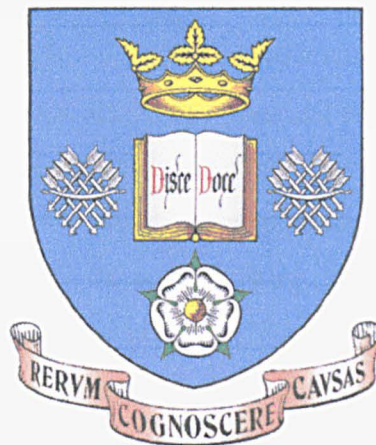


THE UNIVERSITY OF SHEFFIELD



DEPARTMENT OF MECHANICAL ENGINEERING

MODELLING SMART FLUID DEVICES
USING COMPUTATIONAL FLUID DYNAMICS

DARREN JOHN ELLAM

SUBMITTED: November 2003

A thesis submitted to the University of Sheffield as part of the requirements for the
fulfilment of the Degree of Doctor of Philosophy.

ABSTRACT

The apparent slow development and uptake of smart fluid technology has been suggested to be partly due to the inherent non-Newtonian nature of the fluids. To improve matters, it is desirable to determine practical pre-prototype performance. This is possible with a continuum approach and by solving the basic governing equations. Analytical methods are limited to the simplest devices. Therefore, the most practical way forward was hypothesised to be with existing highly developed CFD packages. This thesis investigates the possibility of using CFD to model smart fluid flow.

Initially, the feasibility of modelling basic isothermal, steady, one-dimensional flow was investigated. The procedure was then extended into modelling two-dimensional flow. Here the CFD method was used to investigate some practical problems involving a second perpendicular flow to naturally replace heated fluid. In addition, a smart fluid seal problem was resolved.

The procedure was extended in order to investigate unsteady flow. For a CFD clutch run-up model, problems were identified in an existing analytical solution. To help verify the CFD model, an experimental study was carried out. For the results to agree, an inertial boundary condition has to be developed that allows the inertia of the outer rotor to be included in the CFD model. Here the fluid dynamics affect the rotor dynamics and vice versa.

A constitutive model of a viscoelastic form was found to be most appropriate for modelling sudden changes in excitation. This allowed CFD responses to correspond well with experimental results carried out on an ER fluid Rayleigh step-bearing rig.

The usefulness of CFD for determining the generation and transfer of heat, in addition to temperature distribution, was investigated by comparing CFD results to both experimental and semi-empirical analysis.

In conclusion, CFD as a pre-prototyping tool promises to be very useful. However, it is only as good as the continuum assumption allows it to be. The procedure is also limited by how well the constitutive equation can be determined and by the detail and quality of fluid property data.

ACKNOWLEDGMENTS

Foremost, I need to express my gratitude to my supervisor Mr. Bill Bullough for his expertise and guidance during the course of the project. Secondly, I must thank Professor Ray Atkin from the University's Department of Mathematics for his help with the mathematical aspects of this project, and for all his support and encouragement. I am also extremely grateful to Dr. Roger Stanway for his support and guidance on how to put a thesis together.

Special thanks go to technician Mr. Jim Hodgson in the Mechanical engineering department for machining and assembling all the device parts that I required. Dr. Richard Tozer must be acknowledged for maintaining the high voltage unit used for exciting the ER fluid. I am grateful to Smart Technologies, formally known as ER fluid developments, for allowing me to use their rheometer.

It may come as a surprise that it was only until a year into this project that I discovered my dyslexia disability. I must thank my brother for suggesting that I take a test, and the University's Department of Psychology for their assessment. As a result, I now understand why I struggle with reading and writing. Consequently, I am grateful for the many grammatical corrections made by others to this thesis.

Finally, I must thank my wife Chloe for all her support, and my parents for their encouragement.

TABLE OF CONTENTS

Chapter 1 : Introduction	1
1.1 Smart Machines and Smart Fluids.....	1
1.2 Possible Applications	4
1.3 Computational Methods	6
1.4 Summary: Introduction.....	7
Chapter 2 : Literature Survey	10
2.1 Introduction	10
2.2 Simple Sizing Techniques	10
2.3 Continuum Mechanics.....	11
2.4 Analytical Solutions	14
2.5 Rheometry	17
2.6 Dimensional Analysis for Smart Fluids.....	21
2.7 Numerical Methods (i.e. CFD).....	23
2.8 Summary: Literature Survey.....	25
Chapter 3 : Feasibility Study	29
3.1 Introduction	29
3.2 Computational Fluid Dynamics Package	29
3.3 1D Smart Fluid Flow Examination using the Bingham CFD Model	31
3.4 Smart Fluid Flow Examination in Rayleigh Step Bearing	36
3.5 Non-Uniform Field Distributions	39
3.6 Bayer ER Fluid Test Using a Constant Stress Rheometer.....	42
3.7 Inter-Changeability of Smart Fluid Data and Negative Plastic-Viscosity.....	46
3.8 Summary: Feasibility Study	52
Chapter 4 : 2D Steady State Smart Fluid Flow	78
4.1 Introduction	78
4.2 Analytical Theory: 2D Bingham Plastic Flow between Two Flat Plates.....	79
4.3 CONCENTRIC Clutch with Cooling Through-flow.....	83
4.4 RADIAL Clutch with Cooling Through-flow	87
4.5 Smart Fluid Seals.....	97
4.6 Summary: 2D Steady State Smart Fluid Flow.....	102
Chapter 5 : Smart Fluid Unsteady Flow Response	113
5.1 Introduction	113

5.2	Annular Valve Responsive Study: CFD vs. Analytical Analysis.....	116
5.3	Rayleigh Step Bearing Responsive Study: CFD vs. Experimental	124
5.4	Concentric Clutch Response: Analytical vs. CFD vs. Experimental	135
5.5	Summary: Unsteady Flow	153
Chapter 6 : Heat Transfer in Smart Fluid Devices.....		191
6.1	Introduction	191
6.2	Energy Source Terms	192
6.3	Heat Transfer from a Smart Fluid Radial Plate Clutch Surface	194
6.4	Heat Transfer from a Smart Fluid Concentric Clutch Surface	201
6.5	Comparison of Clutch Designs.....	205
6.6	Summary: Heat Transfer.....	213
Chapter 7 : Conclusion and Further Work		226
7.1	Main Conclusions	226
7.2	Further Work	230
References.....		231
Appendix A : CFD Sub-Routines		235
Appendix B : Publications		238

NOMENCLATURE

<i>a</i>	shear stress in circumferential direction
<i>a_b</i>	acceleration of bob
<i>a_{min}</i>	minimum shear stress for flow to occur
<i>A</i>	area
<i>A_b</i>	constant (for use in constant stress rheometer formulae)
<i>A_d</i>	full area of rotor disc
<i>A_i</i>	radial insulation area
<i>A_s</i>	surface area
<i>b</i>	constant = $(-Gh/2)$
<i>B</i>	output rotor inertial parameter
<i>B_b</i>	constant (for use in constant stress rheometer formulae)
<i>C_b</i>	constant (for use in constant stress rheometer formulae)
<i>C_f</i>	friction coefficient
<i>d_{ij}</i>	local strain rate tensor
<i>D_b</i>	constant (for use in constant stress rheometer formulae)
<i>E</i>	excitation (i.e. for an ER fluid: $E = V/h$)
<i>g</i>	gravitational acceleration
<i>G</i>	1D pressure gradient
<i>G(r)</i>	1D pressure gradient has a function of radius
<i>G_{trans}</i>	pressure gradient on transition from plug to plug-less behaviour
<i>G'</i>	shear modulus
<i>Gr</i>	Grashof Number
<i>h</i>	gap width
<i>h_{plug}</i>	plug width
<i>He</i>	Hedström Number
<i>He_{Re=0}</i>	Hedström Number when $Re = 0$
<i>I</i>	current
<i>I_b</i>	inertia of complete assembly (for use in constant stress rheometer formulae)
<i>I_o</i>	output rotor inertia
<i>j</i>	current density
<i>k_{air}</i>	thermal conductivity of atmospheric air
<i>k_b</i>	bearing term (for use in constant stress rheometer formulae)

k_s	thermal conductivity of casing
L	length
L_c	length of concentric clutch
L_e	electrode length
L_r	length of radial clutch
L_s	surface length
L_x	length in the x -direction
M	mass
M_i	momentum in
M_o	momentum out
n	number of output rotors
N	torque
N_e	torque due to estimated electro-stress effect
N_{eo}	total torque
N_o	torque due to Newtonian nature of fluid
\overline{Nu}	mean Nusselt number
p	pressure
P_{elec}	electrical heating
P_{in}	power in
P_{vis}	viscous heating
\dot{q}_x	flow rate in the x -direction
\dot{q}_z	flow rate in the z -direction
r	radius
r_p	radius of plug boundary
r_1	inner radius
r_2	outer radius
r_i	input radius
r_m	mean radius
r_o	output radius
R	outer plate radius
R_{bi}	ratio between the two viscosity's in the bi-viscous model ($R_{bi} = \mu_s/\mu_e$)
R_c	outer clutch radius on the concentric clutch
R_{cap}	capstan radius
R_r	outer clutch radius on the radial clutch

Re	Reynolds number
Re_y	turbulent Reynolds number
s	constant in the He vs. Re equation
S_b	constant (for use in constant stress rheometer formulae)
t	time
t_d	dynamic response time
t^*	electron hydraulic time constant
t_{min}	minimum possible run-up time dictated by the rotor inertia
t_o	optimum run-up time (no rotor inertia)
t_{ru}	run-up time
t_{rd}	run-down time
T	temperature
T_i	temperature on inner rotor surface (wetted side)
T_s	outer surface temperature
T_m	mean temperature $T_m = T_s/2 + T_\infty/2$
T_o	temperature on outer rotor surface (wetted side)
T_{sh}	temperature of shaft at a known vertical location
T_∞	bulk air temperature
T_{res}	temperature in reservoir
T_p	temperature a pressure tapping
u	velocity in the x -direction
u_o	output speed
u_{inlet}	uniform inlet viscosity
U_{trans}	transitional speed between plug to plug-less flow
U	constant speed of plate
v	in the y -direction
v_b	velocity (for use in constant stress rheometer formulae)
V	voltage
w	velocity in the circumferential direction
y^+	turbulence parameter at wall surface
z	rotor and casing thickness
α	angular acceleration
μ_e	plastic-viscosity
μ_{nn}	non-Newtonian viscosity

μ_o	zero field viscosity (Newtonain)
μ_s	solid viscosity: initial Newtonian viscosity in the bi-viscous model
$\dot{\gamma}$	shear rate
τ	shear-stress
τ_y	yield-stress
τ_{ey}	true yield-stress in bi-viscous model
τ_e	estimated shear-stress due to excitation
τ_o	shear-stress due to the zero field Newtonian viscosity
τ_{ys}	static yield-stress
τ_{ys}	dynamic yield-stress
τ_w	shear stress on wall
ρ	fluid density
ρ_o	operational density
ω	angular velocity
Ω	relative rotational speed
Ω_p	speed at which plugs start to form on outer rotor
\bar{h}	heat transfer coefficient
Δx	cell width
Δt	time-step size
ΔT	temperature difference
ΔA	angular acceleration (for use in constant stress rheometer formulae)
Δp	pressure difference
ΔP_{eo}	total pressure difference
$\Delta \omega$	speed difference across the plug
λ	material property: characteristic relaxation time

CHAPTER 1 :

INTRODUCTION

1.1 Smart Machines and Smart Fluids

In this section, the role that smart fluids¹ can play in the field of smart technology will be outlined. Market potential in the form of existing and possible smart fluid applications is suggested. To further promote commercial development, a computationally based pre-prototyping design methodology is proposed as a sensible way forward.

1.1.1 Smart Machines

The main philosophy behind “smart machines” and “smart structures” involves an inherent capability to flexibly adapt to meet any changes in requirements. Adaptation generally takes place due to a change in the environmental surroundings, e.g. a change of road surface. A smart device in general requires three functions:

- i. Sensors to perceive the environment,
- ii. Intelligence to decide what to do (Central Processing Unit, CPU),
- iii. The ability to change if required, i.e. a change in stiffness, damping, shape, etc.

Sensors and adequate CPUs are already cheaply available. Research is therefore primarily concerned with the third requirement for which “smart materials” and “smart fluids” are available to fulfil this role.

1.1.2 Smart Fluids

In general, a smart fluid operates as a medium between machine parts, and undergoes controllable rheological change through an electrical input.

A paper entitled “The third wave of machines” [1] examines machine history trends and identifies a “dynamic-electronic machine” as the logical follow on to the “dynamic-electromagnetic machine” (i.e. an electric motor). With a smart fluid, these advanced machines are feasible. The machine’s output would be configurable through an electronic signal without any physical adjustment to the machine. Examples include electronically controlled clutches, valves and damping devices.

While the benefits of using a smart fluid are clear, the perceived costs are not. One might expect a smart fluid unit to be more expensive than a conventional mechanical unit. However, the smart fluid unit is likely to be multi-tasking and typically have less

¹ Main examples include Electro-Rheological (ER) and Magneto-Rheological (MR) fluids.

mechanical complexity, thus offering greater reliability and efficiency, and thereby reducing overall costs.

The two main types of smart fluid are Electro-Rheological (ER) and Magneto-Rheological (MR) fluid suspensions. In essence, they both appear to behave as viscoplastic materials with a controllable yield-stress. Alternative forms of smart fluid include any form of configurable fluid such as liquid crystals [2]. Engineers have been waiting to exploit the unique characteristics of ER and MR fluids for almost half a century. It is only recently that adequately developed fluids have become available.

Almost all ER fluids are dispersions of dielectric particles in electrically insulating oil. The dielectric particles are the dispersed phase and the insulating oil is dispersion medium. Under no electric field an ER dispersion behaves like a common dispersion. When an electric field is applied to the ER dispersion, a dielectric mismatch between the suspensions and particles causes the particles to polarise under the influence of an electric field. The polarized particles attract each other due to electrostatic interaction. Consequently, the polarized particles interact and form chain-like or even lattice-like structures, causing the fluid to undergo a significant rheological change. The particle cluster chains cause the resisting power against flow resulting in an ER effect. An ER fluid generally consists of polymer based micron-sized particles and a suitable base fluid may for example be silicone oil, although there is wide of appropriate mixes. An ER fluid is known to react rapidly with response times of the order of 1-2 ms.

The ER phenomenon was first discovered and investigated in depth by Willis Winslow who was granted the first ER fluid patent in 1947 [3]. To date, it is fair to say that no large-scale commercial application of ER fluids has been forthcoming. However, Bridgestone in Japan, Fludicon¹ in Germany and ERFD in England have all developed commercial ER fluids.

While Winslow was investigating the ER effect, Jacob Rabinow discovered the MR effect [4]. He applied for the first MR patent in 1947 [5]. The MR fluid is a suspension consisting of soft, magnetisable particles and is excited through a magnetic field. Unlike its ER counterpart, there have been some recent successful MR applications.

The constitutive equations for ER and MR fluids appears to be similar. Under zero excitation, ER and MR fluids display Newtonian behaviour. With increased excitation,

¹ This is the correct spelling.

both fluids exhibit a roughly proportional increase in yield-stress (τ_y). This behaviour approximately fits a Bingham plastic model (Fig. 1.1). Table 1.1 compares the key characteristics of ER and MR fluids.

		ER fluid	MR fluid
yield strength	kPa	2 to 8	50 to 100
viscosity no field	mPa.s	100 to 200	200 to 300
temperature range	°C	10 to 130	-40 to 150
current/flux density	mA/cm ²	2 to 30 (depends on temperature)	can be energised using permanent magnets
fluid density	kg/m ³	1000 to 2000	3000 - 4000
response time	ms	1-2	10-20

Table 1.1: Comparable properties of ER and MR fluids.

As indicated in Table 1.1, the superior yield-stress magnitude of the MR fluid continues to make it the preferred choice. However, a faster response and simpler mode of application keeps the ER fluid in contention for the immediate future. In addition, there are rumours of very high strength ER fluids being developed. Perhaps the most significant point here is not the absolute strength of new fluids, but the possibility of being able to use a lower voltage source to produce a reasonable yield-stress.

1.1.3 Market Potential for Smart Fluids

The yield strength developed by a smart fluid is a good indication of its usefulness. Some complain that ER yield strengths are lower than initially promised¹, but in time they should inevitably improve. Before this is likely to happen, some successful commercial applications are required. Up until now this catalyst for ER fluid development has not been forthcoming.

Now that commercial applications are being pursued, smart fluid performance should continue to improve, thus helping to increase market demand. Pessimistic attitudes towards smart fluids that continue to hold back progress should change when revenue starts to flow. It appears to be a good time to enter this market now that long running problems are finally beginning to be overcome. Such problems include developing economically viable commercial fluids that possess high enough yield stresses. Other factors include being able to characterise the fluid data so that it can be useful at the design stage.

With a phenomenon involving electronically controllable resistance to flow, it

¹ There are many compromises to be reached when making an ER fluid.

takes little imagination to foresee the potential uses. It is, however, only of late that some small-scale commercial applications have materialised that are all mainly MR-based. These mechanisms have generally been developed to solve tasks difficult to achieve by other means and therefore justifying the cost. Commercial applications include a unique MR fluid lens grinding method [6] [7], active damping systems [8] applied to seat suspension systems, and prosthetic limbs, active suspension systems [9] being used in a luxury car and some race cars, also MR brakes are being used in aerobic exercise machines [8].

A significant reason for the slow progress in bringing a smart fluid device to the market place is the non-Newtonian nature of fluids. In the early days, smart fluids were often thought to behave as Newtonian fluids above the yield-stress [10]. This simplistic approach leads to a lack of appropriate universal methods of characterisation. Ignoring the non-Newtonian nature of smart fluids results in a situation where it is difficult to compare fluid data and predict device performance. For pre-prototyping purposes, the ability to predict practical device performance is highly desirable when developing a complex product.

1.2 Possible Applications

The basic modes of possible operation for a smart fluid are illustrated in Fig. 1.2, all of which employ narrow gap geometry. This basic, electrically configurable, shear force phenomenon has interested engineers for decades and recently some successful commercial applications have materialised.

1.2.1 Smart Fluid Clutch & Brake Systems

Here the shear mode of operation is utilised. Key benefits include:

- i. Electrically controlled transmission.
- ii. No laterally moving mechanical parts, resulting in increased efficiency and reliability.
- iii. Fast speed of response and controlled take up of power.

The main disadvantage involves viscous heating. In a small-scale device, thermal equilibrium may not be sustainable. For larger scale industrial machines, additional cooling may be necessary. In addition, whilst the clutch is engaged, an electrical power input is applied that must be dissipated. Possible uses of such a device are now considered.

Used as a braking system, the speed of the load can be electrically reduced. Although viscous heating effects will occur, all braking systems suffer from heating,

and this system may offer improvements over current braking systems. Although for the same voltage when the temperature increases, so does the current, and so an increase in power input is required.

As a transmission system, linking an input (engine) to an output (load) significant viscous heating will only occur during engagements. Once the clutch is locked at a steady speed, the yield-stress can be reduced whilst retaining engagement. Being able to smoothly engage will reduce stresses that could result in lower specifications of machine parts, thereby giving a reduction of weight and costs.

Operating as a gearbox, the device is allowed to slip, thereby regulating the amount of torque transmitted to the output. The system would be responsive and hardwearing. Inefficiency resulting from viscous heating might be acceptable for applications lacking alternative methods. One suitable application could be simulating the rapid changes in torque on a Formula One racing engine for testing purposes.

Promising smart clutch systems include fast-acting actuators. A high inertia input would serve as an energy source ready to be tapped into at a moments notice¹. If the output is to be stopped with speed and precision, or reversed to create reciprocal motion, a second clutch is required [11]. It has been suggested that such devices are well suited for robotic systems [12]. The need for a second clutch is highlighted in eqn(1.1), which shows the ratio between run-up (t_{ru}) and run-down (t_{rd}) times for a single clutch device when the acceleration (α) is assumed linear. The ratio between the two is essentially the torque when excited ($N = N_e + N_o$) to that when un-excited ($N = N_o$).

$$N = I_o \alpha \Rightarrow \frac{t_{rd}}{t_{ru}} = \frac{N_e + N_o}{N_o} \approx \frac{N_e}{N_o} \quad \text{here } (N_e \gg N_o). \quad (1.1)$$

To significantly reduce costs and device size it would be advantageous to design a reciprocal device using only one clutch. It may be possible to achieve such a device using a planet gear system. Fig. 1.3 shows one example of my attempt to design such a device.

Basic analytical models are possible for predicting basic steady state isothermal behaviour of these devices [13]. It would however seem that solving more geometrically complex models involving heat transfer and unsteady flow will necessitate the use of computational methods.

¹ The system can be likened to stepping onto an escalator rather than waiting for an elevator.

1.2.2 Smart Fluid Valves and Dampers

A smart fluid valve suffers from being an open system device, requiring a relatively large amount of smart fluid that is expensive. Such devices have been investigated in some depth [14, 15]. On a small scale, they have been used as part of a damping system and developed into high frequency actuators adequate for use in loud speakers [16]. Under steady isothermal flow, the valve has been successfully modelled [14]. To model a whole damping system in an unsteady state, computational methods are essential.

There are several ways to go about building a smart damper. A simple narrow channel device would be a good starting point. Current commercial products are MR-based. This is due to the main manufacturer (Lord Corporation) preferring to focus their research into MR fluids. It is possible to model smart dampers analytically [17]. However, it would be advantageous to include heating effects and again this seems only feasible using computational methods.

1.2.3 Other Applications

The most obvious smart fluid systems prefer relatively high yield strengths. Perhaps, however, the best applications will be those that come about from less obvious applications that make do with low yield strengths. Such applications may possibly be found in the field of macro-sized engineering where required fluid volumes and yield strengths should be very small. On a similar basis, Smart Fluid Technologies are developing a brail computer display for the blind using a weak ER fluid.

1.3 Computational Methods

With a continuum fluid approach, direct analytical solutions will be limited and solution of complex practical problems will require numerical methods. Commercial computational fluid dynamic (CFD) software can be used for such purposes with specifically written programs for viscoplastic materials.

The CFD method involves solving numerically the full set of governing equations by a semi-iterative method. This is achieved by splitting the fluid domain into a finite number of cells. A nodal point represents a small element of fluid and stores the flow parameters for that particular control volume. During the iterative process, neighbouring nodes interact with one another. When this interaction reaches a steady state, the flow field is said to have converged.

Several CFD solvers have been developed. Some codes fare better than others on different types of flow problem. Different solvers may use different numerical techniques but the basic principle is the same. That is, they solve the exact governing

equations by discretising the flow. For a smart fluid there is likely to be a limit to how representative a homogenous continuum can ultimately be. Nevertheless, a CFD approach should be able to correct for some basic non-continuum behaviour.

1.4 Summary: Introduction

After over half a century since the discovery of ER and MR phenomena, smart fluid applications are now finally being developed. The potential for creating new and exciting applications is enormous. A significant problem is the inherent difficulty in designing suitable fluids. In addition, a lack of appropriate universal fluid characterisation makes predicting pre-prototype device performance even more difficult.

The need for a standardised approach to characterising smart fluid behaviour has been identified. Standardised data could then be used as part of a CFD based pre-prototyping methodology for predicting basic device performance. This tool would improve the commercial utilisation of smart fluid technology.

1.4.1 Project Aims and Objectives

The initial objective was to review current approaches in order to identify suitable fluid characterisation and modelling methods. With reference to analytical models and reliable experimental results, the feasibility of modelling smart fluids using CFD based techniques was then investigated. After solving steady state problems, the method was extended into unsteady and non-isothermal regimes.

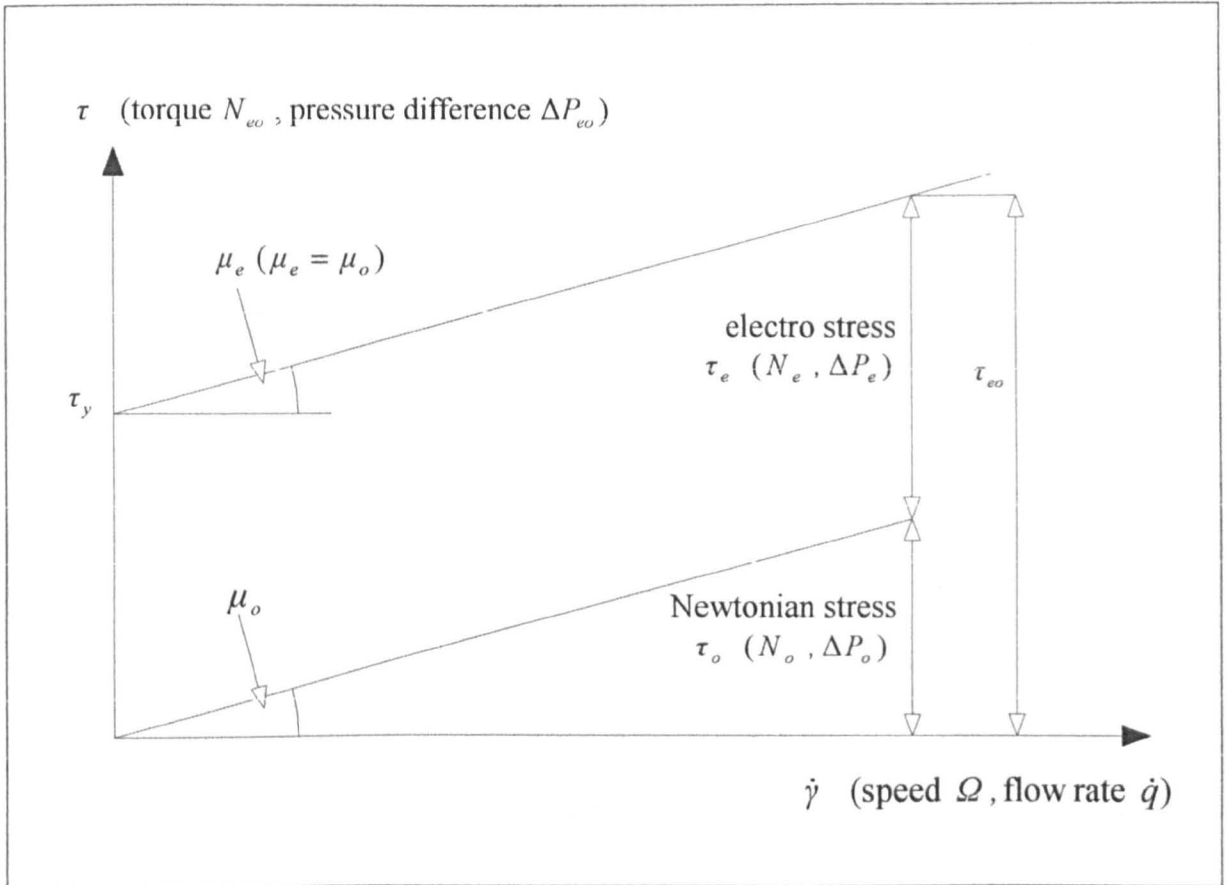


Fig. 1.1: Ideal Bingham plastic flow curve for ER and MR fluids.

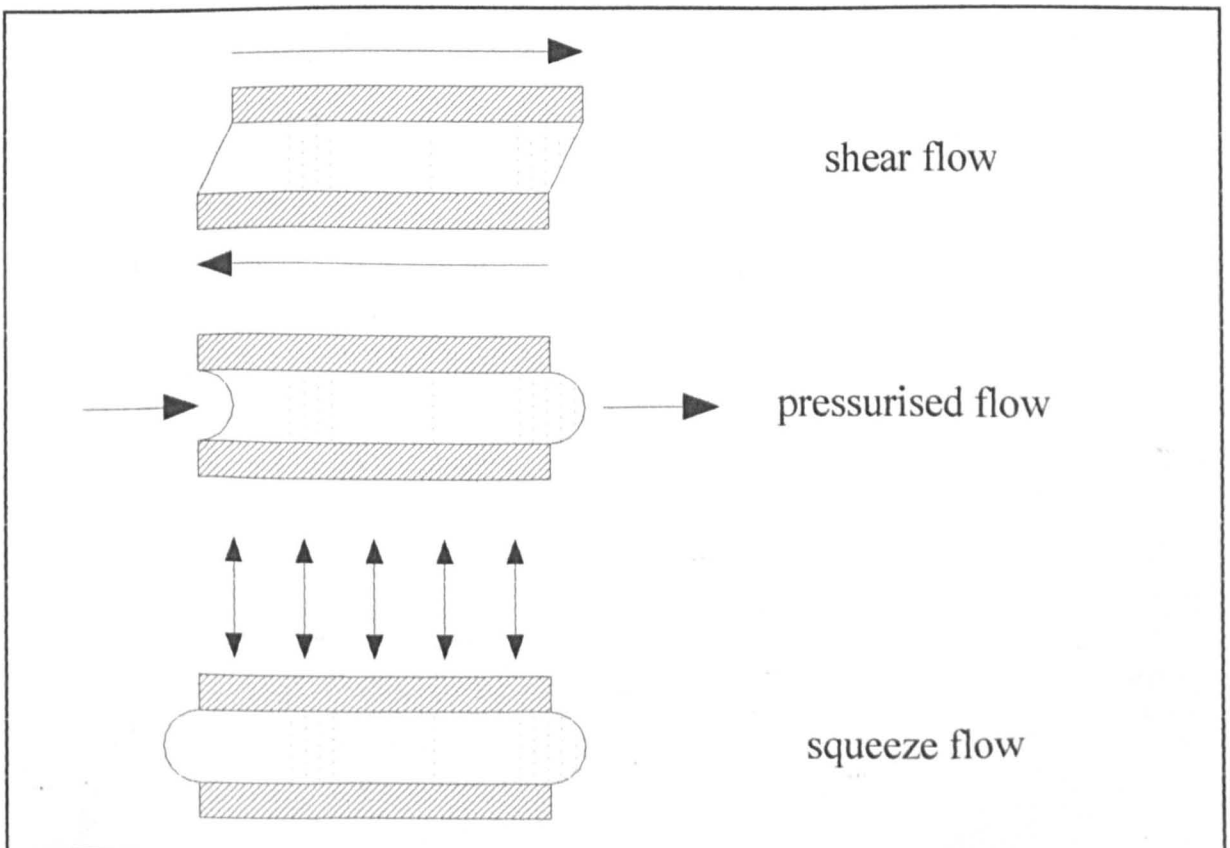


Fig. 1.2: Basic modes of application for smart fluids.

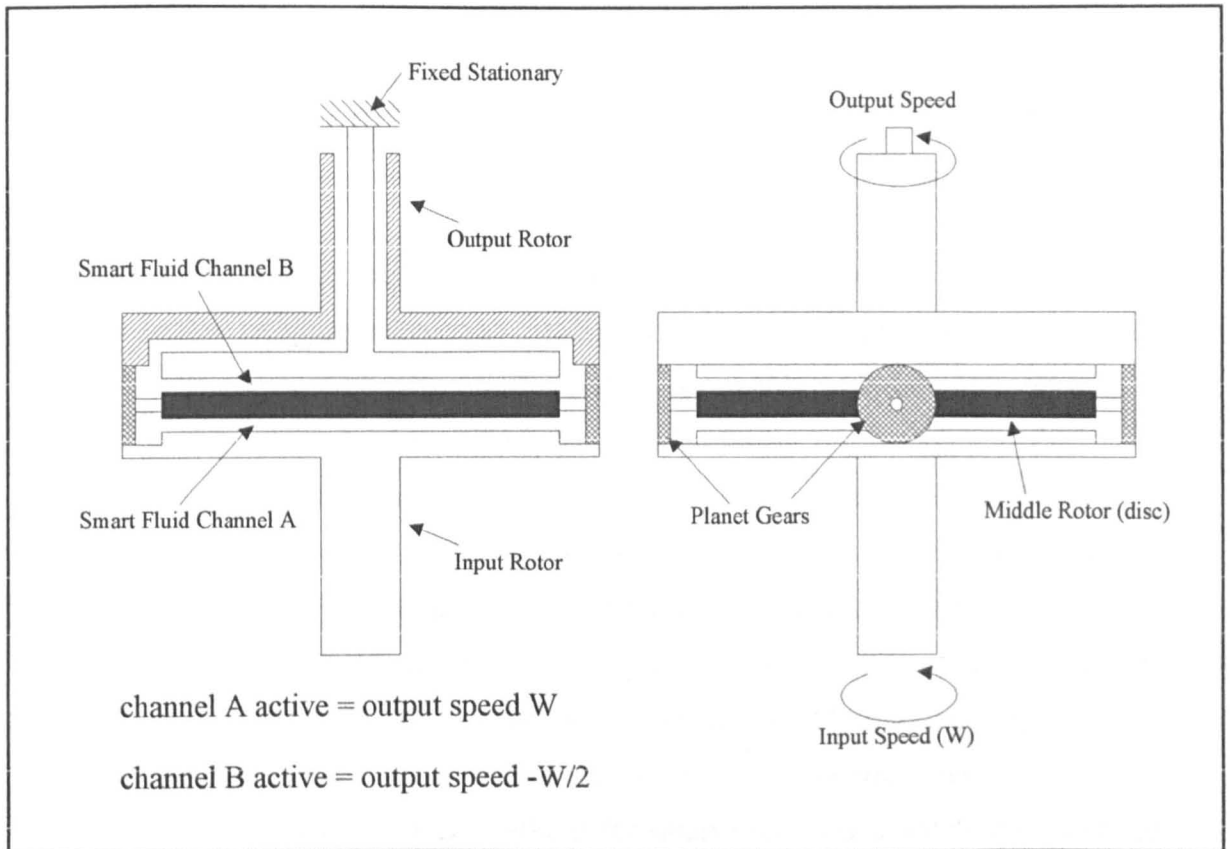


Fig. 1.3: An example of a single reciprocal clutch device using a planet gear system.

CHAPTER 2 :

LITERATURE SURVEY

2.1 Introduction

The previous chapter identified a requirement for improved modelling and characterisation techniques for smart fluids. Difficulties in pre-prototyping inhibit the successful development of commercial products. A possible practical CFD approach to pre-prototyping a smart fluid device was therefore proposed.

Understanding the mechanics of a smart fluid would allow the output characteristics of a smart fluid device to be predicted. A practical pre-prototyping tool for estimating device performance would aid the development of smart fluid products. In addition, the ability to test the feasibility of proposed concepts would speedily aid the assessment of tentative designs. The economic benefits would be further improved if a small-sample rheometer test were sufficient to acquire the fluid properties.

This chapter reviews current methods for smart fluid flow quantification with the aim of identifying improved approaches. Simple but effective sizing techniques are first investigated. More sophisticated approaches are then reviewed in which viscoplastic models are used to gain solutions of the governing equations of motion. A dimensional analysis approach is explained. Rheology is studied in relation to determining smart fluid properties. Finally, the potential of using CFD in this field of study is investigated. The work presented here is an extension of work published in [18].

2.2 Simple Sizing Techniques

Basic performance estimation can be achieved by studying the output characteristics of simple smart fluid devices (Fig. 2.1). After converting the data into a flow curve, $\{\tau \text{ vs. } \dot{\gamma}\}$ the fluid is then approximated as a Bingham plastic with a plastic-viscosity equal to the zero-field value (μ_0), as illustrated in Fig. 1.1. The yield-stress (τ_y) is taken to be equal to the electro-stress (τ_e), which is calculated as the total shear-stress effect (τ_{eo}) minus the Newtonian effect (τ_o) [19] [20]:

$$\tau_y = \tau_e = \tau_{eo} - \tau_o \quad \& \quad \mu_e = \mu_0 \quad \text{where} \quad \tau_o = \mu_o \dot{\gamma} \quad (2.1)$$

The gap size (h) is found to have no significant effect on the fluid properties obtained [14] [21] [22]. This indicates that the fluid can be treated as continuum due to the large gap-size/particle ratio. An expression is now needed to relate τ_y to an excitation (E). For an ER fluid one of the following expressions may be used [23]:

$$\tau_y = \alpha E^2 \quad \text{or} \quad \tau_y = \alpha(E - E_o) \quad \text{or} \quad \tau_y = \alpha(E - E_o)^2 + \beta(E - E_o), \quad (2.2)$$

where α , β and E_o are properties of the fluid material. The appropriate relation will depend on the particular fluid. Adopting this approach will allow design formulae to be derived, thus allowing calculations for a device in which the flow is steady, isothermal and laminar.

Example One: Concentric Clutch

A torque (N) is required to maintain a relative speed difference (Ω). Previous clutch data is used to determine τ_e , allowing $\tau_y = f(E)$ to be established. The overall torque for different clutch configurations is then predicted using:

$$N_{eo} = 2\pi L r^2 (\tau_e + \tau_o) \quad \text{with} \quad \tau_o = \mu_o \frac{r\Omega}{h} \quad \text{and} \quad \tau_e = \frac{N_e}{2\pi r^2 L}. \quad (2.3)$$

Example Two: Annular Valve (Poiseuille Flow Mode)

The total pressure difference (ΔP_{eo}) over a length (L) gives rise to a flow rate (\dot{q}). A balance of the forces allows $\tau_y = f(E)$ to be determined:

$$2\pi r h \Delta P = 2\tau 2\pi r L \Rightarrow \tau_y = \tau_e = \frac{h}{2L} (\Delta P_{eo} - \Delta P_o) \quad \text{where} \quad \Delta P_o = \frac{6\mu_o L \dot{q}}{\pi r h^3}. \quad (2.4)$$

For different valve configurations, ΔP_{eo} is now predicted using:

$$\Delta P_{eo} = \Delta P_o + \Delta P_e \quad \text{with} \quad \Delta P_e = \frac{2L\tau_e}{h}. \quad (2.5)$$

The assumption that the total stress is a simple summation of both the electro and Newtonian stresses results in the linear characteristics (N_{eo} vs. Ω) and (ΔP_{eo} vs. \dot{q}), as shown in Fig. 1.1. The simplicity of the technique enables a fast but very crude estimation of the basic steady state performance. For the valve, it can clearly be seen from eqn(2.5) that high ratios of L/h are desirable, as this gives large pressure differences. An assumption is made that at any excitation, μ_e remains the same. This may not be true, and μ_e can have significant effects on solutions when $\dot{\gamma}$ is large. In addition, τ_y is approximated equal to τ_e which presumes $\mu_e = \mu_o$.

2.3 Continuum Mechanics

To accurately model the flow of a smart fluid using continuum mechanics, it is important to understand the fluid's rheology. Although smart fluids are mainly suspensions, in the non-excited state they display Newtonian behaviour over a wide

range of flow conditions and geometry. Hence, the particles within the dispersant are not introducing any severe non-Newtonian behaviour. This is likely to be due to the particles being micron-sized as opposed to macro-sized.

On a microscopic scale, the micron-sized particles are visible. In the immediate future, there is little prospect for deriving applicable fluid behaviour laws for difficult geometries from micro-structural considerations. However, on the macroscopic scale the particles are no longer visible, allowing the smart fluid to be considered as a homogenous continuum. The behaviour can then be described in terms of continuum properties such as velocity, pressure, density and temperature, as well as space and time derivatives.

2.3.1 Governing Equations and Non-Newtonian Viscosity

The differential governing equations for isothermal flow, of a liquid continuum, upon which any useful mathematical pre-prototyping tool would be built upon, can be written in Cartesian tensor notation as:

$$\begin{array}{c} \text{rate of gain} \\ \text{of density} \\ \frac{\partial \rho}{\partial t} \end{array} + \begin{array}{c} \text{mass} \\ \text{flux} \\ \frac{\partial}{\partial x_i} (\rho u_i) \end{array} = 0 \quad (2.6)$$

$$\begin{array}{c} \text{rate of} \\ \text{change of} \\ \text{momentum} \\ \frac{\partial}{\partial t} (\rho u_j) \end{array} + \begin{array}{c} \text{momentum} \\ \text{flux} \\ \frac{\partial}{\partial x_i} (\rho u_j u_i) \end{array} = \begin{array}{c} \text{term due to} \\ \text{static pressure} \\ -\frac{\partial p}{\partial x_j} \end{array} + \begin{array}{c} \text{term due} \\ \text{to deformation} \\ \text{stresses} \\ \frac{\partial \tau_{ij}}{\partial x_i} \end{array} + \begin{array}{c} \text{body} \\ \text{forces} \\ \rho g_j + F_j \end{array} \quad (2.7)$$

If the above differential equations are to be solved, a rheological expression is required to represent the ‘stress tensor’ (τ_{ij}). For this expression, a constitutive equation can be written in a generalised form [24], in which d_{ij} is the ‘local strain rate tensor’:

$$\tau_{ij} = \mu_{nm} e_{ij} \quad \text{in which} \quad \mu_{nm} = f(\dot{\gamma}) \quad \text{where} \quad d_{ij} = \left(\frac{\partial u_i}{\partial x_j} + \frac{\partial u_j}{\partial x_i} \right) \quad (2.8)$$

Here the stress tensor is being expressed as a function of the local shear-rate ($\dot{\gamma}$). The term μ_{nm} is the ‘non-Newtonian viscosity’¹ also referred to as the ‘apparent’ or ‘effective’ viscosity. To obtain the function μ_{nm} is the main task in the field of rheology, and usually involves curve-fitting exercises. When μ_{nm} is a constant, the partial

¹ Non-Newtonian viscosity is a term used in some CFD manuals and is a good description.

differential equations (2.6) & (2.7) are the well-known Navier-Stokes equations for flow.

For 2D and 3D flows, it is possible for the resultant magnitude of shear-stress to be greater than τ_y , whilst the individual components have magnitude less than τ_y [25]. The resultant magnitudes of τ_{ij} and d_{ij} are given as:

$$\tau = \sqrt{\frac{1}{2} \tau_{ij} \tau_{ij}}, \quad \dot{\gamma} = \sqrt{\frac{1}{2} d_{ij} d_{ij}}, \quad (2.9)$$

$$\text{and then } \mu_m = \tau / \dot{\gamma}, \quad (2.10)$$

is the corresponding non-Newtonian viscosity at each discrete point. The Bingham plastic equation, being the simplest viscoplastic constitutive model, is often used to characterise MR and ER fluids. Accurate representation of experimental data [14] supports the use of this model. For simplicity, the plastic-viscosity (μ_e) is often taken to be equal to the zero-field (μ_0) value (Fig. 1.1):

$$\tau = \tau_y + \mu_e \dot{\gamma},$$

$$\text{hence, } \mu_m = \mu_e + \frac{\tau_y}{\dot{\gamma}}, \quad \tau > \tau_y \quad (2.11)$$

$$d_{ij} = 0, \quad \tau < \tau_y.$$

The Bingham plastic equation is a two-parameter model and variations are possible. One may suit a particular smart fluid better than another (see [24]):

$$\text{Casson: } \sqrt{\tau} = \sqrt{\tau_y} + \sqrt{\mu_e} \sqrt{\dot{\gamma}}, \quad \text{i.e. 2 parameters,}$$

$$\text{Herschel-Bulkley: } \tau = \tau_y + m |\dot{\gamma}|^{n-1} \dot{\gamma}, \quad \text{i.e. 3 parameters,} \quad (2.12)$$

$$\text{Shulman: } \tau = \left[\tau_y^{1/m} + (\mu_e \dot{\gamma})^{1/n} \right]^m \quad \text{i.e. 4 parameters.}$$

Many assumptions are necessary in order to obtain a solution. It is therefore suggested that the use of any model other than the Bingham plastic equation is futile, in an attempt to gain a more accurate solution. A good review of viscoplastic constitutive equations can be found in [24]. In complex confined geometries, great care is required to ensure that assumptions leading to the Bingham plastic model are not violated [26].

2.3.2 Bi-viscous Constitutive Equation

For the Bingham model, μ_m approaches infinity as $\dot{\gamma} \rightarrow 0$ {eqn(2.11)}. This may cause

a problem for a CFD package. An alternative approach is to use a shear-rate limit ($\dot{\gamma}_y$, corresponding to τ_y), above which the fluid behaves as a Bingham plastic. Below this limit, the material behaves as a Newtonian fluid that is so heavily viscous that it can be thought to resemble a solid. This model also makes practical sense. The un-yielded region is being treated like a heavily viscous fluid, as opposed to a relatively weak solid material. This model is called the bi-viscous model and is expressed in Fig. 2.2 and as follows:

$$\begin{aligned} \tau &= \tau_y + \mu_e \dot{\gamma} & , & \quad \tau > \tau_{ey} \\ \tau &= \mu_s \dot{\gamma} & , & \quad \tau < \tau_{ey} \end{aligned} \quad (2.13)$$

$$\text{with } R_{bi} = \mu_s / \mu_e. \quad (2.14)$$

where R_{bi} is a ratio between the two viscosities. For ER plate squeeze film dampers practical flow solutions are obtained by setting $R_{bi} = 10^4$ [17].

2.4 Analytical Solutions

To derive a solution, the governing equations need to be simplified further. For example, incompressible and laminar flow can be assumed. Further simplifications are usually made by considering the flow to be one dimensional (1D) and time-independent. Steady state acceleration terms are usually assumed negligible, placing a limit on the magnitude of the velocity variables. With these assumptions, eqn(2.6) & eqn(2.7) reduce to:

$$\frac{\partial u}{\partial x} = 0 \quad \text{and} \quad \frac{\partial p}{\partial x} = \frac{\partial \tau_{xy}}{\partial y} . \quad (2.15)$$

Equation(2.15) can then be integrated to obtain τ_{xy} , which then equals the Bingham plastic equation:

$$\tau_{xy} = \frac{\partial p}{\partial x} y + C \quad , \quad \tau_{xy} = \tau_y + \mu_o \frac{\partial u}{\partial y} . \quad (2.16)$$

Plug Flow

In some sections of the flow, $\tau < \tau_y$ can result in areas of fluid flowing as a solid body. This phenomenon is known as plug flow. By assuming no-slip boundary conditions and applying the appropriate conditions on the boundary of plug sections ($\tau = \pm \tau_y$), the constant (C), the plug regions and the velocity profiles can be obtained. It is then a simple matter to determine the overall flow-rates and/or forces. One-dimensional, ideal

Bingham plastic flow has been extensively dealt with in the literature for a variety of simple geometries [24].

2.4.1 Example One: 1D Annular Valve Solution

The flow in an annular valve caused by a pressure difference ΔP_{eo} , can be modelled as 1D Poiseuille flow between two plates if gap size (h) is much smaller than the mean radius (r_m).

Equation (2.15) indicated that the shear-stress varies within h , thus allowing the presence of a central plug region with size dependent on the pressure gradient $G (= \Delta P_{eo}/L)$. A full analysis [24] gives the Buckingham equation for flow rate expressed as,

$$\dot{q} = \frac{\pi r \Delta P_{eo} h^3}{6 \mu_e L} \left[4 \left(\frac{L}{h \Delta P_{eo}} \right)^3 \tau_y^3 - 3 \left(\frac{L}{h \Delta P_{eo}} \right) \tau_y - 1.0 \right], \quad (2.17)$$

in which the limiting pressure gradient before which flow can occur is:

$$\frac{\Delta P_{eo}}{L} > \frac{2 \tau_y}{h}. \quad (2.18)$$

Fig. 2.3 shows how eqn(2.17) compares to the more simplistic approach described in section 2.2, when representing real experimental data for an ER valve [14]. The flat plate assumption is found to be acceptably valid when the gap size is much smaller than the mean radius [23] [27].

2.4.2 Example Two: Concentric Cylinder Clutch

Here a clutch consists of two annular rotors with wetted surfaces (r_i and r_o), separated by a distance of h . The movement of one rotor relative to the other causes 1D Couette flow. In a practical device, $h \ll r_m$, allowing the possibility of modelling the clutch as if there is flow between two flat plates.

Flat Plate Bingham Plastic Solution

$$\frac{\partial \tau}{\partial y} = 0 \Rightarrow \tau = \text{constant} = \tau_y + \mu_e \dot{\gamma} \Rightarrow N = 2\pi L r^2 \left(\tau_y + \mu_e \frac{r\Omega}{h} \right). \quad (2.19)$$

A constant shear-stress across the gap prevents plug flow. A torque (N) equals the amount required to overcome the yield-stress, plus a Newtonian contribution. This is effectively the same solution as that described in section 2.2.

Cylindrical Geometry Bingham Plastic Solution

When considering flow between concentric cylinders, a radial distribution of shear-stress arises. Stress is lower on the outer rotor, allowing the possibility for a plug to form when τ on the outer rotor is less than τ_y . Within the yielded region r_i to r_p :

$$\tau(r) = N/2\pi Lr^2 = \tau_y + \mu_e r \frac{\partial \omega}{\partial r}. \quad (2.20)$$

The radius r_p at which the plug forms can be derived from eqn(2.20):

$$r_p = \sqrt{\frac{N}{2\pi L\tau_y}}. \quad (2.21)$$

Any plug thickness therefore diminishes as the torque is increased, and a higher value of τ_y makes plug behaviour more likely. Integration of eqn(2.20) gives a velocity profile valid between r_i and r_p [13]. When the boundary conditions, $u(r_i) = 0$ m/s and $u(r_p) = r_p\Omega$, are applied the following is given:

$$\Omega = \frac{N}{4\pi\mu_e L} \left(\frac{1}{r_i^2} - \frac{1}{r_p^2} \right) - \frac{\tau_y}{\mu_e} \ln \frac{r_p}{r_i}. \quad (2.22)$$

Obtaining N vs. Ω involves solving eqn(2.21) & eqn(2.22). For flow completely within the gap ($r_p = r_o$):

$$\Omega = \frac{N}{4\pi\mu_e L} \left(\frac{1}{r_o^2} - \frac{1}{r_i^2} \right) - \frac{\tau_y}{\mu_e} \ln \frac{r_o}{r_i}. \quad (2.23)$$

The presence of the plug results in a non-linear torque-speed relationship at low speeds as shown in Fig. 2.4. When the fluid is on the point of being plug-free, $r_p = r_o$. Substituting this into eqn(2.23) gives the plug speed limit:

$$\Omega_p = \frac{\tau_y}{\mu_s} \left(\frac{r_i^2}{2r_o^2} - \frac{1}{2} - \ln \frac{r_o}{r_i} \right). \quad (2.24)$$

As shown in Fig. 2.4 the presence of a plug gives a non-linear torque-speed relationship at low speeds.

2.4.3 Radial Distributions in Excitation

When allowing a radial distribution of E , the choice of model to relate yield-stress {i.e. eqn(2.2)} is found to have significant effects on the resulting flow profiles; some allow plugs to be present under certain conditions, while others do not. Until the specific relationship is known, it is probably safe to assume that when the gap size is

much smaller than the mean radius, there is a near uniform field strength across the gap [23] [27]. This approach leads to a good representation of experimental data and must therefore represent a reasonable assumption. Note that for MR fluids, the field strength can be complex and often has a non-linear distribution and thus specific solutions may be called for.

2.4.4 Limitations of Analytical Theory

For a hydrodynamic step bearing, one-dimensional governing equations for 1D combined Poiseuille and Couette flow between flat plates can be derived. The solution indicates under which speed and pressure conditions plug flow will occur [28]. However analytical equations relating wall speed to flow rate and pressure drop have so far only been achieved for the condition of zero net flow rate. It can be concluded that even for a relatively simple case there is a limit to what can be achieved analytically.

Approximate 2D Bingham plastic solutions are obtainable for various other devices such as a concentric clutch with cooling flow [29]. The solution requires the gap size to be very small, and for steady state acceleration terms to be neglected. In an engineering context, assumptions of these kinds could be impractical.

2.5 Rheometry

Rheology is the study of the deformation and flow of matter. As indicated in section 2.3.1, a pre-prototyping mathematical tool requires some continuum fluid properties to determine the stresses. More specifically the following function needs to be established:

$$\mu_m = f(\dot{\gamma}, T, E, t). \quad (2.25)$$

It is anticipated that an adequate formulation would be similar to the Bingham plastic model. This is, however, neither necessary nor important. The essential requirement is only to obtain eqn(2.25). Rheometry will now be reviewed in some detail in relation to establishing smart fluid characteristics.

2.5.1 Characterisation

In general, a smart fluid is a viscoplastic material with a yield-stress dependent on excitation. The viscosity (μ_m) is a continuum property arising from a molecular network of binding forces that resist flow. Viscosity can be a function of six variables: chemical nature, temperature, pressure, shear-rate, time and excitation. The chemical nature of a batch of fluid is fixed and pressure should have negligible effects in all but the extreme cases. This leaves the four variables of concern as indicated in eqn(2.25).

A smart fluid is usually a suspension and therefore classed as a “particulate system”. According to the Warren Spring Laboratory [30], under steady shear granulo-viscous behaviour should be expected and under dynamic shear some thixotropic behaviour might also be expected. On a positive note, normal forces and viscoelastic behaviour are more associated with polymeric systems. In addition, since the particles in the suspension are so small, thixotropic behaviour may not be significant.

Some smart fluids may exhibit some form of thixotropic behaviour. That is, they will show time-dependent properties. Over time, given suitable conditions, the structure might build up either at rest or under excitation. The potential for significant thixotropic behaviour is somewhat daunting, for the subject is a very complex one. It was decided to proceed with caution and expect minimal thixotropic properties, whilst bearing in mind that in time this assumption might have to be revised. If necessary, time characteristics can be measured [13], but these measurements can only really be made of use within CFD modelling. When a smart fluid device is allowed to lock (i.e. with the fluid at zero relative velocity), hysteresis effects are likely to be encountered [22]. This phenomenon is explainable and does not constitute a true fluid/time property. This is a source of common confusion.

Characteristic Time Factor λ

A high Deborah number (λ/t) defines solid behaviour. If an event happens quickly enough, solid behaviour will be displayed. At low shear-rates, the elastic nature can usually be neglected. However, at high shear-rates it cannot. This is in principle why rheometers work in the low shear-rate range. With very rapid changes in stress due to changes in excitation, solid-like behaviour might be expected, for which viscoelastic formulations may be required.

Yield-stress

For a smart fluid, the yield-stress is generally recognised as the most important fluid parameter, for it indicates its potential usefulness. The recognised definition of yield-stress is the value of stress required for flow to occur. Fig. 2.5 illustrates the difference between static yield-stress (τ_{ys}) and dynamic yield-stress (τ_{yd}). The latter is seen to be an apparent yield-stress rather than the true yield-stress. Instead of cutting the τ -axis at an angle, the flow curve can continue to dip with decreasing strain-rate. Some rheologists even question the existence of a yield-stress in a fluid. Nevertheless, τ_{yd} still proves a useful parameter. For an ideal viscoplastic material (Bingham plastic) $\tau_{ys} = \tau_{yd}$.

In practice, above a certain strain-rate most viscoplastic fluids behave approximately as a Bingham plastic.

To obtain the real behaviour at low shear-rates, sophisticated equipment is required. This may eventually constitute an essential area of study. However, for the time being such considerations are not essential. What is required initially is a sufficiently accurate flow curve to allow eqn(2.25) to be inferred. This relation will possibly contain a parameter representing yield-stress, but is not a necessity of the technique being employed.

Other Important Considerations

End effect and edge errors are a consequence of device geometry not corresponding exactly to the theoretical formulation, and must be considered in some situations. Wall slip can occur when the mixture separates into two phases at the shearing surface and will affect rheometer results. Such behaviour is not expected to be of much importance for single-phase fluids with a small particle size [30].

At high speeds, phase separation could occur, and this possibly implies that a low shear-rate device should be used. For relatively low values of τ_y at high $\dot{\gamma}$, $\mu_m \rightarrow \mu_e$ (i.e. the viscosity equals that of the base fluid). This further suggests that the low shear-rate data is of the greater importance. In addition, cavitations may occur at high speeds.

During measurement, the fluid should be homogeneous and any excitation should be uniform. These considerations rule out cone-on-plate rheometer types for ER fluids.

2.5.2 Types of Rheometer

There are a large number of viscometer and rheometer designs on the market. Prices range from a few thousand pounds to over half a million pounds and each design will have its own set of features reflected in the price. Ideally, the correct one to use should not be dictated by financial considerations, but dependent on criteria such as:

- is it important to measure normal stresses and/or complex dynamic moduli?
- the required temperature range,
- the nature of the fluid and the required accuracy,
- are shear creep and recoil functions and/or stress relaxation considerations?

The four main types of rheometer are; parallel plate, flow in an annular gap, pipes/capillaries and parallel disc/cone. To cover a required range of $\dot{\gamma}$, two different types may even need to be used. The particular nature of the fluid to be tested is a very important consideration.

Coaxial Cylindrical Rheometer

These are widely used due to their relative cheapness and ease of operation. The fluid is contained in an annular gap and the governing equations are as given in section 2.4.2. If the data does not agree with the perceived formulae then explicit formulae can be utilised [30]. Controlled stress viscometers that measure the shear-rate as opposed to the traditional controlled shear-rate designs are becoming more common.

ER Fluid Developments (ERFD) was a company based in the UK which specialised in ER fluid-based technology. They designed and developed a specific constant stress rheometer for the USA army [31]. The device allowed yield-stress, plastic-viscosity and current density to be obtained. Measurement of yield-stress is absolute and dependent upon the geometry and applied stress. Data acquisition is to within one second to minimise heating problems. Rotational speed during the drop of the weight is dependent on the fluid properties, acceleration of the weight and the viscous drag of the fluid.

Cone-on-Plate Rheometer

These devices are quite common, use a small sample and are easy to operate. Problems involving particle jamming and obtaining constant excitation fields are potential major problems.

Parallel plate Rheometer

Parallel plate viscometers are growing in popularity. Fluid can be held within the gap by surface tension, or a disc can rotate within a housing. The speed of rotation and the torque due to viscous drag are measured. For particulate systems, the problem of particle jamming can be overcome, however the shear-rate does vary with radius:

$$\dot{\gamma} = \frac{r\Omega}{h}. \quad (2.26)$$

Again, explicit formulae can be used [30].

Tube Rheometer

Here a relationship between flow rate and pressure drop is used to calculate the fluid properties. A relatively large sample is required. Explicit formulae can be used to calculate $\dot{\gamma}$ [31]. The method is time consuming, but large shear-rates can be measured and the fluid is not exposed to atmosphere.

2.5.3 Common Rheometers used for Smart Fluids

Two predominant methods are used for obtaining smart-fluid data, the annular valve

and cylindrical viscometer (concentric clutch). Rheology flow curves that are determined using these methods from different devices do not always agree [32]. Usually the shear-stress on the boundary is adequately measured. The discrepancy arises when calculating $\dot{\gamma}$. For simplicity, the Newtonian equations (which must assume a Newtonian profile), are often used to calculate $\dot{\gamma}$. These relations become increasingly less valid depending upon the scope of the deviation from the traditionally expected Newtonian velocity profile. Caution must therefore be taken when faced with any experimentally derived fluid data.

Cylindrical Viscometer (Couette Flow)

The shear-rate and shear-stress for a viscoplastic fluid (except at very low speeds where plugs may be present), can be accurately determined using the equations below:

$$\dot{\gamma} = \frac{r_w \Omega}{h}, \quad \tau = \frac{N}{2\pi r_m^2 L} \quad (2.27)$$

Here r_w is the radius of the rotating cylinder (the other cylinder is stationary) and r_m is the mean radius, which must be significantly larger than the gap width. Due to a slight variation in shear-rate at very low rotational speeds, a plug may become attached to the outer cylinder. This situation is avoidable if a suitable radius is chosen.

Annular Valve (Poiseuille Flow)

$$\tau_w = \frac{h}{2} \frac{dp}{dL}, \quad \dot{\gamma}_w = \frac{2\dot{q}}{bh^2} \left(2 + \frac{d(\ln \dot{q})}{d(\ln \tau_w)} \right) \quad (2.28)$$

These two equations give the conditions at the wall [30]. The second term in the second equation is relevant for viscoplastic flow. The shear-rate is therefore calculated using numerical integration, which makes this method less accurate than the Couette flow method due to the difficulty in getting the derivative.

Bingham Plastic Model

An alternative approach is to assume that the smart fluid is an ideal Bingham plastic. The plastic-viscosity can be assumed equal to the no-field viscosity (μ_b). The analytical solutions presented in the next section for a concentric clutch and annular valve can then be used to determine τ_y .

2.6 Dimensional Analysis for Smart Fluids

Non-dimensional variables allow experimental data to be represented in a meaningful and graphical form. Hedström [13] used dimensionless parameters to produce a

convenient graphical form of representing the Buckingham equation (section 2.4.1). The relevant parameters are friction coefficient (Cf), Reynolds number (Re) and Hedström number (He). These parameters can be written in the general form:

$$Cf = f(Re, He),$$

$$Cf = \frac{\tau}{\rho \bar{u}^2}, \quad Re = \frac{\rho \bar{u} h}{\mu}, \quad He = \frac{\tau_y \rho h^2}{\mu^2}. \quad (2.29)$$

Using an average velocity and taking the viscosity as the no-field value, experimental data can be converted into Cf and Re . Using, for example a Bingham plastic model, He can be obtained from the experimental results. Re gives an indication of the magnitude of deformation (shear rate) and He is an indication of the strength (yield stress) of the fluid.

If a particular smart fluid is well characterised by the Bingham model then the technique should provide an accurate and useful collation of data as shown in Fig. 2.6 for a MR valve [33].

2.6.1 Numerical Algorithm

When this technique was applied to ER valve and clutch data [14] [34] [32], it was observed that He diminished with increasing flow rate. This suggests that τ_y is dependent on $\dot{\gamma}$. This is explainable, as the greater the deformation rate, the less the particles can form chains and contribute to providing resistance to flow. Determining exactly why this behaviour occurs is not necessary; the deviation from ideal Bingham plastic behaviour can be accounted for with the use of an algorithm. The variation of He can be approximated as [14] [34] [32]

$$He = He_{Re=0} - s Re, \quad (2.30)$$

where s is a constant. A relationship can be derived to infer the value of He at $Re = 0$ in terms of the excitation level. Such a relationship can be determined using a static clutch device, or by extrapolation of fluid data to the zero velocity axis. The constant (s) can be taken as an averaged value, or again a more exact relationship can be determined in terms of the excitation level.

2.6.2 Applications and Limitations

The above technique allows device performance to be predicted regardless of whether the smart fluid has a constant electro-stress effect or not. It has been effectively applied to valves and clutches. The approach is, however, limited to devices in which the geometry and flow field can be simply characterised. Accounting for combined Couette

and Poiseuille flow will be complicated, if not impossible. The procedure here involves assuming a Bingham plastic constitutive model, with μ_e equal to the zero-volts plastic-viscosity. This modest assumption could explain why He is found to decrease with increased Re [eqn(2.29) & eqn(2.30)]. This seems to suggest that the fluid is becoming weaker with increased shear-rate. This may explain why the following algorithm, eqn(2.30), arises. If the fluid was a true Bingham plastic, He should not be dependent on Re (i.e. the degree of shear-rate). Obtaining the relation is contentious and involves the best fitting of data points.

2.7 Numerical Methods (i.e. CFD)

2.7.1 How CFD Can Work for Smart Fluids

Equation (2.9) allows the “magnitude” of the local shear-rate ($\dot{\gamma}$) to be determined for every cell location. A constitutive model then allows μ_{mn} ($=\tau/\dot{\gamma}$) to be determined for each cell location. Each individual cell is then essentially treated as a Newtonian fluid for which the Navier-Stokes equations apply. The velocity gradients at each cell face influence μ_{mn} of the adjoining cells. For a domain in which enough cells are chosen, the problem can be solved using a semi-iterative method, until the whole domain converges to a solution.

Computational difficulties due to un-yielded sections of fluid having a zero shear-rate can be avoided by treating the entire material as a fluid using the bi-viscous constitutive model (section 2.3.2).

One-Dimensional Flow

An early investigation into using a commercial CFD package to model an ER valve was described by Kinsella *et al.* [35]. This treated essentially a 1D problem. Some of the results are representative of the 1D analytical solution and experimental results. However, after studying this work for myself, an employed ‘empirical grid evaluation technique’ appears to be ill conceived. This arises from a misinterpretation of convergence and nodal positioning. There is no need to apply such a method. Also the suggestive use of an algorithm (section 2.6.1) in the main code to represent a better approximation of fluid is ill conceived.

Two-Dimensional Flow

For a small gap size, an approximate 2D solution can represent a concentric clutch with an axial cooling flow [25]. An analytical solution gives the flow rate in terms of the rotor speed and pressure difference. CFD solutions are found to be approximately in

agreement with this solution. For practical values of rotational speed (0 - 5000 rpm) the torque is found to be unaffected by the cooling flow.

2.7.2 Main Advantages of CFD Approach

Solutions Unobtainable by Analytical Means

With the governing equations being difficult to solve for a hydrodynamic flow, a solution is only available when the net flow rate is zero [28]. A CFD model should be capable of solving this situation and many other more practical cases when the net flow rate is not zero. In addition, complex hydrodynamic geometry can also be studied.

Unsteady Flow

For an ER fluid, the finite time (t^*) required for the fluid properties to change in response to voltage is found to be less than one millisecond [22]. This offers the potential for very rapid response mechanisms to be built. The fluid and device inertia thereafter imposes a limit on how fast a device can actually respond. The separation of the true response time from unsteady recordings of a step type excitation input is a complex and tedious operation [36]. By assuming an instantaneous change in rheological properties, CFD can be used directly to estimate the response by solving the governing equations in the time domain.

For 1D flow it is possible to obtain approximate analytical solutions to time-dependent flows [37], [38] and [39].

Heat Transfer

In general, a smart fluid will operate in shear and will thus incur some viscous heating. Modelling heat transfer using CFD is generally relatively straightforward for a whole host of complex geometries. It should only be a matter of solving the energy equation along with usual momentum equations. All fluid properties, including electrical conductivity, can easily be included as a function of temperature within the CFD method. Furthermore, for an ER fluid, an extra sub-routine could be used to include a heating source due to the flow of current.

More Representative Models

Within the CFD methodology, complex constitutive equations that accurately represent experimental rheometer data can be readily used. The CFD method requires the function $\mu_{nm} = f(\dot{\gamma})$ for each excitation. In practice, the best way to enter this data may be of the form $\{\tau \text{ vs. } \dot{\gamma}\}$ for which the parameters are dependent upon E and/or $\dot{\gamma}$. The parameter representing τ_y could be a function of $\dot{\gamma}$, as indicated in section 2.6.

Four parameter models are usually too complex for use in analytical solutions, but can easily be utilised in CFD models such as Carreau [40]:

$$\frac{\mu - \mu_o}{\mu_s - \mu_o} = \frac{1}{(1 + (K\dot{\gamma})^2)^m} \quad (2.31)$$

2.7.3 Complete Model

Commercial CFD code is already widely used to obtain real engineering solutions. These include complex non-isothermal flows, which accommodate complex geometry by virtue of highly developed AutoCAD meshing software. With a commercially available code, the vast majority of the required programming has already been done. If required the software can be customised by the addition of suitable subroutines.

Once an effective fluid model is obtained, the objective is to use CFD to model machines that have elaborate geometry. This model may involve non-uniform field distributions, unsteady and non-isothermal flows, and fluid properties that can vary with temperature as well as with the applied field and deformation rate.

In some respects, the necessity of attempting to achieve such accuracy still needs to be determined. For example, gap widths are generally very small, and thus fluid temperature variations may be insignificant. In addition, one must remember that there is likely to be a limit as to how representative a homogenous continuum can ultimately be. Nevertheless, CFD promises to be a formidable tool.

2.8 Summary: Literature Survey

Offsetting traditional Newtonian formulations with an electro-stress provides some form of basic characterisation. An alternative approach using the Bingham plastic equation provides a superior representation and gives an indication of the fluid's flow profiles. Exploitation of this continuum approach is very limited using direct analytical equations. Even for the simplest flows, the formulations soon become too complex. The only sensible way forward is to use a CFD approach with a bi-viscous formulation.

To make the most of the CFD technique, a rheometer requiring a small sample of fluid is necessary to provide data for the shear-stress model eqn(2.25). A possible rheometer for this purpose is the radial disc rheometer.

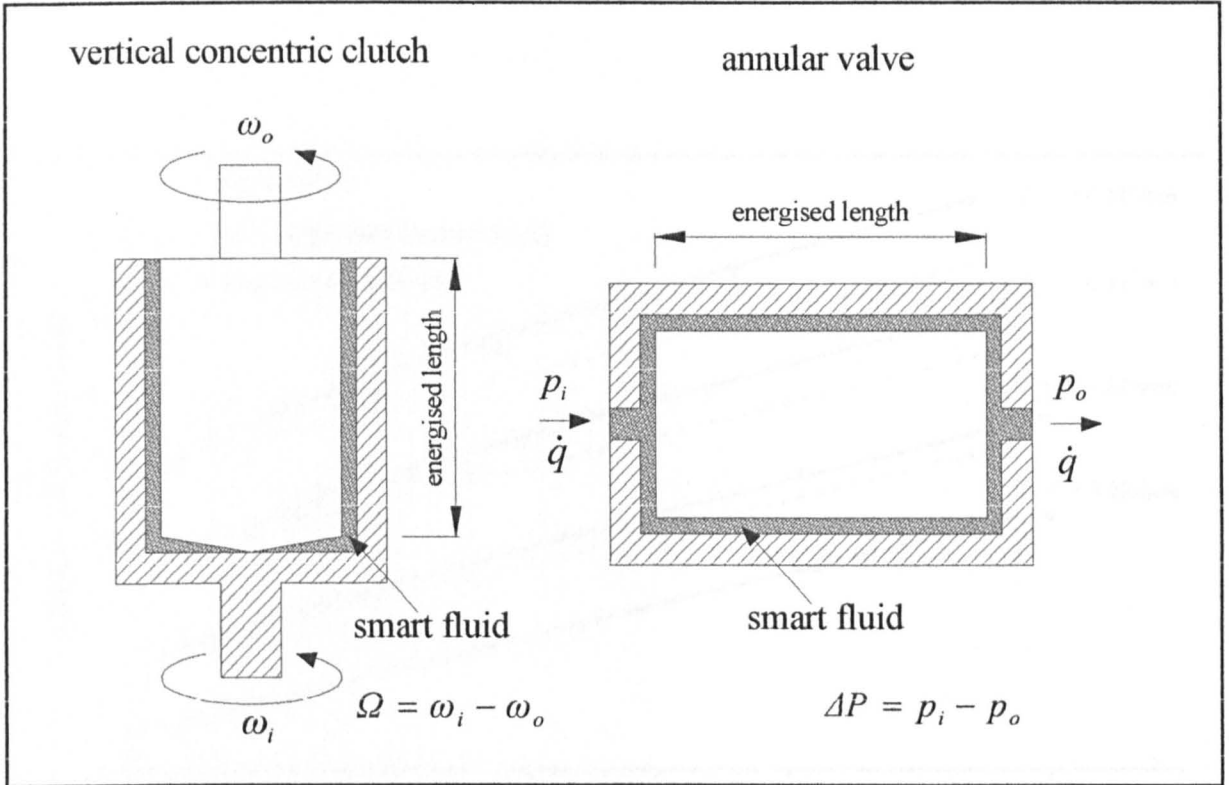


Fig. 2.1: Examples of basic smart fluid devices: concentric clutch and flow control valve.

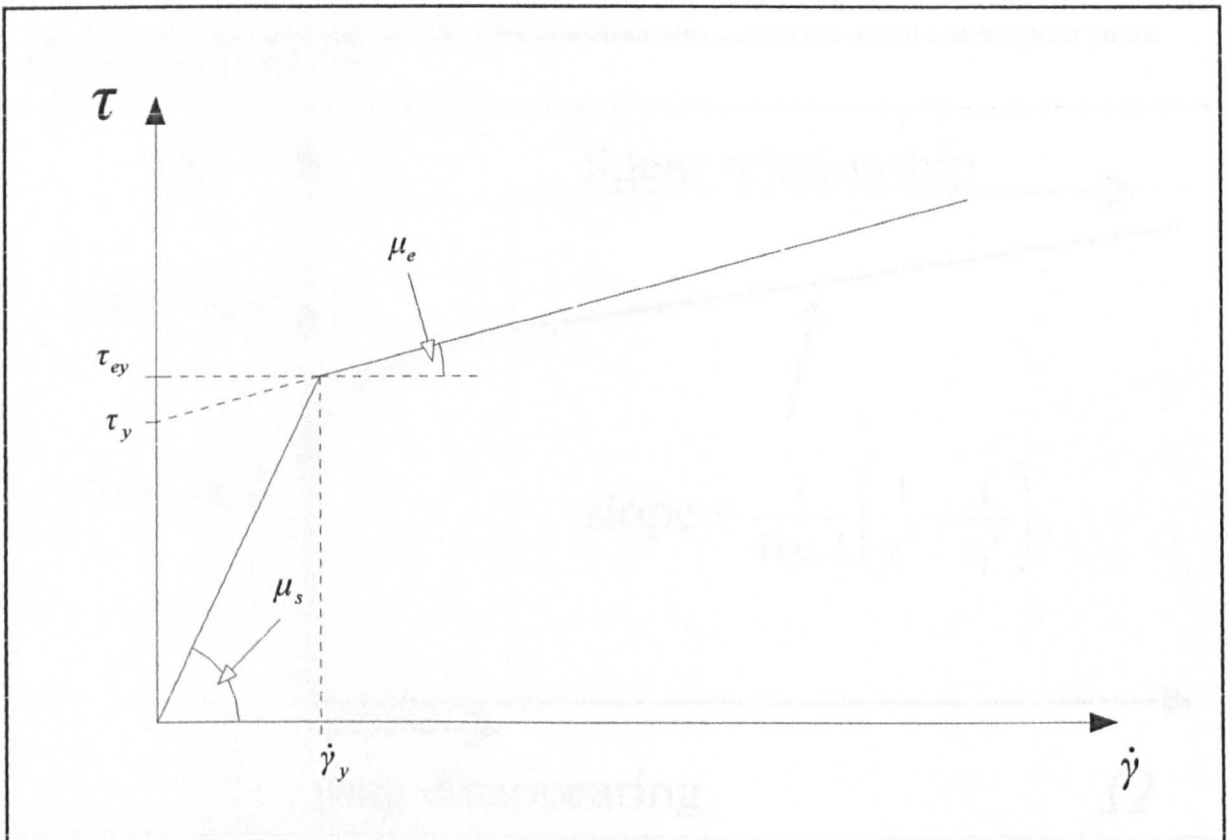


Fig. 2.2: Bi-viscous model: Shear-stress versus shear-rate.

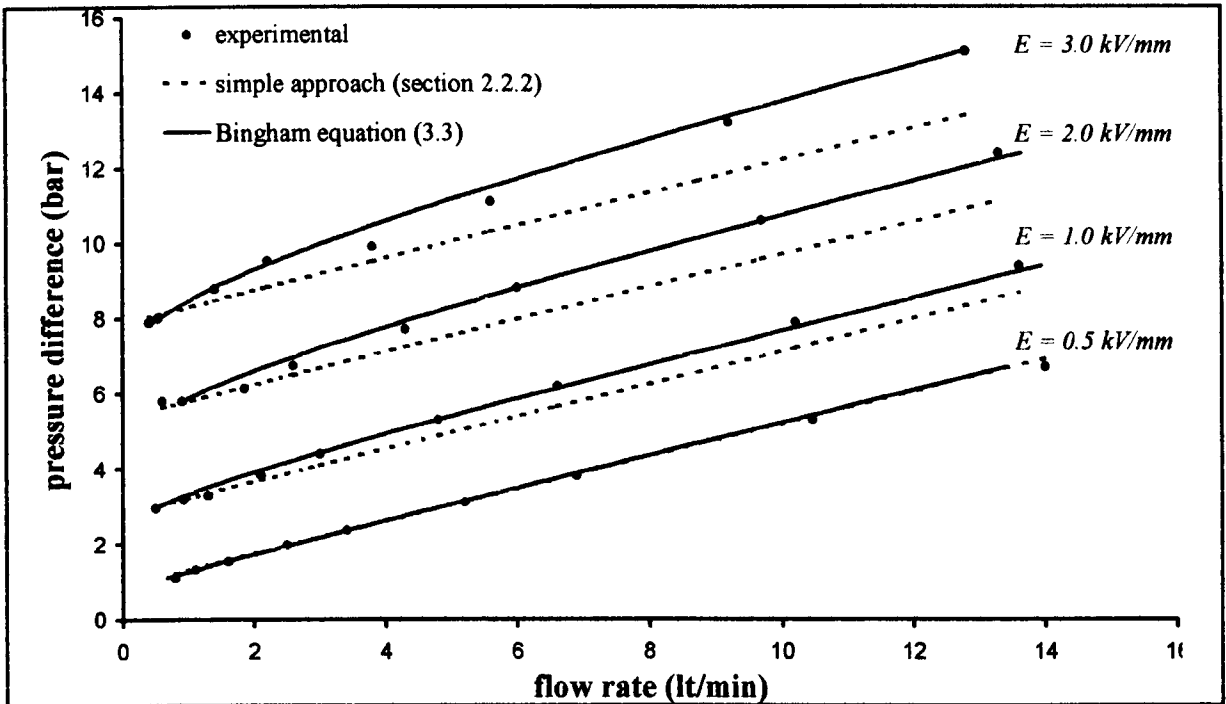


Fig. 2.3: Experimental results on a ER valve compared with a simplistic model and Bingham plastic solution. Value data from [14].

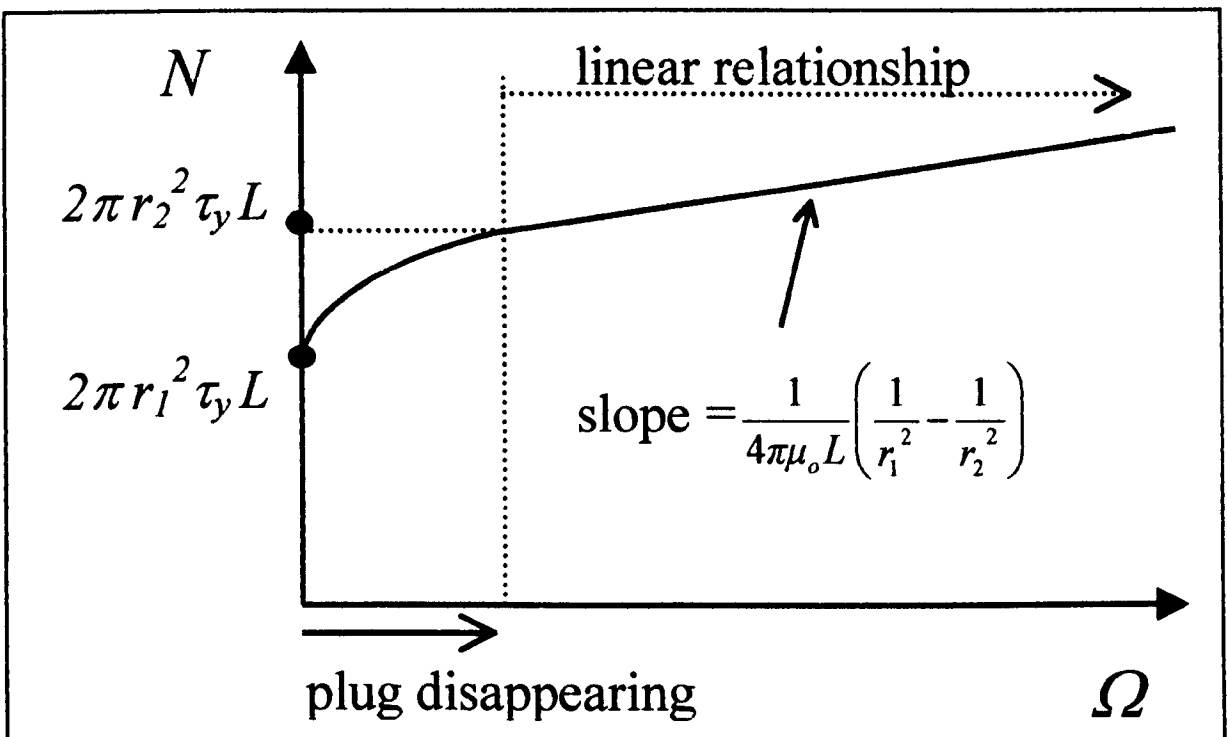


Fig. 2.4: Analytical equation for concentric clutch with a Bingham plastic fluid medium. Non-linear N vs. Ω relationship due to plug presence at low speeds.

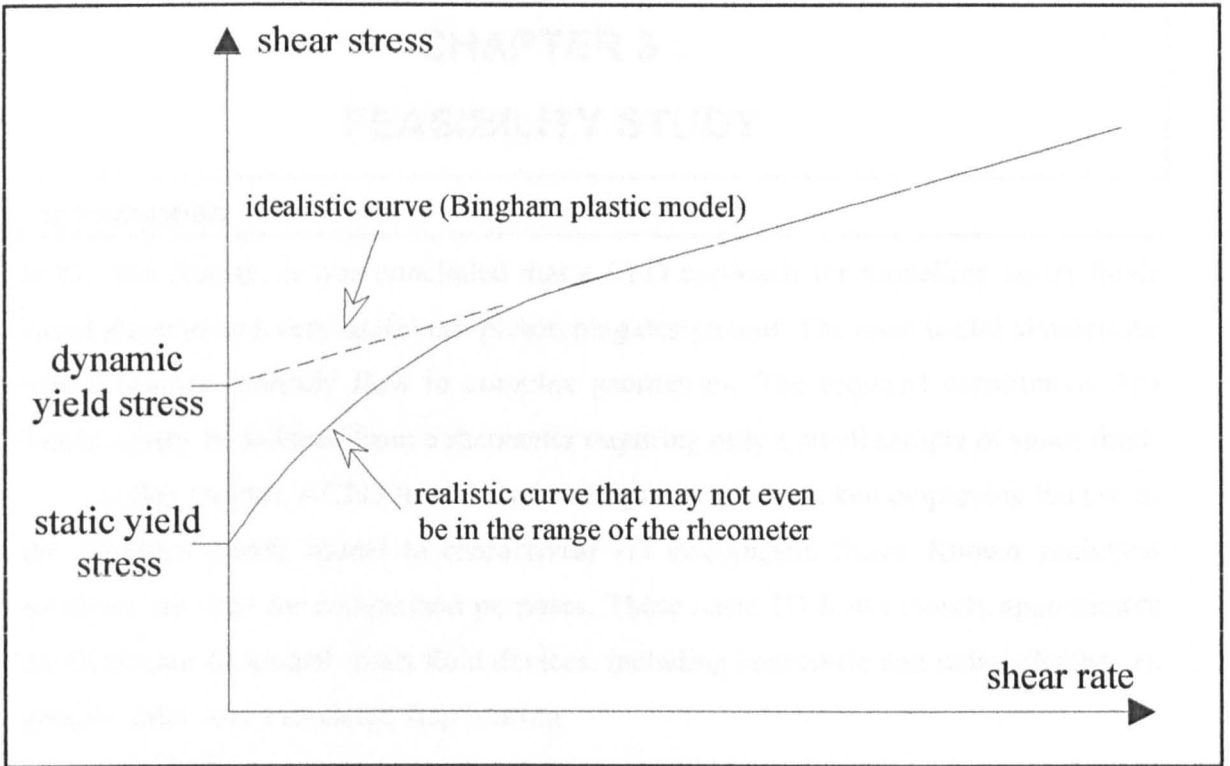


Fig. 2.5: Definition of yield-stress.

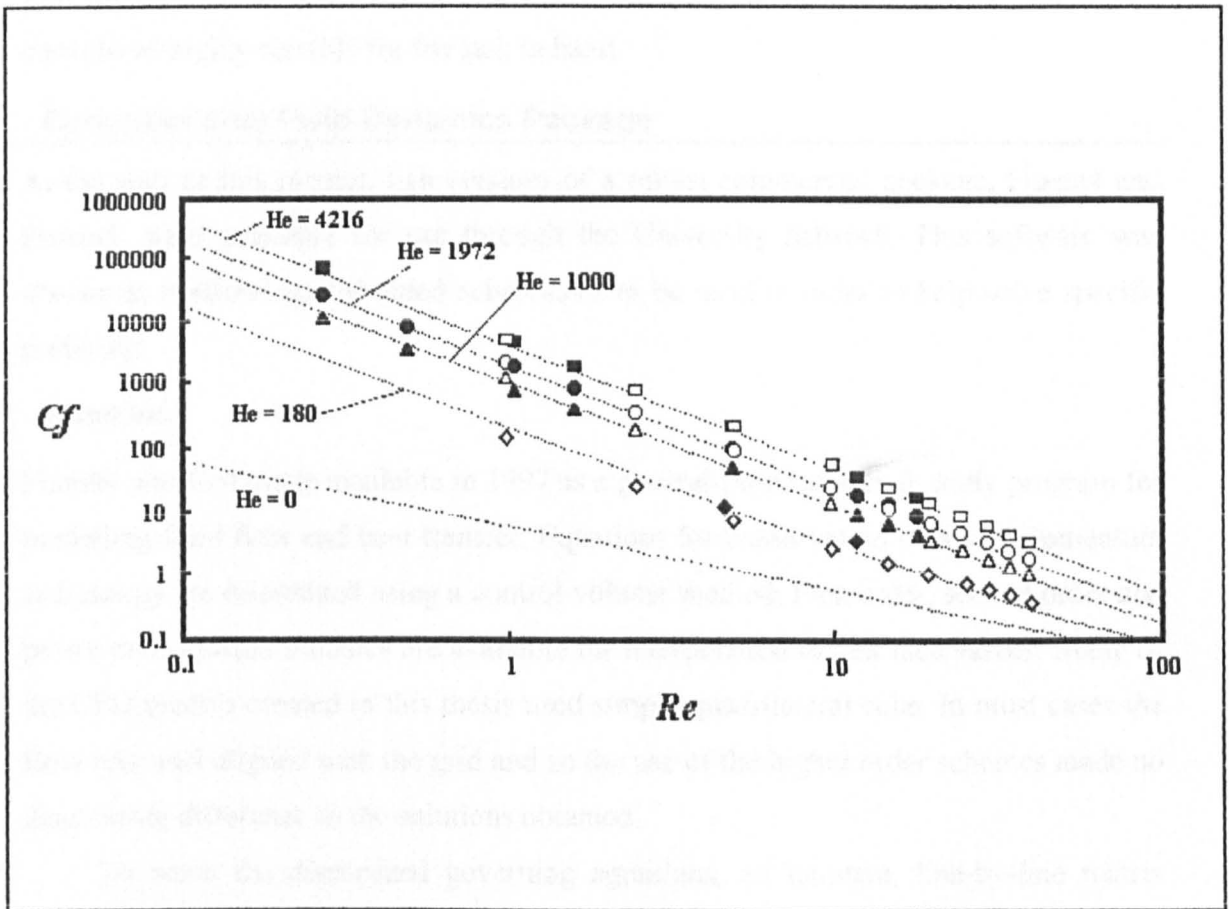


Fig. 2.6: MR valve results presented using He , Re and C_f numbers [33].

CHAPTER 3 :

FEASIBILITY STUDY

3.1 Introduction

In the last chapter, it was concluded that a CFD approach for modelling smart fluids could prove to be a very useful pre-prototyping design tool. The most useful simulations would resolve unsteady flow in complex geometries. The required constitutive data would ideally be inferred from a rheometer requiring only a small sample of smart fluid.

In this chapter, a CFD feasibility investigation is undertaken employing the use of the Bingham plastic model to characterise 1D viscoplastic flows. Known analytical solutions are used for comparison purposes. These basic 1D flows closely approximate the behaviour of several smart fluid devices, including concentric and radial clutches an annular valve and a Rayleigh step bearing.

An ER fluid is characterised using a specific rheometer designed to measure ER fluid properties. At this juncture, this was the only available rheometer, but it was considered highly suitable for the task in hand.

3.2 Computational Fluid Dynamics Package

At the start of this project, two versions of a robust commercial package, Fluent4 and Fluent5, were available for use through the University network. This software was chosen as it allows user-defined subroutines to be used in order to help solve specific problems.

3.2.1 Fluent Inc.

Fluent4 was first made available in 1997 as a general-purpose user-friendly program for modelling fluid flow and heat transfer. Equations for conservation of mass, momentum and energy are discretized using a control-volume method. First order, second order and power law, upwind schemes are available for interpolation of cell face values. Many of the CFD models created in this thesis used simple quadrilateral cells. In most cases the flow was well aligned with the grid and so the use of the higher order schemes made no discernable difference to the solutions obtained.

To solve the discretized governing equations, an iterative, line-by-line matrix segregated solver is used. A block diagram giving an overview of the solution process is shown in Fig. 3.1. A pressure-velocity coupling method is required and for most cases, the default SIMPLE algorithm was found to work just as well as the other available models. For some transient models, the PISO pressure-velocity coupling algorithm

helped to give faster convergence. The solution procedure is speeded up using a multigrid method that computes corrections on a series of coarser grid levels. Fluent5 is more powerful than Fluent4 and includes options to use a coupled solver and unconformable grids with advanced grid adaptation tools.

3.2.2 Convergence

The residual sum can be described as the imbalance between a cell variable and its neighbouring values summed over the whole computation mesh. On a computer with infinite precision, the residuals should decay to zero when convergence is achieved. In reality, the residuals decay and then level out at a small value. The size of the residuals can be used to judge when convergence has been reached – a value of 1×10^{-3} is used as the default convergence criteria for the main variables. However, work on this thesis has found that successful convergence of a smart fluid model requires this criterion to be much smaller ($< 1 \times 10^{-5}$). In fact, it is difficult to judge convergence this way. Variable history monitoring is nearly always required. This involves monitoring variable outputs such as torque, velocity, pressure etc. at influential locations. For example over time, the value of torque on a wall will level out once the solution converges.

3.2.3 Bingham CFD Model

The bi-viscous formulation (see section 2.3.2 and Fig. 2.2) describes an un-yielded region as a highly viscous fluid that effectively behaves as a solid in comparison to a yielded region. Equation (2.13) can be rewritten in a manner suitable for use in CFD:

$$\begin{aligned} \mu_{nm} &= \frac{\tau_y}{\dot{\gamma}} + \mu_e & \text{for } \tau > \tau_{ey} & \text{ or } \dot{\gamma} > \dot{\gamma}_y \\ \mu_{nm} &= \mu_s & \tau < \tau_{ey} & \dot{\gamma} < \dot{\gamma}_y \end{aligned} \quad (3.1)$$

Equation (3.1) allows the cell viscosity to be determined. With high enough values of μ_s , it is anticipated that a CFD bi-viscous solution will be indistinguishable from the Bingham plastic solution. This formulation is not a true Bingham plastic and shall therefore be referred to as the “Bingham CFD model”. The effect that μ_s has on a solution needed to be investigated thoroughly.

Test One: 1D Couette Flow between Concentric Cylinders

A bi-viscous formulation for an concentric clutch () is compared to the Bingham plastic solution presented in section 2.4.2. Movement of one rotor relative to the other causes 1D Couette flow. Between r_p and r_2 , $\Delta\omega$ across the plug is determined by setting $\tau_y = 0$ and $\mu_e = \mu_s$ in eqn(2.23):

$$\Delta\omega(r_p \text{ to } r_2) = \frac{N}{4\pi\mu_s L} \left(\frac{1}{r_p^2} - \frac{1}{r_2^2} \right). \quad (3.2)$$

Equations (2.21), (2.23) and (3.2) can now be solved simultaneously¹ to give the bi-viscous solution. Fig. 3.4 shows the effect of μ_s on the velocity profile when the speed is low enough for the presence of a plug. Here $\mu_s > 1000$ Pa is required so as to make the Bingham plastic and bi-viscous solutions comparable as shown in Fig. 3.4. Increasing μ_s increases the gradient in the un-yielded region of the bi-viscous model (Fig. 2.2) making it more comparable to the more recognised Bingham plastic model (Fig. 1.1).

Test Two: 1D Poiseuille Flow between Parallel Plates

A bi-viscous formulation for an annular valve is now compared to the Bingham plastic solution presented in section 2.4.1. 1D flow is caused by the application of ΔP_{eo} . The bi-viscous solution is obtained using eqn(2.17), modelling the plug section as a Newtonian fluid with viscosity μ_s . Fig. 3.5 shows the effect of μ_s on the velocity profile. Here $\mu_s > 100$ Pa is adequate to make the two solutions comparable.

In conclusion, the bi-viscous model is comparable to the Bingham plastic equation provided that μ_s is sufficiently large so that $\tau_{ey} \approx \tau_y$; a value of $\mu_s = 1000\mu_e$ seems to be adequate. The bi-viscous formulation thereby promises to be a suitable constitutive model for CFD use. Above a specific value, a further increase in μ_s has no observable effect on the solution. It is noted that a smaller value puts less strain on the CFD solver. It is therefore not good practice to set an unrealistically large number in order to be safely above the required value.

3.3 1D Smart Fluid Flow Examination using the Bingham CFD Model

The numerical CFD package had first to be validated before it could be used with any confidence. Available computational power had to be shown to be powerful enough to at least model basic 1D Bingham flows. Using the 1D flow assumption, models for concentric and radial clutches, and an annular valve were formulated.

In the previous section, a constitutive ‘‘Bingham CFD model’’ was proposed that would effectively behave like the Bingham plastic equation. An elaborate model relating τ_y , μ_e and E is not required since no specific experimental data is being used at this stage. Unless otherwise stated, default CFD parameters were used. All the models

¹ An iteration-based spreadsheet (Microsoft Excel) was used.

are for steady, 1D, isothermal, incompressible flow.

3.3.1 Flow Mode: Annular Valve

1D Poiseuille flow in an annular valve (Fig. 3.32) was modelled. With no extra complications, the exact radial geometry of this device could be modelled, allowing radial effects to be taken into consideration. It was however prudent to keep the problem in line with the analytical flat plate solution. Modelling of this flow should be, in principle, straightforward. However, difficulties that arose will be discussed.

The flat plate assumption requires only half the domain to be modelled when a 'symmetry line' boundary condition is used. Flow is caused by the application of ΔP_{eo} or vice-versa, and can be expressed using eqn(2.17).

CFD Model: Annular Valve

The following table summarises the CFD model used in this section.

Software	Fluent4, finite volume, segregated solver	
Physical Model	2D, steady, laminar, incompressible, isothermal flow	
Fluid Properties	viscosity (Bingham CFD model), density (constant), $\mu_s = 100\mu_e$	
Discretisation of flow equations.	interpolation scheme	1st order for all equations
	pressure-velocity	SIMPLE
	grid (x, y)	80 (x-dir) x 10 (y-dir)
Boundary Conditions	upper outer wall	no slip wall condition
	symmetry line	symmetry condition
	inlet and outlet test2	velocity inlet & pressure outlet respectfully
	inlet and outlet test3	velocity inlet & fully developed outlet respectfully

Table 3.1: Summary of CFD model used to solve steady 1D annular valve flow.

Due to the nature of the CFD package, a 2D grid must be used. The upper side of the grid was set to be a stationary wall and the lower side a line of symmetry. Since flow is uniform, in principle only a small number of cells are required in the axial x -direction. However, L/h is large, so a sizeable number of cells are needed to keep cell aspect ratio reasonable. A value of $\mu_s = 100\mu_e$ was used in the simulations.

Inlet and Outlet Conditions

There are several ways in which to set the inlet and outlet boundary conditions. Specifying a uniform velocity, $u_{inlet} = \dot{q} / h2\pi r_m$, sets a corresponding flow-rate, \dot{q} . The method requires a certain inlet length for the uniform velocity profile to develop. Through looking at the velocity profiles this was found to be only a few gap sizes h in

length, but does depend on how many cells are used. This condition is likely to be encountered experimentally, unlike a fully developed profile at the inlet as the analytical theory assumes. The outlet can be set to be either a fully developed or static pressure condition.

An alternative set of boundary conditions is to impose a pressure gradient (G) using a uniform pressure boundary condition. This method requires no attention to flow development lengths. It is numerically wrong to use an inlet pressure condition with a fully developed condition¹.

Newtonian Model: Determining which Set of Inlet and Outlet Conditions to Use

It was prudent initially to test the CFD model on a Newtonian fluid. Fluent4 was used with default solution parameters on a 20 x 20 grid ($h = 0.5$ mm and $L = 100$ mm). To determine if convergence had occurred variable, histories of velocity were recorded on the centre line.

The converged results using a pressure boundary condition are presented in Fig. 3.6. Next, the velocity inlet and pressure outlet boundary condition was tested and the results are shown in Fig. 3.7. It is observed that nearly 10 times fewer iterations are now required. The use of a fully developed outlet condition was found to make little difference. A plot of pressure along the symmetry-line (Fig. 3.8) indicates that 20 cells along the axis is a required minimum. To get a better solution, more cells at and near the inlet are needed. Alternatively, a section of the length can be set aside as an inlet pipe in which a uniform inlet velocity develops. At a point where the pressure gradient is adequately developed, the velocity profile is seen to compare well with analytical theory (Fig. 3.9). It can be concluded that 20 cells within the gap is adequate.

An inlet velocity was now set to imply a theoretical value for G of 300 bar/m across a Bingham fluid of strength $\tau_y = 5$ kPa, $\mu_e = 100$ mPa.s. The results (Fig. 3.10) show that 20 times more iterations are now required to reach a solution, and convergence is very slow. Convergence occurs when the residual for u -velocity is somewhere between 1×10^{-6} and 1×10^{-7} . The grid is too sparse near the inlet to adequately determine the pressure gradient (Fig. 3.8). The velocity profile does, however, fit the analytical theory well at a point where G is properly developed (Fig. 3.9). Fig. 3.11 and Fig. 3.12 further indicate the importance of reducing the residuals past the default setting.

¹ Only an experienced CFD user knows that it is not allowed, there is no physical reason why it cannot be used.

Final Results from Annular Valve Model

Solutions are now computed on a larger grid (80x200) to give a more accurate pressure profile. For a variety of fluid properties \dot{q} was set using u_{inlet} and G was determined. Parameters were chosen to illustrate certain types of behaviour. The results are presented in Fig. 3.13. Over the full range, the CFD results correspond very closely with the analytical theory. Although μ_e appears insignificant in comparison to τ_y , in the equation for μ_m , μ_e is found to be significant. This is due to the presence of large shear-rates at the walls. In conclusion, the results from the CFD model were found to be in excellent agreement with the analytical solution.

3.3.2 Shear Mode: Concentric Clutch

As discussed in section 2.4.2, the simplest model of this device involves flow between two flat plates of dimensions $L \times 2\pi r_m$, separated by a gap width (h). The analytical theory is more complicated when radial geometry is considered, with a non-uniform shear-rate allowing the possibility of plug flow. In comparison, no extra difficulty is encountered when setting up a CFD model with radial geometry. The analytical model relating torque (N) at speed (Ω) for both flat plate and radial geometry is given in section 2.4.2.

CFD Model: Concentric Clutch

The following table summarises the main CFD model used in this section.

Software	Fluent4, finite volume, segregated solver	
Physical Model	2D, steady, laminar, incompressible, isothermal flow	
Fluid Properties	viscosity (Bingham CFD model), density (constant)	
Discretisation of flow equations	interpolation scheme	1st order for all equations
	pressure-velocity	SIMPLE
	grid (x, y) [axisymmetric]	10 (x-direction) x 20 (y-direction)
Boundary Conditions	outer cylindrical wall	no slip wall condition
	inner cylindrical wall	circumferential speed

Table 3.2: Summary of CFD model used to solve steady 1D for in a concentric clutch.

The grid is constructed using axisymmetric geometry. The inner and outer wall radii are set at r_1 and $r_2 = r_1 + h$, ($r_m = r_1/2 + r_2/2$). Flow is 1D, limiting variations in velocity to the radial direction only. The axisymmetric option assumes circumferential flow to have both zero velocity and pressure derivatives; no cell density is therefore required in this direction. For the axial direction, zero derivatives allow a cyclic boundary condition to be used. The inner cylinder speed was set to rotate with a constant angular speed. A

schematic of the CFD model is shown in Fig. 3.14.

CFD Concentric Clutch Results

For a given speed, the torque can be determined using a wall forces command, and plotted against the analytical bi-viscous solution. Results are presented in Fig. 3.15. Over the full range, the CFD results are found to correspond very closely with the theory. For the smallest mean radius used, the difference between the two analytical theories (flat plate and radial geometry) for torque was found to be less than 0.1 %, and so only the radial geometry theory is shown in Fig. 3.15.

One should expect to see a plug profile at low speeds as shown in Fig. 3.16. However, the plug formed does not correspond with velocity profiles from the bi-viscous solution. Upon investigation, it was discovered that the CFD software was applying the constitutive model incorrectly. Equation (3.1) was being used as the constitutive equation but no consideration was given to $\dot{\gamma}_y$. The viscosity is simply allowed to run away until it equals μ_s . Clearly this is not the correct way to apply the model. The solution to this problem involves writing a new sub-routine to calculate the correct viscosity.

Fig. 3.17 shows that when the correct formulation of the Bingham CFD model is used, the results make sense. To get the Bingham plastic flow profile, a value of at least 1000 mPa.s is required. This is in accordance with the prediction in section 3.2.3.

3.3.3 Smart Fluid Radial Clutch

Plugs should not occur in this type of device even though the shear-rate varies in the radial direction. In its simplest form, the device is approximated by assuming flow between two flat discs separated by a distance (h). The analytical equation for torque is given by:

$$N = \int_{r_1}^{r_2} r \cdot 2\pi r \left(\tau_y + \mu_c \frac{r\Omega}{h} \right) dr = \frac{\pi \mu_c \Omega}{2h} (r_2 - r_1)^4 + \frac{2\pi \tau_y}{3} (r_2 - r_1)^3. \quad (3.3)$$

CFD Model: Radial Clutch

The following table summarises the main CFD model used in this section.

Software	Fluent4, finite volume, segregated solver	
Physical Model	2D, steady, laminar, incompressible, isothermal flow	
Fluid Properties	viscosity (Bingham CFD model), density (constant)	
Discretisation of flow equations	interpolation scheme	1 st order for all equations
	pressure-velocity	SIMPLE
	grid (x, y) [axisymmetric]	20 (x-dir) x 30 (y-dir)
Boundary Conditions	inner	symmetry line
	outer (w4)	wall [w-velocity] = (rΩ/h)x]
	left hand side (w1)	wall
	right hand side (w2)	wall [w-velocity = rΩ]

Table 3.3: Summary of CFD model used to solve steady 1D flow in a radial clutch.

The model is relatively straightforward to simulate. The wall velocity is set to be dependent on r (i.e. $w = r\Omega$). The end wall is set to have a linear velocity profile so that it is in line with the theoretical solution. In practice this wall, which physically holds the fluid in, will be either stationary or moving.

Over a range of parameters, the CFD results (Fig. 3.18) are found to compare extremely well with the analytical theory. This requires convergence to be reached, for which the default convergence criterion needs to be ignored. Convergence was better judged by comparing the shear-stresses on both plates.

3.4 Smart Fluid Flow Examination in Rayleigh Step Bearing

A more complicated 1D analytical solution is now compared to a CFD model. Here the performance of a Rayleigh step bearing (Fig. 3.19) is evaluated, firstly when the film medium is a Newtonian fluid and secondly when it is a Bingham plastic. The flow occurring in this device is mainly 1D, even though both Couette and Poiseuille types of flow are both present.

A dynamic bearing is an application of the hydrodynamic effect. A smart fluid bearing could provide a variable hydrodynamic load. This could be of use in some applications, e.g. catering for sudden load changes in a smart adaptive system if nano ER/MR fluids are forthcoming.

3.4.1 Analytical Theory

A detailed description of the analysis for combined 1D Couette and Poiseuille flow between two plates can be found in [28] and [41]. Fluid occupies the region ($0 \leq y \leq h$) between two flat parallel plates. The plate at $y = 0$ moves with a particular speed (U) in the x -direction, whilst the other plate at $y = h$ is stationary. Depending upon the

direction and/or magnitude of τ_y , μ_e , U , pressure gradient (G) and gap size (h), various flow situations can be observed. The movement of the lower plate causes Couette flow; a pressure gradient in the x -direction causes Poiseuille flow. The following velocity field is assumed:

$$u_x = u(y) \quad , \quad u_y = u_z = 0. \quad (3.4)$$

The only non-zero stress component takes the form:

$$\tau_{xy} = Gy + C, \quad (3.5)$$

with C being a constant to be determined. Using the Bingham plastic constitutive equation and relevant no-slip boundary conditions, a governing equation can be derived.

Central Plug Occupying Region $0 < y_1 \leq y \leq y_2 < h$

The most practical situation in which $G > 0$ and $U > 0$ is considered. Taking $\tau_{xy} = -\tau_y$, τ_y & $du/dy = 0$ at y_1 and y_2 respectively, and using eqn(3.5) leads to:

$$h_{plug} = y_2 - y_1 = \frac{2\tau_y}{G}, \quad C = -\frac{1}{2}G(y_1 + y_2). \quad (3.6)$$

Here the plug width (h_{plug}) is therefore independent of the plate speed, and the plug is central provided that $2\tau_y/G < h$. Combining eqn(2.11) and eqn(3.5) gives:

$$\mu_e \frac{du}{dy} = Gy + C + \tau_y. \quad (3.7)$$

Integrating eqn(3.7) and considering the flow in the separate parts, results in the following velocity profiles:

$$\mu_e u = \frac{1}{2}Gy^2 + (C + \tau_y)y + \mu_e U \quad \text{for the region } 0 \leq y \leq y_1, \quad (3.8)$$

$$\mu_e u = -\frac{1}{2}G(h^2 - y^2) - (C - \tau_y)(h - y) \quad \text{for the region } y_2 \leq y \leq h, \quad (3.9)$$

$$u_{plug} = u(y_1) = u(y_2) \quad \text{for the region } y_1 \leq y \leq y_2. \quad (3.10)$$

With an integration between $y = 0$ and $y = h$ the flow rate can be acquired:

$$\frac{\dot{q}}{Uh} = \frac{1}{6} \frac{h^2}{\mu_e U} G \left\{ \left(\frac{y_1}{h} \right)^3 - 2 - \left(\frac{y_2}{h} \right)^3 + 3 \frac{y_2}{h} \right\}. \quad (3.11)$$

The flow rate is now given in terms of the pressure gradient (G) and unknown plug boundaries y_1 and y_2 .

Step Bearing Model: $h_2 = \text{zero}$

Equation (3.11) is applicable to the situation when $h_2 = \text{zero}$ as shown in Fig. 3.19. Because h_1 is now the only gap width $h_1 = h$. Since $h_2 = \text{zero}$, the net flow rate is zero and it is possible to derive the following formulae from eqn(3.11):

$$\frac{h^2}{\mu U} G = a + bB + cB^2. \tag{3.12}$$

	<i>a</i>	<i>b</i>	<i>c</i>	
$0 \leq B \leq 20$	6.00	2.63	-1.41×10^{-2}	(3.13)
$10 \leq B \leq 70$	8.21	2.29	-1.34×10^{-3}	

For a Newtonian fluid:

$$G = \frac{6\mu_e U}{h^2} \tag{3.14}$$

In addition, the velocity profile reduces to:

$$\mu u = -\frac{1}{2} G y^2 - \left(\frac{Gh}{2} + \frac{\mu U}{h} \right) y + \mu U. \tag{3.15}$$

3.4.2 CFD vs. Analytical Solution

To numerically solve the continuum flow equations, the segregated CFD solver was employed.

Newtonian Flow

Software	Fluent4 and Fluent5, finite volume, segregated solver	
Physical Model	2D, steady, laminar, incompressible, isothermal flow	
Fluid Properties	viscosity (Newtonian), density (constant)	
Discretisation of flow equations	interpolation scheme	1st order for all equations
	pressure-velocity	SIMPLE
	grid (x, y) [y = vertical direction]	20 x 20
Boundary Conditions	upper wall (stationary)	zero velocity wall condition
	lower wall (moving in +ve)	constant velocity wall condition
	inlet on the left hand side	pressure inlet (0 Pa)
	wall on the right hand side	zero velocity wall condition

Table 3.4: Summary of CFD model used to solve steady 1D annular valve flow.

Using Fluent4, a model was set up to correspond to that in Fig. 3.19 and Table 3.4. A grid analysis was undertaken to determine the required density of cells to represent the

flow. In Fig. 3.20, the exact analytical solution for pressure (solid red line) is compared to CFD results for varying grid sizes. A sparse grid (10 cells in the y -direction) fared well, but to get very close to the exact solution more cells were required (20 cells in y -direction). With 20 cells in the x -direction, the aspect ratio is very large. However, since the flow is laminar and 1D, a 20x20 grid is adequate. This is demonstrated over a wide range of parameters in Fig. 3.21. To further demonstrate the agreement between CFD and analytical theory, velocity profiles are shown in Fig. 3.22.

Bingham CFD model

Work on the Bingham CFD model was carried out using Fluent5. Computation using Fluent4 was very slow. Here, as before when using the Bingham CFD model, consideration of convergence was found to be vitally important. The analytical solution is compared to CFD solutions in Fig. 3.23. The agreement here can be seen to be very good. To help determine if convergence had been met, the pressure values at certain locations were monitored. A comparison of velocity profiles results in good agreement, as shown in Fig. 3.24.

3.4.3 Concluding Remarks

If an adequate CFD model with correct convergence criteria is utilised for a given plate speed with $h_2 = 0$, the resulting pressure gradients and velocity profiles correspond very closely with the analytical solution. This is in contrast to poorly matching data found in [42], which is mainly a result of inexperience on the part of the CFD operator in setting a correct model and understanding convergence. The fact that both mathematical solutions correspond, considerably reduces the probability of errors in each method. Hence, it is very likely that the analytical and CFD solutions are correct.

It is worth remembering that the Bingham plastic analytical solution could not be solved directly. If the geometry was even more complicated, involving for instance a change in gap-width/s along the bearing length, as found in most hydrodynamic situations, then there would be little scope for deriving a useful analytical relation relating geometry, speed and pressure. In contrast, providing the field distribution is calculated (see section 3.5) then this situation should prove no problem in CFD.

3.5 Non-Uniform Field Distributions

For a given smart fluid, some uncertainty will exist in exactly how its properties vary with field-strength (E). The situation may worsen if the field distribution itself is uncertain, the severity of which depends on the type of field being imposed (electric or magnetic) and the geometry of the situation. However, the situation will improve when

more accurate rheometer data is available.

A magnetic field could be calculated by external means and then superimposed onto the CFD grid. Each cell would then have its own finite value of field strength. For the simplest geometry, all cells would have the same value of E . Alternatively, for specific cases, algorithms may be available for estimating E , depending upon both cell location and time. This thesis is concerned mainly with ER fluids, so these methods have not been considered further.

In an ER fluid, it would be highly useful to be able to calculate the electric-field distribution within the CFD simulation. For example, the user would specify which electrodes are live and which are earthed. This is entirely possible by solving an additional user-defined scalar transport equation:

$$\frac{\partial}{\partial x_i} \left(\frac{\partial \phi_k}{\partial x_i} \right) = S_{\#k} \quad (3.16)$$

Here the flow does not affect the field. The equivalent expression, which may be more familiar, is as follows:

$$\text{div } E = 0, \text{ curl } E = 0. \quad (3.17)$$

A specific value voltage or flux then needs to be set at all boundary conditions. The CFD package can now calculate the voltage distribution. A subroutine can then use this data to calculate the average magnitude of excitation (E) (volts/metre) for each cell location:

$$E = \sqrt{E_y \cdot E_y} \quad (3.18)$$

This value will be used to calculate τ_y and ultimately μ_{nn} {eqn(3.1)}.

3.5.1 ER Bingham CFD model

An example of a sub-routine written to calculate the excitation field and return the fluid viscosity¹ value is shown in Table A.1(Appendix A).

Example One: Annular Valve with Middle Section Excited

To test the sub-routine, an annular valve (see Fig. 3.25; $L = 60$ mm & $h = 0.5$ mm) was modelled using an axisymmetric grid 120 x 20, split equally into three sections. A constant inlet flow rate of 16.47 Lt/min was imposed. The first test involved setting all

¹ Because fluent5 does not calculate the fluid shear-rate correctly in axisymmetric geometry, the sub-routine also calculates the shear-rate.

electrodes (valve walls) to zero voltage and comparing the simulation to the Newtonian analytical solution. In the second test, the upper voltage was set to 2500 V. This should generate a uniform field throughout the whole valve giving a yield-stress of 5 kPa, for which eqn(2.17) should hold true. Finally, only the middle third section was excited. The results shown in Fig. 3.26 are in excellent agreement. In the final case, it can be seen that dp/dx equals that of the unexcited and excited case in the appropriate regions.

Example Two: Flow between Two Parallel Plates with a 180 Degree Bend

An analytical solution to a smart fluid problem involving anything other than flow between flat plates soon becomes very demanding. This need not be the case using CFD. An example would be a problem involving Poiseuille flow between two flat parallel plates with a 180-degree bend. The geometry of this is shown in Fig. 3.27. The 'ER Bingham CFD model' is used with the inner wall excited to 2500 volts and the outer earthed at zero volts.

The solutions for voltage contour distribution and velocity profiles are shown in Fig. 3.27 and Fig. 3.28 respectively. At this stage, other than making sure that the CFD solution is fully converged and adequately discretized¹ there is no way to verify that the solution is correct. There will, be a point when one can no longer verify the solution by any means other than experimentation. The reason for using the CFD method as a pre-prototyping tool is precisely that analytical methods are too difficult to achieve for problems such as this one. As far as one can tell, the solution makes perfect sense and looks correct. The central fluid appears to be rotating around the bend with an angular velocity. Thus, the instantaneous velocity increases with radius across the plug region and can be observed in Fig. 3.28

3.5.2 Previous Work

Concentric Geometry

For an ER fluid, the excitation field across a gap width would typically be assumed to equal V/h . However, in concentric geometry the excitation field would obey:

$$E = \frac{V}{\ln(r_2/r_1)} \frac{1}{r}, \quad (3.19)$$

giving a non-linear excitation (depending on the severity of r_1/r_2) that deviates from the usual linear assumption. Using eqn(3.19) the error involved when assuming a constant excitation in a concentric geometry is illustrated in Fig. 3.29. For an extreme case when

¹ This is done by monitoring any change in flow with further iteration and accessing grid independency.

$r_i = 10$ mm, a deviation of 5.0 % is seen. For a more practical case with $r_i = 30$ mm, the error is only 1.0 %. Other errors in a smart fluid model, such as uncertainty about the fluid's properties, would be much greater. It is therefore not prudent for the time being to pay much attention to this effect.

Papers [23] & [27] have however investigated such behaviour. Here interesting effects can be observed, such as cancellation of plug effect in a concentric clutch due to higher excitation near the inner rotor. The effect depends on the particular model for τ_y .

Concentric Geometry Effect in CFD

The 'Bingham CFD Model' should pick up the concentric distribution effect described above. However this was found not to be true, as the CFD package did not use the right coordinate system to calculate E . This is a similar problem to that found previously, when the CFD package was not calculating the shear-rate correctly¹. It was deemed uneconomical to spend time correcting the problem at this juncture. It will probably be rectified in later versions of Fluent anyway.

3.6 Bayer ER Fluid Test Using a Constant Stress Rheometer

A constant-stress viscometer on loan from ERFD², was used to characterise a silicon-based ER fluid from Bayer AG (3565 50%). The fluid was unused but several years old and separation of the base fluid was evident. The fluid, still in its original five-litre container, was mounted in a paint stirrer and repeatedly agitated for several days until it appeared to be fully homogenous. The properties of the fluid might have changed due to its age, so it had to be re-characterised.

This type of rheometer is similar in design to the widely used coaxial cylindrical rheometer. However, instead of applying a constant shear rate through a constant speed difference, an attempt is made to apply a constant shear stress. A constant shear stress causes the rotating bob (Fig. 3.27) to accelerate. Using the Bingham plastic constitutive model it is possible to calculate the theoretical acceleration. It is thus possible to determine fluid properties by looking at recorded velocity data.

3.6.1 Theory and Description of Apparatus and Calibration

The rheometer has Couette geometry with radii of capstan: $R_{cap} = 19.5$ mm, bob: $r_1 = 25$ mm and cup: $r_2 = 25.5$ mm. The source of constant stress is a hanging weight of

¹ This is a problem when using the CFD axisymmetric model - the correct shear rate is thus calculated in the user-defined subroutine for the smart fluid.

² ER Fluid Developments (ERFD), now known as Smart Technologies.

variable mass (M). A schematic of the apparatus is shown in Fig. 3.30. An experiment is recorded using the data acquisition system. A displacement versus time fitting routine determines the acceleration. Circulation of water through a double-walled cup was provided using a pump heater system. This allowed the temperature of the fluid specimen to be controlled.

A force balance gives:

$$Ma_b = Mg - I/R_{cap}^2 a_b - k_b v_b - (\text{viscous torque})/R_{cap}, \quad (3.20)$$

where k_b is a bearing term, a_b [ms^{-2}] is acceleration, v_b [ms^{-1}] is velocity and I_b is the moment of inertia of the complete assembly. For a Newtonian liquid, the viscous force equates to:

$$F = 4\pi L_b \mu_e v_b / (1/r_2^2 - 1/r_1^2) R_{cap}^2 = D\mu_e v_b, \quad (3.21)$$

where L_b is the length of the bob and D is made up of equipment constants. Substituting eqn(3.21) into eqn(3.20) gives:

$$a_b = Mg/(M + I_b/R_{cap}^2) - (k_b + D\mu)v_b/(M + I_b/R_{cap}^2). \quad (3.22)$$

Thus, a plot of a_b against v_b should, in principle, be a straight line with an intercept (A_b) and slope (S_b):

$$\text{where } A_b = Mg/(M + I_b/R_{cap}^2), \quad (3.23)$$

$$\text{and } S_b = \frac{k_b + D_b \mu_e}{M + I_b/R_{cap}^2} = \frac{k_b}{(M + I_b/R_{cap}^2)} + \frac{D_b \mu_e}{(M + I_b/R_{cap}^2)} = B_b + C_b \mu_e. \quad (3.24)$$

These two values are calculated from the raw data by the program, and printed out at the end. It can be seen that the intercept (A_b) is a function only of the apparatus and the weight used. If the fluid is Newtonian, then A_b is not a function of the temperature or the cup contents. For a Bingham plastic, the extra viscous torque is now derived as:

$$N_e = D_b R_{cap}^2 \tau_y \ln \frac{r_2}{r_1}. \quad (3.25)$$

This value of viscous torque inserted into the basic equation decreases the value of A_b measured, while the plastic-viscosity acts through the S_b term. It can be shown that:

$$\Delta A_b = \tau_y \ln \frac{r_2}{r_1} D_b R_{cap} / (M + I_b/R_{cap}^2). \quad (3.26)$$

ΔA_b is computed as an angular acceleration, and must be multiplied by the capstan

radius to give m/sec^2 . In eqn(3.26) all the values are apparatus constants and/or known from the calibration. It is also clear that ΔA_b cannot be greater than the no-field value of A for that weight, and this puts a limit on the value of yield-stress that can be measured with any given weight. The rheometer was calibrated using standardised Newtonian fluids.

3.6.2 Method

The heater and computer were turned on. A fluid sample was placed within the gap. Rotating the bob allowed any air gaps to escape. Once the required temperature was reached, testing could commence. The weights were checked to be safely in place and the correct electric field magnitude was set. An automated process was then set in motion; the weight was raised, there was then a short pause and the electric field was switched on before the weight fell. Current density was read and recorded manually before the weight drops. Both speed and any pressure gradients were deemed low enough for any cavitation effects to be avoided. In addition, due to micro size of the particles any wall effects are not considered important. The process took about 15 seconds, allowing the procedure to be repeated four to six times for each setting. The values of A and S for each run are automatically written to a database. After some initial practice runs, three sets of accurate data were taken.

First Set of Data

It was considered likely that some re-separation of the ER fluid had occurred. Therefore, before testing, the fluid was shaken for one hour on a paint-mixing machine. Throughout the tests a driving weight of 6kg was used. Testing was conducted at room temperature ($\sim 20^\circ\text{C}$), $\sim 25^\circ\text{C}$, $\sim 30^\circ\text{C}$, $\sim 35^\circ\text{C}$ and $\sim 40^\circ\text{C}$. Increments of 0.2 kV were used. The same fluid was used throughout the testing procedure.

Fig. 3.31 shows the results for τ_y . It is difficult to make an exact fit to the data, but the trend is obvious. The change in τ_y for different temperatures is seen to be minimal at some voltages but up to 50 % at others. Fig. 3.32 shows the corresponding plastic-viscosity values. Above 0.5 kV the value becomes negative. Again, there is no major difference between results at different temperatures, although at 40°C the plastic-viscosity (μ_t) starts increasing again, when the voltage rises above 2 kV. This may be a result of an increase in electrical conductivity when both the temperature and voltage are high.

Second Set of Data

It was envisaged that a second set of testing would correspond with the first set. A new

fluid sample was used. The results are shown in Fig. 3.33 & Fig. 3.34.

Third Set of Data

The procedure was repeated again, this time changing the fluid sample at each temperature. The results are shown in Fig. 3.35 & Fig. 3.36.

3.6.3 Discussion of Results

Yield-stress

To help analyse the results for τ_y at each temperature, they have been placed on a separate graph. Results at 25°C, 30°C and 40°C are shown in Fig. 3.37, Fig. 3.38 and Fig. 3.39 respectively. The results tie together well at some voltages and temperatures, while at other values the discrepancy can be up to 500 Pa. This can be explained as follows. Each fluid sample came from the same bottle. However, each subsequent sample had been subjected to a higher degree of mixing prior to testing, in order to see if this had any effect on the results. This was done by placing the fluid container on a paint shaker for various lengths of time making the fluid more homogenous. It appears to have done so, for on average the last test resulted in much higher τ_y values. In addition, for the last set of tests a new sample was used for each temperature. Once the fluid breaks down (around 2.5-3.0 kV) at high temperatures the fluid may be damaged (some partial chains may fuse together). At the end of a test run, the fluid was indeed found to be damaged. This was due to a current discharge at high voltages that fuses particles together into globules. In addition, it was evident that partial chains had sunk and settled on the bottom of the capstan. This was not expected to happen and may be due to the fluid being old and/or not totally dispersed.

Plastic-viscosity

Results for the plastic-viscosity (μ_e), at 25°C 30°C 40°C are shown in Fig. 3.40, Fig. 3.41 and Fig. 3.42 respectively. At 25°C and 30°C the results are reasonably consistent, although the discrepancy can be up to 50 mPa.s. However, at 40°C discrepancies of up to 150 mPa.s are seen.

Comparison with Manufacturers Results

A manufacturer's specification was available for comparison with the results taken at 40°C. The manufacturer's methods are questioned later (section 3.7). It is, however, possible to infer an estimation of τ_y from their data, and conclude that the values of μ_e are small and possibly negative. In Table 3.5 the manufacturer's data is seen to favourably compare with the constant-stress viscometer results.

Excitation	Manufacturer's Data	Constant Stress Rheometer
kV/mm	Pa	Pa
1.5	700	750
2.0	1100	1300
2.5	1600	1800
3.0	2100	2300

Table 3.5: Comparison of rheometer yield-stress values to the manufacturer's data.

Concluding Comments

The method seems reasonable for obtaining typical values of τ_y . However, the results for μ_e are too scattered to be of any real use in a program that is supposed to predict accurate performance. The idea of a negative plastic-viscosity is also disconcerting and will need to be investigated.

In the absence of any other accurate data, the results are of some use. The final set of data should be assumed the best set of data (Fig. 3.35, Fig. 3.36). This set had the maximum amount of pre-shaking and a new sample was used at each temperature (i.e a fluid sample that may have been damaged at high voltage was not subsequently used for the next temperature range).

3.6.4 Conclusion

These results were based upon a relatively limited knowledge of rheometry that was acquired from a combination of studying the literature and some basic practical experience. However, if in the future it becomes necessary to consider the more complex time-dependent behaviour, it will be necessary to work with experts in the field.

The characterisation of the ER fluid using a specifically designed test facility provided mixed results. The results agree approximately with the manufacturer's data for basic values of yield-stress. However, the data is not consistent enough to be used in CFD pre-prototyping methodology, particularly for values of plastic-viscosity. It is now proposed that a better type of rheometer could be based on the form of a radial plate device.

3.7 Inter-Changeability of Smart Fluid Data and Negative Plastic-Viscosity

This section tackles the problem of inter-changeability of fluid data obtained from different devices. In addition, the concept of a negative value of plastic-viscosity (μ_e) is investigated. Such values were obtained for an ER fluid in the constant stress rheometer detailed in section 3.6.

At first sight, provided μ_{mn} remains positive, the concept of a negative value of μ_e may seem feasible (Fig. 3.43). In conventional terms, we have a situation in which the shear-rate ($\dot{\gamma}$) actually decreases as the shear-stress (τ) is increased. This is a confusing concept. Alternatively, shear-stress reduces as the shear-rate is increased. This makes some sense; maybe as $\dot{\gamma}$ increases, the fluid structure resisting flow could be breaking down, thus reducing its ability to resist load.

The point can be made that flow will not occur when $\tau < \tau_y$, and therefore, μ_e cannot be negative [43]. However, one also could argue that this need only be the case for flow to be initiated.

3.7.1 Numerical Algorithm to Correct non-Bingham Plastic Behaviour

If the CFD pre-prototyping methodology for smart fluids is to be effective, then fluid data from one type of rheometer should match that from another. For the Bayer 3635 ER fluid tested in section 3.1, the original manufacturers data is available. These data sets, obtained on a clutch and annular valve device, should correspond with one another. A study using the manufacturer's Bayer 3635 ER fluid data in [32] and a similar problem in [34] show that sets of data from a clutch and annular valve do approximately correspond. For this agreement to be evident the dimensional method employing He , Re and Cf outlined in section 2.6 is used. This procedure uses a numerical algorithm {eqn(2.30)} that effectively suggests that the fluids yield-stress becomes weaker with increased shear-rate. This loosely ties in with the idea that a smart fluid could have a negative value of μ_e .

It was suggested in [44] that a numerical algorithm {eqn(2.30)} is unique to an ER fluid and can thus be used to improve a CFD-based Bingham plastic constitutive model. The method requires a value of Re to be known, thereby allowing He and hence τ_y to be calculated. It is difficult to define Re on a cell-by-cell basis. Even defining an average Re value based on the overall geometry would be limited to only the simplest geometry. The suggestion in [44] is really a misconception based on a fundamental misunderstanding of how CFD works. In addition, the suggestion that a wall refinement technique is required is also a misunderstanding. Here concepts of convergence and cell aspect ratios have not been fully understood.

In a CFD based technique there is no need to assume $\mu_e = \mu_o$ and thus to convert values of shear-rate to Re , or values of τ_y to He . Doing so undermines the whole purpose of using CFD in the first place.

3.7.2 Inter-changeability of fluid data

Without employing the dimensionless procedure used in [32] the inter-changeability of the data from an annular clutch and valve device was investigated. The fluid data is the same as that used in [32] which uses the dimensional analysis procedure.

Cylindrical Clutch Data

Low shear-rate data at 40 °C was obtained by the manufacturer's (Bayer) using a small cylindrical Couette device [$r_2 = 11.2$ mm (stationary), $h = 0.55$ mm, $L = 32.3$ mm]. The data is presented by the manufacturer in the form of a flow curve data (i.e. τ vs. $\dot{\gamma}$) and was calculated using the following relationships:

$$\tau_w = N/2\pi r_2^2 L, \text{ and } \dot{\gamma} = \Omega r_1/h. \quad (3.27)$$

The shear stress would have been better derived using a mean radius ($r_m = r_1 + r_2$). Furthermore, the estimation of $\dot{\gamma}$ is only strictly valid if the fluid is fully sheared; this is not the case if wall plug is present. Using this information, a corrected τ vs. $\dot{\gamma}$ curve was calculated and is shown in Fig. 3.44.

By assuming a Bingham plastic form and that $\mu_e = \mu_o$ holds true, eqn(2.21) can be used to determine if any of the data is in the plug regime. In addition, eqn(2.23) can be used to calculate a value of τ_y for each data point. The procedure suggests that most of the data is in the plug regime (Fig. 3.44), which severely limits the usefulness of the data and indicates a degree of misunderstanding on the part of the manufacturers. Even worse, if $\mu_e < \mu_o$, as appears to be the case (Fig. 3.44), then all the data points could easily fall within the plug regime.

As reported in [32] the value of yield-stress does indeed appear to reduce with increased shear rate (Fig. 3.45). However, this is assuming that the ER fluid can be characterised using the Bingham plastic equation with $\mu_e = \mu_o$. Furthermore, eqn(2.23) that is used to calculate the τ_y is only valid for plug-less flow. Thus, it is not right to infer from these results that the yield-stress decreases with increased shear-rate. In fact, if μ_e was to be slightly smaller than μ_o then such an effect will be cancelled out.

Since most of the data (if not all depending on what value of μ_e is chosen) is in the plug regime it would appear the Couette data is of little use. However in section 3.2.3 a spreadsheet was created that calculated the torque profile in the plug regime. In a curve fitting exercise, using $\mu_e = 55$ mPa.s for all voltages, a value of yield-stress was chosen that allowed the Bingham plastic clutch theory to tie up with the clutch data on a reasonable basis (Fig. 3.44). The procedure is contentious, but no more so than the

methods used in [34].

In summary, the clutch data that appears to be mostly in the plug regime has been utilised to determine values of the τ_y at certain voltages. This was done using the Bingham plastic clutch theory with the assumption that $\mu_e = \mu_o = 55$ mPa.s.

Annular Value Data

High shear-rate was obtained at 40 °C by the manufacturer using a small annular value [$r_2 = 6.5$ mm, $h = 0.75$ mm, $L = 100$ mm]. Again, the data is presented by the manufacturer in the form of a flow curve data using the following relationships:

$$\tau_w = \Delta p \cdot h / 2L, \text{ and } \dot{\gamma} = 6\dot{q}/bh^2. \quad (3.28)$$

The method for determining stress is appropriate, but the method for determining $\dot{\gamma}$ can only really be applied to a Newtonian fluid. Equation (3.28) was used to reproduce the original valve data (Δp vs. \dot{q}). It should now be possible to use the Bingham plastic fluid data from the clutch to predict the valve data. Since the excitation values, used on both devices do not correspond, the following relationship was used to infer τ_y (Fig. 3.46):

$$\tau_y(\text{Pa}) = 387E^{1.49} \quad \text{note: } E (\text{kV/mm}) \quad (3.29)$$

For an ER fluid τ_y is usually a function of an E or E^2 {eqn(2.2)}. Here $E^{1.49}$ arises in order for the curve to fit the yield-stress values from the clutch data well, and is similar to that used in [34]. A linear curve is often used, however the manufactures data indicates the relationship is slightly non-linear, thus eqn(3.29) is believed to be a better means of inferring yield-stress at higher excitations.

Using the CFD valve model from section 3.3.1, with $\mu_e = 55$ mPa.s and eqn(3.29) values of pressure were calculated for given values of flow rate. The CFD results are compared to the experimental valve in Fig. 3.47.

Discussion of results

The agreement between the predicted valve results using the Bayer clutch fluid data and the actual experimental values are not perfect. However, the Bayer clutch data is considered to be mostly in the plug regime, the results are surprisingly good. Furthermore, the agreement is just as good as in [34]. Thus, there seems to be no need to consider the yield-stress to be shear-rate dependent using a numerical algorithm {eqn(2.30)}. Any indication that the yield-stress reduces is likely to be due to the plastic-viscosity being taken to equal non-field viscosity. Thus it is important to have

original Couette flow data that is of good enough quality (thus away from plug-regime) so that is possible to occur values of yield-stress and plastic-viscosity.

3.7.3 Negative Plastic-viscosity

Using the CFD models tested previously (section 3.3), the concept of a negative value of plastic-viscosity (μ_e) was investigated. Fig. 3.43 shows the flow curve of a Bingham plastic with a negative μ_e .

Perhaps a good way to understand this phenomenon is using the non-Newtonian viscosity concept, eqn(2.11), as used in the CFD approach. Fig. 3.43 indicates μ_{mn} at three different values of $\dot{\gamma}$. Here the consequence of a negative μ_e is to simply reduce μ_{mn} at a greater rate with $\dot{\gamma}$, than when μ_e is positive. A complication will arise when $\dot{\gamma}$ is large enough for μ_{mn} to become negative. This simply can never be the case, so it is assumed that at some stage the fluid will become sufficiently sheared such that any smart fluid effect is broken down and the fluids minimum viscosity is that when there is no-field:

$$\mu_{\max} = \mu_o. \quad (3.30)$$

Here we are no closer to understanding if a negative μ_e is allowed. The best way to proceed is to test the concept using previous CFD models.

Annular Valve with a Negative Plastic-viscosity

An annular valve for which the Bingham plastic solution {eqn(2.17)} applies can be investigated when the plastic-viscosity is negative. As demonstrated in Fig. 3.48, the flow rate approaches infinity as μ_e is reduced to zero. This is because when μ_e equals zero the shear-rate can increase with no increase in shear-stress.

A CFD model of a valve, known to be correct was used. The results obtained when $\mu_s = 100$ Pa are displayed in Fig. 3.48 for a 2 kPa fluid. When μ_e is positive, the CFD results fit the theory. When $\mu_e = 0$ Pa.s, the solution does not converge. The condition in eqn(3.30) was applied, and as shown in Fig. 3.48 a converged solution was obtainable for a value of $\mu_e = 0$ Pa.s. The model even works when μ_e is negative - the lower the value the weaker the fluid and the greater the flow rate.

Shear Flow between Flat Plates with Negative Plastic-viscosity

The annular valve problem is relatively complex. A simple shear flow between two plates was therefore investigated. A periodic condition is applied to a 50x10 grid of dimensions 2.5 mm by 0.5 mm. The bottom plate was set to move with speed 1.5 m/s,

which sets shear-rate of 3000 /s.

For a Bingham plastic fluid medium, the theoretical shear force is given by eqn(2.19). This equation seems to hold true when μ_e is negative, and is plotted in Fig. 3.49 for a 2 kPa fluid. Also shown in this figure are corresponding CFD solutions, which are in excellent agreement when μ_e is greater than or equal to zero. However, when μ_e is negative, the agreement is poor. A plug shaped velocity profile forms (shown in Fig. 3.50) whereas a linear shear profile is expected. If a linear profile is initialised then the solution agrees but then starts to diverge upon further iteration, indicating a clear problem. Various things were tried in order to eliminate potential causes. The grid size was investigated, periodic conditions were eliminated as a cause, alternative solution parameters were used, a concentric geometry was tested. However, the solution remained the same.

A further attempt to achieve the expected solution was carried out. The actual flow curve data dictated by the Bingham plastic equation was transformed into [μ_{mn} vs. $\dot{\gamma}$]. CFD requires the data to be in this form, and this is precisely what Fluent does upon solution. Power law curves were then used to match the data. Upon doing so it is difficult to tell which power law curves were derived using negative or positive values of μ_e . One thing that is for certain, is that solutions derived using a positive plastic-viscosity give the expected solution, and ones with a negative plastic-viscosity still give the same unexpected solution as before.

3.7.4 Conclusion

The validity of a negative plastic-viscosity, suggested by the constant stress viscometer results (section 3.6), was scrutinised. A practical dimensional approach suggests a negative value may be plausible - with increased shear-rate the structure may be breaking down and thus the shear-stress it can support is reduced. However, this may be due to the plastic-viscosity (μ_e) being taken to equal the no-field value (μ_e).

Mathematically the concept of a negative μ_e is not plausible. For flow to occur τ must be greater than τ_y . Thus at this stage it is implausible to derive analytical equations using negative values of μ_e . For analytical work to be used to verify CFD results, μ_e will have to remain positive.

It can be concluded that for the simplest shear flow CFD does not appear to be compatible with the concept of a negative plastic-viscosity. If the actual shear-stress falls with increased shear-rate, then the solution appears to always diverge, whichever equation is used. This may be due to the concept being fundamentally flawed.

Alternatively, the CFD package in its current form may not be able to handle the idea and thus may need modifying.

To fully understand this perplexing problem, more consideration is required. The plastic-viscosity is only significant in smart fluid devices that exhibit a relatively high shear-rates such as in an annular valve. As a result it was decided that time was best utilised elsewhere. As a result the debate is still open, however I suspect that the problem lies with the use of the Bingham plastic model in rheometer procedure, and that negative values are impossible.

3.8 Summary: Feasibility Study

There appears to be no problem in solving basic steady state 1D smart fluid problems. There may be an issue with computing time for more complicated flows, especially if pressure boundary conditions are used. A specific ER fluid rheometer provided realistic ER fluid results. However, these results are deemed not to be very accurate. Perhaps a radial plate rheometer would be the best way forward, as suggested in section 2.5.2. Some major issues have been tackled involving the concept of a negative plastic-viscosity.

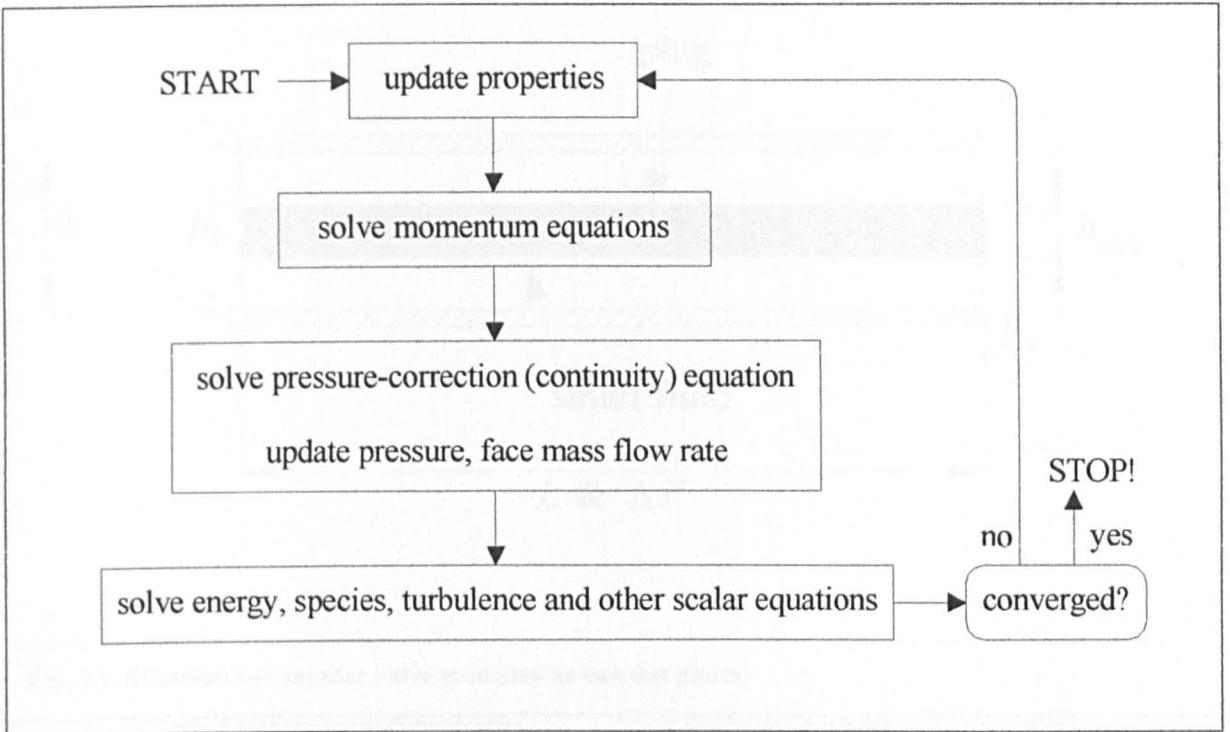


Fig. 3.1: Overview of segregated solution method used in Fluent4 and Fluent5.

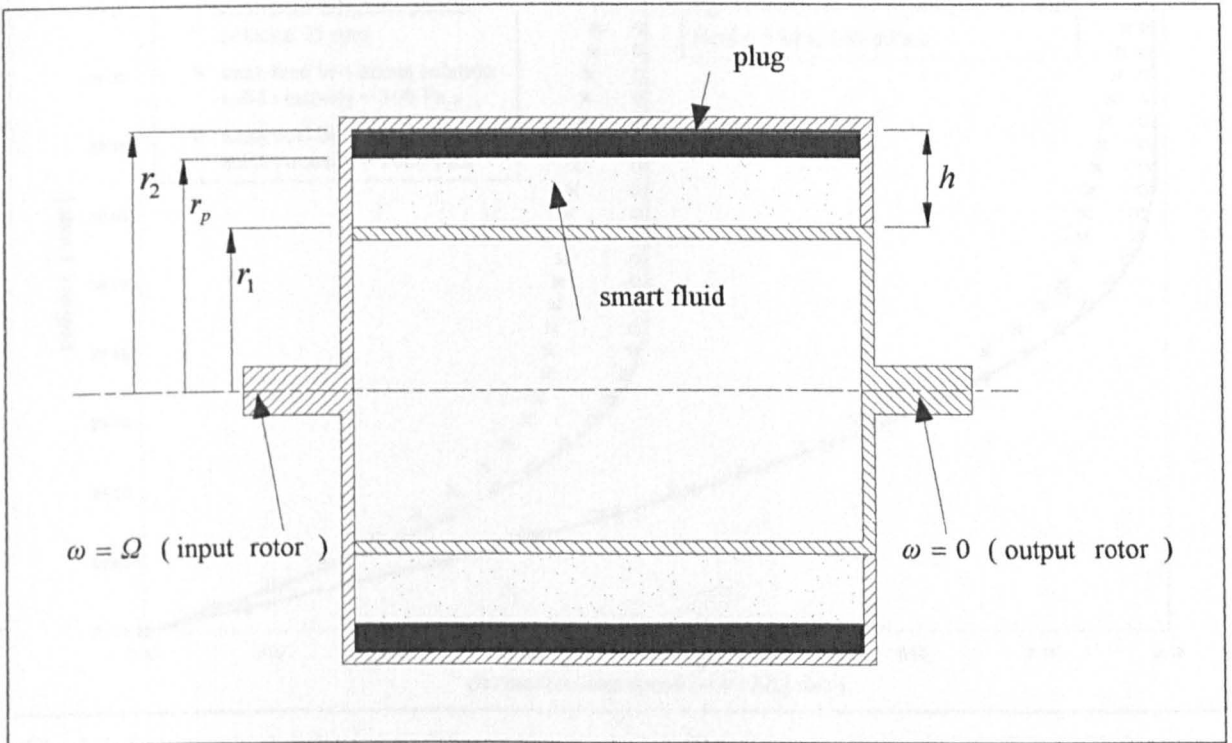


Fig. 3.2: Schematic of concentric clutch with a plug formation.

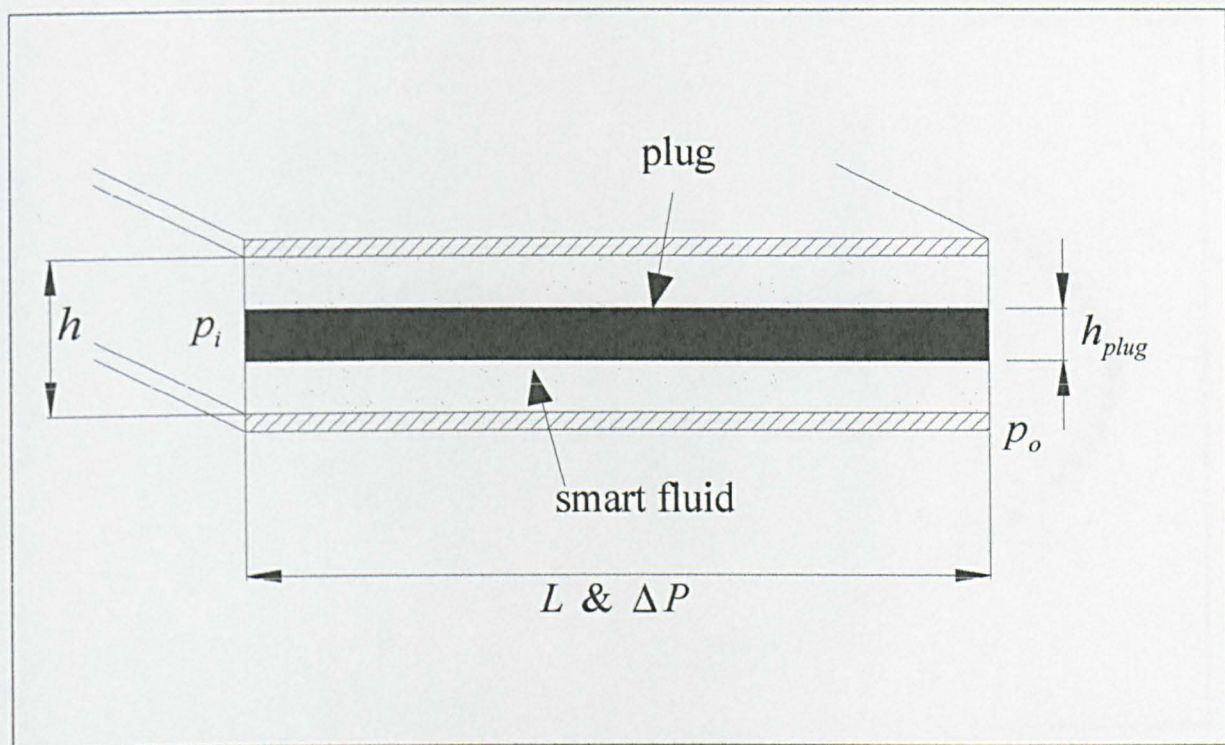


Fig. 3.3: Schematic of annular valve modelled as two flat plates.

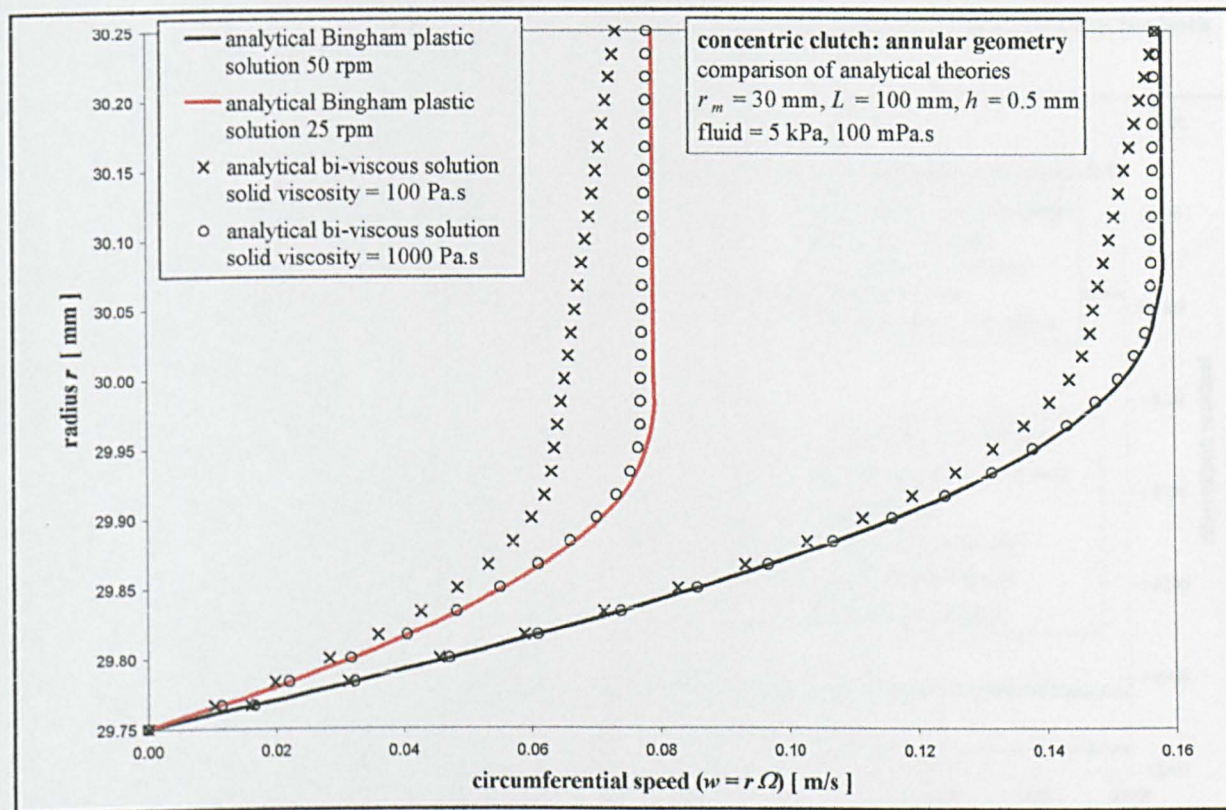


Fig. 3.4: Concentric clutch model with annular geometry. Comparison of velocity profiles at 25 & 50 rpm for both bi-viscous vs. Bingham plastic equations. The speed is low enough for plugs to form on the outer rotor.

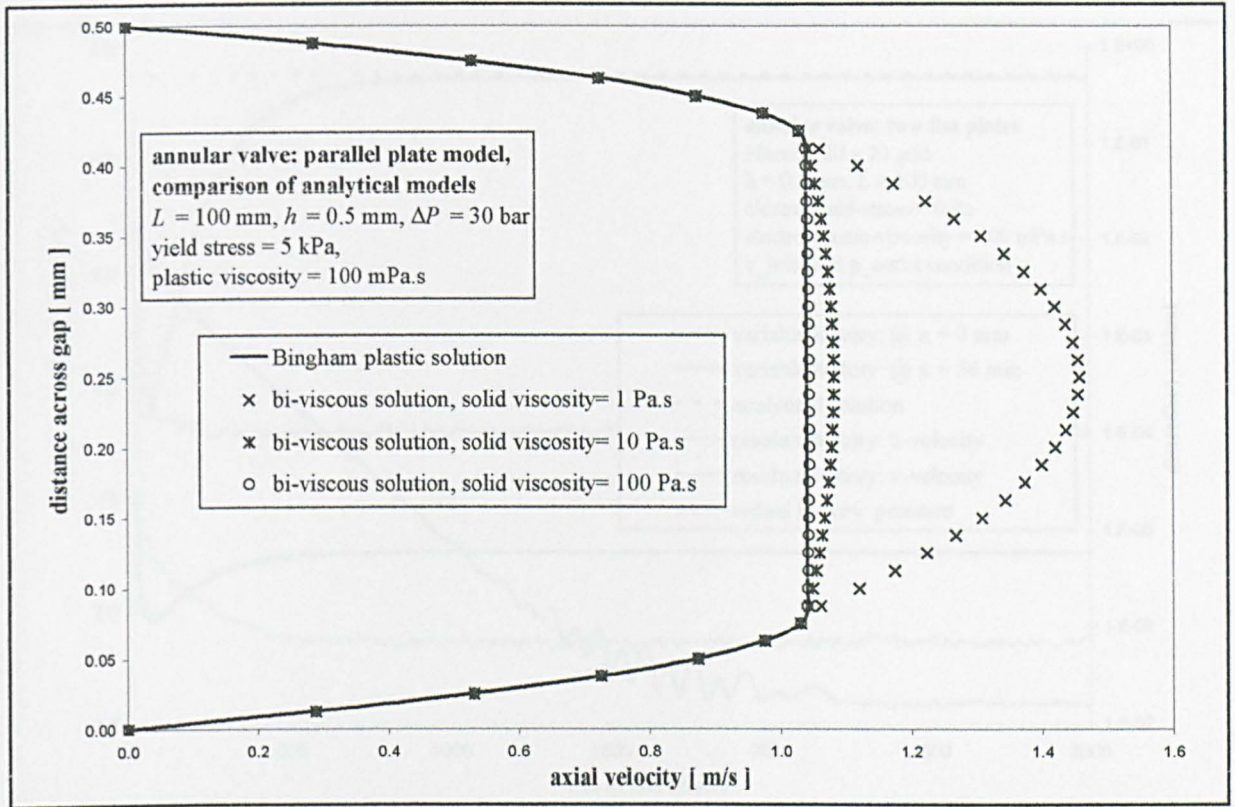


Fig. 3.5: Annular valve modelled as flow between flat plates. Comparison of velocity profiles for both bi-viscous vs. Bingham plastic equations.

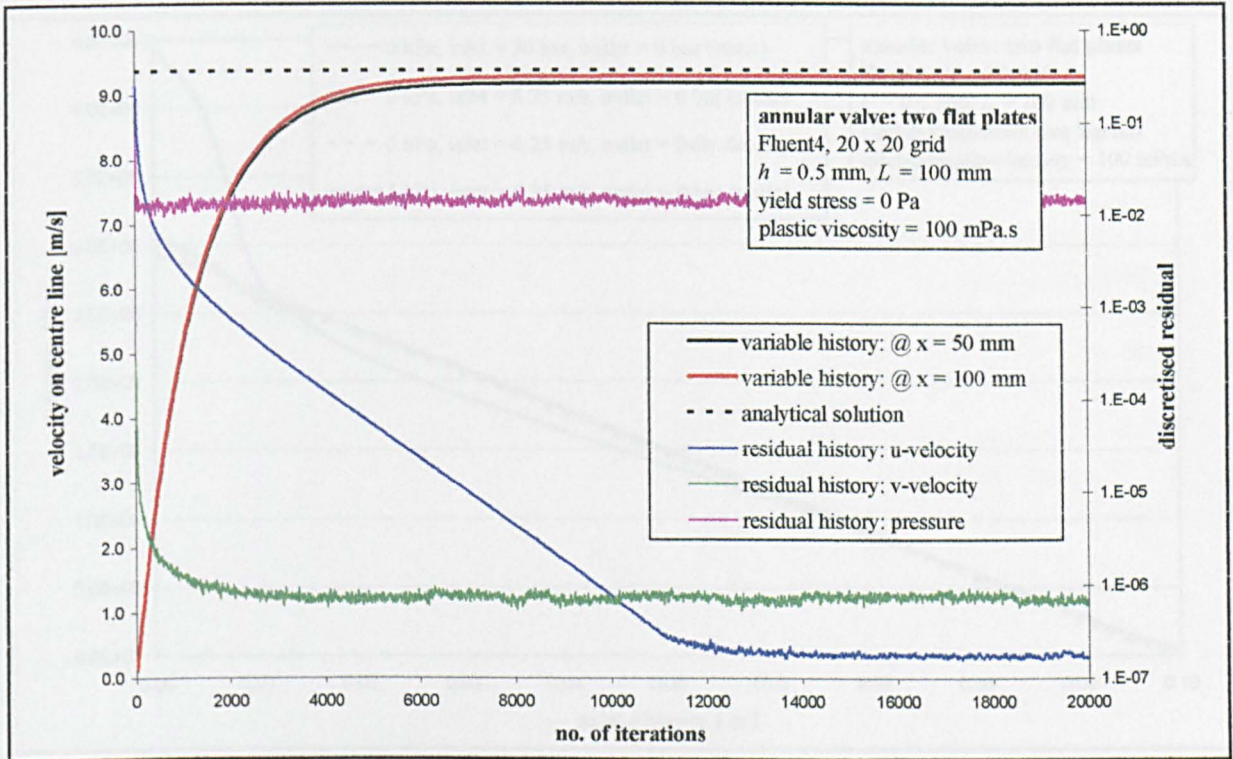


Fig. 3.6: CFD annular valve modelled as two flat plates with Newtonian fluid medium. Convergence test when pressure boundary conditions are used.

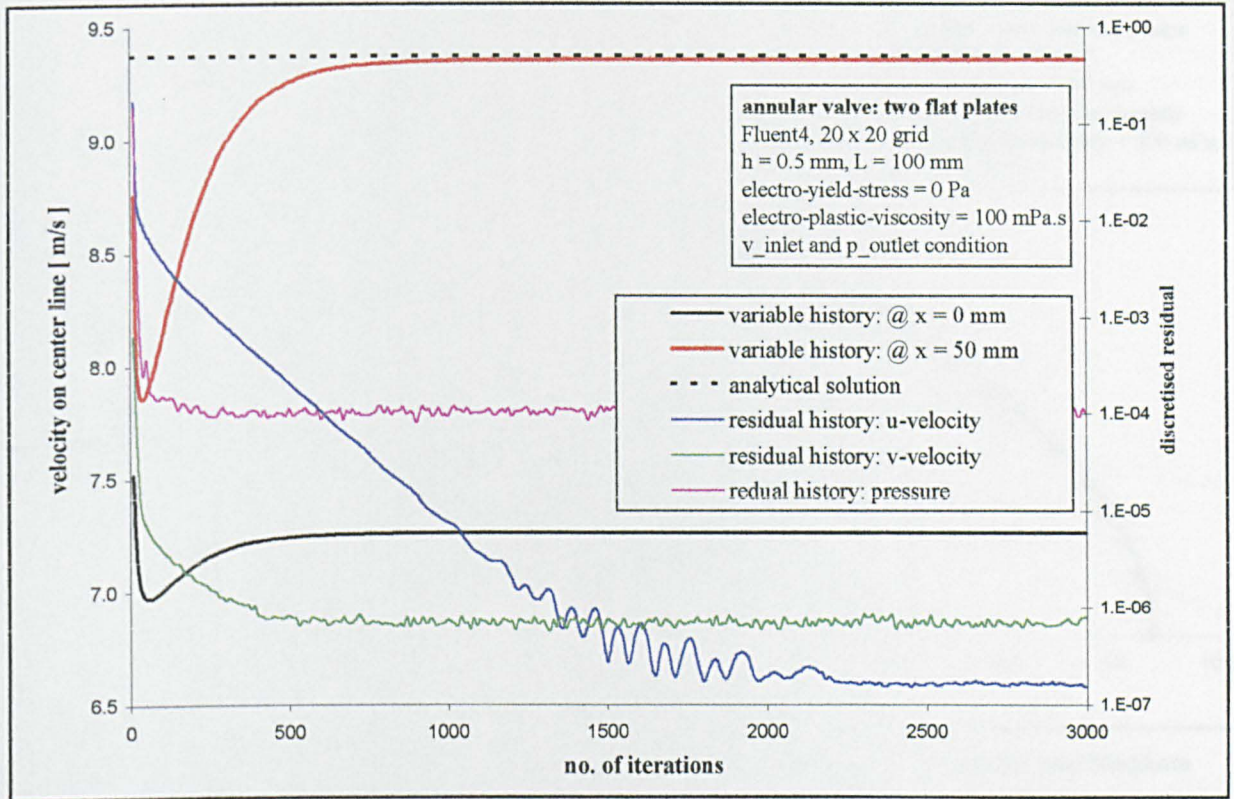


Fig. 3.7: Annular valve modelled as two flat plates. Newtonian fluid medium. Convergence test when a uniform inlet velocity and a pressure outlet boundary condition are used.

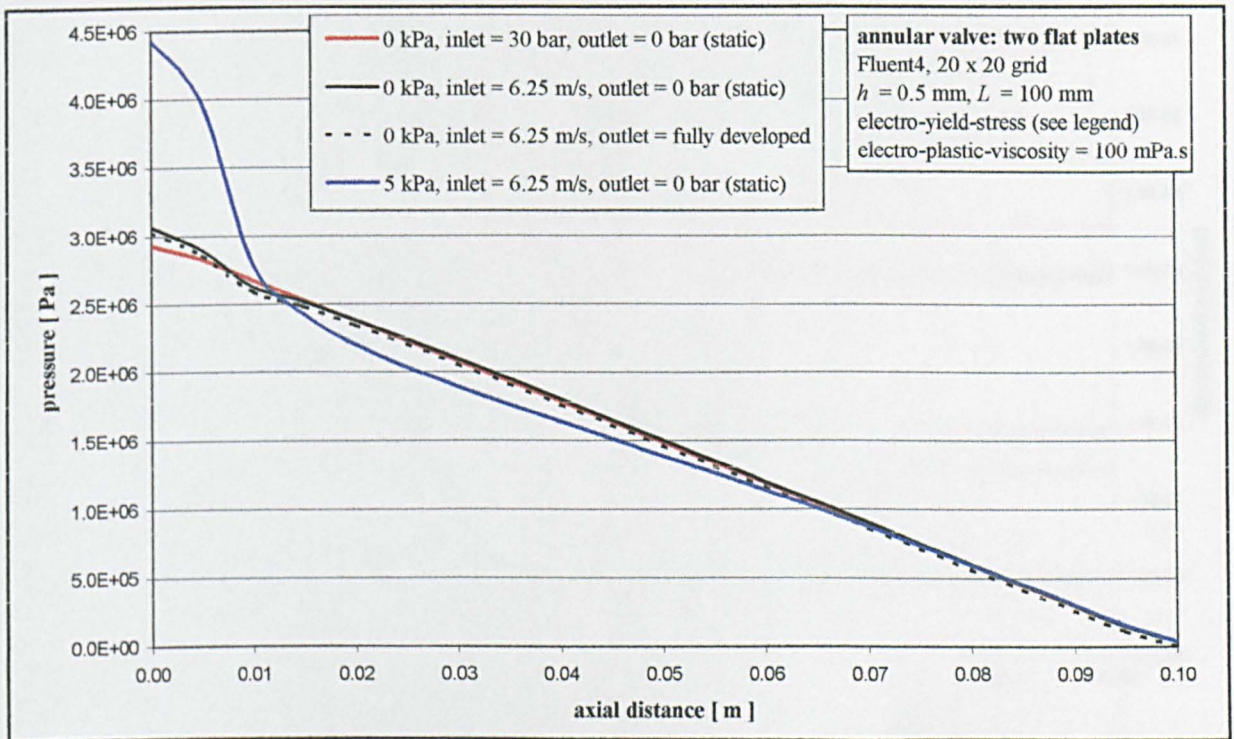


Fig. 3.8: Annular valve modelled as two flat plates. Pressure profile along symmetry line for the different methods of applying boundary conditions.

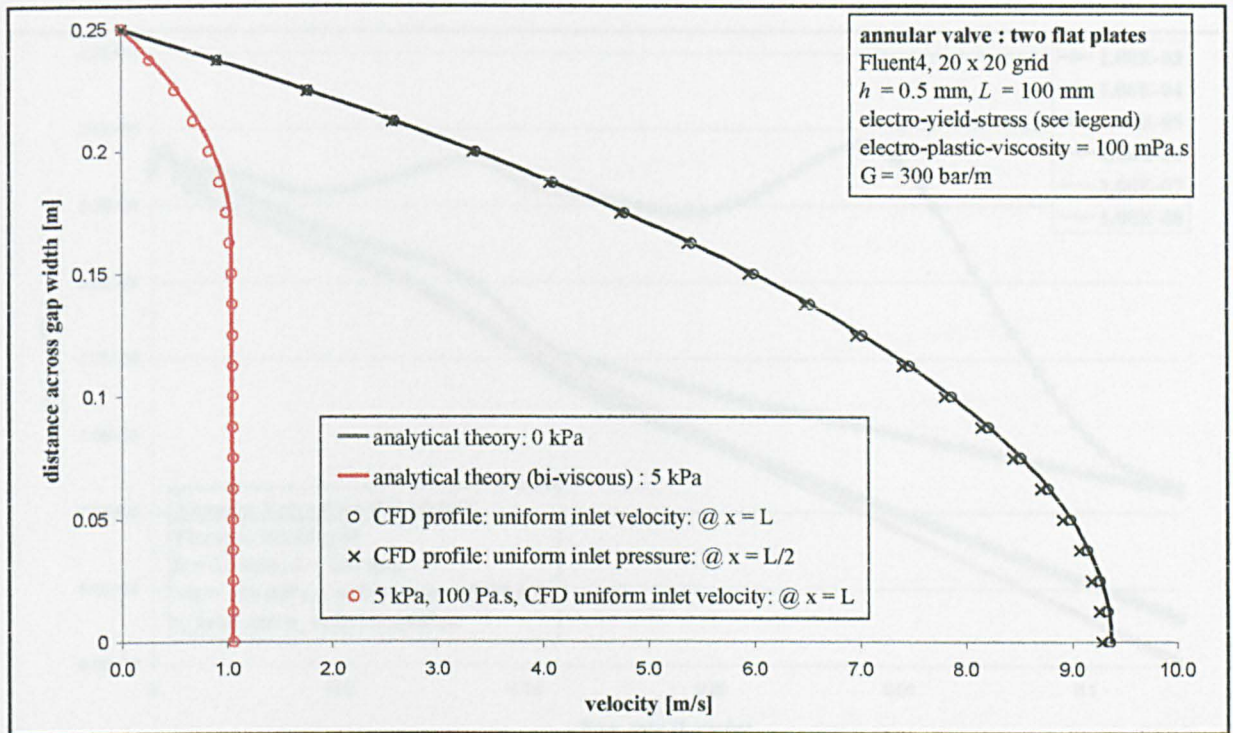


Fig. 3.9: Annular valve modelled as two flat plates. Velocity profiles for a Newtonian and Bingham plastic fluid medium compared with the analytical profile.

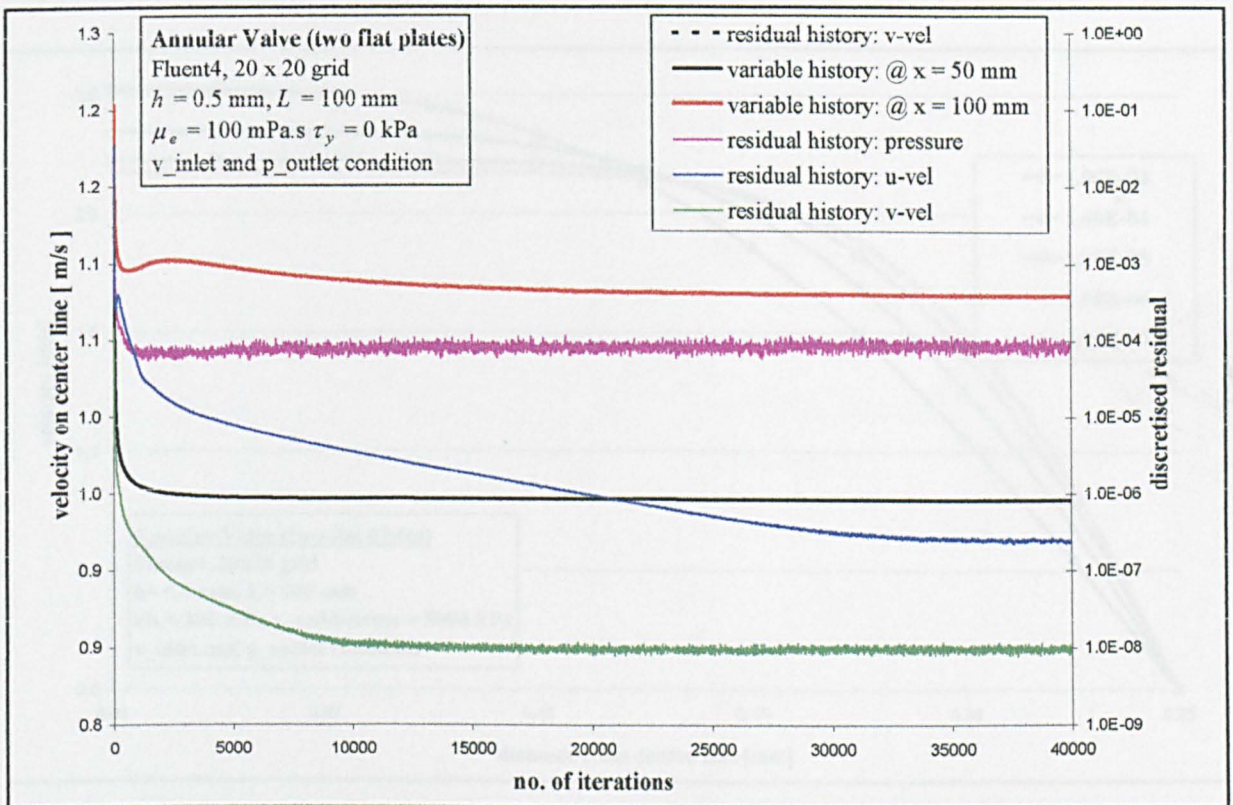


Fig. 3.10: Annular valve with Bingham fluid medium modelled as two flat plates. Convergence test when a uniform inlet velocity and a pressure outlet boundary condition are used to set the flow-rate.

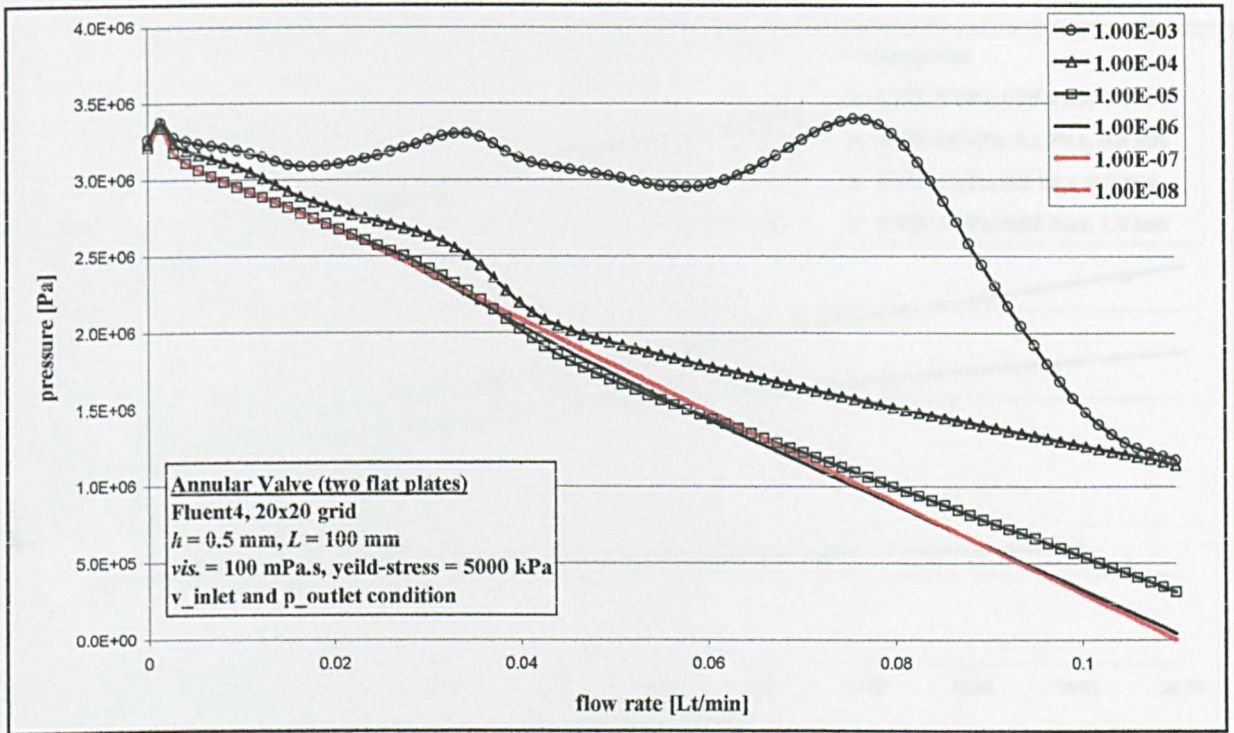


Fig. 3.11: Annular valve modelled as two flat plates. Bingham fluid medium. Convergence test: pressure on the centre line during convergence.

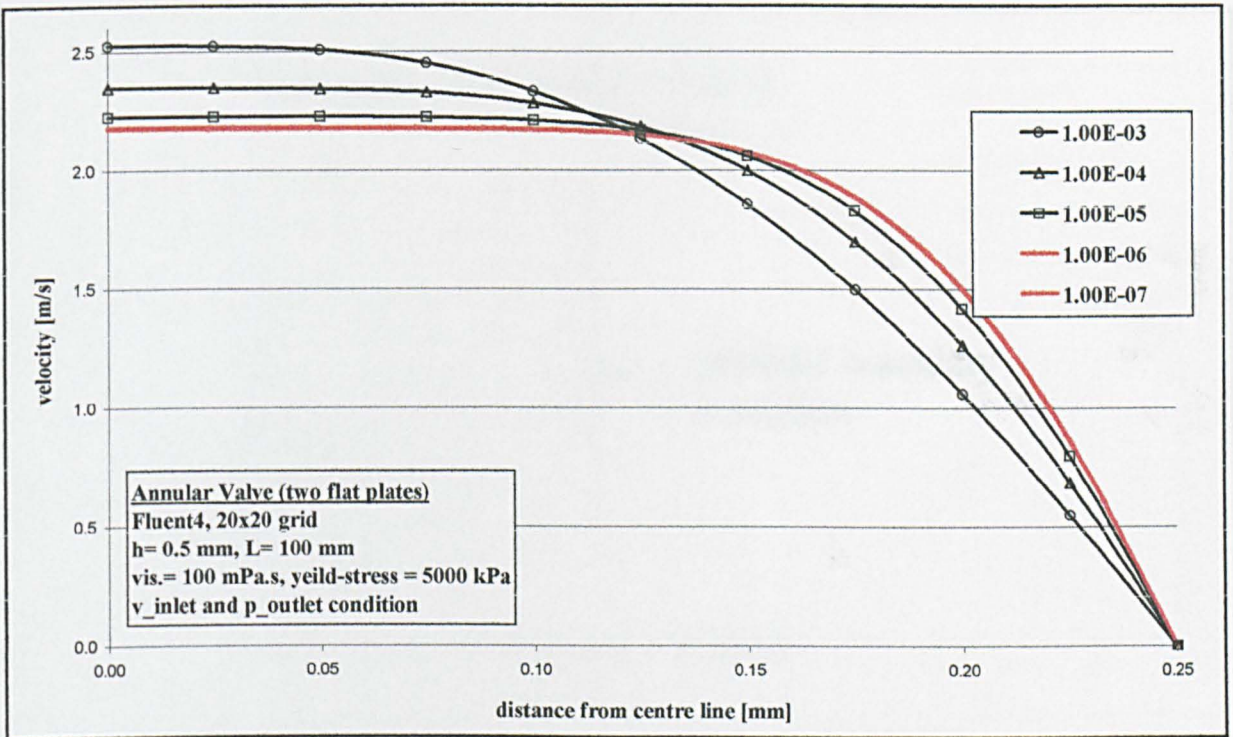


Fig. 3.12: Annular valve modelled as two flat plates. Bingham fluid medium. Convergence test: velocity profile at outlet during convergence.

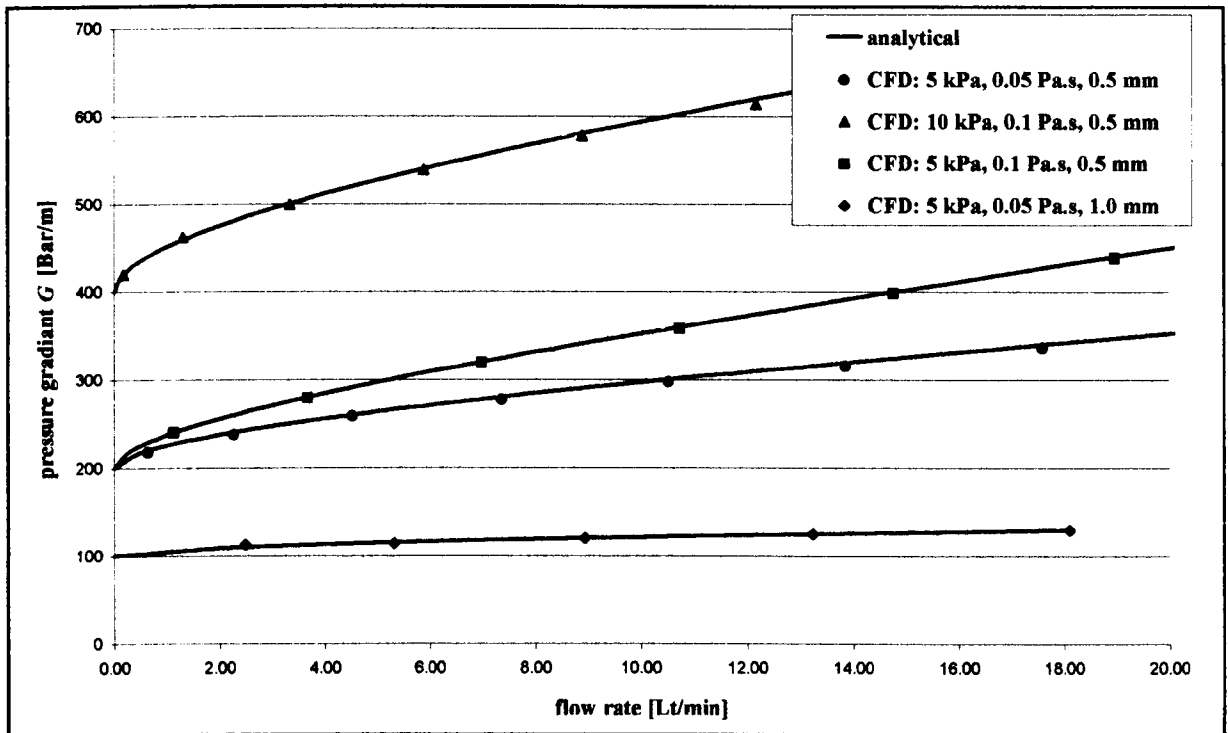


Fig. 3.13: Annular valve with Bingham fluid medium modelled as two flat plates. CFD comparison with analytical theory for a variety of parameters.

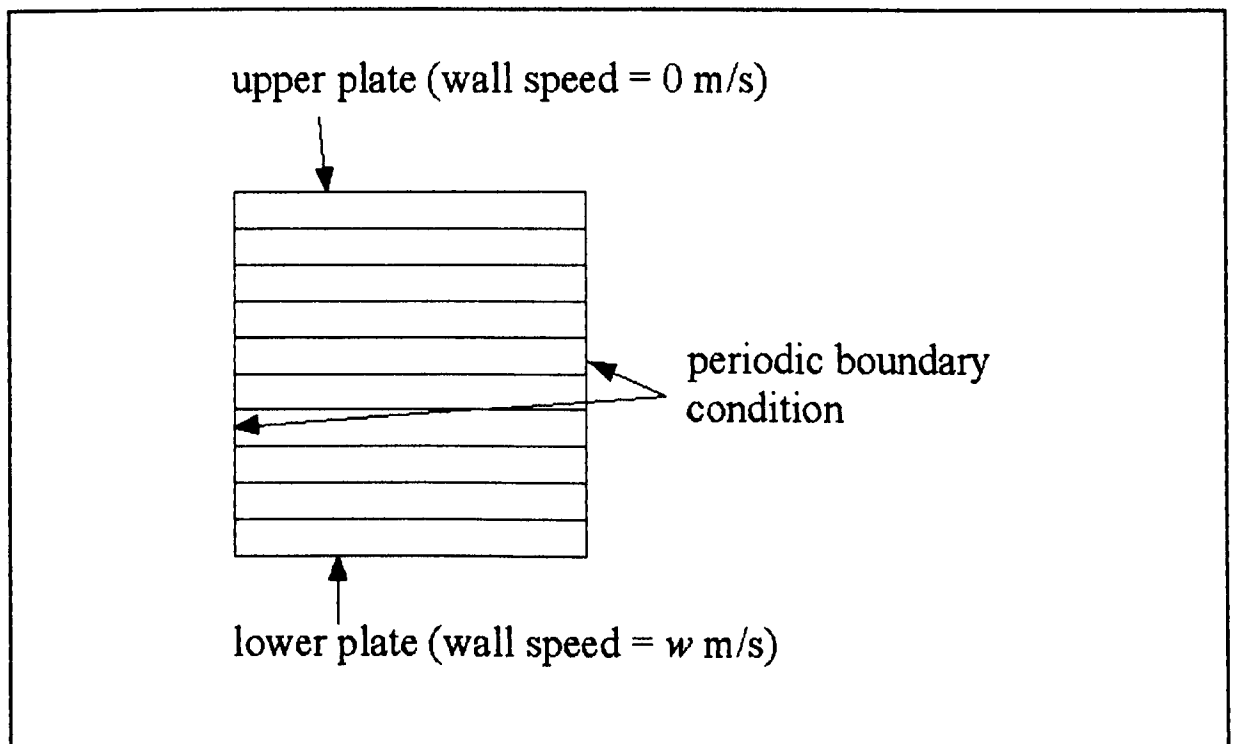


Fig. 3.14: Schematic of CFD model for concentric clutch, 1 x 10 cells

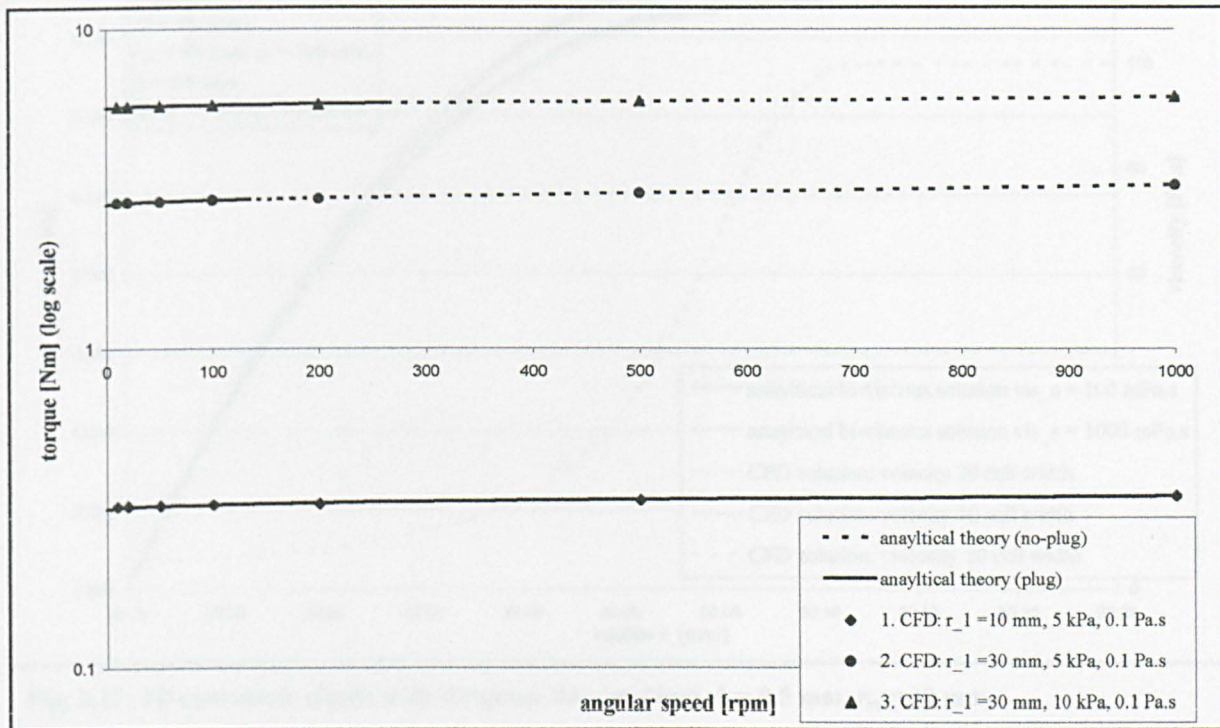


Fig. 3.15: 1D Bingham flow in concentric clutch. $h = 0.5 \text{ mm}$, $r = r_m$, $\mu_s = 1000 \text{ Pa}$.

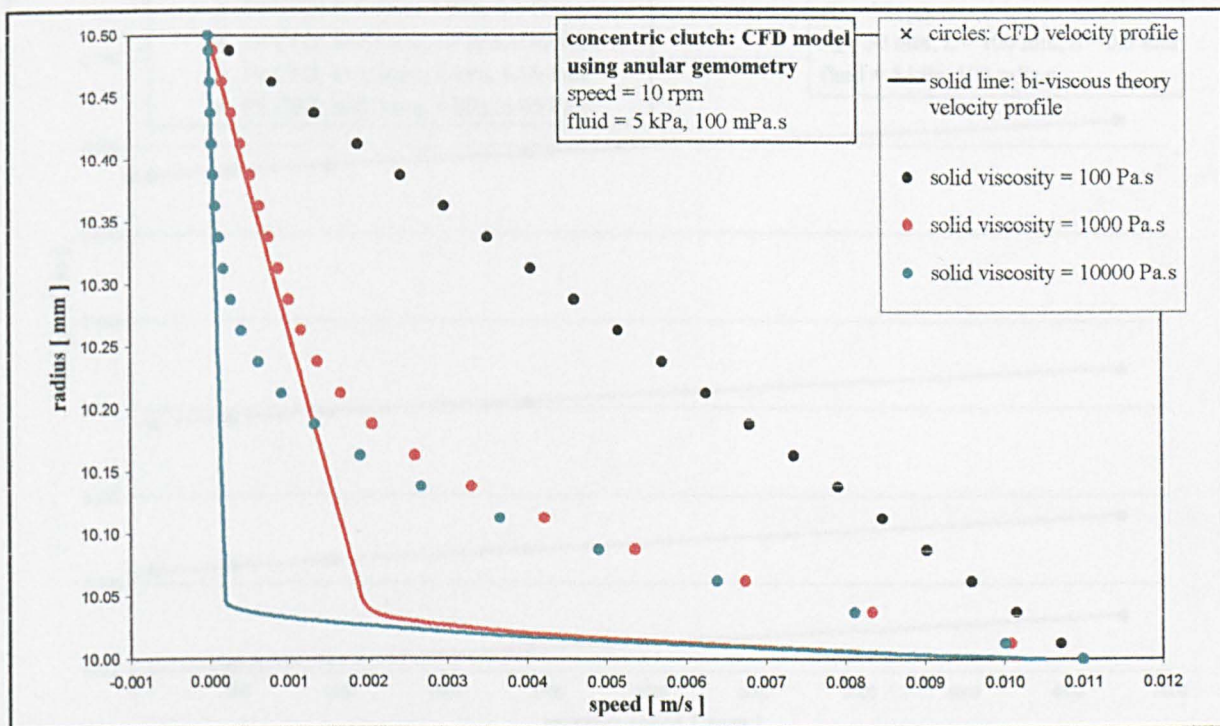


Fig. 3.16: Concentric clutch using Bingham CFD model. Here the CFD profiles become more plug like as μ_s is increased, but do not agree with theory. $r_I = 10 \text{ mm}$ at 10 rpm.

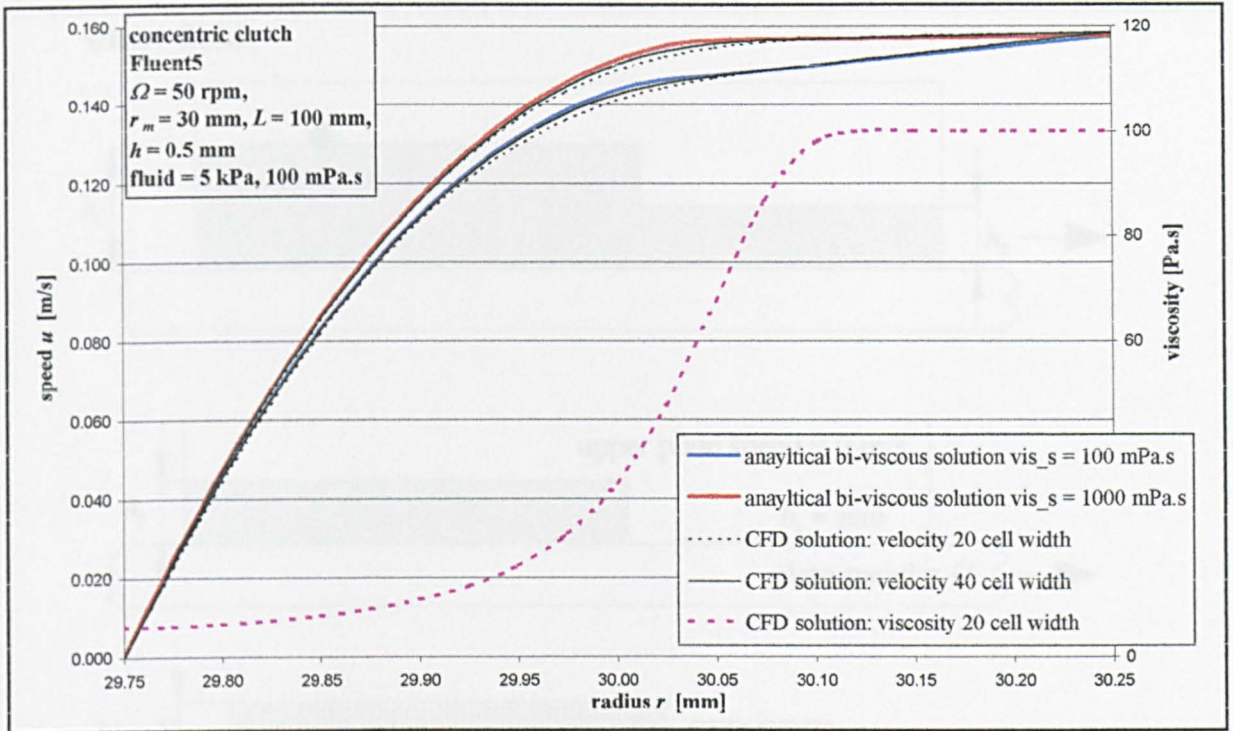


Fig. 3.17: 1D concentric clutch with Bingham flow medium. $h = 0.5$ mm, $r_m = 30$ mm.

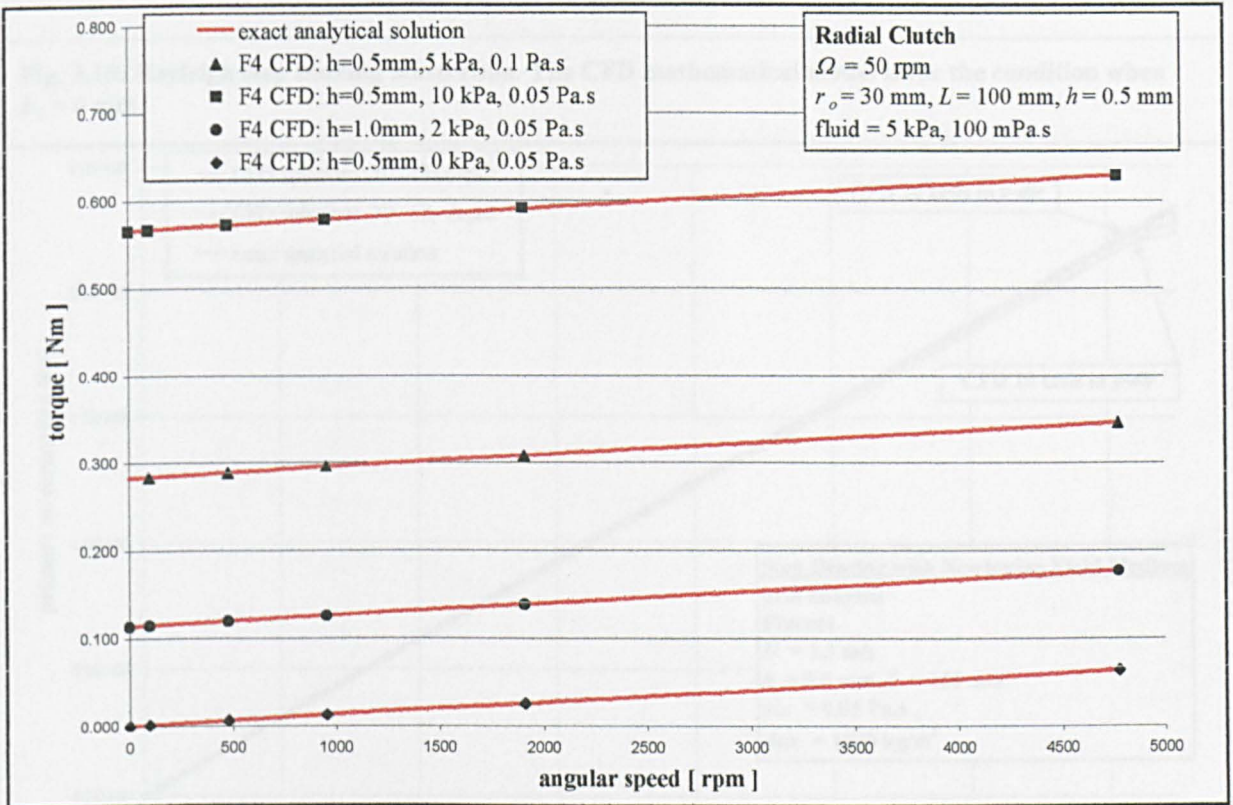


Fig. 3.18: 1D radial clutch with Bingham flow medium. Here the Fluent4 CFD predictions for torque (N) agree with analytical theory. $h = 0.5$ mm, $r_o = 30$ mm.

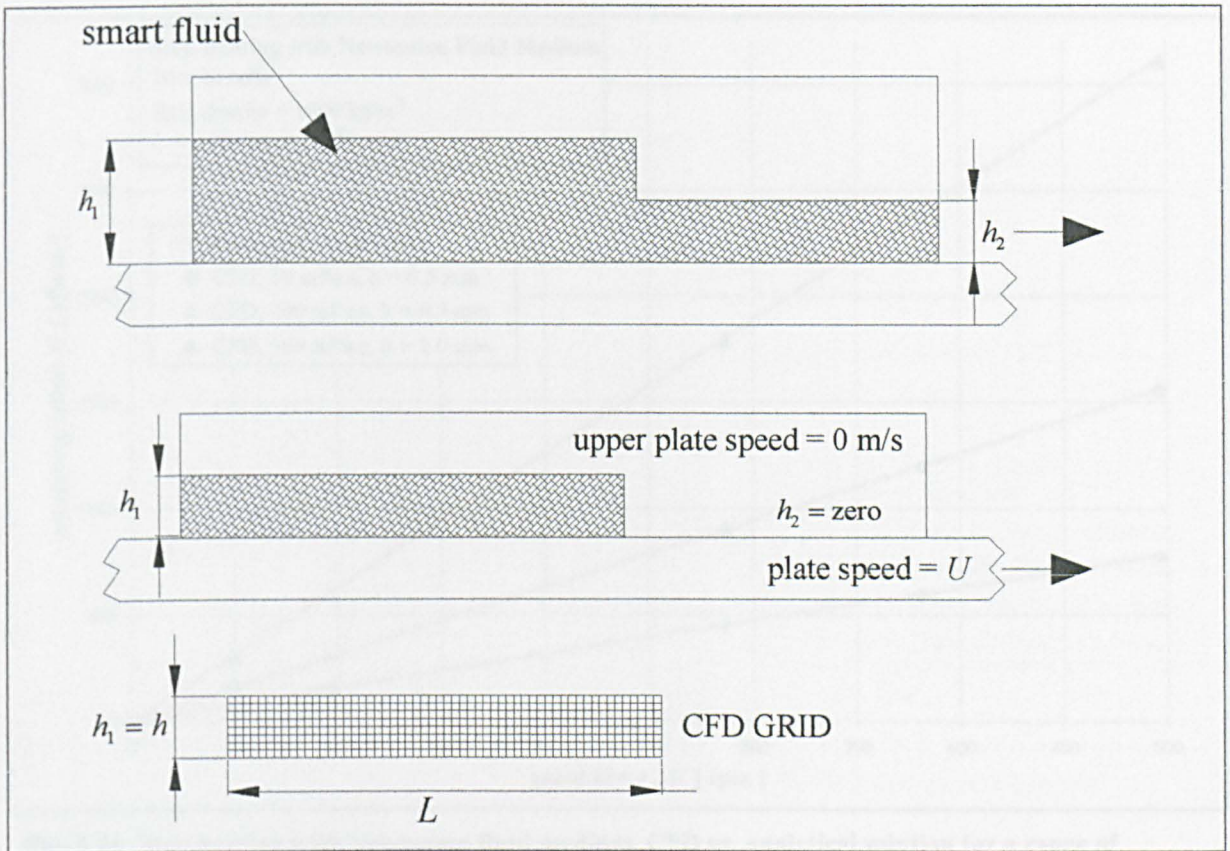


Fig. 3.19: Rayleigh step bearing illustration. The CFD mathematical model is for the condition when $h_2 = 0 \text{ mm}$.

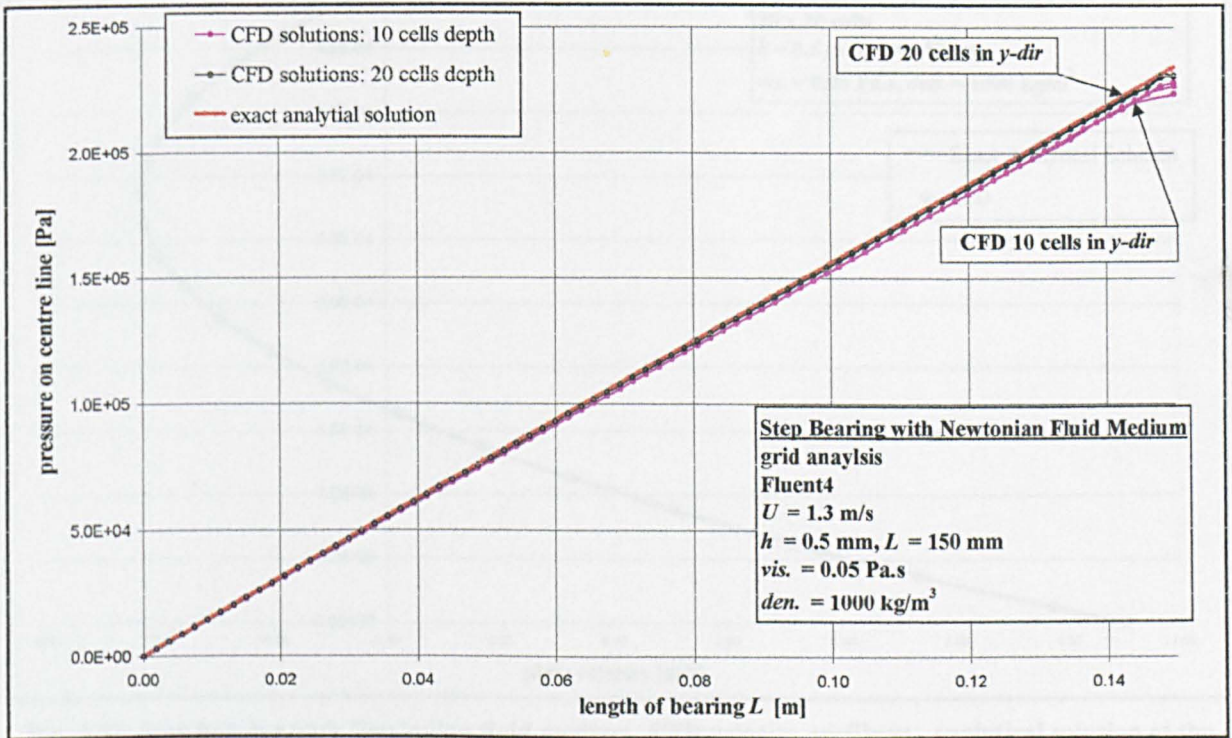


Fig. 3.20: Rayleigh step bearing with Newtonian fluid medium. CFD grid analysis.

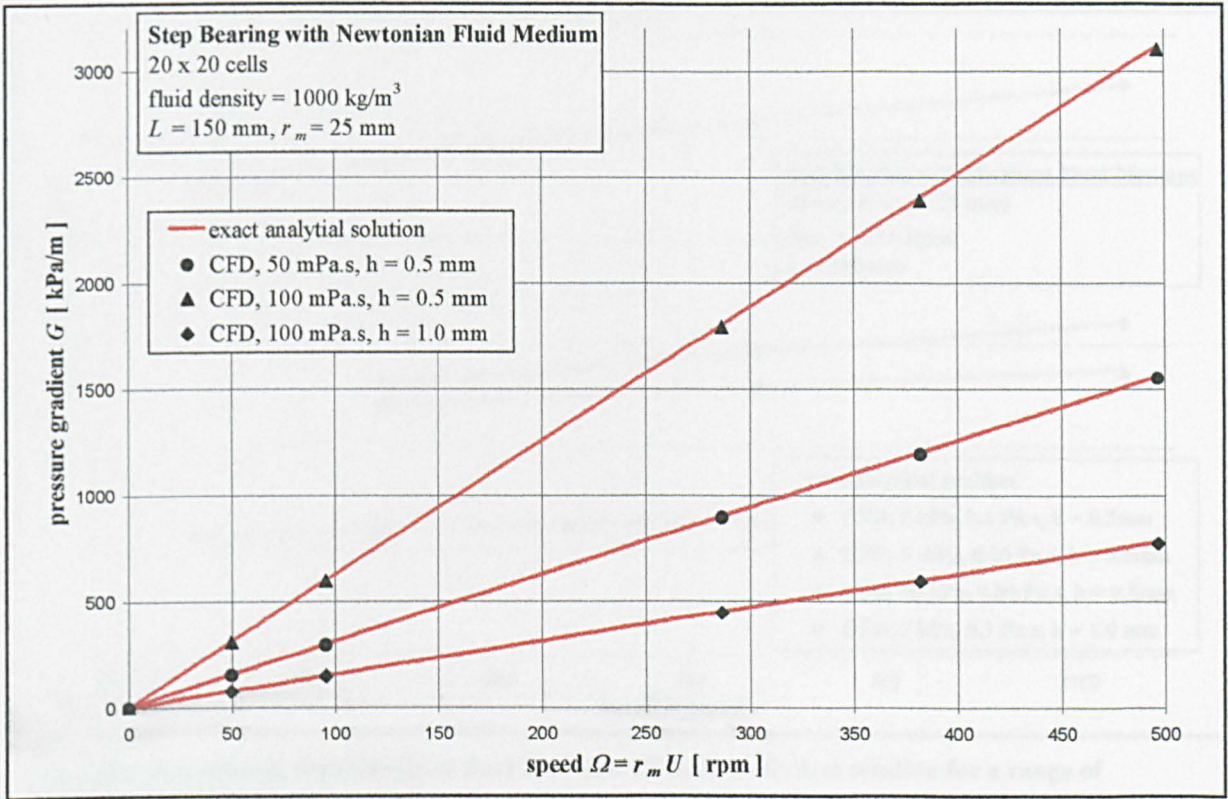


Fig. 3.21: Step bearing with Newtonian fluid medium. CFD vs. analytical solution for a range of parameters.

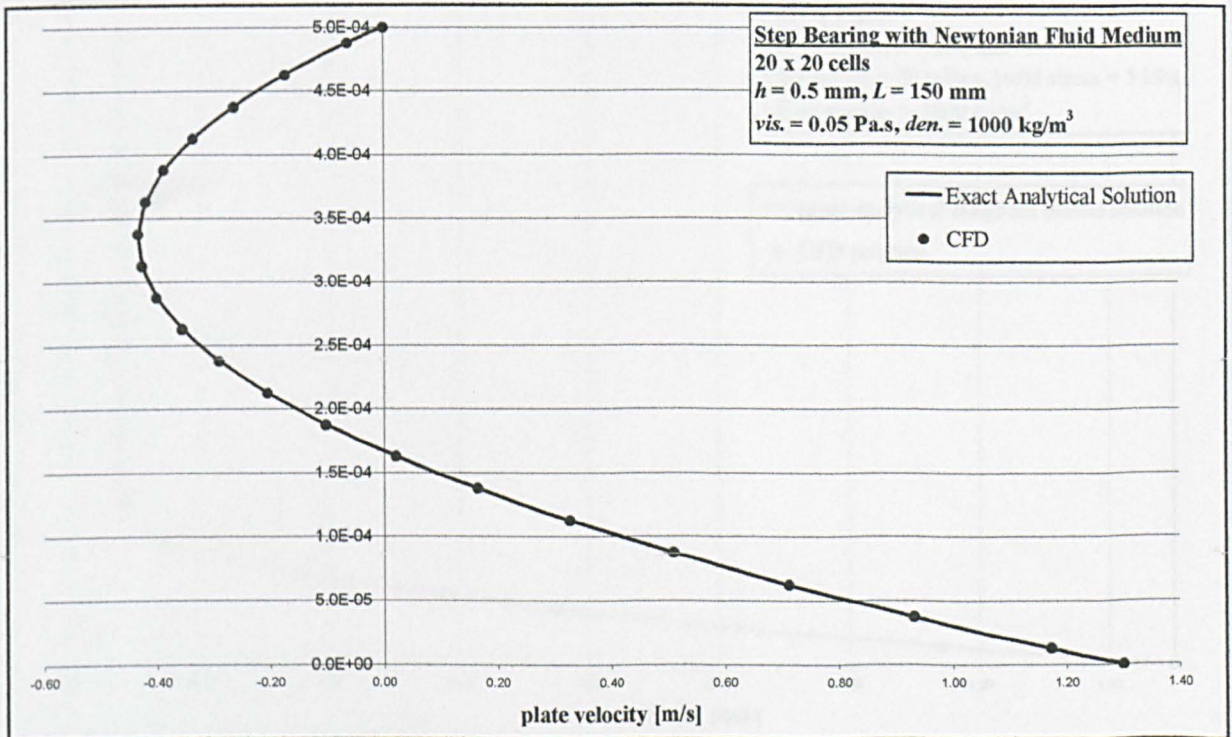


Fig. 3.22: Step bearing with Newtonian fluid medium. CFD velocity profile vs. analytical solution at the inlet to the bearing. The net flow-rate is zero.

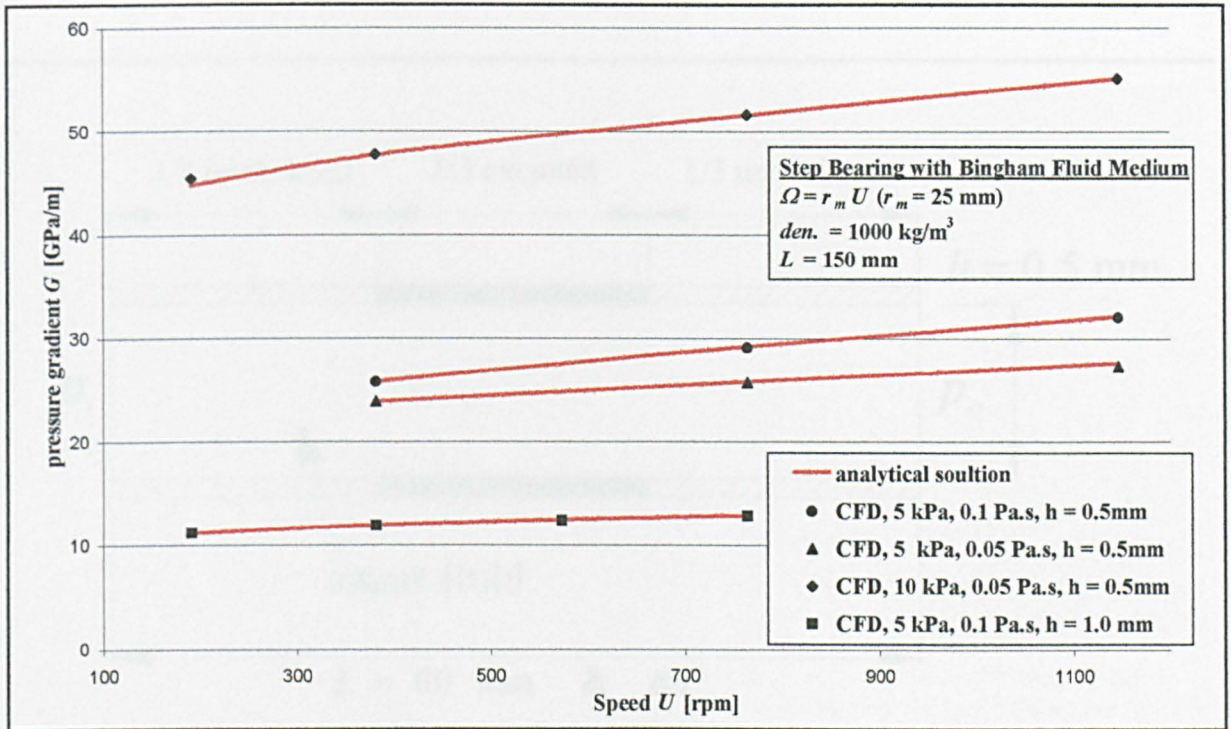


Fig. 3.23: Step bearing with Bingham fluid medium. CFD vs. analytical solution for a range of parameters.

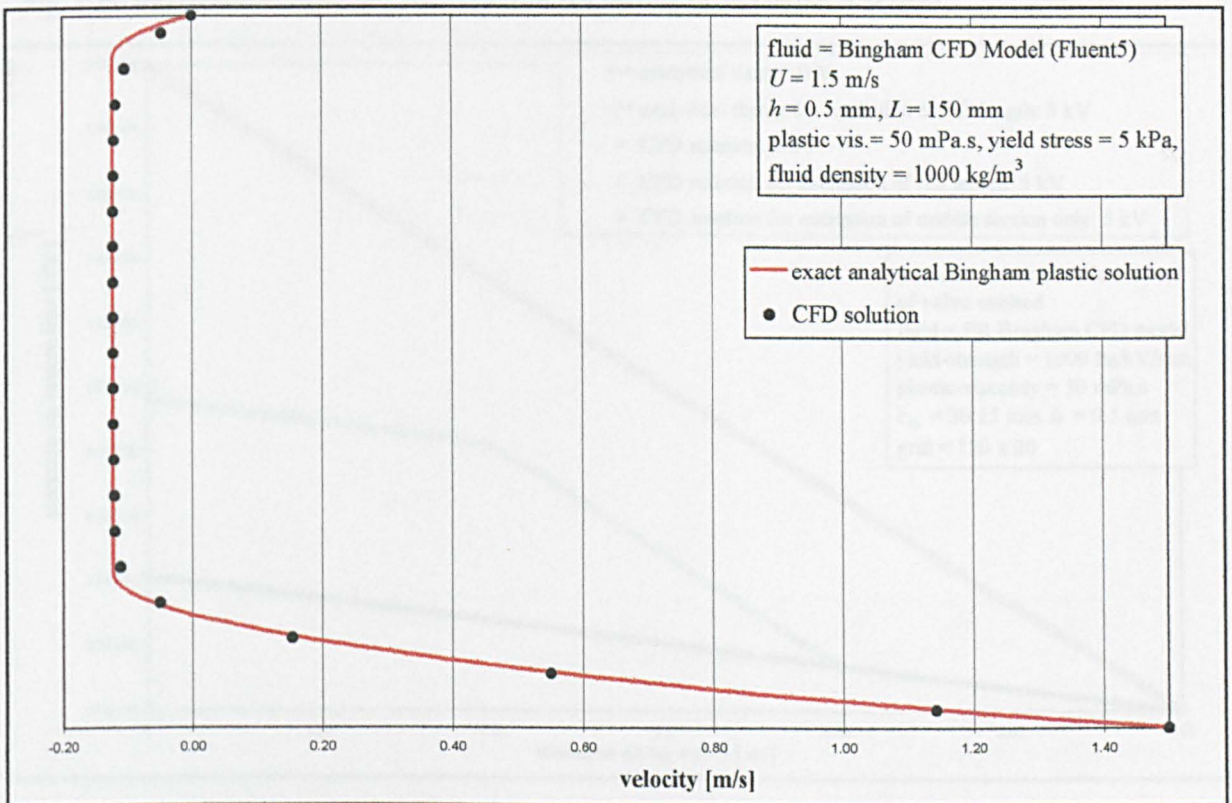


Fig. 3.24: Step bearing with Bingham fluid medium. CFD vs. analytical velocity profile. For large plugs more cells will be required near the walls.

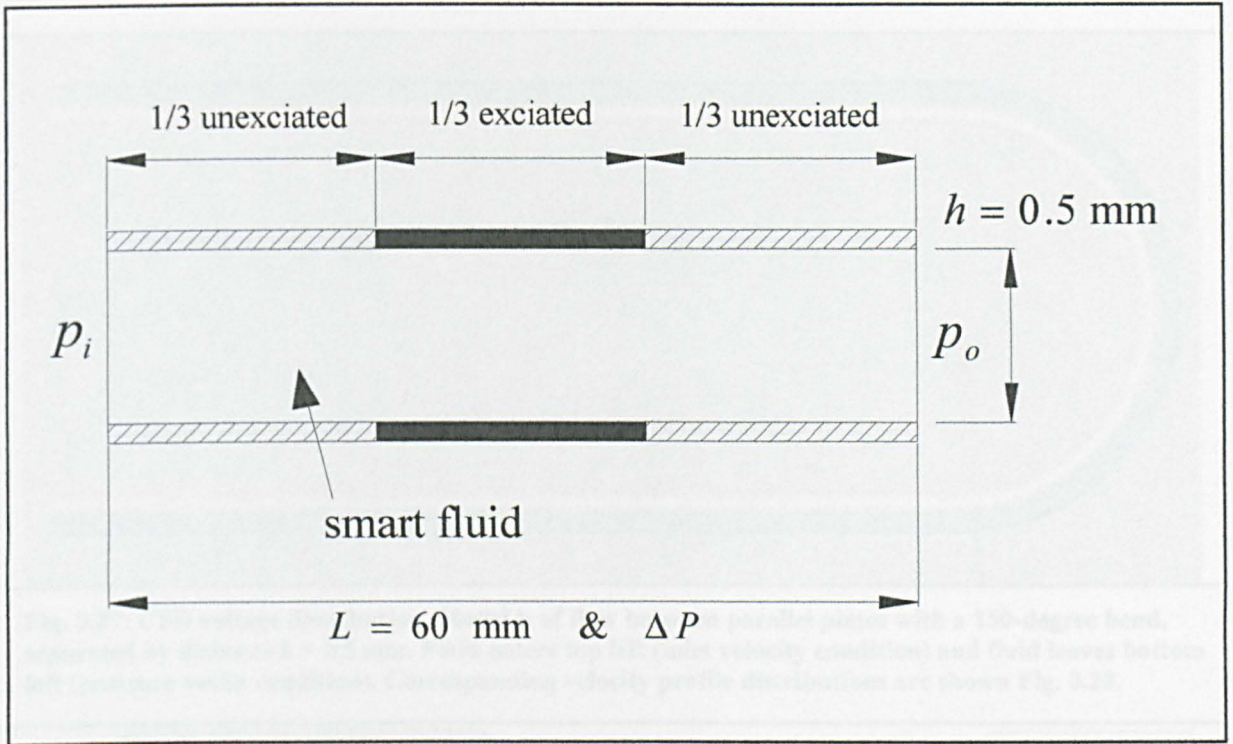


Fig. 3.25: Schematic of annular valve in which the middle third section is excited.

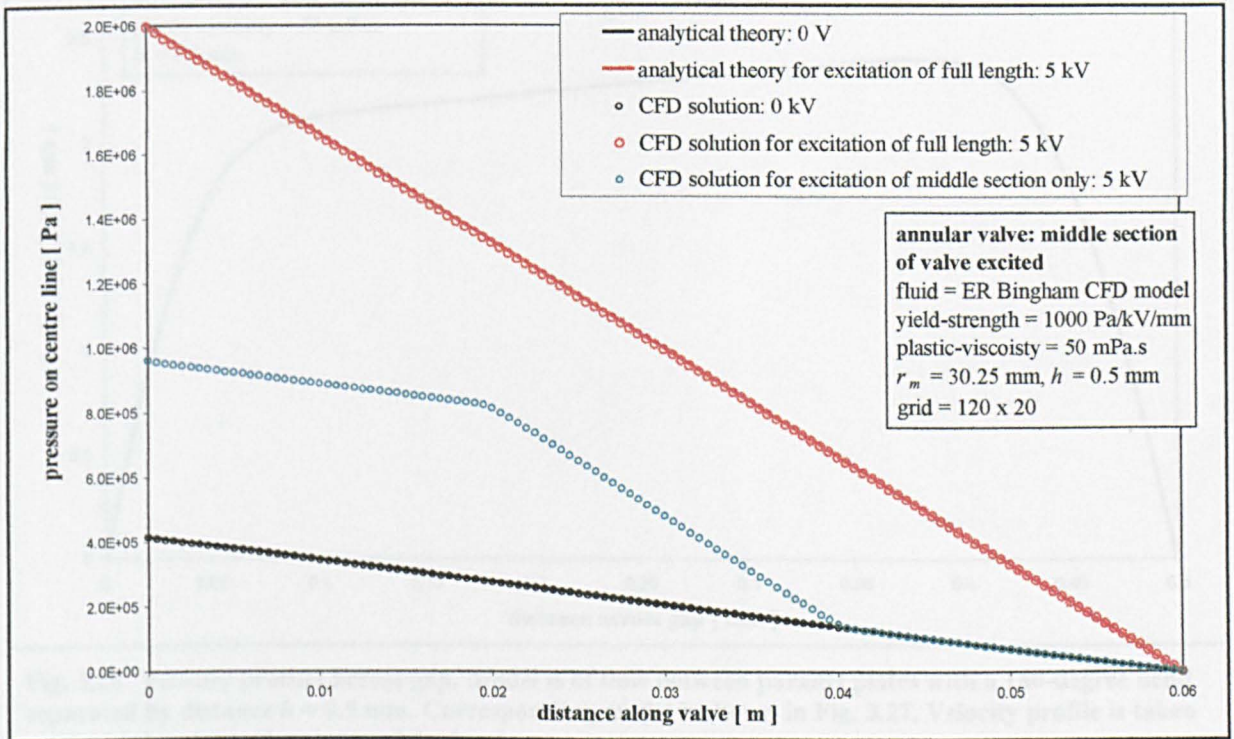


Fig. 3.26: Annular valve in which the middle third section is excited using the ER Bingham CFD model.

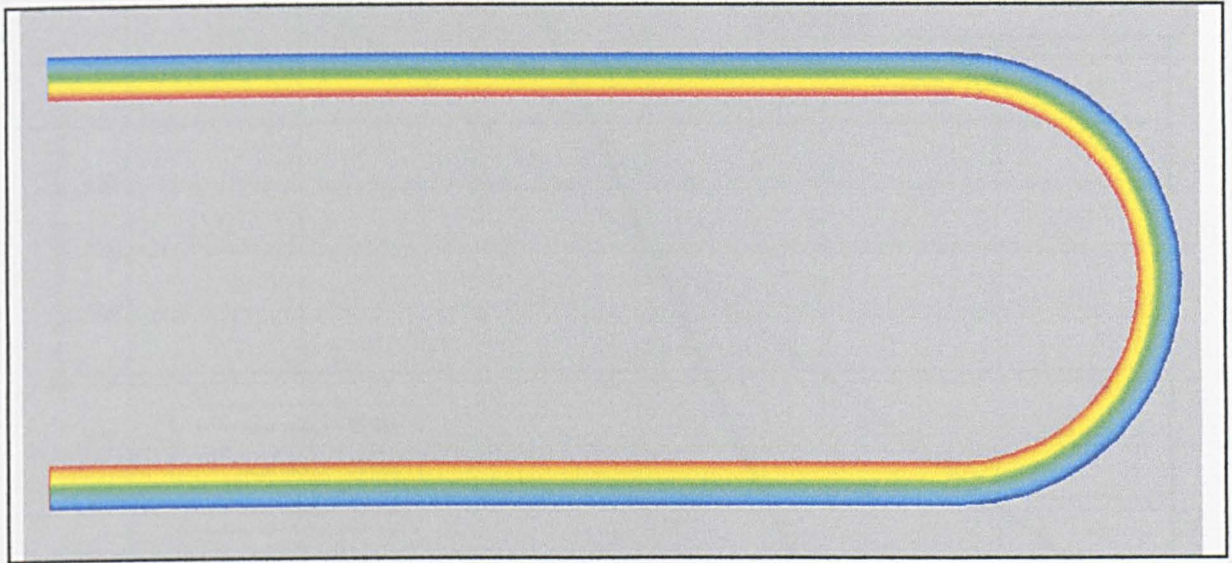


Fig. 3.27: CFD voltage distribution. Model is of flow between parallel plates with a 180-degree bend, separated by distance $h = 0.5$ mm. Fluid enters top left (inlet velocity condition) and fluid leaves bottom left (pressure outlet condition). Corresponding velocity profile distributions are shown Fig. 3.28.

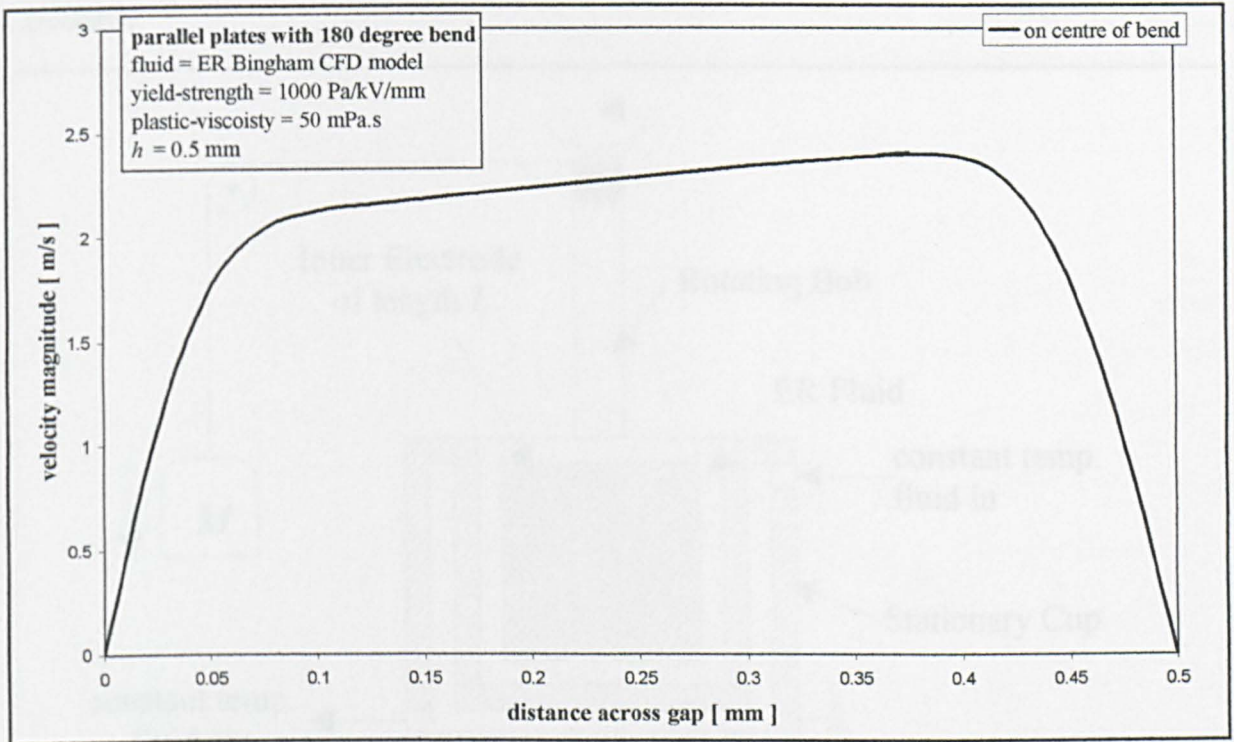


Fig. 3.28: Velocity profiles across gap. Model is of flow between parallel plates with a 180-degree bend separated by distance $h = 0.5$ mm. Corresponding model is shown in Fig. 3.27. Velocity profile is taken on the horizontal at the centre of the bend.

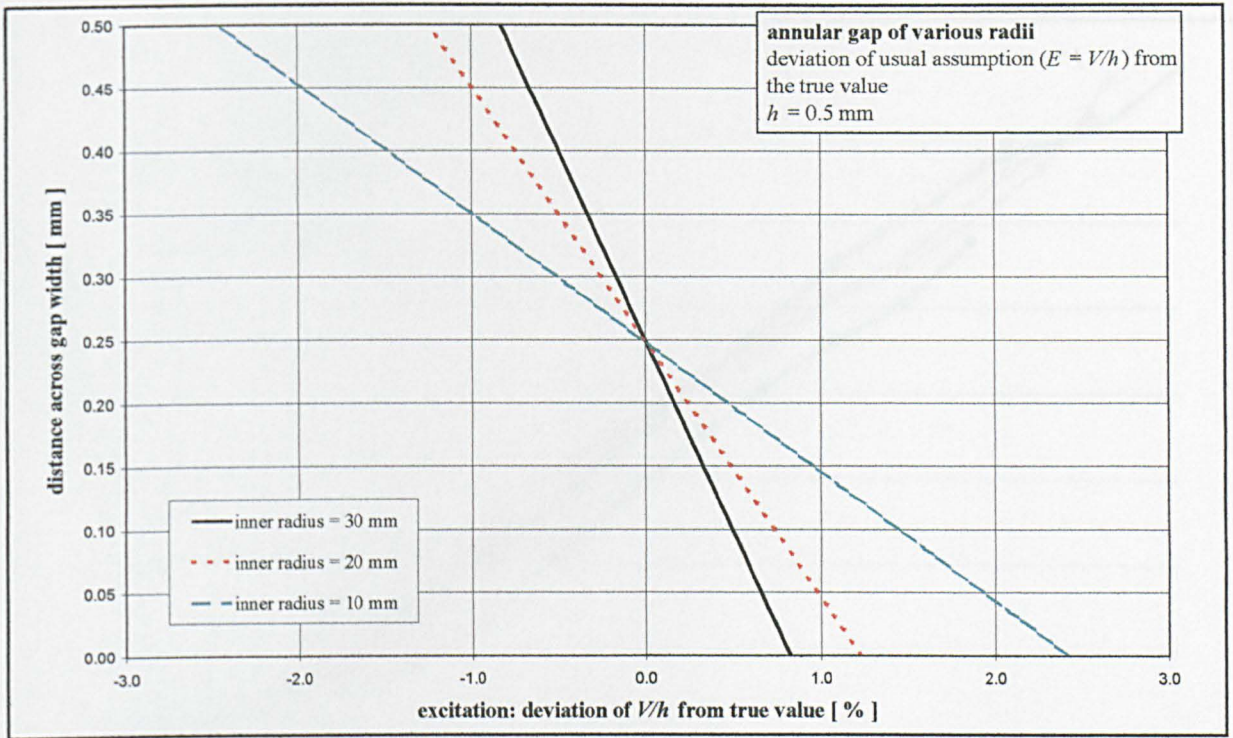


Fig. 3.29: Illustration of the small error involved when assuming a constant excitation in a concentric geometry.

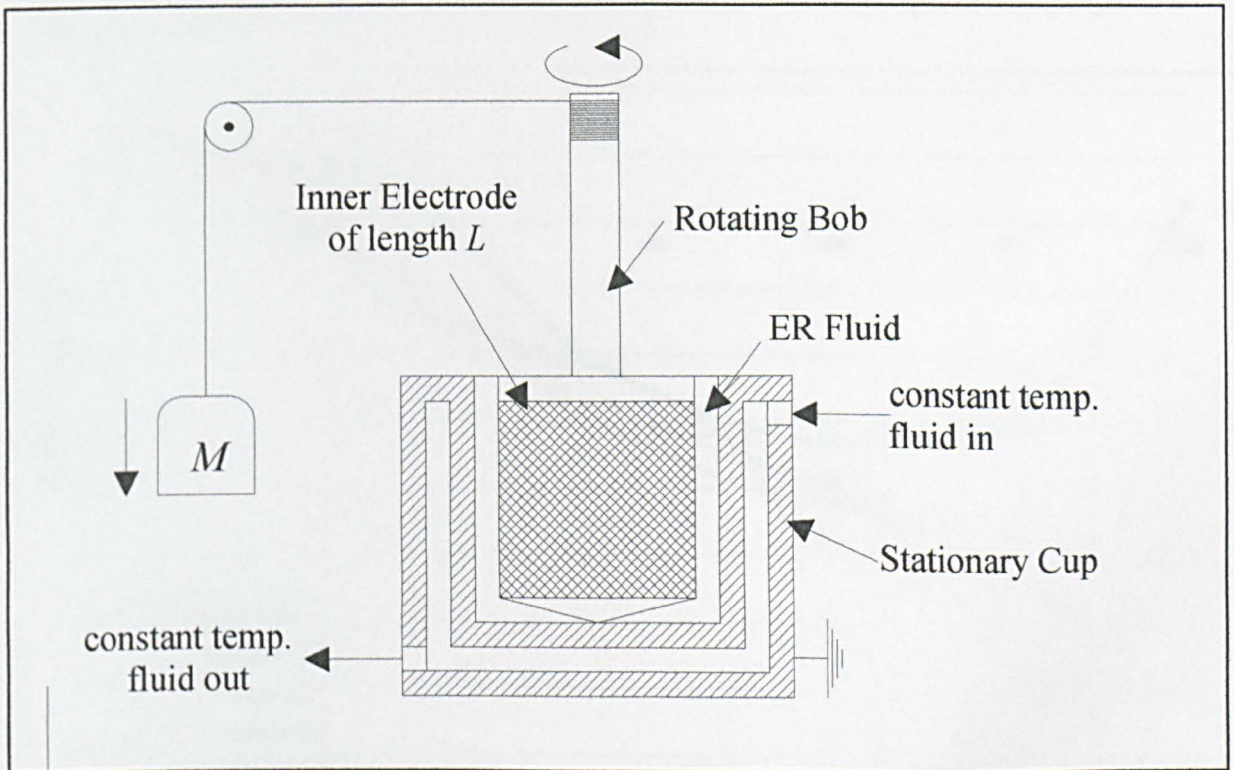


Fig. 3.30: Schematic of ERFD rheometer. The inner electrode is excited with DC voltage through a high voltage cable that runs down the centre of the shaft.

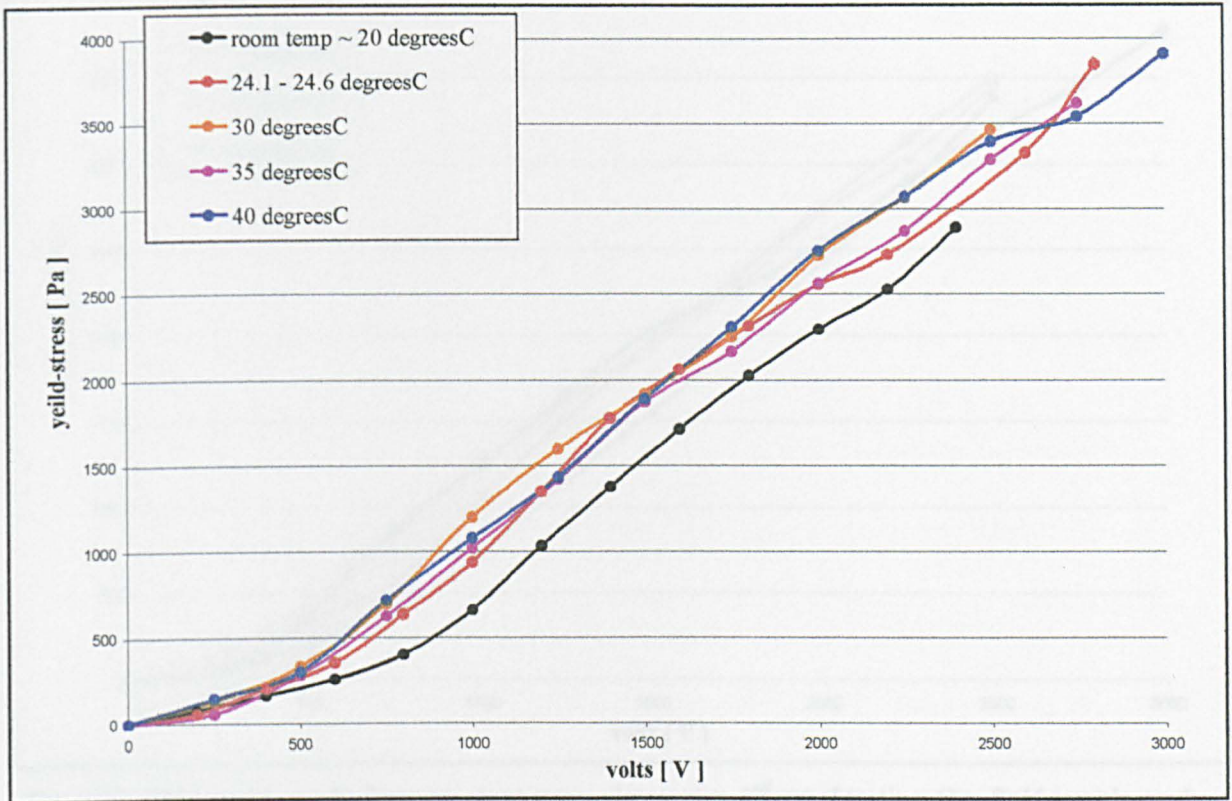


Fig. 3.31: Yield-stress results from constant stress viscometer. 1st set of testing. One fluid sample used throughout the test.

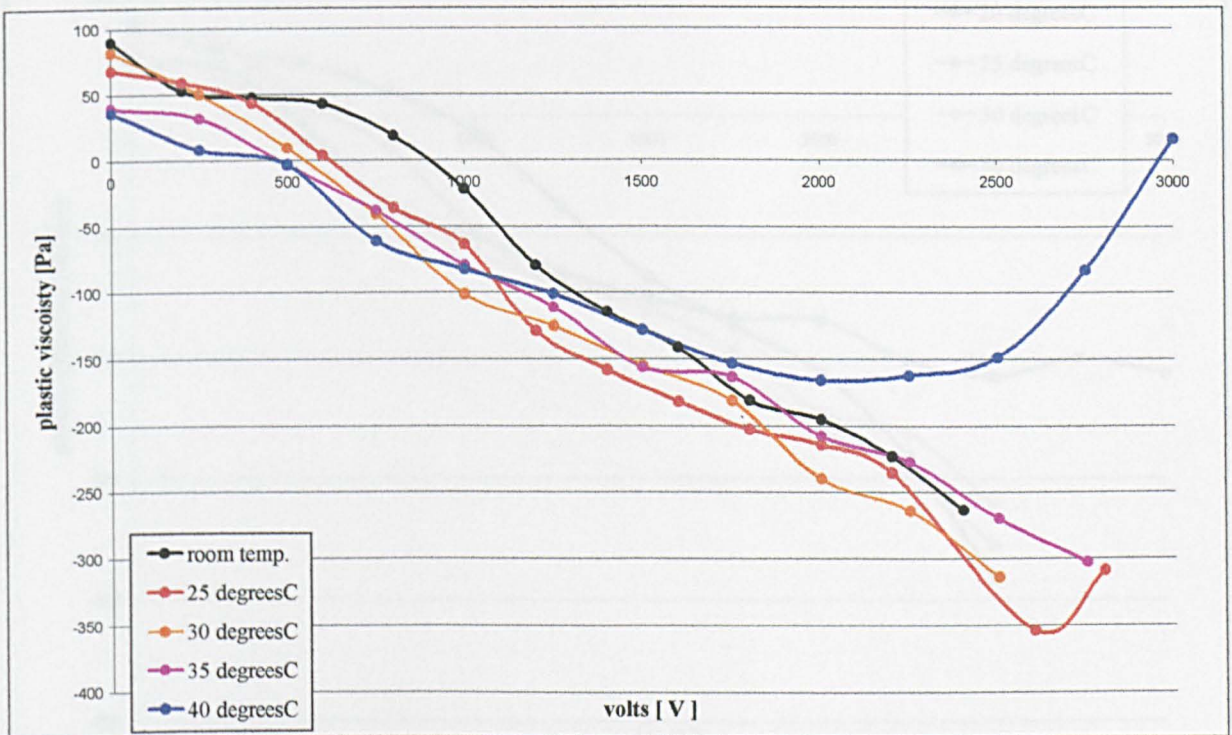


Fig. 3.32: Plastic-viscosity results from constant stress viscometer. 1st set of testing. One fluid sample used throughout the test.

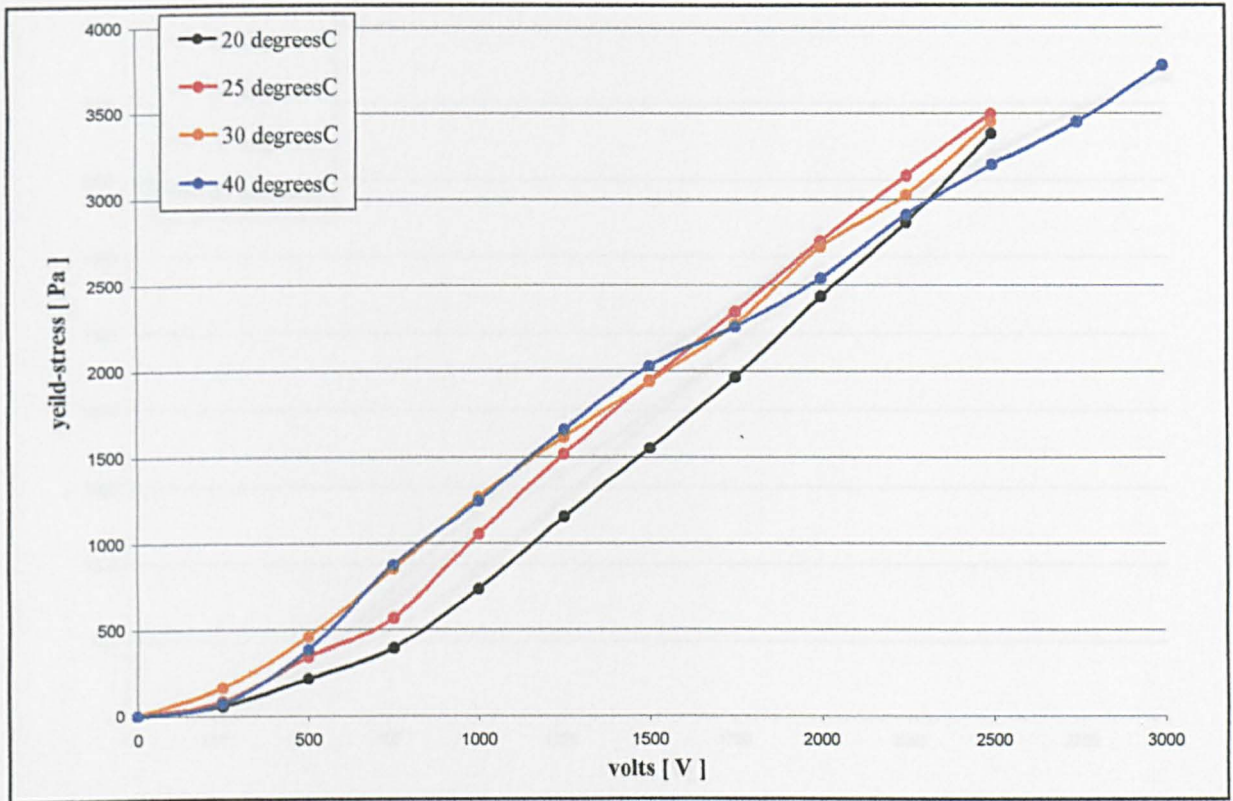


Fig. 3.33: Yield-stress results from constant stress viscometer. 2nd set of testing. One fluid sample used throughout the test.

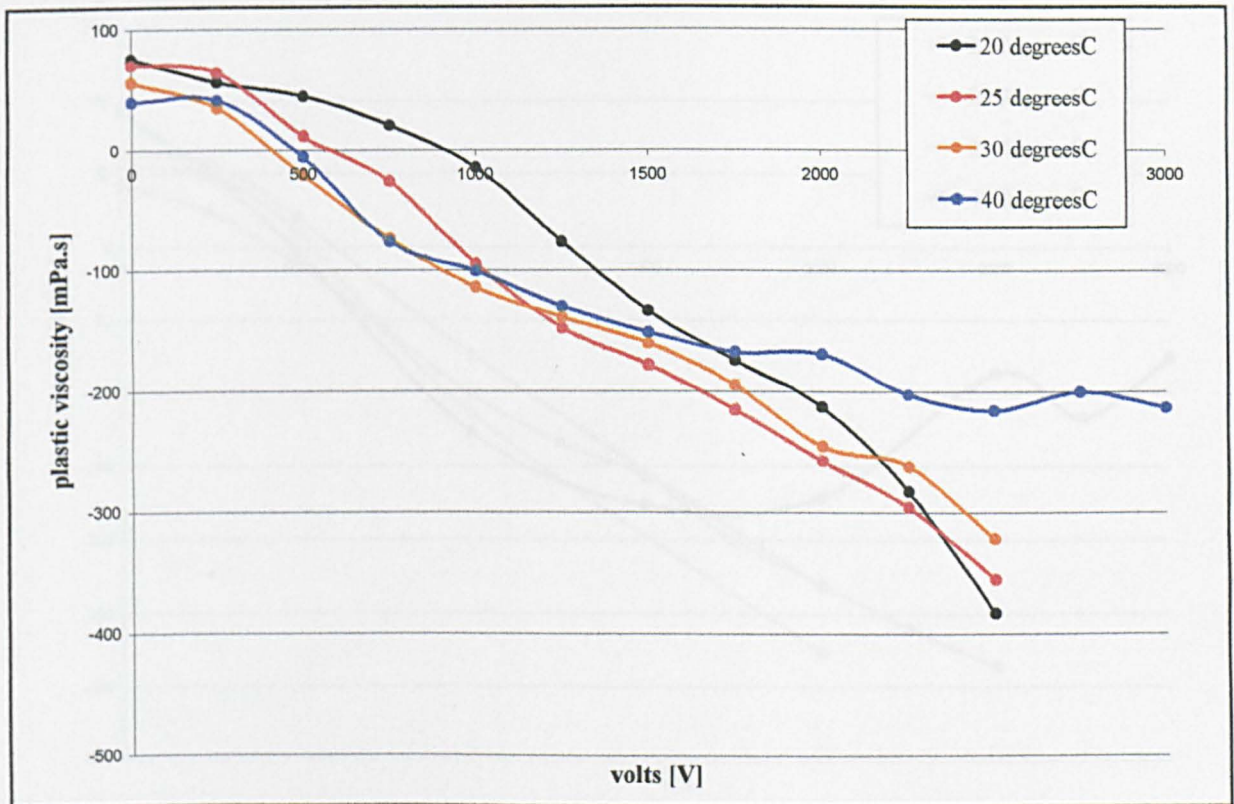


Fig. 3.34: Plastic-viscosity results from constant stress viscometer. 2nd set of testing. One fluid sample used throughout the test.

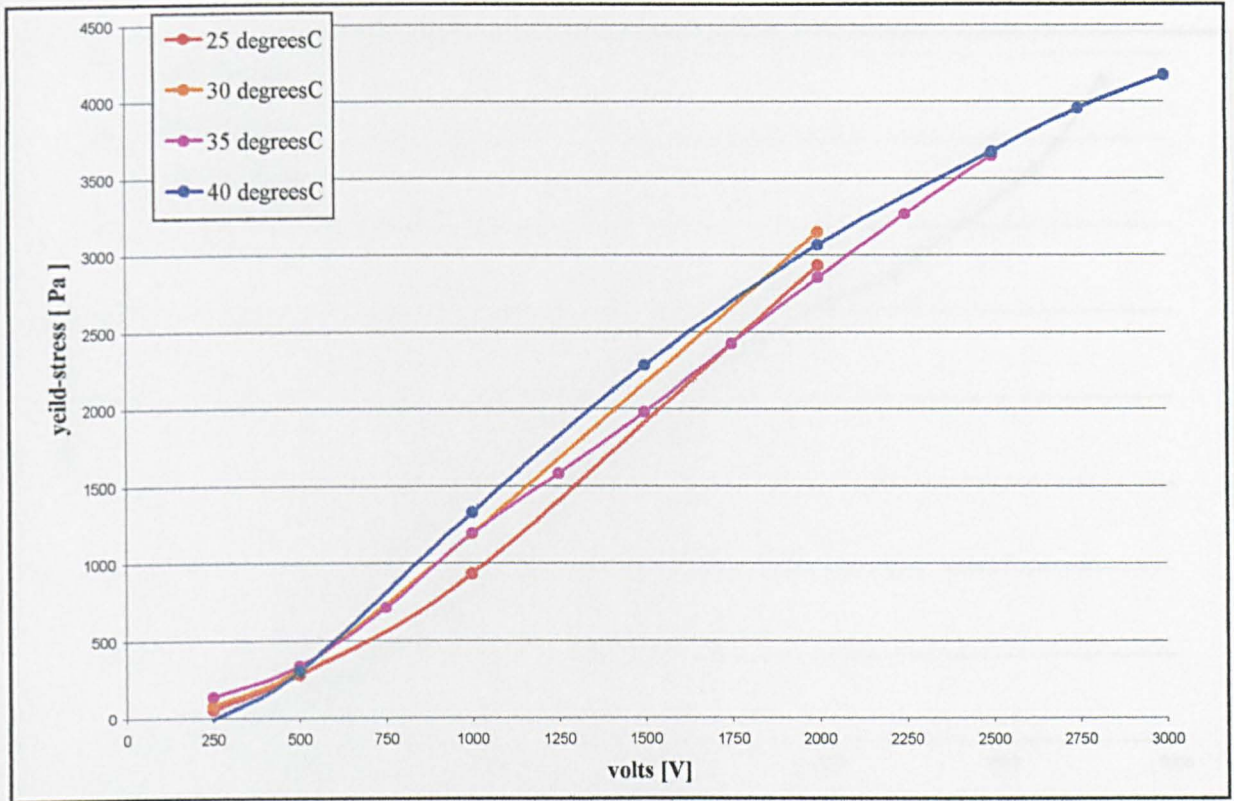


Fig. 3.35: Yield-stress results from constant stress viscometer. 3rd set of testing. New fluid sample used for each temperature.

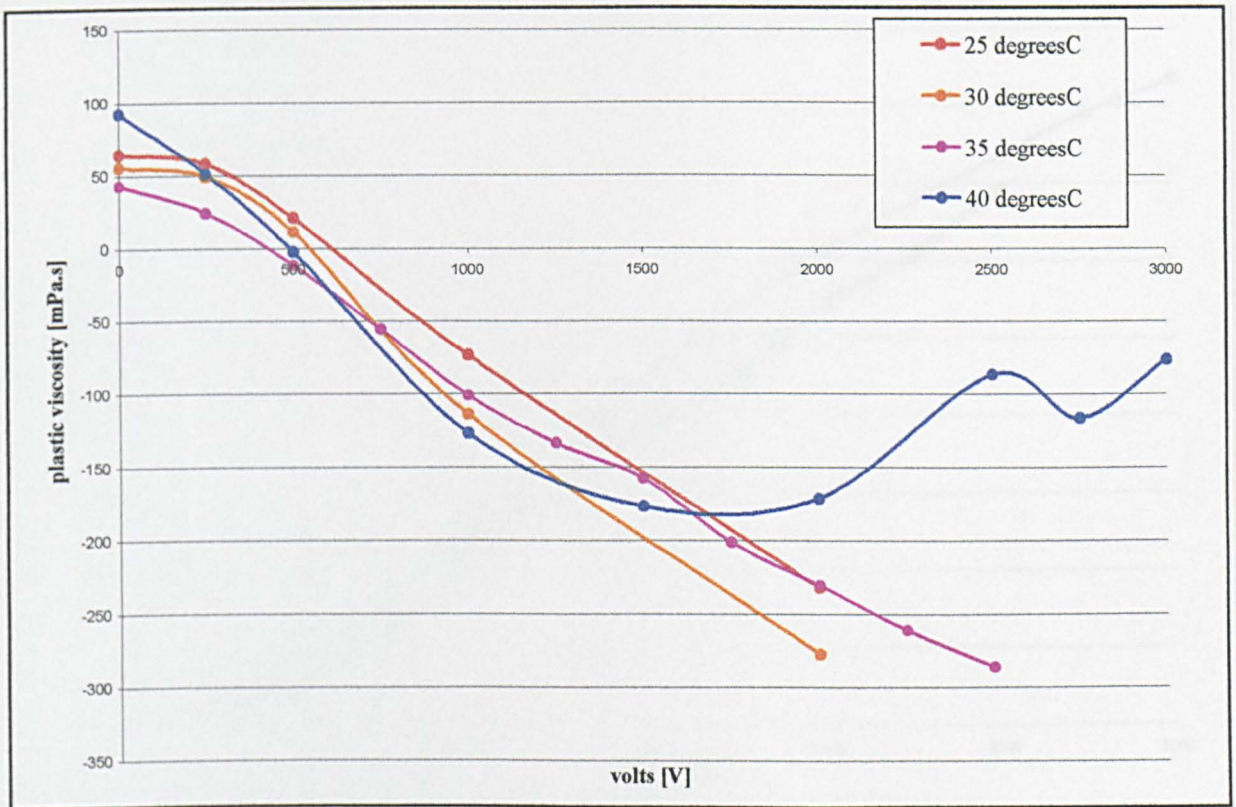


Fig. 3.36: Plastic-viscosity results from constant stress viscometer. 3rd set of testing. New fluid sample used for each temperature.

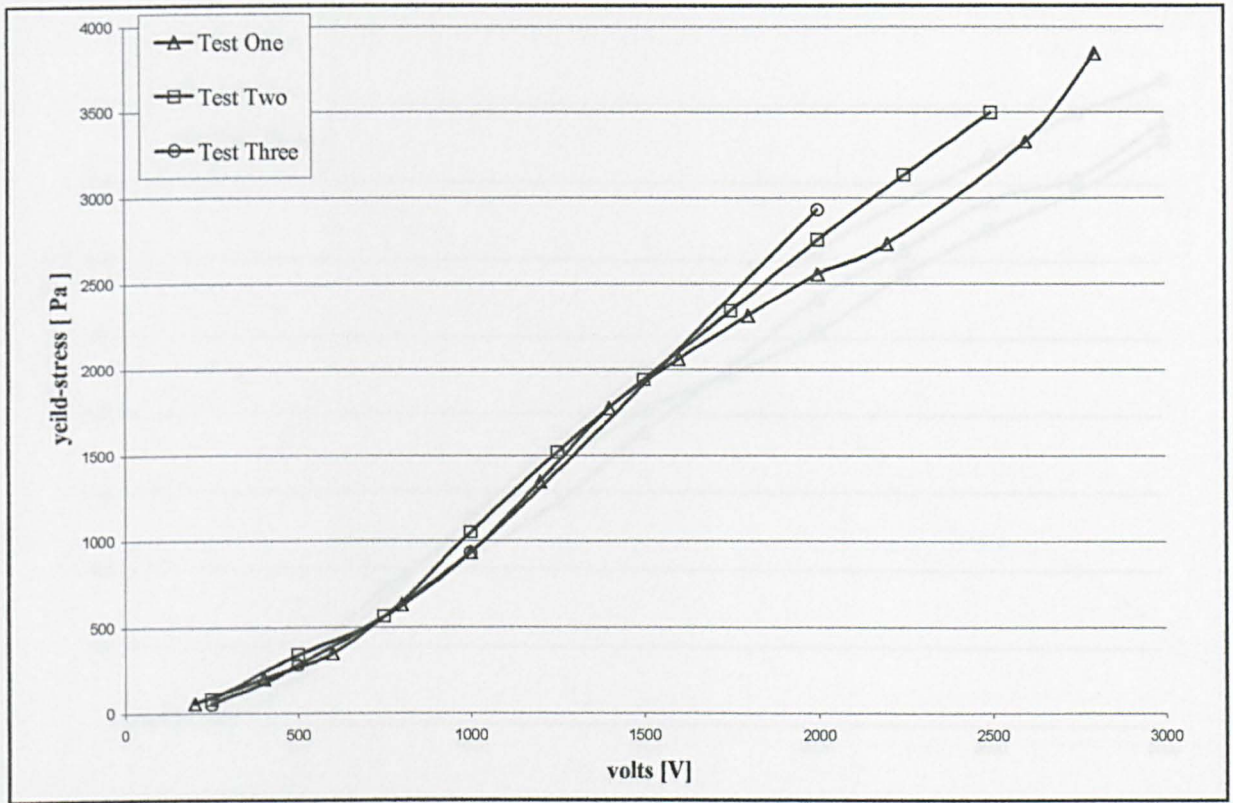


Fig. 3.37: Yield-stress results from constant stress viscometer at 25°C.

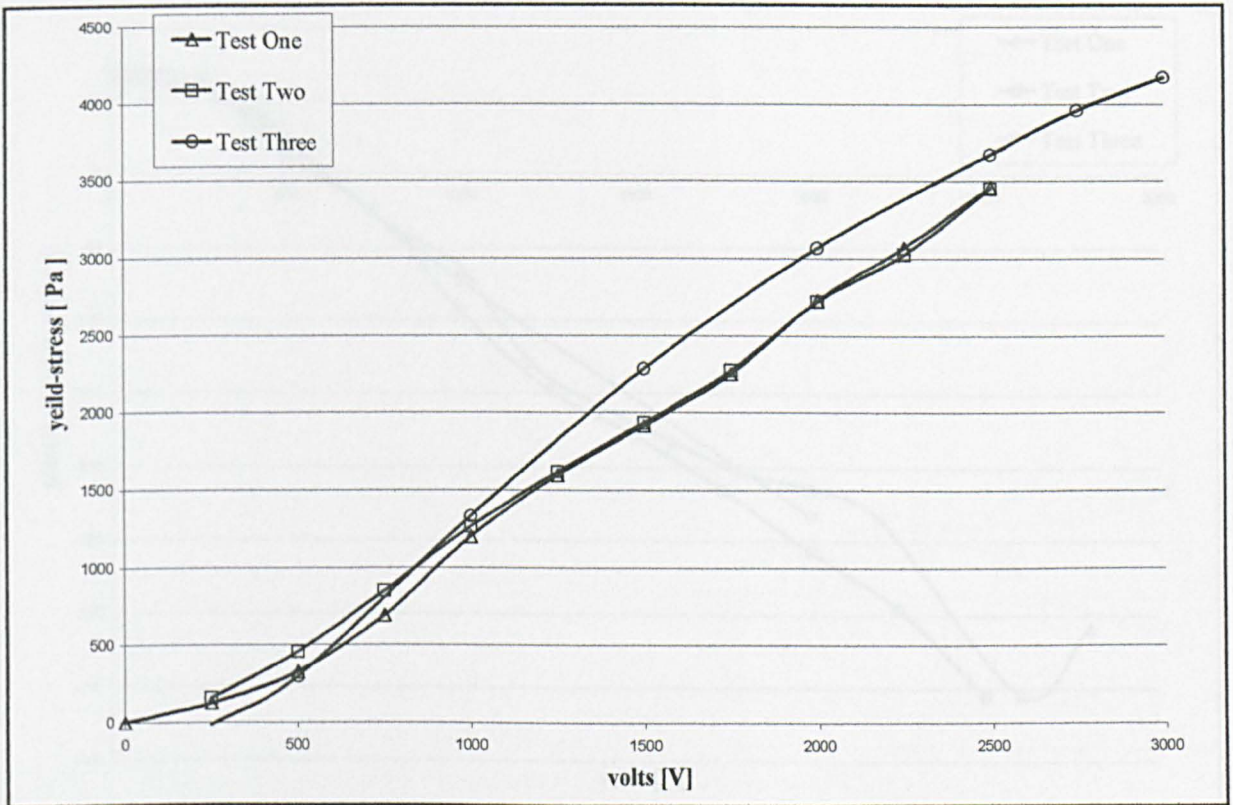


Fig. 3.38: Yield-stress results from constant stress viscometer at 30°C.

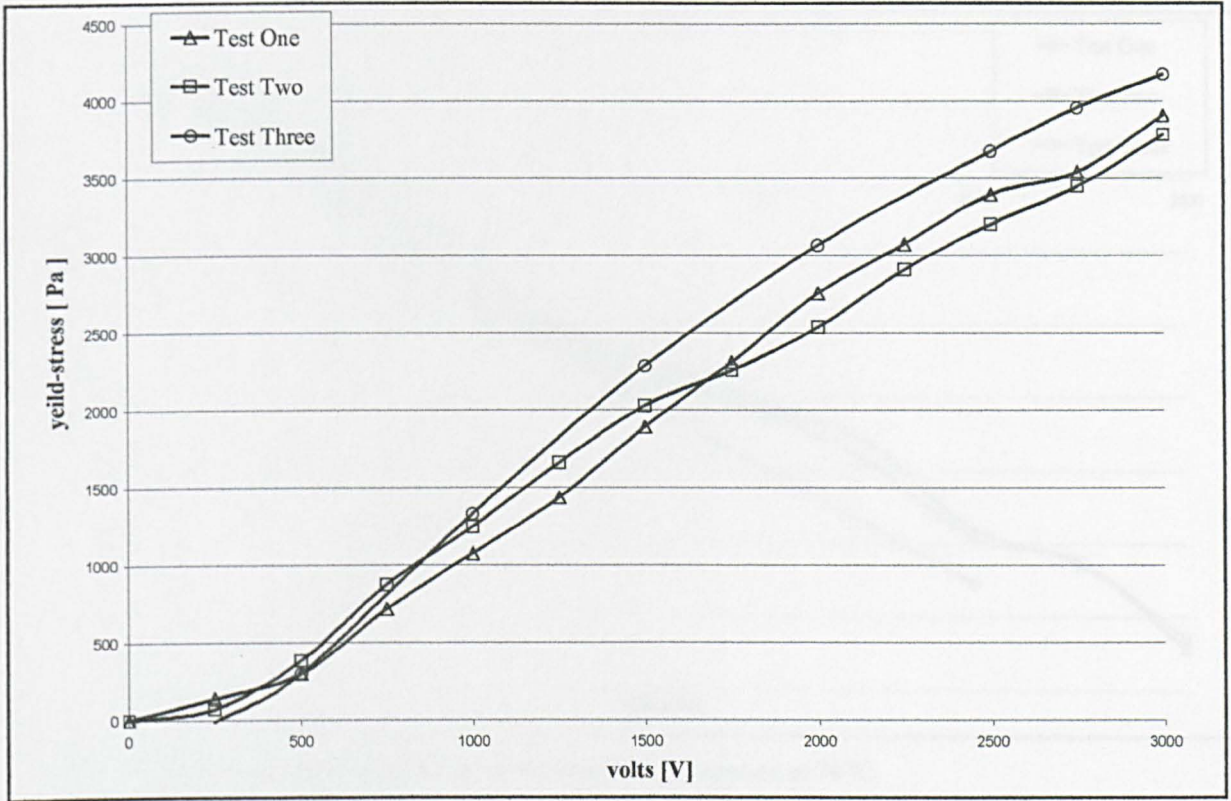


Fig. 3.39: Yield-stress results from constant stress viscometer at 40°C.

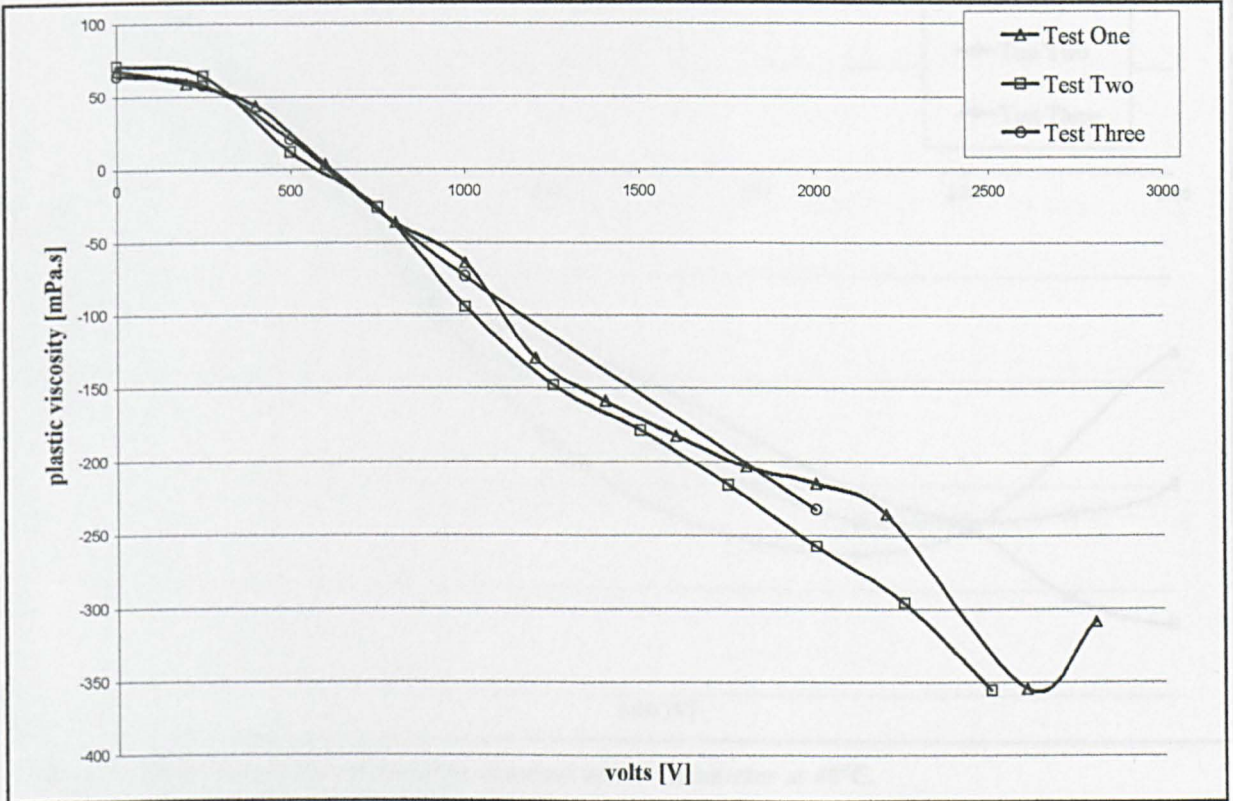


Fig. 3.40: Plastic-viscosity results from constant stress viscometer at 25°C.

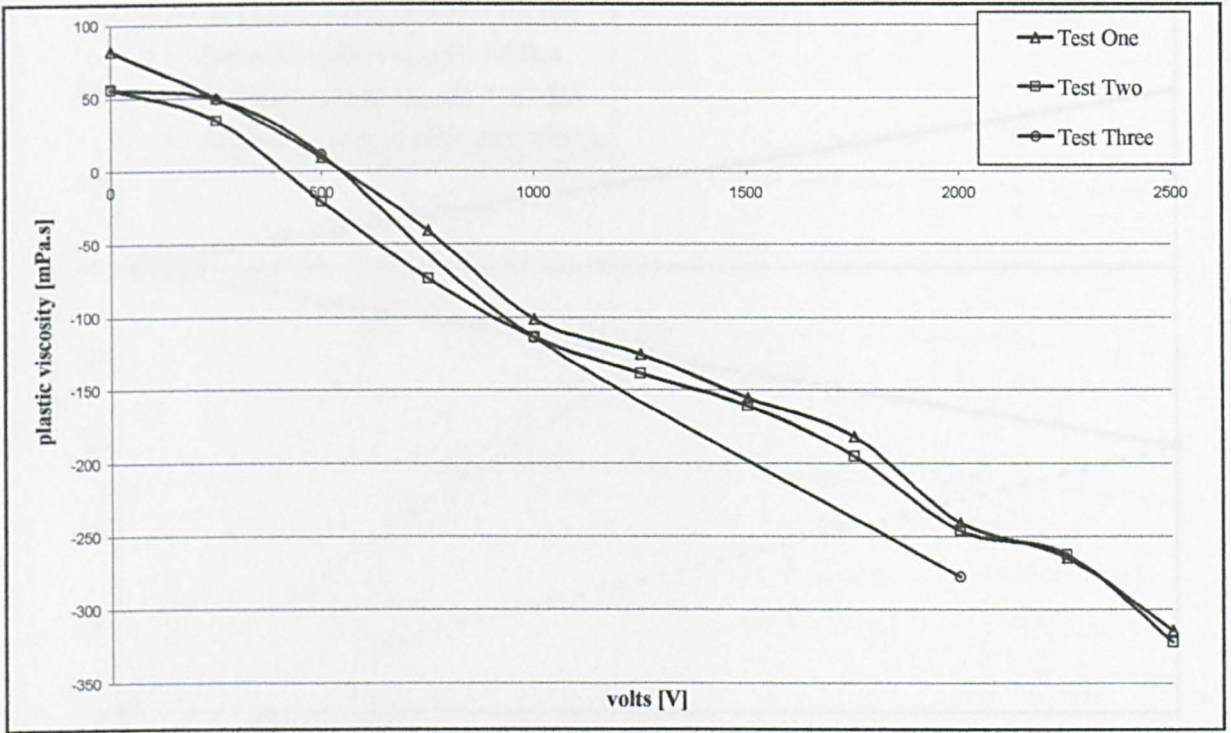


Fig. 3.41: Plastic-viscosity results from constant stress viscometer at 30°C.

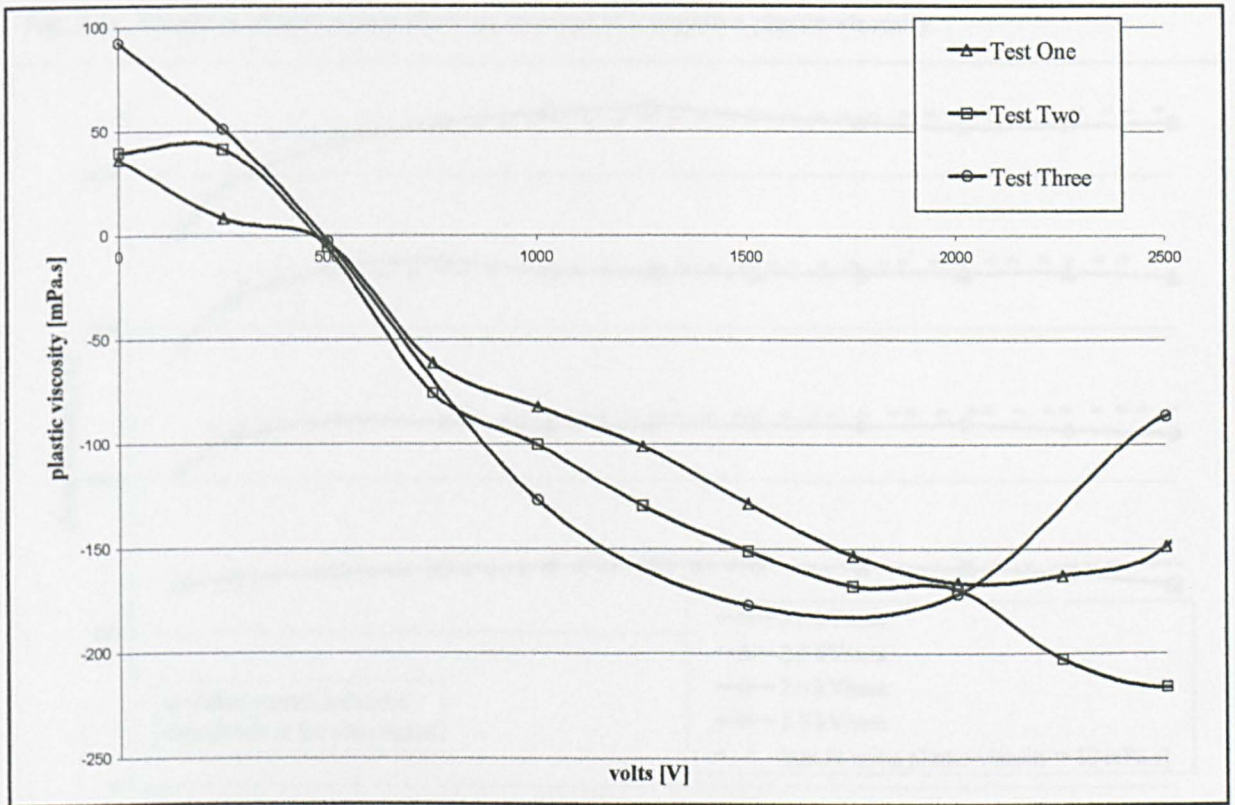


Fig. 3.42: Plastic-viscosity results from constant stress viscometer at 40°C.

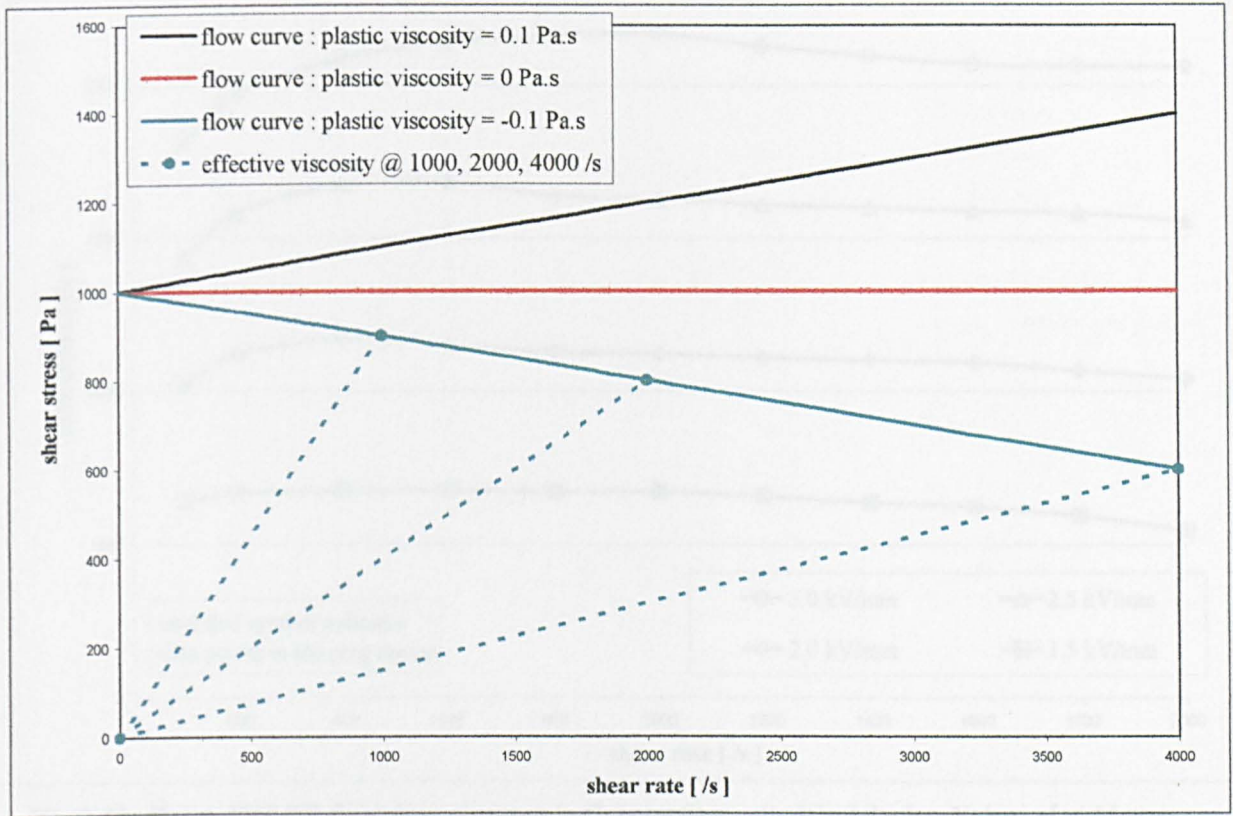


Fig. 3.43: Bingham plastic model showing concept of a negative plastic-viscosity.

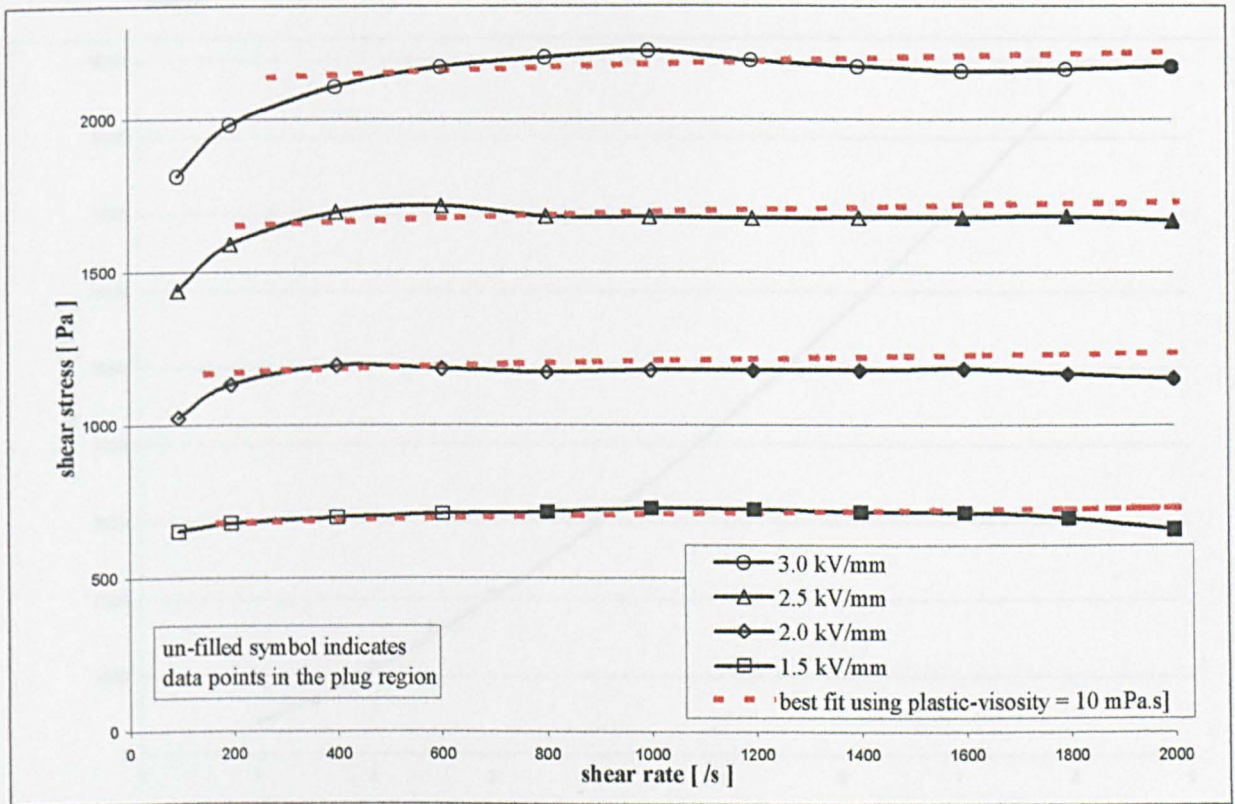


Fig. 3.44: Flow curve for a Bayer 3565 ER fluid obtained in Couette flow cylindrical device. Temperature = 40 °C

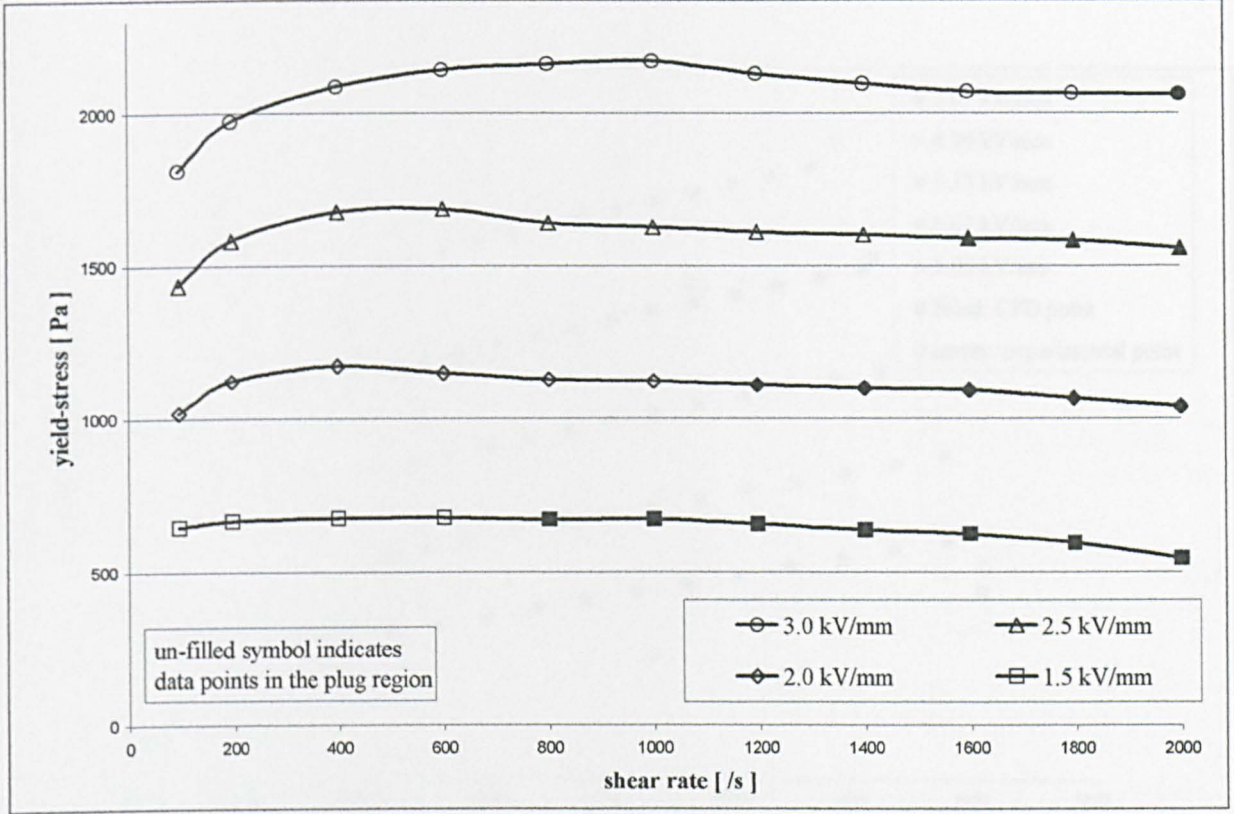


Fig. 3.45: Bayer 3565 ER fluid data obtained in Couette flow cylindrical device. Values of yield-stress calculated using eqn(2.23) with $\mu_e = 55$ mPa.s. Only data points in the plug-less regime are valid.

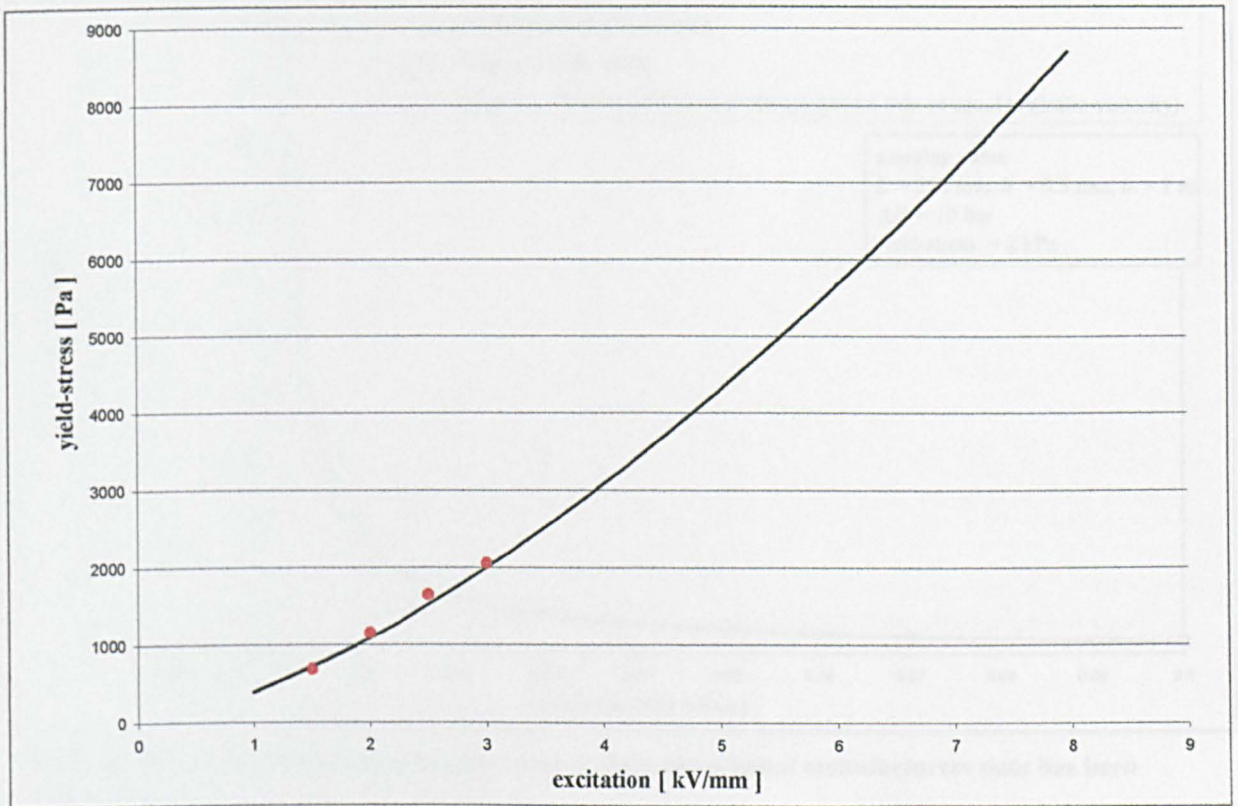


Fig. 3.46: Flow curve for a Bayer 3565 ER fluid obtained in Couette flow cylindrical device. Temperature = 40 °C

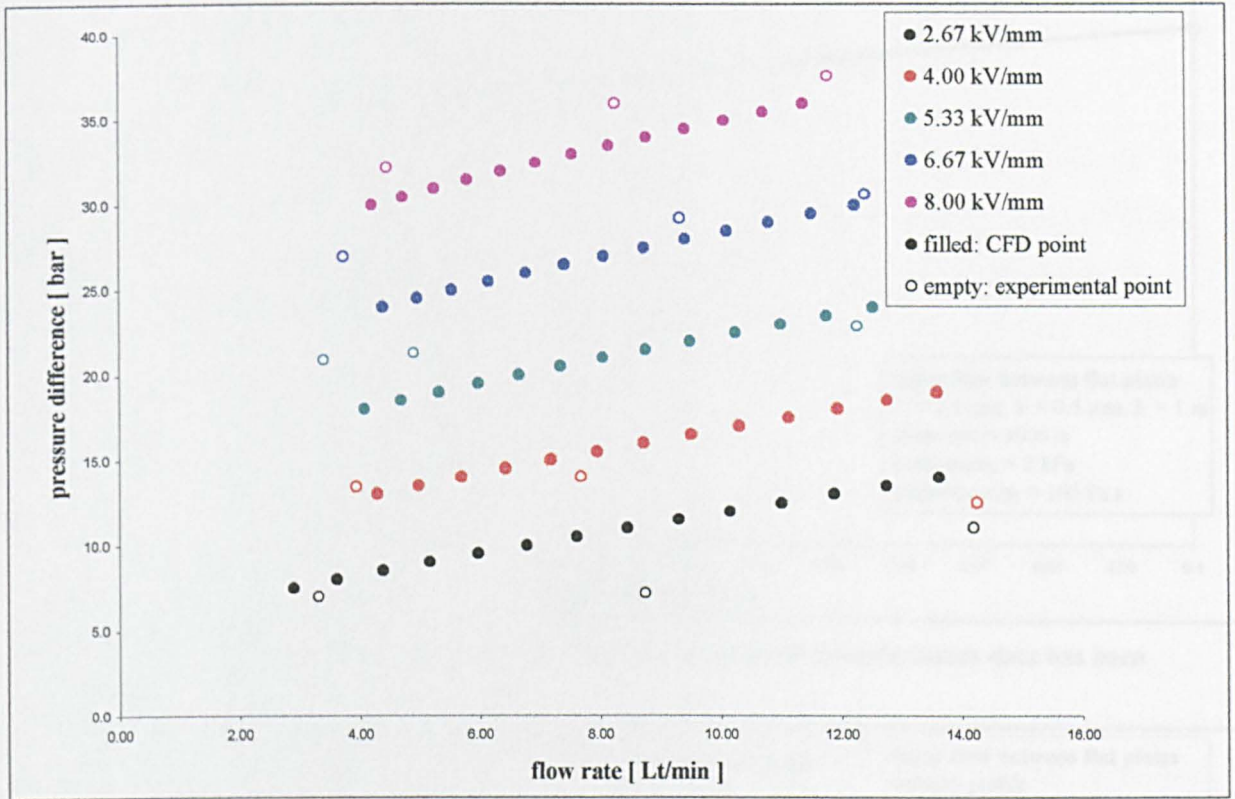


Fig. 3.47: Valve data for a Bayer 3565 ER fluid. Temperature = 40 °C

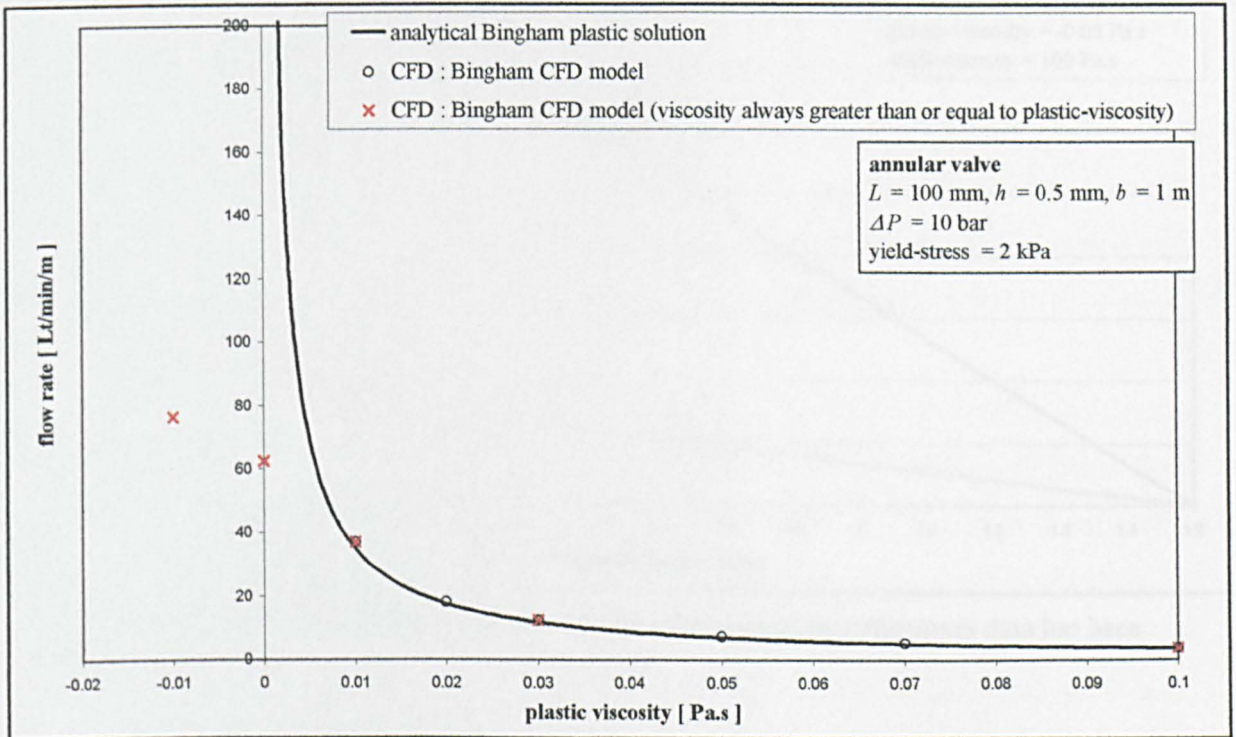


Fig. 3.48: Flow curve from a Couette flow device. Here the original manufacturers data has been corrected.

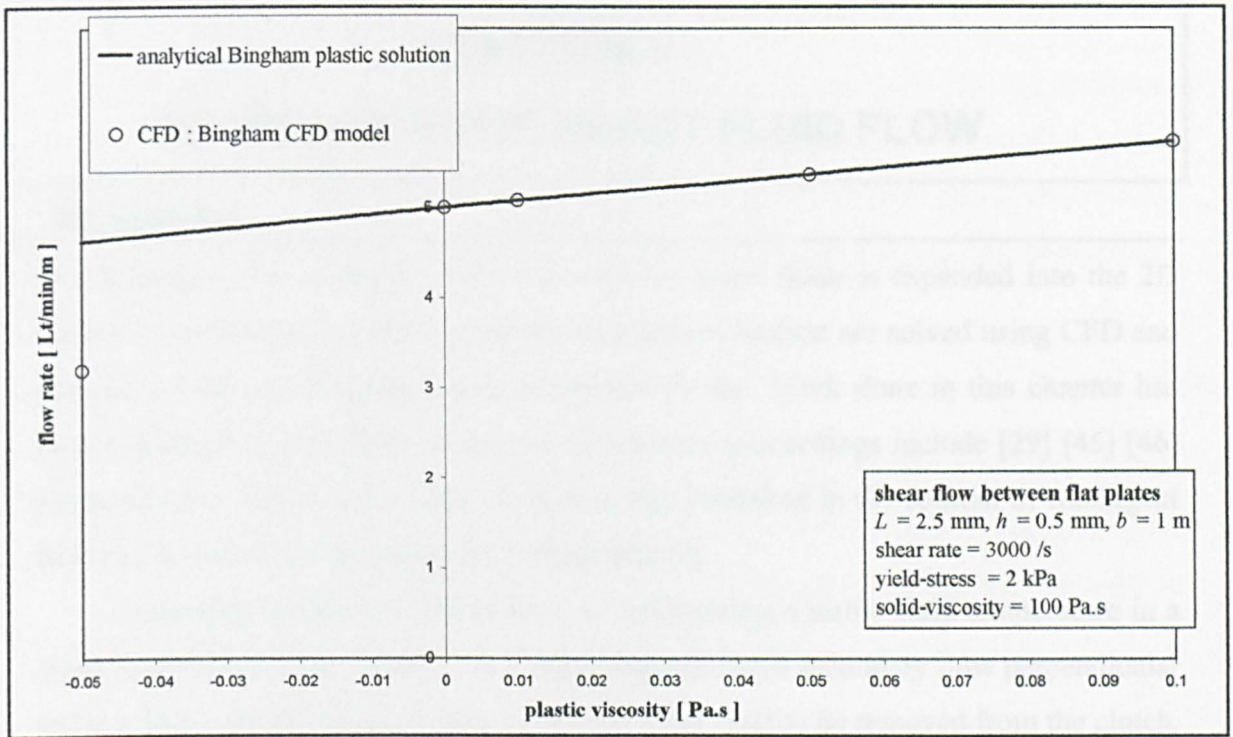


Fig. 3.49: Flow curve from a Couette flow device. Here the original manufacturers data has been corrected.

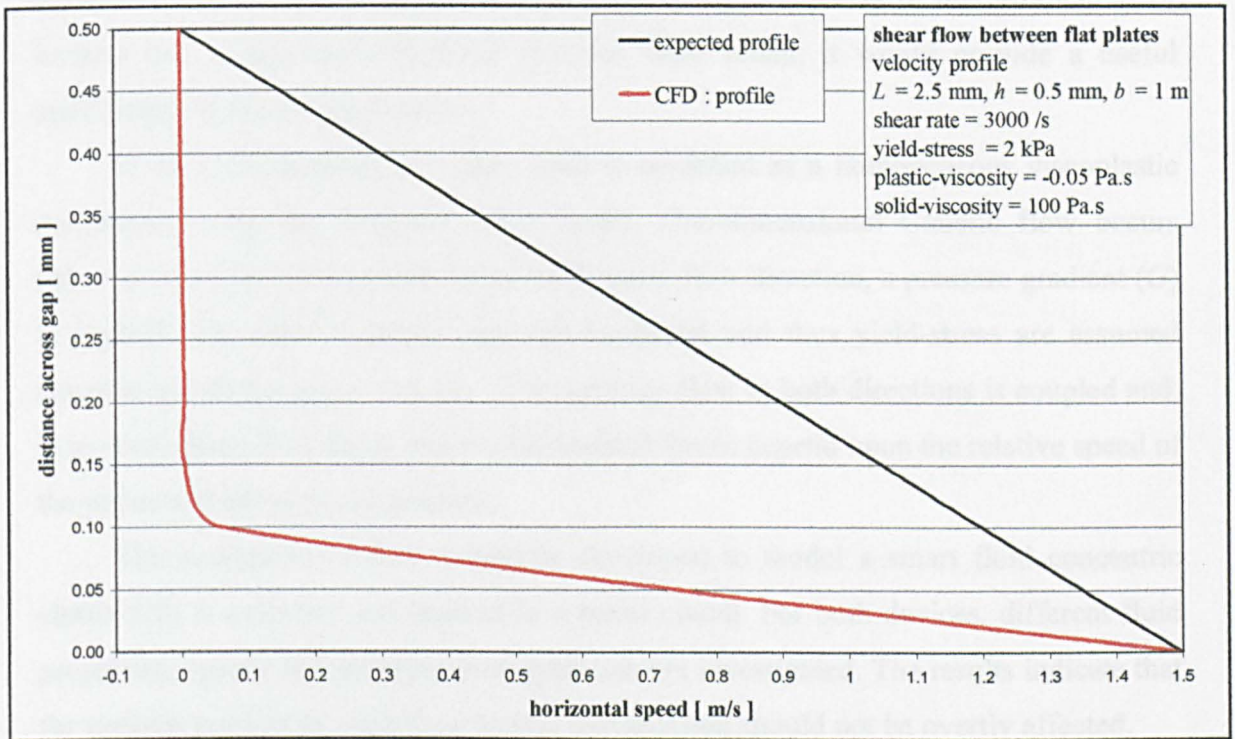


Fig. 3.50: Flow curve from a Couette flow device. Here the original manufacturers data has been corrected.

CHAPTER 4 :

2D STEADY STATE SMART FLUID FLOW

4.1 Introduction

In this chapter, the successful 1D CFD work on smart fluids is expanded into the 2D regime. Two-dimensional flow problems of practical interest are solved using CFD and compared with the Bingham plastic analytical theory. Work done in this chapter has been published in four different papers. Conference proceedings include [29] [45] [46] (Appendix B). Work on the smart fluid seal was published in the Journal of Intelligent Material Systems and Structures [47] (Appendix B).

A possible solution to the problem of maintaining a stable fluid temperature in a smart fluid clutch is examined. It has been proposed that a secondary flow perpendicular to the torque transmitting direction would allow hot fluid to be removed from the clutch. An analytical solution to this problem is possible but relatively complex. The resulting equations need to be solved numerically [25]. A CFD solution to this problem is of interest and if agreement between the two were found, it would provide a useful verification of the two approaches.

In the CFD method, the smart fluid is modelled as a homogeneous viscoplastic continuum using the Bingham CFD model. One-dimensional Couette flow occurs between two plates. Perpendicular to the Couette flow direction, a pressure gradient (G) is applied. The flow is steady, and the excitation and thus yield-stress are assumed constant across the gap-width (h). The resulting flow in both directions is coupled and, in general, these flow fields and the transmitted forces depend upon the relative speed of the plates and the pressure gradient.

The analytical solution originally developed to model a smart fluid concentric clutch [25] is extended and applied to a radial clutch. For both devices, different fluid properties, speeds and axial pressure gradients are investigated. The results indicate that for realistic rates of through-flow torque transmission should not be overtly affected.

Utilising the 2D concentric clutch CFD model, a further problem is resolved. This problem deals with flow in a concentrically located rotating smart fluid shaft seal. Incompatible reports of the effect of rotational speed on sealing capabilities exist. The discrepancy is explained when the effect of radius ratio, rotational speed, axial pressure gradient and the fluid properties on leakage flow rate are investigated using a CFD model.

4.2 Analytical Theory: 2D Bingham Plastic Flow between Two Flat Plates

An analytical solution developed by Atkin [48] is now summarised. Fig. 4.1 illustrates the geometry used. A distance (h) in the z -direction separates two parallel plates, between which 2D, fully developed, isothermal flow of a homogeneous, incompressible continuum with fixed Bingham plastic properties [23] occurs. The velocity components are assumed to be:

$$v_x = u(z), \quad v_y = v(z), \quad v_z = 0. \quad (4.1)$$

The Poiseuille type flow is caused by a pressure gradient, $G(= dp/dy = \Delta P/L)$, and the Couette type flow occurs due to the speed difference between the plates. For simplicity, one plate ($z = h$) is always considered stationary, with the other ($z = 0$) moving at constant speed (U). The boundary conditions are therefore:

$$u(0) = U, \quad u(h) = 0; \quad v(0) = v(h) = 0. \quad (4.2)$$

4.2.1 Governing Equations

In the absence of body forces the momentum equations (section 2.3.1) are:

$$\rho \left(\frac{\partial v_i}{\partial t} + v_j \frac{\partial v_i}{\partial x_j} \right) = - \frac{\partial p}{\partial x_i} + \frac{\partial \tau_{ij}}{\partial x_j}. \quad (4.3)$$

In the manner described in section 2.3, the Bingham plastic constitutive model [23] is used to represent the stress tensor (τ_{ij}) in terms of the deformation rate tensor (d_{ij}):

$$\tau_{ij} = \begin{cases} \left(\frac{\tau_y}{\dot{\gamma}} + \mu_o \right) d_{ij} & \tau > \tau_y \\ \dot{\gamma} = 0 & \tau < \tau_y \end{cases} \quad \text{where} \quad e_{ij} = \frac{\partial v_i}{\partial x_j} + \frac{\partial v_j}{\partial x_i} \quad \text{and} \quad \tau = \pm \sqrt{\frac{1}{2} \tau_{ij} \tau_{ij}} \\ \dot{\gamma} = \pm \sqrt{\frac{1}{2} e_{ij} e_{ij}}. \quad (4.4)$$

For the velocity field given by eqn(4.1) the only non-zero rate of strain components are given by:

$$d_{xz} = d_{zx} = \frac{du}{dz}, \quad d_{yz} = d_{zy} = \frac{dv}{dz}, \quad (4.5)$$

and using eqn(4.4) the resulting non-zero shear stresses are:

$$\tau_{xz} = \left(\frac{\tau_y}{\dot{\gamma}} + \mu_e \right) \frac{du}{dz}, \quad \tau_{yz} = \left(\frac{\tau_y}{\dot{\gamma}} + \mu_e \right) \frac{dv}{dz}, \quad (4.6)$$

$$\text{where } \dot{\gamma} = \sqrt{\left[\frac{du}{dz}\right]^2 + \left[\frac{dv}{dz}\right]^2}. \quad (4.7)$$

The equations of motion {eqn(4.3)} reduce to:

$$\frac{d}{dz}\tau_{xz} = 0, \quad -\frac{dp}{dy} + \frac{d}{dz}\tau_{yz} = 0, \quad (4.8)$$

which can be integrated to give:

$$\tau_{xz} = a, \quad \tau_{yz} = Gz + b, \quad (4.9)$$

where a and b are constants, $G = dp/dy$ and so, using eqn(4.4):

$$\tau = \sqrt{\tau_{xz}^2 + \tau_{yz}^2} = \sqrt{a^2 + (Gz + b)^2}. \quad (4.10)$$

From equations (4.6), (4.7), (4.10) it follows that:

$$\mu_e \frac{du}{dz} = a \left(1 - \frac{\tau_y}{\tau}\right), \quad \mu_e \frac{dv}{dz} = (Gz + b) \left(1 - \frac{\tau_y}{\tau}\right). \quad (4.11)$$

The equations obtained by substituting eqn(4.10) into eqn(4.11) can be integrated to determine the velocity components u and v that satisfy the boundary conditions {eqn(4.2)}. It follows from the analysis in case (i) and (ii) below that to satisfy the boundary conditions on v , $b = -Gh/2$.

For flow to occur τ must be greater than τ_y which is a positive constant. From eqn(4.10) flow can only occur if $(a^2 + b^2)^{1/2} > \tau_y$. There are two cases to consider:

$$(i) \quad \tau_y < |a| \quad \text{and} \quad (ii) \quad |a| < \tau_y < (a^2 + b^2)^{1/2}.$$

Case (i) No-Plug Regime $|a| > \tau_y$

If $|a| > \tau_y$ then τ is always greater than τ_y and flow occurs across the whole gap with no plugs present. A direct integration of eqn(4.11), using eqn(4.10) and the boundary conditions {eqn(4.2)}, results in the velocity components:

$$u = U - \bar{U}(z), \quad v = V(z), \quad (4.12)$$

where

$$\mu_e \bar{U}(z) = |a| \left[z - \frac{\tau_y}{G} \left\{ \sinh^{-1} \left(\frac{Gz + b}{|a|} \right) - \sinh^{-1} \left(\frac{b}{|a|} \right) \right\} \right], \quad (4.13)$$

$$\mu_e V(z) = \frac{Gz^2}{2} + bz - \frac{\tau_y}{G} \left[\sqrt{a^2 + (Gz + b)^2} - \sqrt{a^2 + b^2} \right] \quad (4.14)$$

Both velocity components are therefore dependent upon G and thereby affected by a change in the pressure gradient. An integration of the velocity profile eqn(4.14) gives the flow rate in the y -direction as:

$$\dot{q}_y = -\frac{L_x Gh^3}{12\mu_e} + \frac{L_x}{\mu_e} \left\{ \frac{\tau_y h}{4G} \sqrt{G^2 h^2 + 4a^2} - \frac{\tau_y a^2}{G^2} \sinh^{-1} \left(\frac{Gh}{2|a|} \right) \right\}, \quad (4.15)$$

where L_x is the length of plate in the x -direction. To satisfy the condition $u = U$ at $y = 0$ it follows that:

$$\mu_o U = |a| \left[h - \frac{2\tau_y}{G} \sinh^{-1} \left(\frac{Gh}{2|a|} \right) \right]. \quad (4.16)$$

This equation can be used to determine $|a|$.

Case (ii) Plug Flow Regime $|a| < \tau_y$

In this flow regime the possibility of yield surfaces arise. A solution with a central plug, which is symmetric about the mid-plane $z = h/2$, is derived. The plug boundaries can be determined by using the condition that $\tau = \tau_y$ in eqn(4.10). This gives a plug thickness of:

$$h_p = z_2 - z_1 = \frac{2}{G} \sqrt{\tau_y^2 - a^2}, \quad (4.17)$$

which must be less than the gap-width (h). This inequality leads to a critical condition on the pressure gradient for flow to occur. The derivation of the velocity components is now more involved. The final velocity components can be written in the form:

$$u = \begin{cases} U - \bar{U}(z) & 0 \leq z < z_1 \\ U/2 & z_1 \leq z \leq z_2 \\ \bar{U}(h-z) & z_2 < z \leq h \end{cases}, \quad v = \begin{cases} V(z) & 0 \leq z < z_1 \\ V(z_1) & z_1 \leq z \leq z_2 \\ V(h-z) & z_2 < z \leq h \end{cases}. \quad (4.18)$$

where \bar{U} and $V(z)$ are given by eqns(4.13) & (4.14). Again the condition $u = U$ at $y = h$ gives:

$$\mu_e U = |a| \left[h - \frac{2\sqrt{\tau_y^2 - a^2}}{G} \right] - \frac{2|a|\tau_y}{G} \left[\sinh^{-1} \left(\frac{Gh}{2|a|} \right) - \sinh^{-1} \left(\frac{\sqrt{\tau_y^2 - a^2}}{|a|} \right) \right]. \quad (4.19)$$

An integration of the velocity profile u gives the flow rate expression:

$$\dot{q}_y = 2L_x \left[\int_0^{z_1} V(z) dz + V(z_1)(z_2 - z_1) \right] = 2L_x (\dot{q}_1 + \dot{q}_2), \quad (4.20)$$

$$\begin{aligned} \dot{q}_1 = \frac{1}{\mu_e} \left[-\frac{Gz^2}{12} (3h - 2z) + \frac{\tau_y z}{2G} \sqrt{G^2 h^2 + 4a^2} \right. \\ \left. + \frac{\tau_y}{2G} \left(\frac{h}{2} - z \right) \sqrt{a^2 + G^2 \left(\frac{h}{2} - z \right)^2} + \frac{\tau_y a^2}{2G^2} \sinh^{-1} \left(\frac{G}{|a|} \left(\frac{h}{2} - z \right) \right) \right]_0^{z_1}, \end{aligned} \quad (4.21)$$

$$\dot{q}_2 = (0.5h - z_1)V(z_1). \quad (4.22)$$

Plug and Plug-Less Flow

It is useful to know which conditions are required for flow to occur, and for a changeover from the no-plug to plug regime. At the limiting condition for flow to occur $\tau = \tau_y$. This condition in eqn(4.10) gives:

$$\frac{a^2}{\tau_y^2} + \frac{b^2}{\tau_y^2} = 1 \Rightarrow \frac{a^2}{\tau_y^2} + \frac{G^2}{\left(\frac{2\tau_y}{h} \right)^2} = 1 \quad (4.23)$$

Fig. 4.1 (b) illustrates this relationship. The switch from plug to plug-less regime occurs when $a = \tau_y$. For a given value of G , the values of flow rate and plate speed at the point of transition between plug and plug-less flow can be calculated using eqn(4.15) (\dot{q}_{trans}) and eqn(4.16) (U_{trans}) respectively with $a = \tau_y$. If a given value of G is below $2\tau_y/h$ then a minimum stress (a_{min}) is required for flow to occur - this can be deduced from eqn(4.23):

$$a_{min} = \sqrt{\tau_y^2 - \frac{G^2 h^2}{4}}. \quad (4.24)$$

4.2.2 Conclusion

If $|a| > \tau_y$, then shear-stress from the Couette flow alone is strong enough to ensure the fluid is sheared throughout with no plugs present. In this case, for a given value of G and U , a is given by eqn(4.16) and the resulting flow rate (which is dependent on G and

a) is given by eqn(4.15). However if $|a| < \tau_y$, then flow can only occur if G is sufficiently strong enough to help overcome the fluid yield-stress. A plug will be present which is symmetric about along the centre line, a is now given by eqn(4.19) and the resulting flow rate is given by eqn(4.20).

The equations are quite complex. To obtain a , equations (4.16) and (4.19) must be solved numerically. Care must be taken, as the opportunity for human error is high. The equations governing the 2D flow/stress field give rise to two flows that are coupled.

4.3 CONCENTRIC Clutch with Cooling Through-flow

A theoretical concentric cylinder clutch was examined in a pre-prototyping exercise in order to estimate the effect of a secondary, axial, cooling flow on torque transmission. The through-flow was investigated using the analytical theory presented in section 4.2 and CFD analysis.

The ‘2D Bingham plastic flat plate theory’ was originally developed to analyse this particular problem [48] where gap-width (h) is much smaller than the clutch’s mean radius (r_m). Solutions to the analytical theory and CFD results from undergraduate projects [49] and [50] have been presented in the International Journal of Modern Physics [25]. Here the CFD and analytical results do not correspond very well. This appears to be due to a lack of appreciation in understanding how to obtain a correctly converged solution. The following CFD results that utilise an adequate grid density and convergence procedure agree well with the analytical solution.

4.3.1 Theoretical Model: 2D Concentric Clutch

Within the fluid gap-width (h), the field strength is assumed constant, and flow occurs in both the circumferential and axial directions. The former is caused by rotation of the inner rotor, and the latter is due to the difference in pressure between inlet and outlet along the axis.

4.3.2 Analytical Solution

Given that $h \ll r_m$, the flow is approximated to that between two flat plates. The inner rotor corresponds to the lower plate ($y = 0$) moving with speed $U (= r_1 \Omega)$ in the x -direction whilst the upper plate ($y = h$) is fixed. The steady state torque (N) is then given by:

$$N = 2\pi h r_m^2 |a| L_y. \quad (4.25)$$

Since the clutch is approximated as two flat plates, a mean radius must be used when calculating the torque. This was not done previously in [49], and can affect the results

slightly due to an r^2 effect.

The equations were solved numerically using a spreadsheet¹. Values of the parameters h , r_m , L_x , Ω , Δp , τ_y and μ_e were entered allowing the spreadsheet to calculate values of G and b . A Newton-Raphson method then solves eqn(4.16) or (4.19) for a . If $G < 2\tau_y/h$, eqn(4.24) can be used to obtain a_{min} . The transition pressure gradient (G_{trans}) between plug and plug-less flow regimes is determined when $a = \tau_y$ is used in eqn(4.16) or (4.19) and solved using a Newton-Raphson method. Equation (4.15) or (4.20) can then be used to calculate flow rate. Care must be exercised because the equations are quite complex and errors can be made when entering them into the program.

4.3.3 CFD Model: 2D Concentric Clutch

The following table summarises the CFD model used in this section.

Software	Fluent4, finite volume, segregated solver	
Physical Model	2D, steady, laminar, incompressible, isothermal flow	
Fluid Properties	viscosity (Bingham CFD model), density (constant)	
Discretisation of flow Equations	interpolation scheme	1st order for all equations
	pressure-velocity	SIMPLE
	grid (y, z) [z = radial direction]	40 (axial) x 40 (radial)
Boundary Conditions	outer rotor	wall, zero velocity condition
	inner rotor	set circumferential velocity
	inlet	inlet axial velocity
	outlet	fully developed

Table 4.1: Summary of CFD model used to solve 2D concentric clutch with through-flow.

Without having to make the flat plate approximation, the same problem was solved under identical flow assumptions using the CFD method. The clutch was modelled using an inner and outer cylindrical wall. All derivatives in the tangential direction are zero, allowing an axisymmetric grid to be used. A uniform inlet velocity was used to set the flow rate (\dot{q}_y) (using a mean radius r_m). The length of the clutch was increased by 20% to allow space for the parabolic velocity profile to develop. This was ample room to allow the profile to develop. Since the flow aligns with the grid, a first order power law interpolation scheme was found to be adequate in determining cell face values. To allow convergence the residuals had to be reduced considerably more than the default values. It also proved advantageous to increase the under relaxation values for

¹ Done using Microsoft Excel.

w-velocity and viscosity equations to a value closer to 1.0.

4.3.4 Results: 2D Concentric Clutch Model

In some areas, the CFD results are found to be in very good agreement with the analytical predictions. In other areas, the correlation is poor. This inconsistency is due to the analytical flat plate assumption being less valid for representing cylindrical geometry at lower speeds where wall plug behaviour can be found.

Fig. 4.2 displays results of torque vs. rotational speed for a 10 kPa fluid under various levels of pressure gradient (G). To fully test the comparison between the CFD package and analytical theory, some large values of G were chosen in order to put the flow in both plug and plug-less regimes. Here a uniform inlet velocity was used in order to achieve a theoretical value of G as indicated by the analytical model. As a result, the corresponding values of flow rate shown in Fig. 4.3 are in perfect correlation. Referring back to Fig. 4.2, when $G = 0$ bar/m there is no axial flow and the torque profile is seen to be unaffected and is thus the familiar N vs. Ω for a smart clutch device. However, for larger values of G , the effect on torque becomes evident.

As discussed in section 2.4.2, below a certain speed (Ω_p), given by eqn(2.24), a plug would be attached to the outer wall due to the concentric geometry, in which case the flat plate assumption, used for the analytical model, is less valid. Equation (2.24) applies only to the case when $\dot{q}_y = 0$ Lt/min. However, its value is still likely to be of some use in indicating whether the flat plate assumption is valid or not. As indicated by eqn(4.10), for the same Ω an increased value of G , reduces the shear-stress (a), which would result in Ω_p being underestimated. Bearing in mind that the CFD results have been obtained for the cylindrical geometry, this behaviour is indicated in Fig. 4.2. Below Ω_p , the CFD points match the analytical theory less well than above Ω_p . The torque dips at very low speed due to plug presence on the outer rotor.

When $G > 2\tau_y/h$, a minimum value of a before flow can occur is not required (see Fig. 4.1 (b)). This effect is shown in Fig. 4.4 for a 6 kPa strength fluid. Here the yield-stress has effectively been removed and no initial torque is required before flow can occur. The corresponding flow rates are shown in Fig. 4.5. Here for the 8 and 10 kPa fluid, no axial flow occurs at zero speed because $\tau < \tau_y$.

It is useful to look at how the flow rate affects the torque (N vs. \dot{q}_x) as in Fig. 4.6 at a speed of 600 rpm for 2 and 10 kPa at 100 mPa.s. Increased flow rate is seen to diminish torque. The corresponding values of G required to obtain \dot{q}_y are shown in

Fig. 4.3. For the same plate speed (U), with increased pressure gradient (G), circumferential shear-stress ($|a|$) decreases and a transition from case (i) ($|a| > \tau_y$) to case (ii) ($|a| < \tau_y$) can occur. The transition point occurs at higher flow rates with decreasing τ_y and Ω . Flow rates greater than 1.0 Lt/min intuitively seem to be too high for such a small device and thus flow is always likely to be in the plug regime.

Finally, the velocity profiles must be considered. In case (i) there is no plug and $w(h/2) = W/2$, whereas in case (ii), the region $z_1 \leq z \leq z_2$ is occupied by a plug moving with this speed in the transverse direction. The axial component is symmetric about $y = h/2$ with maximum speed at $y = h/2$, in case (i). In case (ii), the plug moves with speed $v(z_1)$ in this direction. These features agree with the profiles obtained from the CFD as shown in Fig. 4.7 and Fig. 4.8.

4.3.5 Discussion

When G is increased to 100 bar/m and 300 bar/m the torque profile is affected, i.e. the pressure gradient is reducing the value of a . The effect is quite severe at 300 bar/m, and the value reduces significantly at low speed. Within the range of practical operation, when Ω is relatively large and G small, a change from plug flow to plug-less flow occurs. A value of 100 bar/m seems large but for a 10 kPa fluid this gives a flow rate less than 1.0 Lt/min at 1000 rpm. However, the clutch is unlikely to operate in a fully active slipping state 100 % of the time. During the cycles when the clutch is un-active (e.g. during disengagements) $\tau_y = 0$ kPa and significant amounts of axial flow will occur, thus helping to remove heated fluid.

When the axial flow rate is zero, the torque remains relatively independent of speed, provided μ_e is small. This is not the case when pressure is applied so as to force an axial flow rate. At low speeds, G can dominate and a lot of torque can be lost. The severity depends upon the magnitude of G . For high values of G , the situation can be likened to a clutch device operating with a fluid that has no static yield-stress. Such a set-up may be useful in certain forms, for example as a speed-limiting device¹. It can also be noted that at low speeds viscous heating is less of a problem and thus large values of G are not required.

When considering this device to be a valve as opposed to a clutch, unusual $\{\Delta p \text{ vs. } \dot{q}_x\}$ curves are formed. If the device is forced to rotate then no initial G need be overcome for flow to occur. This could help give a better range of operation in a smart

fluid valve. When the flow rate is less than the critical value as predicted by the analysis, no plug is present, whereas above this value there is a central plug.

The number of cells within the gap width that are needed in order to achieve a grid independent solution, was found to be greater than that required for Newtonian flow. This is due to the velocity profile being more complex. Default convergence criteria were found to be insufficient. It is mainly a lack of consideration to these two important points that gave poor comparable results in previous work [25].

It is clear that for practical cases ($\dot{q}_z \approx 1.0 \text{ Lt/min}$, based on rudimentary heat balance calculation) the linear approximation based on $|Gh/2a| \ll 1$ is not valid. The consequence of this is that there will be a drop in pre-set torque with increased through-flow. However, the results show that the severity of this loss in output is quite small, allowing for an otherwise impractical (due to heating effects) device to be contemplated.

On this occasion, the CFD indicated that the original plug-less flow theory ($\tau > \tau_y$) was insufficient. This led to the development of the plug flow analysis ($\tau < \tau_y$).

4.4 RADIAL Clutch with Cooling Through-flow

A theoretical two plate radial clutch is now examined in a pre-prototyping exercise. With a similar aim to the previous section, the effect of a secondary radial cooling flow on pre-set torque transmission is estimated. The through-flow is investigated using CFD analysis and the results are partially verified by developing the Bingham plastic 2D parallel plate theory (section 4.2).

This situation is more complex than before, as the pressure gradient that causes flow is no longer constant. This imposes difficulties in the analytical solution. The pressure profile has to be obtained numerically as when CFD is used. Once this profile is calculated using a CFD model, it can be used in the analytical theory to obtain values of torque and flow-rate.

Again, the smart fluid is considered a homogeneous, incompressible continuum with constant values of yield-stress and plastic-viscosity. The Bingham equation is utilised and analysis assumes steady, 2D, laminar and isothermal flow.

4.4.1 Theoretical Model

The two discs are separated at a distance (h) in the z -direction as shown in Fig. 4.9. Flow occurs in both the circumferential (θ) and the radial (r) directions. The former is

¹ As the speed increases, the torque resisting motion would also quickly increase.

caused by the relative angular speed (Ω) of the plates (Couette flow), whereas the latter is due to a pressure difference between the inlet and the outlet radii (Poiseuille flow). For simplicity, one plate ($z = 0$) is always considered stationary, whilst the other ($z = h$) rotates with constant speed Ω . The velocity components are assumed to be:

$$v_r = v_r(r, z), \quad v_\theta = v_\theta(r, z), \quad v_z = 0. \quad (4.26)$$

4.4.2 Analytical Solution

An analysis of the deformation rate tensor (d_{ij}) shows that provided $h \ll r$, the dominant terms are d_{rz} , d_{zr} , $d_{z\theta}$ and $d_{\theta z}$. This is equivalent to neglecting the normal stresses. As centrifugal acceleration terms are expected to be relatively small, steady state acceleration terms are also neglected. Under the approximation $h \ll r$, the dominant terms in the momentum equations {eqn(4.3)} are then:

$$-\frac{\partial p}{\partial r} + \frac{\partial \tau_{rz}}{\partial z} = 0, \quad \frac{\partial \tau_{\theta z}}{\partial z} = 0, \quad \frac{\partial p}{\partial z} = 0 \quad \{\text{cf. eqn(4.8)}\} \quad (4.27)$$

These partial differential equations can be integrated to give:

$$\tau_{rz} = G(r)z + b(r), \quad \tau_{\theta z} = a(r), \quad p = p(r), \quad (4.28)$$

in which $b(r)$ and $a(r)$ are arbitrary functions of r and so are arbitrary constants at a given radius and:

$$G(r) = \frac{dp}{dr}. \quad (4.29)$$

The magnitude of resultant shear-stress at radius (r) is:

$$\tau(r) = \sqrt{\tau_{rz}^2 + \tau_{\theta z}^2} = \sqrt{a(r)^2 + (G(r)z + b(r))^2}. \quad (4.30)$$

Equation (4.30) is equivalent to eqn(4.10) at a given radius (r). In this case, from eqn(4.4),

$$\tau_{rz} = \left(\frac{\tau_y}{\dot{\gamma}} + \mu_e \right) \frac{dv_r}{dz}, \quad \tau_{\theta z} = \left(\frac{\tau_y}{\dot{\gamma}} + \mu_e \right) \frac{dv_\theta}{dz}. \quad \{\text{cf. eqn(4.6)}\} \quad (4.31)$$

It follows that eqn(4.2), eqn(4.11), eqn(4.13), eqn(4.14), eqn(4.16), eqn(4.17), eqn(4.18) & eqn(4.19) are relevant for this situation at radius (r) when the following replacements are made:

$$u_r = v, \quad u_\theta = u, \quad r\Omega = U, \quad \text{and } a, b, G \text{ depend upon } r. \quad (4.32)$$

Once again to satisfy the boundary conditions on v_r :

$$b(r) = -G(r)h/2. \quad (4.33)$$

Torque

The torque required to keep the plate moving at speed Ω is given by:

$$N = \int_{r_i}^{r_o} dr \int_0^{2\pi} r^2 a(r) dr d\theta = 2\pi \int_{r_i}^{r_o} r^2 a(r) dr \quad (4.34)$$

In the couple case the total torque is calculated at discrete radii and summed over the range r_i and r_o so that:

$$N = 2\pi \sum_{r_i}^{r_o} r^2 a(r) \delta r \quad (4.35)$$

When $Gh/2a \ll 1$ and $U = r\Omega$ then eqn(4.16) reduces to:

$$a(r) \approx \frac{\mu_e r \Omega}{h} + \tau_y, \quad (4.36)$$

giving from eqn(4.34):

$$N = \frac{\mu_e \pi \Omega}{2h} (r_o^4 - r_i^4) + \frac{2\pi \tau_y}{3} (r_o^3 - r_i^3). \quad (4.37)$$

This expression is the same as for the case when there is no axial flow ($G(r) = 0$).

Flow Rate: Plug-Less Flow $|a(r)| > \tau_y$

An integration of the radial velocity profile gives the flow rate at radius (r) as:

$$\dot{q}_r = -\frac{G(r)h^3\pi r}{6\mu_e} + \frac{2\pi r}{\mu_e} \left\{ \frac{\tau_y h}{4G(r)} \sqrt{G(r)^2 h^2 + 4a(r)^2} - \frac{\tau_y a(r)^2}{G(r)^2} \sinh^{-1} \left(\frac{G(r)h}{2|a(r)|} \right) \right\}, \quad (4.38)$$

{cf. eqn(4.15) note $L_x = 2\pi r$ }.

Flow Rate: Plug Flow $|a(r)| < \tau_y$

The radial flow rate at radius (r) is a summation of flow in the plug-less region plus that of the plug:

$$\dot{q}_r = 2\pi r \left[2 \int_0^1 u_r(r, z) dz + u_r(r, z)(z_2 - z_1) \right] = \dot{q}_1 + \dot{q}_2, \quad \text{note (4.39)}$$

$$L_x = 2\pi r$$

$$\begin{aligned} \dot{q}_1 = \frac{2\pi r}{\mu_e} & \left[-\frac{G(r)y^2}{12}(3h-2z) + \frac{\tau_y z}{2G(r)} \sqrt{G(r)^2 h^2 + 4a(r)^2} \right. \\ & + \frac{\tau_y}{2G(r)} \left(\frac{h}{2} - z \right) \sqrt{a(r)^2 + G(r)^2 (0.5h - z)^2} \\ & \left. + \frac{\tau_y a(r)^2}{2G(r)^2} \sinh^{-1} \left(\frac{G(r)}{|a(r)|} \left(\frac{h}{2} - z \right) \right) \right]_0^{z_1}, \end{aligned} \quad (4.40)$$

$$\dot{q}_2 = 2\pi r (0.5h - z_1) u_r(r, z_1). \quad \text{\{cf. eqn(4.20), eqn(4.21) \& eqn(4.22)\}} \quad (4.41)$$

If we consider radial flow only (Poiseuille flow only $a(r) = 0$) eqn(4.39) reduces to,

$$\dot{q}_r = \frac{\pi r h^3 G(r)}{6\mu_e} \left[1 + 3 \left(\frac{\tau_y}{hG(r)} \right) - 4 \left(\frac{\tau_y}{hG(r)} \right)^3 \right]. \quad (4.42)$$

With appropriate change in notation, this equation is the same as that presented in [24].

Pseudo-Plug Flow

If $|a(r)| > \tau_y$ flow will occur across the whole gap. However if $|a(r)| < \tau_y$ flow can only occur if a central pseudo-plug region is present. The term pseudo-plug is used because in this geometry it is impossible to have a solid central section moving at constant speed. However, at given radius the velocity profiles have a central section in which the speed is constant.

4.4.3 CFD Model: 2D Radial Clutch

The following table summarises the main CFD model used in this section.

Software	Fluent4, finite volume, segregated solver	
Physical Model	2D, steady, laminar, incompressible, isothermal flow	
Fluid Properties	viscosity (Bingham CFD model), density (constant)	
Discretisation of flow Equations	interpolation scheme	1 st order for all equations
	pressure-velocity	SIMPLE
	axisymmetric grid	80 (in gap-width) x 100 (along the radius)
Boundary Conditions	upper disc	wall, zero velocity condition
	lower disc	wall, with circumferential velocity $r\Omega$
	inlet	inlet axial velocity
	outlet	static pressure outlet

Table 4.2: Summary of CFD model used to solve 2D radial clutch with through-flow.

The problem outlined above was solved using Fluent4. The same flow and fluid assumptions already outlined apply. However, the lubrication assumption $h \ll r$ is not required and furthermore the steady state acceleration terms are not be neglected.

Since all derivatives are zero in the tangential direction, a 2D axisymmetric grid was used. A uniform inlet velocity boundary condition allowed the flow rate, \dot{q}_r , to be set, a static zero pressure condition was used for the outlet. A fully developed condition is not correct. One wall is set to be stationary and the other set to rotate with angular speed Ω . Increasing grid resolution produces a model that more accurately simulates the continuum problem. However, this comes at the expense of computational speed therefore engineering judgement had to be exercised. Since the flow aligns with the grid a first order power law interpolation scheme was adequate to determine cell face values.

4.4.4 Results: 2D Radial Clutch

Poiseuille Flow Only

The case of radial flow only was initially studied, for which pseudo-plug profiles were found. In the analysis, eqn(4.17) suggests that the plug size will increase with radius when G decreases with radial position. To maintain mass continuity, the velocity of the fluid reduces; this results in a more dominant plug at greater radii, due to a reduction in deformation rate. This behaviour can be observed in Fig. 4.10.

The pressure profile can be numerically differentiated to determine $G(r)$ at discrete values of radius. If the CFD profile is correct then eqn(4.42) must yield a constant value of \dot{q}_r at all radii, if mass is to be conserved. Initial tests showed disagreement at small radii that could not be fully attributed to flow development. The

discrepancy was found to be due to a lack of cell density in the radial direction. Unlike the concentric clutch case, the pressure profile is non-linear particularly at and near the inlet radius. Increasing cell density resulted in good agreement over most of the radius range. The initial 5 mm of the CFD flow field conforms to mass continuity but does not correspond to theory. A flow development length that is required for the uniform inlet velocity to develop, results in a pressure profile that does satisfy the assumptions of the theory.

Coupled Flow

The CFD model was used to find how N is affected by higher flow rates. As $G(r)$ increases, $|a(r)|$ decreases, and eventually there is a crossover from case (i) to (ii). For every computed flow field $G(r)$ was determined numerically, allowing $a(r)$ to be calculated using the relevant equation. This allowed the total torque to be evaluated by summing the values at each discrete radius (eqn(4.35)). This was achieved by importing CFD data into a spreadsheet that allowed each CFD point to be checked.

A grid analysis showed that 80 cells in the axial direction gave grid independent answers. To achieve an accurate pressure field over the full radius required about 400 cells. However, the majority of torque is generated well away from the inlet. This meant that only 100 cells in the radial direction were required for a grid independent answer. Considering the geometry $(r_o-r_i)/h$ a grid of 80 x 100 cells was chosen. Engineering judgment was therefore used to set up a practical grid; the validity of which is demonstrated in the following results.

Fig. 4.11 and Fig. 4.12 show N and Δp behaviour over a wide range of τ_y and flow rates at two typical speeds of operation. At 600 rpm there is a ~50% drop in N at 6 Lt/min at each value of τ_y , whilst at 1200 rpm the severity of the coupling loss is much less (~20%). For a constant pressure difference, it can be noted that reducing the speed also reduces the flow rate.

Next, the effect of the geometry is considered. When there is no radial flow, doubling the gap size halves the shearing rate and likewise the Newtonian contribution to torque. Nevertheless, for practical parameters the Newtonian shear-stress is small in comparison to the yield-stress contribution, meaning that there is only a small loss in N . In terms of coupling effect as shown in Fig. 4.13, doubling the gap size results in a significantly better scenario. The ratio between circumferential/radial velocities is doubled, resulting in a greater Couette flow domination and less coupling.

As shown in Fig. 4.13 a 17 % increase in radius from 30 to 35 mm gives a 91 %

increase in torque. Such an increase also results in a higher ratio of circumferential/radial velocity in this new section - radial velocity decreases with radius while circumferential velocity increases. At 6 Lt/min the loss in torque is now ~40% as opposed to ~50% previously, so the overall increase in torque due to the extra 5 mm is more than 60% - this is a significant consideration.

In the absence of radial flow, μ_e only contributes to the Newtonian term, which is typically very much smaller than the yield-stress term. Fig. 4.14 shows that a high plastic-viscosity can give a much greater Newtonian contribution, but this has little effect in terms of coupling.

We now look at the velocity profiles. Fig. 4.15 and Fig. 4.16 show the radial and circumferential velocity profiles when the conditions 5 kPa at 0.8 lt/min are used. In this case, both plug and parabolic regions are present. The pseudo-plug regime is observed at small radii at and near the inlet when the Poiseuille flow is dominating. At larger radii at and near the outlet, Couette flow dominates and the plug-less regime is present.

The pseudo-plug propagates from being present only at the inlet to the full radius at greater radial flow rates. When the Poiseuille flow is dominant at all radii, the plug size is seen to increase with radius in a similar way to that observed for the Poiseuille case (Fig. 4.10). It can be noted that near the outlet where most of the torque is generated the circumferential velocity profiles are relatively linear.

Required Range

To emphasise parameter effects and show good agreements between theory and CFD, results have been presented over a relatively large range [0-6 lt/min]. To determine an approximation of the magnitude required for a practical situation, a basic heat balance calculation is carried out. Evaluating the power input and the amount of energy the smart fluid can carry away gives the following relationship:

$$\Delta T = \frac{QN}{\rho C_v \dot{q}} \quad (4.43)$$

Even for low values of τ_y , the overall majority of the work done on the smart fluid is that needed to overcome the yield-stress of the fluid. It is therefore the yield-stress, as opposed to the plastic-viscosity, that is mostly responsible for heat generation. A yield-stress of 10 kPa was seen to generate a torque of 0.6 Nm (Fig. 4.11). To stop the fluid rising by more than 2°C, a flow rate of 0.5 Lt/min is therefore required. In comparison, a yield-stress of 20 kPa requires 1.0 Lt/min.

A flow rate of 1.0 Lt/min is therefore a substantial cooling flow for this situation,

and over the operational range of [0 - 1.0 Lt/min] it can be seen that there is very little drop in pre-set torque (Fig. 4.17). In this range, we are predominately in the plug-less flow regime, the importance of which simply means that the circumferential flow is dominating.

4.4.5 Discussion

Constitutive Theory

In the analytical analysis, when the plug has a constant width, the region can simply be treated as a rigid body that moves at constant speed; the fluid mechanics is not applied in the plug region and there is no misuse of the model. Nevertheless, is this approach valid when the plug width varies? Such problems are considered by Lipscomb *et.al* [26] who state that in complex flow geometries, solid plug regions cannot exist. Interestingly they suggest the use of the bi-viscous model, which is in fact the same as the Bingham CFD model that has been used. The theory in this chapter has been re-derived using this bi-viscous model. As a result, the flow profiles in both yielded and un-yielded regions had to be modified. The expressions for N and \dot{q} contain extra terms, but these are negligible for high values of μ_s . To help simplify matters, the theory presented here is for high values of μ_s , thus the same as using a Bingham plastic constitutive model. The results clearly show that the CFD method, which uses a bi-viscous approach, is comparable to the analytical theory. It can be concluded that the discontinuity that has been highlighted in the Bingham plastic constitutive model is not significant – in comparison to yielded regions, the fluid mechanics in any plug region is unimportant.

ER fluids and MR fluids are expected to have very high values of μ_s , the magnitude of which is therefore of little importance. It should however be noted, that some shear thinning fluids are characterised by having a noticeable value of μ_s at low shear-rates, which then starts to decrease as particle interactions start to become significant. The CFD model used here could be a very useful tool for modelling such fluids. It can also be noted that at high enough shear-rates, all materials and suspensions display Newtonian behaviour, as the Bingham plastic model μ_{nm} tends towards the plastic-viscosity at high deformation rates.

Steady State Assumption

The main difference between the analytical and CFD model was that the former neglected steady state acceleration terms in the momentum equations. A simple conservation of momentum calculation shows that the output torque will be less than the input:

$$M_i - M_o = \dot{m}v_i - \dot{m}v_o \quad \text{since} \quad \dot{m}v_i \gg \dot{m}v_o$$

it follows that,

$$M_o = M_i - \dot{m}v_i \tag{4.44}$$

This first became known from initial CFD results. The difference between the torque on the input and output plates is only noticeable at large flow rates and at low τ_y for which the extra loss in N is only 6%. In the estimated practical flow range of [0-1.0 Lt/min], the difference is less than 1%. The CFD torque values presented here are those that correspond to the input plate. Finally, the theory neglects any loss in torque, and so to make an accurate comparison the input plate that must be considered.

4.4.6 Main Indications of Appraisal

The results show that provided the Couette flow is dominating, the pre-set torque is relatively unaffected by the radial flow. The presence of pseudo-plugs is not desirable in so much as it means that Poiseuille flow is dominating. On a more practical point, the presence of a plug means that the difference between plate speeds is distributed over a smaller distance, resulting in greater shear-rates and hence more significant viscous heat generation.

Fluid manufacturers try to design smart fluids to have a low plastic-viscosity. This gives a low Newtonian shear-stress contribution, and consequently a constant shear-stress over a relatively large range of shear-rates, that can be manipulated by changing τ_y through the field strength. The viscosity is found to have little effect in terms of the severity of the coupling effect. However, although the Newtonian contribution is small, for fluids that display low τ_e , it can be quite significant as the rate of heat generation increases with speed. It is therefore an advantageous characteristic if for the same pressure the flow rate increases with increased speed.

A larger gap size results in a lower radial velocity and therefore less coupling effect for the same flow rate. However, a larger gap size requires a bigger power supply to generate the same field strength. A compromise in this respect is therefore required.

There are other consequences of having a through-flow. The condition that must be satisfied at the outer radius for flow to occur can be rewritten as:

$$\sqrt{\frac{G(r)h^2}{2} + a(r)^2} > \tau_y \tag{4.45}$$

Provided that $G(r) > 2\tau_y/h$, even when both clutch plates are stationary the smart fluid will always be in a sheared flowing state. The requirement of a limiting torque before

any flow occurs is therefore eliminated. This suggests that the clutch cannot support any load, but in practice, as soon as there is any circumferential flow the radial flow rapidly becomes much less dominant, allowing the clutch to support torque. The ability to support load will rapidly vary from zero at $\Omega = 0$, to a substantial value as Ω develops. The severity of the change will depend on $G(r)$, h and τ_y .

The ability to vary N over a wide range is now possible by controlling the shear-rate, which before was not possible due to low plastic viscosities and having to overcome an initial limiting torque. Such a device characteristic may be utilised in various applications such a rapid self regulating controller, a damper, and devices that need to be readily taken from zero to non-zero Ω through control of τ_y .

If the inability to support little load at very low speed is undesirable then the pressure can simply be reduced so that $G(r) > 2\tau_y/h$, for which at $\Omega = 0$ rad/s the shear-stress is given by:

$$G(r)^2 h^2 / 4 + a(r)^2 = \tau_y. \quad (4.46)$$

In practice, for a clutch operating with the dimensions and parameters outlined in this chapter at the estimated low flow rates, the range is such that there will always be a considerable amount of load-supporting ability at zero speed.

Applications

The radial plate clutch may eventually be designed to induce its own through-flow because of the centrifugal action on the parallel fluid film. This would be most easily controlled if supplied from an external fluid source, or by the centrifugal flow induced by the clutch plates, as when slipping or locked.

Due to a more severe coupling effect at high yield-stresses, and the necessity of simplistic design, smart fluid type clutches would seem to benefit from ER Fluids as opposed to MR fluids. However, with a higher gap width the coupling effect may be acceptable for high yield strength fluids.

Complex Model

In essence, it can be concluded that that there is good agreement between CFD and theory. Any discrepancy appears to be due to a lack in the number of cells to accurately represent the continuum model. The initial aims of this work have therefore been fulfilled. For the required flow range to keep the smart fluid thermally stable the loading capabilities are little affected.

The analytical theory in this chapter is useful with regard to getting an overall

view of the problem and in this case allowed the CFD results to be verified. However, it is not readily adaptable to other flow conditions. In practice, CFD will be needed eventually to predict prototype performance, and even test concepts in the absence of analytical techniques.

4.5 Smart Fluid Seals

In this final section contradicting reports on the effects of rotational speed on the sealing capabilities of smart fluid seal are resolved with the aid of a CFD model. Effects on leakage rate of radius ratio, rotational speed and axial pressure gradient as they interact with fluid properties are illustrated.

Experiments based on steady, 2D flow induced by a pressure gradient in the axial (shaft) direction and rotary motion in the other (circumferential) direction, have been carried out using ER fluids by Atkin et. al. [51]. The results indicate that the motion in the circumferential direction of one surface with respect to the stationary surface, always causes flow to take place in a direction appropriate to that of the pressure gradient inducing it. In a second analysis carried out by Kordonski and Gorodkin [52], no equivalent theory is supplied, but experimentally a MR fluid seal was found to withstand a significant axial pressure gradient without leakage occurring. Since the constitutive equation for ER and MR fluids is understood to be similar, (both materials being modelled as a Bingham plastic), these conflicting results are in need of examination.

In the previous sections we have seen that the viscoplastic continuum analysis (albeit in some cases approximated by the absence of centrifugal terms and limited by use of the lubrication assumption) compares well with the CFD results in both radial plate and concentric cylindrical clutch cases [45] and [29]. Here CFD is used to resolve the apparent paradox between the results reported previously [51] and [52].

From the outset, due caution has to be exercised at low shear-rates when the exact properties of the various fluid types are not fully known. This could be due to the presence of surfactant and anti coagulant additives.

4.5.1 Theory

Again the parallel plate theory presented in section 4.2 can be used to help resolve this problem. Here the problem to investigate is whether flow occurs in the axial direction when the clutch rotates, or does the ER fluid behave like a seal.

When the gap-width (h) is very small compared to the mean radius (r_m) of the electrodes, the flow is considered to be between two flat plates; $z = 0$ which moves with

speed $U (= r_1\Omega)$ and a fixed plate $z = h$ (see Fig. 4.18 a schematic). The pressure gradient $G (= dp/dy = \Delta P/L)$ is in the y -direction. If $u(z)$ and $v(z)$ denote the velocity components in the x - and y - directions, the problem is the same as that described in section 4.3 and so all the results derived there apply here.

4.5.2 CFD Model: Smart Fluid Seal

The problem outlined above was also solved using CFD. As before a concentric axisymmetric geometry was used. This is possible because, as stated in the earlier assumptions, all derivatives in the tangential direction are zero. The flat plate approximation adopted in the theoretical analysis does not have to be made here. The fluid is therefore confined by an inner and outer cylindrical wall boundary condition. The inner cylindrical wall is set to rotate at a tangential speed $U = r_1\Omega$. Uniform pressure conditions are set at the inlet and outlet, allowing a pressure difference to be set over a certain seal length. The model here differs from the concentric clutch model in section 4.3.3, in the way that a flow is imposed using pressure boundary conditions. As a result, convergence is very slow but no flow development length is required. Previously a constant velocity boundary condition was used in order to set a flow rate.

It is important to determine an adequate cell density for the CFD model to correctly represent a continuum. In the radial direction, it was found that 20 cells are adequate. In theory, fewer cells are needed in the axial direction because the flow is not changing with distance in that direction. However, it is important not to skew the cells severely and so 100 cells are used in that direction.

4.5.3 Review

The aim of this section is to consider why some experimental results in [51] and the 2D Bingham plastic flat plate theory, derived in section 4.2, suggest that it is impossible to have an effective smart fluid seal when the shaft is rotating, whilst other experimental results in [52] for MR fluids indicate that the opposite is true. A list of the values of the relevant parameters used by these authors is given in Table 4.3; those indicated by an asterisk (*) are estimates.

	Atkin et. al. [51]	Kordonski & Gorodkin [52]
yield-stress	ER fluid: 256-1500 Pa	MR fluid: ~ 5-10 kPa *
shaft diameter	60 mm	20 mm
gap width	1-2 mm	0.075-0.15 mm
shaft speed	500-2000 rpm (~ 50-200 rad/s)	< 250 rpm (~ 25 rad/s)
pressure gradient	1000Pa/10mm = 0.1 GPa/m	10 min, 300 max GPa/m *

Table 4.3: Seal parameters used in Atkin et. al. [51] and Kordonski and Gorodkin [52]

The experiments by Atkin et.al. [51] were conducted in the range $|a| > \tau_y$. However, from the magnitudes of the yield-stress and speed, it appears that the results reported in Kordonski and Gorodkin [52] could be in the range $|a| < \tau_y$, when in the parallel plate case there is a central plug. It seems pertinent at this point to consider any effects that occur due to the cylindrical geometry. For purely rotational flow ($v = 0$) between two concentric cylinders with radii r_1 and r_2 ($r_1 < r_2$), caused by either cylinder rotating with an angular speed (Ω) and the other stationary, it is possible to have flow in only part of the gap with a plug attached to the outer cylinder at small enough speeds. The angular speed (Ω_p) at which the plug disappears for a Bingham plastic material is given by eqn(2.24). For $\Omega > \Omega_p$ there is flow across the whole gap. Estimates of Ω_p are given in Table 4.4.

	r_1	$r_2 - r_1$	τ_y	μ_e	Ω_p
	mm	mm	Pa	Pa.s	rad/s
Kordonski & Gorodkin [52]	10	0.15	10000	0.1	22
	10	0.15	10000	0.5	11
Atkin et. al. [51] on smaller shaft	30	2.00	1000	0.1	44
	10	2.00	1000	0.1	4963

Table 4.4: Speed (Ω_p) required to exit the plug regime.

The value of Ω_p is significantly affected by the fluid properties. It can be concluded from line 3 Table 4.4, and Table 4.3 that experimental work in Atkin et. al. [51] is likely to have been carried out at rotational speeds greater than Ω_p (the limiting speed for plugs) when the theory predicts flow across the whole gap. This conclusion is further validated by the fact that the results (within experimental error) do match up to the theory. However, with the same parameters and a smaller shaft radius very high speeds are needed. As illustrated in line 1 in Table 4.4, and Table 4.3 for a smaller shaft [52] the limiting speed is much higher than many of the experimental speeds used. This consequently means that plugs are likely to be present which goes some way to

explaining why it may be possible to have full sealing.

4.5.4 CFD Analysis

Further insight into the effect of the relevant parameters when flow is present in both axial and circumferential directions is gained from the CFD analysis. Since shaft diameter is likely to be a significant factor, results were obtained for two sizes corresponding to the apparatus used in Atkin et. al. [51] and Kordonski and Gorodkin [52]. To highlight the important parameters, an orthogonal array, which limits the total number of simulations to 16, was used (Taguucci Analysis). Table 4.5 below shows the flow rate results for all 16 simulations. Also indicated is the theoretical transition speed Ω_p .

No.	Ω rad/s	Gap Size mm	Yield Stress kPa	Vis. Pa.s	dP/dz GPa/m	Shaft radius 10 mm			Shaft radius 30 mm		
						Ω limit eqn. (5)	Flow Rate [Lt/hr] Diff = from theory		Ω limit eqn. (5)	Flow Rate [Lt/hr] Diff = from theory	
						rad/s	CFD	Diff[%]	rad/s	CFD	Diff[%]
1	10	0.5	10	0.05	10	492	0.20	84.8	55	4.03	60.7
2	30	0.5	10	0.10	20	246	4.71	40.3	28	39.85	30.8
3	10	0.2	10	0.10	10	40	0.05	47.1	4	0.64	12.4
4	10	0.5	5	0.05	20	246	7.47	38.8	28	60.71	26.5
5	30	0.2	10	0.05	20	79	0.41	46.7	9	4.21	14.5
6	30	0.5	5	0.10	10	123	4.51	36.4	14	35.56	23.0
7	10	0.2	5	0.10	20	20	0.44	37.5	2	3.52	20.8
8	30	0.2	5	0.05	10	40	0.43	28.6	4	4.06	6.7
Average						161	2.28	45.0	18	19.07	24.4

Table 4.5: Smart fluid seal parameters and results used in Taguucci analysis

Here the values of Ω are close to the range used in Kordonski and Gorodkin [52]. For the chosen range of parameters the results from the CFD simulations differ from those of the flat plate theory, the variation ranging between 7 % - 85 %, the largest discrepancy occurring when $\Omega \ll \Omega_p$ (simulation 1). The flow profiles corresponding to simulation 1 when $r_1 = 10$ mm are shown in Fig. 4.19. The circumferential velocity is seen to exhibit plug-like behaviour, corresponding to high values of μ_{nn} , and the axial velocity is non-symmetric. The plug-like region is attached to the outer cylinder and extends over almost half the gap. The large discrepancy indicates that the flat plate approximation is inapplicable and that it is necessary to consider the cylindrical geometry. Other large discrepancies indicate that for this range of parameters care has to be taken when using the flat plate approximation. Care in interpreting the results of Fig. 4.19 should be exercised because of the concentric cylindrical arrangement and the selection of the value of μ_s . It must be noted that no constant velocity plug per se is evident.

The CFD results are used in Fig. 4.20 to show the average effect of each parameter. A considerably lower flow rate on the smaller shaft can now be seen. At the relatively low speeds of 10 and 30 rad/s the shaft speed is found to be relatively unimportant. The yield-stresses and pressure gradients are found to have an almost linear effect, i.e. doubling the yield-stress halves the flow rate. As clearly represented in Fig. 4.20, the significant parameter of most interest appears to be the gap size. It must be noted that the resulting flow rates are quite small (litres/hour).

It can also be shown that for smaller Ω_p/Ω (less extensive plug behaviour) the results are generally closer. In addition, in all cases of larger r_m/h values (30 mm shaft), the results are considerably closer (Table 4.5). Over the range of parameters that were chosen the gap size is a more significant factor than yield-stress and pressure gradient. In addition, it was found that the plastic-viscosity and rotational speed are generally less important.

4.5.5 Discussion

The present analyses indicate that, the results in Atkin et. al. [51] and Kordonski and Gorodkin [52] can both be reconciled. Although the analyses predict that there is leakage when rotation occurs, for some range of parameters this may be very small (see Table 4.5). For all parameter values taken in Table 4.5 it is found that smaller flow rates are obtained with a smaller shaft radius. Since this model only approximates the real fluid, the flow rate could be zero as found experimentally in Kordonski and Gorodkin [52].

Whilst the eqn(2.24) for Ω_p used to predict the occurrence of plugs in cylindrical geometry is restricted to purely rotational flow, the CFD results, which allow for flow in both the circumferential and axial directions, substantiate the occurrence of a plug-like region attached to the outer cylinder. The CFD analysis also allows for the effect of the relevant parameters on flow rate to be investigated and indicates that the gap width and the shaft radius are the most significant.

For some parameter values shown in Table 4.5, there are large discrepancies between the values for flow rates predicted by the CFD and those that follow from the theoretical analysis in which the flow is taken to be between two parallel flat plates. Here the speeds were chosen to be within the range used in Kordonski and Gorodkin [52]. However, in the earlier work where higher speeds are used, very good agreement is found between this theory and the results from CFD. This indicates that care has to be taken when replacing the cylindrical geometry by two parallel flat plates.

Finally, in all the analysis presented, the excitation field is assumed constant across the gap. For further work, the effect of a non-uniform field distribution could be included in both theoretical analysis and CFD.

4.6 Summary: 2D Steady State Smart Fluid Flow

The essential results are very promising. In the CFD models, the true radial geometry was modelled using an axisymmetric grid. The analytical model for the concentric clutch and seal problem used a flat plate approximation. Above the minimum speed, at which a wall plug should have disappeared, the flat plate assumption becomes quite valid and agreement between CFD and theory is very good. This minimum speed can be estimated using eqn(2.24). The radial clutch problem the analysis could only be used to partially check the CFD results.

With the confidence in the basic method gained from this work, more complex CFD modelling can now be contemplated involving more difficult geometry, heat transfer and unsteady modes of operation. The CFD software already has a very sophisticated input and output interface and the internal code can be adapted using subroutines. This allows for the modelling of realistic fluids in which the main fluid property (μ_{nn}) can be dependent on field strength, temperature, deformation rate and even the time domain.

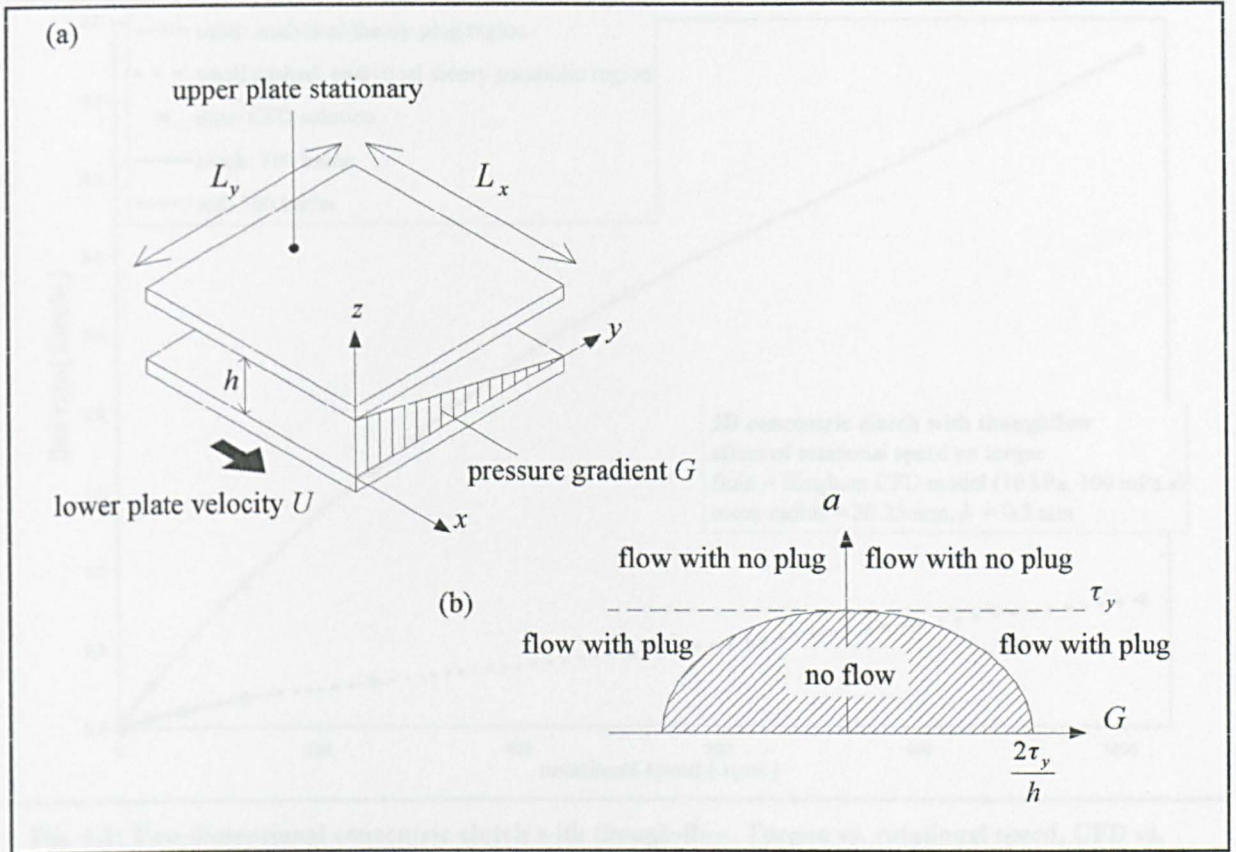


Fig. 4.1: Atkin's two-dimensional Bingham plastic flat plate analytical model.

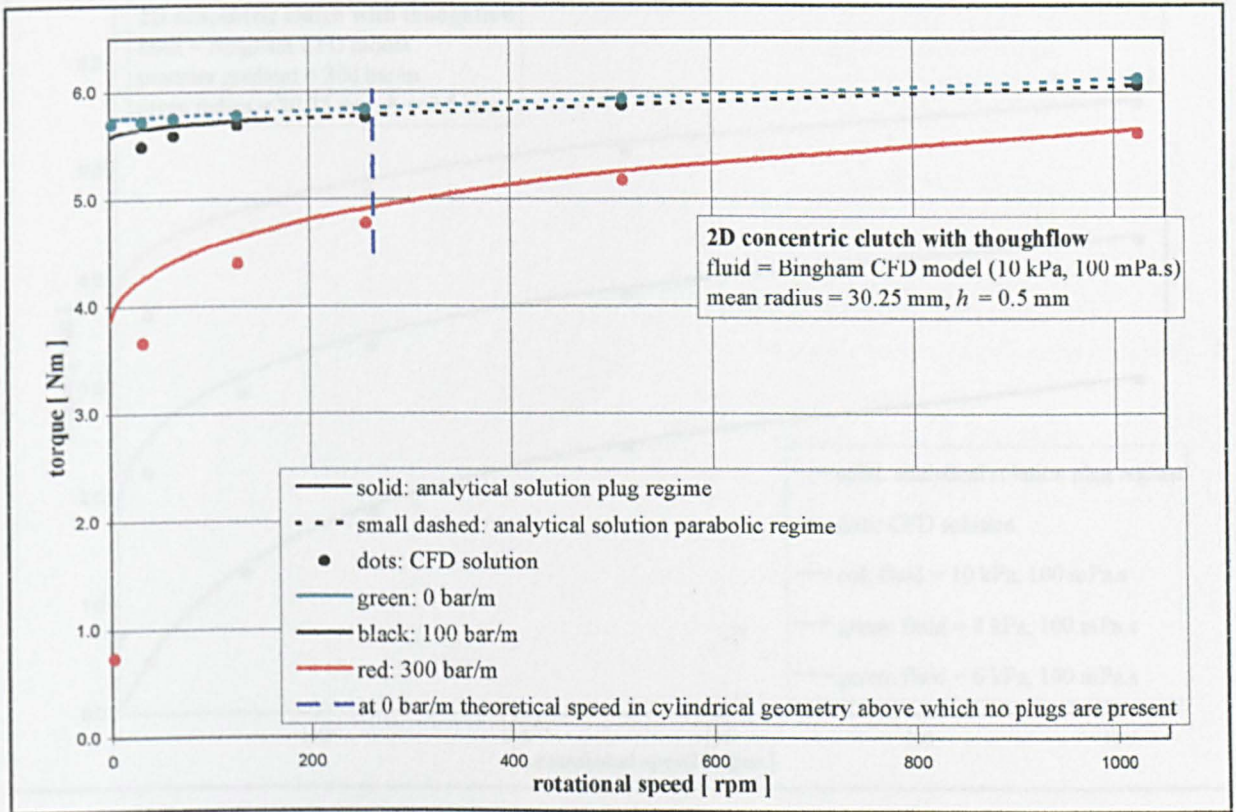


Fig. 4.2: Two-dimensional concentric clutch with through-flow. Torque vs. rotational speed, CFD vs. analytical results for constant values of pressure gradient G . The corresponding values of flow rate are shown in Fig. 4.3.

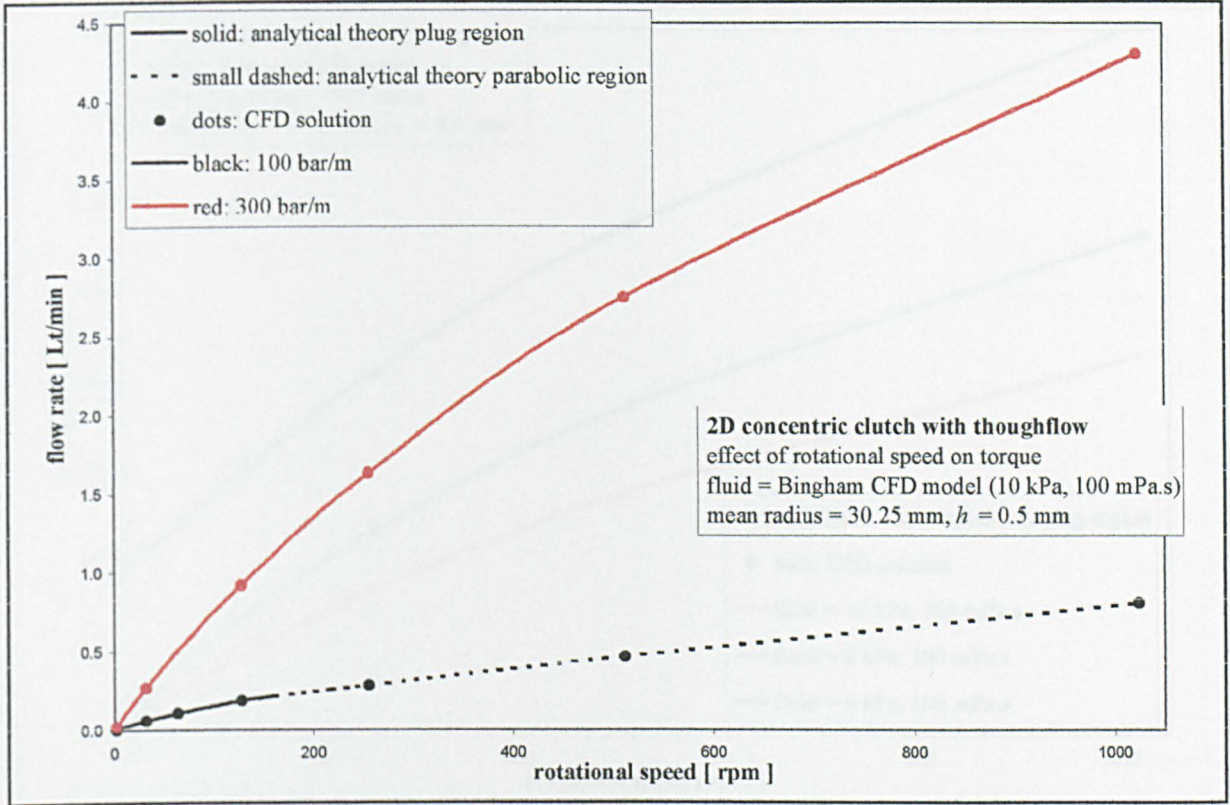


Fig. 4.3: Two-dimensional concentric clutch with through-flow. Torque vs. rotational speed, CFD vs. analytical results for theoretical constant values of pressure gradient G .

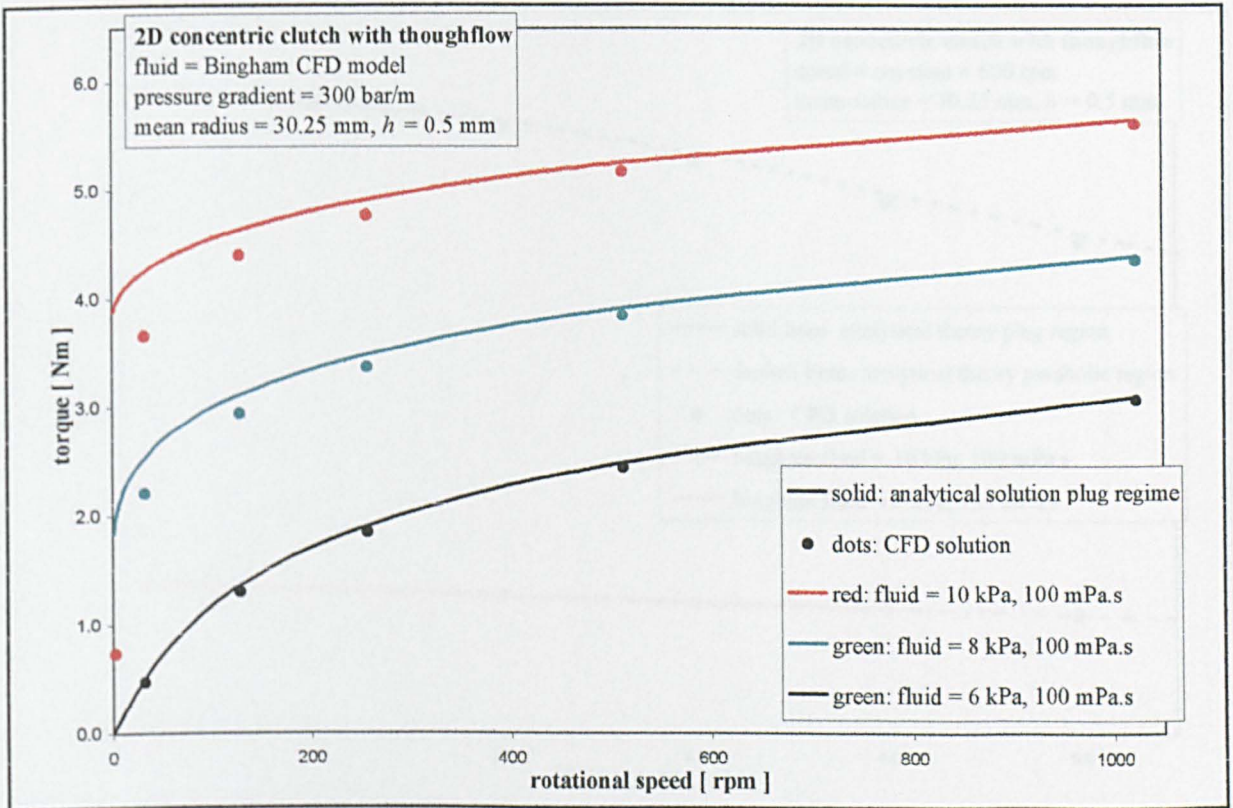


Fig. 4.4: Two-dimensional concentric clutch with through-flow. Torque vs. rotational speed, CFD vs. analytical results for different values of yield strength.

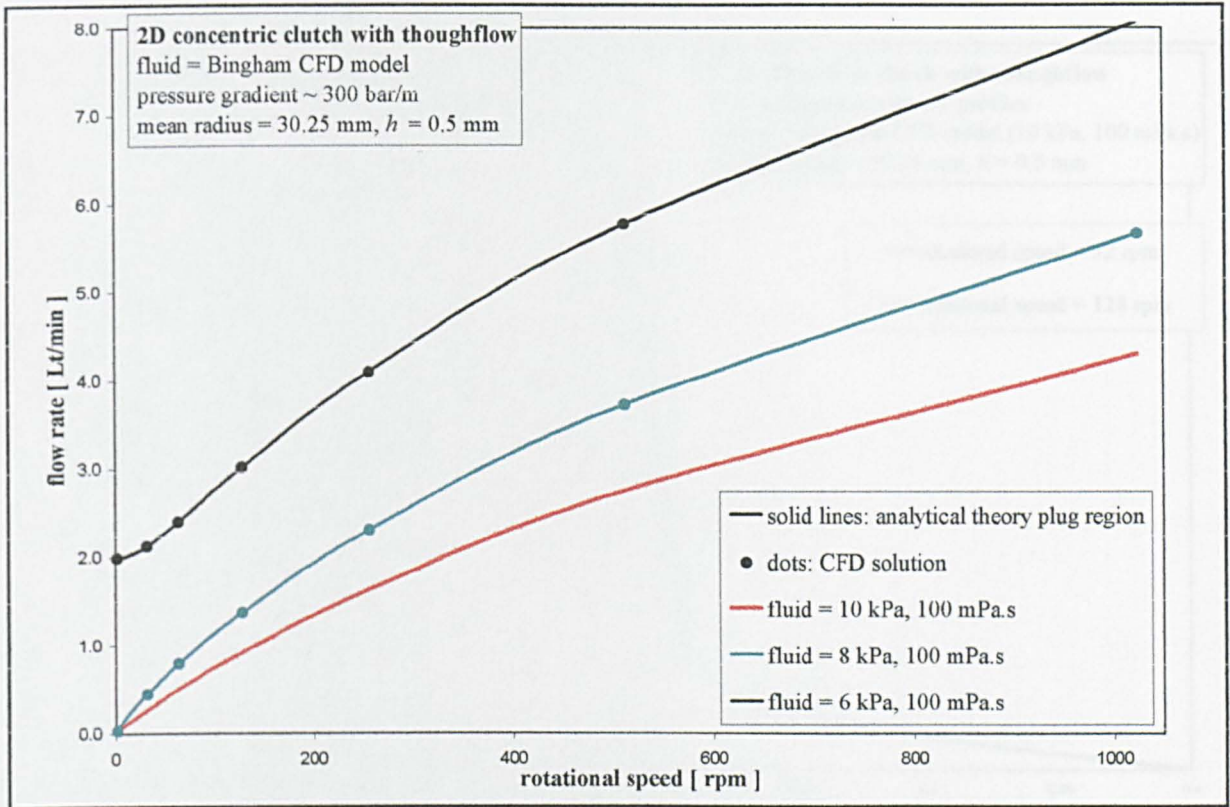


Fig. 4.5: 2D concentric clutch with through-flow. CFD vs. analytical results for constant values of pressure gradient G . The corresponding values of flow rate are shown in Fig. 4.3.

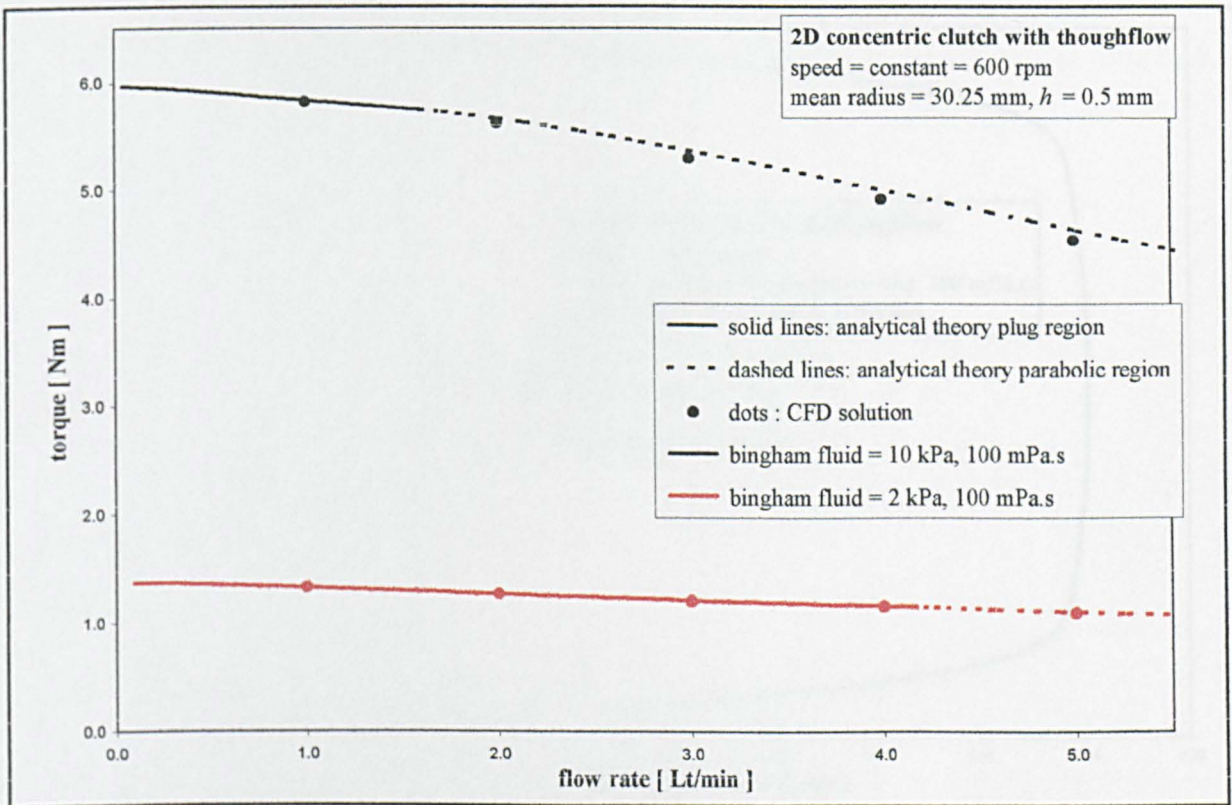


Fig. 4.6: 2D concentric clutch with through-flow. CFD vs. analytical results for constant values of pressure gradient G . The corresponding values of flow rate are shown in Fig. 4.3.

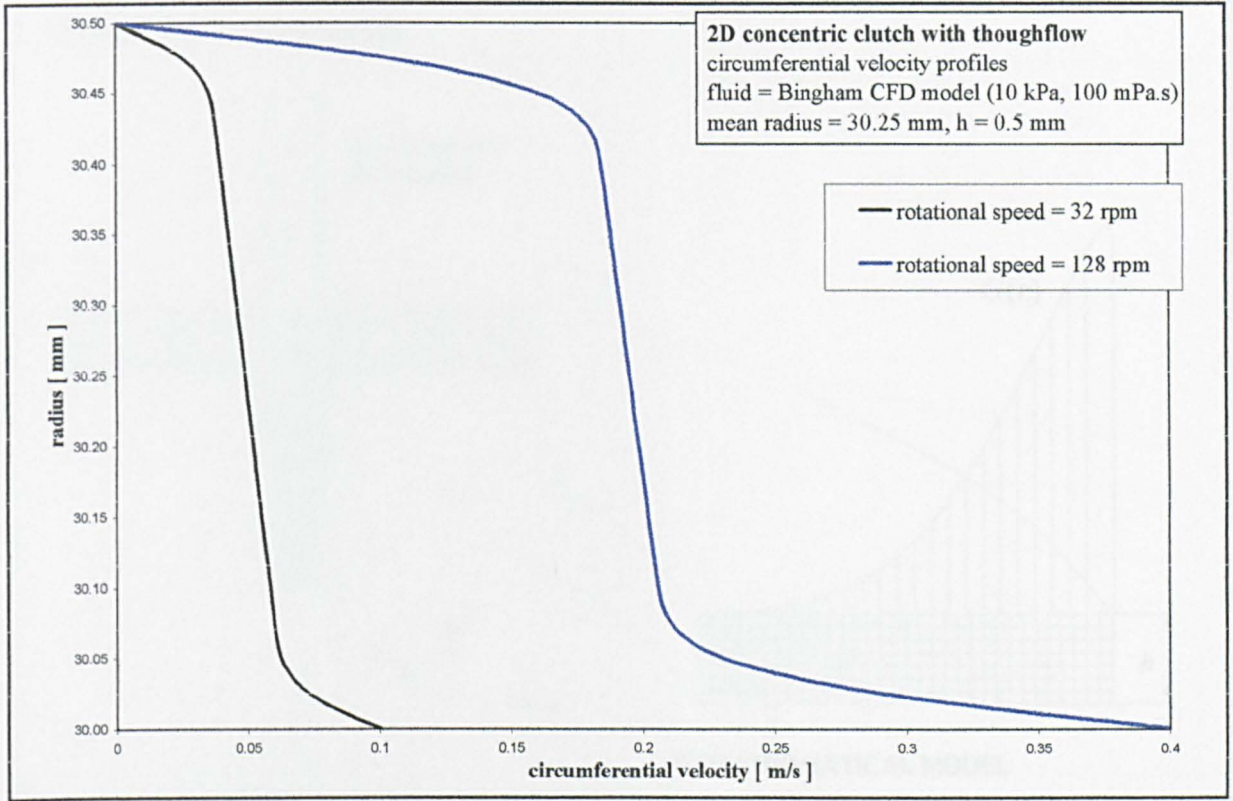


Fig. 4.7: 2D concentric clutch with through-flow. Circumferential velocity profiles.

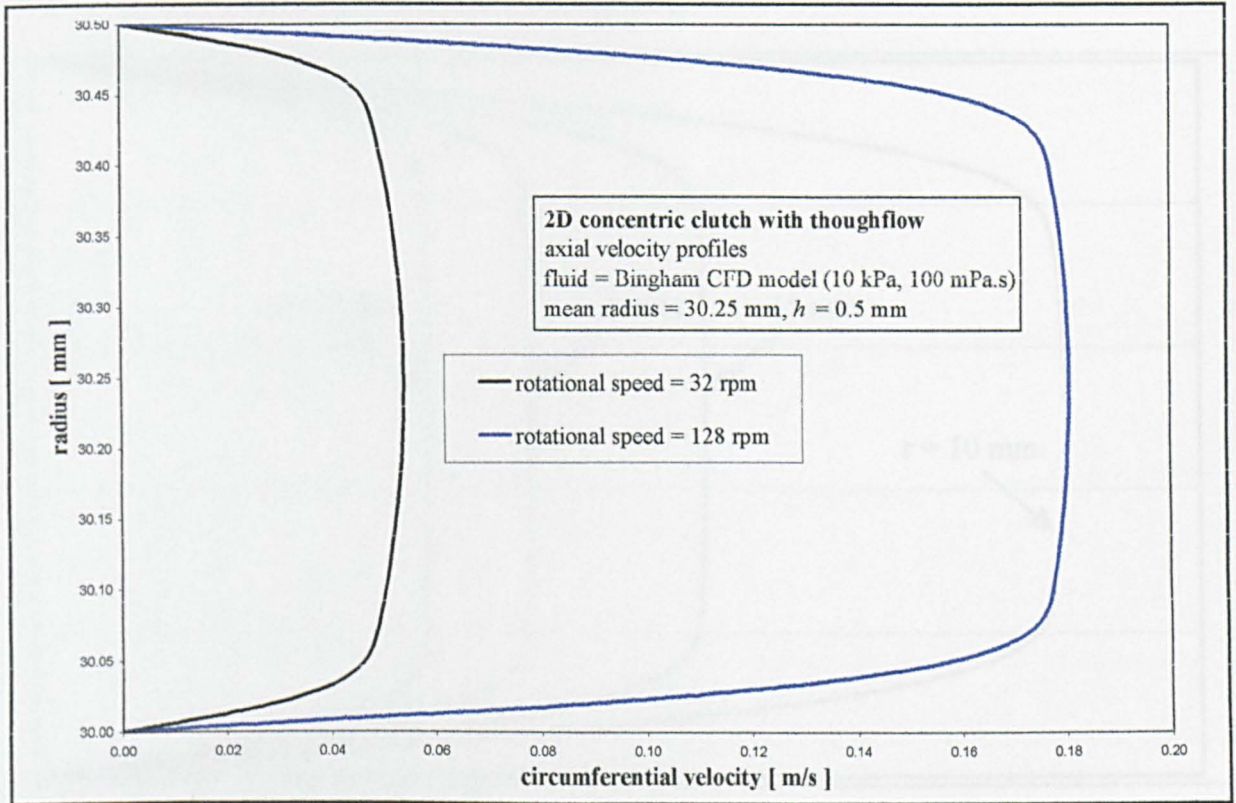


Fig. 4.8: 2D concentric clutch with through-flow. Axial velocity profiles.

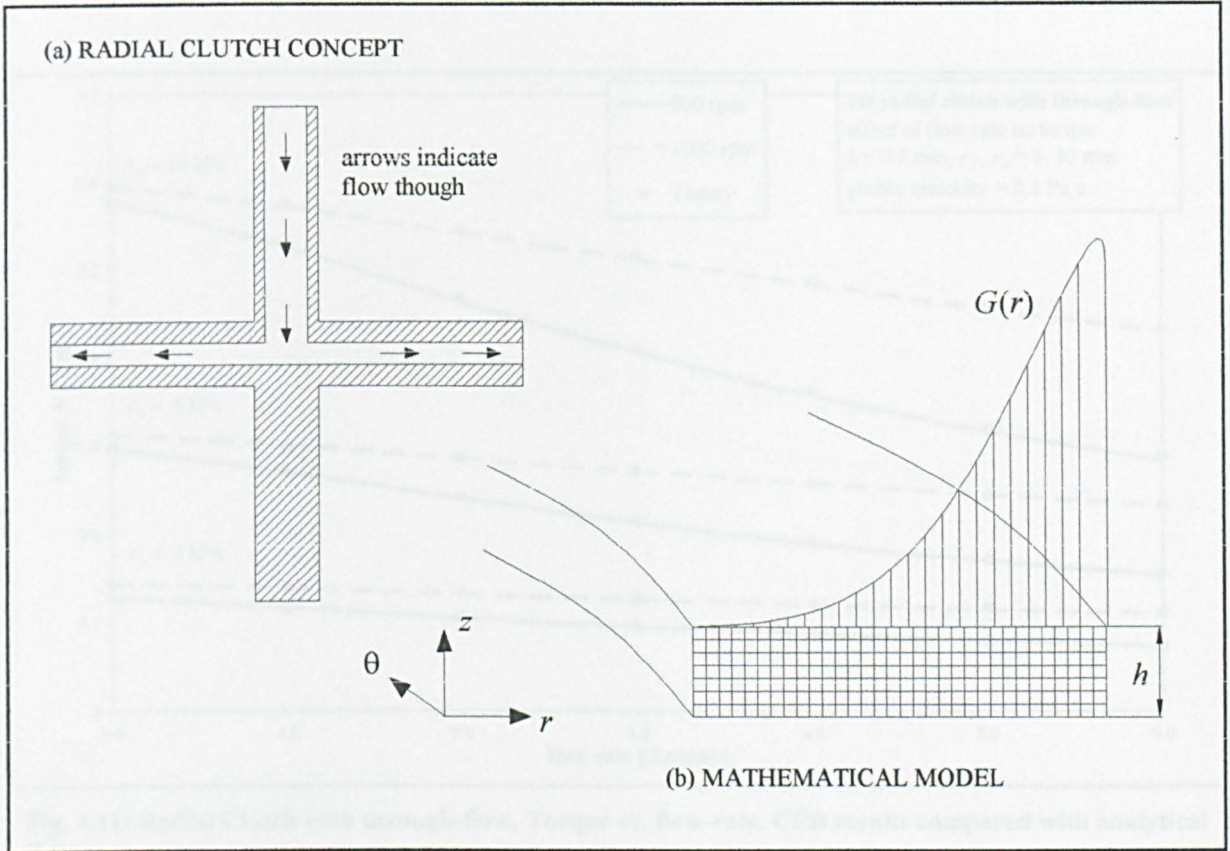


Fig. 4.9: Schematic of 2D radial clutch with through-flow.

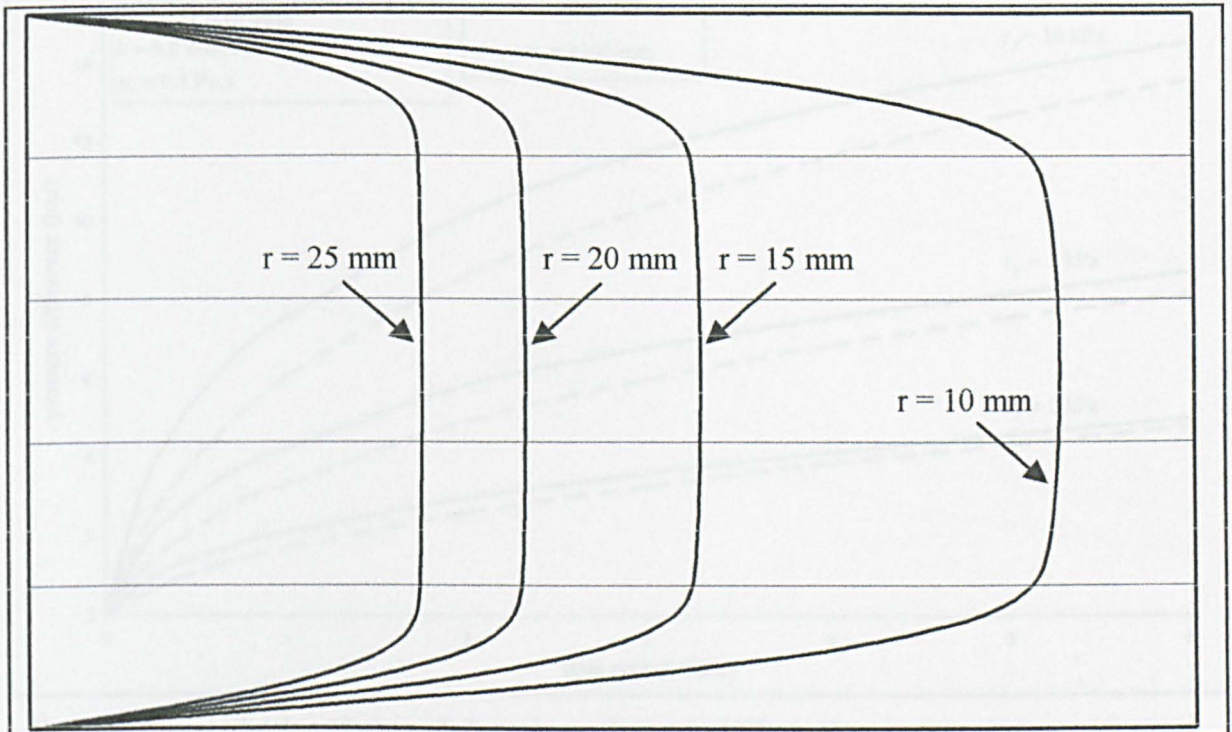


Fig. 4.10: 2D radial clutch with through-flow. Radial velocity profiles for the case of Poiseuille flow only (i.e. no angular speed).

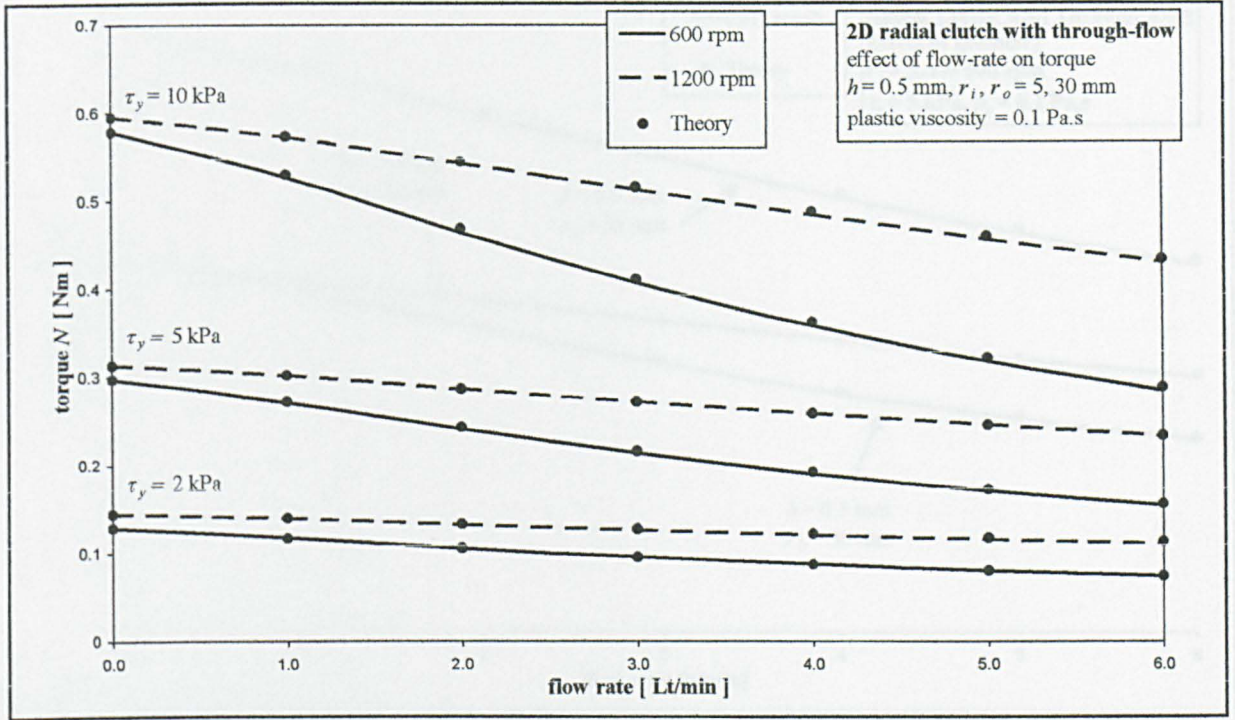


Fig. 4.11: Radial Clutch with through-flow. Torque vs. flow-rate. CFD results compared with analytical theory.

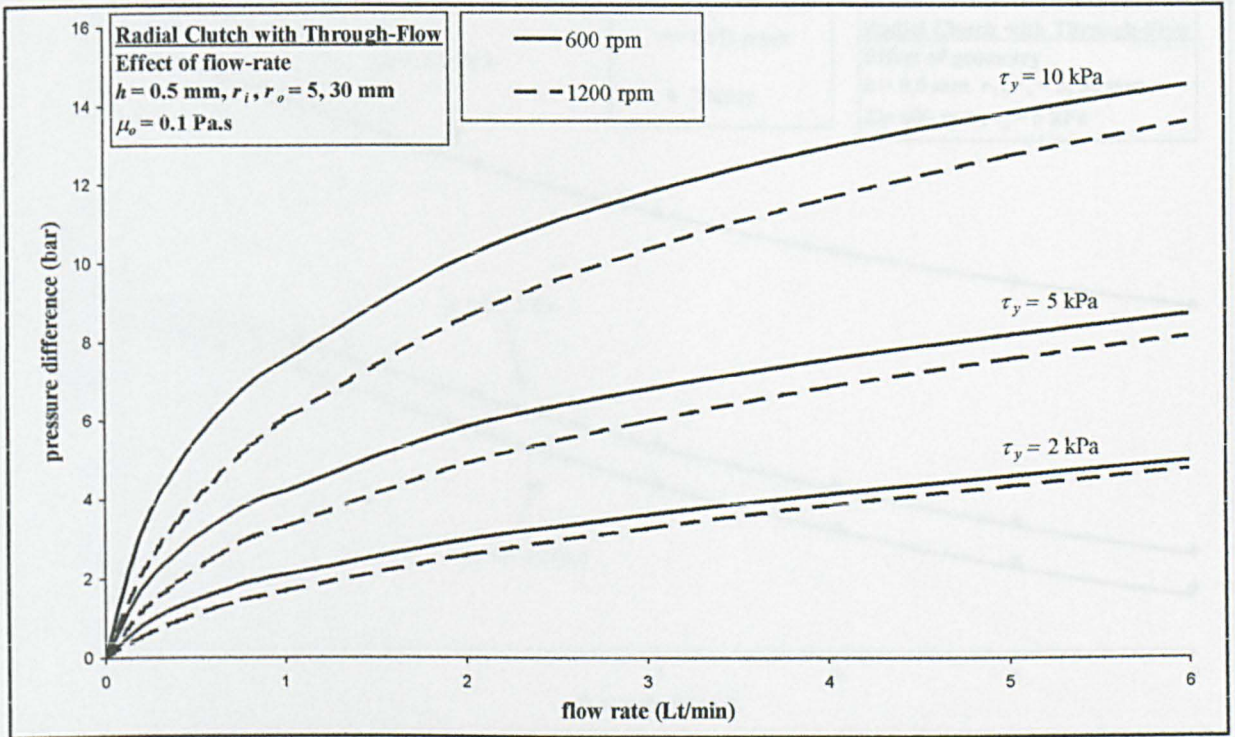


Fig. 4.12: Radial Clutch with through-flow. dp vs. flow-rate. CFD results.

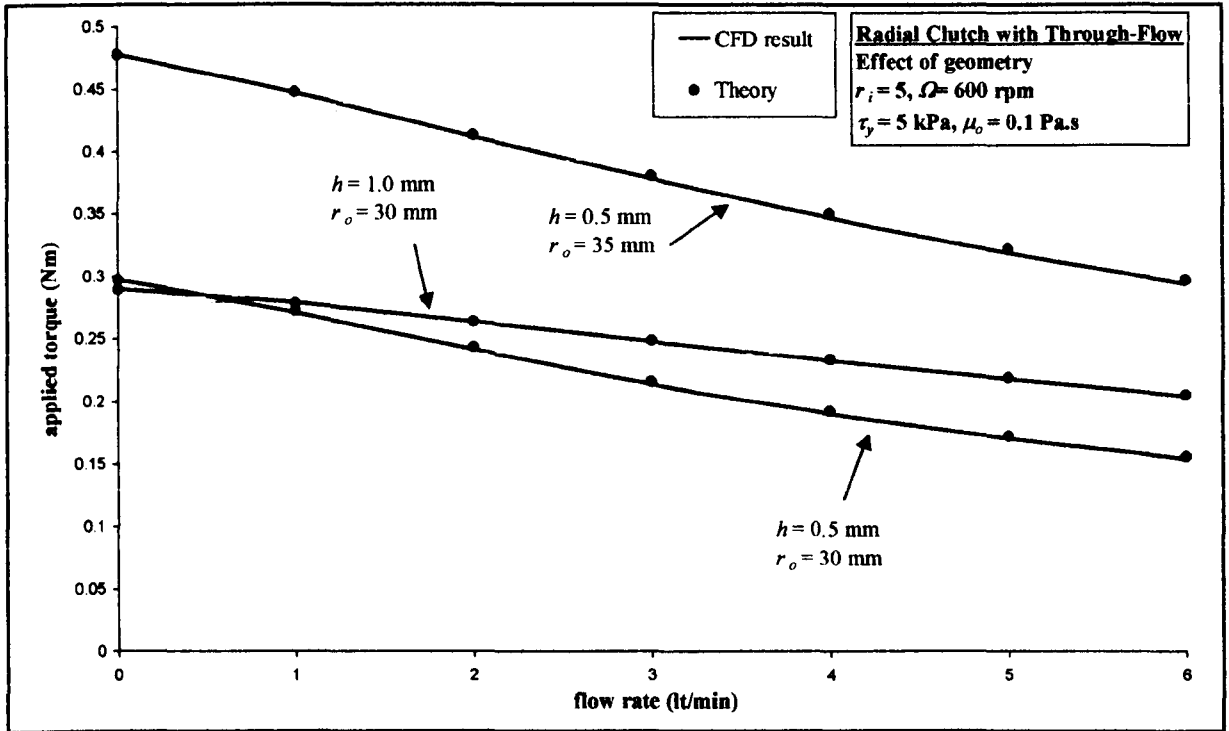


Fig. 4.13: Radial Clutch with through-flow. Effect of geometry. CFD results compared with analytical theory.

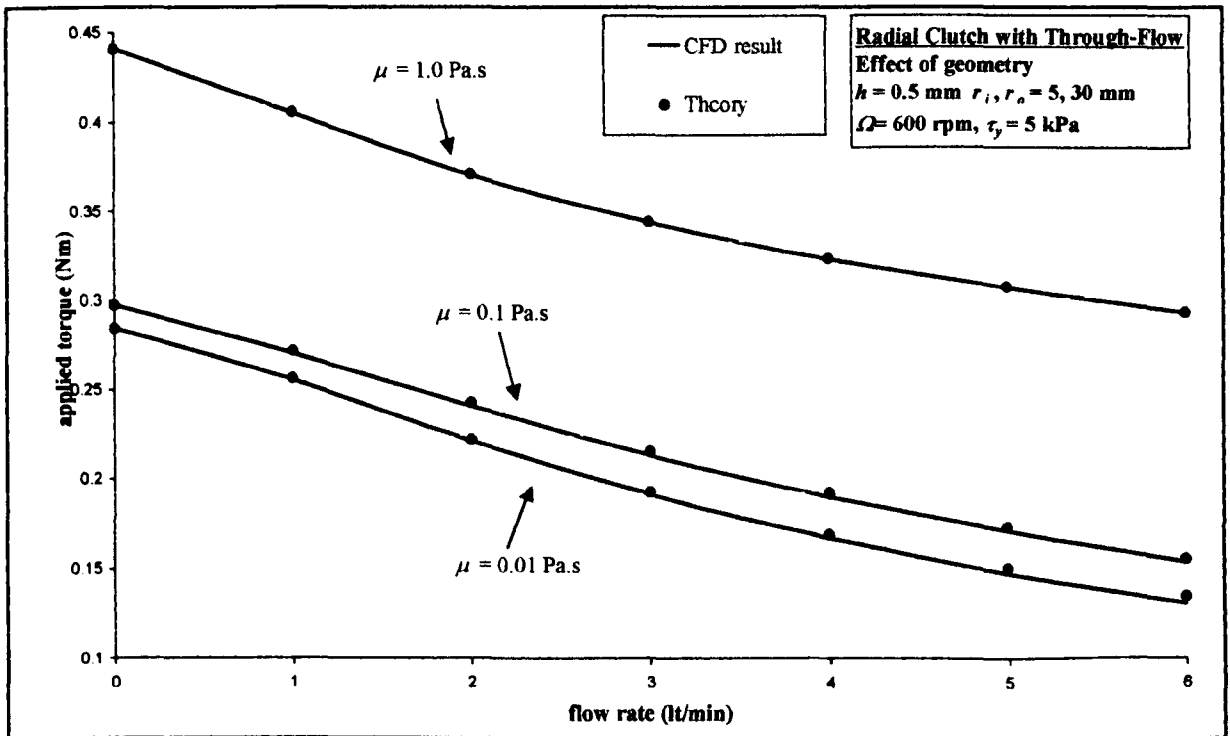


Fig. 4.14: Radial Clutch with through-flow. Effect of geometry. CFD results compared with analytical theory.

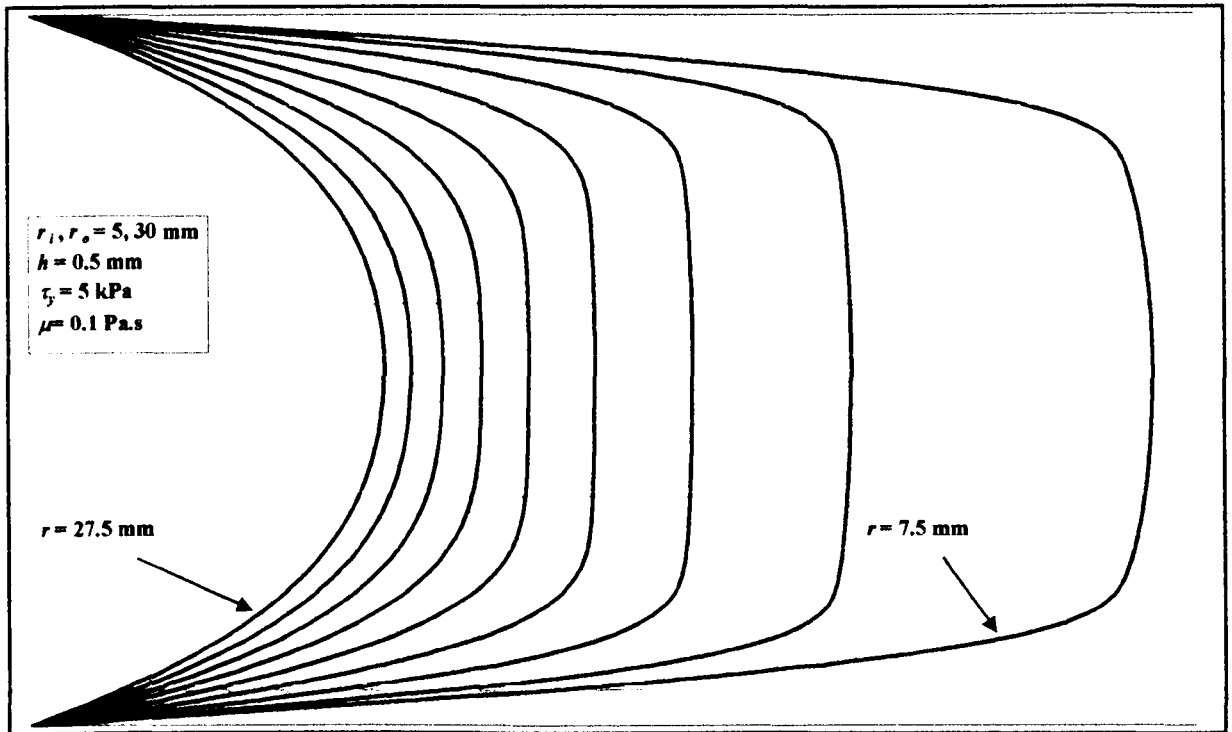


Fig. 4.15: Radial Clutch with through-flow. Radial velocity profiles. $\Omega = 600$ rpm, $\dot{q} = 0.8$ Lt/min

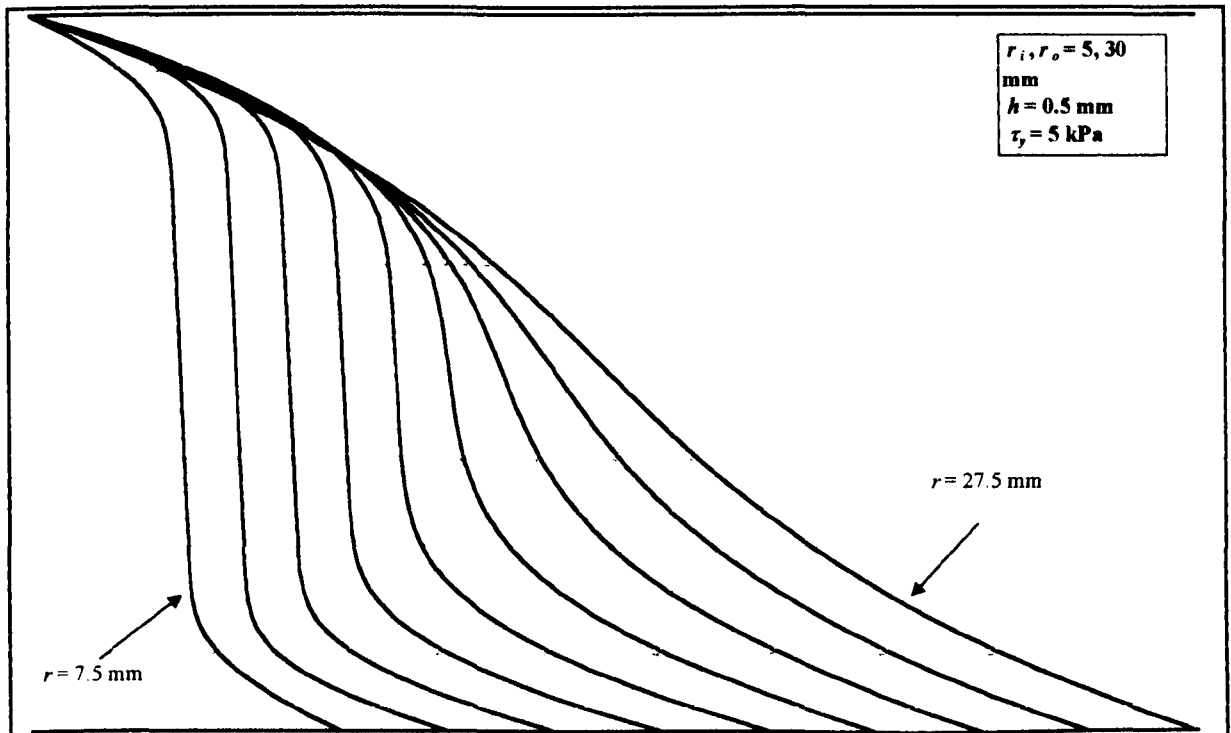


Fig. 4.16: Radial Clutch with through-flow. Circumferential velocity profiles. $\Omega = 600$ rpm, $\dot{q} = 0.8$ Lt/min

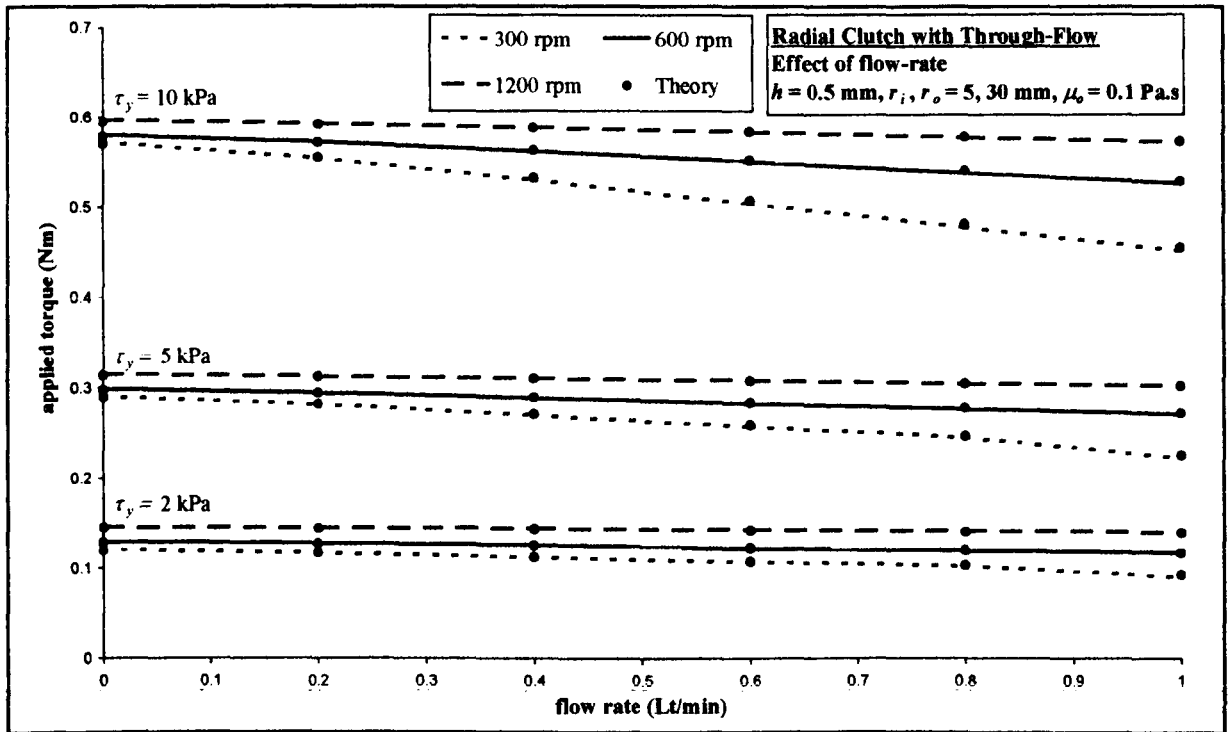


Fig. 4.17: Radial Clutch with through-flow. Torque vs. flow-rate. CFD results compared with analytical theory.

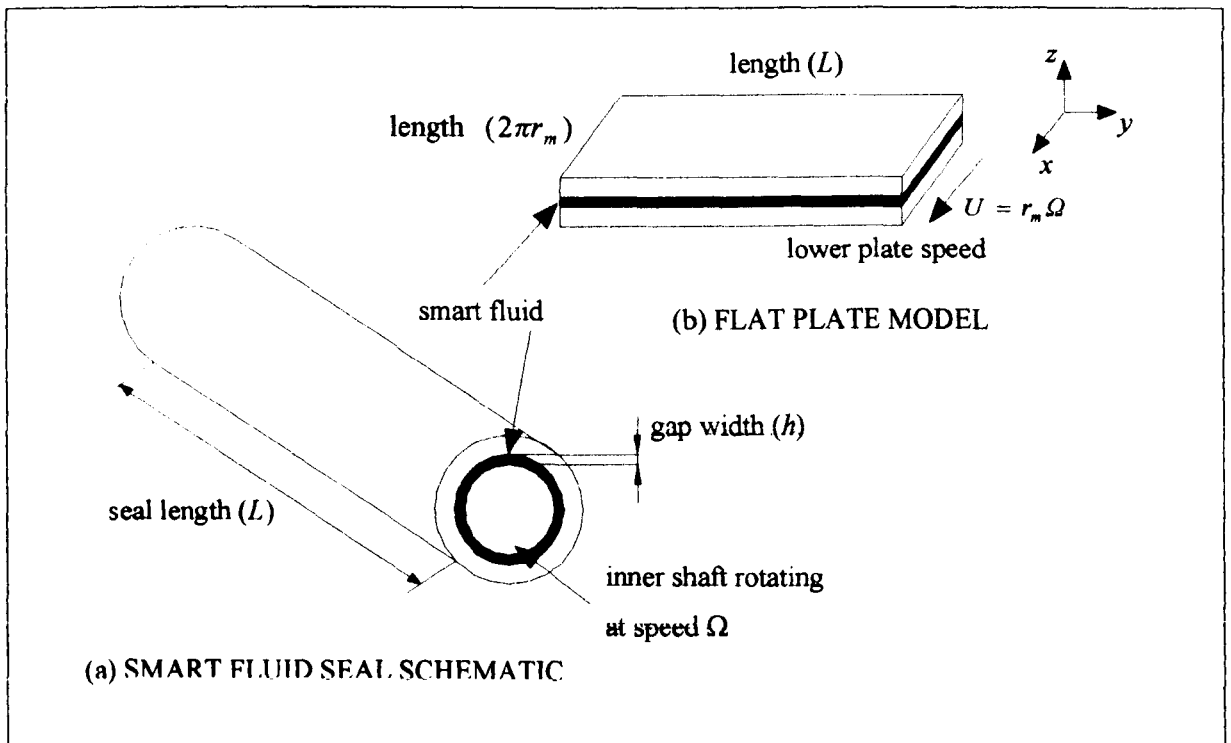


Fig. 4.18: Schematic of smart fluid seal and how it can be modelled as flow between flat plates.

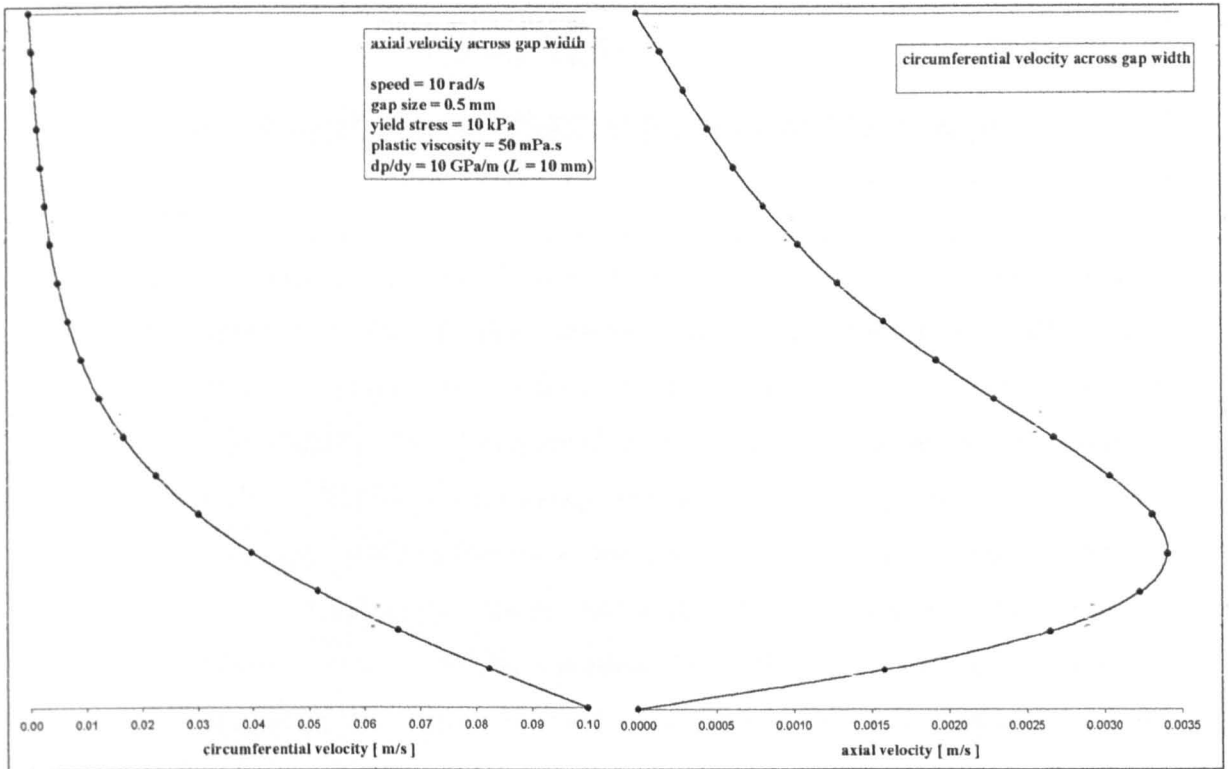


Fig. 4.19: Smart fluid CFD results, velocity profiles for case no. 1 on the 10 mm shaft. Circumferential (left) and axial (right).

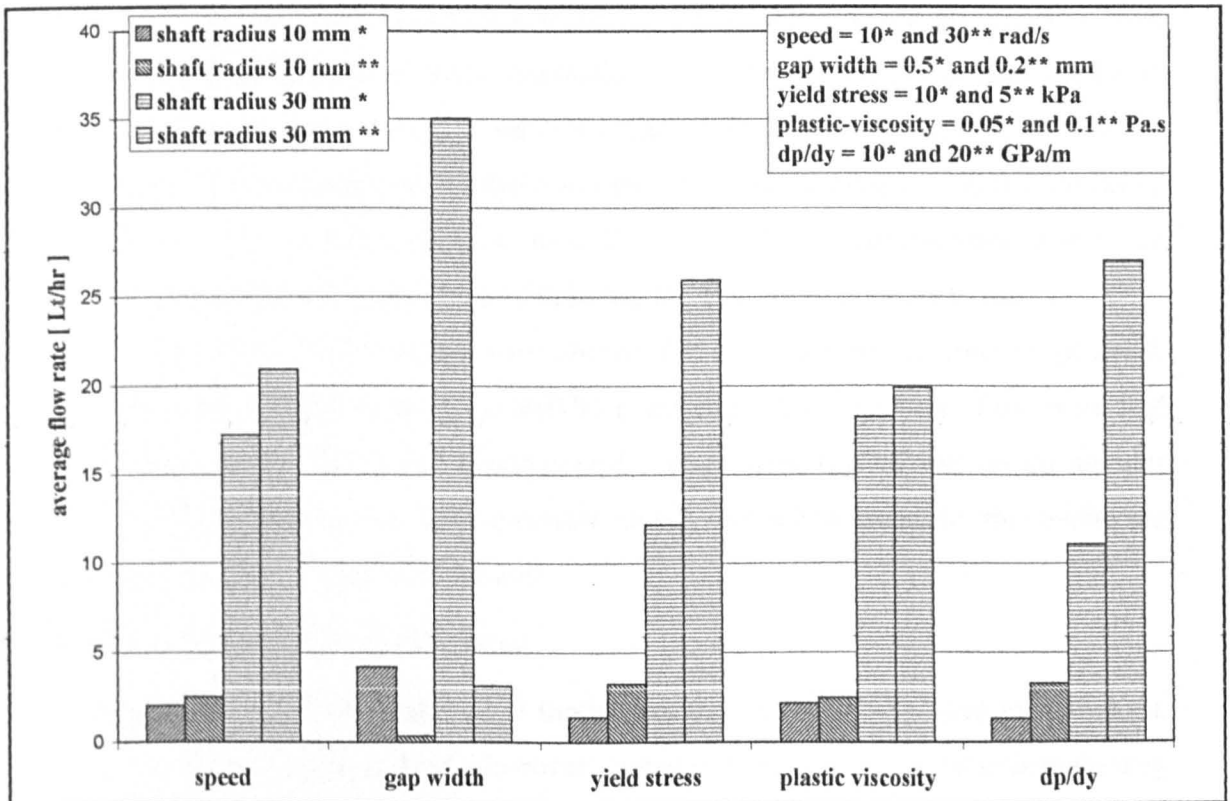


Fig. 4.20: Effect of each parameter on average flow rate using CFD simulation results.

CHAPTER 5 :

SMART FLUID UNSTEADY FLOW RESPONSE

5.1 Introduction

This chapter is primarily concerned with the modelling of time-dependent flows of smart fluids using CFD. The optimum utilisation of a smart fluid device will involve unsteady operation. It is therefore useful to be able to model the unsteady flow of a smart fluid. Remarkable little mathematical research has been done for this mode of operation. Even smart fluid data is generally presented in the steady state.

The inclusion of additional terms in the governing equations of motion adds an increased level of complexity, further indicating the need for a CFD approach. Analytical solutions of the governing equations of motion is possible for some basic devices including smart fluid valves [37] [53] and clutches [38] [39]. However, in some areas these studies were found to disagree with CFD analysis. Reasons for these differences had to be identified.

One of the main advantages of a smart fluid is its ability to rapidly transmit large forces and torques in an electrically controlled way. The speed of response will be an important factor in determining whether a smart fluid device outperforms alternative mechanisms. The dynamics of the fluid and the coincident hardware will dictate limits of operation. An understanding of how the basic fluid characteristics affect the dynamics of operation will also help in deciding the best form of fluids to use.

Several smart fluid devices were chosen for investigation. In order to proceed, definitions and possible methods of modelling unsteady flow of a smart fluid were laid down. Subsequently, CFD and experimental studies were carried out on an annular valve, Rayleigh step bearing and concentric clutch, and where possible, the results are compared with earlier analytical studies.

5.1.1 Modelling Unsteady Smart Fluid Flow

Within this thesis, the Bingham CFD model has been successfully used to model the steady state flow of a smart fluid. However, dynamic behaviour in the time domain may not even be of a continuum nature, meaning that great care must be exercised. For example when the particles are moving the fluid may not be homogenous.

This subject area is far from being fully understood, mainly due to its inherent complexity. In particular, the characterisation of fluids and assignment of fluid properties are areas in which further work is necessary. Much more research and

collaboration with specialised rheologists is required. For this to happen, more interest in the subject must first be stimulated. This should occur as more applications continue to appear on the market. For the time being, it is necessary to use existing equipment, until the cost of more appropriate rheometers can be justified¹.

However, progress can be made by setting down some basic assumptions and proceeding forward with caution. If the results are found to be unsuitable then the original assumptions can be re-evaluated. The particles in a smart fluid are usually micro-sized, therefore at least to some extent it is thought that the fluid can be characterised in terms of macroscopic properties.

Denoting the time associated with the fluid dynamic response as t_d , and the time associated with changes in rheology as t^* , in general, it would seem reasonable to approximate the maximum possible response time as:

$$t_{\max} = t^* + t_d. \quad (5.1)$$

Any actual response is expected to be faster than t_{\max} due to t^* occurring in unison with time t_d . The time t^* is often referred to as the 'electron hydraulic time constant'.

Electron Hydraulic Time Constant (t^*)

An ER clutch apparatus can help to determine t^* [12]. Experimentation is carried out with a constant relative speed difference between the electrodes, high enough such that no plugs are present. Hence, the velocity profile can be approximated as linear and should remain the same before and after excitation. In this situation, $t_d = 0$ s and so the time for the torque to increase is attributed to t^* . Typical results using an ER fluid indicates that t^* is fast at 1-2 ms [12]. Exactly what physical properties affect t^* is debatable. It will depend to some extent on the particular constitution of fluid. A mechanism to describe the development of the yield-stress is still not fully available [54] [55] [56] [57]. Although it is thought that t^* is determined by chaining time (dipole orientation in an ER fluid). Nevertheless, it is understood that charged particles move very fast, possibly making t^* look negligible comparison to t_d in some flows. If t^* is found to be small compared with t_d , then to all intents and purposes it may be possible to consider the rise in τ_y to be instantaneous. For an ideal viscoplastic material, t^* would represent the time required for the yield-stress to kick in. The real situation is likely to

¹ During this study a detailed proposal to design and build an ER/MR rheometer in collaboration with Ravenfield Designs Limited (Makers of Viscometers and Scientific Instruments) was submitted to the EPSRC. Unfortunately, it was turned down, probably due to the expense involved.

be more complicated.

Fluid Dynamic Response Time (t_d)

The actual time associated with a change in flow is the fluid dynamic response (t_d). Conceptually, this response depends upon how fast information can be transferred through the smart fluid, thus the stiffer the fluid medium, the faster the response. In general, with a large non-Newtonian viscosity¹ and a small fluid gap, the dynamic response is expected to be fast.

5.1.2 Viscoelastic Model

As discussed in section 2.5.1, if a fluid is hit fast enough it will respond elastically. Since accelerations are expected to be high, such behaviour is likely to be associated with smart fluids. It may therefore prove necessary to introduce viscoelastic effects. Simplistically, visco-elasticity causes a delay in the transmission of information. A more suitable constitutive equation for a particular smart fluid may involve a shear-modulus G' [58]. One such model [36] gives the shear-stress as follows:

$$\tau(t) = \tau_e + \tau_o = \tau_y \left[1 - \exp\left(-\frac{G'}{\tau_y} \dot{\gamma} t\right) \right] + \mu_e \dot{\gamma} \quad (5.2)$$

One way to help interpret this model is to assume that the change in yield-stress (τ_y) is instantaneous, and to consider the delay in the development of the electro-stress² (τ_e) as a consequence of the shear modulus (G'). The resulting time constant from eqn(5.2) is:

$$\left(\frac{G'}{\tau_y} \dot{\gamma} \right)^{-1} \quad (5.3)$$

In Fig. 5.1 and Fig. 5.2 this viscoelastic constitutive model is compared to the Bingham CFD model which has been successfully used up until now, within this thesis, for steady flow. With increasing time, the viscoplastic constitutive model begins to represent the original Bingham CFD model. It is important to consider the range of $\dot{\gamma}$, for example, with $G' = 10$ kPa, the shear-stress from both models is comparable, after 1 ms when $\dot{\gamma} > 2000$ /s, and after 10 ms when $\dot{\gamma} > 400$ /s.

As shown in Fig. 5.1, with the viscoelastic model there is no physical yield-stress (τ_y) to overcome before flow occurs. As with the Bingham CFD model, this

¹ At a constant shear-rate of only 1000 /s, and a yield-stress of only 1000 Pa.s, $\mu_{nn} \approx 1.0$ Pa.s.

² Shear-stress due to the excitation minus the Newtonian contribution.

is a desirable aspect when solving the governing flow equations. The entire smart fluid always exists as a fluid. This is in contrast to the ideal Bingham plastic model, where one must identify any un-yielded regions ($\dot{\gamma} = 0$ /s) and then consider how these solid regions affect the flow.

When using the Bingham CFD model, plug velocity profiles arise and compare well with the ideal Bingham plastic solution when μ_s is sufficiently large (see Fig. 3.5). For the viscoelastic model (as shown in Fig. 5.2), at very low shear-rate the viscosity becomes increasingly large with time. A more appropriate model may require a maximum viscosity (μ_s) to be imposed. As with the Bingham CFD model an appropriate value of μ_s , may prove to be 100-1000 times greater than μ_e . This value gives results comparable to the ideal Bingham plastic equation (see section 3.3.1). Thus a modified model that uses a maximum cut off viscosity (μ_s), will subsequently be referred to as the viscoelastic Bingham CFD model.

5.2 Annular Valve Responsive Study: CFD vs. Analytical Analysis

In a practical operation, the flow of a smart fluid in an annular valve would be unsteady. Various studies have therefore been carried out in order to understand behaviour in this mode of operation [37], [15], [36], [53]. Experimentally measuring the response is difficult due to compressibility effects in the connecting pipes and so forth. The distinct advantage of a mathematical approach is that measuring devices such as flow-rate meters, pressure tappings and connecting pipes do not interfere with the fluid mechanics of the idealised system.

The response due to a change in excitation was investigated using the Bingham CFD model and the new viscoelastic Bingham CFD model. The device was modelled as 1D flow between two flat plates (Fig. 5.3). The valve operates as an open system with fluid flowing into the valve at one end and out at the other. In section 3.3.1 the steady flow situation was investigated using the Bingham CFD model and the results agreed very well with the analytical Bingham plastic analysis.

A mode of operation that the valve could typically experience is a rapid change in flow-rate (\dot{q}), due to a change in excitation, with ΔP_{eo} remaining approximately constant or vice versa. Using the line of reasoning outlined in section 5.1.1 the dynamic speed of response (t_d) can be investigated. This would help in optimising the valve design and assist in determining suitable applications that the device could fulfil.

5.2.1 Response using VISCOPLASTIC model

The fluid dynamic response (t_d) of an isolated valve was obtained for a step change in

excitation. This should give some indication of the size of an optimum response time. The change in τ_y is from a value of zero and is assumed instantaneous. Here the actual fluid property response (t^*) is therefore not being considered. In a real smart fluid, a small but finite time is required for the new fluid structure to form; this may need to be considered later. The fluid flow is also assumed incompressible and isothermal.

Analytical analysis of the problem when $G (= \Delta P/L)$ remains constant and is subject to a step-change in E has previously been investigated by [37] and [53]. Whittle *et.al* [37] simplified the problem by approximating the flow to that between two flat plates. The solution indicates that time constants are given by:

$$t_n \approx \frac{\rho h^2}{4\pi^2 n^2 \mu_e}, \quad (5.4)$$

where h is the gap-width, μ_e is the plastic viscosity, and n is number of terms. Here the yield-stress is not believed to affect the response time. However, would not τ_y , (considered by many as the most significant smart fluid parameter) affect the dynamic response time (t_d)? An analytical and numerical solution of the same problem by Li *et.al* [53] suggests that τ_y does indeed affect t_d .

CFD Model: Flow Rate Response to an Instantaneous Excitation

The following table summarises the CFD model used in this section.

Software	Fluent5, finite volume, segregated solver	
Physical Model	1D, laminar, incompressible, isothermal flow	
Fluid Properties	Bingham CFD model and viscoelastic Bingham CFD model	
Discretisation of flow Equations	interpolation scheme	1st order, PRESTO for pressure
	pressure-velocity	SIMPLE
	unsteady flow	1st order implicit
	uniform grid (x, y)	3 (x-direction) x 20 (y-direction)
Boundary Conditions	valve wall	no slip wall condition
	centre line	symmetry condition
	pressure difference	periodic condition

Table 5.1: Summary of the CFD model used to determine the flow rate response in a smart fluid annular valve.

As found in section 5.1.1, obtaining a solution takes 100 times longer when a constant pressure difference is set in preference to a flow rate. Unfortunately, the model does require a constant value of G to be set. Computing time was therefore improved by using a periodic boundary condition so that only a few cell widths are necessary

(Fig. 5.3). It was also envisaged that reaching convergence at each time-step would not be a problem because the flow field from the previous time-step would closely match that of the next one.

The new CFD model was initially verified for steady flow using equations in section 2.4.1. Increasing the under-relaxation factor for the momentum equations to 0.9, drastically reduced the time required to reach convergence. For the unsteady model, using the PESTO scheme for the discretization method for pressure, also improved convergence times. Fig. 5.4 demonstrates how care is necessary in order to ensure true convergence at each time-step. In this figure the flow rate curve appears to be fine, but with the flow rate per iteration also being monitored, it is clear that convergence is not being reached at each time-step. To improve the solution, an increase in the number of iterations per time-step and/or a smaller time-step is required. A time-step of 1×10^{-7} s with 100 iterations/time-step was found to be adequate¹. In conclusion, care and patience had to be exercised in order that the resulting solution had been converged correctly with confidence.

Discussion of CFD Results: Flow Rate Response to an Instantaneous Excitation

A Tagucci approach [59] was utilised to obtain a good indication of the effects of the various parameters, while testing the CFD model for a wide range of parameters from only eight simulations. For each case, it was important to make sure that eqn(2.18) was satisfied, in order to maintain flow after excitation. The parameters and results are summarised in Table 5.2.

model number	parameters					theory			initial parameters		CFD		dynamic response time t_d	
	yield stress	pressure gradient	fluid density	plastic viscosity	gap width	initial flow rate	final flow rate	ratio of plug width to gap width	wall shear rate	wall shear stress	initial flow rate	final flow rate	Whittle et al formula summed over 20 terms	CFD (99% of final steady state value)
	kPa	bar/100mm	kg/m ³	Pa.s	mm	Lt/min/m	Lt/min/m	%	/s	Pa	Lt/min/m	Lt/min/m	ms	ms
a	5	60	1500	0.050	0.50	750	389	33.3	300000	15000	751	402	0.30	2.76
b	10	60	1500	0.100	1.00	3000	1556	33.3	300000	30000	3004	1612	0.61	5.20
c	5	120	1500	0.100	0.50	750	564	16.7	300000	30000	751	565	0.15	1.31
d	5	60	3000	0.050	1.00	6000	4514	16.7	600000	30000	6007	4530	2.43	20.00
e	10	120	1500	0.050	1.00	12000	9028	16.7	1200000	60000	12014	9072	1.21	9.69
f	10	60	3000	0.100	0.50	375	56	66.7	150000	15000	376	61.7	0.30	2.87
g	5	120	3000	0.100	1.00	6000	5252	8.3	600000	60000	6007	5280	1.21	7.15
h	10	120	3000	0.050	0.50	1500	778	33.3	600000	30000	1502	805.2	0.61	5.27

Table 5.2: Tagucci parameters and results for an annular valve; viscoplastic response due to instantaneous excitation.

The function of the Tagucci approach is to help determine the approximate affect of each parameter on the dynamic response time (Fig. 5.5). Since the differences in

¹ Even so, it did take up to 24 hours to iterate a full solution.

response times are large, the Tagucci results are only approximate. Fig. 5.5 suggests that doubling fluid density increases the response time by a factor of two; this is in accordance with eqn(5.4). This is expected, because doubling the density doubles the fluid's inertia, and thus it will take twice as long to reduce its speed. The gap width is found to be very significant. Fig. 5.5 indicates that the effect is greater than h^2 , but less than the h^3 indicated by eqn(5.4). Increasing the gap width will increase the overall weight of fluid to be stopped. In addition, the shear-rate and thus the fluid shear stresses will also be reduced; both of these factors will contribute to a longer response time. The pressure gradient (which eqn(5.4) suggests has no effect on the time constant), is indeed found to only have a small effect on the response time. The reason for this is as follows: When τ_o is greater than τ_e , a change in G gives a proportional change in the mean shear-rate and thus shear-stress. In this case, if G is increased, the fluid shear stresses that resist motion also increase, and counterbalancing effects occur. For the chosen parameters, the statement that $\tau_o \gg \tau_e$ is not fully justified, and so G is indeed found to have a small effect. The plastic-viscosity is found to have an effect in line with eqn(5.4). However the yield-stress is also seen to have an affect on t_d and is not a parameter in eqn(5.4). Conceptually the CFD results make sense; the larger the non-Newtonian viscosity {eqn(2.11)}, the faster the flow rate will be reduced to its final steady state profile. The relative contribution of τ_y and μ_e to the magnitude of μ_{nn} depends on $\dot{\gamma}$. In this device, the shear-rates are high¹, and so the value of $\tau_o = \mu_e \dot{\gamma}$ can be on a par with τ_y . Thus, both τ_y and μ_e should affect t_d .

Fig. 5.6 indicates that the flow rate change is non-linear. This is not surprising, as the shear-rate and thus shear-stress do not remain constant throughout the event. As shown in Table 5.2, the results before the event agree very precisely with steady state analytical prediction. In addition, when the plug width is less than one third of the gap width the event also agrees very closely with analytical prediction. When this is not the case, the difference in flow rate is up to 10 %. This is because an improved grid should really be used when the plug region is large². However, for this analysis a 5 % difference is quite acceptable. The velocity profiles for case *a* are shown in Fig. 5.7 and clearly indicate how the plug rapidly forms. As anticipated, the results in Table 5.2 indicate that the CFD response time is longer than that predicted by eqn(5.4).

¹ Within the valve the shear-rate varies, but becomes very large in proximity to the wall.

² When the plug is large, fewer cells remain for resolving the remaining flow.

Discussion

In order for the results to be deemed reliable, it is vitally important to determine the reason for the difference between these CFD results and the analytical prediction of Whittle *et.al.* [37]. Both mathematical methods are solving the same basic equations, and the same outer boundary conditions are being used. However, one difference is in the constitutive model used. The analysis in [37] uses the Bingham plastic equation, whereas the CFD solution uses the bi-viscous model, which (for the reasons outlined in section 3.2.3) is referred to as the Bingham CFD model. As investigated in section 3.2.3, when μ_s is large then the models should give comparable results. Up until now, this has conclusively been found to be the case. The problem is therefore not thought to be due to the technical difference in the constitutive model.

Another difference between the solutions involves the plug region. In the CFD model, a plug is an extremely high viscous region. In contrast the equations in [37] do not produce a plug shaped profile. Outside the identifiable plug region the correct profile is produced. However, inside the plug region, the Bingham plastic equation is not valid. The density of the fluid in this region will affect the solution. However, what seems to have been overlooked by Whittle *et.al* [37] is that the shape of the velocity profile in the plug region will also affect the fluid's momentum. This point has also been commented on by Li *et.al* [53] who suggest that the solution derived in [37] does not properly account for a balance of momentum for the plug flow region.

It is now suggested that, the plug (whose actual width increases with time (Fig. 5.7)) must surely have a direct effect on the flow response time due to the following conceptual reason. Once a plug forms it has a certain momentum¹. In [37] the velocity profile is such that the momentum of the plug region is undervalued. As a result, the calculated response time is faster than it really should be. Furthermore, in a solid, force and velocity are transferred across a material virtually instantaneously, compared to in a fluid where the material shears, and thus there is a delay in the transmission of information. A higher yield-stress results in a larger plug, and so the dynamic response is faster.

To achieve a direct comparison between all three solutions, a CFD model was set up to precisely match a situation solved in both Whittle *et.al* [37] and Li *et.al* [53]. The pressure gradient is set as constant (12.5 bar/100 mm). The initial CFD velocity profile with $\tau_y = 0$ kPa was found to agree exactly with that in [37] and [53]. This confirmed

¹ mass x velocity

that the parameters in all three models were likely to be the same. The overall flow rate response was then calculated for $\tau_y = 2$ kPa. For the CFD model, the change in velocity profiles is shown in Fig. 5.8. The form in which the profiles change over time is the same in all three models. However, as predicted above, the solution derived in [37] gives a faster overall response time. For example, after 0.1 ms the maximum velocity has reduced to ~ 1.5 m/s in [37] and 2.7 m/s in [53]. As indicated by Fig. 5.8, the CFD model gives a speed of approximately 2.7 m/s after 0.1 ms, and therefore seems to be in agreement with the solution derived by Li *et.al.* [53].

To verify that a lower yield-stress does indeed give a slower response, it was decreased from 2.0 kPa to 1.0 kPa. Fig. 5.9 shows the flow rate response for both fluid strengths. It can be seen that after 2 ms the flow rate of the 2.0 kPa fluid is closer to its final steady value than the 1.0 kPa fluid.

Conclusion

It can be concluded that the viscoplastic model, which assumes an instantaneous change in yield-stress, can be used to determine a flow rate response. However, since the change in the stress is instantaneous, very small time-steps with a significant amount of iterations per step are required. This takes a significant amount of time even when a very small grid is used. Strong similarities in the form and shape of the response are found between the CFD results and the analytical works discussed previously [37] [53]. However it can be concluded that Whittle *et.al* [37] under predicts the fluids initial momentum and therefore the response time. This is due to the Bingham plastic equation not being valid in the plug region. The results presented here also call into question their statement that the yield-stress does not affect the response time.

5.2.2 VISCOPLASTIC CFD Model: Valve Shut Down Time due to an Instantaneous Excitation

The CFD model used here is the same as that used above, with parameters chosen such that after excitation, $\tau_y < Gh/2$, and thus the flow is stopped. The time it takes for the flow to stop is called the shut-down time (t_c). This work was done to further verify the CFD model against an available analytical solution. Li *et.al.* [53] provide an expression that estimates the shut-down time:

$$t_c \approx \frac{\rho h^3 |G|}{16\mu_e \tau_y}, \quad (5.5)$$

where h is the gap-width, μ_e is the plastic viscosity, G is the pressure gradient, and τ_y is the yield stress.

Using the refined CFD model from section 5.2.1, summarised in Table 5.1 the flow rate response was calculated for two different values of yield-stress (Table 5.3). The two flow rate responses are shown in Fig. 5.10.

Parameters					Shut Down Time t_c		
yield stress	pressure gradient	fluid density	plastic viscosity	gap width	Li et.al. formula	CFD	difference
Pa	bar/100mm	kg/m ³	mPa.s	mm	ms	ms	%
2000	2	1500	100	1.00	0.938	0.760	18.9
5000	2	1500	100	0.50	0.047	0.028	40.3

Table 5.3: Annular valve shut down time results due to instantaneous excitation.

The order of magnitude calculated for t_c by both the CFD solution and eqn(5.5) is similar at each yield-stress, but the actual magnitudes differ. The difference is as great as 40 % for the higher yield-stress. The reason for this is two fold. Firstly eqn(5.5) is only an approximate result and does over-predict the actual results obtained in [53] by roughly 10 %. However, perhaps more importantly, the CFD model under-predicts t_c for the following reason. The plug expands until it occupies the entire gap (Fig. 5.11). As this happens, the CFD grid becomes increasingly less valid, due to fewer cells being left to properly resolve the flow between the wall and the plug. At least 5 cells are required to resolve a shear flow satisfactorily. However, using this grid there are less than five cells remaining in the non-plug region once the plug reaches 75 % gap-width. To get a more accurate solution, an improved grid with more cells near the outer wall is required. In addition, the grid can be refined as the solution progresses; this can even be done automatically using later versions of Fluent.

5.2.3 Response using VISCOELASTIC model

As discussed in the two previous sections 5.2.1 & 5.2.2, important information has been gained using the viscoplastic Bingham CFD model. In particular, the yield-stress was highlighted as an important parameter. Previously this parameter had been suggested not to contribute to the flow response time. The strategy of initially using a simple constitutive model and proceeding forward with caution has proven successful. Thus, the next step was to test an improved, more sophisticated model.

The theoretical viscoplastic flow rate response is very fast; indeed faster than indicated by experimentation, although here it is difficult to differentiate out an isolated valve response from unsteady experimental data. Since the response has been indicated to be fast, it is likely that some visco-elasticity may be occurring. The alternative viscoelastic constitutive model {eqn(5.2)} is now investigated.

Viscoelastic Bingham CFD Model Test

Equation (5.2) was written into a subroutine as shown in Table A.2 (Appendix A). An initial test involved a simple shear flow between two parallel plates. Initial parameters are $\tau_y = 0$ Pa, $\mu_e = 0.1$ Pa.s and $\dot{\gamma} = 3000$ /s [$u = 0, 1.5$ m/s, $h = 0.5$ mm]. The shear modulus (G') is chosen to be 1×10^4 . At time $t = 0$ s, an instantaneous formation of τ_y ($=5$ kPa) takes place, but does not immediately take effect due to visco-elasticity. The shear-rate is not expected to change; only the viscosity μ_{nn} should increase. Fig. 5.12 shows μ_{nn} changing over a period of 1.0 ms. Although the test was basic, the model did appear to be working correctly.

Flow Rate Response for a Constant Pressure Difference

The proven CFD set-up for the valve used in section 5.2.1 is now used with the viscoelastic Bingham CFD model replacing its viscoplastic equivalent. On investigation, a time-step size of 1×10^{-5} s with 100 iterations/step proved to be a satisfactory solution procedure. Note that the time-step need not be as previously.

Fig. 5.13 shows the effect of using different values of G' (100 Pa, 500 Pa, 1000 Pa and 10000 Pa) for a solution with the remaining parameters the same as in case c in Table 5.2. For all but very low values of G' , very little difference can be seen when compared with the previous Bingham CFD model solution. In fact, the flow rate response for $G' = 10000$ Pa (shown in Fig. 5.13), overlaps the original viscoplastic solution. The reason for the small effect of G' becomes apparent if the high shear-rates are considered. Table 5.4 indicates that the initial shear-stress on the valve wall is six times the actual yield-stress, in which case $\tau_o \gg \tau_e$. A quick study of eqn(5.2) shows that G' affects only τ_e and not τ_o . In addition, the lower the value of G' , the longer the full development of yield-stress takes. The CFD results are therefore as expected.

Parameters							initial parameters		ratio of G' and yield stress	final steady state flow rate		dynamic response time (90 % of final value)	difference between a and b
yield stress	plastic viscosity	solid viscosity	shear modulus (G')	density	pressure gradient	gap width	wall shear rate	wall shear stress		theoretical	CFD		
Pa	mPa.s	Pa.s	Pa	kg/m ³	bar/100mm	mm	/s	Pa	Lt/min/m	Lt/min/m	ms	ms	
5000	100	1000	10000	1500	120	0.50	300000	30000	2.00	564	565	b 0.435	0.030
5000	100	1000	1000	1500	120	0.50	300000	30000	0.20	564	565	a 0.465	
5000	100	1000	500	1500	120	0.50	300000	30000	0.10	564	565	0.505	
5000	100	1000	100	1500	120	0.50	300000	30000	0.02	564	565	0.805	
5000	100	1000	10000	1500	60	0.50	150000	15000	2.00	194	195	b 0.825	0.115
5000	100	1000	1000	1500	60	0.50	150000	15000	0.20	194	195	a 0.940	
5000	100	1000	100	1500	60	0.50	150000	15000	0.02	194	195	2.650	
10000	100	1000	10000	1500	60	0.50	150000	15000	1.00	55.6	55.9	b 1.480	
10000	100	1000	1000	1500	60	0.50	150000	15000	0.10	55.6	55.9	a 4.510	3.030
10000	100	1000	100	1500	60	0.50	150000	15000	0.01	55.6	55.9		

Table 5.4: Parameters and results for an annular valve; viscoelastic response due to instantaneous excitation.

If the average shear-rate is halved through reducing G then τ_o is much smaller and

G' should be able to have more effect on the response time. This is found to be true as the CFD results in Fig. 5.14 and Table 5.4 indicate. For the same parameters albeit with half the pressure gradient, a small G' value clearly gives a longer response time.

The effect of τ_y is now considered. In the viscoplastic model, a larger value of τ_y caused the flow to reduce more quickly. With the viscoelastic, as shown in Fig. 5.15 and Table 5.4, the same effect is not quite so obvious. In this case it is the ratio of G'/τ_y that is significant, rather the individual magnitudes.

Pressure Response for a Constant Flow Rate

An alternative CFD set-up was required in order to model a pressure response. Here the flow rate remains constant, and a step change in excitation causes a pressure rise. To save computing time, a flat plate model with a symmetry line was utilised. A 20x20 grid was used and the full valve length was modelled. A uniform inlet was used to set the flow rate, and a zero pressure was set at the outlet. This model was similar to the earlier steady state model, which is known to be satisfactory. As before, an initial uniform steady solution with zero excitation ($\tau_y = 0$ Pa) was calculated and saved. All other parameters and procedures remained the same as before.

A flow rate was chosen to give a final pressure difference of 30 bar for a 5 kPa fluid. This value equates to 0.71 Lt/min, when a mean radius of 25 mm is assumed, and gives an initial wall shear-rate of 75000 /s, and thus a wall shear-stress of 7500 Pa. Thus, τ_o is of the same order as τ_e , and therefore the value of G' is found to have a significant effect on the pressure response time (Fig. 5.16). As shown in Fig. 5.17 a small yield-stress gives a faster pressure response. Conceptually this should be anticipated as the fluid is weaker and the change in the shape of the velocity profile is minimal. However one needs to be careful in trying to interpret such a result, because the ratio of G'/τ_y , {eqn(5.3)} will affect the response time. For the 1.0 kPa and 5.0 kPa fluid, this ratio is 5.0 and 1.0 respectively. The higher this ratio, the quicker the generation of yield-stress and so the faster the response should be.

The effect of changing μ_e was investigated and the results are shown in Fig. 5.18. Here the plastic-viscosity is halved, and has a significant effect on the overall shear-stress, but does not really change the response time. This is because G' has no effect on μ_e .

5.3 Rayleigh Step Bearing Responsive Study: CFD vs. Experimental

In this section, the response of a smart fluid Rayleigh step bearing was investigated using CFD and experimental methods. The MR fluid hydrodynamic effect has already

found successful commercial application in grinding high quality lenses [7] [60]. Here the increased pressure due to the hydrodynamic effect and localized high viscosity result in a non-contact method for the removal of material from a lens surface. The ability to rapidly and controllably vary the local pressure force without any mechanical contact is a desirable industrial aim. The potential for the application of a highly responsive mechanism of controllable pressure is probably substantial. For example, pressure could be used to control a lifting force, or as part of a hydraulic system. The overall usefulness of a smart fluid hydrodynamic effect is likely to be determined by how fast the response can be. Determining this factor, as well as developing the overall CFD pre-prototyping design methodology, was the main basis for this piece of work.

Steady state CFD analysis on a Rayleigh step bearing was carried out in section 3.4. A linear pressure gradient (G) is generated due to a plate speed (U) and yield-stress (τ_y) – this is the hydrodynamic effect. Here results from analytical and CFD analysis were found to correspond well. The work is now extended to determine unsteady response behaviour. To this author's knowledge, there is no easy analytical solution to this unsteady flow problem. A numerical method is therefore required, hence the need to use CFD. In the absence of an analytical solution, an experimental study was undertaken in order to verify the unsteady CFD results.

Tribology is an inherent feature associated with devices such as the one being studied here. A smart fluid can be likened to a variable viscosity lubricant, which is obviously extremely useful. Tribology in relation to smart fluids is beginning to be dealt with by researchers, and is proving to be an interesting and perplexing subject. For example, elasto-hydrodynamic lubrication (as associated with ball bearings) proves difficult since the fluid particles prefer not to travel under the ball. For the purposes of this project, modest attention will be paid to tribological considerations. The prime concern is to study and model the basic continuum behaviour.

Experimental work from Leek *et.al.* [41] shows a pressure response due to a step change in excitation to be relatively slow (>100 ms). With the pressure response being considerably slower than expected, Leek *et.al.* gave their own work a tough examination. They concluded that they could not conceive of any further unexamined aspect of their technique that would cast doubt upon the validity of their pressure response data. Having studied this work it is clear that obtaining a set of pressure data is not at all straightforward. A hole in the bearing is necessary if a pressure reading is to be acquired. This in turn will locally disrupt the electric field.

5.3.1 CFD Model: Pressure Response Using the Bingham CFD Model

The following table summaries the CFD model used in this section.

Software	Fluent5, finite volume, segregated solver	
Physical Model	2D, laminar, incompressible, isothermal flow	
Fluid Properties	viscosity (Bingham CFD model)	
Discretisation of Flow Equations	interpolation scheme	1st order, PRESTO for pressure
	pressure-velocity	SIMPLE
	unsteady flow	1st order implicit
	under-relaxation	pressure (0.7), momentum (0.7), density (1.0)
	grid (x, y, z)	20 (x-direction) x 20 (y-direction) (y = radial direction)
Boundary Conditions	upper wall	no slip wall condition
	lower wall	x-velocity = U m/s
	inlet	pressure boundary condition
	end	no slip wall condition

Table 5.5: Summary of CFD model used to solve unsteady 1D flow in a smart fluid valve.

With the length $L \gg h$ and the pressure gradient being uniform along the length, it would be advantageous to use period boundary conditions in order to reduce the number of required cells. However, this is not possible due to a flow reversal at the end of the bearing length. Hence, the whole bearing geometry needs to be modelled.

At $t = 0$ s the flow is steady and there is no excitation. The initial flow is thus computed using a steady state model with $\tau_y = 0$ Pa. This data was then substituted into the unsteady model as the initial flow condition.

After some initial tests, a grid {20 x 20 cells (150 mm x 0.5 mm)} was deemed adequate for acquiring steady state results. The next step was to determine a suitable unsteady solution procedure; i.e. the time-step size and number of iterations/time-step. Some results of a parameter size study are shown in Fig. 5.19. Here the solution was highly time-step size dependent, the pressure response was spiky, and thus the results were not reliable. To improve matters, a much smaller bearing length was used ($L = 10h$) giving smaller and hence better cell aspect ratios. As can be seen in Fig. 5.20, the response was no longer spiky and much more realistic.

Results from a new criteria study (Fig. 5.21) indicated that a reliable solution required a very small time-step, and that a 20x20 size grid was adequate. Increasing the grid size in the vertical direction appeared to affect the solution. However, it was found that with an increased number of vertical cells, more iterations/time-step were required.

For only a relatively weak smart fluid of 1 kPa, the pressure response was found to be very fast with $t_d < 0.2$ ms (Fig. 5.21). However, a convincing pressure rise could not be obtained, even with a very small time-step of 1×10^{-7} s. This is likely to be due to the unrealistic nature of the model being employed, with the yield-stress and thus shear-stress changing instantaneously at $t = 0$ s. In reality, there would be a small but finite time over which the yield-stress would develop. Consequently, the results obtained using this model appear anomalous.

5.3.2 CFD Model: Pressure Response Using a Viscoelastic Bingham CFD Model

As indicated above, the viscoplastic model is unrealistic as the yield-stress develops instantaneously at $t = 0$ s. A much better approach could involve using the viscoelastic Bingham CFD model that was outlined in section 5.1.2 and used in section 5.2.3 to model the valve. The same CFD procedure was used with only the constitutive equation changed. The change in shear-stress is smooth, and consequently the results look more realistic (Fig. 5.22). This figure clearly shows that the results are time-step independent above a size of 0.1 ms. Furthermore the results are seen to be grid independent. The pressure response for a 1000 Pa fluid can be observed to be of the order of 0.5 ms (see Fig. 5.22).

For the viscoelastic model the value of G' influences the time in which the yield-stress develops and therefore has a specific effect on the pressure response time. This is shown to be the case in Fig. 5.23 for some typical values of G' . Changing the speed did not have any drastic effect on the pressure response time (Fig. 5.24), although a higher speed does appear to give a slightly faster response. Because the shear rates are relatively low, the plastic viscosity is found to have a minimal effect on the solution (Fig. 5.25). In addition, changing the gap width (and hence the shear rate) also did not have much of an effect on the pressure response time (Fig. 5.26).

The value of yield-stress is seen to have a significant effect on the response time (Fig. 5.27). However, this is more to do with the ratio G'/τ_y rather than the actual magnitude of τ_y . Equation (5.2) dictates that the larger the value of G'/τ_y the faster the yield-stress will develop, and should thus give a faster response time. This is indeed the case, has illustrated in Fig. 5.23.

Conclusion

Due to a more realistic steady change in shear-stress, the viscoelastic Bingham CFD model appears to give a much more reliable result than the viscoplastic Bingham CFD model. Without doubt, the CFD study indicates that the response is very fast. These

results seem to indicate that the time scale of the response recorded by Leek *et.al.* [41] is faster by several orders of magnitudes than their results suggest. This is promising because Leek *et.al.* were surprised by how slow their experimental pressure responses were.

The response is seen to be in two stages (Fig. 5.27 and Fig. 5.28). The initial rapid response is due to the sudden change in μ_{mn} and the velocity profile changes considerably and quickly. This change in μ_{mn} is not instantaneous but is delayed by the ratio G'/τ_y . The second stage is slower, but still relatively fast, here the velocity profile is still changing but more slowly until it finally reaches its steady state value.

5.3.3 Experimental Investigation

The CFD model has a net zero flow-rate. This condition is experimentally repeatable using a Rayleigh step bearing with $h_2 = 0$ (Fig. 3.19). An experimental study utilising an ER fluid in a hydrodynamic step bearing was therefore undertaken in order to resolve the discrepancy between the results obtained by CFD and by Leek *et.al.* [41].

This was also a practical test of the smart fluid CFD pre-prototyping methodology. Because experimental responses in [41] appeared to be slow, an unsteady smart fluid CFD model was utilised to shed some light a problem. Apart from the cost associated with having access to CFD software, very little resources were required to do this. With the CFD results appearing to indicate that the results in [41] are indeed slow, a new experimental study is now justified.

5.3.4 Initial Experimental Rig

Experimental Set-up and Procedure

An existing viscosity pump was adapted. The main design details are illustrated in Fig. 5.29. Care was taken to ensure that arcing and fluid leakage would not occur¹. The inner rotor draws fluid in from a small reservoir. The fluid outlet is blocked, and so the fluid flows in along the inner rotor and flows back out again along the stationary outer casing. The temperature was monitored using k-type thermocouples (0.1°C) at locations indicated in Fig. 5.29.

To make sure the device worked as envisaged, a Newtonian Tellus 37 oil was used as an initial test medium. This was a worthwhile procedure as many problems were identified. A constant speed should generate a constant pressure recording that should in turn agree with the mathematical steady state analysis (section 3.4.1). Initial pressure

¹ ER fluid is expensive.

results agreed well with analysis at low speeds (50-100 rpm), but became very poor as the speed was increased (400 rpm - 34 % error).

Flat Plate Assumption

A possible reason for the discrepancy was that flat plate assumption and omission of side end effects in the analysis were inadequate. The first assumption was investigated using two different meshes based on the cylindrical bearing geometry. Examples of these meshes are shown in Fig. 5.30; one mesh is more representative of the true step bearing than the other. A speed of 500 rpm was chosen, as experimental discrepancy is particularly high at this speed. The pressure gradient along the bearing was found to be indistinguishable to that using the flat plate assumption solution (difference < 2 %). The flat plate approximation was therefore considered adequate, and not likely to be a factor for any significant discrepancy in the experimental results. A 3D grid was then set-up to determine if end effects influenced the overall solution. Again, no significant difference in pressure distribution was found that could account for the experimental difference.

Frictional Heating

Once the device was assembled, a considerable torque had to be applied to obtain rotation. This meant that a significant amount of frictional heating was being generated. To make sure the device did not leak, the end pieces had to be screwed on relatively firmly (Fig. 5.29).

The main bulk of generated heat is likely to occur due to friction between the end pieces and rotor mountings. The torque required to rotate the inner rotor was measured to be approximately 4 Nm. This torque, multiplied by the rotational speed, equals a sizable amount of input energy (200 watts @ 500 rpm). This would not normally be expected to cause a major problem, but the inner rotor is electrically and therefore also thermally insulated. The end pieces are made from Perspex and therefore have a low thermal conductivity, and consequently the frictional heating is dissipated into the steel rotor. Heat will then leave the inner rotor mainly by conduction through the ER fluid and the outer casing, and then into the atmosphere through convection. It is therefore not surprising that after the device was run for only a few minutes, it was noticeable that the shaft had become significantly hotter than the main casing.

This situation was crudely simulated using a simple CFD model¹. The temperature in the reservoir (T_{res}) was found to be up to five degrees less than the temperature at pressure transducer (T_p). In addition, the model was thermally unstable. The values used

¹ CFD heat transfer is dealt with in detail in Chapter 6.

in this model are estimates, but it is clear that frictional heating was a major problem. With the actual temperature of the fluid in the channel being much higher than estimated, the viscosity being used in the steady mathematical analysis {eqn(3.14)} was an overestimate, thus providing an explanation for the large discrepancy with the experimental results.

In addition, the PTFE bearings that keep the input rotor central soon became damaged. As a result, the pressure readings oscillated with amplitude of up to 50% of *the average reading, and with a frequency equal to the constant rotational speed. This situation was improved by replacing the inner PTFE bearings with more durable brass ones.*

Improved Results

Using the modifications to the rig outlined above, and operating at low speeds for short periods it was possible to obtain some good results using a Tellus 37 oil medium. However, the set-up was still thermally unstable, with the temperature increasing rapidly even at low speeds.

One set of results was obtained by setting a constant speed and recording the pressure at intervals as the temperature increased. During this procedure, the viscosity of the oil decreases and thus the pressure should do likewise in accordance to eqn(3.14). This procedure was applied at speeds of 300, 400, 450 & 500 rpm and the results are shown in Fig. 5.31. Due to the speed at which the temperature increased it was difficult to get accurate simultaneous temperature readings at all locations. As a result, only the temperatures in the side bearing locations were recorded. The temperature between one side of the channel and the other was found to vary by up to 1.5 °C. This was expected as one bearing may be tighter than the other, and hence generate more heat.

The results shown in Fig. 5.31 agree as well as can be expected. The pressure is justifiably less than that predicted, as the wiper does not act as a perfect block and thus some fluid can get around the edges. Another set of results shown in Fig. 5.32 illustrates how the generated pressure increases with speed for a relatively constant temperature. This was achieved by turning off the motor and allowing the rig to cool down before it could be used again; the next reading was then taken once the appropriate temperature had been reached.

ER fluid Tests

Using the adapted viscosity pump, a procedure was established that provided reliable results indicative of the steady state analysis {eqn(3.14)}. However, with an ER fluid medium no reliable results could be achieved. This was for a variety of reasons, but

mainly because the viscosity pump had not been originally designed or machined with the degree of accuracy required to serve as an ER fluid device. The gap-width simply varied too much such that the excitation and thus yield-stress varied considerably and no realistic pressure response could be ascertained.

In an attempt to improve matters the inner end pieces were redesigned in order to hold the inner in a more centrally located position. However, it was then discovered that the left and right sections of the casing that held the end pieces were not quite co-axially located and thus when the device was assembled the inner rotor was held fast by the forces of friction. It was impossible to achieve a compromise and so a new rig had to be designed and machined.

5.3.5 Experimental Set-up and Procedure: New Rig

Due to the problems discussed above with the adapted viscosity pump, it was necessary to design and build a new experimental rig specific for the job in hand. The main significant design improvement was the use of two roller ball bearings. These would provide a means of locating the inner shaft so that it is concentric with the outer. In general, the design was such that it could easily be produced in the workshop with the required accuracy. The main design features are shown in Fig. 5.33 and Fig. 5.34.

The speed was set roughly using a mechanical speed gauge. However, for each result, the input speed was recorded using a tachometer and so the average speed was accurately known. This speed was then used to calculate the theoretical pressure at the location of the pressure transducer ($L = 114$ mm).

5.3.6 Newtonian Results from New Rig

Initially Newtonian Tellus 37 oil was used to determine the applicability of the theoretical model to the experimental set-up. The pressure recording oscillated with a frequency equal to the input rotor speed (Fig. 5.35) and so an average pressure was taken. A summary of some typical results is shown in Table 5.6.

gap width	rotor speed	average fluid temperature	fluid viscosity	pressure at length 3/4 length ($L = 114$ mm)					
				experimental			CFD	difference	
				average	amplitude			bar	%
mm	rpm	°C	Pa.s	bar	bar	%	bar		bar
0.5	510	25.0	0.0703	2.31	~ 0.30	12.99	2.62	0.31	11.79
0.5	398	25.0	0.0703	1.84	~ 0.25	13.60	2.04	0.21	10.11
0.5	295	25.0	0.0703	1.41	~ 0.18	12.74	1.51	0.10	6.62
0.5	190	25.0	0.0703	0.91	~ 0.11	12.14	0.97	0.07	7.02
0.5	102	25.0	0.0703	0.50	~ 0.07	14.03	0.52	0.02	4.33
0.5	503	31.0	0.0554	1.77	~ 0.24	13.53	2.04	0.27	13.00
0.5	405	31.0	0.0554	1.45	~ 0.20	13.80	1.64	0.19	11.74
0.5	301	31.0	0.0554	1.07	~ 0.14	13.06	1.22	0.15	12.11
0.5	211	31.0	0.0554	0.78	~ 0.10	12.87	0.86	0.08	9.26
0.5	111	31.0	0.0554	0.42	~ 0.06	14.39	0.45	0.03	7.49

Table 5.6: New Rayleigh step bearing rig. Some typical results using Tellus 37 oil.

The temperature was found to remain uniform within the outer casing (locations T_1 , T_2 , T_3 and T_4 are shown in Fig. 5.29). However, once the device was running, the temperature at location T_5 (Fig. 5.33) measures the actual fluid temperature and this remained higher than those at the other locations. It was difficult to measure the inner shaft temperature with any accuracy due to the shaft being in rotation. The best indication of the true fluid temperature was to use the temperature at location T_5 only. The assumption is that since the casing temperature is approximately uniform, the fluid film temperature would also be uniform.

As shown Fig. 5.35, the recorded pressure has an amplitude and period. The period equals the rotational speed. The fluctuation was therefore likely to be due to a small variation in the gap width as opposed to the result of any trapped air. As indicated in Table 5.6 for different speeds the amplitude of the oscillations is approximately 13-14% of the total amplitude, this would indicate a gap width variation of 3-4 %. With the gap-width, being only 0.5 mm this is not too surprising. In addition, this situation was a dramatic improvement on initial results that indicated a 20-30 % variation in gap-width. Here the machinist had made the inner bearings out of Nylon as opposed to the specified Tufnel which was simply too soft. After a small remake, the results are now seen to be much better.

As indicated in Table 5.6 and Fig. 5.36 the experimental results are below the theoretical values. This is to be expected because some pressure fluid will escape under and around the lateral nylon seal (Fig. 5.33). As the speed is increased, the percentage difference between theory and experimental results increases. This is most likely to be due to an error in the mean fluid viscosity used to calculate the pressure {eqn(3.14)}. As the speed increases so does the heat transfer, thus making it more difficult to infer a

correct temperature and thus an accurate value of the fluid viscosity ().

5.3.7 ER Fluid Results from New Rig

The ER fluid characterised in section 3.6 was used as the fluid medium for experimentation. As before, the bearing was set to rotate at a constant speed. A constant DC voltage was then applied using a switching box design to do so very quickly [61]. Results of input speed, pressure, voltage and current are recorded on the digital oscilloscope. Initial and final steady state pressures should correspond with the steady state theoretical pressure (section 3.4.1).

Since the available fluid data was not accurate, an upper and lower estimate was calculated and the experimental result should fall within this range. Although it is somewhat unfortunate that exact comparisons for pressure magnitude could not be achieved at least indications of the response time can be seen.

5.3.8 Zero voltage Results from New Rig

For the condition of zero voltage the results should be essentially Newtonian and thus similar to thus of Tellus 37 oil in section 5.3.6. A summary of some experimental results is shown in Table 5.7.

data set			1	1a	2a	3a	4a	12b						
experimental	speed	rpm	265	265	488	495	267	251						
	temperature	°C	23.5	26.6	27.0	28.5	30.0	26.0						
	excitation	kV	0.0	0.0	0.0	0.0	0.0	0.0						
	final pressure	bar	1.13	1.07	1.80	1.82	0.97	0.93						
CFD			lower estimate	upper estimate										
	yield-stress	Pa	0	0	0	0	0	0	0	0	0	0		
	plastic-viscosity	Pa.s	0.060	0.070	0.060	0.700	0.060	0.070	0.060	0.070	0.055	0.070	0.060	0.070
	theoretical pressure	bar	1.2	1.3	1.2	13.5	2.1	2.5	2.2	2.5	1.1	1.4	1.1	1.3
	difference	%	2.1	16.1	7.2	92.0	15.5	27.5	15.3	27.4	9.2	28.6	14.8	27.0

Table 5.7: New Rayleigh step bearing rig. Typical results for ER fluid medium with no volts applied.

The table illustrates that for the lower estimate of plastic viscosity the steady state pressure is a few percent lower than the theoretical pressure – this is in line with the Newtonian Tellus oil results. As shown in Fig. 5.37 the pressure is seen to oscillate with a frequency equal to the rotational speed. The amplitude is seen to be nearly 15 % of the total pressure. The bearings are manufactured with a very high tolerance. Thus, the inner casing is obviously not machined to the required accuracy¹. A smooth surface to

¹ The standard achieved is supposedly the best that the workshop can produce.

an accuracy of at least 0.01 mm was required; this was visibly not the case. As a result, the inner rotor is not located co-axially with the required accuracy and thus the gap-width and pressure oscillate with a frequency equal to the speed. This is very unfortunate because the situation will be even worse then the fluid is excited – the yield-stress is a function of E and this will alternate with the gap width ($E = V/h$).

5.3.9 ER fluid Results from New Rig

As discussed above the fact that gap-width does not remain constant is indeed more of a problem when the ER fluid is excited. This is illustrated in Fig. 5.38 in which a pressure response can clearly be seen, however it is difficult to determine an exact response time. This is essentially due to a varying gap width causing unsteady flow/pressure. Fig. 5.38 is not the worst result; through trial and error it was possible to work out where best to locate the bearings in order minimise the problem. If time had permitted, it would have been better to machine a new casing to a better tolerance. This was the second rig built to examine this problem and since it would take time for the workshop to produce a new one, which can only be presumed to be of a better standard than the previous, it was decided to proceed using the current design. Although the results are not ideal, it is possible to identify an approximate response time. For example, the pressure response in Fig. 5.38 appears to be less than 20 ms and in Fig. 5.39 appears to be less than 30 ms.

Table 5.8 shows some of the better results for a variety of parameters.

data set			5	6	9	13	8a	26b
experimental	speed	rpm	110	70	257	125	125	250
	temperature	°C	27.0	28.0	28.0	38.0	32.0	32.0
	excitation	kV	1.2	1.2	1.2	1.2	1.2	1.0
	approx. response time	ms	20	20	20	30	20	20

Table 5.8: New Rayleigh step bearing rig. Some typical results for ER fluid medium with volts applied.

Although it is difficult to identify a final steady state pressure, the magnitude at the pressure tapping after excitation is approximately only half that of the steady state theoretical prediction {eqn (3.12)}. These predictions use the yield-stress results from section 3.6 and a plastic-viscosity equal to no-field value. The experimental pressure is expected to be less than the theoretical prediction due to mathematical model being perfectly pressurised. The value of yield-stress is likely to be quite accurate and was found to be approximately the same at a variety of temperatures (Fig. 3.33). The value of plastic-viscosity is however in question. A lower value gives a lower pressure and

thus a better comparison with the experimental result. Obtaining a theoretical result using a negative value of plastic-viscosity indicated in by the rheometer results in section 3.6 is still elusive. Since there is no accurate data for plastic-viscosity, it is difficult to proceed further. Perhaps here more collaboration with rheological experts is required. Although studying the magnitudes of pressure is important, the main aim was to investigate the pressure response time.

Response times

From some of the better results it was possible to incur a time associated with pressure response (Table 5.8). One thing that is certain is that it is fast, much faster than the results from Leek *et.al* [41]. Some responses are shown in Fig. 5.38, Fig. 5.39, and Fig. 5.40. The overall shape of the response is similar to the CFD results using the viscoelastic Bingham CFD model (section 5.3.2). To make a direct comparison accurate values of G' are required and these were not available. However, experimental results do appear to be slightly slower than the CFD predictions in (section 5.3.2).

5.3.10 Summary

The results can be improved upon by machining a rig to greater tolerance, and through obtaining and using improved fluid data. The latter will require more collaboration with rheologists. However, the viscoelastic Bingham CFD model appears to predict a pressure faster than the results indicated by Leek *et.al.* [41]. The experimental results carried out on a new Rayleigh step bearing apparatus tend to indicate that the CFD results are correct.

5.4 Concentric Clutch Response: Analytical vs. CFD vs. Experimental

In this final section, the fluid dynamic and rotor inertia effects of a cylindrical smart fluid clutch are investigated. Specifically, the run-up time (t_{ru}) required for one rotor, initially at rest, to reach a constant speed equal to that of the input rotor is studied. Analytical and CFD Bingham plastic time-dependent solutions are considered. Responses are also measured experimentally using an ER clutch. An inertial CFD boundary condition had to be developed in a sub-routine to account for the mass of the accelerating rotor.

The fluid flow is approximated as 1D between two flat parallel plates. This is a reasonable method of modelling the flow as demonstrated in section 3.3.2, provided that $h \ll r_m$. The lower plate was taken as the inner driving cylinder ($r = r_i$) moving at speed $U = r_i \Omega$. The upper plate was taken as the output rotor ($r = r_o$) running at speed $u_o = f(t)$. The flow is steady at and before $t = 0$ s, and is always isothermal.

The effects of fluid and device parameters on t_{ru} were studied. This includes plastic-viscosity (μ_e), yield-stress (τ_y), density (ρ), input plate speed (U) and gap width (h). Identifying limitations and optimum parameters was of prime concern. The length of the clutch rotors (L) simply determines how much torque is produced per metre length and has no effect on solutions.

Literature Review: Analytical Theory

An analytical analysis of the problem described above has been carried out by Whittle *et.al* [38]. Here the authors solve the time-dependent governing equations for a homogenous Bingham plastic continuum material using approximations that they justify. The authors have derived a rough design formula giving an ‘optimum run-up time’ (t_o), that occurs when the output rotor inertia vanishes:

$$t_o \approx Ah^2 \rho / \mu_e \quad \text{where } A = 4.0 \text{ is a constant .} \quad (5.6)$$

This formula is intended to aid the design of devices and fluids by giving an estimate of the fastest possible t_{ru} . However, it was necessary to reassess the validity of this formula, and compare it with CFD results. Parameters not present in eqn(5.6) are U and τ_y . A change in velocity gives a proportional change in $\dot{\gamma}$. Thus when U is twice as large, the viscous shearing force that drags the output rotor up to the same speed also doubles. For a Newtonian fluid, a change in U should therefore have little or no effect on the solution of t_{ru} . However, for a smart fluid, the total shear-stress is much less dependent on $\dot{\gamma}$ and in some cases approximately equal to τ_y ¹. In this situation, logically the run-up time should be longer if U is higher or if τ_y is lower.

5.4.1 Clutch with Newtonian Fluid medium and No Output Rotor Inertia: CFD vs. Analytical

The situation when the fluid dynamics alone solely influence t_{ru} is of initial interest. This is the case when the output rotor has zero inertia, thereby giving an optimum run-up time (t_o). Using an array of parameters in a Tagucci analysis, the average effects of μ_e , ρ , U and h , on t_o can be established. Here $\tau_y = 0$ Pa and values are chosen over a range typical to the application in hand.

Development of CFD Model

The following table summarises the CFD model used in this section.

¹ Shear-rates in a clutch will be relatively small and therefore $\tau_y \gg \tau_o$.

Software	Fluent5, finite volume, segregated solver	
Physical Model	1D, laminar, incompressible, isothermal flow	
Fluid Properties	viscosity (Newtonian), density (constant)	
Discretisation of flow Equations.	interpolation scheme	1 st order for all equations
	pressure-velocity	SIMPLE
	unsteady flow	1 st order implicit
	uniform grid (x, y, z) [$y =$ radial direction]	3 (x -direction) x 20 (y -direction)
Boundary Conditions	upper wall (outer rotor)	no stress wall condition (free surface)
	lower wall (inner driven rotor)	constant speed wall condition
	left and right edges	cyclic condition

Table 5.9: Summary of CFD model used to solve 1D concentric clutch with no rotor inertia.

For 1D flow, all derivatives in the circumferential (x -direction) and axial (z -direction) are zero. As a result, only a few cell widths are required in the x -direction when a periodic boundary condition is used (Fig. 5.41). In addition, the z -direction is automatically taken to be 1.0 m long, thus shear force is reported per metre length. The length in the x -direction is arbitrary and was set to equal to the gap-width length simply the model well proportioned (Fig. 5.41). The wall corresponding to the outer rotor was given a zero-shear-stress condition; this would be the condition imposed if the outer rotor has no mass and therefore zero inertia. Refer to Fig. 5.41 and Table 5.9 for more details.

In order to determine the initial steady state linear velocity profile, the upper plate was set as a standard no-slip wall condition. The solution was then computed and the data saved. This data file was then used to initialise the unsteady solution.

Grid Adequacy, Convergence Criteria and Time-step Size

A value of twenty cells in the y -direction was found to be adequate¹. For convergence, the normalised residual history criteria must be reduced to at least 1×10^{-5} . A criterion of 1×10^{-6} was therefore used to ensure convergence at each time-step was being achieved. In order to record the run-up curve, the x -velocity component on the outer rotor was written to a file at each time-step. Fig. 5.42 shows the velocity run-up curve for different time-step values. Decreasing the time-step to less than 0.1 ms is seen to have little effect. Variable history files written for each time-step allowed convergence to be further verified for each time-step.

¹ This was established using basic steady state formula for clutch $N = f(\text{speed, viscosity, gap size})$.

Results: Newtonian Fluid with No Rotor Inertia

Having determined the correct solution parameters to use for this particular time-dependent solution, a detailed analysis of the problem can be carried out. The chosen parameters and the results are presented in Table 5.10.

simulation number	parameters				run-up time ms	coefficient <i>A</i>
	density	velocity	viscosity	gap width		
	kg/m ³	m/s	Pa.s	mm		
a	1000	1.5	0.05	0.5	12.8	2.558
b	1000	1.5	0.10	1.0	25.6	2.555
c	1000	3.0	0.05	1.0	51.1	2.553
d	1000	3.0	0.10	0.5	6.4	2.564
e	2000	1.5	0.05	1.0	102.5	2.563
f	2000	1.5	0.10	0.5	12.8	2.558
g	2000	3.0	0.05	0.5	25.6	2.554
h	2000	3.0	0.10	1.0	51.1	2.553

Table 5.10: CFD results and Tagucci parameters used for a concentric clutch with a zero yield-stress fluid medium and no load.

In order to determine t_o , a definition must be set. This corresponds to the time required for the speed of the output rotor (u_o) to reach a percentage of the input rotor speed (U).

$$t_o \text{ equals the time when } \frac{u_o}{U} = P\%. \quad (5.7)$$

Since the solution is iterative, it is not sensible for P to equal 100 %. A value of 99.9% was therefore chosen¹. Using this value, the parameter A from eqn(5.6) is found to be consistent at ≈ 2.6 . The results therefore conform to the dimensionally correct formula of eqn(5.6), but with a slightly different constant of proportionality. The CFD result for A is likely to be different to that in eqn(5.6) due to the t_{ru} not being an exact time, whereas the analytical result is.

Fig. 5.43 shows the average effect of each parameter, and clearly suggests that the effect on t_o is as described in eqn(5.6). Fig. 5.44 shows the run-up curves. Curves *a* & *f* overlap one another – doubling the density is cancelled out exactly by doubling the viscosity. The curves show a decreasing acceleration over time. As the plates come up to the same speed, the shear-rate and thus shear-stress decrease giving a reduced acceleration. It is clear from Fig. 5.45 that the velocity profiles throughout the event are non-linear.

5.4.2 Clutch with Bingham Plastic Medium and No Output Rotor Inertia: CFD vs. Analytical

The CFD set-model up in section 5.4.1 was now utilised with the Bingham CFD model

¹ An alternative value would give different results, it is therefore important to be consistent.

in place of the Newtonian fluid. The CFD set-up was first checked to ensure correct results were obtained for a steady state shear. This was done using the steady state analytical equation for torque from section 3.3.2, and the model was found to be adequate.

The run-up situation was then investigated, and as anticipated, t_o was found to be several orders of magnitude faster than that obtained with the Newtonian model. A solution procedure using a time-step size of 1×10^{-6} s, was found to be adequate, but a time-step of 1×10^{-7} s was used to ensure accuracy. This may seem to be at the expense of computational time. However, using a smaller time-step means that each time-step converges more quickly thus justifying the value chosen. To ensure convergence, fifty iterations per time-step were performed.

Results: Bingham fluid with no Rotor Inertia

The chosen parameters and the results are presented in Table 5.11 and the average effect of the parameters is shown in Fig. 5.46.

simulation number	Parameters					run-up time	
	yield stress	velocity	fluid density	viscosity	gap width	Whittle et.al formula	CFD
	Pa	m/s	kg/m ³	Pa.s	mm	ms	ms
a	5000	1.50	1500	0.50	0.50	3.0	0.109
b	10000	1.50	1500	1.00	1.00	6.0	0.110
c	5000	3.00	1500	1.00	0.50	1.5	0.432
d	5000	1.50	3000	0.50	1.00	24.0	0.223
e	10000	3.00	1500	0.50	0.50	3.0	0.106
f	10000	1.50	3000	1.00	1.00	12.0	0.220
g	5000	3.00	3000	1.00	0.50	3.0	0.886
h	10000	3.00	3000	0.50	1.00	24.0	0.217

Table 5.11: CFD results and Tagucci parameters used for a concentric clutch with a Bingham fluid medium and no load.

This time the definition of t_o is quite distinctive as can be seen in Fig. 5.47. Fig. 5.46 illustrates that, within the scope of the Tagucci analysis, the chosen parameters h , ρ , U and τ_y are all important parameters affecting t_o . A gap-width of half the size allows information to travel across the gap roughly twice as fast. A yield-stress twice as large allows roughly twice as much accelerating force. Fluid density has the same effect as in the Newtonian case. As anticipated, U now has an effect; a higher value gives a proportionally longer run-up time. Plastic-viscosity is found to have little effect. As hypothesised earlier, the response time is now several orders of magnitude faster than the Newtonian case. Fig. 5.48 typically shows how the velocity profile changes during an event, and shows how a plug forms and increases until the whole gap is moving at

the same speed. The CFD results are clearly in conflict with the estimation {eqn(5.6)} provided in [38].

5.4.3 Clutch with Inclusion of Rotor Inertia: Analytical Predictions when Fluid Inertial Effects are Neglected

Experimental results using a clutch set-up (presented later), show t_{ru} to be an order of magnitude greater than the t_o CFD results. The difference was attributed to the inertia of the output rotor not being negligible. Accounting for the inertia of the output rotor in the CFD model is in principle straightforward. However, getting the CFD model to function correctly proved very difficult, so in the mean time an approximate analytical solution was formulated in order to get an indication of the size of t_{ru} .

Here the inertia of the fluid is not being considered, making the solution simple, but only valid when the outer rotor inertia (I_o) is dominant. At the outer radius (r_o), the smart fluid imposes a torque (N_o) on inner surface of area (A_o):

$$N_{r=r_o} = I_o \alpha \Rightarrow \tau_{r=r_o} r_o A_o = I_o \frac{1}{r_o} \frac{du}{dt} \Big|_{r=r_o} \Rightarrow \tau_{r=r_o} = \frac{I_o}{A_o r_o^2} \frac{du}{dt} \Big|_{r=r_o} . \quad (5.8)$$

For a Newtonian fluid the shear-rate and hence shear-stress reduce over time, and so eqn(5.8) shows that the acceleration will be highly non-linear. In contrast, for a strong smart fluid ($\tau_e > \tau_o$) in which the shear-stress remains approximately constant, the acceleration would be linear. For a weak smart fluid ($\tau_e < \tau_o$), the plastic-viscosity makes the total shear-stress somewhat dependent on the shear-rate, and so the acceleration would start off being linear, and then gradually become non-linear.

Prediction Using a Constant Stress Assumption

If the known initial shear-stress is to remain constant throughout the event, a useful parameter t_{min} can be derived. This would give the fastest possible run-up time. The stronger the smart fluid, the more valid the approximation would be¹. Since the shear-stress is assumed to remain constant, the acceleration is linear, and from eqn(5.8) it follows that:

$$\tau_{t=0s} = (\mu_{nn})_{t=0s} \frac{U}{h} = \frac{I_o}{A_o r_o^2} \frac{U}{t_{min}} \Rightarrow t_{min} = \frac{I_o h}{2\pi r_o^3 L (\mu_{nn})_{t=0s}} . \quad (5.9)$$

For a Newtonian fluid $\mu_{nn} = \mu_e$, and eqn(5.9) shows that t_{min} is independent of U . Table

¹ $\tau_y \neq f(\text{shear-rate})$, and so the total shear-stress becomes less dependent on shear-rate the larger the values of τ_y become

5.12 shows t_{min} for parameters in the range of initial experimental results, using a Newtonian fluid.

Inertia of output rotor I_o	kgm ³	2.5E-05	2.5E-05	2.5E-05	5.0E-05	2.5E-05
gap width h	mm	0.5	0.5	1.0	1.0	0.5
outer rotor radius r_o	mm	25	25	25	25	50
length L	mm	30	30	30	30	30
viscosity μ_e	Pa.s	0.05	0.1	0.05	0.05	0.05
t_{min}	ms	84.9	42.4	169.8	339.5	10.6

Table 5.12: Minimum possible run-up time (t_{min}) when the rotor inertia is included for a Newtonian fluid medium.

Here t_{min} is now of the same order of magnitude as it was in the initial experimental results, and more importantly is faster.

Using the same assumptions for a smart fluid, then it follows from eqn(5.8) that:

$$t_{min} = \frac{I_o U}{A_o r_o^2} \left(\frac{1}{\tau_y + \mu_e \dot{\gamma}} \right). \tag{5.10}$$

Since τ_y is generally much larger than $\mu_e \dot{\gamma}$, it follows from eqn(5.10) that:

$$t_{ru} \approx \frac{I_o U}{A_o r_o^2} \left(\frac{1}{\tau_y} \right) \Rightarrow u_o(t) \approx \left(\frac{A_o r_o^2 \tau_y}{I_o} \right) t. \tag{5.11}$$

Equation (5.11) suggests that the rotor should run-up linearly, regardless of the value of inertia. Such behaviour was even evident when $I_o = 0 \text{ kg.m}^3$ (see Fig. 5.47). Table 5.13 shows results from eqn(5.11) for parameters in the range used previously. The estimated run-up times are very fast in comparison to the Newtonian fluid case.

inertia of output rotor I_o	kgm ³	2.5E-05	2.5E-05	2.5E-05	2.5E-05	5.0E-05
gap width h	mm	0.5	0.5	0.5	1.0	0.5
outer rotor radius r_o	mm	25	25	25	25	25
length L	mm	30	30	30	30	30
yield stress τ_y	kPa	1.0	5.0	1.0	1.0	1.0
speed Ω	rpm	500	500	250	500	500
run-up time	ms	11.1	2.2	5.6	11.1	11.1

Table 5.13: Approximate t_{min} solution for a Bingham plastic fluid medium assuming a constant stress.

These predictions do not account for the inertial effects of the fluid. However, the times are much larger than the optimum zero inertia times calculated in section 5.4.2 and

therefore indicates that the inertia of the outer rotor has a great influence. This suggests that this simple solution may be relatively correct.

Prediction using a Linear Flow Profile Assumption

An improved approximation was next sought. When the inertia of the rotor is a factor, it may be reasonable to assume that the velocity profile will remain linear, but of variable magnitude throughout the event, in which case the shear-rate is given as follows:

$$\dot{\gamma} = \frac{u_i - u_o}{h} = \frac{U - u_o(t)}{h}. \quad (5.12)$$

Equation(5.8) can now be solved using a backward differencing scheme for the acceleration term,

$$\mu_e \frac{U - u(t)}{h} \approx \frac{I_o}{2\pi r_o^3 L} \frac{u(t) - u(t - \Delta t)}{\Delta t}. \quad (5.13)$$

This equation was easily solved for $u(t)$ within a spread sheet. The results for a Newtonian fluid are presented in Fig. 5.49, and still show that U has no effect on the solution. A faster time is achieved using a higher viscosity and reduced inertia value.

5.4.4 Smart Fluid Clutch CFD Model with Inclusion of Outer Rotor Using an Inertial Boundary Condition

It has been concluded that it will be important to consider the mass of the outer rotor and not just the fluid itself. If CFD software is to prove useful for practical cases, then the dynamics of machine parts, which are being forced to accelerate by the smart fluid, must somehow be included in the model. The relatively up to date Fluent5 CFD software does not offer such a facility. However, user-defined subroutines within Fluent5 allow for the possible development of such a boundary condition.

The shear-stress imposed on the fluid surface by the outer rotor that is accelerating in the positive x -direction is given by:

$$N_o = I_o \alpha \Rightarrow \tau_o = B \left. \frac{du}{dt} \right|_o, \quad (5.14)$$

$$\text{where } B = \frac{I_o}{2\pi r_o^3 L}. \quad (5.15)$$

The acceleration of the outer rotor can be acquired using a 1st order backward difference approximation:

$$\left| \frac{du}{dt} \right|_o = \frac{|u - u_{t-\Delta t}|_o}{\Delta t} \quad (5.16)$$

Using eqn(5.16) and eqn(5.14) a shear-stress boundary condition (τ_o) can now be used in the CFD model. For initial testing purposes, B was typically taken to be:

$$B = \frac{I_o}{2\pi r_o^3 L} = \frac{2.437 \times 10^{-5}}{2\pi \cdot (25 \text{ mm})^3 \cdot 30 \text{ mm}} = 8.488. \quad (5.17)$$

Initial Subroutine for Inertial Boundary Condition

Once the sub-routine (Appendix A - Table A.3) is written, it must be placed in the appropriate directory and compiled so that it is available for selection as a boundary condition. The CFD model previously used for the Newtonian fluid medium was utilised. The zero shear-stress boundary condition was replaced with the user-defined shear-stress condition. After various efforts, the boundary condition was never made to function properly. Typically after one iteration $u(t)$ became very large giving an unrealistic acceleration and consequently rapid divergence. This is a chicken and egg situation; $u(t)$ is an unknown, but is required for use in the user-defined subroutine. Several attempts to improve the situation were made, including incorporating under relaxation terms. After exhausting all ideas, an alternative approach was sought.

Modified Subroutine for Inertial Boundary Condition

In principle, it should be possible to get the shear-stress boundary condition to work properly. In practice, the CFD package prefers to work with velocities. Equation (5.14) can be rearranged to give a boundary condition in terms of velocity:

$$\tau_o = B \left| \frac{du}{dt} \right|_o = B \left(\frac{u_o - u_{o(t-\Delta t)}}{\Delta t} \right) = \mu_{nn} \dot{\gamma} \Rightarrow u_o = \frac{\mu_{nn} \dot{\gamma}}{A} \Delta t + u_{o(t-\Delta t)}. \quad (5.18)$$

As per usual, the correct size and number of iterations per time-step had to be determined. The boundary condition appeared to be working. However, a problem that is evident from Fig. 5.50 was discovered. The value of acceleration at $t = 0$ s is theoretically known¹ and is included in Fig. 5.50 as a dotted line. The shear-rate and consequent shear-stress and acceleration can only possibly reduce over time. Hence, any run-up curve should remain on the right hand side of this dotted line. As can be seen in Fig. 5.50, the opposite is true. The error appears to worsen the smaller the time-step. However, the solution does improve with increasing grid size. It was discovered that the

anomaly arose due to u_o and $u_{o(t-\Delta t)}$ being taken to be equal to adjacent cell centre velocity, rather than the actual wall velocity. Reducing the cell size reduced this error and thus gave a better solution. Reducing the time-step increased the ratio between the step increase in velocity and the actual velocity error, thereby giving a worse solution. Hence, the results are time-step size dependent and are most certainly not a correct solution of the problem in hand.

Corrected Inertial Boundary Condition Subroutine

Since du/dy is known, it is possible to determine the true value of u_o . It is however impossible to correctly obtain the $u_{o(t-\Delta t)}$, since the previous shear-rate is not available for use². A detailed investigation concluded that the following was possibly a way forward:

$$u_{o(t-\Delta t)} \approx (\text{cell center velocity of cell next to the wall})_{(t-\Delta t)} + \left| \frac{\dot{\gamma} \Delta x}{2} \right|. \quad (5.19)$$

Here the shear-rate at time t , and cell width (Δx) are being used to obtain a more accurate value of $u_{o(t-\Delta t)}$. This situation is exactly equivalent to basing the force balance at $y = h - \Delta x/2$ opposed to at $y = h$. When the time-step is small, this approximation should be acceptable. It is therefore important to have a small cell width at the wall. With this additional term the results (as shown in Fig. 5.51), are now on the correct side of the theoretical line. In this figure, it can also be seen that the use of a very small time-step ($< 1 \times 10^{-4}$ s) is inappropriate. This is because the increase in speed per time-step should not be any less than the error in speed due to the approximation, as is explained above.

Partial Verification of Final Model

If the value for the output inertia boundary condition is consequently reduced, then the event should ultimately be the same as is described in section 5.4.1 in which a free surface (no-inertia) boundary condition is used. This situation was investigated and the results are shown in Fig. 5.52. As they should do, the two different boundary conditions are complementary when the inertia value is very low.

¹ at $t = 0$ s the shear-rate and hence force on the outer rotor is known

² known from consultations with Fluent development team

CFD Analysis: Newtonian Fluid with Rotor Inertia

simulation number	Parameters					run-up time
	inertia parameter B	input speed	fluid density	plastic viscosity	gap width	90%
	Pa.s ² /m	m/s	kg/m ³	Pa.s	mm	ms
a	1	1.50	1000	0.50	0.50	203
b	2	1.50	1000	1.00	0.10	261
c	1	3.00	1000	1.00	0.50	202
d	1	1.50	2000	0.50	0.10	261
e	2	3.00	1000	0.50	0.10	268
f	2	1.50	2000	1.00	0.50	396
g	1	3.00	2000	1.00	0.10	208
h	2	3.00	2000	0.50	0.50	400

Table 5.14: CFD clutch results for zero yield-stress with inclusion of rotor load

With the newly developed inertial boundary condition, it was possible to determine more accurately how the inertia of the rotor affects t_{ru} . In addition, the versatility of the boundary condition could be tested for different parameters. This was again done using a Tagucci analysis with parameters as listed in Table 5.14. Results are presented in Fig. 5.53. It is now clear that the value of output rotor inertia is a major factor for the run-up time. The speed (U) is still not a factor for the Newtonian case. In conclusion, the value of rotor inertia is significant. Fig. 5.54 shows that the run-up time is now several hundred milliseconds, this is in line with initial experimental studies.

CFD Analysis: Bingham CFD Model with Rotor Inertia

When using the Bingham CFD model technical difficulties were encountered. When a yield-stress is present, the overall response is faster and so Δt needs to be smaller; the error associated with the correction term in eqn(5.19) is now quite large compared with the Δt term in eqn(5.18). Eventually new documentation came to light that indicated that user-defined memory locations were available for use. This would allow the plate speed to be stored in a memory location so that the previously computed plate velocity was known. In fact three memory locations were used; one to store the actual time-step number, so that the point at which u_o should be updated could be determined; one to store u , and one to store u old.

Again, a Tagucci analysis was employed with parameters as listed in Table 5.15.

simulation number	Parameters					run-up time		
	yield stress	velocity	fluid density	plastic viscosity	inertia parameter B	theory (t_{min})	CFD (t_{ru})	difference
	Pa	m/s	kg/m ³	Pa.s	kg/m ²	ms	ms	%
a	5000	1.50	1000	0.05	5.0	1.46	1.58	7.8
b	10000	1.50	1000	0.10	10.0	1.46	1.53	4.8
c	5000	3.00	1000	0.10	5.0	2.68	3.01	11.0
d	5000	1.50	2000	0.05	10.0	2.91	3.15	7.5
e	10000	3.00	1000	0.05	10.0	2.91	3.07	5.1
f	10000	1.50	2000	0.10	5.0	0.73	0.89	18.2
g	5000	3.00	2000	0.10	10.0	5.36	6.01	10.9
h	10000	3.00	2000	0.05	5.0	1.46	1.65	11.7

Table 5.15: Parameters and results for a concentric clutch with Bingham plastic fluid medium and inclusion output rotor inertia. Theoretical t_{min} is from eqn(5.10).

It is clear from Fig. 5.55 that the yield-stress, input speed and rotor inertia are important parameters. The run-up curves shown in Fig. 5.56 are all reasonably linear; as a consequence the linear assumption used to derive t_{min} {eqn(5.10)} is quite valid and gives a good approximation for t_{ru} (Table 5.15). The actual CFD run-up time is slightly longer; this is due to the fluid inertia having some effect (clear from Fig. 5.55) and from a slight drop in shear-stress due to the fall in shear-rate.

Clutch with Bingham medium and Rotor Inertia: CFD vs. Analytical

Two solutions for high and low output rotor inertia are given by Whittle *et.al* [38]. It was worth comparing these solutions to the CFD counterpart. For the high rotor inertia solution, the parameters are such that $B (= 163.514 \text{ kg/m}^2)$ {eqn(5.15)} is large¹. Fig. 5.57 shows that the corresponding CFD solution is close but not exactly in line with the analytical solution [38]. This appears to be due to the CFD model having a higher initial shear-stress due to τ_o being included in the solution. The analytical solution approximates the rotor inertial acceleration to be due to τ_y alone {equivalent to the derived approximation eqn(5.11)}. The CFD run-up curve looks to be linear but in fact, the initial gradient is slightly larger than that in [38] due to τ_o . Initially $\tau_o = 300 \text{ Pa}$, but then obviously decreases as the shear-rate reduces (Fig. 5.58), while $\tau_y = 2000 \text{ Pa}$ remains constant. For the analytical solution² [38] $t_{ru} \approx 245 \text{ ms}$ and is line with that from eqn(5.11) ($t_{ru} \approx 245 \text{ ms}$). Since eqn(5.11) neglects all fluid inertia it can be concluded that for these parameters the fluid density has very little effect on the overall solution.

¹ For a practical clutch this value would be much lower.

² Result read from printed figure in [38].

Because of the high inertia, the velocity profiles are found to be linear in both the CFD (Fig. 5.58) and analytical solution. The t_{min} solution {eqn(5.10)} is also included on Fig. 5.57, this gives t_{ru} if the initial shear stress and thus acceleration were to remain the same. Here the initial assumption in [38] of a linear form to $u_o(t)$ is quite valid, and thus it is quite understandable that it gives a reasonable result in line with the CFD solution.

The low output rotor solution in [38] is now compared with the corresponding CFD result. The inertia is now much lower, but still relatively high ($B = 14.062 \text{ kg/m}^2$). The CFD velocity profiles (Fig. 5.60) show that the shear-rate becomes much less linear with time. This is in line with the profiles in [38], although on a different time scale as can be seen in Fig. 5.59. Up until about the 3.0 ms the run-up profiles are similar although differ due to the same reason as for the high inertia case. After about 3.0 ms significantly different behaviour occurs and $u_o(t)$ suddenly begins to run-up as if there was no rotor inertia, and the overall time becomes close to that given by eqn(5.6). This is explained by Whittle et.al. [38] to be due to the fact that a critical point has been reached in which acceleration becomes limited by the fluid dynamics. This is surely in error, the shear stress on the rotor cannot just suddenly reduce and so the rotor should still run-up with a similar acceleration. However, before a significant examination into why the solutions are so different, it is useful to present an experimental study of the problem in hand.

5.4.5 Clutch with a Newtonian Fluid Medium: Experimental vs. CFD results

To determine the reliability of the theoretical solutions experimental results in a concentric clutch apparatus were sought. This was achieved by modifying an existing apparatus. The device had been designed to give linear motion and consists of two, dual channel, ER clutches. One clutch was utilised for the experimentation. The clutch had been designed to have low output inertia [62]. To maximise torque for the same rotor inertia a double channel formation is used (Fig. 5.61). To limit the need for seals, and therefore friction, the clutch is mounted vertically. The lower input rotor rotates with constant speed Ω . The fluid rotates with the same angular speed as the input rotor once the output rotor has run up to the same speed.

The output rotor was stripped of all unnecessary parts to reduce its inertia. A release mechanism was built to hold the “output” rotor stationary (Fig. 5.61). Two small servomotors served as tachometers. The upper tachometer could not be mounted co-axially. This was due to the design requiring electrical excitation to be applied through the top cap. A simple gear train was therefore used to mount the upper tachometer as shown in Fig. 5.61.

Experimental Method

The clutch parts are disassembled cleaned and reassembled. The clutch is then filled with Tellus 37 oil from the inner channel; fluid then flows into the outer channel thereby ensuring that all the air is expelled. The experimental procedure is then as follows:

- i. The output rotor is held stationary while the input speed (Ω) is set.
- ii. An approximation of the fluid temperature is obtained using an infra-red thermometer. The thermometer takes a reading on the outer casing that is painted black for maximum thermistivity.
- iii. The output rotor is then released and both the input and output rotor speeds are recorded on a digital oscilloscope.
- iv. The results are then stored and imported into a spreadsheet for analysis.

To achieve different fluid temperatures the output rotor was held stationary while viscous heating took affect. The outer casing is only a few millimetres thick and highly conductive. It is therefore reasonable to assume that fluid temperature is relatively uniform and equal to that measured on the outer surface. For the Tellus 37 the viscosity is given accurately by the following equation [63]:

$$\mu = 0.089 \frac{1 - 0.31t}{1 + 0.94t} \quad \text{where } t = 0.05T_s - 1.0 \quad (5.20)$$

CFD Model and Results

The CFD models from section 5.4.4 were utilised. In order for the single channel CFD models to behave as a dual-channel clutch, the length (L) must be doubled. The value for B is calculated as:

$$B = \frac{I_o}{2\pi r_o^3 L} = \frac{2.9 \times 10^{-5}}{2\pi \cdot (24.5 \text{ mm})^3 \cdot 60 \text{ mm}} = 5.231 \text{ kg/m}^2. \quad (5.21)$$

The mean radius (r_m) of the output rotor was measured at 24.5 mm, this was used to set the wall speed ($U = r_m \Omega$).

All the results (Fig. 5.62, Fig. 5.63, Fig. 5.64, Fig. 5.65 & Fig. 5.66) clearly indicate that t_{ru} is independent on the speed U . As indicated in the figures the CFD and experimental results clearly agree over a wide range of results. The run-up time is not dependent on speed U and is only effected through the viscosity that changes with temperature. Typical run-up time equals 200 ms. These times are not very fast but with a smart fluid the response should be much quicker.

5.4.6 Clutch with an ER Fluid Medium and Rotor inertia: Experimental vs. CFD results

An investigation was now carried out using the same CFD model as in section 5.4.5 for an ER fluid medium. The fluid used was Bayer 3565 50%. The experimental method was now as follows:

- i. The input speed Ω is set to the desired value.
- ii. The voltage supply is set to give the correct excitation.
- iii. An approximation of the fluid temperature is obtained.
- iv. Voltage is applied by switching on 10 V to the switching box.
- v. The output rotor is then released and the velocities are recorded on the digital oscilloscope.
- vi. The results are then imported into a spreadsheet for analysis.

At low speeds and high voltages, excitation actually caused the driving motor to stop stationary. The motor was simply not powerful enough to keep the input rotor rotating while the outer was being held stationary. At high voltages, the yield-stress and forces involved were just too strong in order to be able hold the output rotor stationary, without damaging the apparatus.

Problems encountered

Although significantly faster than the zero excitation case, initial results indicated that t_{ru} was slower than expected. When clutches are locked together, the electrical conductivity is higher than when the fluid is in shear. This is because the fluid can form strong chain like structures when not under shear, providing a favourable means of current transfer. From this an indication of t_{ru} was inferred from recordings of current that was faster than that indicated by the tachometer recording. Stiffening up the apparatus and reducing possibility of slippage in the cogging system gave tachometer recordings consistent with the current recordings¹.

Results and Discussion

All the experimental tests were carried out at least twice. All the results are found to be repeatable and are therefore of high quality. The first set of data (Fig. 5.67) was for zero volts giving t_{ru} curves (~200 ms) typical to those found before for a Newtonian fluid. Using a viscosity corresponding to the correct temperature gives a very close match between CFD and experimentation. For an excitation of 2.0 kV/mm t_{ru} is seen to

¹ Although the gears appeared to be attached tightly, accelerations of 10000 rad/s/s could easily cause slippage.

be linear¹ (Fig. 5.68). As illustrated in Fig. 5.68 agreement between CFD and experiment is good. This is also the case for different temperatures and for higher excitations² as shown in Fig. 5.69 Fig. 5.70. Interestingly at a temperature of 40°C $\mu_e = 0$ Pa.s. In which case t_{ru} should be linear and is indeed so as shown in Fig. 5.71.

5.4.7 Discussion

The CFD and experimental results agree well, and are in accordance with the derived analytical approximations in section 5.4.3. However, there is a fundamental difference between the run-up times given by CFD and the analytical work of Whittle *et.al.* [38]. These differences are summarised in Table 5.16.

Model	Observation	Conclusion
Newtonian fluid medium with no output rotor inertia	Good agreement for t_o between CFD and [38]. (section 5.4.1)	CFD results agree well with eqn(5.6) given by [38].
Bingham plastic medium with no output rotor inertia	eqn(5.6) given by [38] over-predicts the CFD results for t_o by several orders of magnitude. (section 5.4.2)	Eqn(5.6) does not contain a yield-stress or an input speed parameter, and therefore does not predict the results obtained by CFD.
Newtonian fluid medium with output rotor inertia	Very good agreement between CFD and experiment. The inclusion of the output rotor inertia changes the magnitude of the response by a factor ten.	Due to the requirement for the rotor inertia to be considered, eqn(5.6) is no longer valid.
Bingham plastic fluid medium with output rotor inertia	Very good agreement between CFD and experiment. The parameter B is such that the solution given by [38] will indicate that the response is limited by the fluid dynamics and thus t_{ru} is given by eqn(5.6).	[38] is in disagreement with both CFD and experimental results.

Table 5.16: Summary of the clutch run-up results given by Whittle *et.al* [38] and CFD.

When the output rotor inertia (I_o) is high, rough agreement the two mathematical studies is reached (Fig. 5.57). Here the fluid inertia has a negligible effect, helping to keep the velocity profiles linear (Fig. 5.58). In [38], it is suggested that when the output rotor inertia is dominant the rotor accelerates in a linear manner, caused by a constant shear stress ($\tau = \tau_y$). The two different studies therefore agree well when the solution is

¹ The electro-stress is high in comparison to the plastic-viscosity.

² On activation of 3kV/mm the motor was not sufficiently powerful to keep the clutch at 600 rpm.

dominated by rotor inertia.

The disagreement occurs when a more practical case of low output inertia is considered (Fig. 5.59). The solution of Whittle *et.al* [38] indicates that after a certain time, the fluid dynamic response prevents the approximately constant acceleration from continuing. The response is seen to suddenly change and become very slow (Fig. 5.59). This fluid dynamic response appears to be similar, if not the same, as for the case of no rotor inertia with $\tau_y = 0$ Pa (section 5.4.1 - Fig. 5.44). In this case, the final run-up time should be given approximately by eqn(5.6) (i.e. $t_o \approx 23$ ms). The complete run-up curve is not presented in [38], but if the curve is extrapolated, then 23 ms will not be far off the mark - note that the CFD response time is only 4 ms.

When the rotor inertia is not significantly high, [38] appears to suggest that the actual overall response is fluid dynamic limited, and so t_{ru} can be determined using eqn(5.6) (t_o). However, this author believes this to be wrong for the following reasons:

- i. In [38] the fluid dynamic response is said to become dominant because it is slower than the rotor inertia response. This does not make any sense; the fluid dynamic response affects the acceleration of the output rotor, and the inertia of the rotor affects the fluid dynamic response. Therefore neither one can be dominant as they both affect each other.
- ii. The optimum fluid dynamic response time ($t_{ru} = t_o$) is true when $I_o = 0$ kg.m², and thus only the fluid is been accelerated. If any additional inertia were included (i.e. the output rotor) then the laws of motion dictate that t_{ru} must be longer. The CFD and experimental results are in agreement with this logic, the analytical solution is not [38]. In the latter case, adding rotor inertia does not always increase t_{ru} !
- iii. Although the approaches are quite different, when $\tau_y = 0$ Pa, eqn(5.6) for t_o the analytical work [38] does indeed agree with CFD. In fact, the arrangement of the parameters in eqn(5.6) is found to agree precisely with the CFD results. According to [38], eqn(5.6) will also hold true for a Bingham plastic fluid. However, the CFD results indicate that when $\tau_y > 0$ Pa, both τ_y and U now become important parameters. This is understandable when the following is considered. The non-Newtonian viscosity concept¹ gives finite sections of fluid a viscosity equal to eqn(2.13). Initially $\dot{\gamma}$ (and hence μ_{nn}) are uniform across the gap. When $\tau_y = 0$ Pa, typically $\mu_{nn} = \mu_e = 50$ mPa.s. For a 5.0 kPa fluid with a

¹ The concept is the foundation of all the CFD work in this thesis.

shear-rate¹ of 3000 /s, μ_{mn} is now 34 times larger. The initial shear-stress ($\mu_{mn}\dot{\gamma}$) is therefore 34 times larger than before, and thus the acceleration will be much faster for the same fluid density. In addition, (unlike the Newtonian case), for a smart fluid the initial shear-stress does not significantly reduce as the event progresses $\{\tau_y \neq f(\dot{\gamma})\}$, further indicating a faster run-up time.

From an engineer's perspective it is difficult to argue with the above points and thus the validity of the analytical solution is questioned [38]. However both analytical [38] and CFD solutions are essentially solving the same governing flow equations so their results should agree. The reason for the disagreement has to be identified.

One difference between the two approaches is that in [38] the radial geometry is used, and in the CFD model a flat plate approximation was used². However, it is unlikely that this small assumption can explain the fundamental differences in the orders of the run-up times encountered.

Another difference between the two approaches is the choice of boundary condition on the output rotor. The main objective is to determine the velocity function $\{u_o(t)\}$ on this boundary. For a practical CFD solution, a user-defined subroutine was utilised to apply Newton's law of motion on the output rotor, and thus determine its speed. Here no initial assumptions of the form of $u_o(t)$ are taken. Although the CFD solution is iterative, great care was taken to ensure that the time-step sizes and number of iterations per step were appropriate. To obtain the fluid limited solution (t_o), (i.e. when the outer rotor has zero mass), a free surface boundary condition was used. The formula for t_o in [38] appears to have been derived by consideration of a special case of the overall solution only.

In the analytical solution [38], $u_o(t)$ is initially assumed to be linear, due to a constant value of yield-stress, and is in fact equivalent to the derived approximation of eqn(5.11). The value of shear-stress on the output rotor is therefore under-predicted³. An inappropriate negative gradient velocity occurs on the output wall. A condition is therefore imposed to prevent the velocity gradient from becoming negative. This does not necessarily mean that the subsequent solution is now correct – it is still an indirect solution of the problem in hand. This procedure seems dubious.

The analytical solution in [38] does not predict or allow for the formation of

¹ $U = 1.5$ m/s, $h = 0.5$ mm.

² This was done to simplify the CFD model as far as possible.

³ The severity of this inaccuracy depends on the magnitude of shear-rate.

plugs. In the CFD analysis, as soon as the output rotor a plug forms, due to $\tau < \tau_y$. The thickness of this plug increases with time.

5.4.8 Practical Considerations

Only the fluid properties and value of B affect the output acceleration. Of all the fluid parameters, the yield-stress is the most significant (Fig. 5.55), approximately effecting the acceleration in a directly proportionally manner.

If we assume a cylindrical output rotor of thickness (z) and density (ρ_o) then from eqn(5.15):

$$B = \frac{I_o}{2\pi r_o^3 L} = \frac{2\pi r_o^3 L \rho_o z}{2\pi r_o^3 L} = \rho_o z. \quad (5.22)$$

A low value of B would be 2 kg/m^2 ($1000 \text{ kg/m}^3 \times 2 \text{ mm}$); for a dual channel this would be halved to 1 kg/m^2 . This value is low and means that fluid inertia needs to be considered, thus requiring a CFD solution. However, in practice, the inertia will be higher due to a rotor shaft, and most importantly, the inertia of the device it will be attached too. In this case B will be much larger, and eqn(5.10) and eqn(5.11) should prove useful.

5.5 Summary: Unsteady Flow

Using the continuum CFD approach outlined in section 5.1, the response of a smart fluid in several devices was successfully modelled. In the annular valve, both pressure and flow-rate responses due to step changes in excitation were analysed. For the viscoplastic case, analytical studies were available to help verify the results. It was concluded that the work of Whittle *et.al.* [37] was inadequate in not correctly modelling the fluid momentum of the plug section. The yield-stress and plastic viscosity (due to high shear rates) were found to have strong effects on the response time.

For modelling the Rayleigh step bearing the viscoelastic Bingham CFD model proved to give much more realistic results than the viscoplastic Bingham CFD model. An experimental study on Rayleigh step bearing shows that the response is faster than experimental results obtained by Leek *et.al.* [41] who themselves believed that there results were slow. The CFD response appears to be slightly faster than the experimental situation, but this is likely to be due CFD model being ideally pressurised. More accurate fluid data with some idea on the value of G' is required if a more detailed comparison is to be made.

Although the clutch run-up problem was quite simple to solve, the actual

technicalities proved difficult. For the CFD to be useful, the model had to be aware of the mass of influencing parts (output rotor). A formula was derived to act as a CFD inertia boundary condition. Programming this function into Fluent proved difficult¹. However the effort was worthwhile as the results were found to be clearly in line with experimental results for both Newtonian oil and ER fluid mediums. The CFD solution clearly disagrees with the analytical solution of Whittle *et.al.* [38].

¹ Even with help from Fluent.Inc via. Email the sub-routine was difficult to build. This was partly due to the limited documentation describing Fluents' macros.

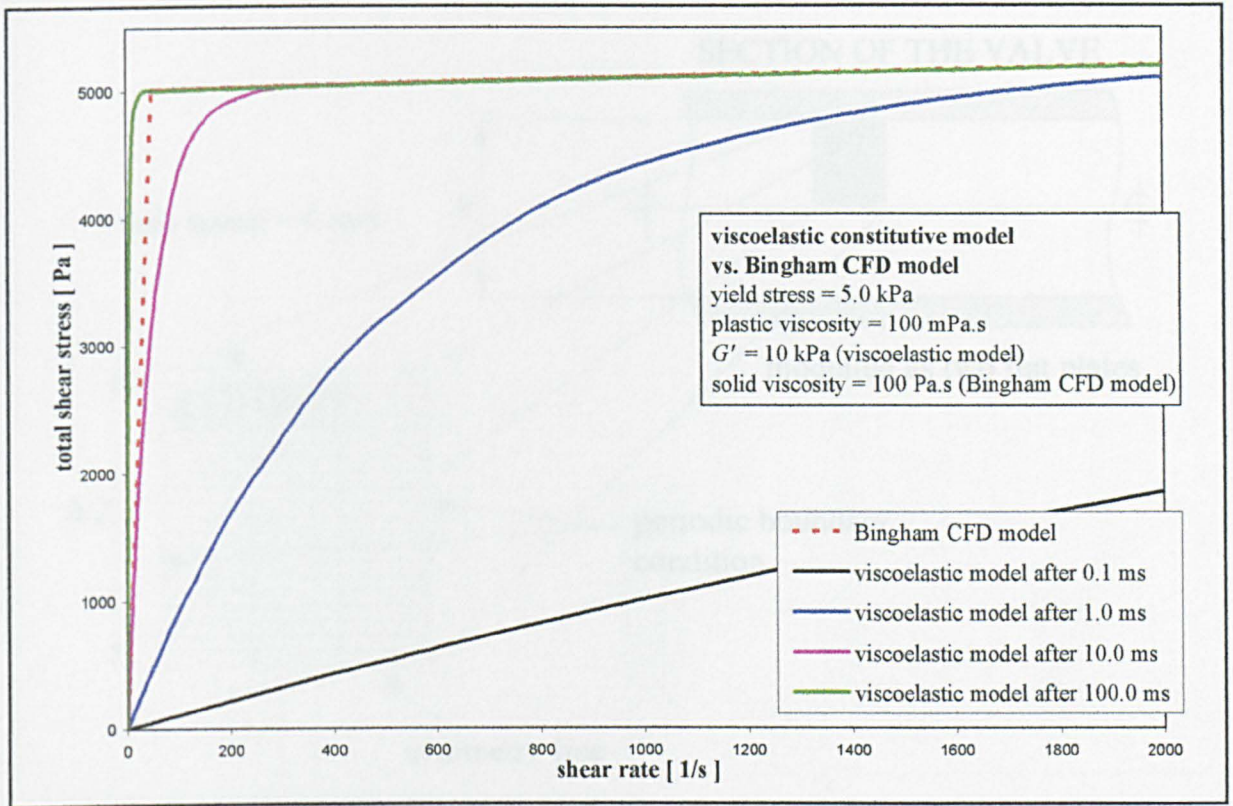


Fig. 5.1: Flow curve showing the comparison of the constitutive viscoelastic and Bingham CFD model at different time intervals. Here the usual Bingham plastic type flow curve becomes recognisable after about 10 ms.

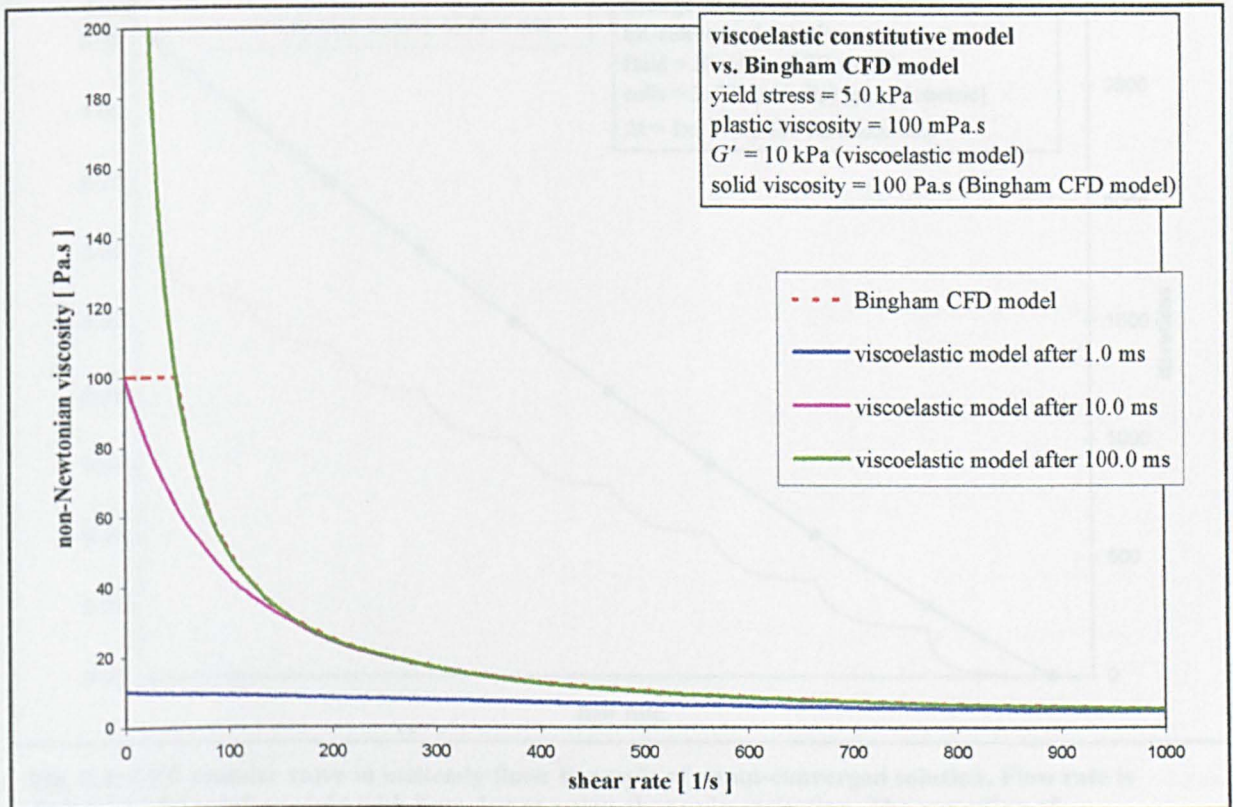


Fig. 5.2: Non-Newtonian viscosity curve showing the comparison of the constitutive viscoelastic and Bingham CFD model at different time intervals.

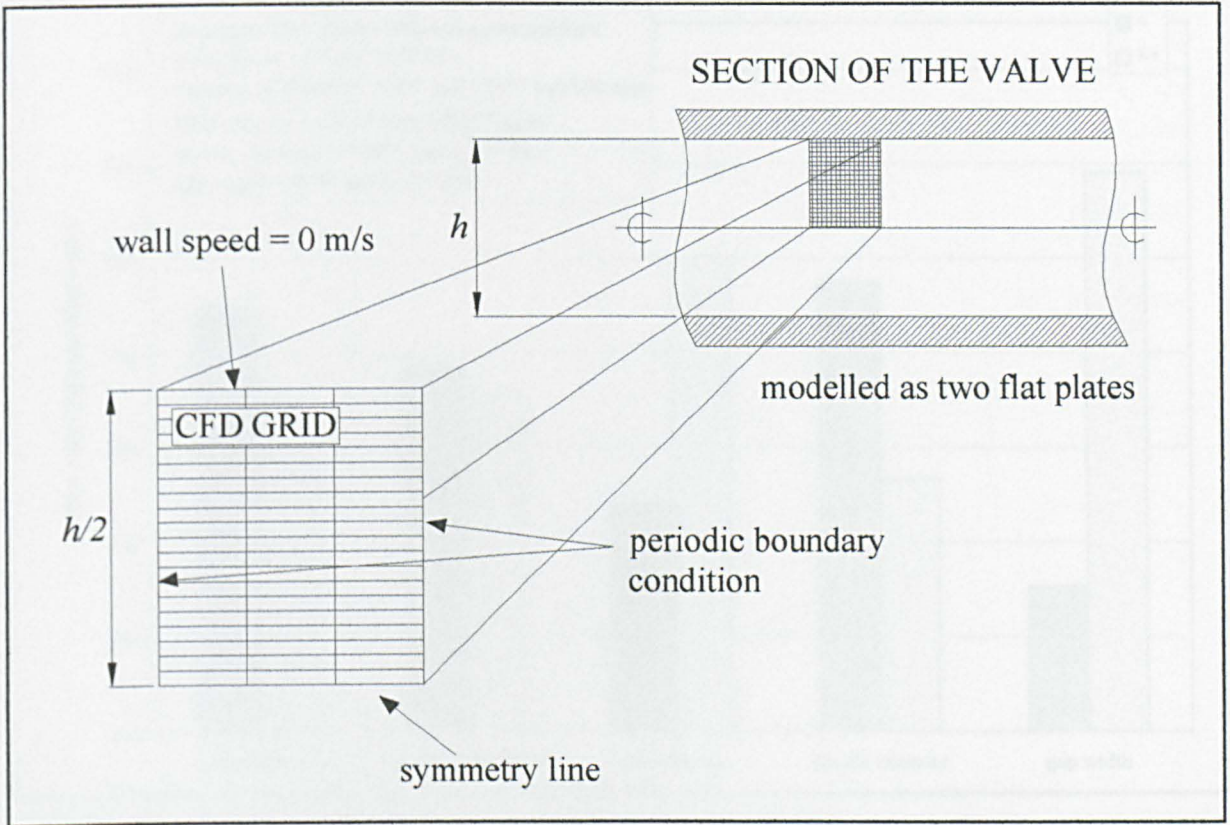


Fig. 5.3: Illustration of annular valve model.

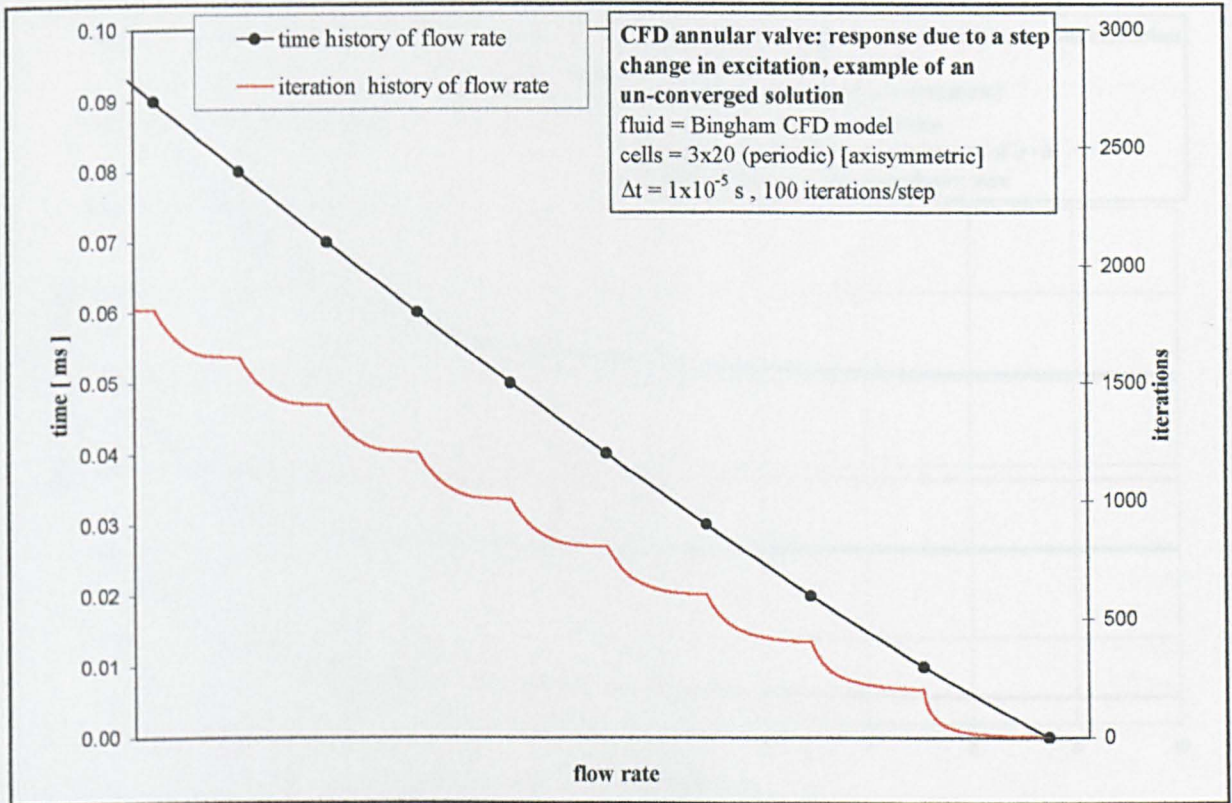


Fig. 5.4: CFD annular valve in unsteady flow: Example of an un-converged solution. Flow rate is decreasing from left to right with time due to a step change in excitation. The recording of flow-rate/iteration clearly shows that convergence is not being fully reached for each time-step.

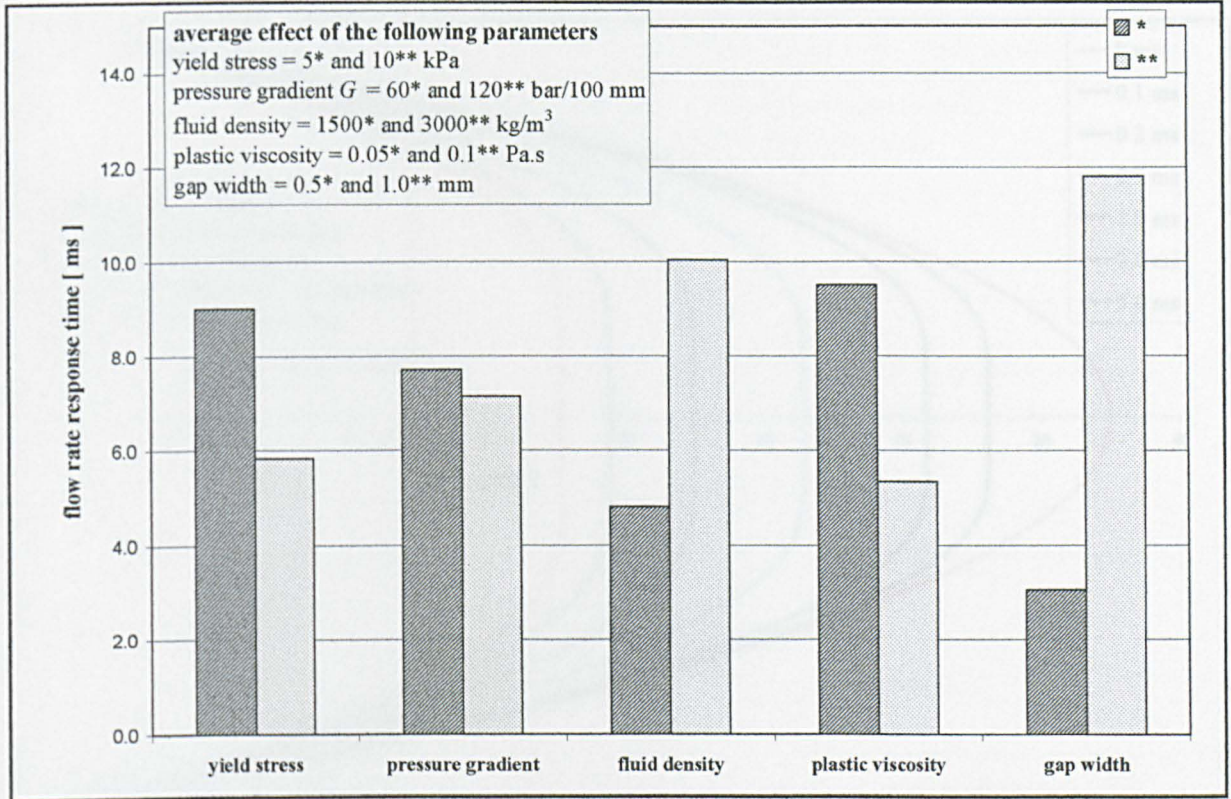


Fig. 5.5: CFD annular valve response due to an instantaneous excitation using the Bingham CFD model ($t < 0$ s, $E = 0$ kV/mm). Tagucci analysis: average effect of each parameter on the response time (t_d).

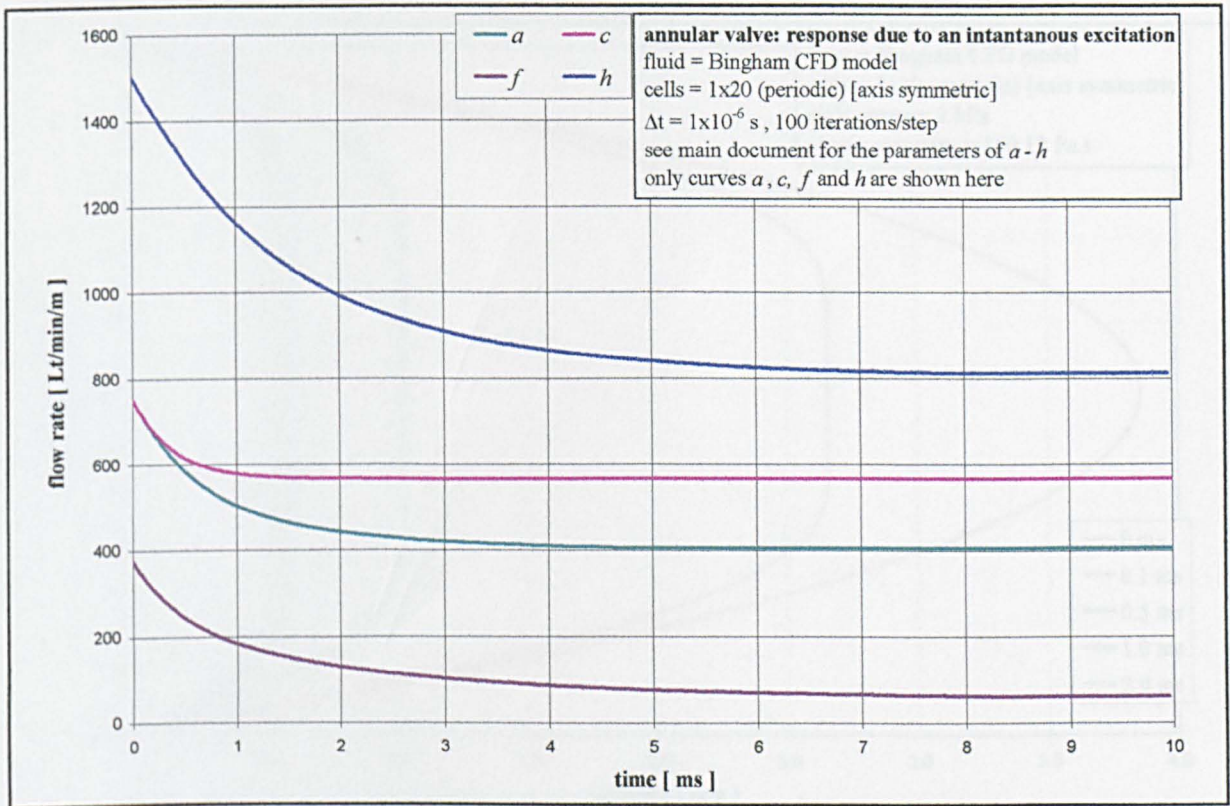


Fig. 5.6: CFD annular valve response due to an instantaneous excitation using the Bingham CFD model ($t < 0$ s, $E = 0$ kV/mm). Tagucci analysis: see Table 5.2 for all parameters. The range of flow is too large to fit all the curves onto one graph. However, the general shape is the same for all curves.

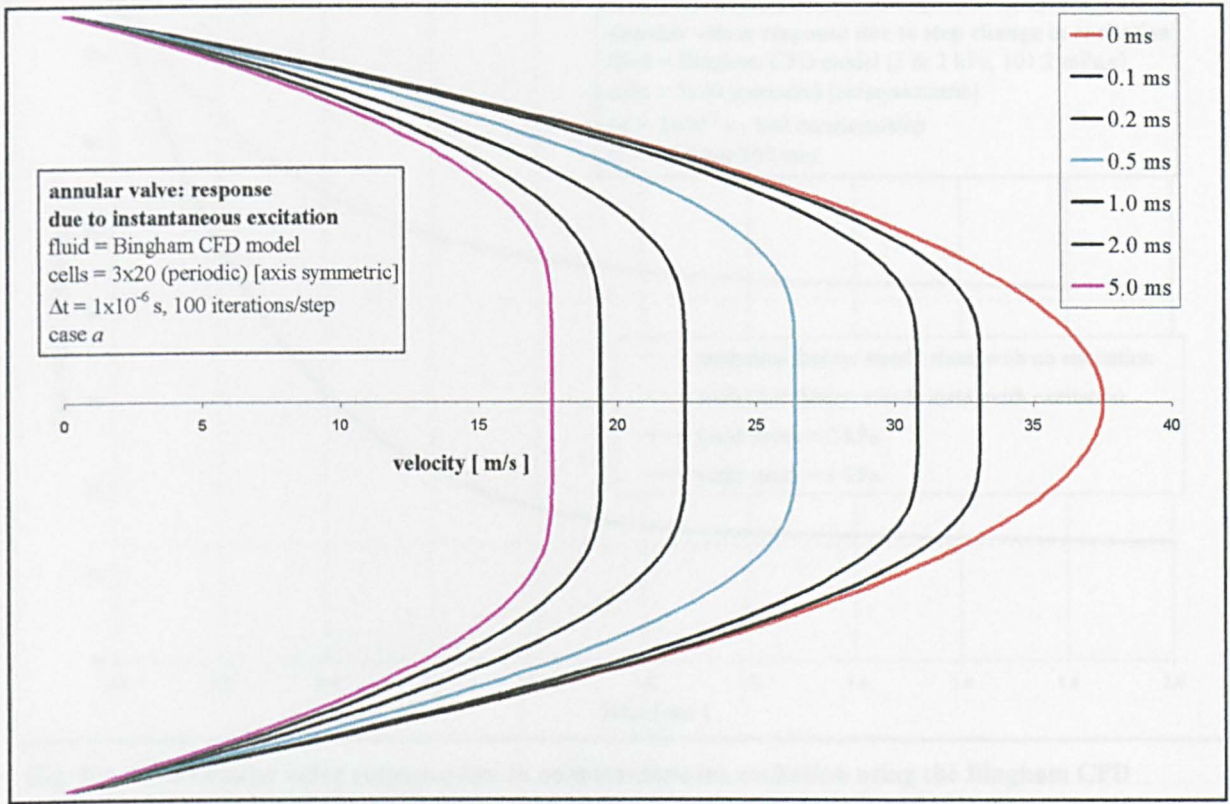


Fig. 5.7: CFD annular valve response due to an instantaneous excitation using the Bingham CFD model. Tagucci analysis: velocity profile case a (See Table 5.2 for all parameters).

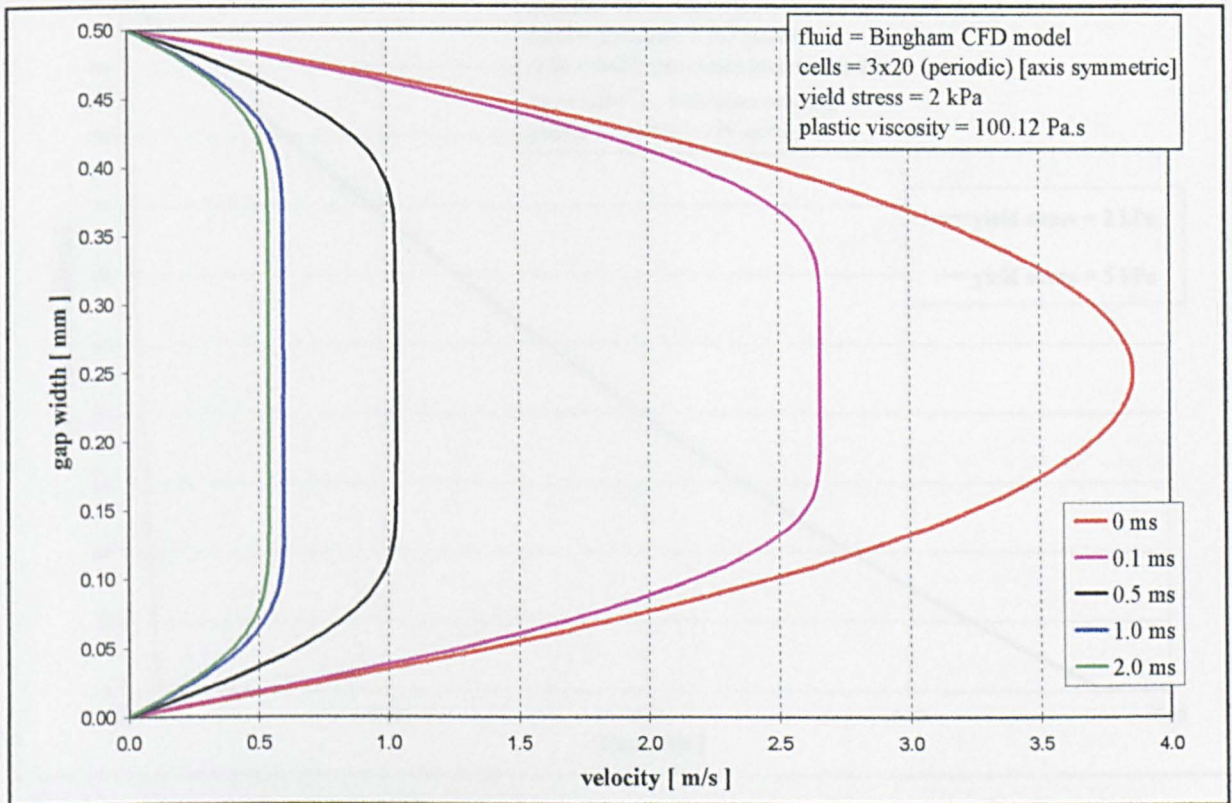


Fig. 5.8: CFD annular valve response due to an instantaneous excitation using the Bingham CFD model. Parameters used to match those used in [37] and [53].

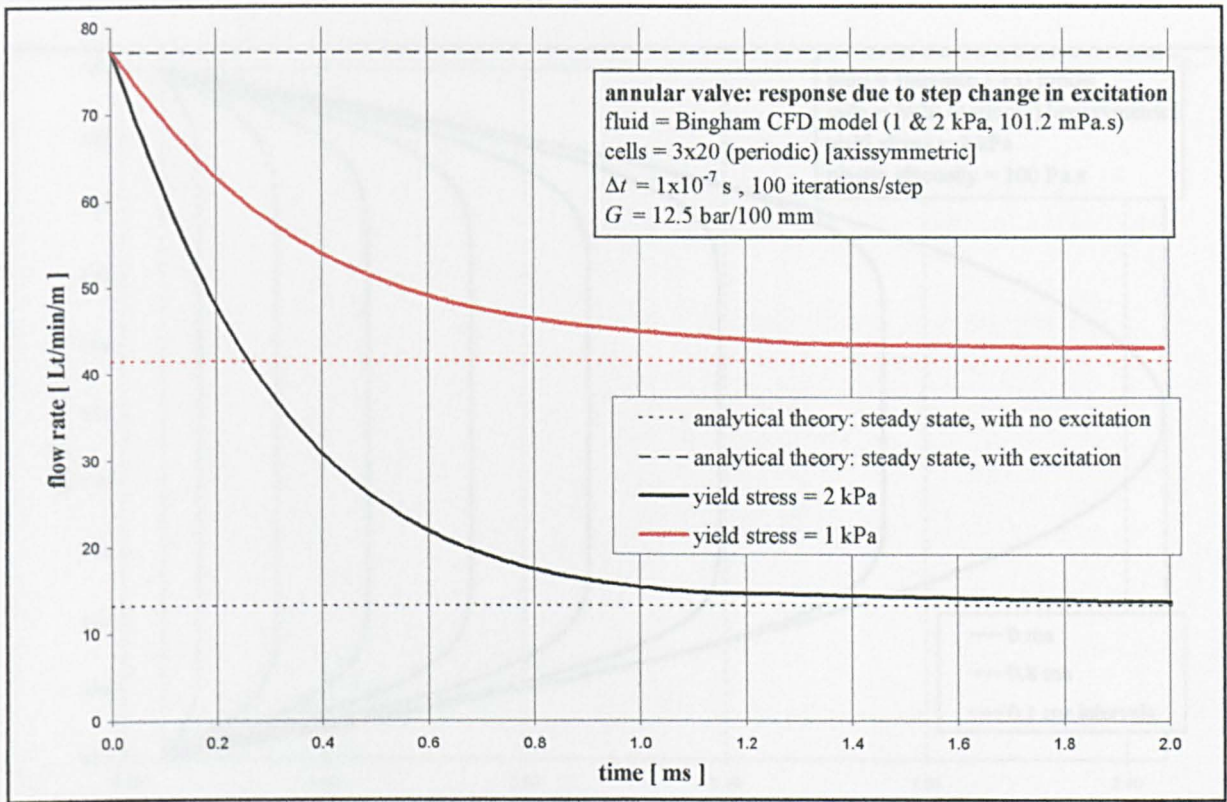


Fig. 5.9: CFD annular valve response due to an instantaneous excitation using the Bingham CFD model. Parameters for the 2 kPa fluid are used to match those used in [37] and [53]. Here the yield-stress is reduced and the flow rate response is seen to be slower.

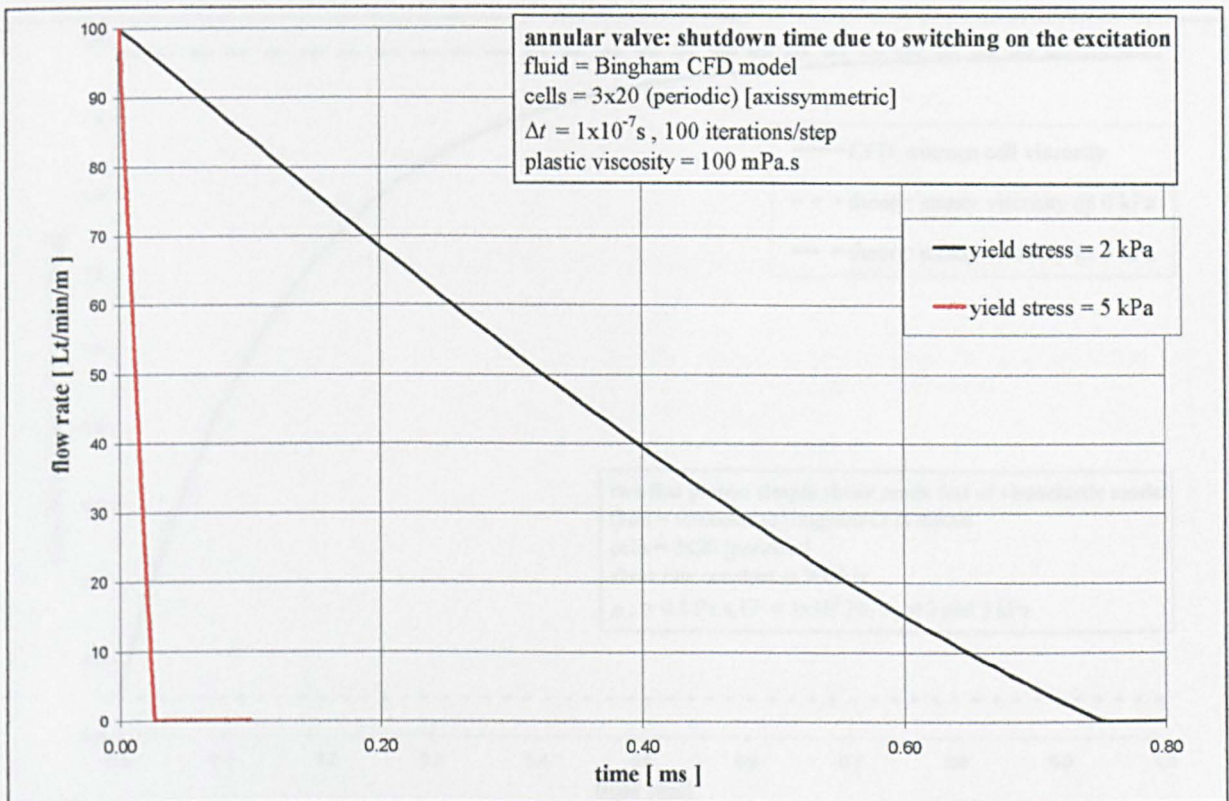


Fig. 5.10: CFD annular valve response due to an instantaneous excitation using the Bingham CFD model. Here the flow rate is being reduced to zero. Velocity profiles for the 2 kPa fluid are shown in Fig. 5.11.

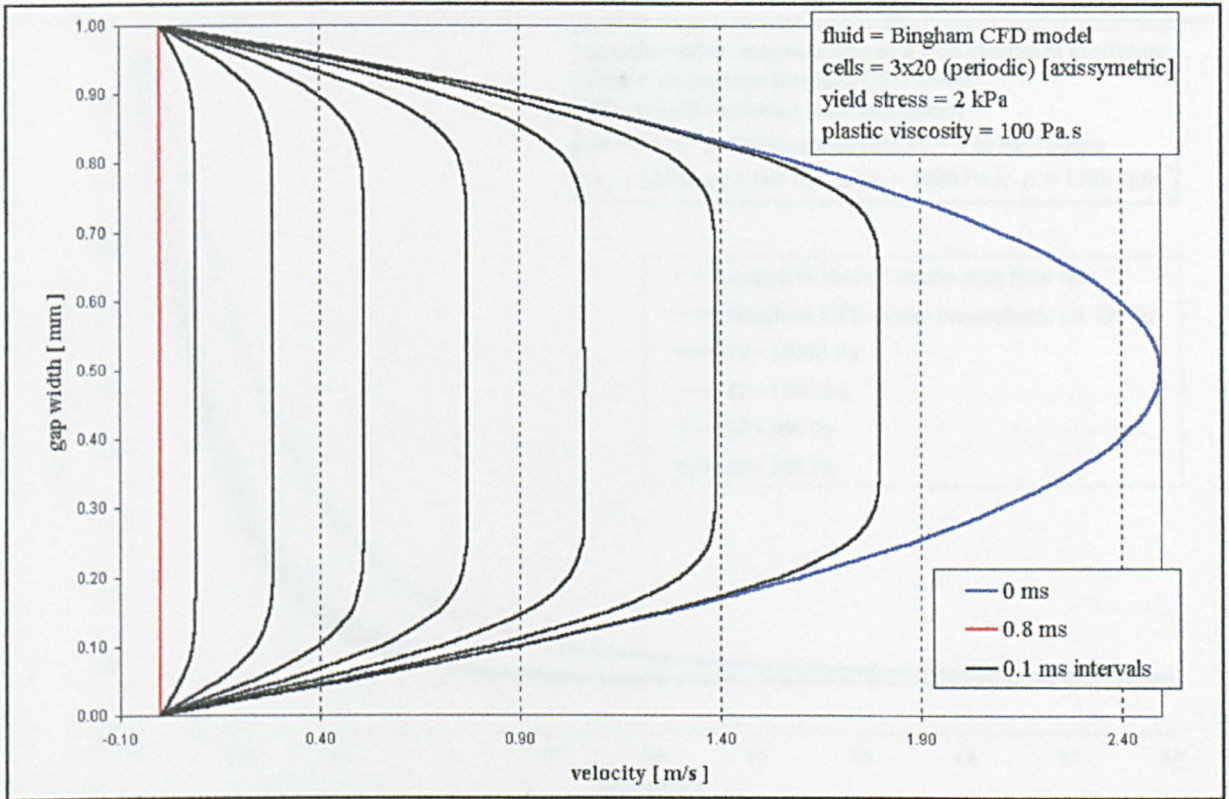


Fig. 5.11: CFD annular valve response due to an instantaneous excitation using the Bingham CFD model. Here the flow rate is being reduced to zero.

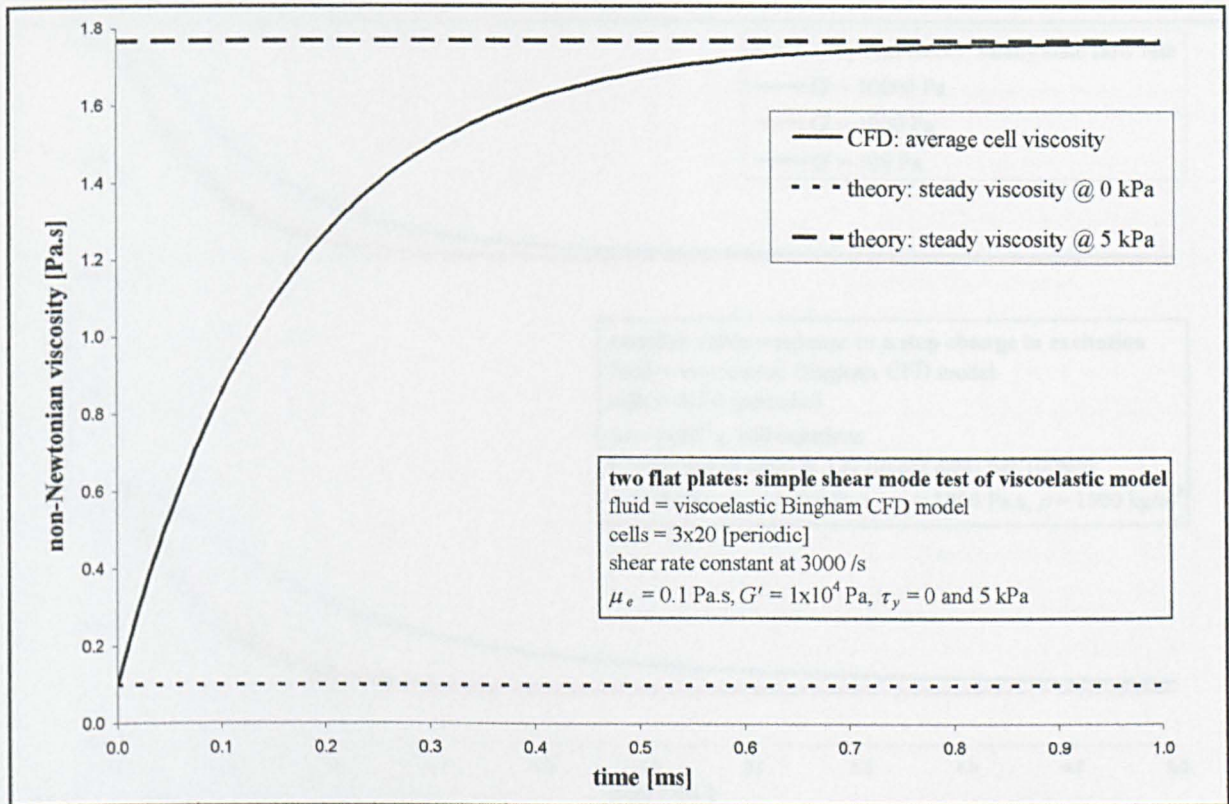


Fig. 5.12: Simple shear mode test of viscoelastic Bingham CFD model {eqn(5.2)}. Flow between two flat plates with a step change in excitation at $t = 0$ s. Here the yield-stress and thus non-Newtonian viscosity change is no longer instantaneous.

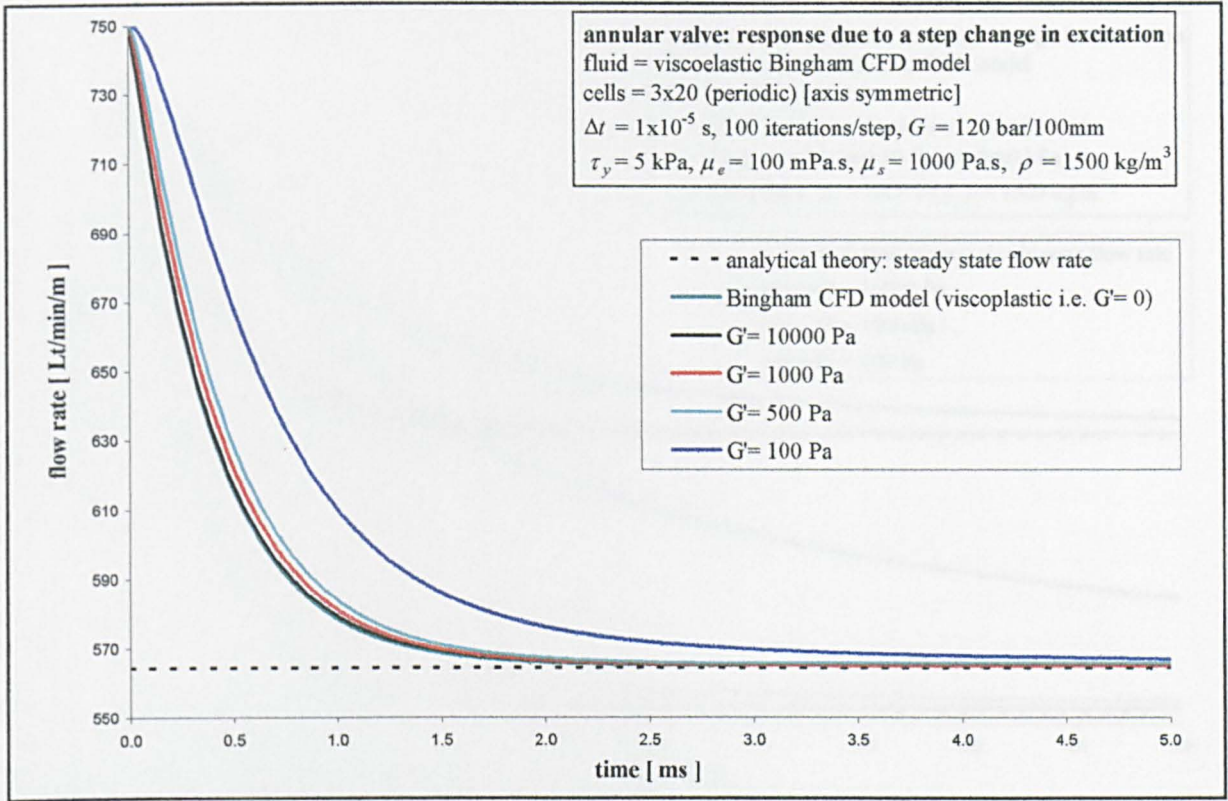


Fig. 5.13: CFD annular valve response due to an instantaneous excitation using the viscoelastic Bingham CFD model. Here it is only when G' is low that any real difference can be seen.

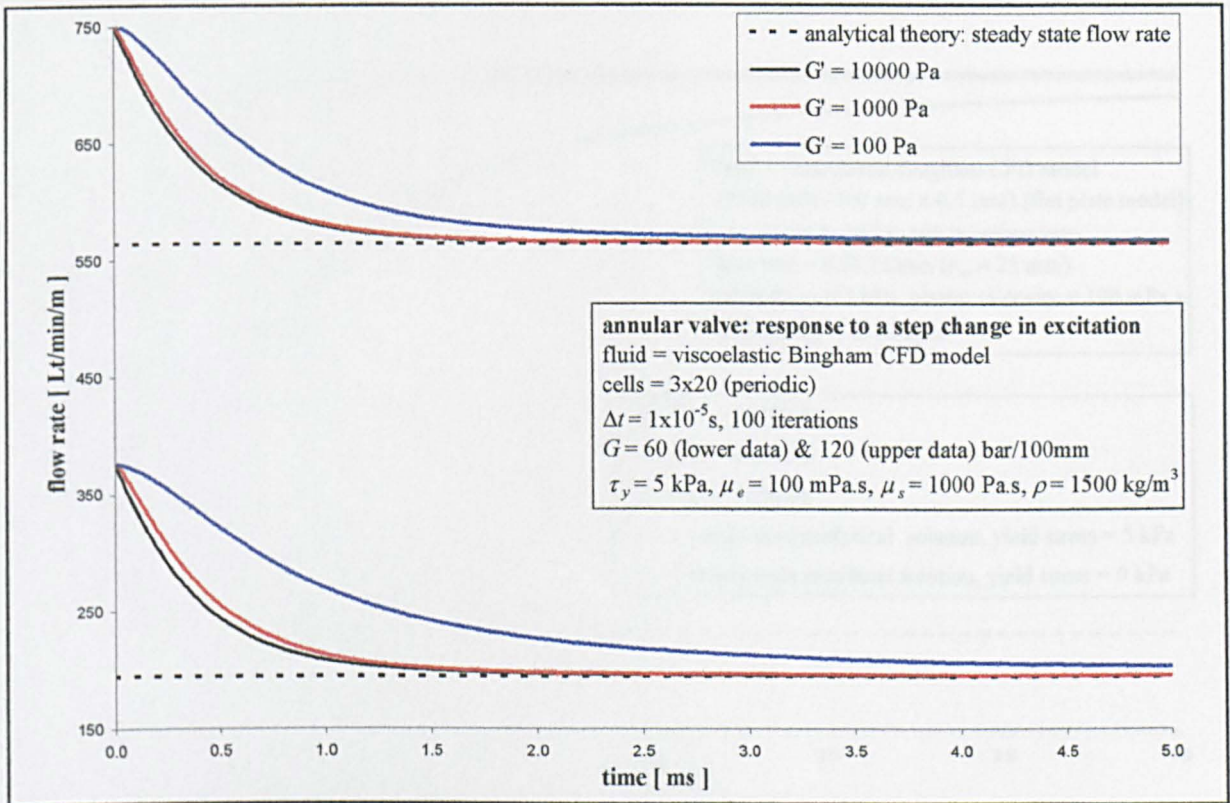


Fig. 5.14: CFD annular valve response due to an instantaneous excitation using the viscoelastic Bingham CFD model. Here the effect of pressure gradient and hence shear rate are investigated.

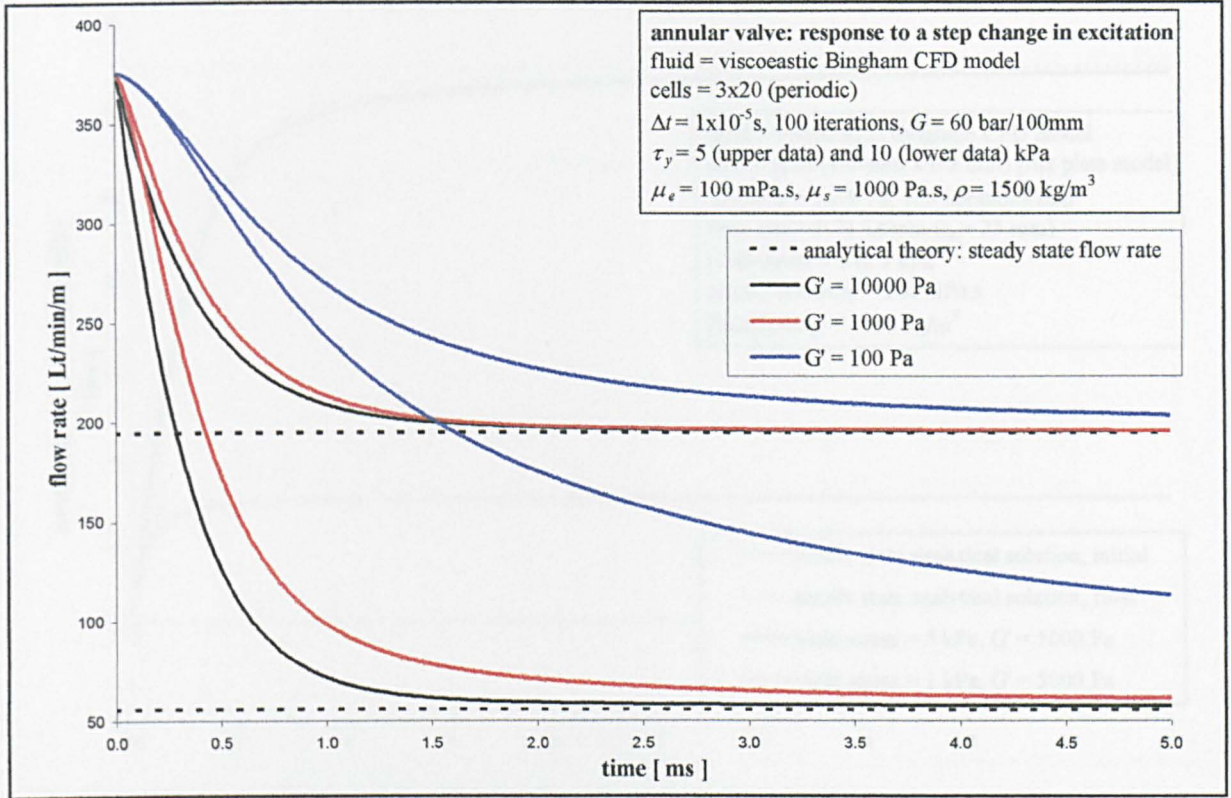


Fig. 5.15: CFD annular valve response due to an instantaneous excitation using the viscoelastic Bingham CFD model. Here the effect of yield-stress is investigated.

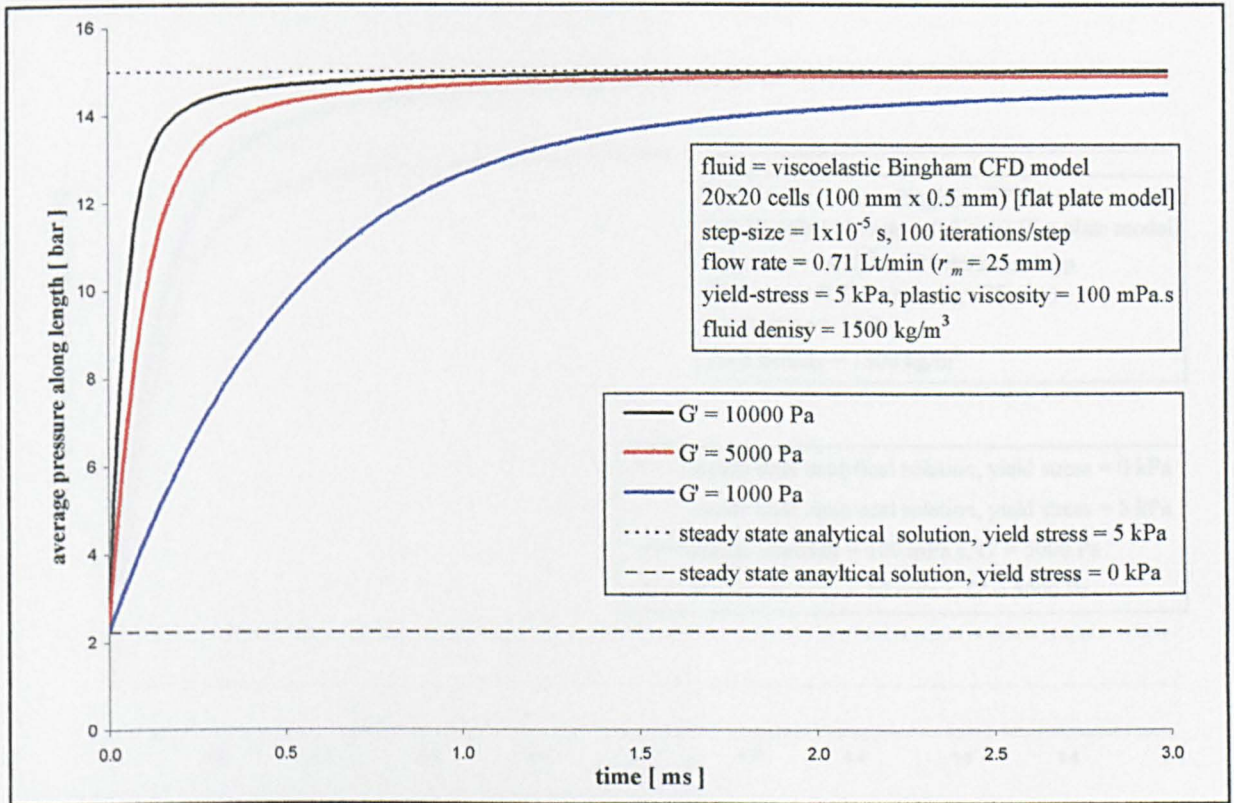


Fig. 5.16: CFD annular valve pressure response due to an instantaneous excitation using the viscoelastic Bingham CFD model. Here the effect of G' is investigated.

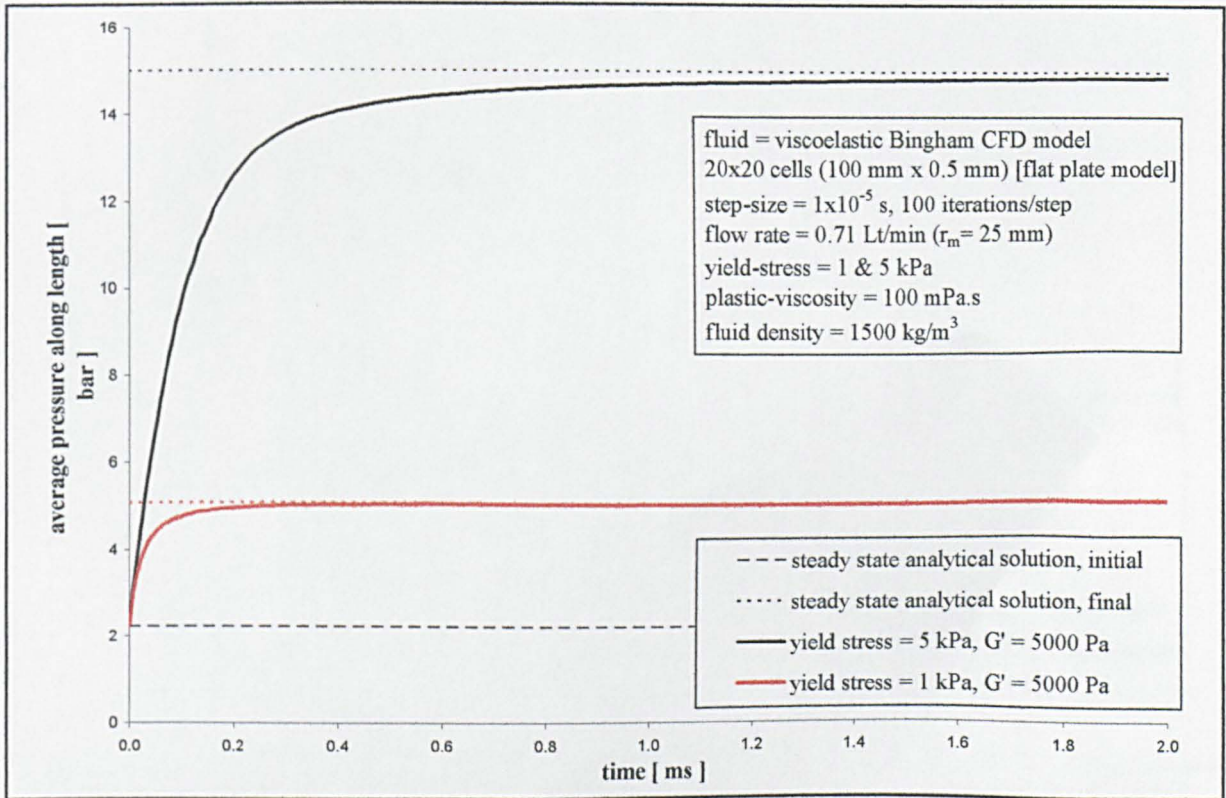


Fig. 5.17: CFD annular valve pressure response due to an instantaneous excitation using the viscoelastic Bingham CFD model. Here the effect of yield-stress is investigated.

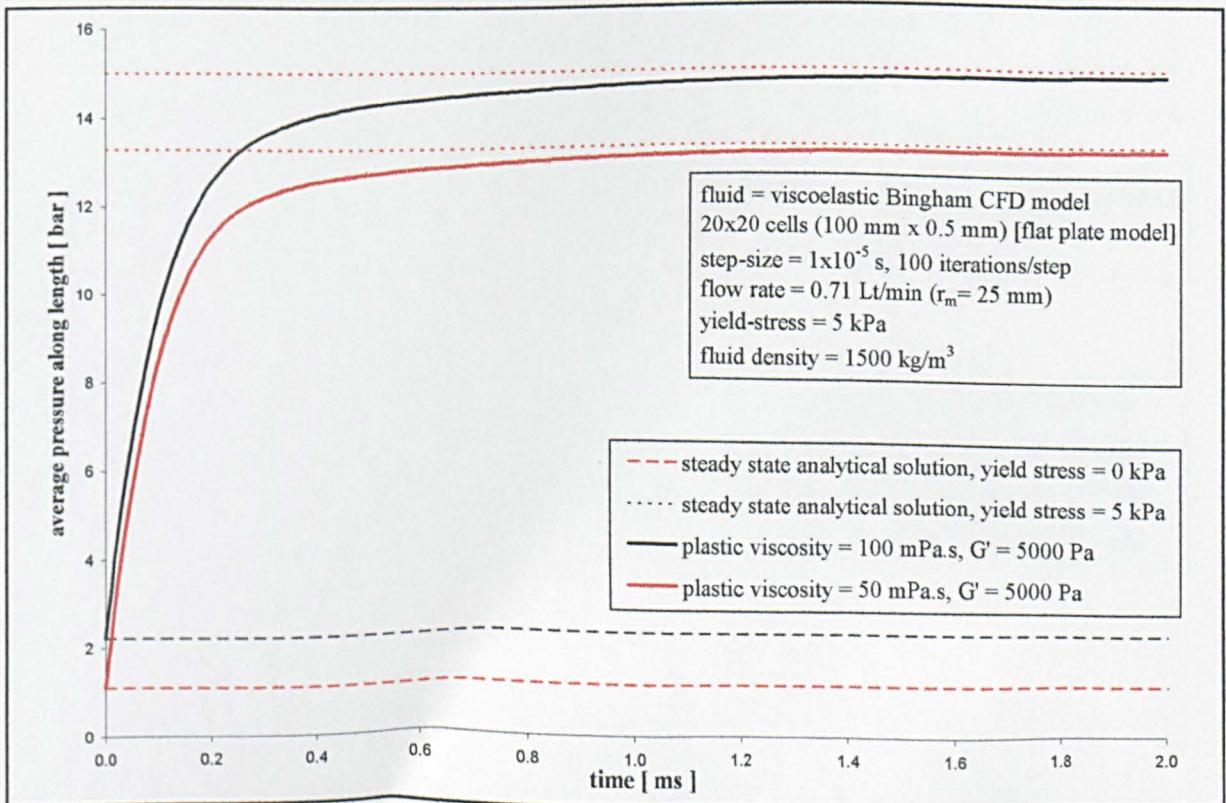


Fig. 5.18: CFD annular valve pressure response due to an instantaneous excitation using the viscoelastic Bingham CFD model. Here the effect of plastic-viscosity is investigated.

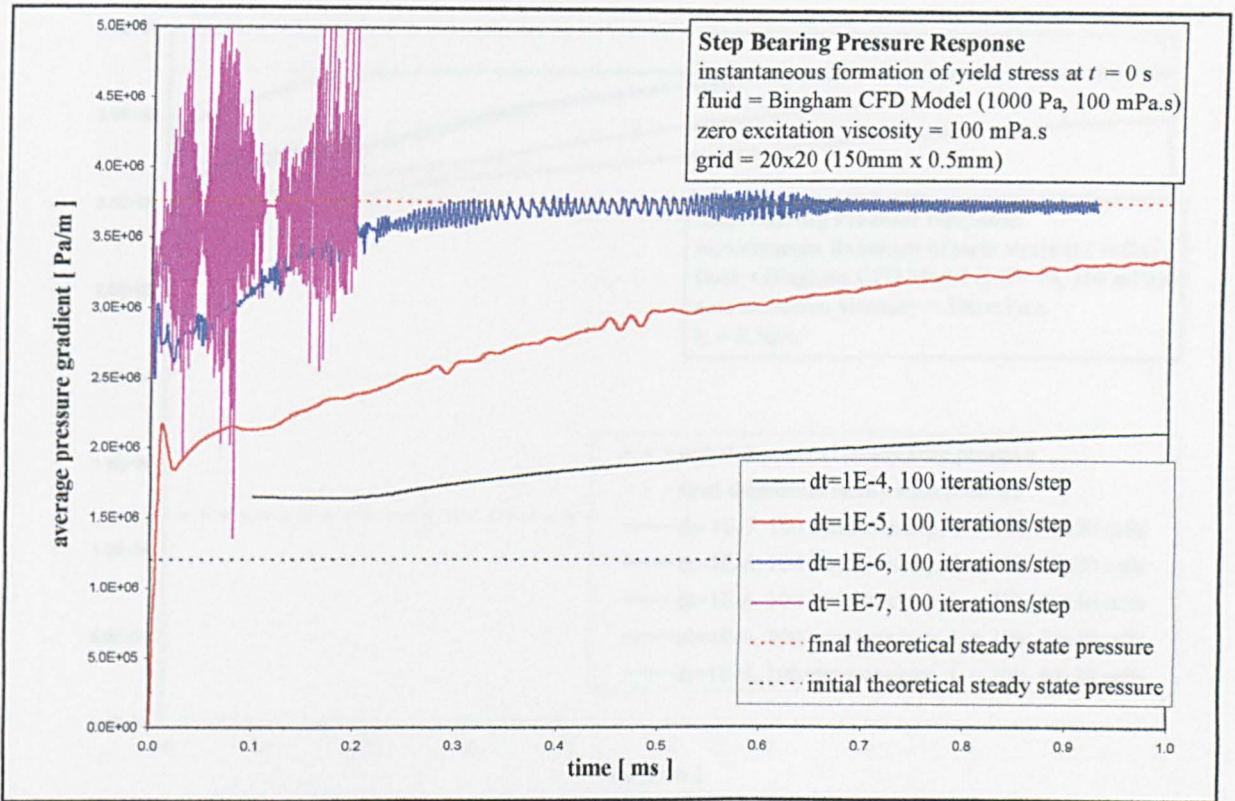


Fig. 5.19: CFD smart fluid Rayleigh step bearing pressure response due to an instantaneous formation in yield-stress. The bearing length and cell aspect ratio are large. Here the result is time-step size dependent and so the solution is not reliable.

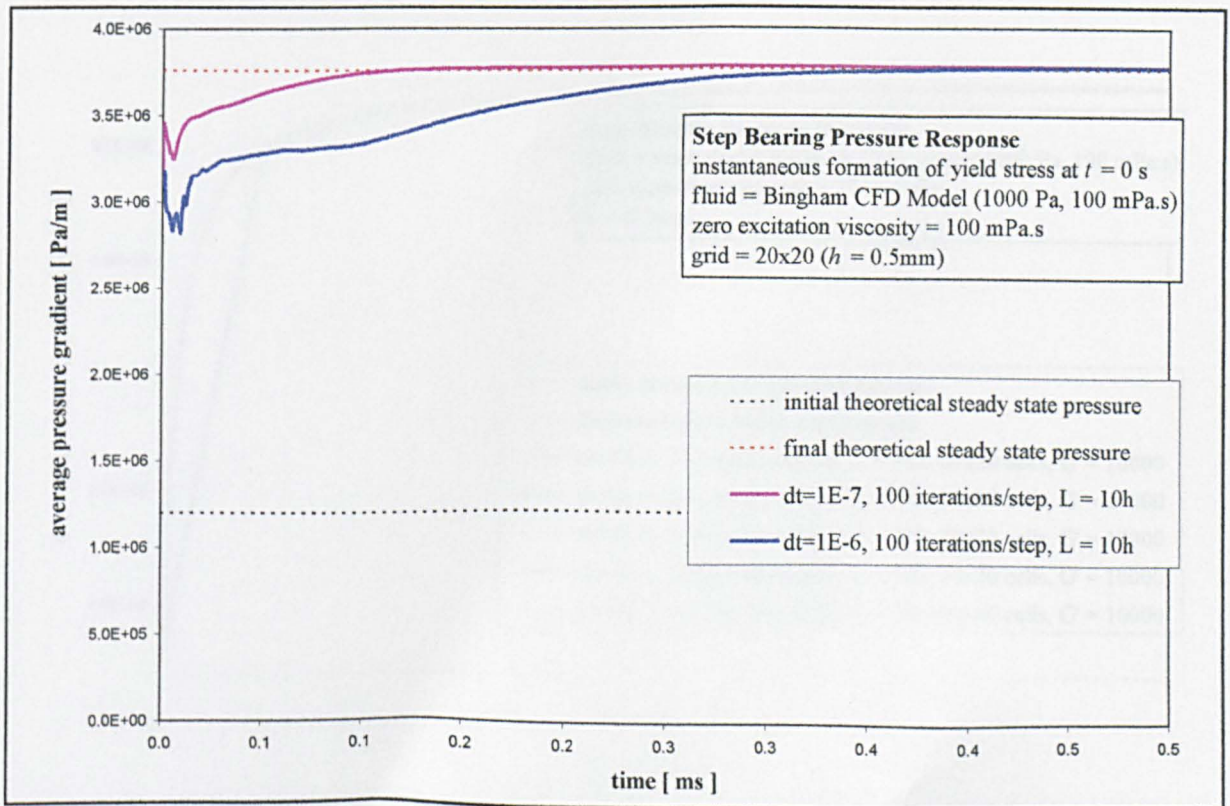


Fig. 5.20: CFD smart fluid Rayleigh step bearing pressure response due to an instantaneous formation in yield-stress. The bearing length and cell aspect ratio are large. Here the solution has been improved by using a smaller cell aspect ratio ($L = 10h$).

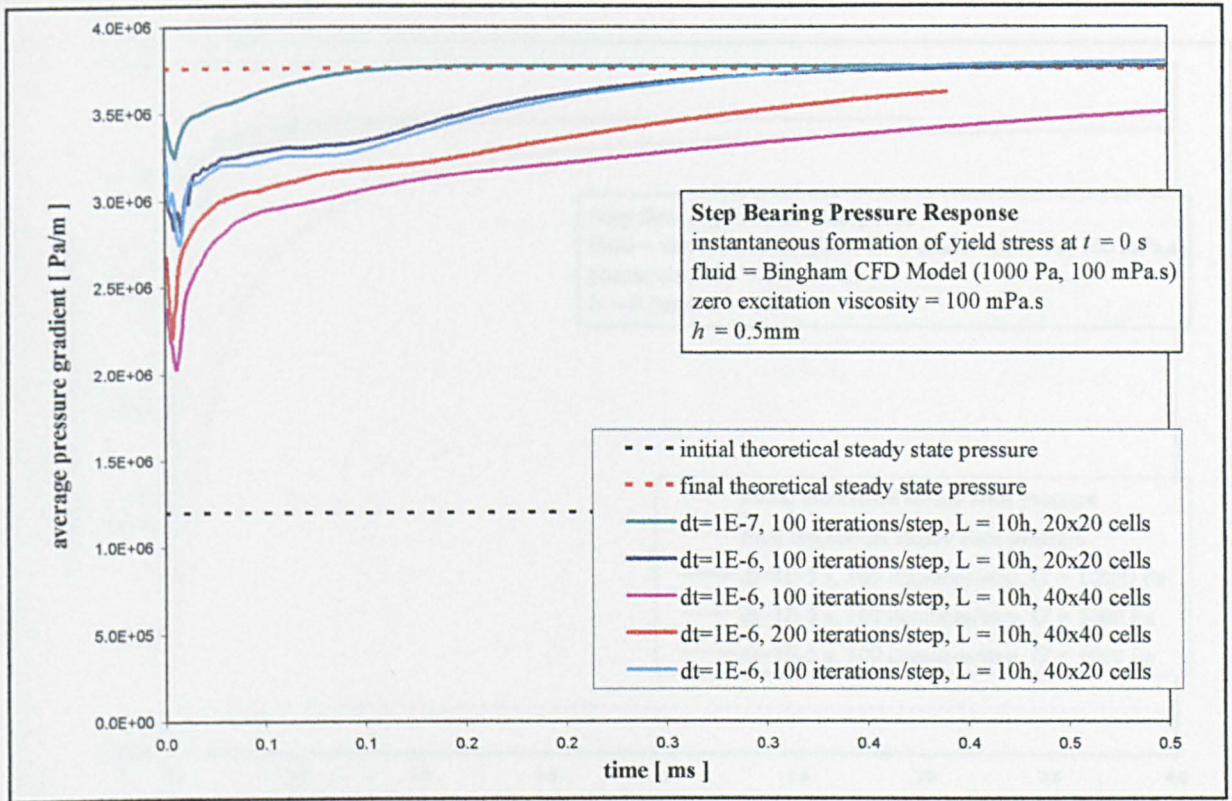


Fig. 5.21: CFD smart fluid Rayleigh step bearing pressure response due to an instantaneous formation in yield-stress. The bearing length and cell aspect ratio are large. Here the effect that the time-step and grid size have on the solution is investigated.

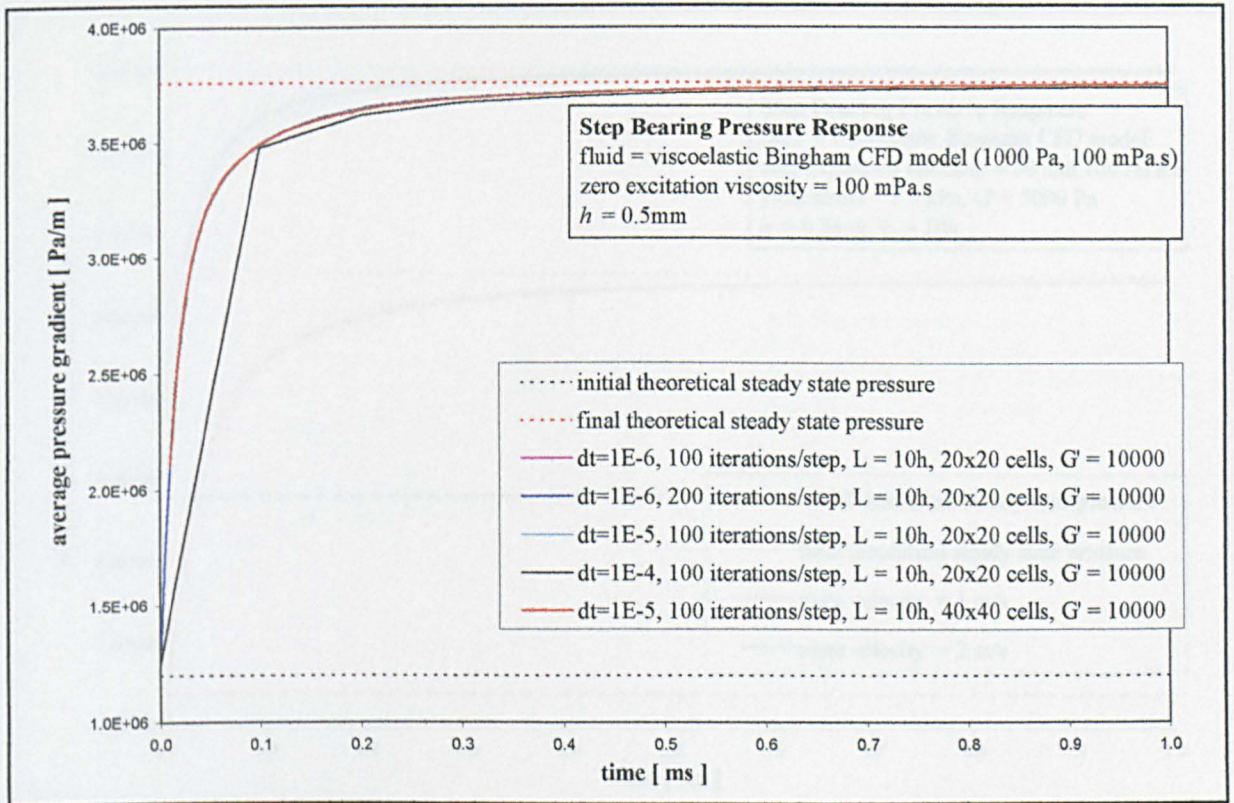


Fig. 5.22: CFD smart fluid Rayleigh step bearing pressure response due to change in yield-stress using the viscoelastic model. Here the effect that the time-step and grid size have on the solution is investigated. All the simulations above a time-step size of 0.1 ms are overlapping one another.

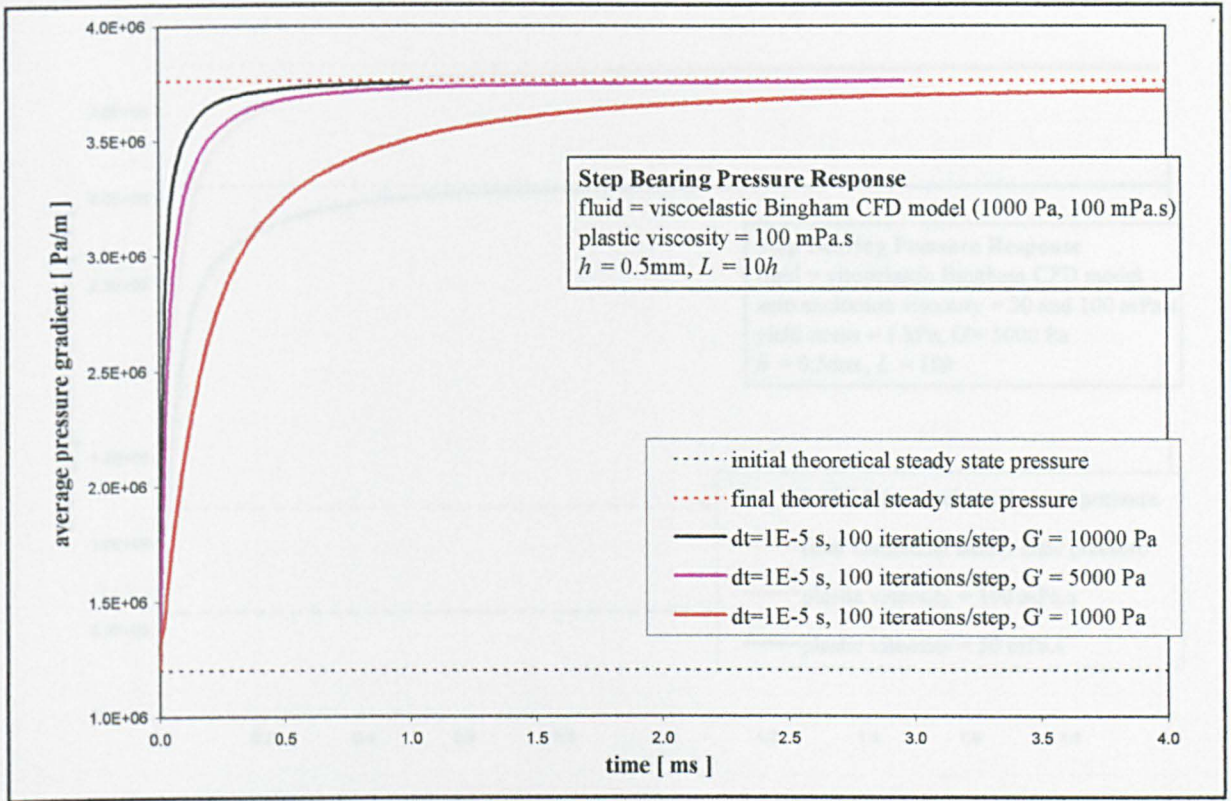


Fig. 5.23: CFD smart fluid Rayleigh step bearing pressure response due to change in yield-stress using the viscoelastic model. Here the effect that G' has on the solution is investigated.

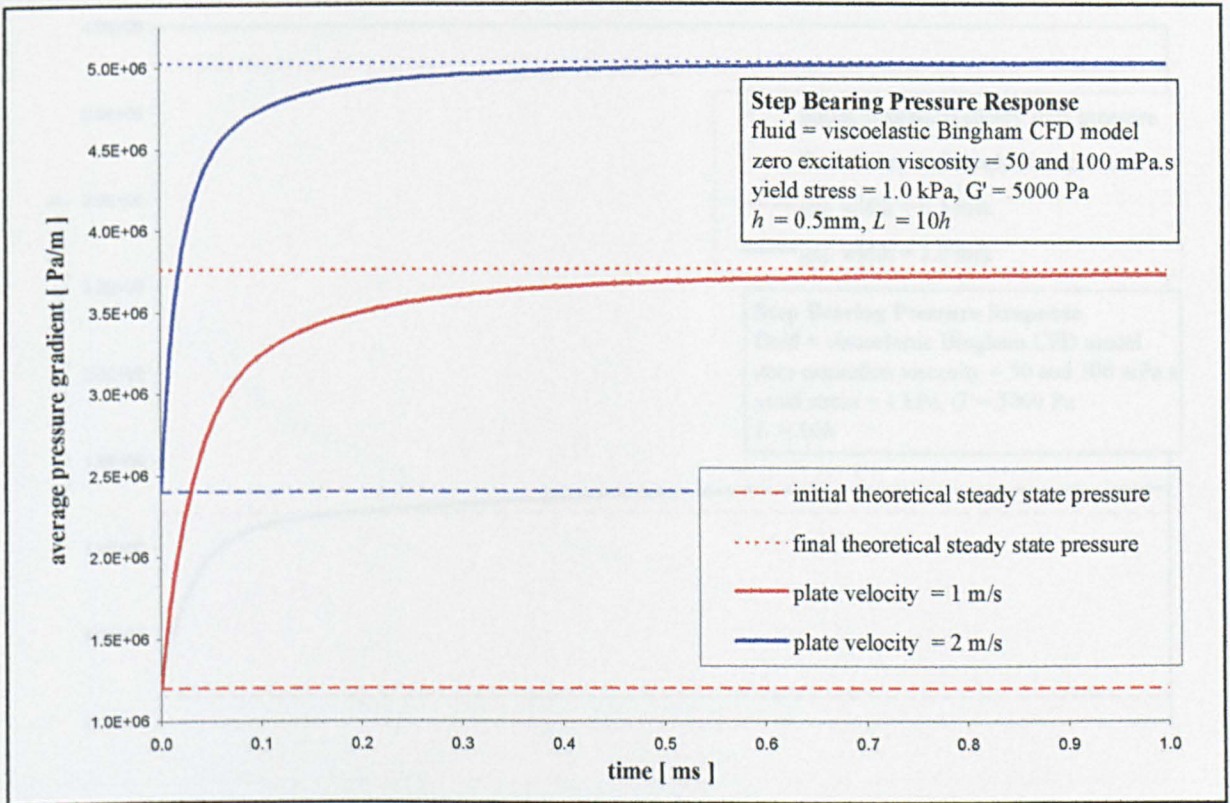


Fig. 5.24: CFD smart fluid Rayleigh step bearing pressure response due to change in yield-stress using the viscoelastic model. Here the effect that plate speed (U) has on the solution is investigated.

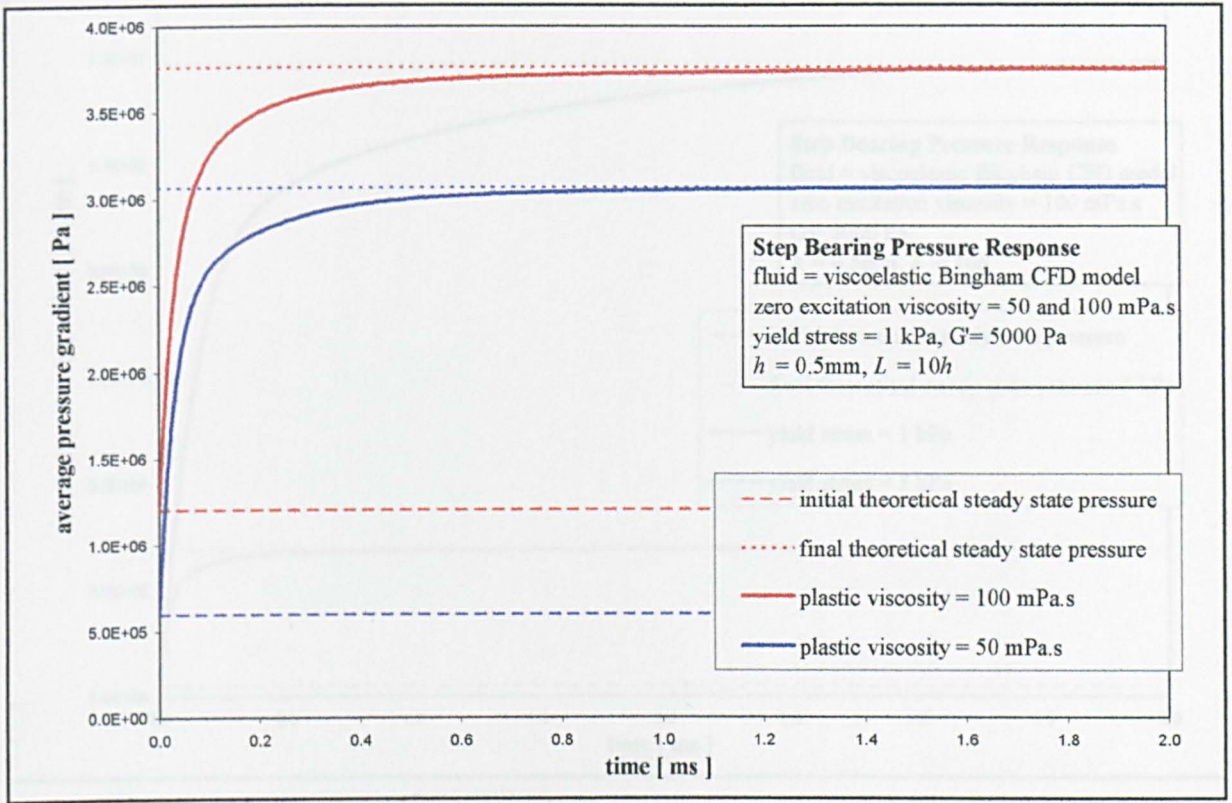


Fig. 5.25: CFD smart fluid Rayleigh step bearing pressure response due to change in yield-stress using the viscoelastic model. Here the effect that plastic-viscosity has on the solution is investigated.

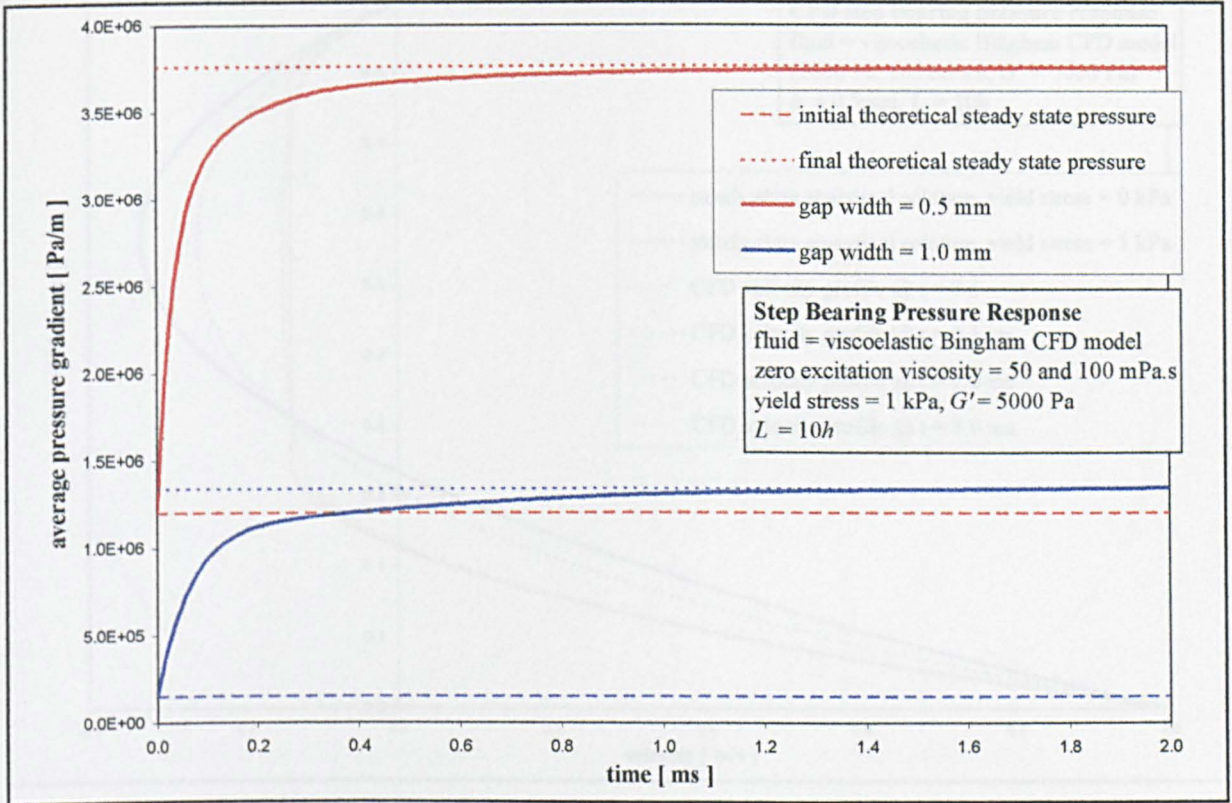


Fig. 5.26: CFD smart fluid Rayleigh step bearing pressure response due to change in yield-stress using the viscoelastic model. Here the effect that gap width (h) has on the solution is investigated.

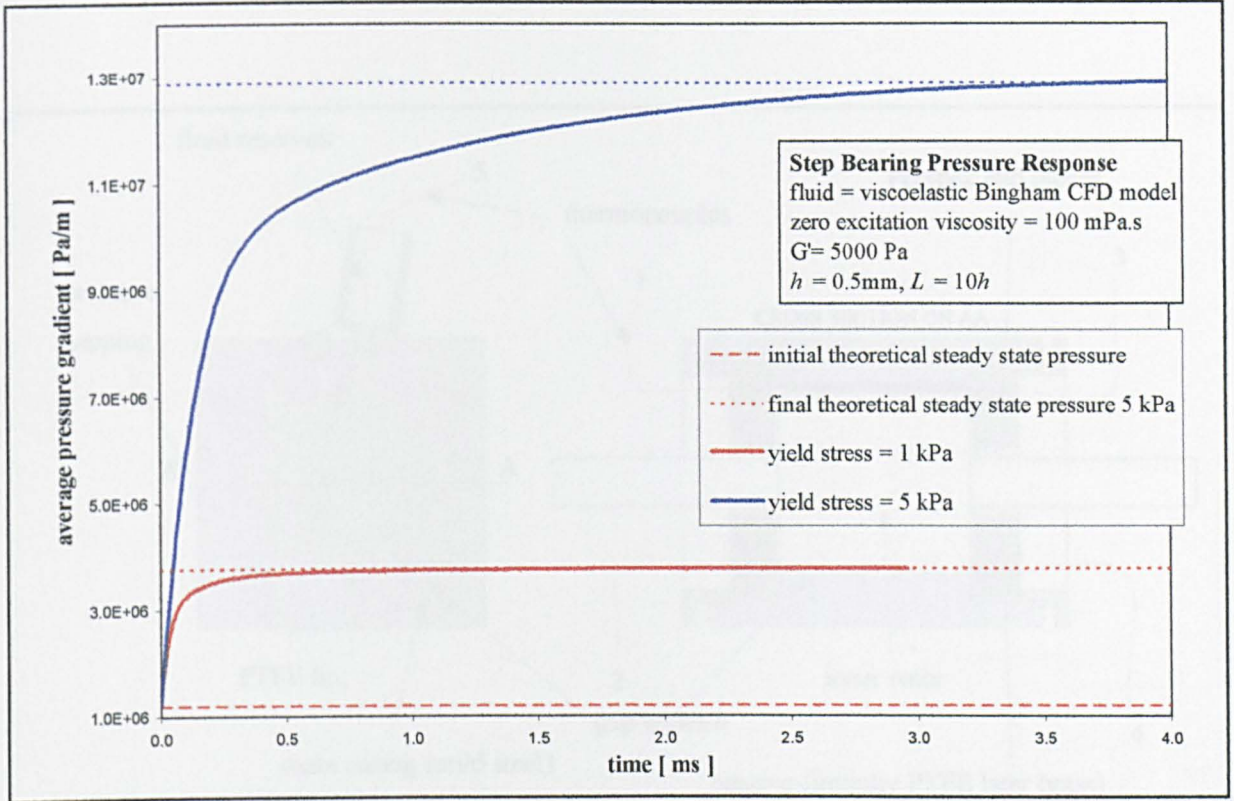


Fig. 5.27: CFD smart fluid Rayleigh step bearing pressure response due to change in yield-stress using the viscoelastic model. Here the effect that yield-stress has on the solution is investigated.

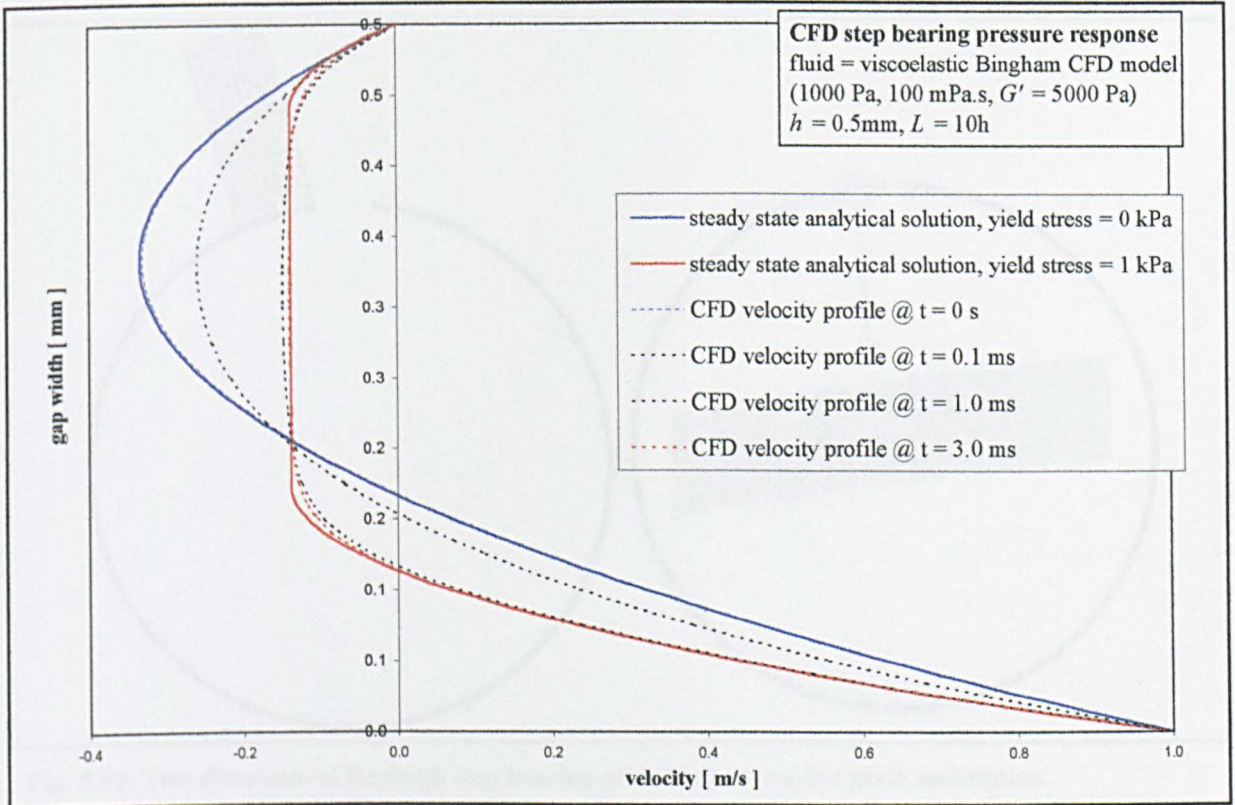


Fig. 5.28: CFD smart fluid Rayleigh step bearing pressure response due to change in yield-stress using the viscoelastic model. Example on how the velocity profile changes over time. Refer to Fig. 3.19 for model arrangement.

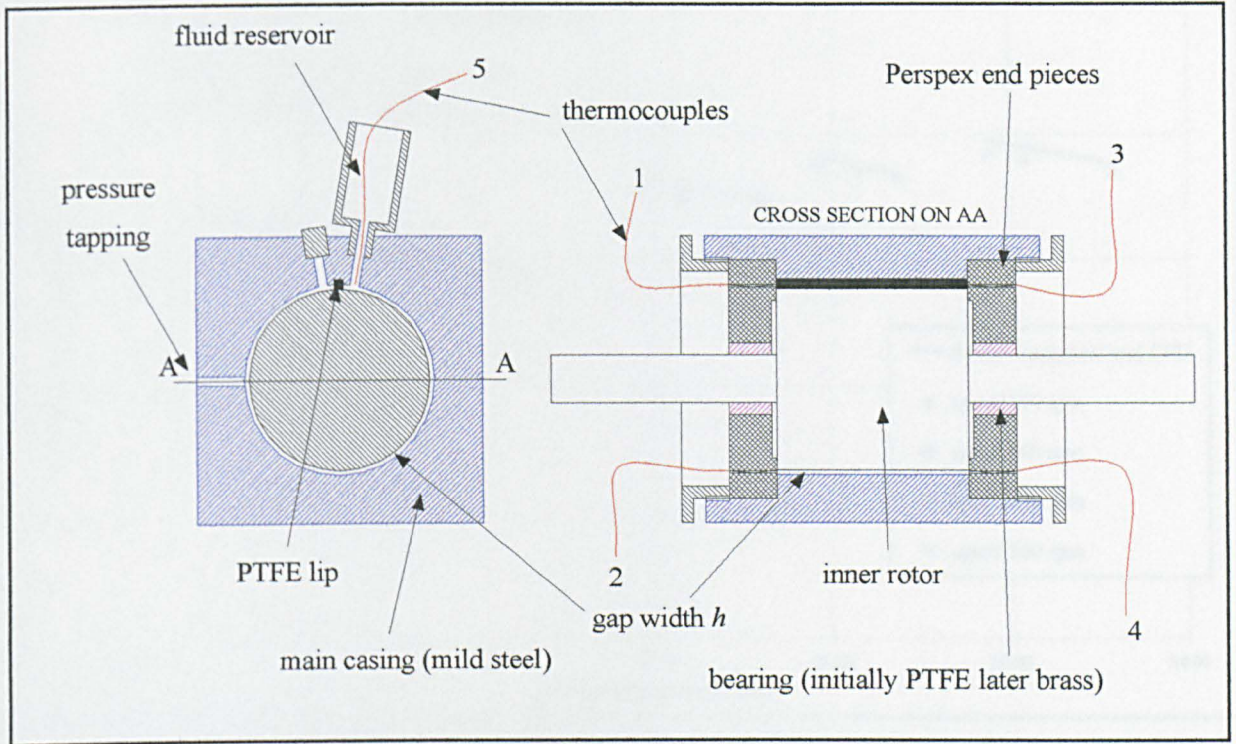


Fig. 5.29: Initial ER fluid Rayleigh step bearing. This is an adapted viscosity pump.

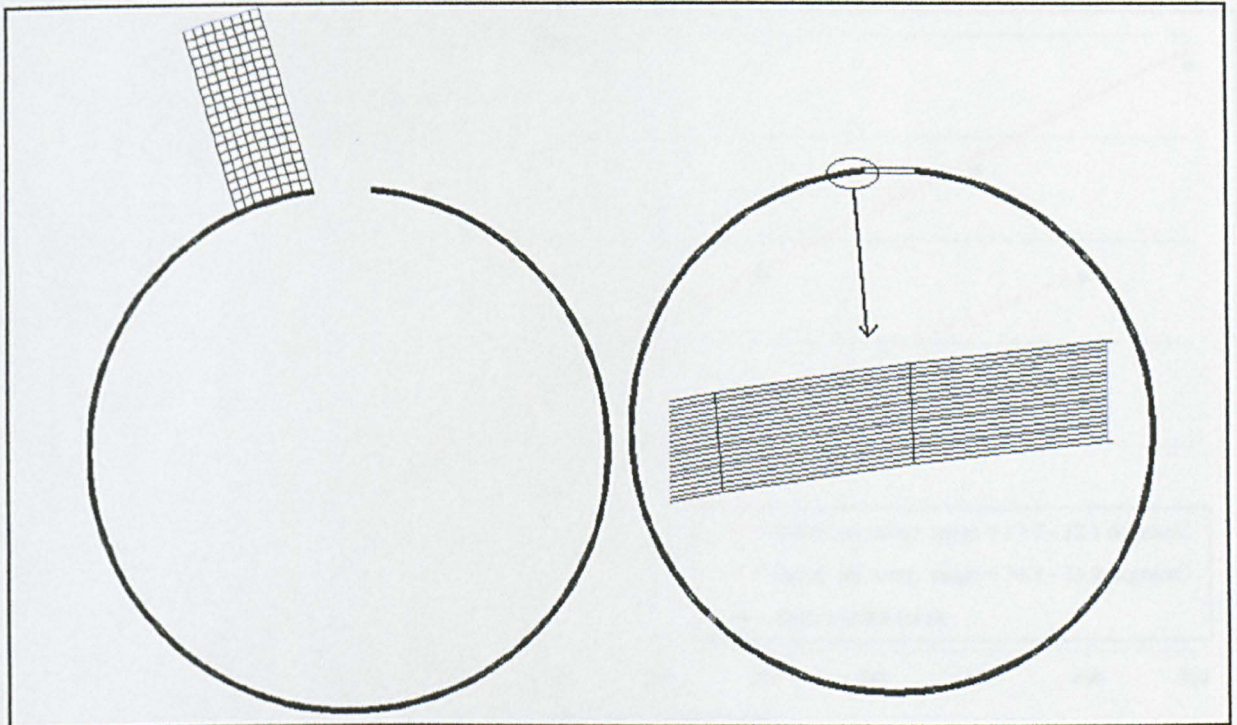


Fig. 5.30: Two-dimensional Rayleigh step bearing grids used to test flat plate assumption.

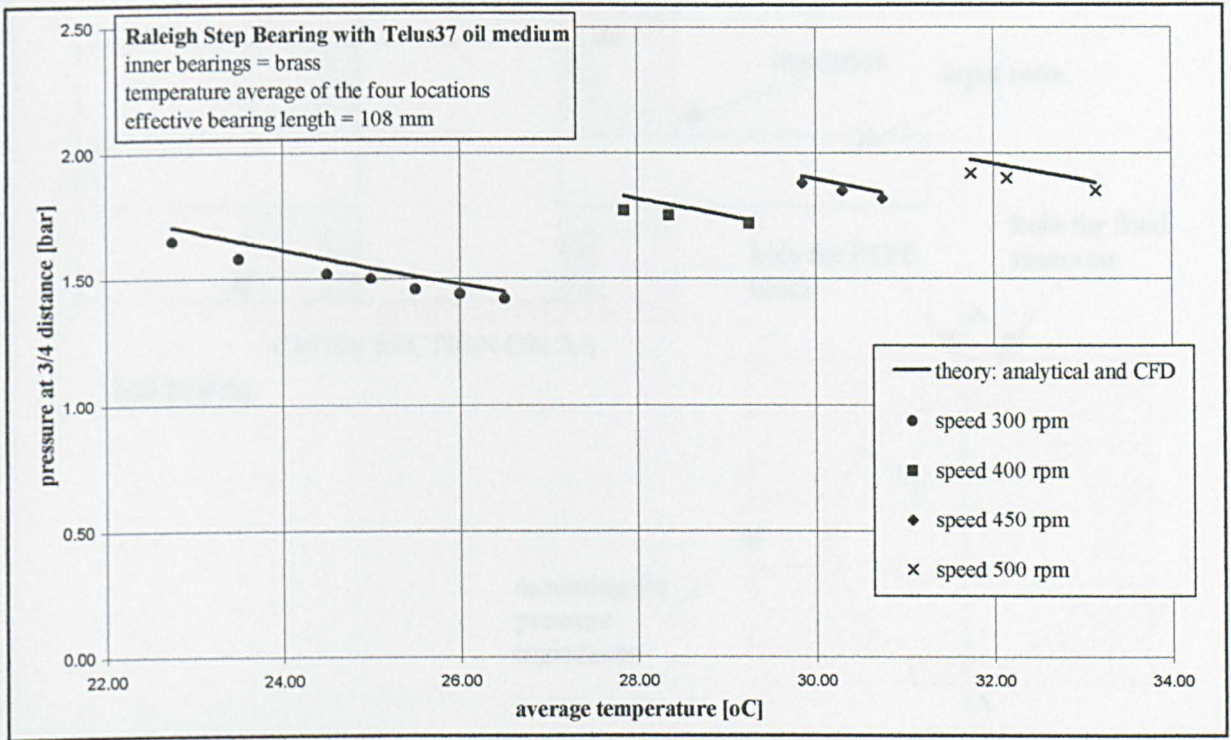


Fig. 5.31: Rayleigh step bearing with Tellus37 oil medium. Experiment vs. theory. Here the temperature was allowed to increase while the bearing speed remained constant.

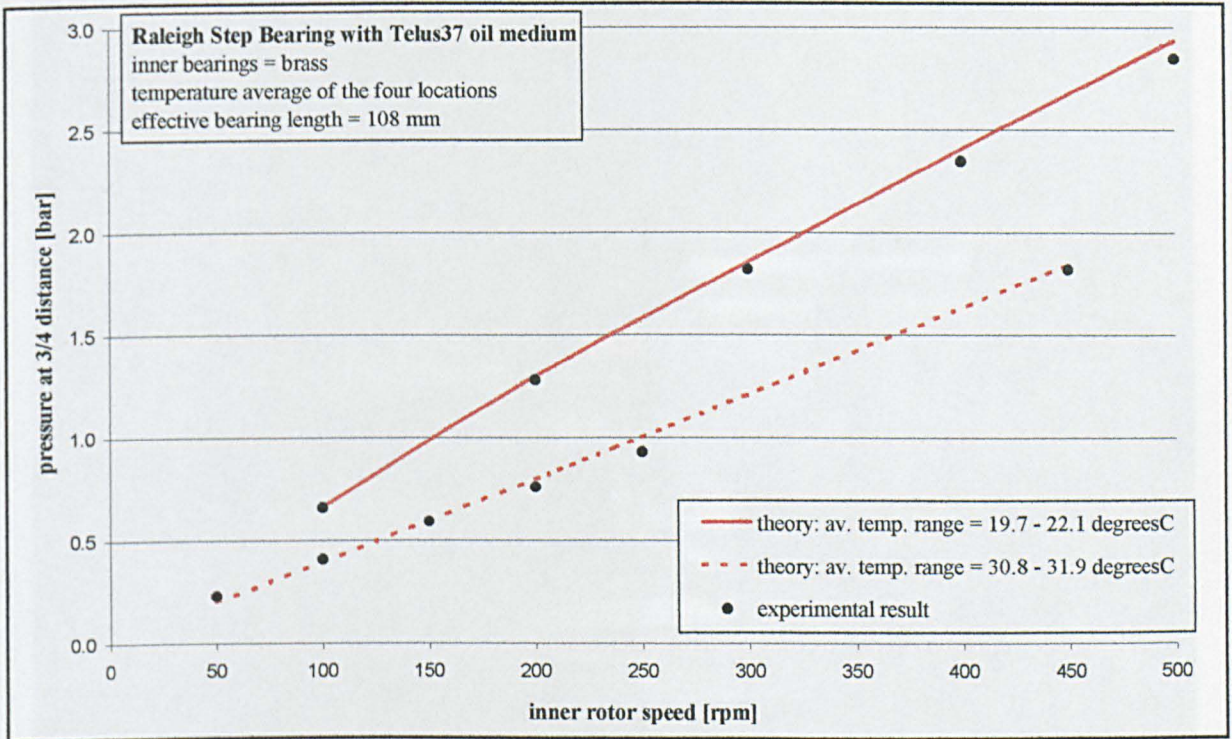


Fig. 5.32: Rayleigh step bearing with Tellus37 oil medium. Experiment vs. theory. Here results were taken for constant values of temperature.

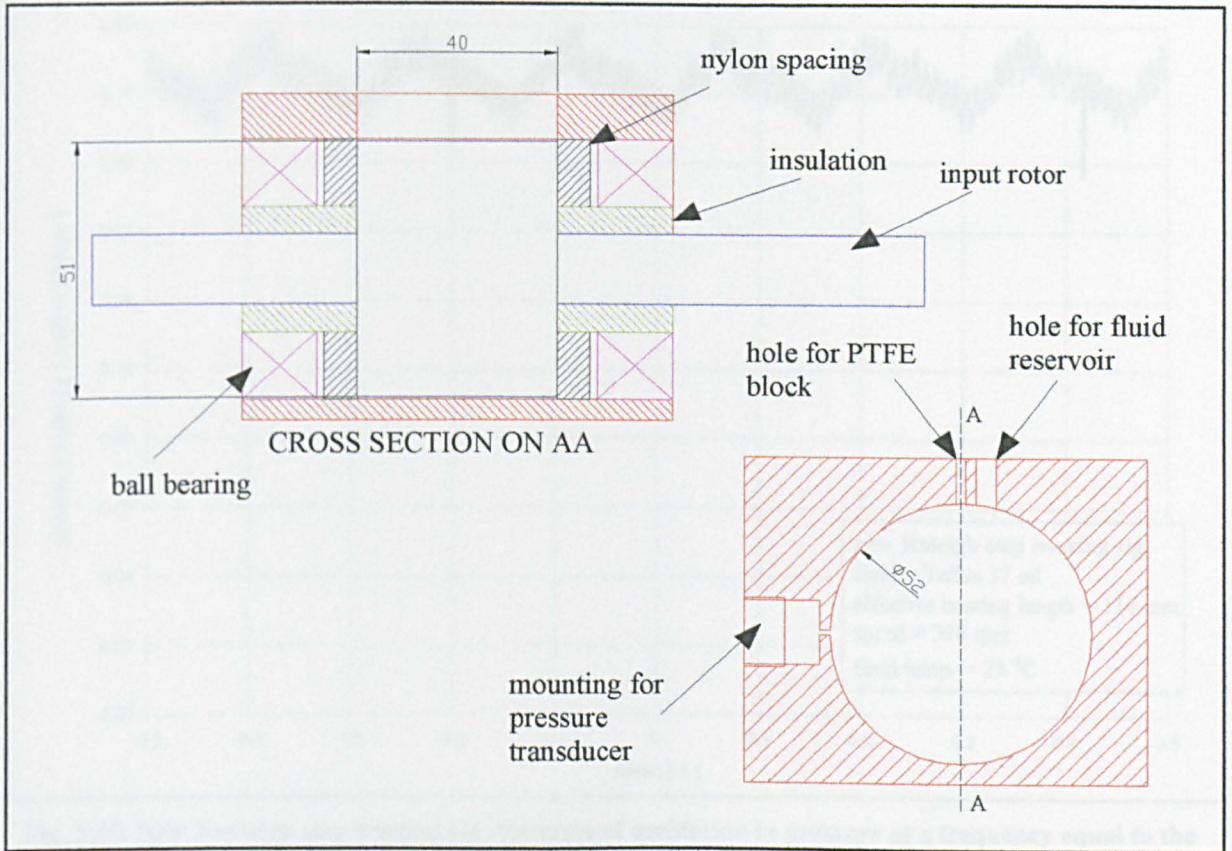


Fig. 5.33: Schematic of the new ER fluid Rayleigh step-bearing rig.



Fig. 5.34: Picture of new ER fluid Rayleigh step bearing rig.

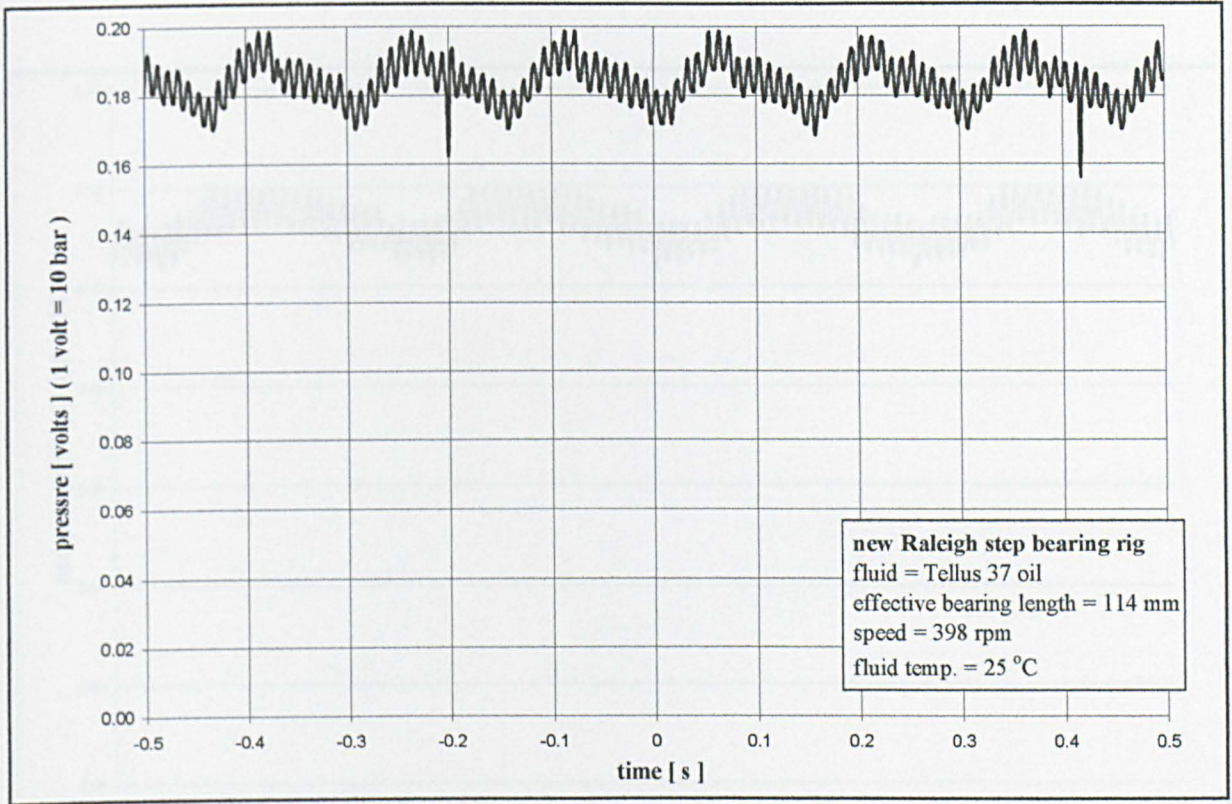


Fig. 5.35: New Rayleigh step bearing rig. Example of oscillation in pressure at a frequency equal to the input speed (398 rpm = 1 rev/ 0.15 s, 6.6 Hz).

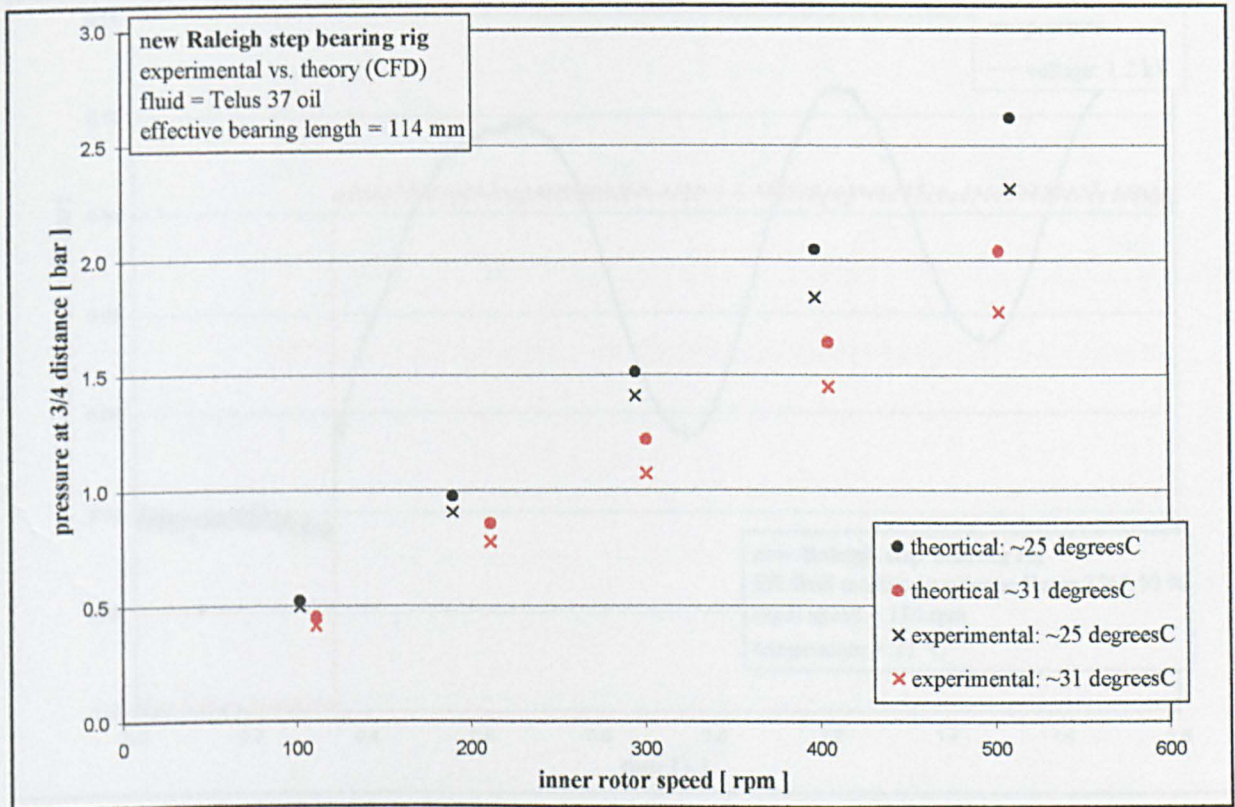


Fig. 5.36: New Rayleigh step bearing rig. Experimental vs. CFD for a Newtonian Tellus 37 oil fluid medium at two different temperatures.

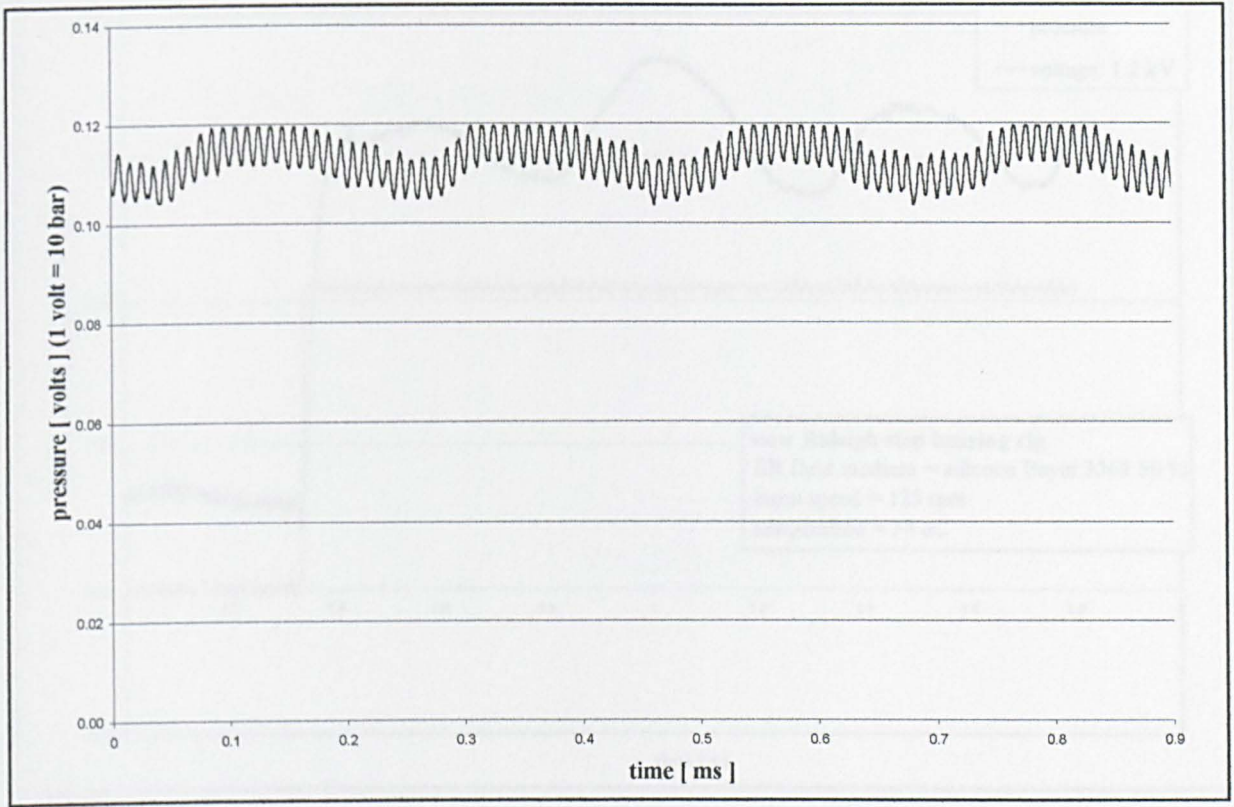


Fig. 5.37: New Rayleigh step bearing rig. ER fluid medium with zero volts excitation. Speed = 265 rpm.

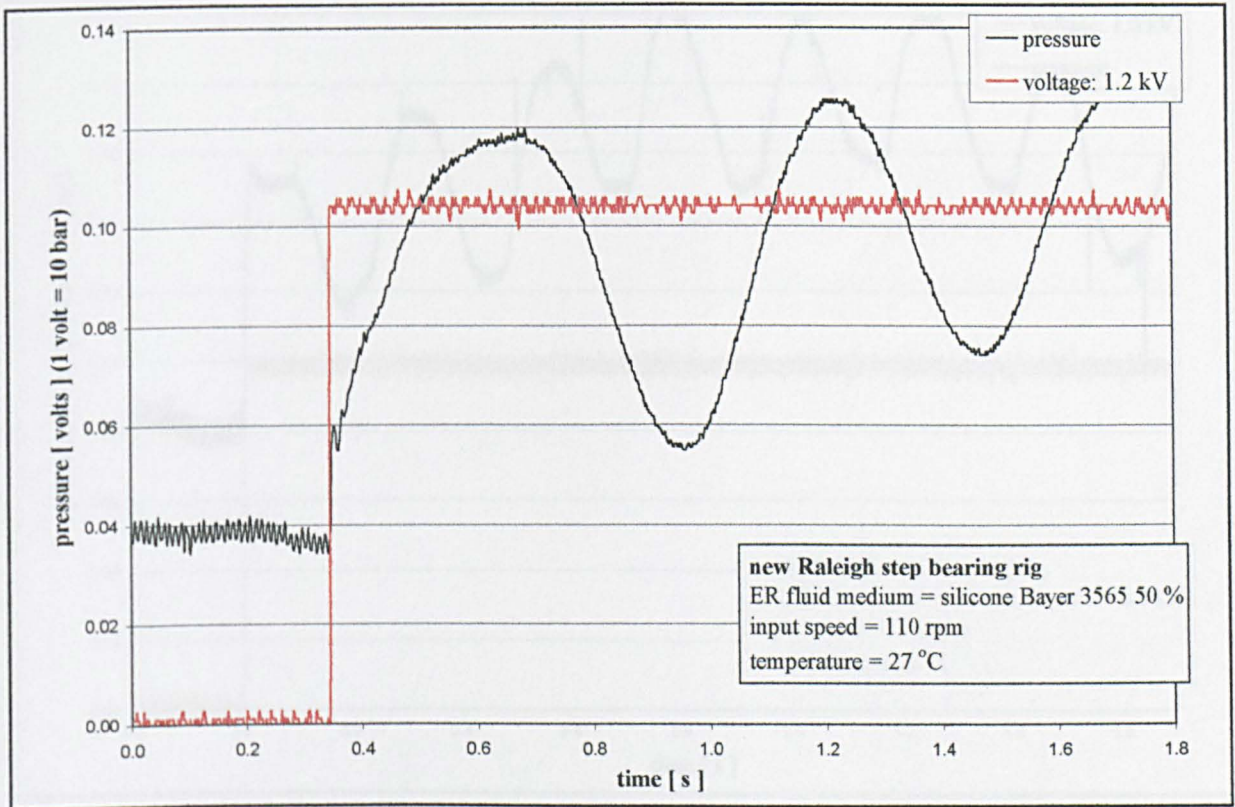


Fig. 5.38: New Rayleigh step bearing rig. ER fluid medium with 1.2 volts excitation. Speed = 110 rpm.

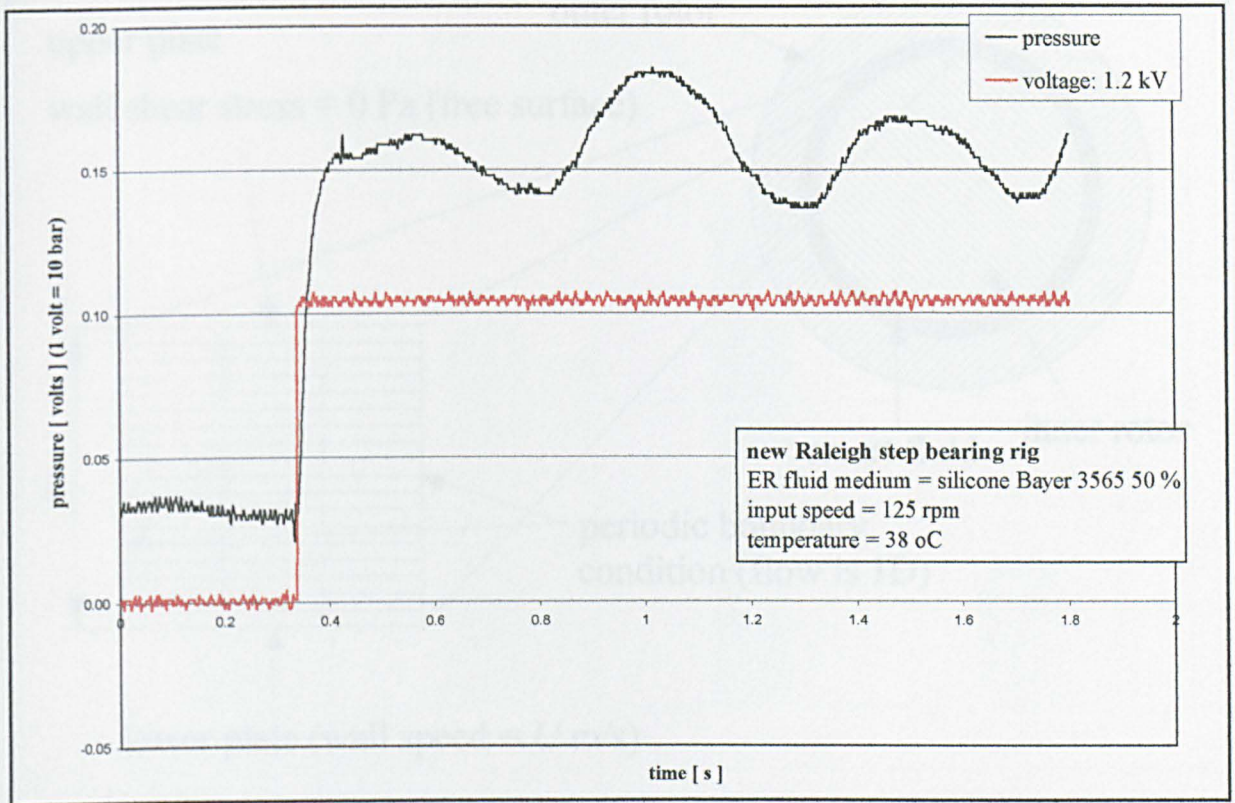


Fig. 5.39: New Rayleigh step bearing rig. ER fluid medium with 1.2 volts excitation. Speed = 125 rpm.

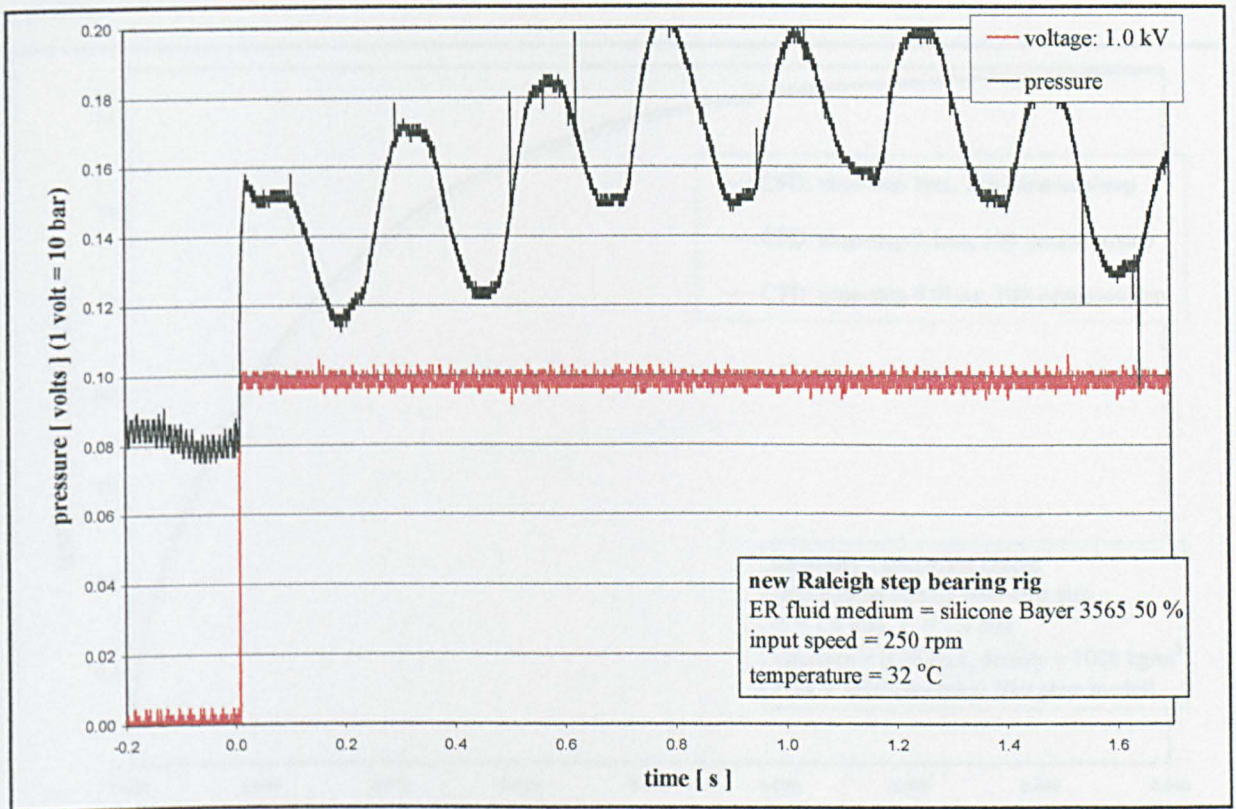


Fig. 5.40: New Rayleigh step bearing rig. ER fluid medium with 1.2 volts excitation. Speed = 250 rpm.

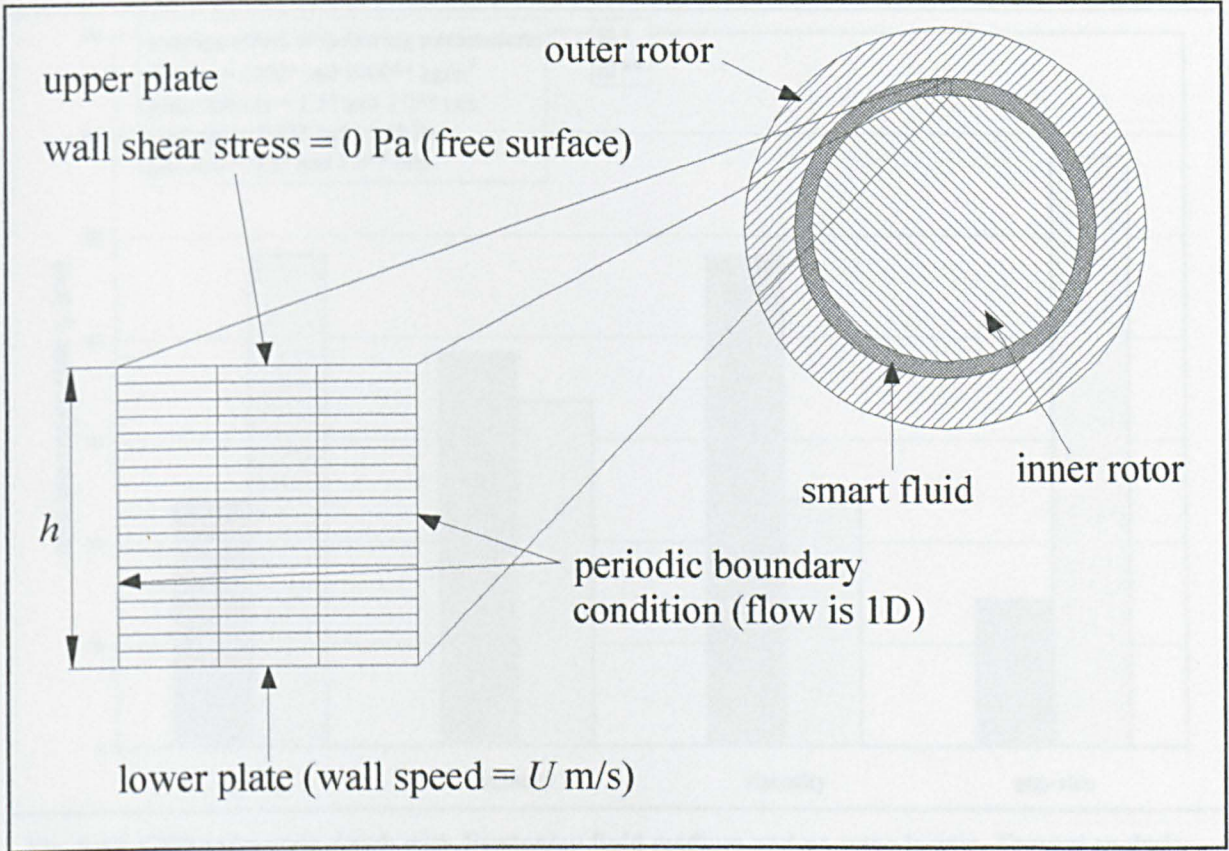


Fig. 5.41: CFD model for a 1D concentric clutch. Outer and inner rotors are approximated as flat plates.

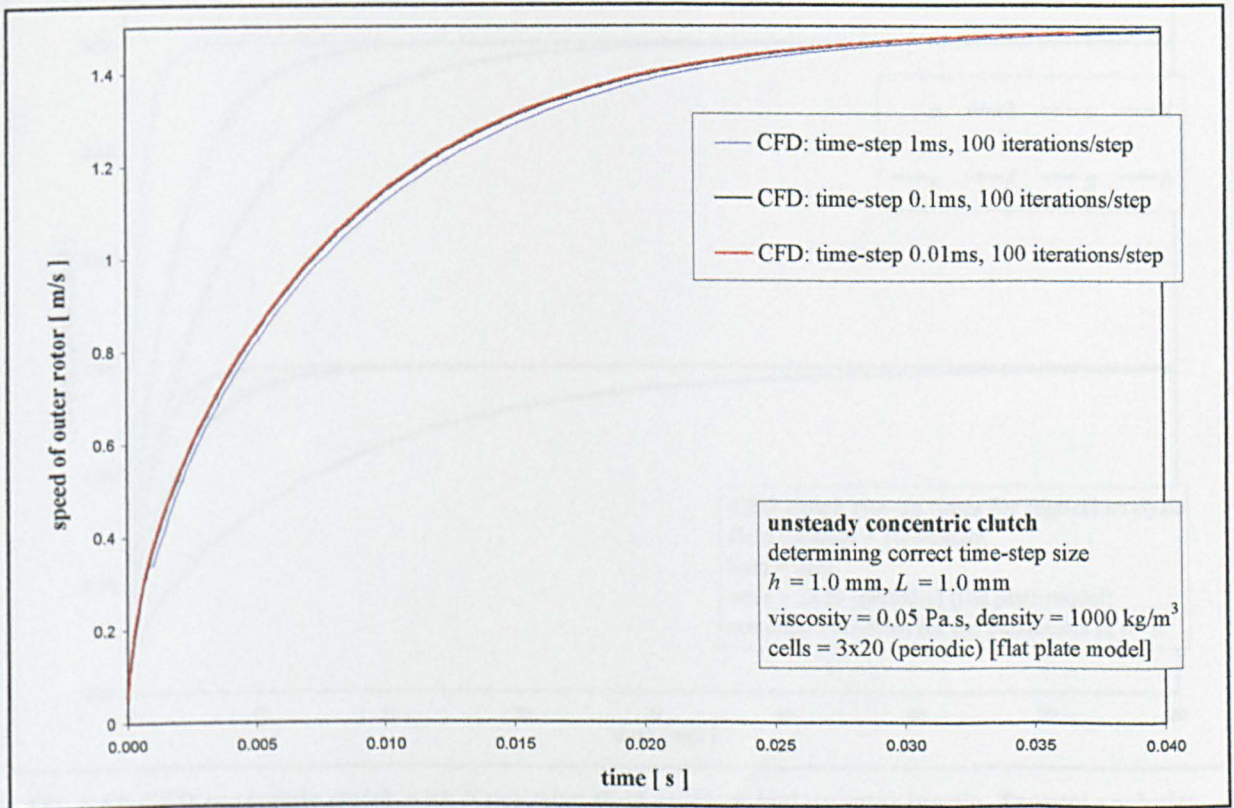


Fig. 5.42: CFD concentric clutch with Newtonian fluid medium and no rotor inertia. Determination of correct time-step size. Data for 0.01 ms and 0.1 ms are overlapping.

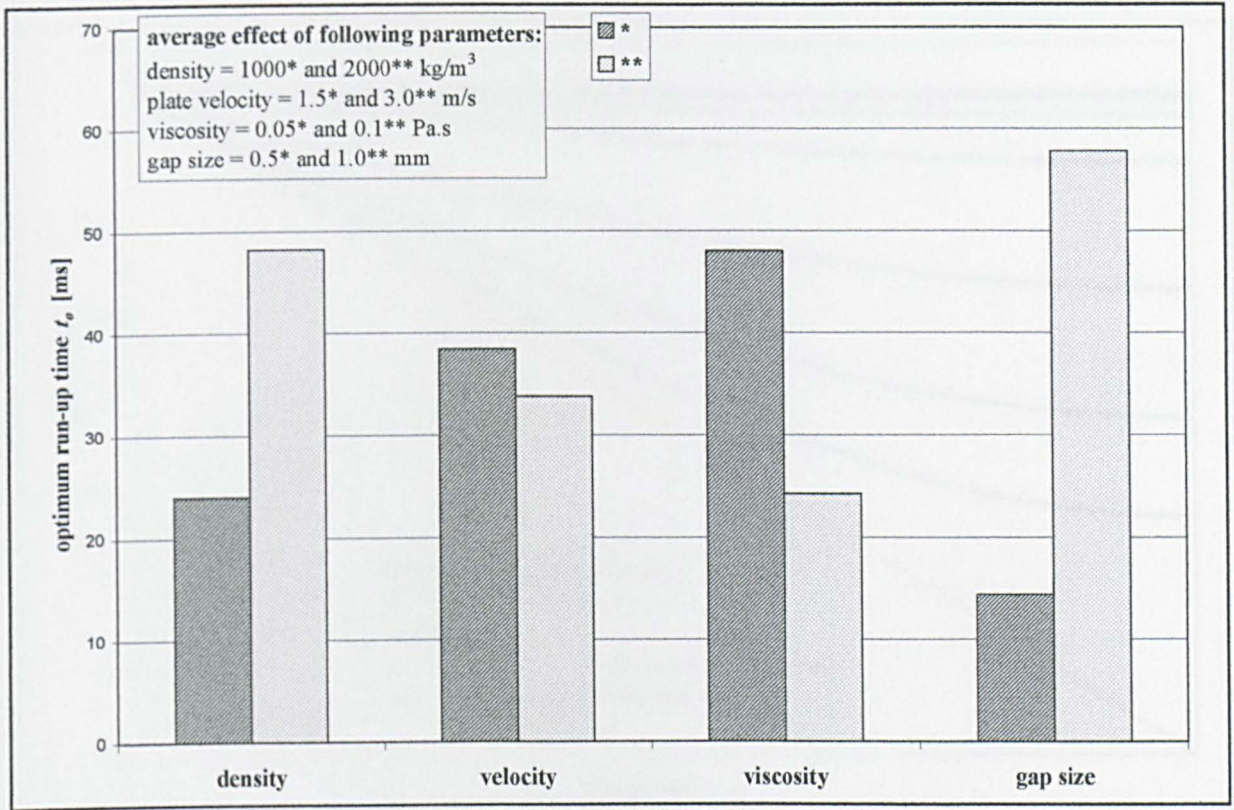


Fig. 5.43: CFD concentric clutch with Newtonian fluid medium and no rotor inertia. Tagucci analysis: average effect of each parameter on clutch run-up time.

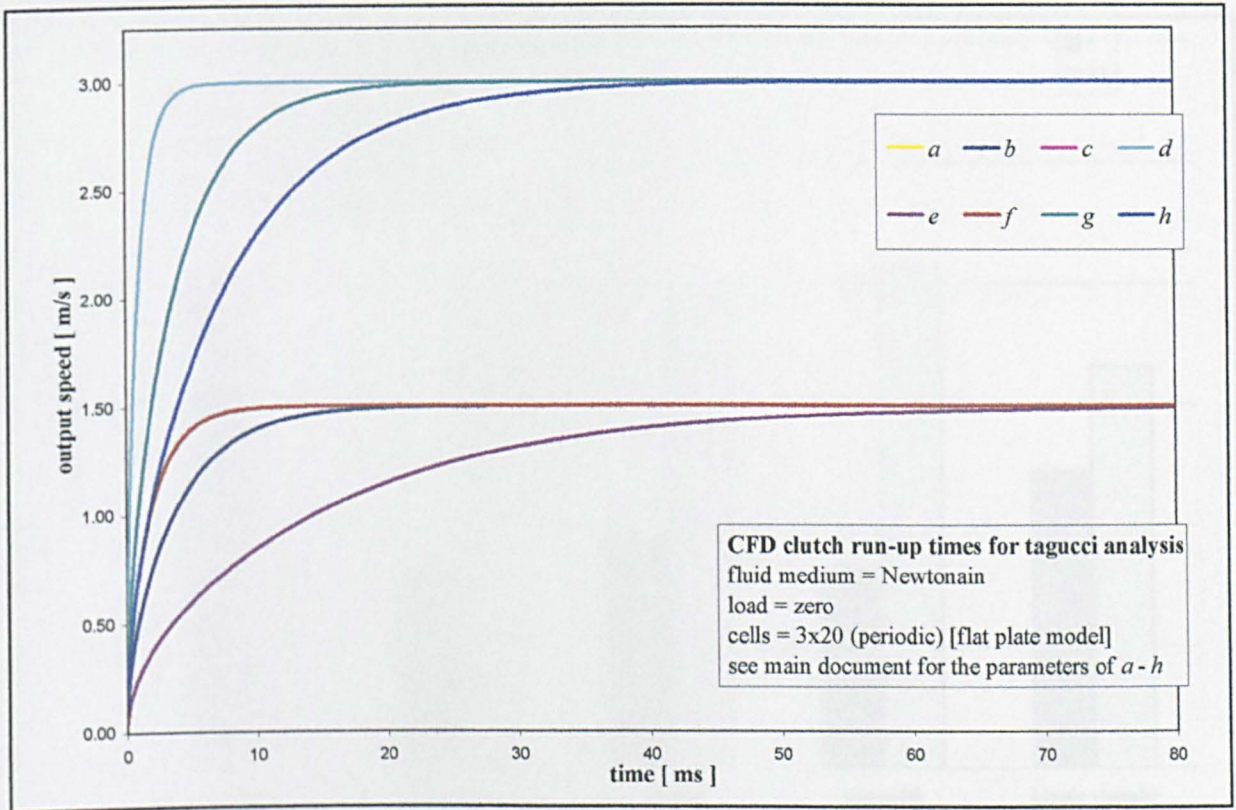


Fig. 5.44: CFD concentric clutch with Newtonian fluid medium and no rotor inertia. Tagucci analysis: run-up curves. See Table 5.10 for parameters. Curves a & f and c & h respectively overlap one another.

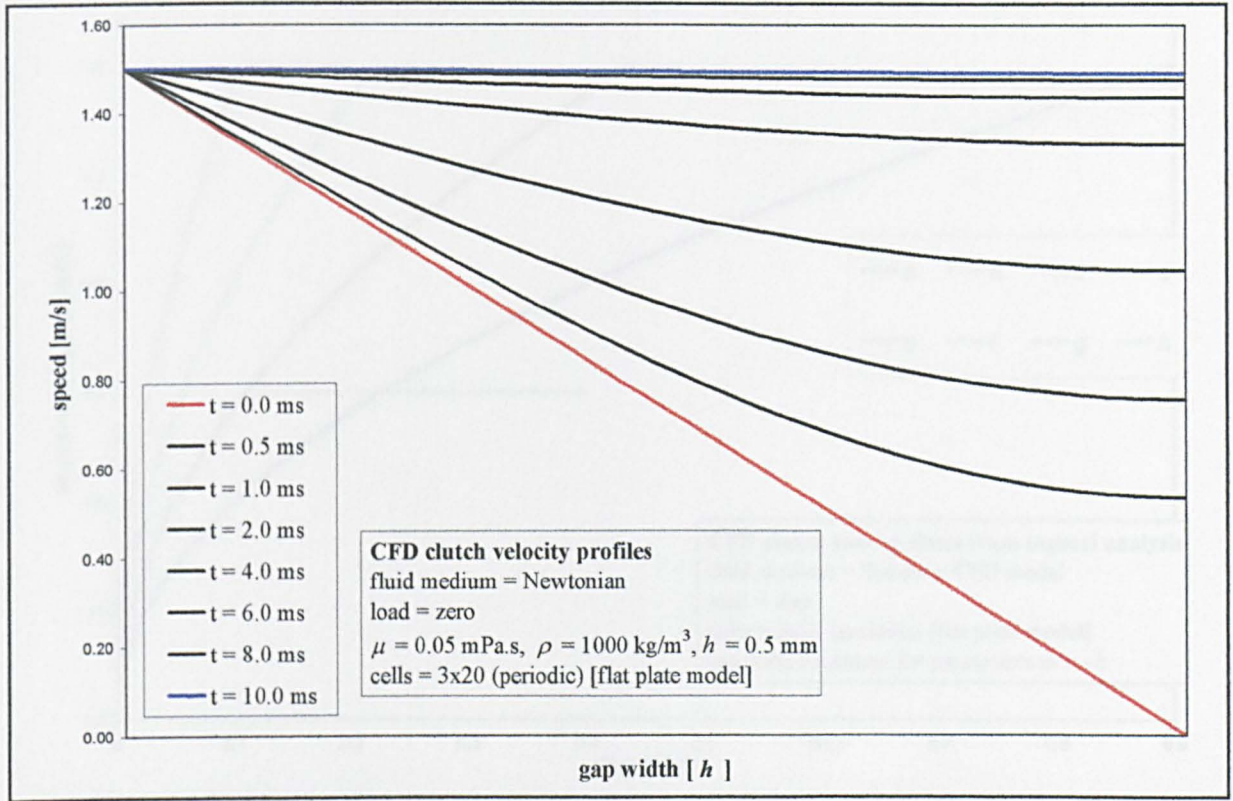


Fig. 5.45: CFD concentric clutch with a Newtonian fluid medium and no rotor inertia. Velocity profile change during the event.

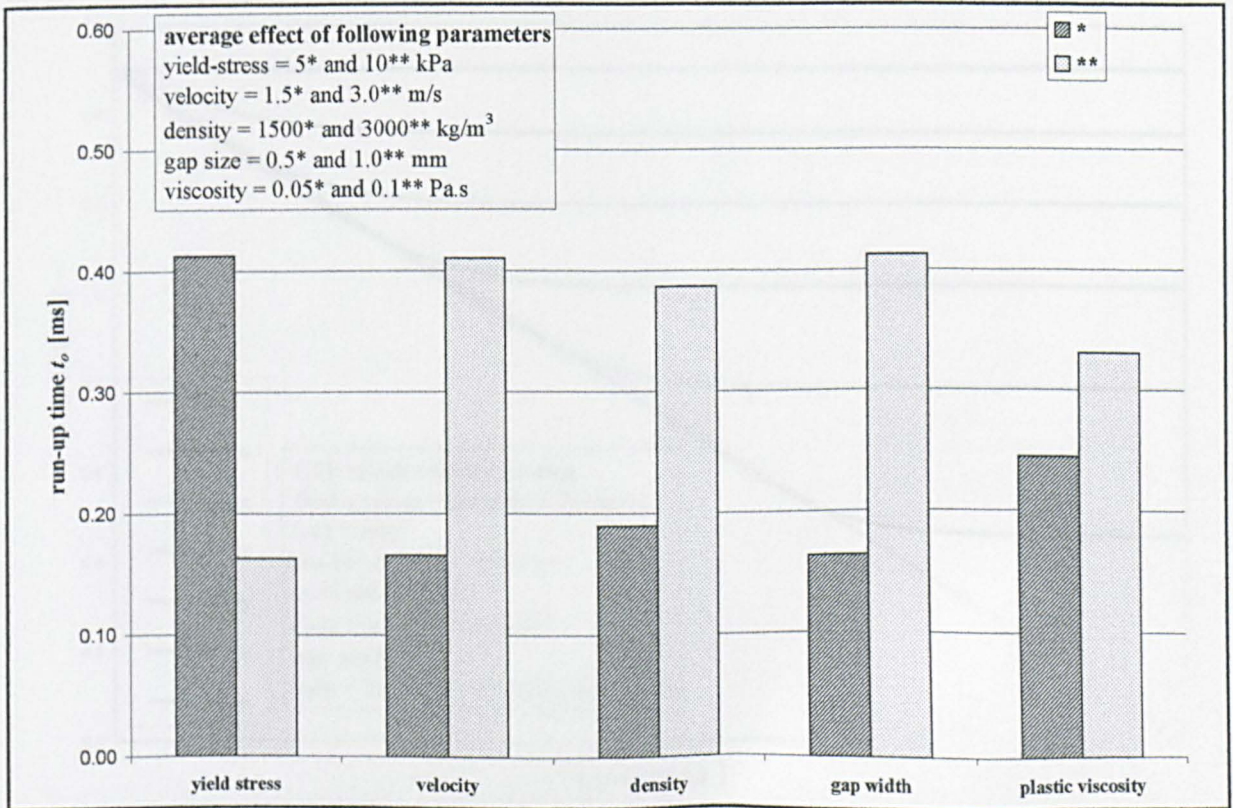


Fig. 5.46: CFD concentric clutch with a Bingham fluid medium and no rotor inertia. Tagucci analysis: average effect of each parameter on clutch run-up time.

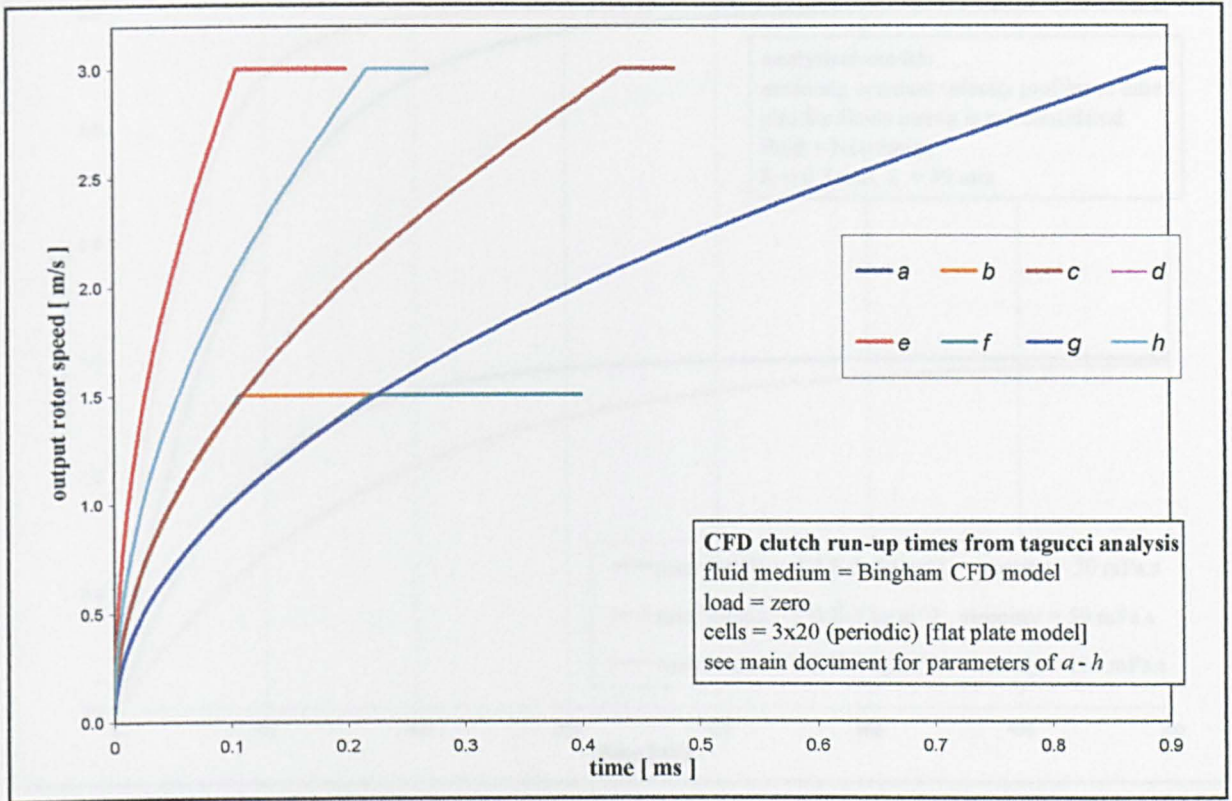


Fig. 5.47: CFD concentric clutch with a Bingham fluid medium and no rotor inertia. Tagucci analysis: run-up curves. See Table 5.11 for parameters. Curves a & b and d & f overlap one another.

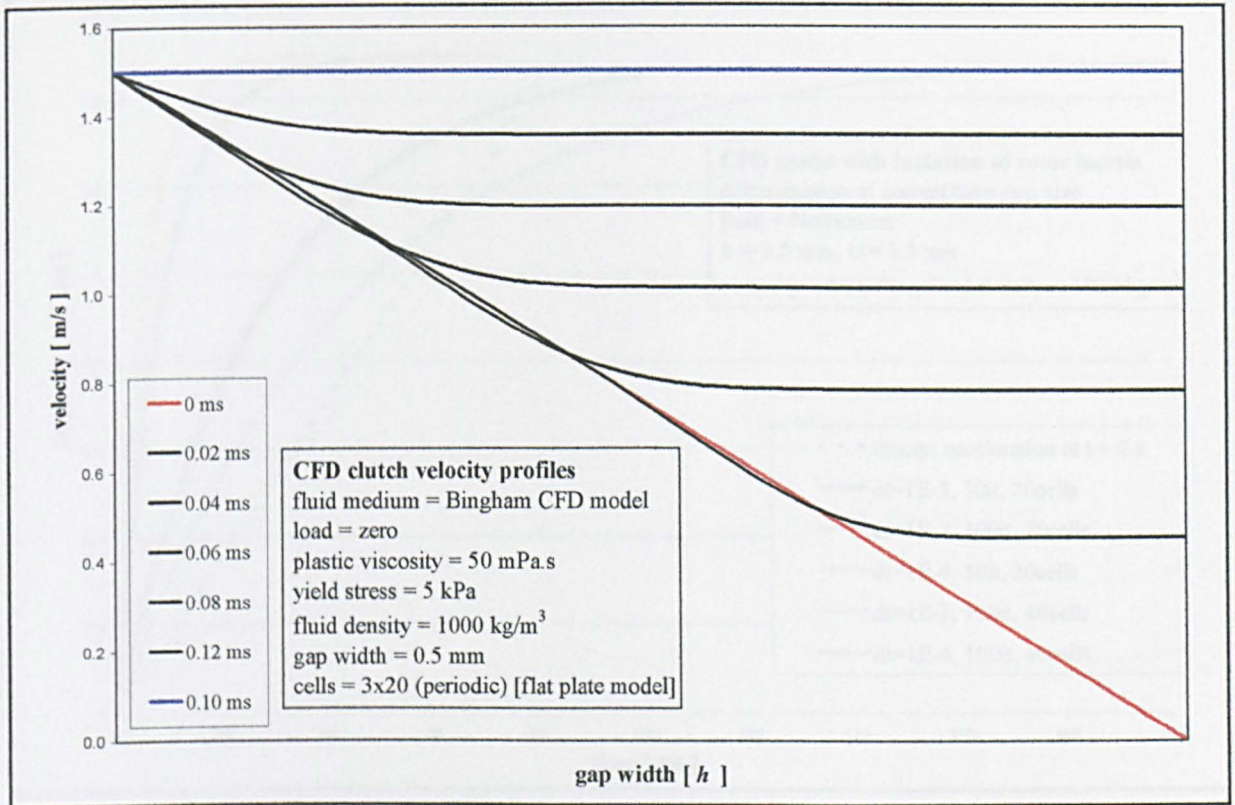


Fig. 5.48: CFD concentric clutch with a Bingham fluid medium and no rotor inertia. Velocity profile change during the event.

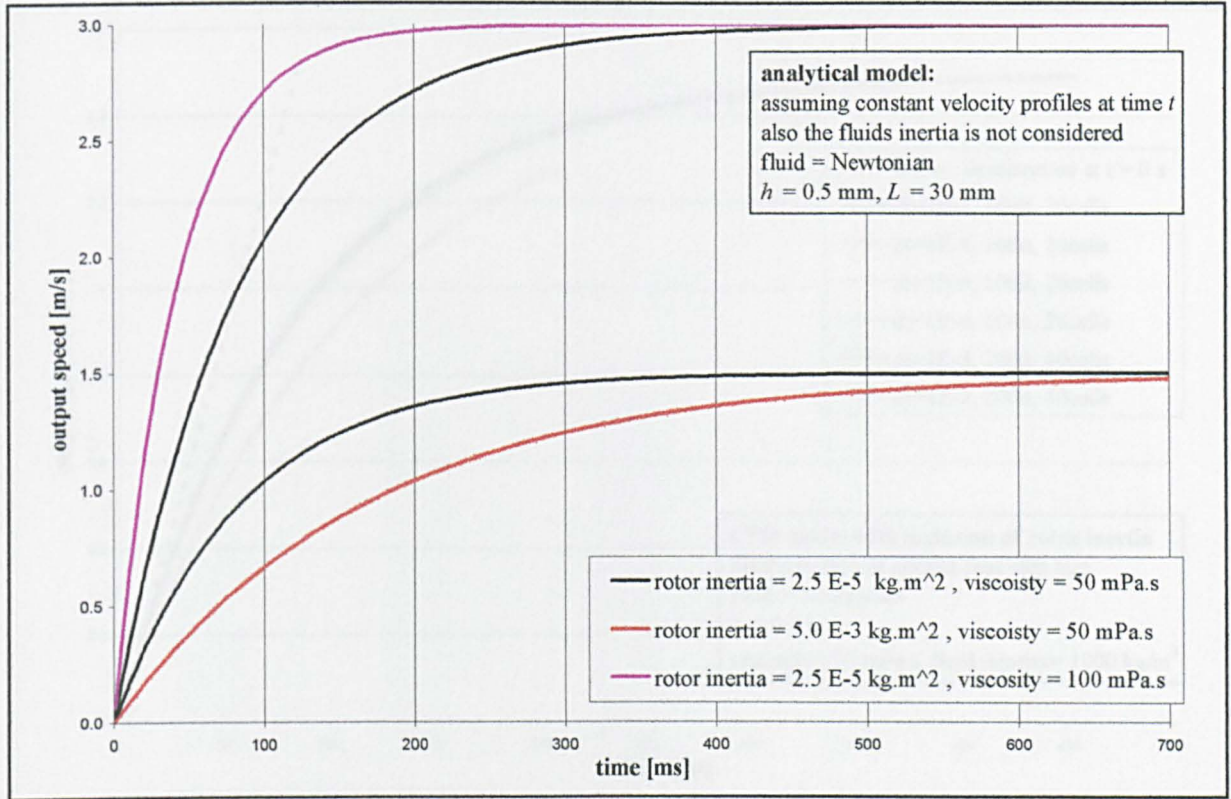


Fig. 5.49: Concentric clutch with Newtonian fluid medium and inclusion of rotor inertia. Analytical solution assuming linear velocity profiles at time t . Solution of eqn(5.13).

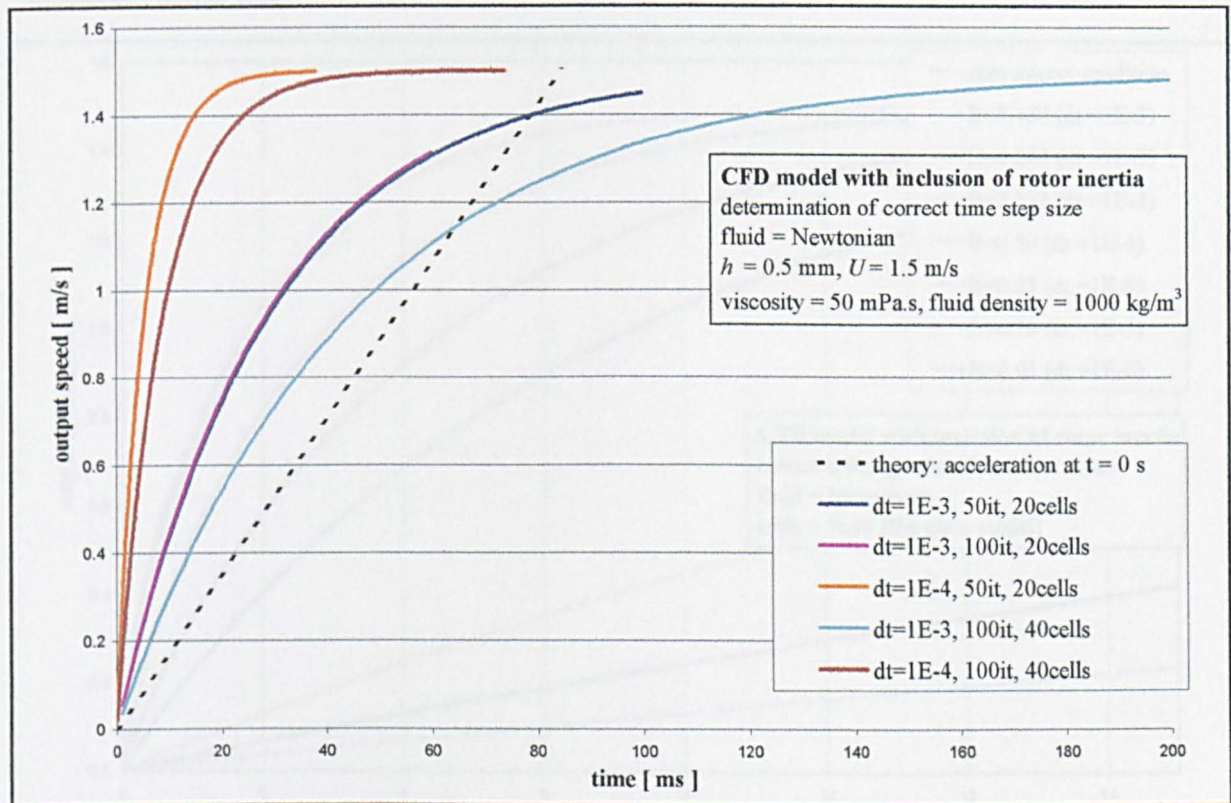


Fig. 5.50: CFD clutch with Newtonian fluid medium and inclusion of rotor inertia. Initial results using the subroutine to incur wall velocity from the shear-stress. The run-up curves should be on the right hand side of the theoretical dotted line.

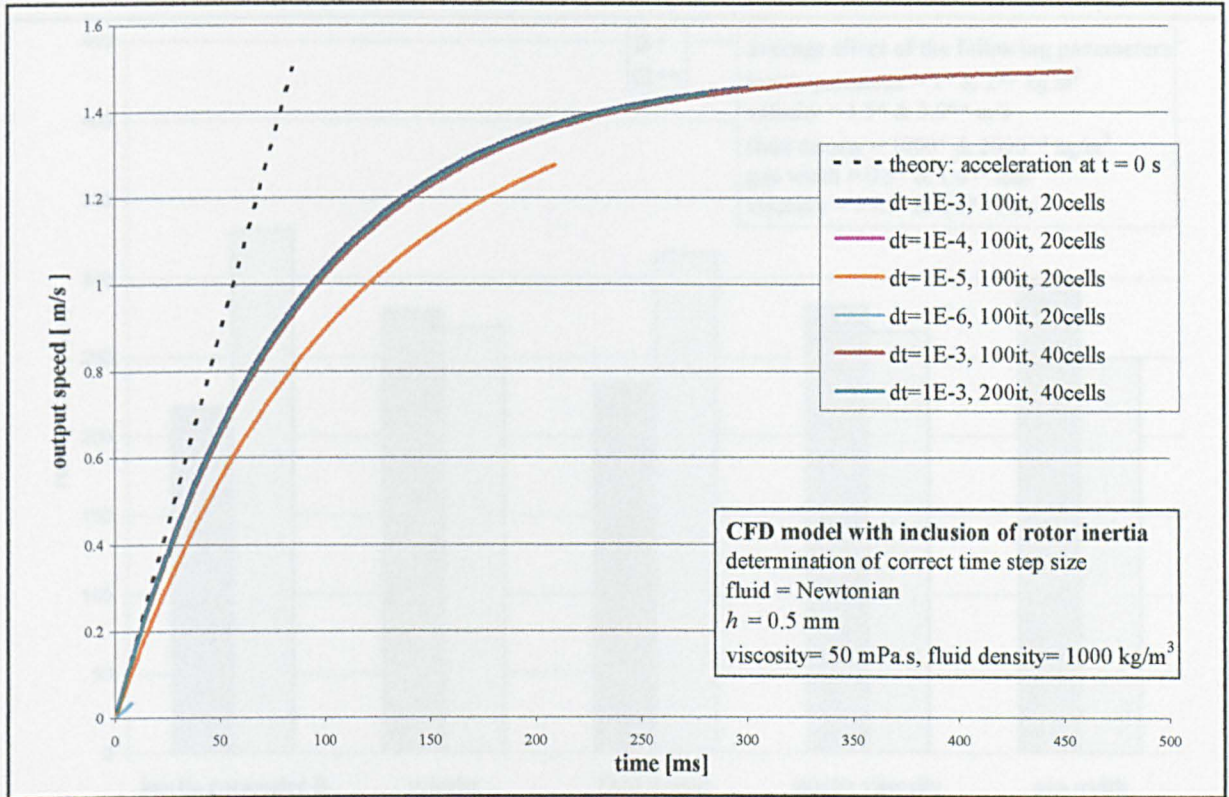


Fig. 5.51: CFD clutch with a Newtonian fluid medium and inclusion of rotor inertia. Results from improved subroutine with correction factor. The run-up curves are now on the correct side of the theoretical dotted line.

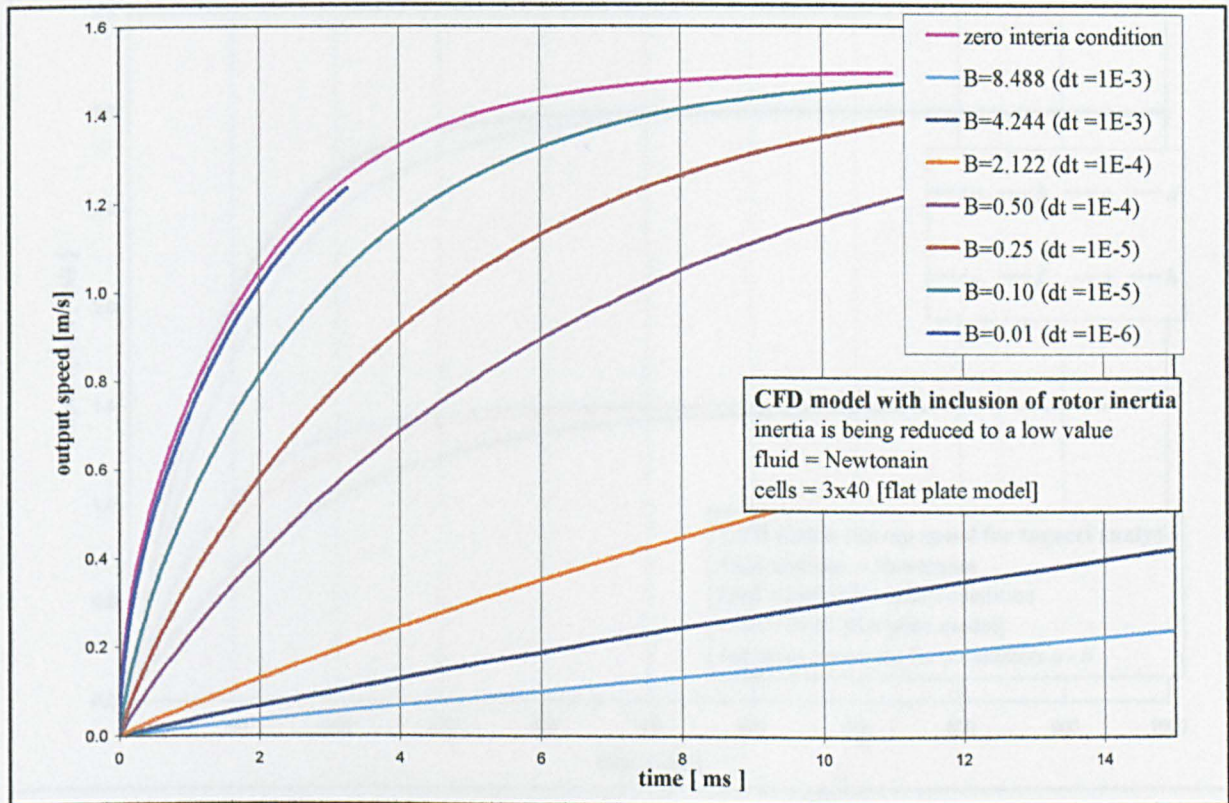


Fig. 5.52: CFD clutch with a Newtonian fluid medium and inclusion of rotor inertia. When Inertia is reduced, the solution is the same has the zero inertia condition.

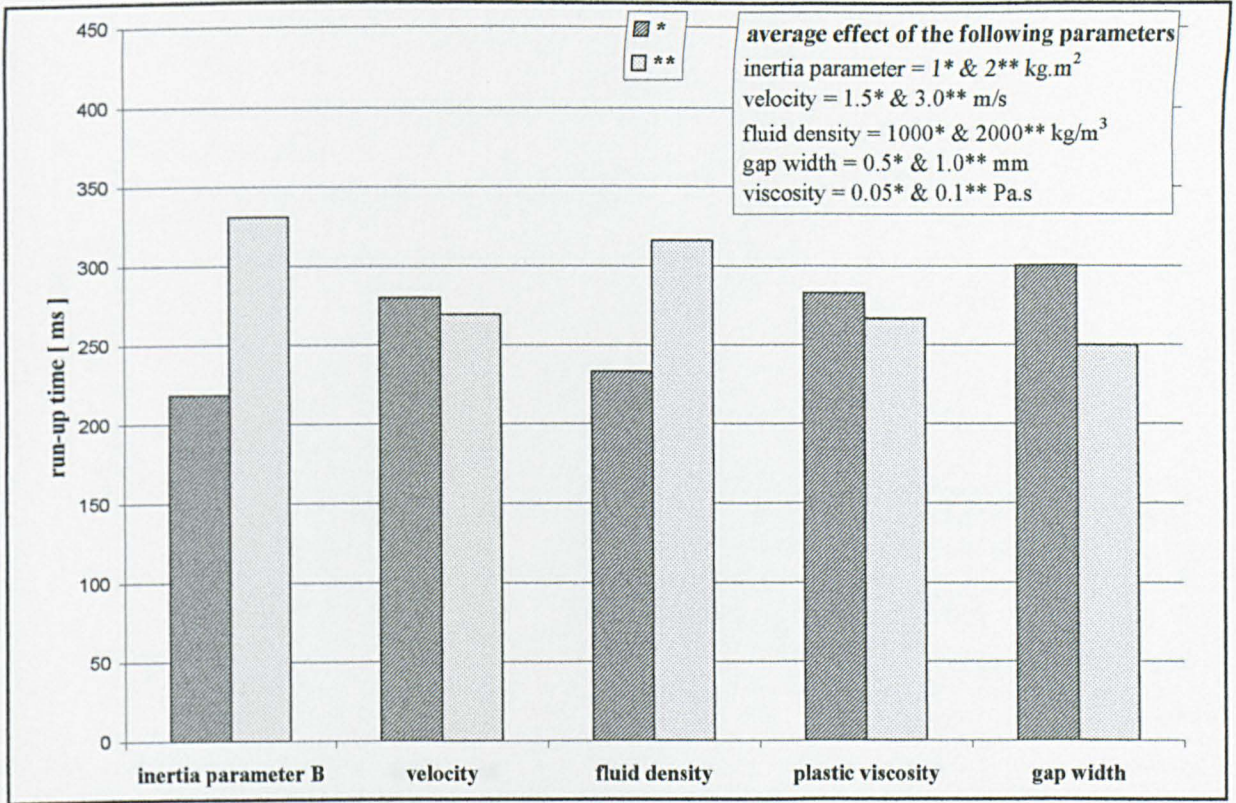


Fig. 5.53: CFD concentric clutch with Newtonian fluid medium and inclusion of rotor inertia. Tagucci analysis: average effect of each parameter on clutch run-up time.

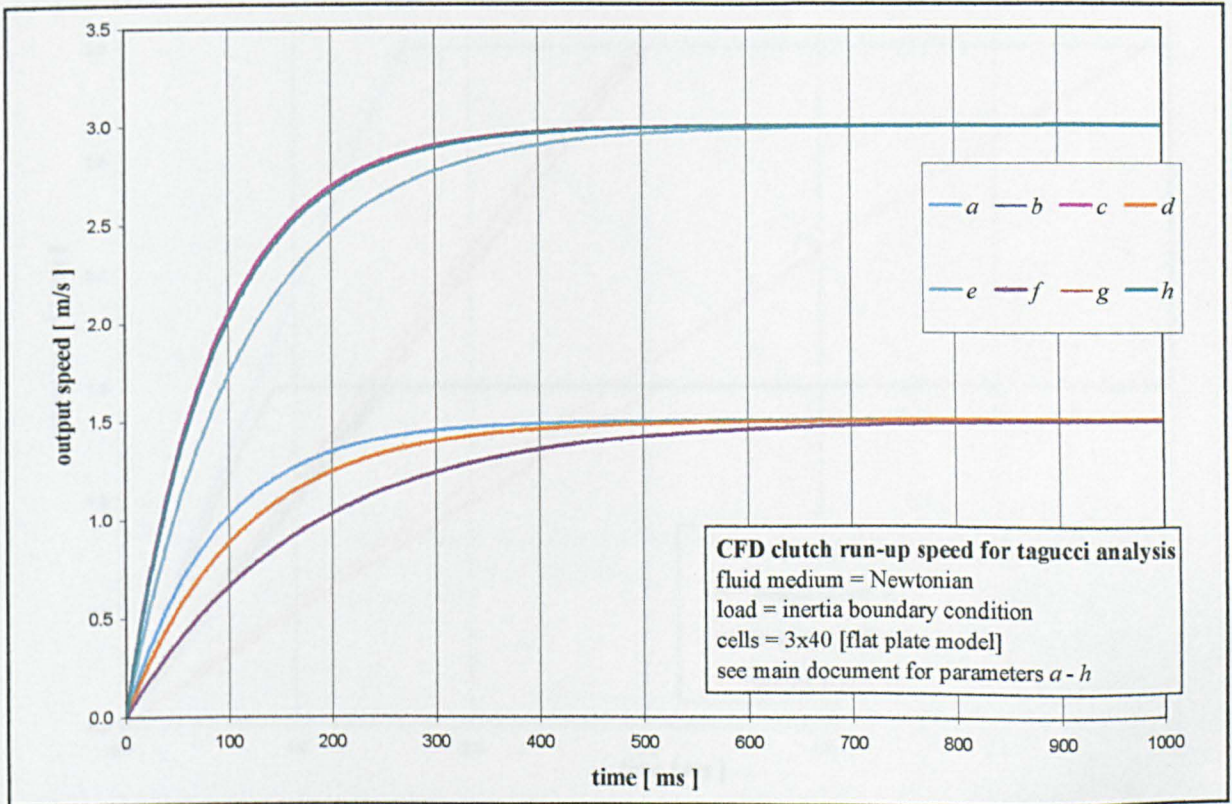


Fig. 5.54: CFD concentric clutch with a Newtonian medium and inclusion of rotor inertia. Tagucci analysis: run-up curves. See Table 5.14 for parameters.

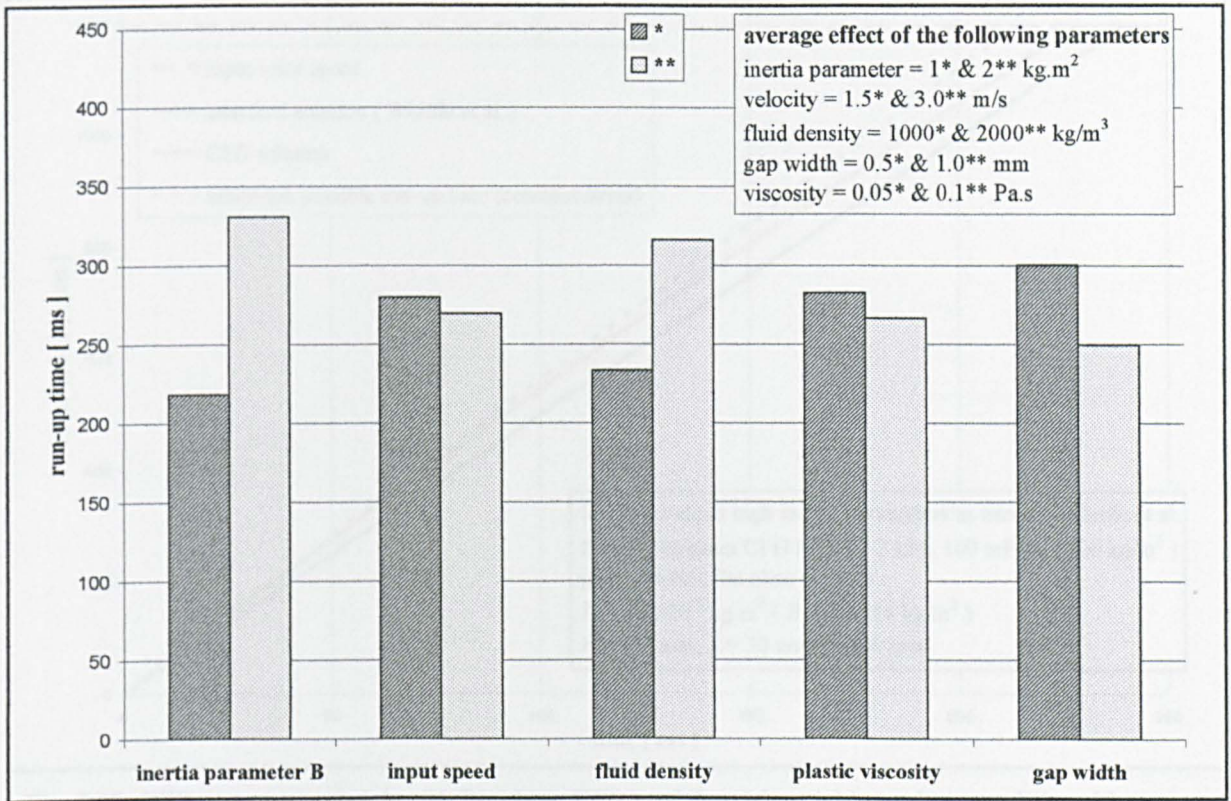


Fig. 5.55: CFD concentric clutch with medium and inclusion of rotor inertia. Tagucci analysis: run-up curves. See Table 5.15 for parameters.

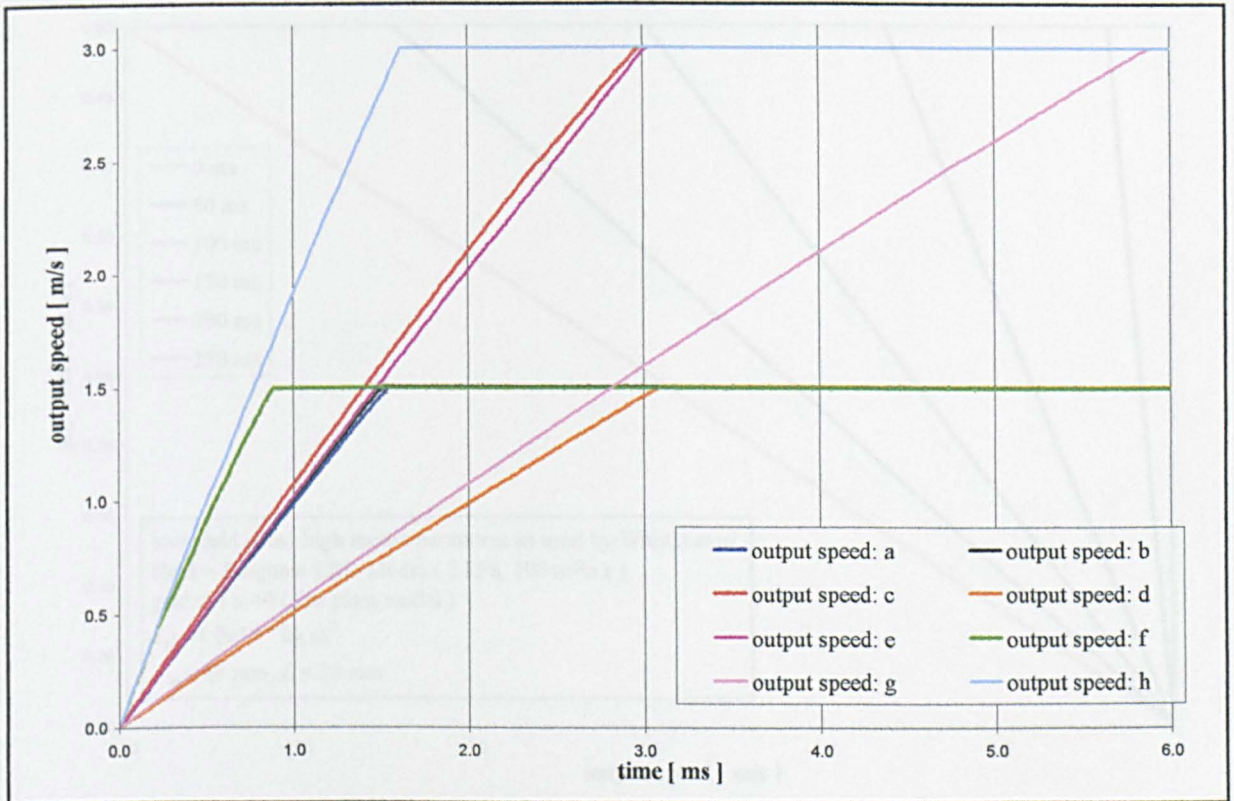


Fig. 5.56: Concentric clutch run-up curves using Bingham CFD model and inertial boundary condition. Tagucci analysis: parameters given in Table 5.15.

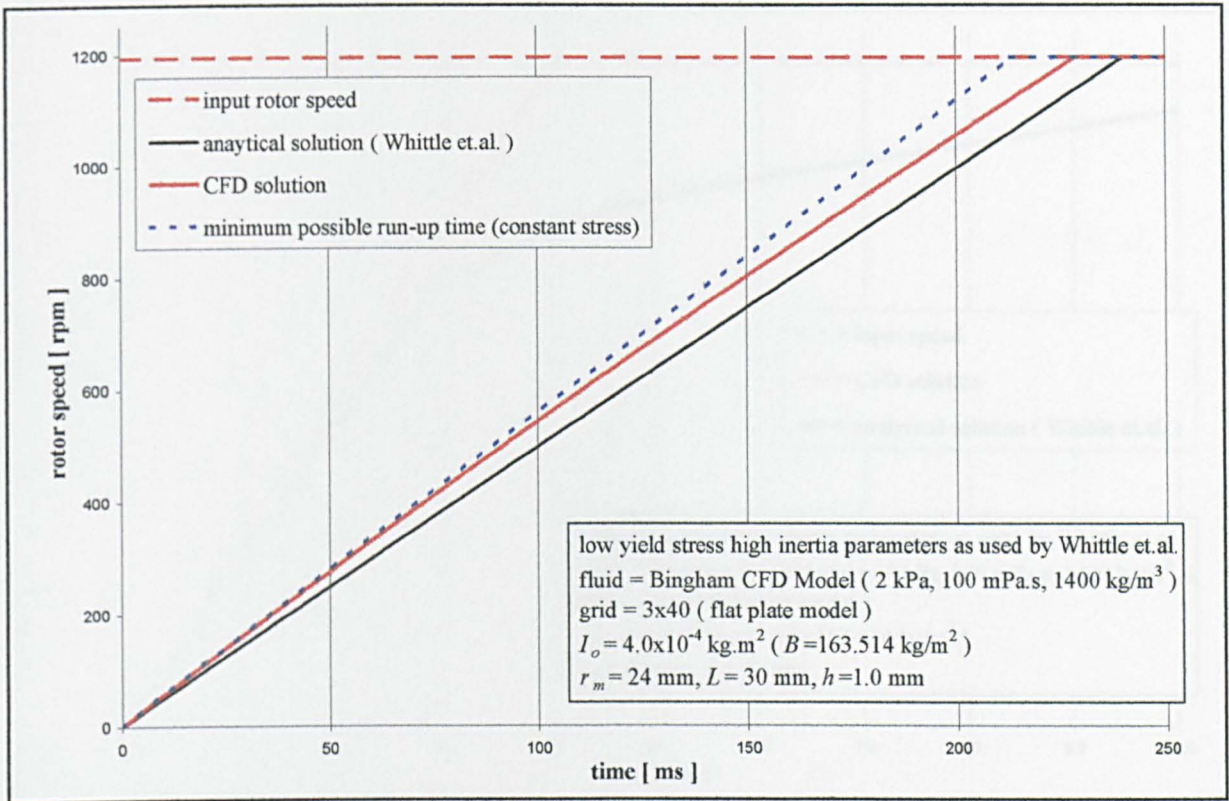


Fig. 5.57: CFD concentric clutch with Bingham CFD model and inertial boundary condition. Linear run-up curves are produced when the output rotor inertia is high. Parameters are the same as those used in [38]. Constant stress solution is from eqn(5.10).

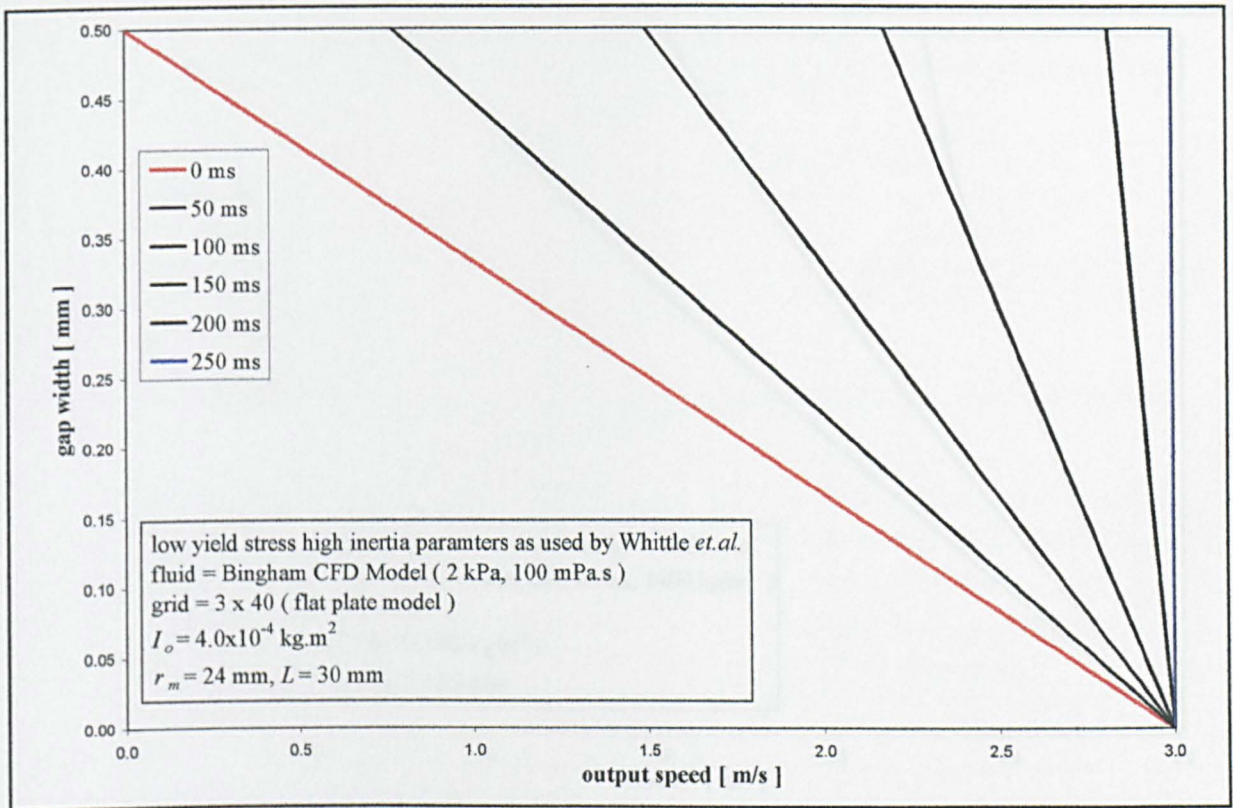


Fig. 5.58: CFD concentric clutch with Bingham CFD model and inertial boundary condition. Linear velocity profiles are produced when the output rotor inertia is high. Parameters are the same as those used in [38].

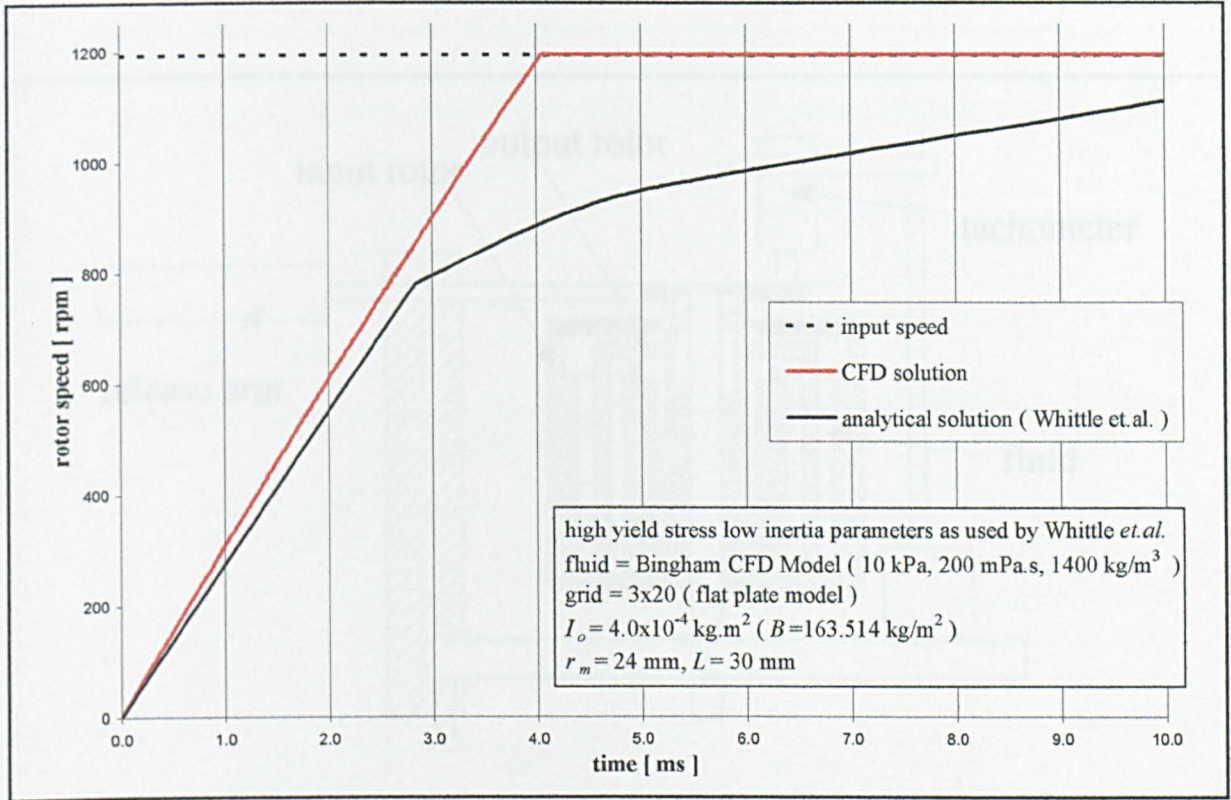


Fig. 5.59: CFD concentric clutch with Bingham CFD model and inertial boundary condition. Linear run-up curves are produced when the output rotor inertia is high. Parameters are the same as those used in [38].

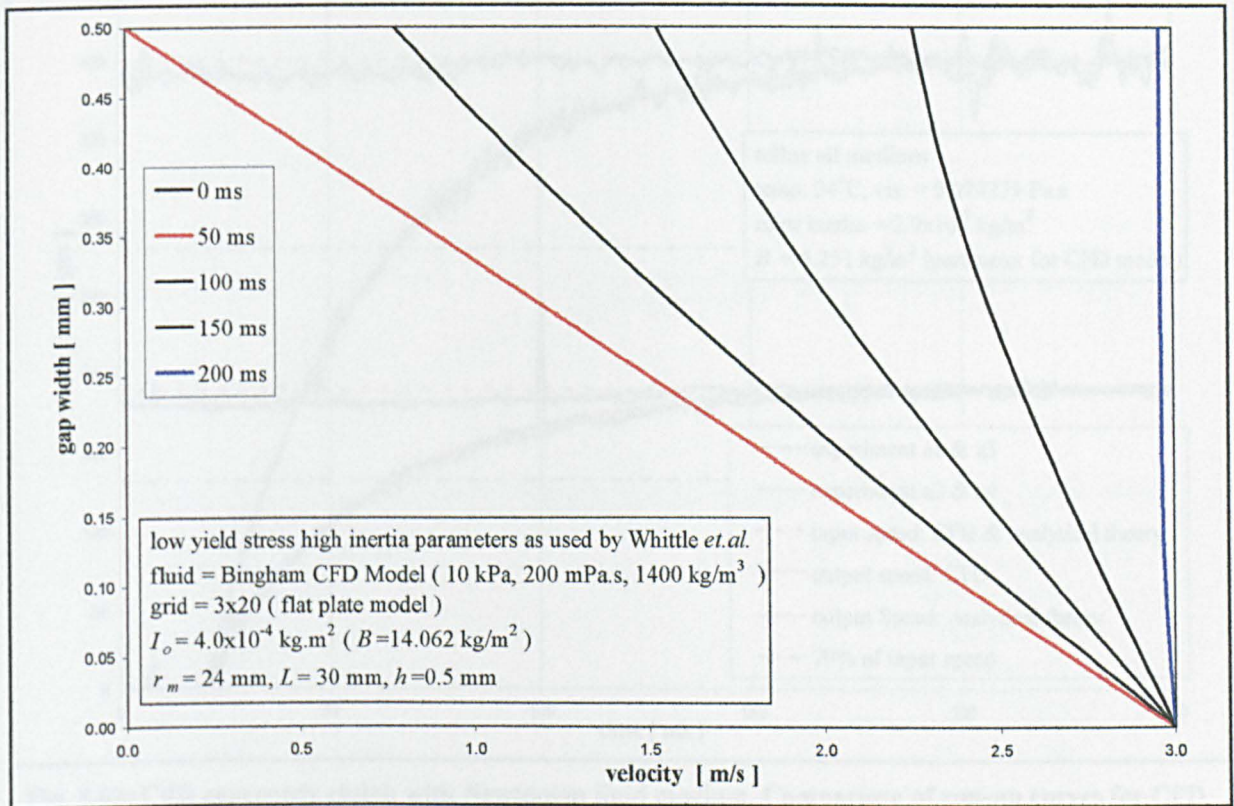


Fig. 5.60: CFD concentric clutch with Bingham CFD model and inertial boundary condition. Linear velocity profiles are produced when the output rotor inertia is high. Parameters are the same as those used in [38].

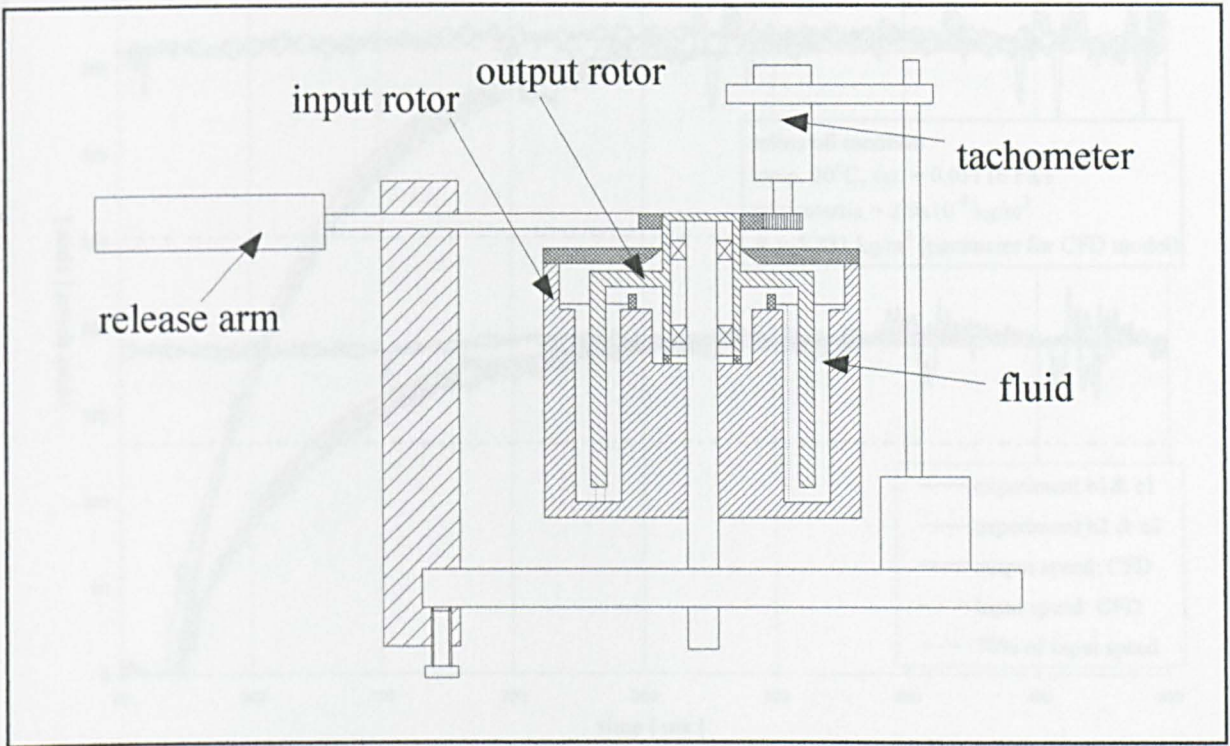


Fig. 5.61: Sketch of the dual channel concentric clutch used for experimentation.

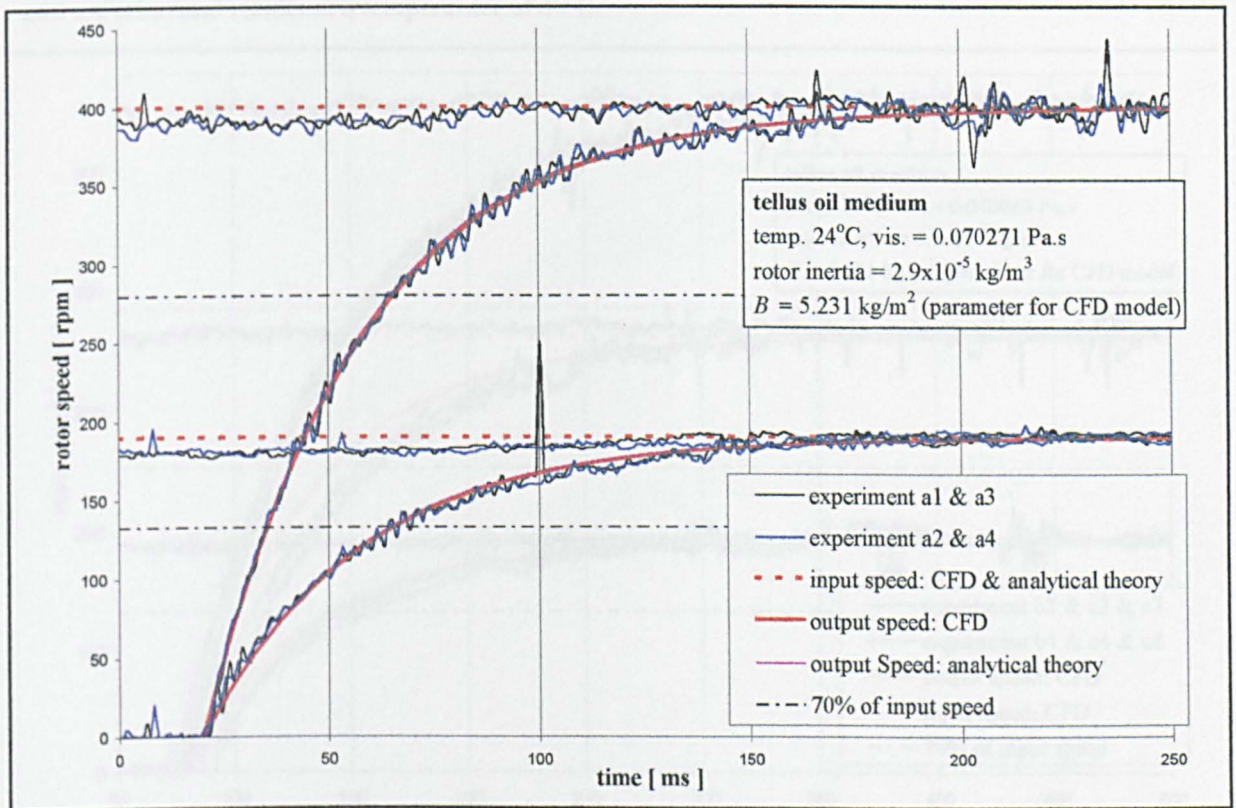


Fig. 5.62: CFD concentric clutch with Newtonian fluid medium. Comparison of run-up curves for CFD and experimental results at a temperature of 24°C. Analytical theory is the solution of eqn(5.13).

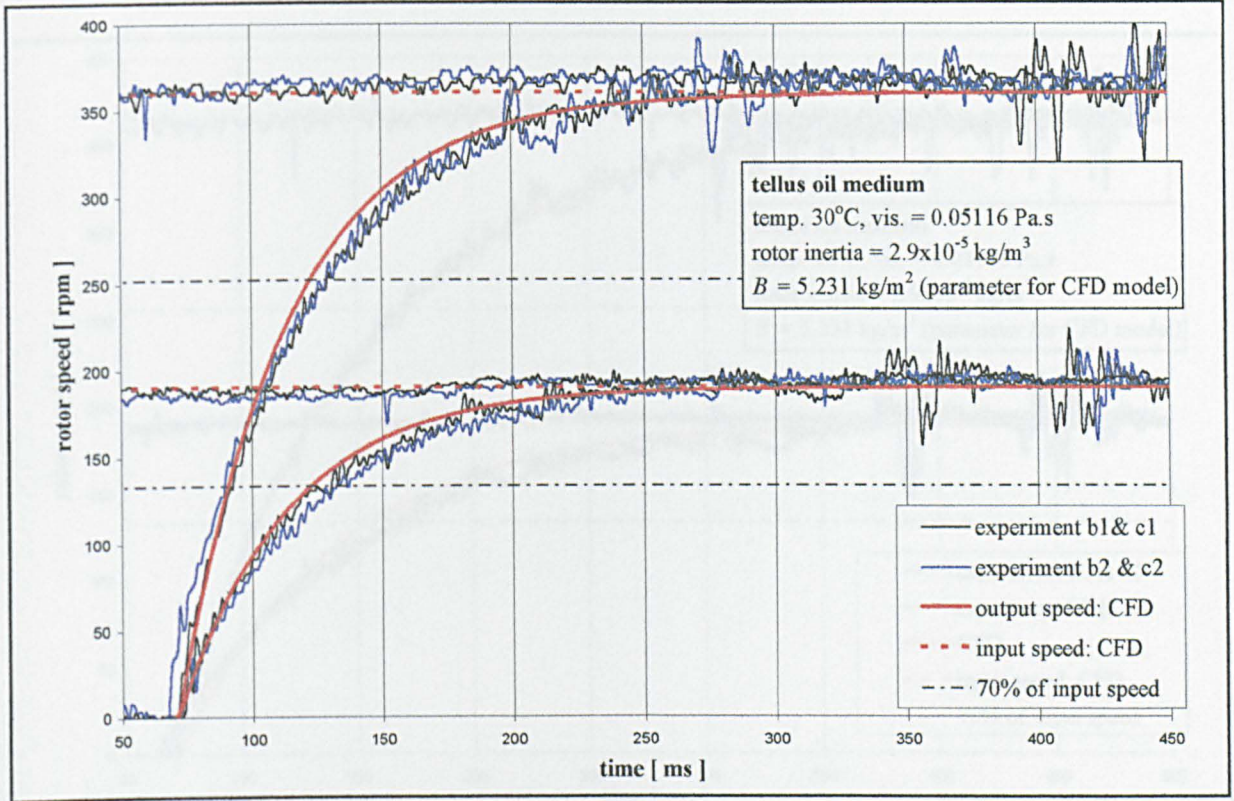


Fig. 5.63: CFD concentric clutch with Newtonian fluid medium. Comparison of run-up curves for CFD and experimental results at a temperature of 30°C.

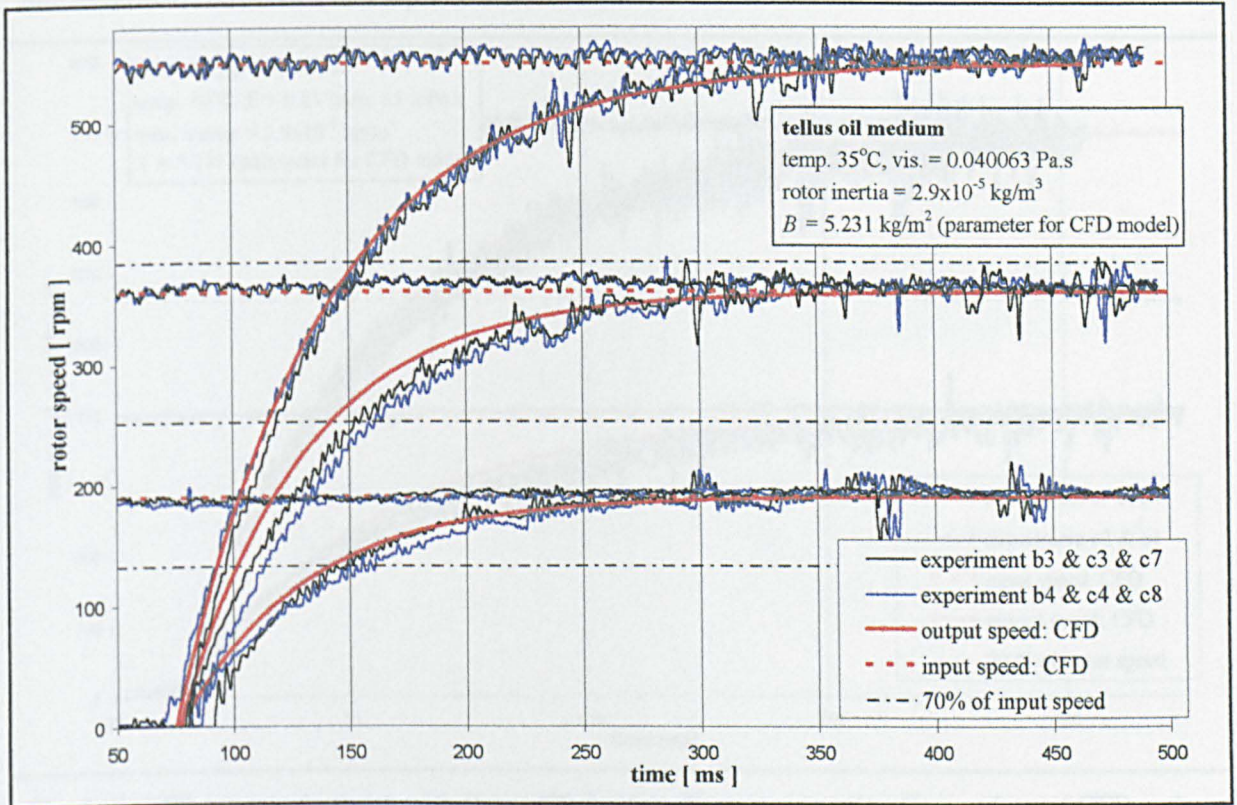


Fig. 5.64: CFD concentric clutch with Newtonian fluid medium. Comparison of run-up curves for CFD and experimental results at a temperature of 35°C.

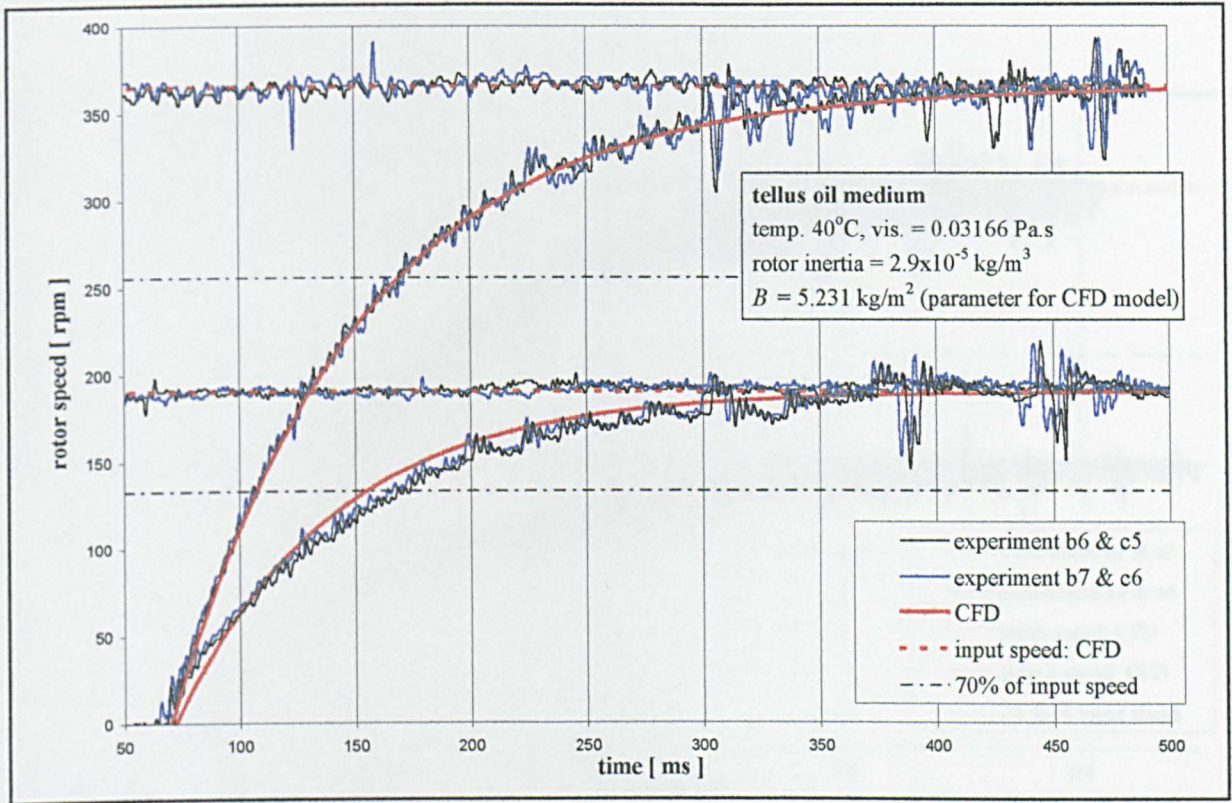


Fig. 5.65: CFD concentric clutch with Newtonian fluid medium. Comparison of run-up curves for CFD and experimental results at a temperature of 40°C.

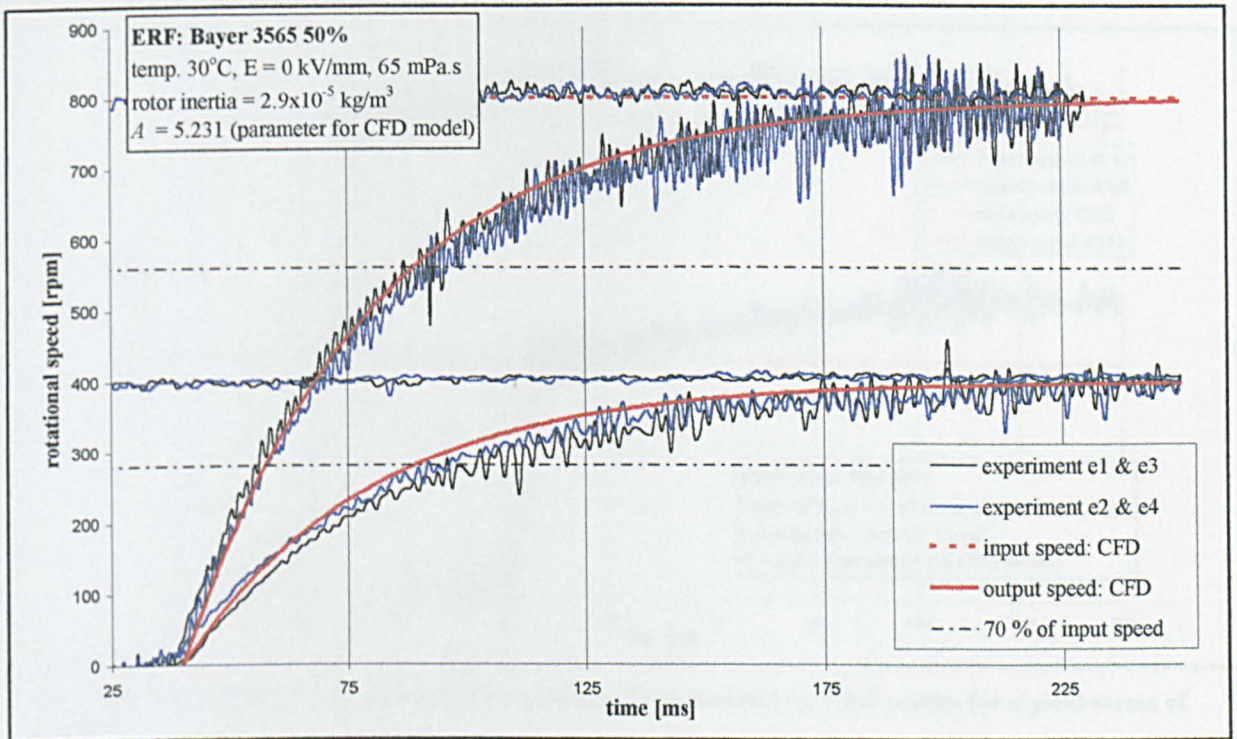


Fig. 5.66: CFD concentric clutch with Bayer ERF fluid medium at zero volts. Comparison of CFD and experimental run-up curves at a temperature of 30°C.

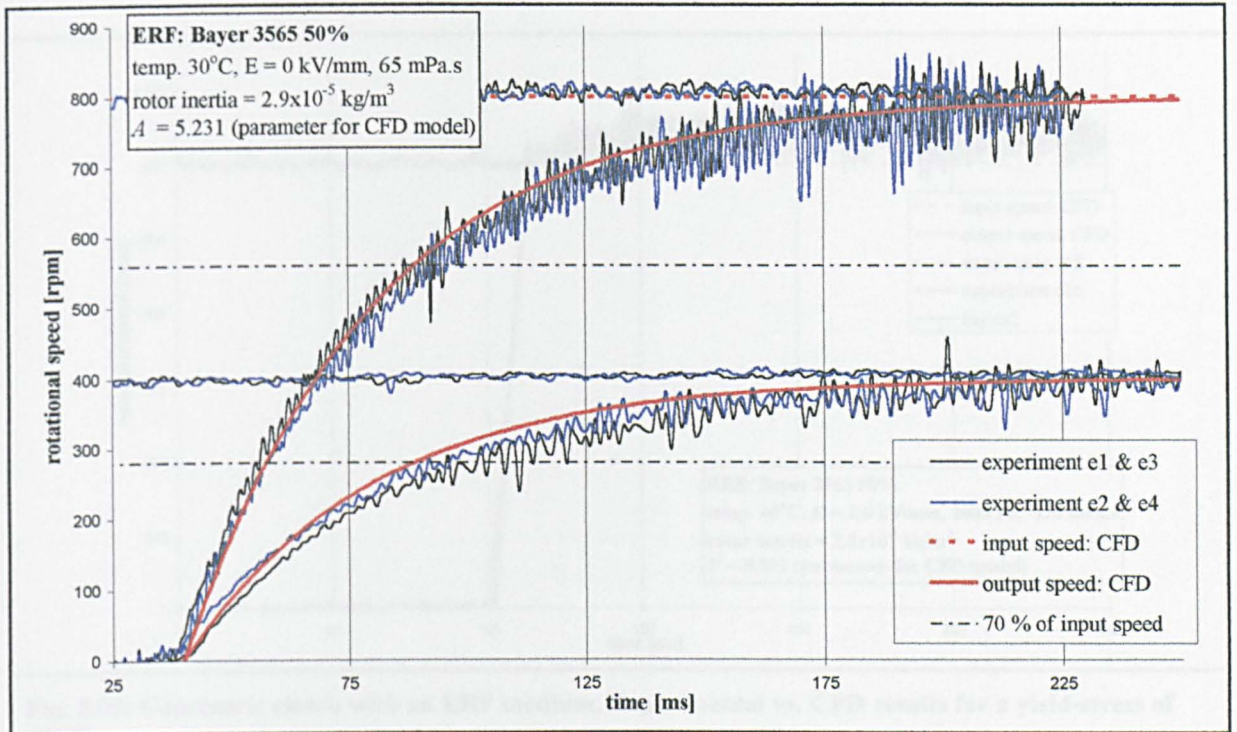


Fig. 5.67: CFD concentric clutch with Bayer ER fluid medium at zero volts. Comparison of CFD and experimental run-up curves at a temperature of 30°C.

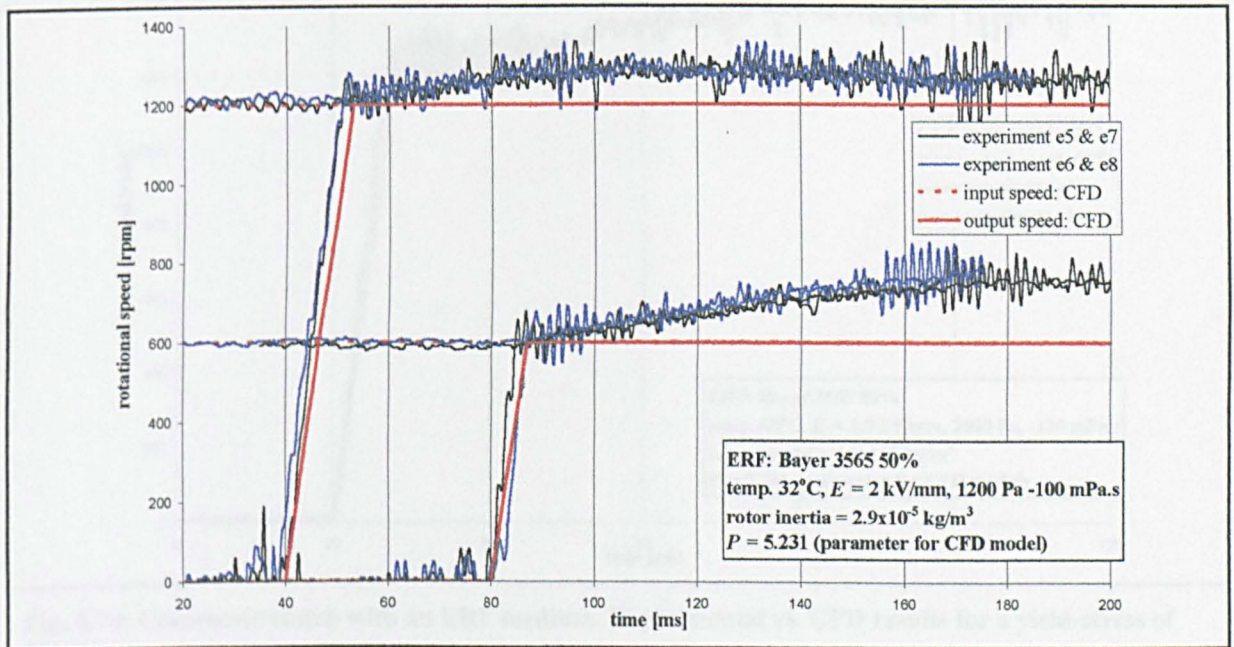


Fig. 5.68: Concentric clutch with an ERF medium. Experimental vs. CFD results for a yield-stress of 1000 Pa.

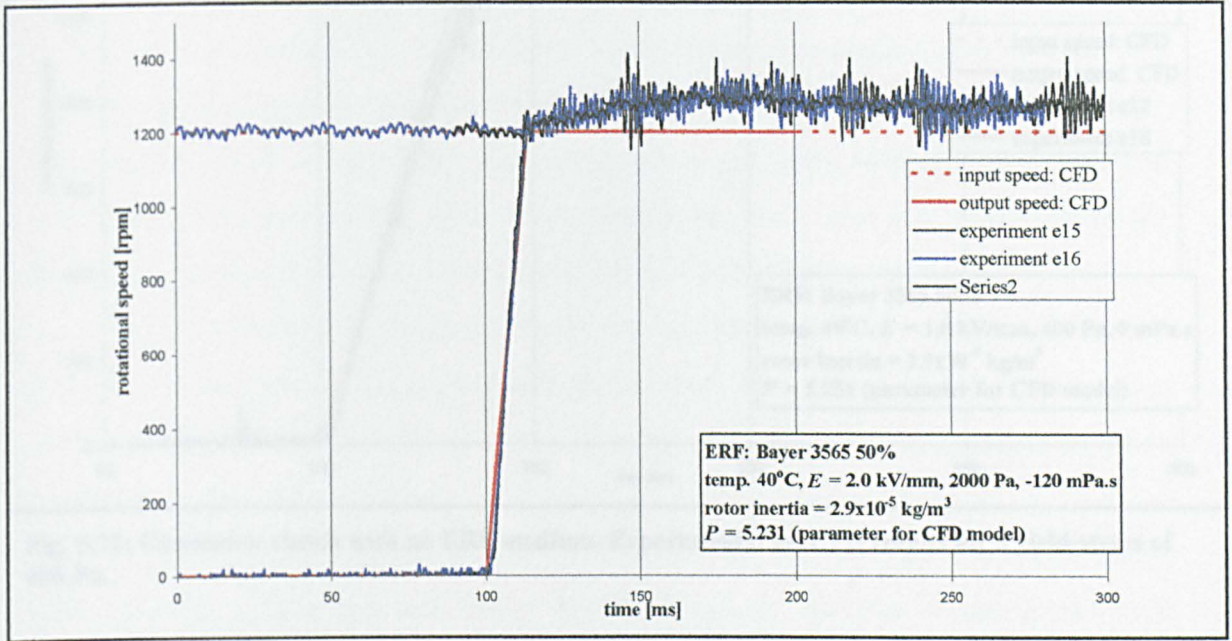


Fig. 5.69: Concentric clutch with an ERF medium. Experimental vs. CFD results for a yield-stress of 400 Pa.

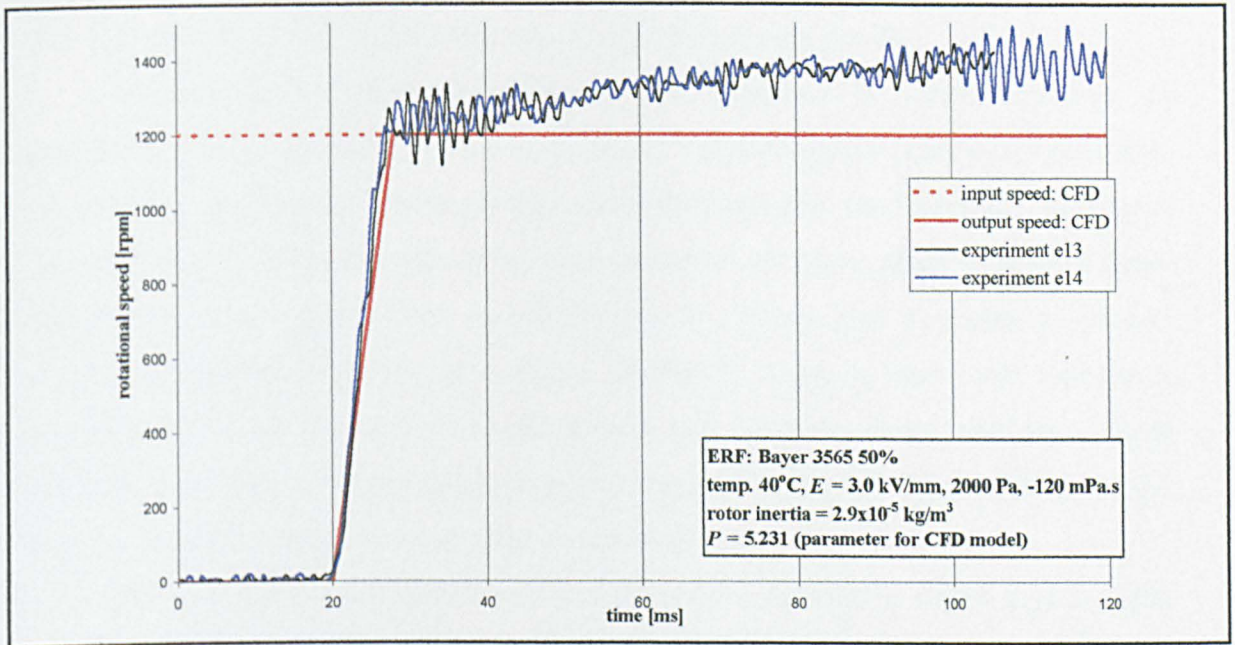


Fig. 5.70: Concentric clutch with an ERF medium. Experimental vs. CFD results for a yield-stress of 400 Pa.

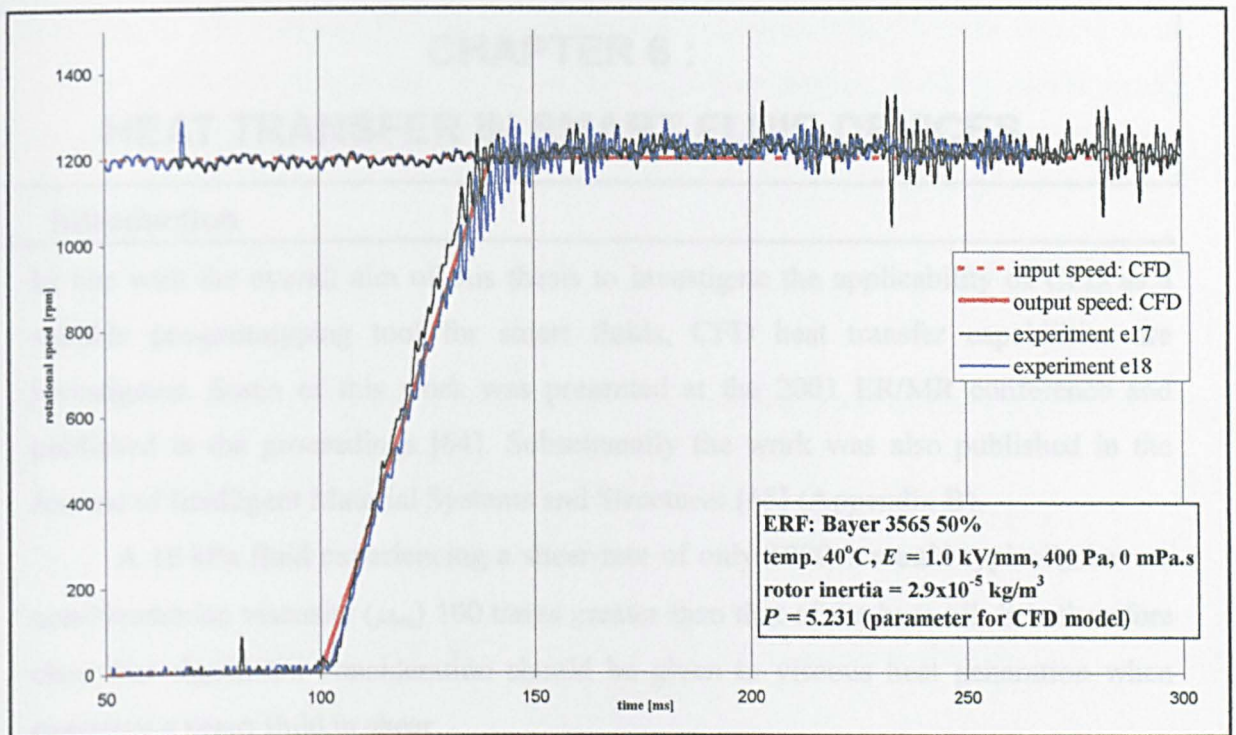


Fig. 5.71: Concentric clutch with an ERF medium. Experimental vs. CFD results for a yield-stress of 400 Pa.

...of a hole but will cover. For an ER fluid, this may be due to electrical breakdown through the fluid. For an MR fluid, the hole line occurs in the coil used to generate the magnetic field. A CFD method of modeling heat generation in an ER fluid due to breakdown is attempted using the concept of a current density.

A smart fluid clutch requires adequate heat dissipation in order to maintain an acceptable fluid temperature. This is particularly important when continuously switching between or within an electronically controlled variable configuration of output resistance. In some instances, multi-plate clutches will be required to provide large input torque in a small, low inertia device. It follows that a means to predict temperature within a device of complex geometry, using a fluid with non-linear properties, will be required for both steady and unsteady flow problems. These difficulties typically indicate a problem best solved by CFD. The majority of the operating regimes are achieved in non-uniformed packages.

Practical steady state heat transfer studies on a concentric clutch and a radial clutch apparatus are carried out in order to investigate, identify the physical parameters for heat transfer, the rate of heat transfer from the clutch surface is calculated. Analytical and experimental methods are used in order to verify CFD results. After gaining a good understanding of the heat loss results problem in both steady and unsteady flow conditions, the best design for both single plate and multi-plate clutches, for the case of a radial clutch, both axial and

CHAPTER 6 :

HEAT TRANSFER IN SMART FLUID DEVICES

6.1 Introduction

In line with the overall aim of this thesis to investigate the applicability of CFD as a suitable pre-prototyping tool for smart fluids, CFD heat transfer capabilities are investigated. Some of this work was presented at the 2001 ER/MR conference and published in the proceedings [64]. Subsequently the work was also published in the Journal of Intelligent Material Systems and Structures [65] (Appendix B).

A 10 kPa fluid experiencing a shear-rate of only 1000 /s would typically have a non-Newtonian viscosity (μ_{nn}) 100 times greater than that of the base oil. It is therefore clear that significant consideration should be given to viscous heat generation when operating a smart fluid in shear.

In general, the generation of a yield-stress requires an electrical input. Consequently a Joule loss will occur. For an ER fluid, this loss is due to electrical conduction through the fluid. For an MR fluid, the Joule loss occurs in the coil used to produce the magnetic field. A CFD method of modelling heat generation in an ER fluid due to conduction is attempted using the concept of a current density.

A smart fluid clutch requires adequate heat dissipation in order to maintain an acceptable fluid temperature. This is particularly important when continually switching in order to achieve an electronically controlled variable configuration of output motion [66]. In some instances, multi-plate clutches will be required to provide large output torque in a small, low inertia device. It follows that a means to predict temperature within a device of complex geometry, using a fluid with non-linear properties, will be required for both steady and unsteady flow problems. These difficulties typically indicate a problem best handled by CFD. The majority of the necessary routines are inherent in most commercial packages.

Practical steady state heat transfer studies on a concentric clutch and a radial clutch apparatus are carried out in order to investigate underlying physical phenomena. For both clutches, the rate of heat transfer from the clutch surface is calculated. Analytical and experimental methods are used in order to verify CFD results. After gaining a good understanding of the basic heat transfer problem in both clutch configurations a study was then undertaken to determine the best designs for both single plate and multi-plate clutches. For the same outer radius dimension, both radial and

concentric clutch designs offer similar dynamic capabilities. It may well be that the heat transfer characteristics of the device dictates the best design. A CFD model could quickly indicate the best design without resorting to prototype experimentation for comparisons.

6.2 Energy Source Terms

6.2.1 Viscous Heating

In the CFD method, the resultant magnitude of shear-stress at a cell centre is given by:

$$\text{resultant magnitude of shear stress } (\tau) = \mu_{nn} \dot{\gamma}. \quad (6.1)$$

The amount of energy that is generated within the cell due to viscous forces is then:

$$\text{heat generated in each cell} = \tau \cdot \text{vol} \cdot \dot{\gamma} \left[\frac{\text{N}}{\text{m}^2} \cdot \text{m}^3 \cdot \frac{1}{\text{s}} = \frac{\text{Nm}}{\text{s}} = \text{watts} \right], \quad (6.2)$$

where *vol* is the cell volume. This is essentially how a CFD package can calculate the viscous energy source of each cell.

For the situation of laminar steady Bingham plastic flow between two flat discs of radius (*R*) separated by distance (*h*), rotating at relative speed (Ω):

$$P_{vis} = N \cdot \Omega = \frac{\pi \mu_e \Omega^2}{2h} R^4 + \frac{2\pi \tau_y}{3} R^3. \quad (\text{from section 3.3.3}) \quad (6.3)$$

This simple analytical model was compared with results from a CFD model. The model consisted of an axisymmetric grid (only 20 x 20 cells). The lower disc is located at $x = 0$ ($\omega = 0$), and the upper disc at $x = h$ ($\omega = \Omega$). To eliminate end effects a linear velocity profile was set on the end wall ($w = R\Omega x/h$). The energy model with viscous heating effects was enabled. All walls were set at a temperature of 300 K¹.

The total heat flux leaving the clutch was determined using the surface heat flux command and compared to eqn(6.3). Over a wide range of parameters, no obvious difficulties were found². For example, Fig. 6.1 shows very precise agreement at two different fluid strengths.

6.2.2 Electrical Heating in an ER fluid Due to Conduction

When electrical current (albeit a low one) passes through an ER fluid, consideration

¹ Otherwise all walls would be by default isothermal.

² For the Fluent5 CFD package it was discovered that viscous heating effects were not being calculated when the axisymmetric swirl model with the coupled solver was used.

may have to be paid to heating through conduction/resistance. The fluid has a resistance in which electrical power is dissipated. The amount of dissipation will depend upon the magnitude of the current and voltage ($P = IV$). It could well be that this magnitude is on a par with the amount of viscous heating. During fluid quantification a current density (j) can be calculated by dividing the local current (I) by the local plate surface area (A_s):

$$j = \frac{I}{A_s} \left[\frac{\mu\text{A}}{\text{cm}^2} \right]. \quad (6.4)$$

Within a cell, the amount of electrical power being generated can be given by:

$$P_{elec} = j \cdot E \cdot vol \left[\frac{\text{A}}{\text{m}^2} \right] \cdot \left[\frac{\text{V}}{\text{m}} \right] \cdot \text{m}^3 = \text{watts}. \quad (6.5)$$

It has been proposed that measurements of current density fit the following function for an ER fluid [31]:

$$j = PE + QE^2. \quad (6.6)$$

Constants P and Q have units [nA/V] and [fA/V^2 or 10^{-15} A/V^2] respectively. They can be found by plotting j/E against E . For $Q = 10$, $j = 16 \mu\text{A/cm}^2$ at 4 kV/mm . $\text{Log}Q$ is a linear function of the concentration of active species in the solid, and this seems to be true of all ER fluids. Q is also sometimes a function of temperature:

$$Q = Q_o \exp\left(-\frac{\Delta H}{RT}\right). \quad (6.7)$$

A plot of $\text{log}Q$ vs. $1/T$ can therefore be used to give a value of ΔH for a given solid.

The CFD model from section 6.2 was modified to include a sub-routine that can calculate the electrical heating. The sub-routine written as shown in Table A.4 (Appendix A) allows a source term (watts/m^3) to be selected in Fluent. One disc is set at zero volts and the other at both 500 and 1500 to give a yield-stress of 1 kPa and 3 kPa.

The sub-routine calculates the magnitude of the excitation in the cell and then determines $j \times E$. Fig. 6.1 shows good agreement with theory for two different excitations. For both excitations, a value of $30 \mu\text{A/cm}^2$ was assumed. This is on the high side corresponding to an ER fluid at a high temperature. For the 3.0 kPa fluid it can be seen that at 70 rpm the viscous and heating effects are on a par. It therefore likely that viscous as opposed to electrical heating effects are going to be more significant.

Conclusion

There is no problem in determining viscous heating. Heating through electrical conduction can be calculated provided the current density is known. The function j is also temperature dependent. However, this model may be too simplistic, as shear-rate is also a factor. A detailed study to determine the function may be required. In most cases, it may be possible to ignore electrical heating effects. It can however be noted that equations (6.3), (6.5) & (6.6) indicate that:

$$P_e = f(E^3) \quad , \quad P_{vis} = f(E^2) \quad \text{where} \quad \tau_y = f(E^2), \quad (6.8)$$

thus for large voltages, electrical heating may be more dominant than viscous heating.

6.3 Heat Transfer from a Smart Fluid Radial Plate Clutch Surface

Heat dissipation from a radial plate clutch was investigated. This was in line with testing the CFD heat transfer capability and is a problem of some interest. Experimental results over a range of angular speeds and fluid gap widths were compared to analytical and CFD solutions.

The upper plate is driven and the lower plate, being thermally insulated, is held stationary. The work rate (ΩN) is equated to the heat transferred into the upper plate. Under thermal equilibrium, energies can be equated to determine temperature gradients. Shear-rate in this radial device varies with radius, inviting concern with respect to temperature gradients along the oil film and plates.

For the experimental study, the working fluid was Tellus 37 oil. Using a smart fluid at this early stage was not necessary. At this juncture detailed thermal properties of a smart fluid are not accurately known, and these would be required if the CFD model were to provide accurate results. In addition, a complication in separating out the electrical heating would also arise.

6.3.1 Radial Clutch Description

The clutch comprises two mild steel (EN3) radial discs (10 mm wide & 85 mm dia.). The upper disc is attached to a motor by a solid shaft of 20 mm dia. of the same material (Fig. 6.2). This shaft is insulated (60 mm length, 36 mm dia.). Gauge blocks (slip gauge) were used to set a gap between the discs, which contains hydraulic oil of known fluid properties (Tellus37).

The bottom plate was held stationary and thermally insulated with use of Tufnol and Kao wool so that a zero heat flux boundary condition could be assumed. Five k-type thermocouples are implanted approximately 1.0 mm away from the wetted

surface, located at radial positions of 0, 10, 20, 30 and 40 mm. To allow for a 1D analysis the outer edges of the device and driving shaft are also insulated.

It was to become clear that determining the amount of heat conducted up through the shaft required a temperature (T_{sh}) to be measured¹. The accuracy of an available infra-red camera that could remotely measure this temperature was deemed inadequate. The temperature T_{sh} was therefore inferred from a near air temperature. To calculate the amount of heat convection from the disc surface, the bulk air temperature (T_{∞}) was also measured.

6.3.2 Experimental Method

All the thermocouples were first checked to be working correctly and calibrated. The gap-size was set at either 0.5, 0.75 or 1.0 mm. Temperature readings were taken and then the motor was set to rotate at 500, 750 or 1000 rpm. Temperature readings were then taken every twenty minutes or so until the temperatures had reached their steady state values. The readings consisted of the five input plate surface temperatures (T_i), two readings above the plate to allow an average T_{∞} to be determined, and the near air temperature (T_{sh}) (Fig. 6.2).

6.3.3 Analytical Model

Very detailed notes on the analysis can be found in [63]². The rate of steady state heat transfer at constant rotational speed is considered. Insulation on lower and circumferential surfaces allows 1D heat transfer to be assumed. Furthermore, it is assumed that all mentioned temperatures are uniform in both radial and circumferential directions - a key assumption that would later be verified by experimental and CFD results.

The solution of heat transfer in the experimental device does not require the detailed distribution of temperature within the individual parts. It is enough to take into consideration just inner T_i and outer T_o temperatures of the rotors (wetted surfaces), disc surface temperature (T_s), surrounding air temperature (T_{∞}) and the shaft temperature (T_{sh}) at known length away from the upper disc surface. Newtonian fluid is situated between the stationary and rotating disc having a viscosity³ that is dependent upon the

¹ A colleague (Dr. V. Oravsky, [63]) had insisted that upper shaft temperature would be equal to the air temperature.

² I had my name removed from this paper due to disagreement on parts of the analysis. My experimental data was used in this paper.

³ Formulae described in [63] to predict manufacturers viscosity specification.

average fluid temperature $(T_i/2 + T_o/2)$:

$$\mu_e = 0.089 \frac{1 - 0.31t}{1 + 0.94t} \quad t = 0.05 \left(\frac{T_i + T_o}{2} \right) - 1.0 \quad (6.9)$$

Heat Balance

Mutual comparison of the heat flows provides a system of equations defining the three unknown temperatures T_s , T_i and T_o :

$$P_{in} = \dot{Q}_{oil} = \dot{Q}_{output\ disc} = \dot{Q}_{shaft} + \dot{Q}_{surface} \quad (6.10)$$

Frictional tangential forces in the fluid generate an amount of heat equal to $N\Omega$:

$$P_{in} = N\Omega = 0.5\pi\mu_e\Omega^2 R^2/h \quad (6.11)$$

This heat is transferred through the oil, output disc and shaft (via conduction):

$$\dot{Q}_{oil} = hA_d(T_i - T_o)/h_{oil} \quad \text{and} \quad \dot{Q}_{output\ disc} = hA_d(T_o - T_s)/h_{output\ disc} \quad (6.12)$$

A proportion of the heat is transferred from the rotating disc into the surrounding air via convection at a rate approximated by Newton's law of cooling:

$$\dot{Q}_{surface} = \bar{h}(A_d - A_i)(T_s - T_\infty) \quad (6.13)$$

The heat transfer coefficient for convection was given using a semi-empirical relationship expressed through averaged Nusselt ($N\bar{u}$), Reynolds (Re) and Prandtl (Pr) numbers [67]. The expression is for a horizontal disc (no shaft) rotating at a speed such that the flow is laminar ($Re < 2.5 \times 10^5$). This expression is assumed appropriate to our model:

$$N\bar{u} = (0.277 + 0.105Pr)Re^{0.5}, \quad \bar{h} = N\bar{u} \cdot k_{air}/R \quad (6.14)$$

Rotating Shaft

To determine \dot{Q}_{shaft} , two different methods are employed. The first (*model-one*), assumes that at a certain vertical position on the shaft the temperature reaches the bulk air temperature (T_∞). The experimental data is then used to determine an empirical coefficient for the shaft ($W/m^2/^\circ C$) so that the theoretical temperatures match experimental ones. This fictive parameter associated with \dot{Q}_{sh} is described as 'calibrating the theoretical model'. The method absorbs all other uncertainties that may be present in the experimental set-up. This model was devised by Dr V. Orskay and is presented in detail in [63]. Unfortunately, I couldn't agree with the applicability of his

model to this problem so a second method (*model-two*) was devised. At the very least *model-one* does not serve the purpose of helping to validate the CFD results; the fictive parameter absorbs all errors allowing the theoretical model to compare well with the experimental results and does therefore not allow the CFD results to be compared on an equal footing.

Model-two assumes that the temperature of the air at a location very close to the shaft (T_{sh}) is representative of the true temperature in the shaft at this location (Fig. 6.2). This allows the conductivity equation to be applied for heat rate through the shaft:

$$\dot{Q}_{sh} = k_{sh} A_{sh} (T_s - T_{sh}) / h_{sh}. \quad (6.15)$$

This method uses the exact experimental device geometry, material properties and measured temperatures, and is thus a more practical and realistic model. That is providing the assumption in determining T_{sh} is appropriate. This assumption is thought to be quite justifiable because very little heat could actually escape from the shaft by convection. This is because the shaft has a small surface area, and the supporting metal structure acts as a large heat sink and consequently a more favourable means for the heat to be dissipated (Fig. 6.2).

Solution

Mutual comparison of the above heat flows, provides a system of equations defining the three unknown temperatures T_s , T_u and T_i . The shaft (T_{sh}) and surrounding air (T_∞) temperatures are known, allowing theoretical T_i to be determined using a spreadsheet which solves the above equations using a simple iterative procedure. In order to do this the fluid air properties are linearised as shown in Table 6.1.

thermal conductivity of steel	$k_s = 51.836 \text{ (W/m.K)}$
thermal conductivity of oil	$k_o = 0.134 \text{ (W/m.K)}$
viscosity of air	$\mu_{air} = 4.40 \times 10^{-8} T_{air} + 5.26 \times 10^{-6} \text{ (kg/ms)}$
density of air	$\rho_{air} = -0.002948 T_{air} + 2.0618 \text{ (kg/m}^3\text{)}$
thermal conductivity of air	$k_{air} = 7.41 \times 10^{-5} T_{air} + 0.00401 \text{ (W/m.K)}$
Prantel Number for air	$Pr_{air} = -1.9 \times 10^{-4} T_{air} + 0.765$

Table 6.1: Linearisation of the fluid air properties, and other material proprieties.

6.3.4 CFD Model

The following table summarises the CFD model used in this section.

software	Fluent5, finite volume, segregated solver	
Physical Model	Flow is laminar in both oil and air regions. Viscous heating terms are included. Buoyancy terms in the air region are included ($g = 9.81\text{ms}^{-2}$).	
fluid properties	air (ρ, μ, k)	properties are linearised and are a function of cell temperature as indicated Table 6.1
	oil (Newtonian)	Tellus 37: properties as a function of cell temperature as indicated by eqn(6.9)
boundary conditions	Insulated walls are set to have zero heat flux. Rotating parts are set to the correct angular velocity. The shaft end is set to temp. T_{sh} . The boundary of the air region is placed at the vertical position equal to the T_{∞} location. This boundary is then set to be equal to atmospheric pressure and temp. T_{∞}	

Table 6.2: Summary of CFD model used to solve a single plate radial clutch with heat transfer model.

The CFD model was set up in comparison to the analytical model that used *model-two* to calculate the heat conduction in the shaft. The exact geometry of the experimental device was used to produce an axisymmetric grid. Table 6.2 outlines which relevant models were used and the boundary conditions that were applied to close the system of equations. CFD involves the full set of Navier-Stokes and energy equations, thereby avoiding the requirement for the semi-empirical heat transfer coefficient for convection as used in theoretical analysis.

Convergence was verified by making sure that the residual history of each equation was sufficiently low and that the net heat-flux through the appropriate parts was the same. Grid sufficiency was met using a built in grid adaptation facility, which increases the grid density in regions where the derivatives of temperature were high.

6.3.5 Results and Discussion: Experimental vs. CFD vs. Numerical

The essential results are shown in Table 6.3. Both experimental and CFD data verified that the assumption of uniform radial temperature distribution in all metal and fluid parts was valid. No variation above 0.1°C on the lower plate was recorded in all experiments. The CFD analysis clearly showed that although there is a radial distribution in shear-rate, the high conductivity of the metal parts distributes the temperature evenly.

gap width	speed	experimental temperature			theoretical input rotor predictions			Q_{sh}/Q_s	
		shaft	bulk air	input rotor	difference from experimental			model-two	CFD
		T_{sh}	T_a	T_l	model-one	model-two	CFD		
mm	rpm	°C	°C	°C	°C	°C	°C		
0.5	500	24.9	25.4	28.1	0.3	2.1	1.8	3.9	3.1
		24.5	24.8	28.3	-0.5	1.5	1.2	3.7	2.9
	750	25.8	25.9	31.8	-0.2	3.1	2.4	2.9	2.2
		25.8	26.0	31.7	0.0	3.2	2.5	2.9	2.2
	1000	26.5	26.3	35.8	-0.7	3.5	2.5	2.4	1.9
		26.5	26.4	35.6	-0.4	3.7	2.7	2.4	1.9
0.75	500	26.6	27.0	29.1	0.1	1.3	0.8	3.9	3.1
		26.6	27.0	29.2	0.1	1.2	0.7	3.9	3.1
	750	26.6	26.5	31.6	-0.5	2.0	1.0	2.8	2.2
		26.4	26.4	31.4	-0.3	2.1	1.1	2.8	3.2
	1000	24.5	24.2	32.3	0.0	3.5	1.7	2.4	1.9
		24.5	24.5	31.7	0.8	4.1	2.3	2.4	1.9
1.00	500	27.4	27.6	29.0	0.5	1.5	0.9	3.7	3.0
		25.6	25.8	27.3	0.6	1.6	1.0	3.7	3.0
	750	25.4	25.4	30.1	-0.4	1.6	0.3	2.8	2.2
		27.1	27.2	31.0	0.2	2.1	0.8	2.9	2.3
	1000	25.4	25.3	32.0	0.3	3.0	1.0	2.4	1.9
		25.3	25.2	31.9	0.3	3.0	0.9	2.4	1.9

Table 6.3: Comparison between measured experimental temperatures and theoretical predictions.

Theoretical *model-one* is seen to give temperature results closer to the experimental results than *model-two*. This is because it allows uncertainties to be absorbed by virtue of the empirical coefficient for the shaft. This parameter is essentially chosen to make the theoretical model fit experimental results and this is why the model both over- and under-predicts the experimental results. *Model-one* is not particularly useful, as the experimental results were needed before any predictions could be made. In my opinion, *model-one* is not based upon sound methodology, and this is why *model-two* was employed.

Theoretical *model-two* is very much less subjective and provides a much fairer means for comparison with the CFD method. The model over predicts the experimental temperature results (by 4.1 °C in one case). The CFD results are also over-predictions but by far less of a margin. These higher reading are to be expected due the theoretical and CFD models being ideally insulated (Fig. 6.2), whereas experimentally it was not. So that a 1D heat flow assumption could be used for the theoretical analysis, most of the apparatus was insulated. As a result, the area assumed ideally insulated is relatively large in comparison to the thermally open surfaces. Although the conductivity of the insulating materials is low, the large surface would give rise to some additional heat loss. This would easily explain the 0.3-2.7 °C over-prediction of the CFD model.

It would appear that theoretical *model-two* does not sufficiently allow enough heat to be dissipated. Apart from the convective part of the model, all aspects are quite

similar to the CFD method, and thus it is likely to be this part of the model that is the problem. The semi-empirical expression used to calculate a heat transfer coefficient (\bar{h}) is for a complete rotating disc, and does not take into account the shaft/wall geometry in the experimental set up (Fig. 6.2). It was however hypothesized [63] that the expression would remain true if the area for convection was based upon the disc area minus the area of the shaft. It was deemed prudent to determine whether the semi-empirical formulae eqn(6.14) was valid. In a CFD simulation, a hypothetical disc was set to rotate in a large region of air, an amount of heat flux was set to leave the disc and enter the atmosphere. The model is summarised in Table 6.4.

software	Fluent5, finite volume, segregated solver	
Physical Model	Flow is laminar in both oil and air regions. Viscous heating terms are included. Buoyancy terms in the air region are included ($g = 9.81\text{ms}^{-2}$).	
fluid properties	air (ρ, μ, k)	properties are linearised and are a function of cell temperature as indicated Table 6.1
boundary conditions	Rotating disc was set to the correct angular velocity. This air boundary condition is then set to be equal to atmospheric pressure and temp. T_∞	

Table 6.4: Summary of CFD model used to solve heat transfer from a rotating disc.

Setting a far field temperature (T_∞) closes the system of governing equations and allows T_s to be determined. As shown in Fig. 6.3 over a range of parameters, remarkably close correlation between theory and CFD was found. A shaft and wall constraint as seen in the experimental set-up was then introduced. Now as shown in Fig. 6.4, the semi-empirical expression over predicts the surface temperature. This would explain why the CFD results are closer to the experimental data than the comparable theoretical *model-two*, and why CFD gives lower values of $\dot{Q}_{shaft} / \dot{Q}_s$. In this case, it is important to note the necessary inclusion of the driving shaft, which carries away a significant proportion of the generated heat.

It can be noted from Table 6.3 that for a gap width of 0.5 mm the shaft temperature increases with speed. The opposite effect is observed for 0.75 & 1.0 mm gap widths. The reason for this is likely to be related to the ratio of power being generated, to that being able to leave through the disc. An increase in Ω allows greater heat convection from the disc that may not be sufficient to counter the increase in viscous heat generation. Therefore, a small gap width in which the heat generation is larger, the shaft may heat up as the speed is increased. In addition, the final shaft temperature is dependent upon the outside air temperature (T_∞) that can differ between

experiments.

6.4 Heat Transfer from a Smart Fluid Concentric Clutch Surface

A second practical investigation involving the dissipation of heat from a concentric clutch surface was carried out. The clutch maintains a steady speed and so the smart fluid is shearing at a steady rate. The problem would further verify the usefulness of CFD. The outer input rotor is driven at a constant speed (Ω), whilst the inner output rotor is held stationary (Fig. 6.5).

Previous Work

Semi-empirical analytical work and some sparse experimental data on this specific problem has already been done [68]. Initially the work by Smyth *et.al.* [68] was reviewed in detail. The procedures are found to be similar to those encountered for the radial clutch (section 6.3). In a state of thermal equilibrium, the analytical theory equates the work rate (ΩN) to heat transferred through the outer casing by conduction and then convection. This allows temperatures to be predicted in relation to the bulk air temperature (T_∞). The device and the analytical model are illustrated in Fig. 6.5.

In this work, it was correctly hypothesized that the model chosen to represent the convection is all-important. The values of Re and Gr dictate the form of convection and an appropriate model for $N\bar{u}$ that in turn dictates the value of \bar{h} (W/m^2). To make the calculation easier, the air properties were linearised (between $20^\circ C$ and $100^\circ C$) and found to accurately correspond with those used in Table 6.1¹.

6.4.1 Analytical Model of Convection from a Rotating Cylinder

The semi-empirical model corresponds with that in [68]. Here the clutch length (L_i) is taken to equal the outer surface length (L_s) (Fig. 6.5). For a mean radius (r_m) the torque (N) results in a frictional heating and input power (P_{in}):

$$P_{in} = N\Omega = 2\pi r_m^2 L_i \cdot \left(\mu_e \frac{r_m \Omega}{h} + \tau_y \right) \cdot \Omega \quad \text{when } \tau_y = 0, \quad P_{in} = \frac{2\pi r_m^3 L_i}{h} \mu_e \Omega^2. \quad (6.16)$$

This heat is dissipated from the outer casing of diameter (D) into the surrounding air of bulk temperature (T_∞) by convection at a rate approximated by Newton's law of cooling:

¹ Properties in [68] are linearised in terms of $^\circ C$, those in Table 6.1 are linearised in terms of Kelvin.

$$P_{in} = \dot{Q}_s = \bar{h}\pi DL_i(T_s - T_\infty). \quad (6.17)$$

Using eqn(6.16), for a given speed, fluid properties, and clutch dimensions, the rate of heat transfer from the clutch surface \dot{Q}_s can be calculated. Once the heat transfer coefficient for convection is known eqn(6.17) can be used to calculate the rotor surface temperature (T_s). This is determined by calculating the mean Nusselt number ($N\bar{u}$) using the semi-empirical relations from [68]:

$$N\bar{u} = 0.456 (Gr \cdot Pr)^{0.25}, \text{ free convection, } Re < (Gr/Pr)^{0.5} \quad (6.18)$$

$$N\bar{u} = 0.18 [(0.5Re^2 + Gr)Pr]^{0.315}, \text{ mixed convection, } Re \leq 5 \times 10^4 \quad (6.19)$$

The non-dimensional parameters are given as:

$$N\bar{u} = \frac{\bar{h}D}{k}, \quad Re = \frac{\rho\Omega D^2}{\mu}, \quad Gr = \frac{\rho^2 \beta g D^3 \Delta\theta}{\mu^2}, \quad (6.20)$$

and the fluid air properties are given as in Table 6.1 using a mean air temperature (T_m):

$$T_m = \frac{T_s - T_\infty}{2}. \quad (6.21)$$

With care, it is a relatively simple matter to use a spreadsheet¹ to solve for T_s . Once T_s is known the output plate temperature (T_o) at r_o can be calculated from the following conduction equation:

$$P_{in} = \dot{Q}_{\text{output rotor}} = \frac{2\pi k_s L_i}{\ln(r_s / r_o)} (T_s - T_o). \quad (6.22)$$

Subsequently the input plate temperature can also be calculated:

$$P_{in} = \dot{Q}_{\text{fluid}} = \frac{2\pi k_f L_i}{\ln(r_o / r_i)} (T_i - T_o). \quad (6.23)$$

It can be noted that when eqn(6.17) is equated with any of the above heat flow equations the lengths L_i are cancelled out. Hence, the clutch length has no effect on the distribution of temperature.

6.4.2 CFD Model of Convection from a Rotating Cylinder

The following table summaries the CFD model used.

¹ Microsoft Excel was used.

software	Fluent5, finite volume, segregated solver	
basic assumptions	Viscous heating terms are included. Buoyancy terms in the air region are included ($g = 9.81\text{ms}^{-2}$).	
turbulence model	RNG $k-\varepsilon$ model with the two layer zonal near wall model.	
fluid properties	air (ρ, μ, k)	ideal gas: properties function of cell temp. as indicated Table 6.1
discretisation of flow equations	interpolation scheme	1 st Order
solver FVM	pressure-velocity	SIMPLE
	grid: smart fluid	20 cells within gap (hexagonal)
	grid: air	tri, fine at the wall to model boundary layer
boundary conditions	See Fig. 6.6.	

Table 6.5: CFD Summary: Concentric clutch model.

There was no problem with the conduction part of the model. However, it was quickly discovered the convection part of the model would be much more difficult to get right. This is because of the effect of buoyancy in the air region. Consequently, the problem is 3D. However, since the clutch length has no effect on the solution the clutch can be considered infinitely long, allowing the problem to be set-up using 2D coordinates as shown in Fig. 6.6.

After investigating several different set-ups the best way to model the all important air region was to put the clutch in a box surrounded by air (Fig. 6.6). In all, there are four material regions: the outer fluid air region, the solid outer shaft region, the inner smart fluid region with gap-width (h) and the solid inner shaft region. Each region had to be correctly specified in the CFD model. The outer rotor is set to rotate at angular speed (Ω). The difficulty now lies in modelling the air region, it was important to take great care in correctly setting all aspects affecting the buoyancy driven flow. This involved following recommendations from the Fluent5 manual [69] for this particular type of flow.

The energy model is turned on and a gravitational body force is set to act in the downward y -direction. An operational density (ρ_o) had to be specified for it used to specify pressure boundary conditions. In the CFD model:

$$p'_s = \rho_o g y + p_s. \quad (6.24)$$

The static pressure set at a boundary is p'_s and so it is important to know the value of ρ_o . This was chosen to correspond to the mean value in the analytical model. In order to

correctly set the pressure on the side boundaries the pressure had to be set as a function of y . However, the precise value of ρ_0 didn't significantly affect the solution provided it was relatively representative (Fig. 6.7).

As recommended in the Fluent5 manual [69], the more accurate body force weighted discretisation scheme for pressure was used. In addition, the discretisation schemes for momentum and energy were increased to second order. The shape and size of the grid was a very important consideration. A combined trilateral (3-sides) and quadreic (4-sides) grid was used (example shown in Fig. 6.8 and Fig. 6.9). This allowed that main area of influence to be economically filled while allowing the remaining air region to be economically filled. This grid would allow the majority of the flow to be well modelled.

A very significant part of the model includes turbulence. The flow is a combination of mixed and forced convection ($Re > 10^3$), and so it is important to consider turbulence. There are several available turbulence models available for use. The flow here is not particular complex and so the obvious choice was the popular tried and tested $k-\varepsilon$ model. This model is generally accepted to be robust, economical and accurate for a wide range of flows. The RNG $k-\varepsilon$ variation was used because is well suited for modelling swirling flows.

A significant part of the model included a turbulent wall function. Having chosen the RNG $k-\varepsilon$ model, the standard wall function model would be the obvious choice, as it requires only a minimal number of cells near the clutch wall surface. For this model the turbulence wall parameter¹ (y^+) must be $> 30\sim 60$ for a near wall region log-law to be valid. However, it proved impractical to get a practical value of y^+ without making the mesh ludicrously coarse. A course grid at the wall meant it was difficult to adequately resolve temperature gradients. The Two Layer Zonal near wall model was therefore used. This model requires at least 10 cells to be within the viscosity-affected near wall region ($Re_y < 200$) and most ideally for $y^+ = 1.0$. This was achievable by increasing the grid density in the near wall region, though a combination of adapting cells which had high temperature gradients, and near wall cells with y^+ values greater than 1.0. Fig. 6.11 illustrates a check that there are at least 10 cells in the $Re_y < 200$ region.

6.4.3 Results and Discussion

The main parameters were chosen to correspond with those used by Smyth *et.al.* [68].

¹ y^+ : dimensionless parameter representing the distance from the wall to the first adjacent cell, is only a parameter in the fist cell next to wall.

These parameters with overall results are shown in Table 6.6. The Reynolds number is well above the value $\{(Gr/Pr)^{0.5}\}$ required to enter the mixed¹ convection regime. Furthermore, Re remains below the value (5×10^5) required for eqn(6.19) to remain valid.

parameters	fluid gap width	mm	0.5	0.5	0.5	0.5	0.5	0.5
	mean fluid radius	mm	30.25	30.25	30.25	30.25	30.25	30.25
	rotor diameter	mm	80	80	80	80	80	80
	input rotor speed	rpm	500	750	1000	500	750	1000
	fluid yield stress	kPa	0	0	0	500	500	500
	plastic viscosity	mPa.s	50	50	50	50	50	50
	mean air temp.	°C	20.0	20.0	20.0	20.0	20.0	20.0
theory	Re		21656	31995	41931	20303	29672	38538
	free or forced convection		mixed	mixed	mixed	mixed	mixed	mixed
frictional heating	theory	watts	48	107	191	198	333	492
	CFD		47.6	106.9	190.3	197.3	331.8	490.2
	difference	%	-0.1	-0.4	-0.4	-0.9	-1.2	-1.5
main surface temp.	theory	°C	28.3	34.5	41.6	54.7	65.3	76.0
	CFD		26.45	34.85	46.85	47.85	65.85	91.85
	difference		-1.9	0.3	5.3	-6.8	0.5	15.8

Table 6.6: Comparison of results between CFD and theoretical predictions for heat transfer in a concentric clutch.

For low values of viscous heating, there is good agreement between the semi-empirical model and the CFD result. Such agreement can be seen in Fig. 6.12 for un-excited fluid ($\mu_e = 50 \text{ mPa.s}$ & $\tau_y = 0 \text{ kPa}$) over a range of 500-1000 rpm. The semi-empirical theoretical results correspond well with those in Smyth *et.al.* [68]. Thus, it is likely that the theoretical semi-empirical model has been correctly implemented.

Under excitation, for a yield-stress of 500 Pa, frictional heating is greatly increased. The CFD model predicts the same amount of heating as the theoretical model (Table 6.6). However, the difference in the theoretical temperatures is more severe Fig. 6.12. Nevertheless, the coloration is still within a suitable range considering the simplicity of the semi-empirical model. Fig. 6.13 shows a typical example of the temperature distribution

6.5 Comparison of Clutch Designs

In this section, concentric and radial clutch designs are compared. Only the steady state situation is considered in which significant viscous heating occurs due to a constant rotor speed difference (Ω). In order to produce a competitive commercial device it is

¹ combined free and forced convection

important to consider acceleration ($\alpha = N_{eo}/I_o$) and control ratio (N_e/N_o) in addition to the overall magnitude of N_{eo} . Here N_{eo} is the overall torque, N_o is the no-field torque, and N_e is the torque from the smart fluid effect ($= N_{eo} - N_o$). The angular acceleration (α) is only the value at the instant when the output rotor is released. However, as found in section 5.4, the shear stress and thus α will remain approximately constant for a practical device. To maximise this acceleration, the output rotor would be made from lightweight material, whereas the input rotor would consist of a heavier, high conducting material to maximize heat dissipation and help reduce regulation.

6.5.1 Torque and Acceleration Comparison

By assuming a uniform casing and rotor thickness (z), it is possible to derive approximate equations for torque and inertia based upon the number of internal rotor channels (n). Here the input and output shafts are not considered, as they will affect the results equally in each clutch design.

Multi Channel Concentric Clutch

With reference to Fig. 6.14, the following applies to a multi-channel concentric clutch with each rotor of mean radius (r_m), electrode length (L_e), outer casing length and radius (L_c and R_c respectively), and number of internal rotors (n):

$$N_{eo} \approx \sum_n 2 \left\{ 2\pi r_m^2 L_e \left(\tau_y + \frac{\mu_e r_m \Omega}{h} \right) \right\}, \quad (6.25)$$

$$I_c \approx \sum_n 2\pi \rho z r_m^3 L_e, \quad (6.26)$$

$$\text{when } n=1 \quad \frac{N_{eo}}{I_c} = \frac{2}{\rho z} \left(\frac{\tau_y}{r_m} + \frac{\mu_e \Omega}{h} \right), \quad (6.27)$$

$$R_c = (r_m)_{\max} + (h + 1.5z), \quad L_c = L_e + 2(z + h) \quad (\text{outer casing dimensions}) \quad (6.28)$$

Multi Channel Radial Clutch.

With reference to Fig. 6.15 the equivalent equations for a radial clutch with outer casing length and radius (L_r and R_r respectively), and number of inner rotors (n) are:

$$N_{eo} = 2n \left\{ 2\pi r_m^3 \left(\frac{\tau_y}{3} + \frac{\mu_e r_m \Omega}{4h} \right) \right\}, \quad (6.29)$$

$$I_r = \frac{1}{2} \rho n \pi z r_m^4, \quad (6.30)$$

$$\frac{N_{eo}}{I_r} = \frac{2}{\rho z} \left(\frac{4}{3} \frac{\tau_y}{r_m} + \frac{\mu_e \Omega}{h} \right), \quad (6.31)$$

$$R_r = r_m + (h + z), \quad L_r = 2n(z + h) + z \quad (\text{outer casing dimensions}). \quad (6.32)$$

Some important conclusions can now be drawn. The radial clutch torque is dependent upon r_m^3 . For the concentric clutch, the torque is dependent upon r_m^2 , but L_e also plays a role. For a single rotor, dual channel clutch ($n = 1$), $N_o \ll N_e$, then for the same torque {eqn(6.25) = eqn(6.29)} and mean radius, the lengths L_e , L_r and L_c can be determined:

$$L_e = \frac{1}{3} r_m \quad \text{giving} \quad L_r = 3z + 2h \quad \& \quad L_c = \frac{1}{3} r_m + 2z + 2h \quad \text{here} \quad (z \approx h) \ll r_m. \quad (6.33)$$

Here the concentric design length (L_c) is therefore much larger than the radial design length (L_r). Also, for the same torque {eqn(6.25) = eqn(6.29)}, when $N_o \ll N_e$, and with $L_e = r_m$ then:

$$r_m|_{\text{concentric}} = 0.69 r_m|_{\text{radial}}, \quad L_r = 3z + 2h \quad \& \quad L_c = r_m + 2z + 2h \quad \text{here} \quad (z \approx h) \ll r_m. \quad (6.34)$$

Here the concentric device is 69 % smaller in the radial direction but is significantly larger in the axial direction. The concentric design may therefore be more suited to radial confined geometry but will always be much longer than the radial clutch design for the same torque output. In addition, the ratio of N_e/N_o in the radial design is 25 % greater than in the concentric design. It can be noted that for both devices a smaller radius gives greater acceleration. On an acceleration basis, for a single dual channel ($n=1$) and when N_o is small, the radial clutch is more favourable by 33 %.

For a single dual channel ($n=1$), on a size-by-size basis, the radial clutch seems to be much better. For the radial design, adding more channels makes no difference to the acceleration. However, adding more channels to the concentric design will slightly improve the acceleration as α {eqn(6.26)} improves as the radius decreases.

6.5.2 Heat Transfer Comparison (Single Rotor Clutch)

Single rotor ($n=1$) dual channel, horizontal axis, radial (Fig. 6.14) and concentric (Fig. 6.15) clutch designs are now compared on a heat transfer basis.

Semi-Empirical Analytical Model

For a mean radius (r_m), casing dimension (z) and gap size (h), the overall case geometry (R_r & L_r) for the radial clutch is known {eqn(6.32)}. For the concentric design, L_e is also required. Due to the high thermal conductivity of the outer casing, the surface temperature (T_s) is likely to be approximately uniform. Thus, T_s is assumed to be uniform at all points on the clutch surface. Shafts will have similar effects in each design and are therefore not included. For a given speed, eqns (6.25) & (6.29) are used to determine N_{eo} . Using Newton's law of cooling, T_s can be calculated for a given bulk air temperature (T_∞):

$$P_{in} = N_{eo}\Omega = (T_s - T_\infty)(A_r\bar{h}_r + A_a\bar{h}_a). \quad (6.35)$$

Here $A_r\bar{h}_r$ and $A_a\bar{h}_a$ are the average rates of heat dissipation by convection in radial and axial directions respectively. These coefficients are dependent on the condition of the surrounding air flow, and are calculated using a mean Nusselt number ($N\bar{u}$) determined from the following semi-empirical formulas [67]:

$$(N\bar{u})_a = 0.4(Re^2 + Gr)^{0.25}, \quad Gr = \rho^2 \beta g R^3 \pi^{1.5} \Delta\theta / \mu^2, \quad (\text{vertical disc}). \quad (6.36)$$

$$(N\bar{u})_r = 0.18[(0.5Re^2 + Gr)Pr]^{0.315}, \quad Gr = \rho^2 \beta g D^3 \Delta\theta / \mu^2, \quad (\text{horizontal shaft}). \quad (6.37)$$

The electrode length (L_e) required for the concentric clutch model was chosen to make T_s equal in both clutch models. In summary, r_m , z , h , Ω , τ_y , μ_e and T_∞ are chosen. This allows T_s to be calculated for the radial clutch. For the same parameters, L_e is then calculated to obtain the same T_s for the concentric clutch model. The calculation was done in a spreadsheet with the air fluid properties being dependent on the mean temperature $(T_s + T_\infty)/2$.

CFD Model

In sections 6.3 and 6.4, CFD was used to model convective heat from the clutch surface. Here the convection problem investigated was two-dimensional. In this section, the aim was to analyse a three-dimensional convection problem. However, after initial attempts, it was deemed uneconomical to model this three-dimensional problem. This was partly due to the huge number of cells and thus computational time required, and inexperience in setting up a complex, buoyancy driven convective air problem. Given enough time and computational resources, solution to this problem is obviously achievable, but is not in the remit of this study. The objective here is to study the application of CFD to smart fluids, rather than model complex convective air problems.

In the previous sections, semi-empirical formulae from [67] have already been verified by CFD to be applicable. Even if the semi-empirical formulae are not entirely accurate, they are still appropriate for making an impartial comparison of the two clutch designs.

However, the CFD procedure is still useful for checking the approximations for torque and viscous heating found using eqn(6.25) and eqn(6.29). In addition, most significantly, the main assumption of a uniform surface temperature can be checked for validity.

When setting up the CFD model four regions had to be specified. The two fluid regions were the smart fluid and surrounding air, and two solid material regions included the inner output rotor and outer casing. The outer casing was surrounded with a 10 mm thickness of air which itself was closed off using a pressure boundary condition with temperature T_s . The inner rotor was set to rotate with speed Ω . All solution parameters were left at default values.

Results

For the parameters, $r_m = 30$ mm, $h = 0.5$ mm, $z = 1.0$ mm and $T_\infty = 25$ °C, the surface temperature (T_s) for radial clutch design can be calculated. The electrode length (L_e) can then be determined in order to achieve the same T_s in both clutch designs. This allows torque and acceleration for both designs to be compared. The results shown in Table 6.7, Fig. 6.16 and Fig. 6.17 indicate that for the same T_s , the radial clutch offers more acceleration. Also for the same T_s , the overall size and consequent surface area of the concentric design is larger than the radial one. This allows it to convert more heat, and thus can generate slightly more torque for the same surface temperature. However the acceleration from the radial device is still greater and the over size is smaller than the concentric design.

yield-stress		r_y	kPa	5				5				10				10				
plastic-viscosity		μ_p	mPa.s	50				100				50				100				
speed		Ω	rpm	250	500	750	1000	250	500	750	1000	250	500	750	1000	250	500	750	1000	
radial design	total torque	N_{eo}	analytical	Nm	0.572	0.579	0.585	0.592	0.579	0.592	0.605	0.619	1.138	1.144	1.151	1.158	1.144	1.158	1.171	1.184
			CFD		0.581	0.589	0.596	0.604	0.588	0.603	0.617	0.632	1.154	1.163	1.171	1.179	1.162	1.177	1.192	1.207
			difference	%	1.5	1.7	1.8	1.9	1.6	1.8	1.9	2.1	1.4	1.6	1.7	1.8	1.5	1.6	1.8	1.9
	viscous heating	P_m	analytical	Watts	15.0	30.3	46.0	62.0	15.2	31.0	47.6	64.8	29.8	59.9	90.4	121.2	30.0	60.6	92.0	124.0
			CFD		15.2	30.7	46.7	63.1	15.4	31.5	48.4	65.9	30.1	60.8	92.0	122.9	30.4	61.7	93.7	126.7
			difference	%	1.5	1.3	1.5	1.7	1.6	1.6	1.8	1.7	1.1	1.5	1.7	1.4	1.5	1.8	1.9	2.1
casing length	L_c	mm		4.0	4.0	4.0	4.0	4.0	4.0	4.0	4.0	4.0	4.0	4.0	4.0	4.0	4.0	4.0	4.0	
casing radius	R_c	mm		31.5	31.5	31.5	31.5	31.5	31.5	31.5	31.5	31.5	31.5	31.5	31.5	31.5	31.5	31.5	31.5	
acceleration	α	$\times 10^3 \text{ rad/s}^2$		165	167	169	171	167	171	175	179	329	331	333	335	331	335	338	342	
concentric design	total torque	N_{eo}	analytical	Nm	0.636	0.647	0.657	0.666	0.643	0.661	0.678	0.694	1.264	1.277	1.289	1.299	1.271	1.292	1.310	1.328
			CFD		0.650	0.663	0.675	0.685	0.658	0.678	0.697	0.715	1.282	1.302	1.314	1.325	1.290	1.318	1.338	1.357
			difference	%	2.2	2.4	2.7	2.8	2.3	2.5	2.7	2.9	1.4	1.9	1.9	2.0	1.5	2.0	2.1	2.2
	viscous heating	P_m	analytical	Watts	16.6	33.9	51.6	69.7	16.8	34.6	53.3	72.7	33.1	66.9	101.2	136.0	33.3	67.6	102.9	139.0
			CFD		16.9	34.4	52.6	71.5	17.1	35.2	54.4	74.6	33.5	67.9	102.9	138.5	33.7	68.7	105.1	142.1
			difference	%	1.5	1.5	2.0	2.5	1.6	1.6	2.1	2.5	1.2	1.5	1.6	1.8	1.3	1.6	2.1	2.2
casing length	L_c	mm		14.07	14.09	14.09	14.07	14.03	14.00	13.96	13.91	14.09	14.12	14.13	14.13	14.07	14.07	14.06	14.04	
casing radius	R_c	mm		32.0	32.0	32.0	32.0	32.0	32.0	32.0	32.0	32.0	32.0	32.0	32.0	32.0	32.0	32.0	32.0	
acceleration	α	$\times 10^3 \text{ rad/s}^2$		125	126	128	130	126	130	134	138	247	249	251	253	249	253	257	261	
surface temperature	T_s	$^\circ\text{C}$		340.6	358.8	373.2	385.7	341.1	360.2	375.7	389.6	381.9	417.9	446.0	470.3	382.4	419.3	448.6	474.3	

Table 6.7: Comparison between measured experimental temperatures and theoretical predictions.

The relative performances between the clutch designs can be expressed as a ratio between the radial and concentric design results. For a variety of fluid properties and speeds, this ratio does not change by more than a few percent (see Fig. 6.17). Fig. 6.17 clearly shows that for the same mean radius and surface temperature, the radial clutch gives approximately 10% less torque but 30% more acceleration than the concentric clutch. In addition the radial clutch length is more than half that of the concentric clutch. Fig. 6.18 shows how T_s increases with speed. The plastic-viscosity is found to play a noticeable but relatively insignificant role, due to it having a minimal effect on N_{eo} .

The CFD results for torque and generated heat agree to within 1-3 % of the analytical approximations (Table 6.7). The CFD values are slightly different due to rotor end effects, which are not accounted for in the semi-empirical solution. In the CFD model, the actual surface temperatures are found to be much higher than semi-empirical solution; this is because the CFD convective model is two-dimensional, when it should really be there-dimensional. However, since the smart fluid properties are not set to be temperature dependent the conductive model inside the clutch is still quite valid and allows the distribution and differences in temperature to be analysed. In both designs, only a very small variation in temperature occurs within the clutch itself and thus the uniform surface assumption is quite valid (Fig. 6.19). In which case, the constant surface temperature assumption appears to be valid. The high thermal conductivity of the outer casing evens the out surface temperature. In the radial design, the temperature is seen to be greater at a higher radius due to increased shearing.

6.5.3 Heat Transfer Comparison (Multi-Plate Clutch)

The single rotor study shows that the radial clutch type is a more favourable design – for a smaller size the radial device gives a similar torque output but more acceleration than the concentric design. It can be noted that for the radial design, increasing the casing length has no direct effect on α {eqn(6.31)}. However, this is not true for the concentric design in which the unused space below the first outer rotor can be utilised with more blades. A multi-plate clutch device was therefore studied next.

Practical sizes of casing were chosen (L & R). This dictated the number (n) of double channel segments that can be accommodated in both design configurations. Using a similar method as to that described in section 6.5.2, for a particular speed and fluid properties, the amount of torque, viscous heating and surface temperature could be calculated for both devices. In practice, the smart fluid properties will be a function of temperature. Since the shear rates are relatively low, the plastic-viscosity plays no significant role, in which case it is only the assumption that the yield-stress is the same for all temperatures that is in question. However, as can be seen in Fig. 3.31 a smart fluid is often designed to have a yield-stress that remains quite constant over a range of temperature, thus making this assumption a valid one.

Again, CFD models were used to check the validity of the constant surface temperature assumption and the accuracy of the magnitudes of torque and viscous heating.

Summary of Model

The input parameters are as followings, $h = 0.5$ mm, $z = 1.0$ mm, $\tau_y = 1.0$ kPa, $\mu_e = 50$ mPa.s, $\Omega = 250$ rpm and $T_\infty = 25$ °C. Several practical configurations of outer casing geometry were investigated (R & L). The input speed and yield-stress have only a proportional effect on the magnitude of viscous heating. It was discovered that even for relatively low values, significant viscous heating occurs, to the extent that the temperature rises way above the range in which the air properties were linearised. To reduce viscous heating, an additional criterion had to be set. This was that the clutch would be in shear for only 10 % of the time. This would be a more practical realistic state of operation:

running in shear 100 % of the time unrealistic mode of operation $P_{in} = N_{eo}\Omega$,

running in shear 10 % of the time realistic mode of operation $P_{in} = 0.1N_{eo}\Omega$.

The clutches are still being modelled as an unsteady problem, but with only 10 % of the

heating that would occur in an excited clutch in permanent shear. This is perfectly fine for the clutch comparison objective in hand, however if results that are more detailed were required an unsteady problem would result that could only realistically be solved using a CFD model.

Although the geometry is more complex, in essence the CFD model is no more complicated. In order to reduce the torque and thus viscous heating to correspond with the analytical model $\mu_{nn} = 0.1\mu_{nn}$ was set.

Results

Table 6.8 and Fig. 6.20 show the main results. Looking at the ratios of relative performance (Fig. 6.20) there is now virtually no difference between the two designs. For the same casing dimensions, torque, acceleration and surface temperatures are very similar.

yield-stress		τ_y	Pa		1000	1000	1000	1000
plastic-viscosity		μ_e	mPa.s		50	50	50	50
speed		Ω	rpm		250	250	250	250
casing length		L	mm		30	60	60	30
casing radius		R	mm		30	60	30	60
radial design	total torque	N_{eo}	analytical	Nm	0.102	18.70	2.048	9.35
			CFD		0.101	18.32	1.980	9.12
			difference		%	-1.4	-2.1	-3.4
	viscous heating	P_{in}	analytical	Watts	2.68	49.0	5.36	24.5
			CFD		2.64	48.2	5.29	23.8
			difference		%	-1.5	-1.6	-1.3
acceleration	α	rad/s ²		3634	18691	36338	18691	
surface temperature	T_s	analytical	°C	32.0	55.5	36.6	42.3	
concentric design	total torque	N_{eo}	analytical	Nm	1.021	18.71	2.155	8.86
			CFD		1.000	17.83	2.054	8.48
			difference		%	-2.1	-4.9	-4.9
	viscous heating	P_{in}	analytical	Watts	2.67	49.0	5.64	23.2
			CFD		2.61	48.1	5.52	22.6
			difference		%	-2.4	-1.8	-2.2
acceleration	α	rad/s ²		35245	18419	35245	18419	
surface temperature	T_s	analytical	°C	31.9	55.5	37.2	41.4	

Table 6.8: Comparison between measured experimental temperatures and theoretical predictions.

Table 6.8 illustrates how acceleration is greatly enhanced by reducing the outer radius of the clutch and that increasing the length of the clutch has no effect on acceleration. The CFD results for torque and viscous heating are seen to agree well with theory. Any difference is due the CFD model being more realistic with field distribution not being uniform at the rotor ends.

It appears that for a multi-plate clutch, both radial and concentric designs fare equally well. The CFD results do however illustrate one other major consideration,

namely how well heat generated in the annular gaps can be conducted into the outer casing. To maximise acceleration the output rotor is likely must be constructed of a lightweight material that is expected to have a low thermal conductivity. This hinders heat transfer from the outer casing. The thermal conductivity of the inner rotor was set to equal that of nylon. Typical temperature distribution within the radial and concentric clutch designs are shown respectively in Fig. 6.21 and Fig. 6.24. The result of the nylon output rotor is to hinder heat transfer and thus contribute to areas of increased temperature. This is more of a problem for the concentric clutch, but by only a few degrees. For example, with dimensions ($R = 60\text{mm}$, $L = 60\text{ mm}$), the difference between maximum and minimum temperatures within the clutch is $2.3\text{ }^{\circ}\text{C}$ for concentric design (Fig. 6.22) and $1.5\text{ }^{\circ}\text{C}$ in the radial design (Fig. 6.24).

6.5.4 Conclusion

The above study suggests that both radial and concentric clutch designs perform approximately equally. However, in the case that inner rotor is made of a low conducting material, it will be difficult to dissipate heat from the inner channel. As a result, the multi-plate radial clutch seems to be slightly better. Furthermore, a radial design does not exhibit plug behaviour over its full range of operation thus generally leading to lower viscous heating.

6.6 Summary: Heat Transfer

As is evident from comparisons of the experimental and theoretical data for a viscous clutch device set-up, the correct magnitudes of heat transfer can be effectively predicted. For a more complex set-up, such as a multi-plate clutch in an unsteady operation, CFD promises to be a simple and important tool for heat transfer evaluation.

In the experimental studies, the viscous medium was Newtonian Shell oil. Heat transfer in non-Newtonian fluids is a complex subject. However, it is proposed that modelling heat transfer in smart fluids need not be that complicated due to the following reasons: All smart fluid devices operate within a very narrow channel, for which the distribution of temperature across the gap width is likely to be nominal as indicated in this study. Using CFD, the most important variable (yield-stress) can be easily entered as a function of temperature, excitation and shear rate. Furthermore, correctly determined non-Newtonian velocity profiles will give the rate of heat generation on a cell-by-cell basis.

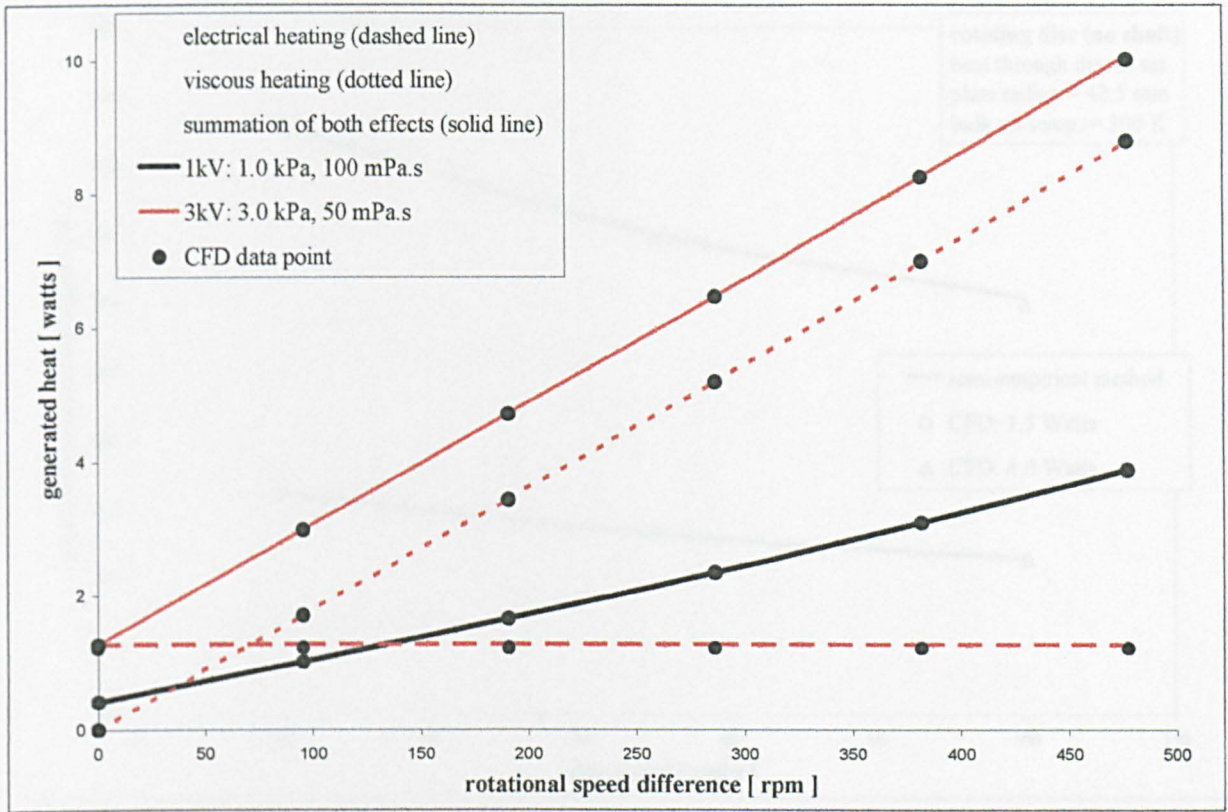


Fig. 6.1: CFD single channel radial clutch model ($R = 30 \text{ mm}$, $h = 0.5 \text{ mm}$) to determine viscous and electrical conduction source terms. $j = 30 \mu\text{A}/\text{cm}^2$.

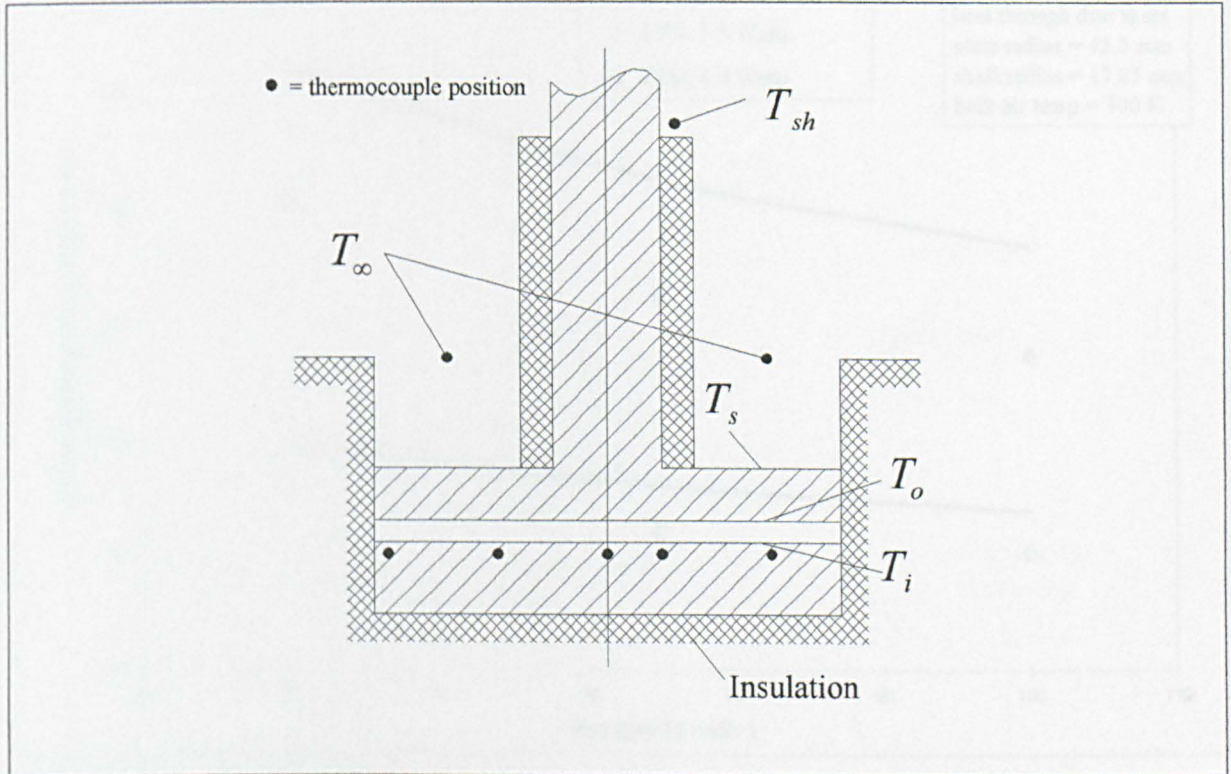


Fig. 6.2: Schematic of radial clutch experimental set-up.

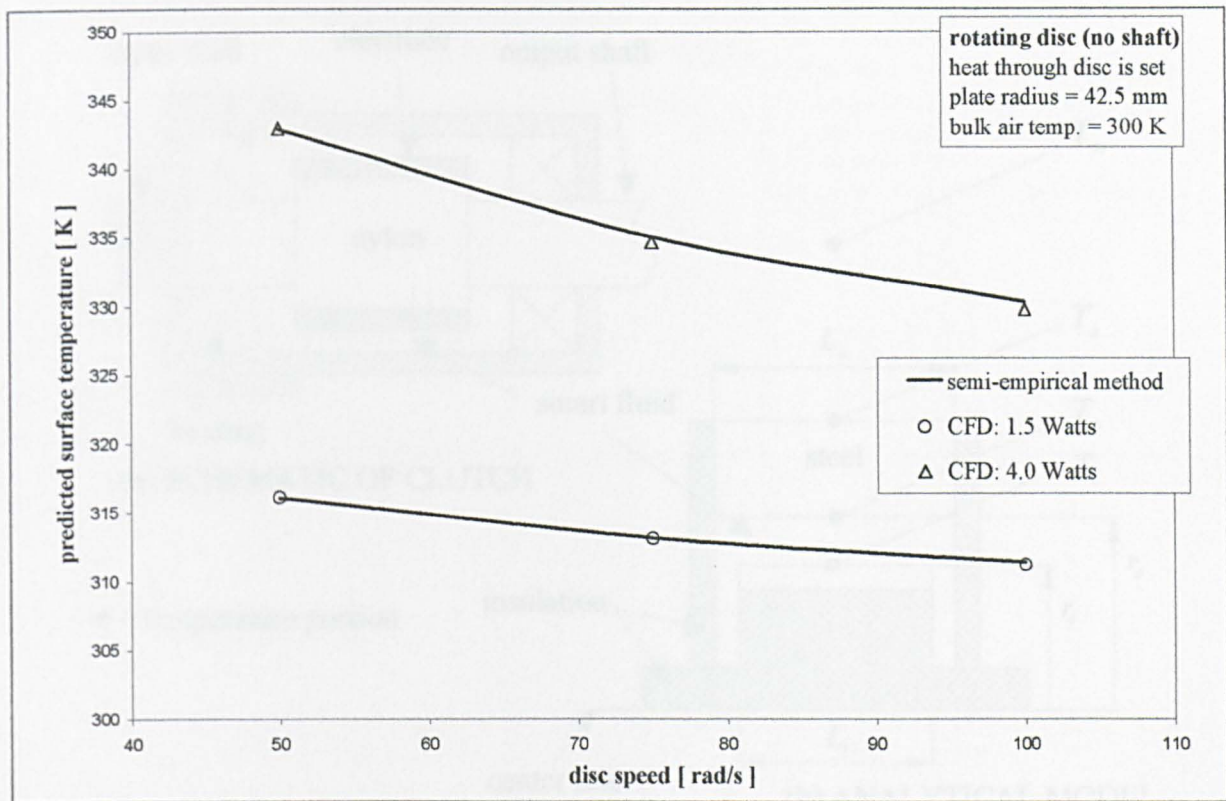


Fig. 6.3: Test of semi-empirical formulae: Rotating disc in air (no shaft and wall constraint).

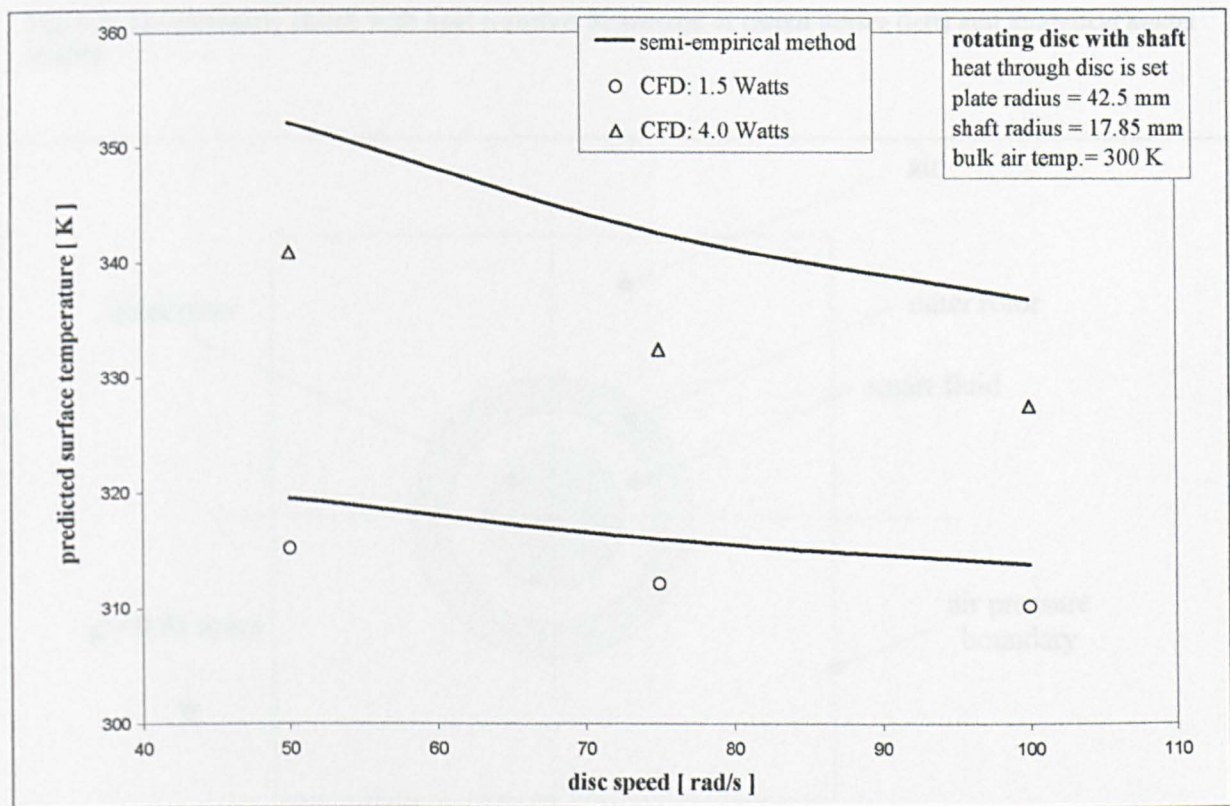


Fig. 6.4: Test of semi-empirical formulae: Rotating disc in air (shaft and wall constraint included).

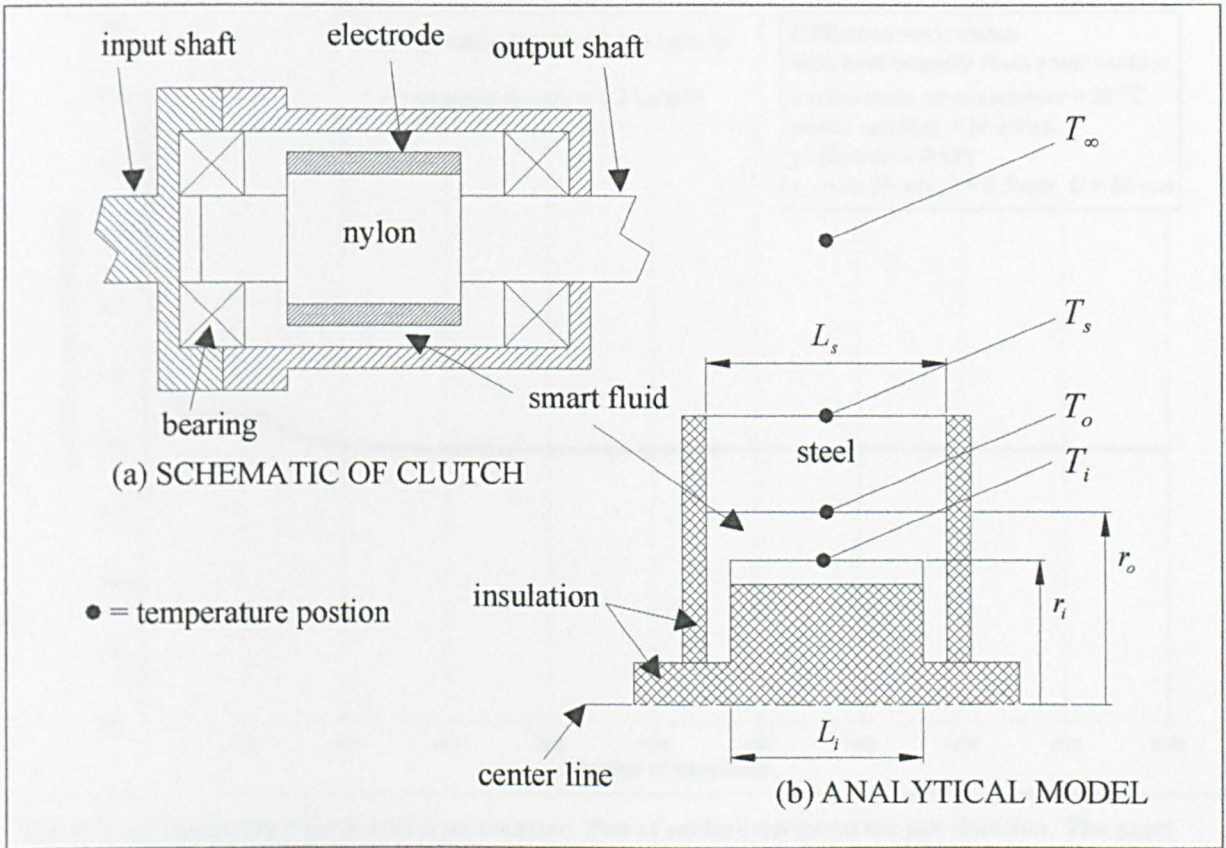


Fig. 6.5: 2D concentric clutch with heat transfer. Schematic of clutch device (left) and analytical model (right).

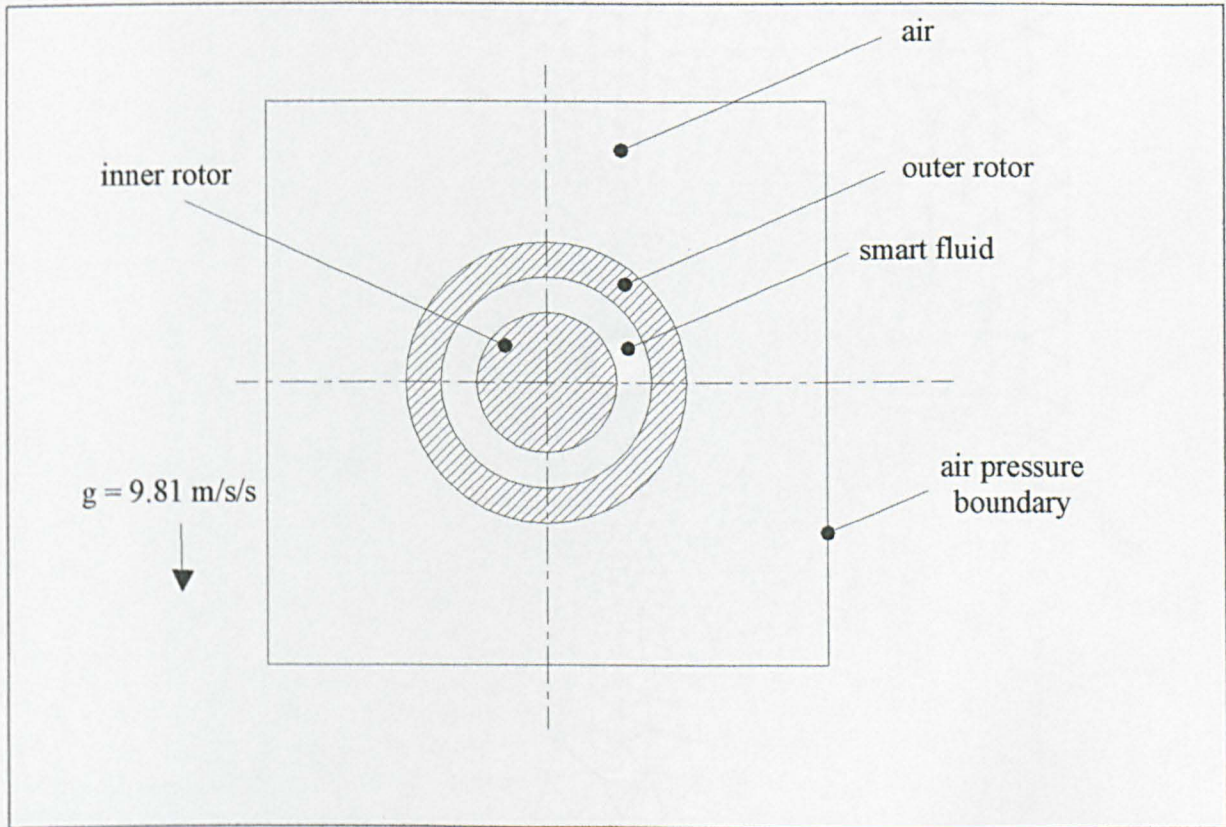


Fig. 6.6: 2D concentric clutch with heat transfer. Schematic of CFD model.

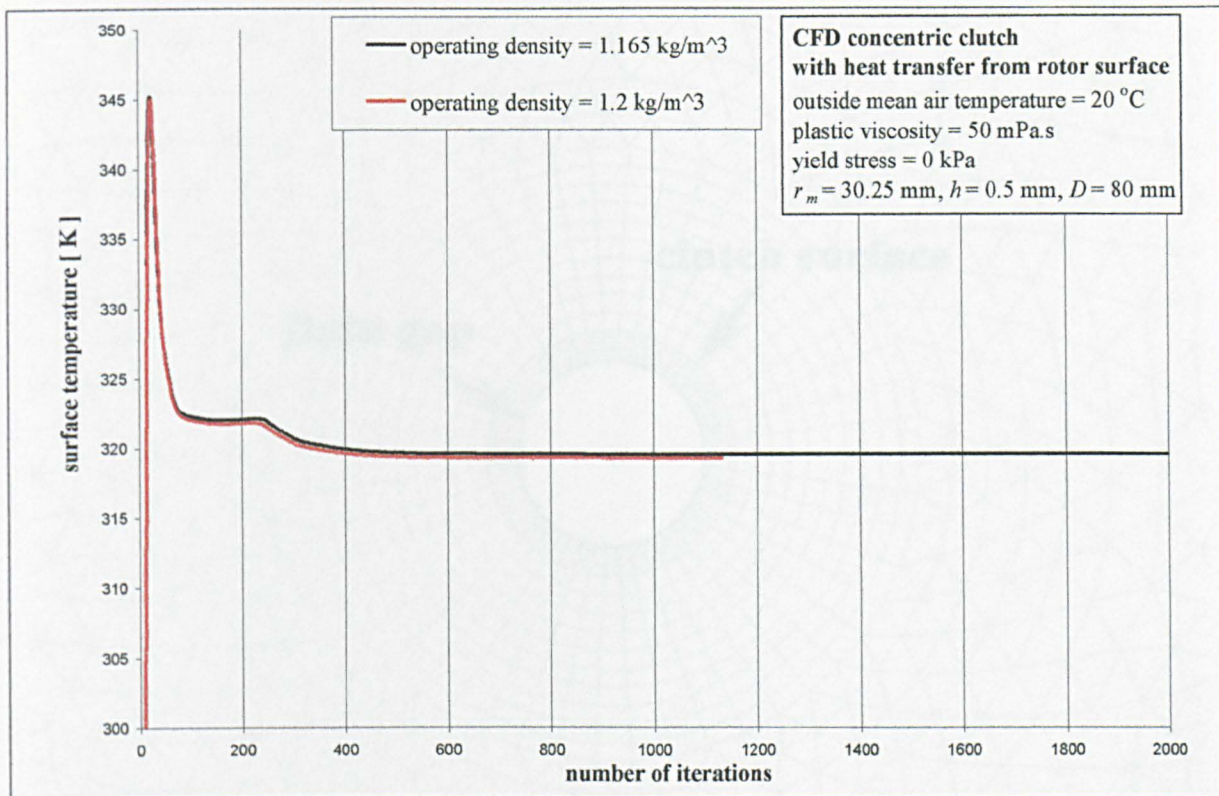


Fig. 6.7: 2D concentric clutch with heat transfer. Plot of surface temperature per iteration. The exact value of operating density does not significantly affect the solution.

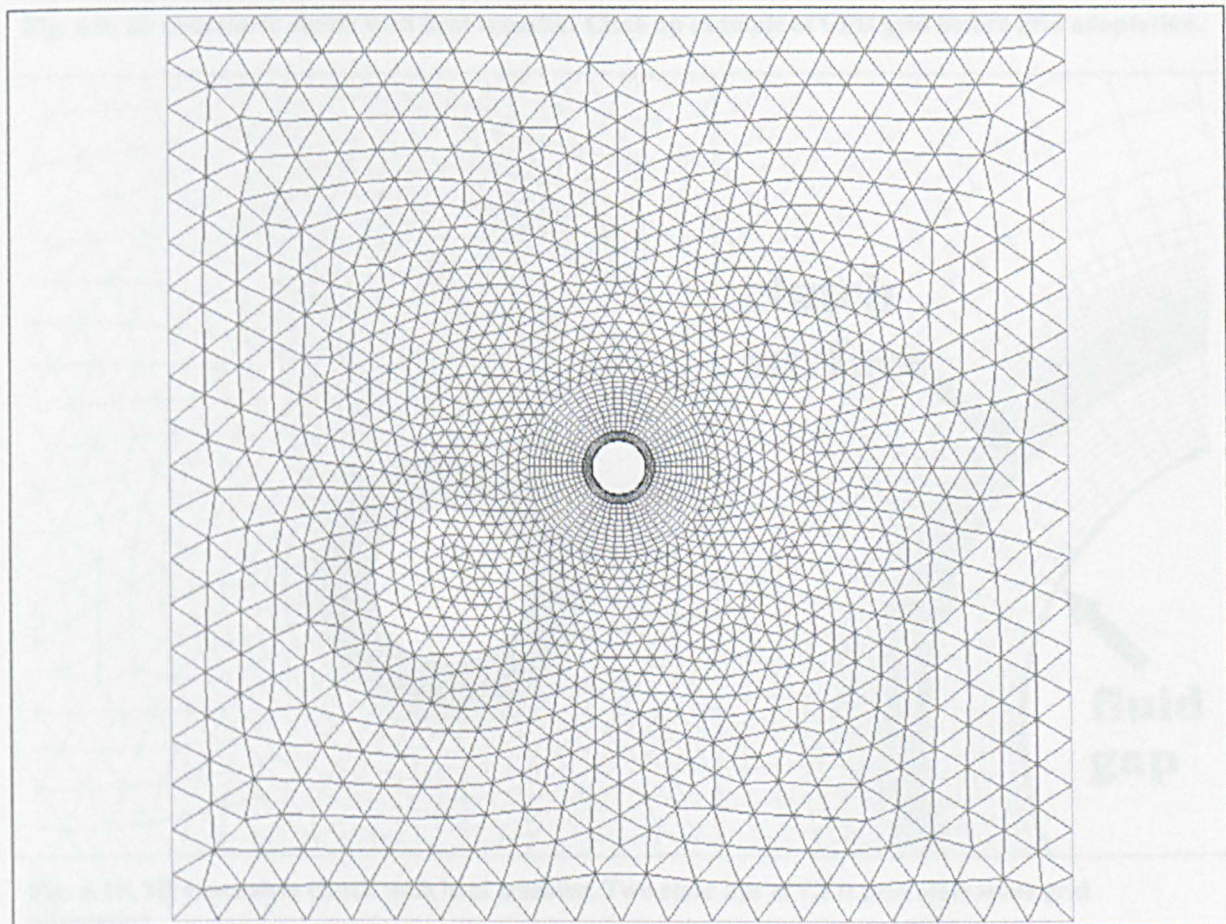


Fig. 6.8: 2D concentric clutch with heat transfer. CFD grid uses both trilateral and quadratic cells.

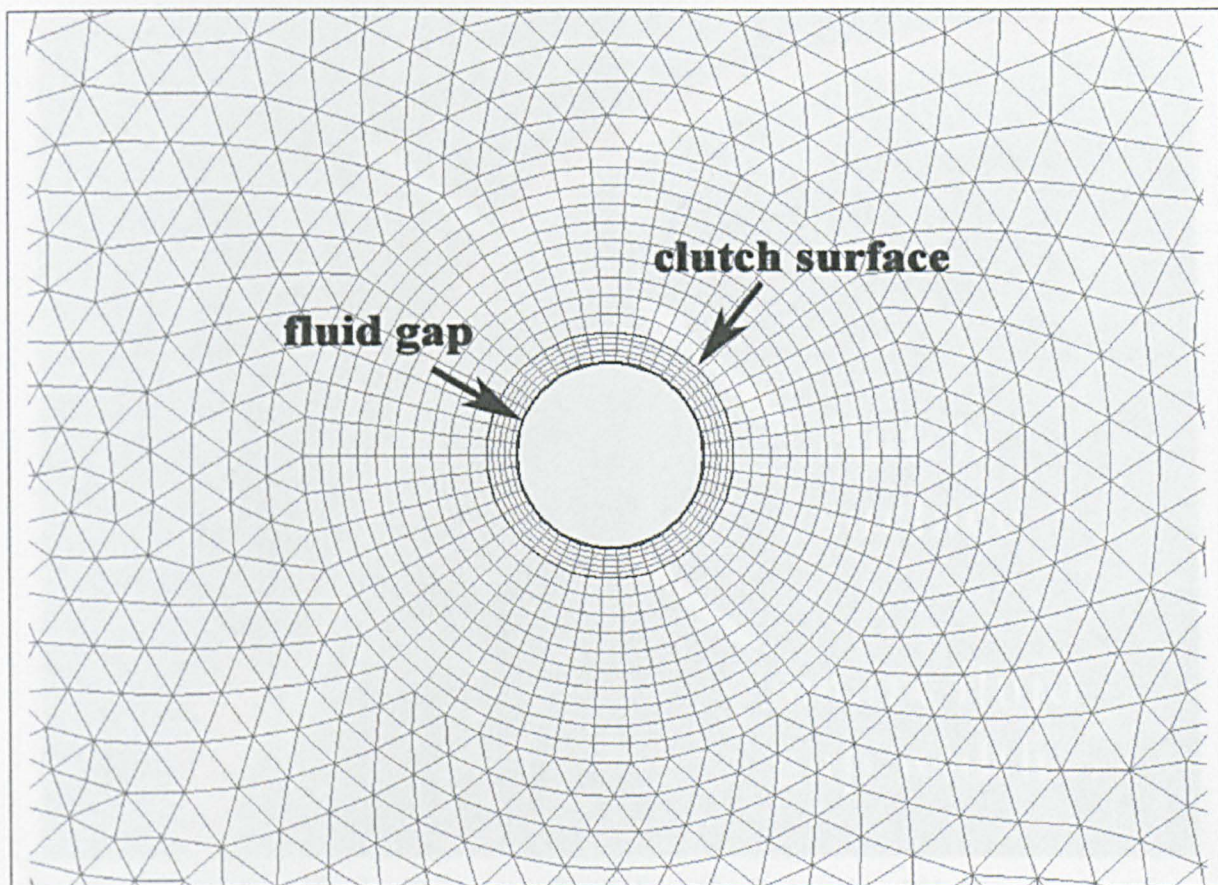


Fig. 6.9: 2D concentric clutch with heat transfer. Close up example of CFD grid before grid adaptation.

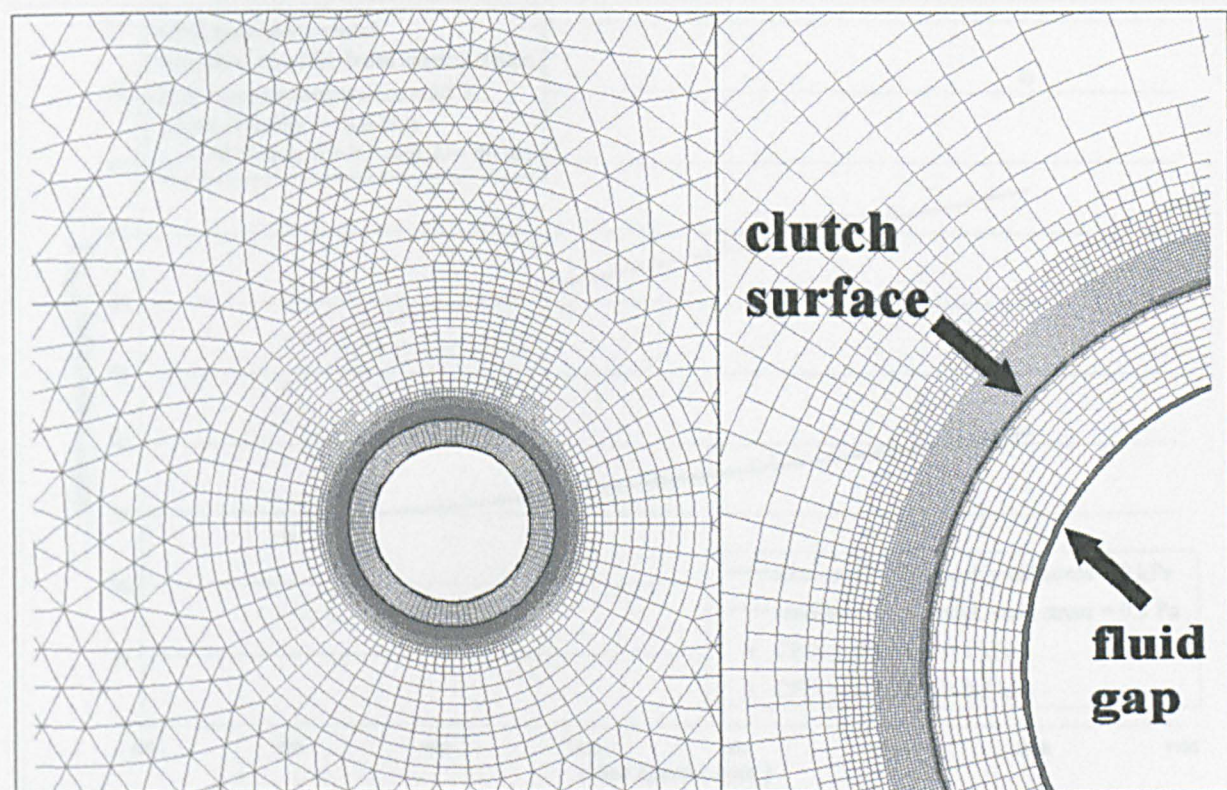


Fig. 6.10: 2D concentric clutch with heat transfer. Two close ups of CFD grid after some grid adaptation.

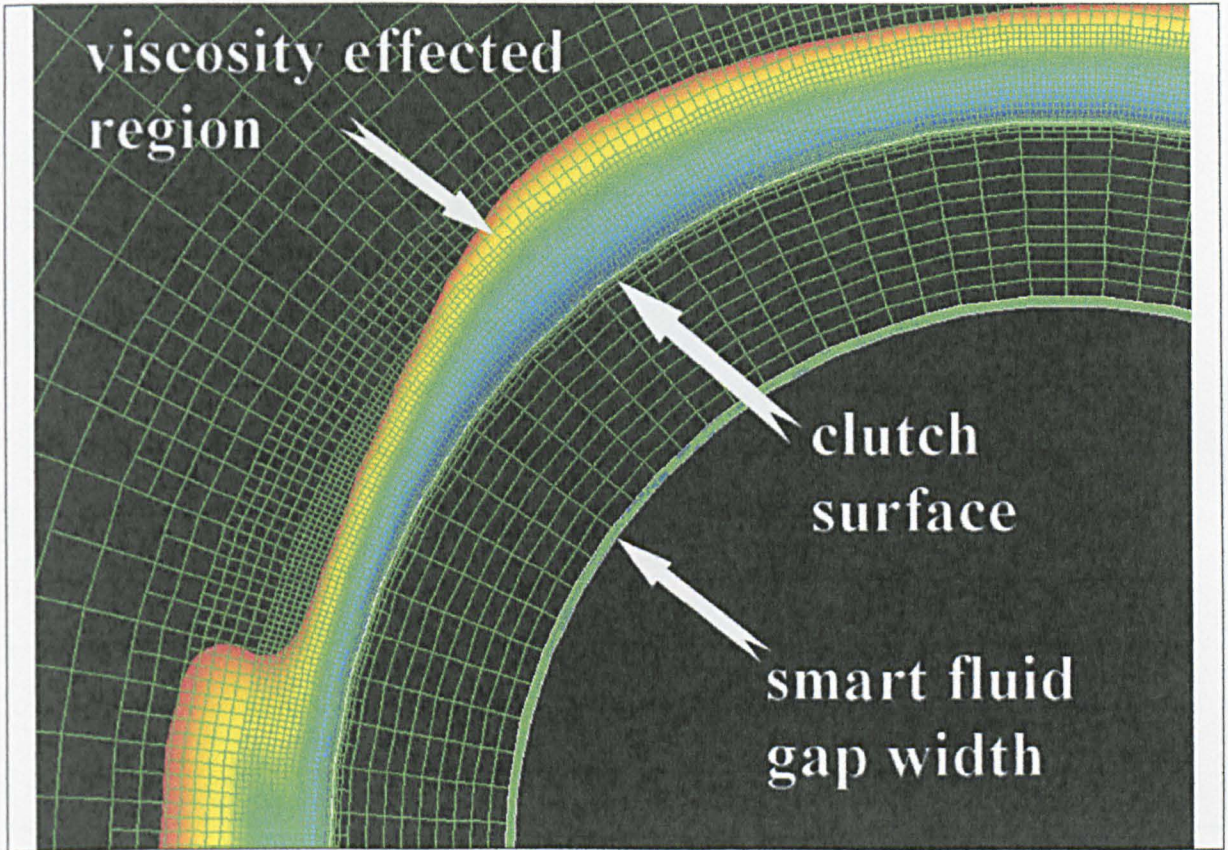


Fig. 6.11: 2D concentric clutch with heat transfer. At least 10 cells must be within viscosity-affected near wall region ($Re_y < 200$) for the Two-Layer Zonal near wall turbulence model to be valid.

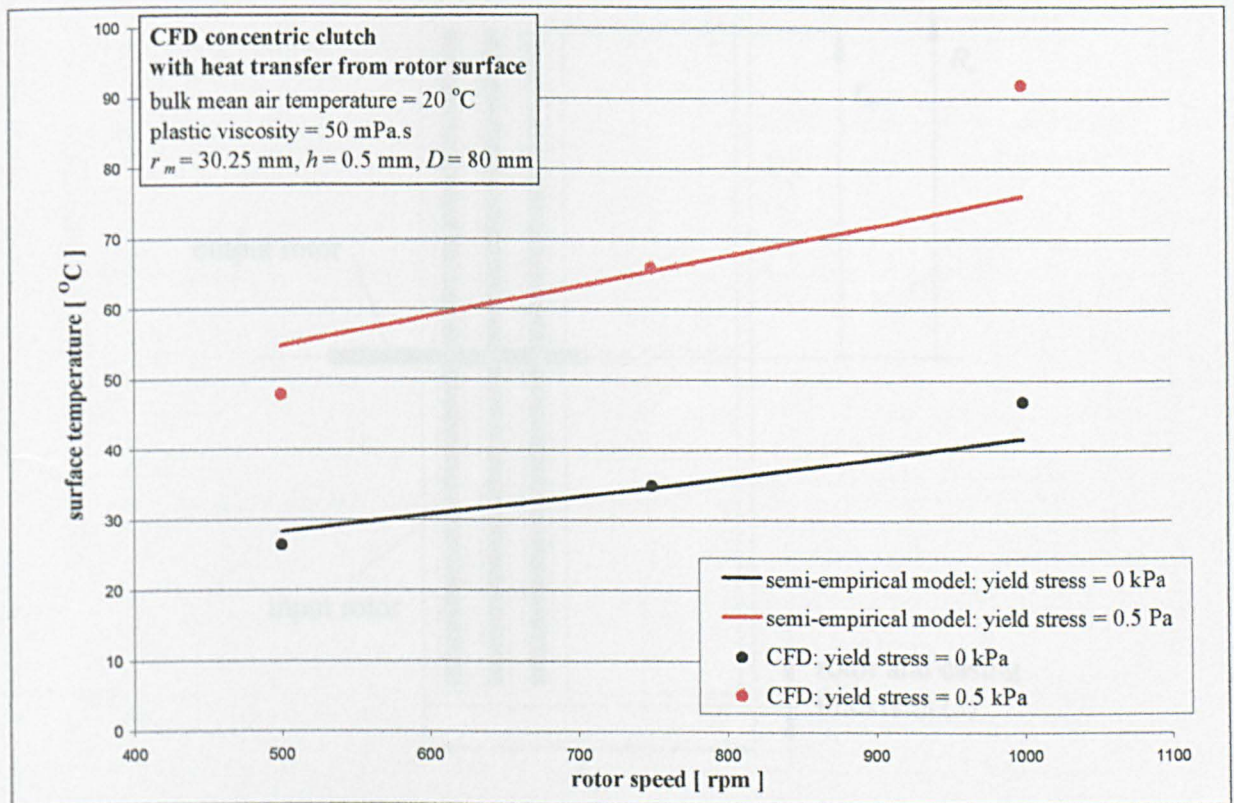


Fig. 6.12: 2D concentric clutch heat transfer model. CFD vs. semi-empirical model.

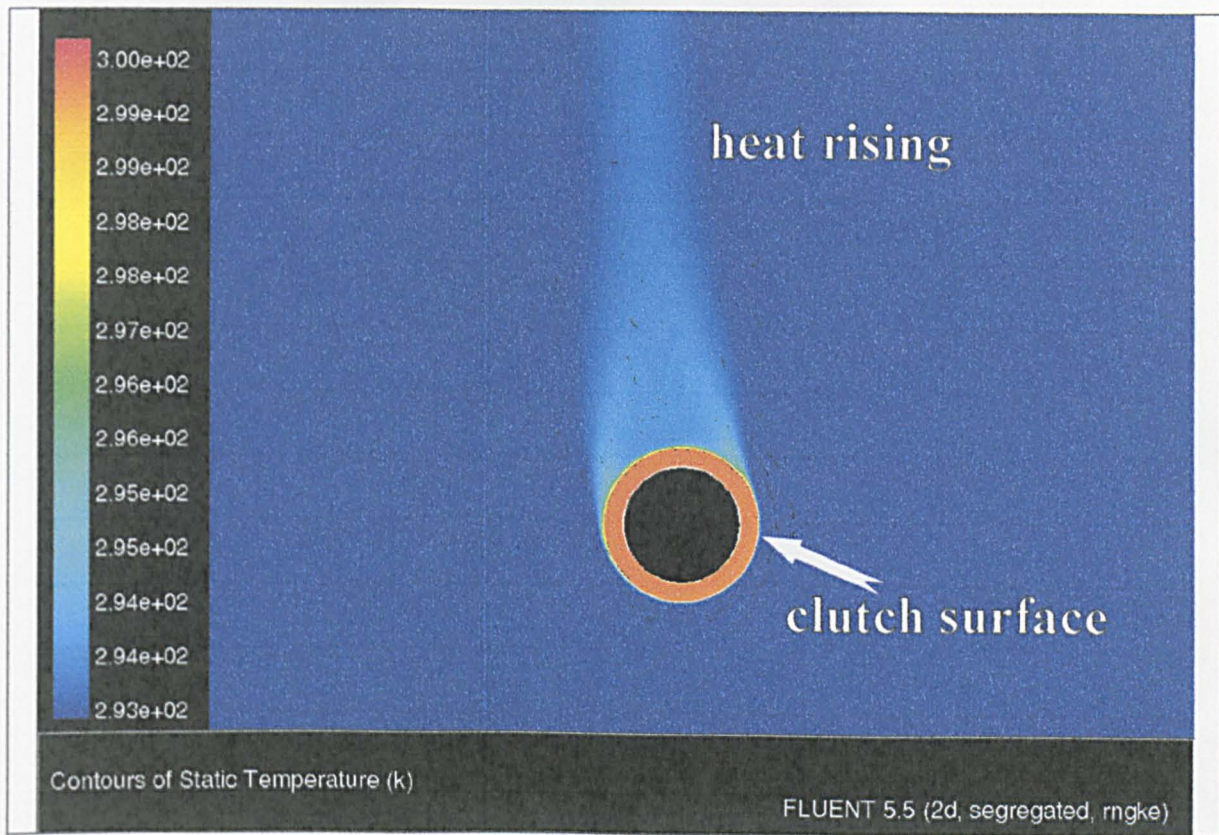


Fig. 6.13: 2D concentric clutch heat transfer model. Temperature distribution at a speed of 500 rpm.

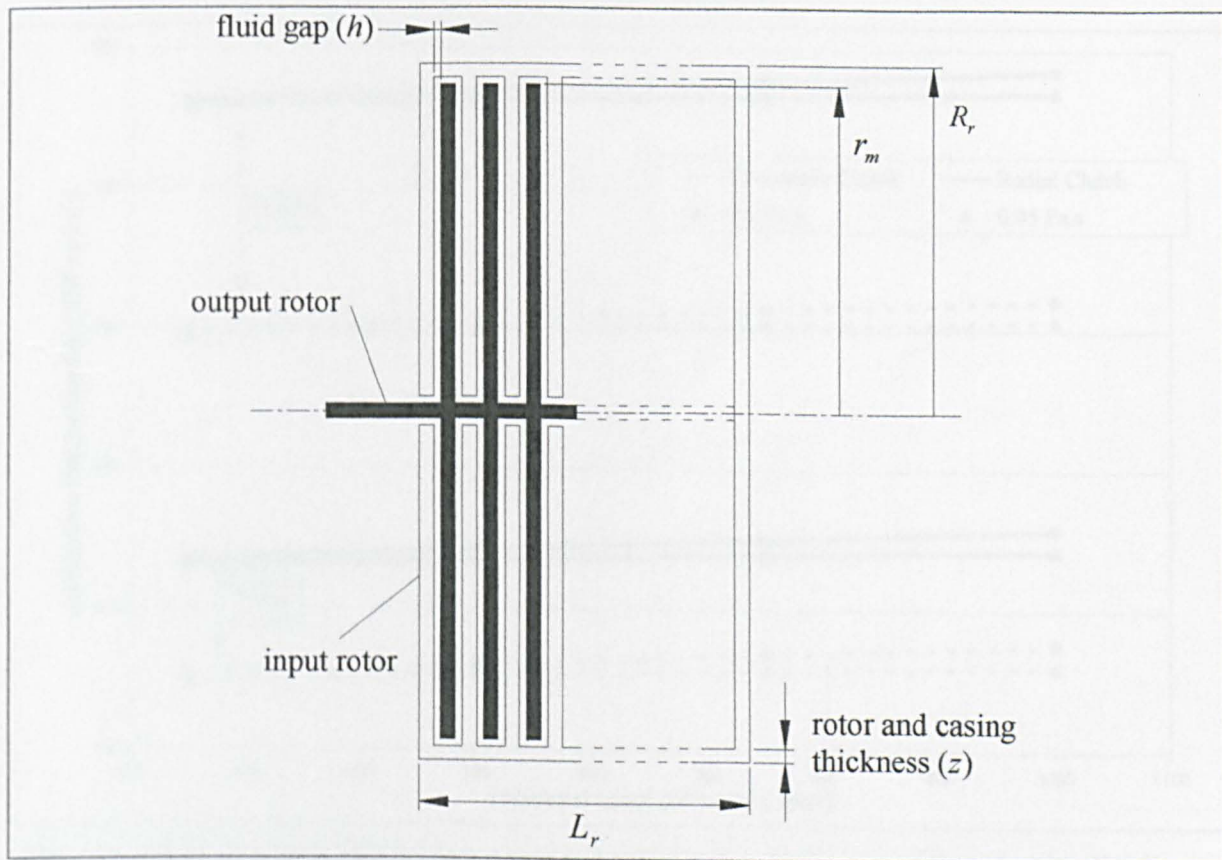


Fig. 6.14: Radial clutch geometry for a multi channel device.

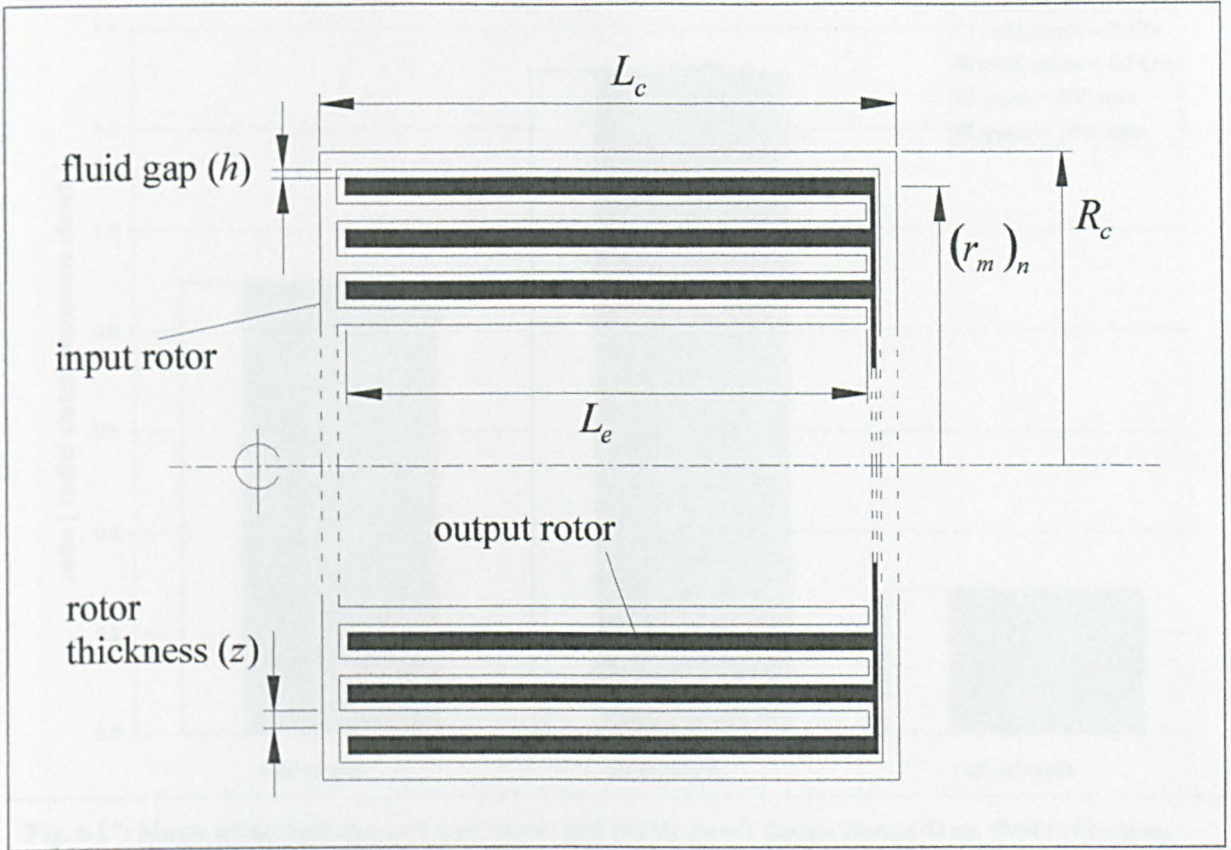


Fig. 6.15: Concentric clutch geometry for a multi channel device.

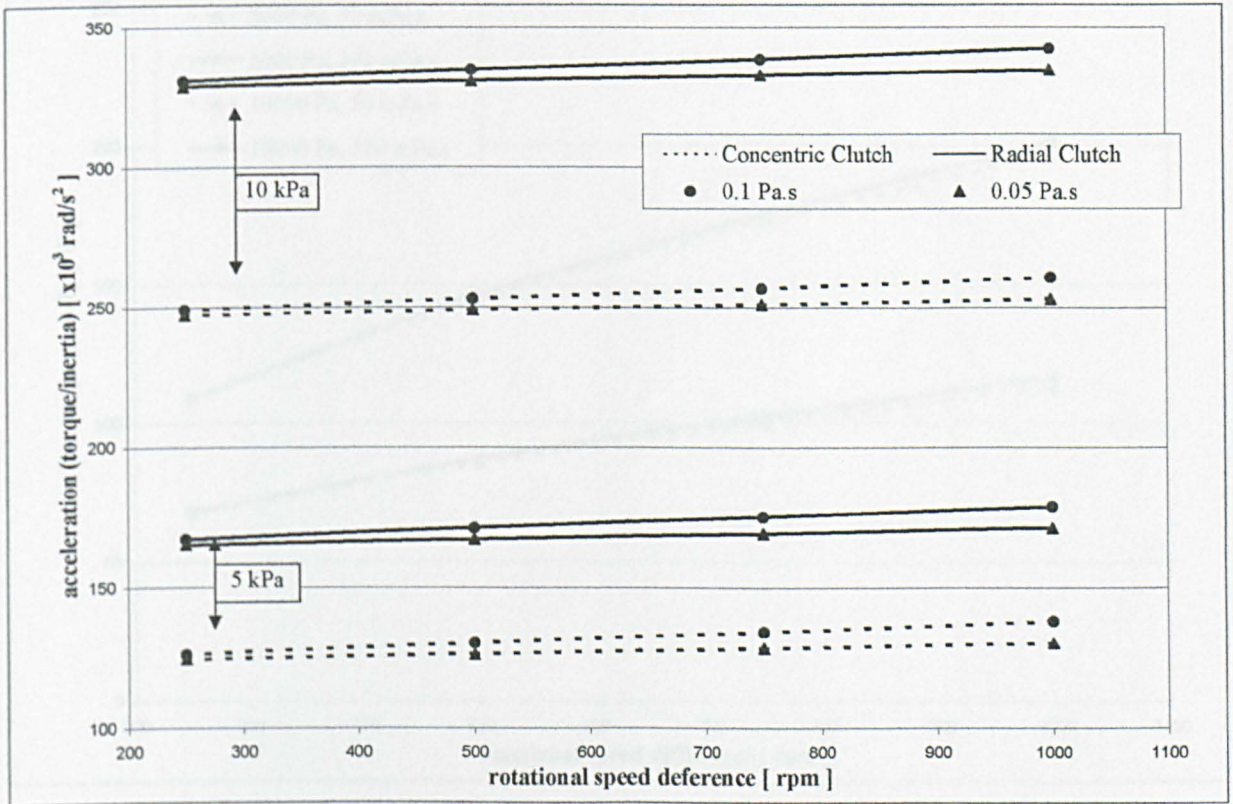


Fig. 6.16: Single rotor dual channel concentric and radial clutch design comparison. Acceleration is calculated for the same clutch surface temperatures.

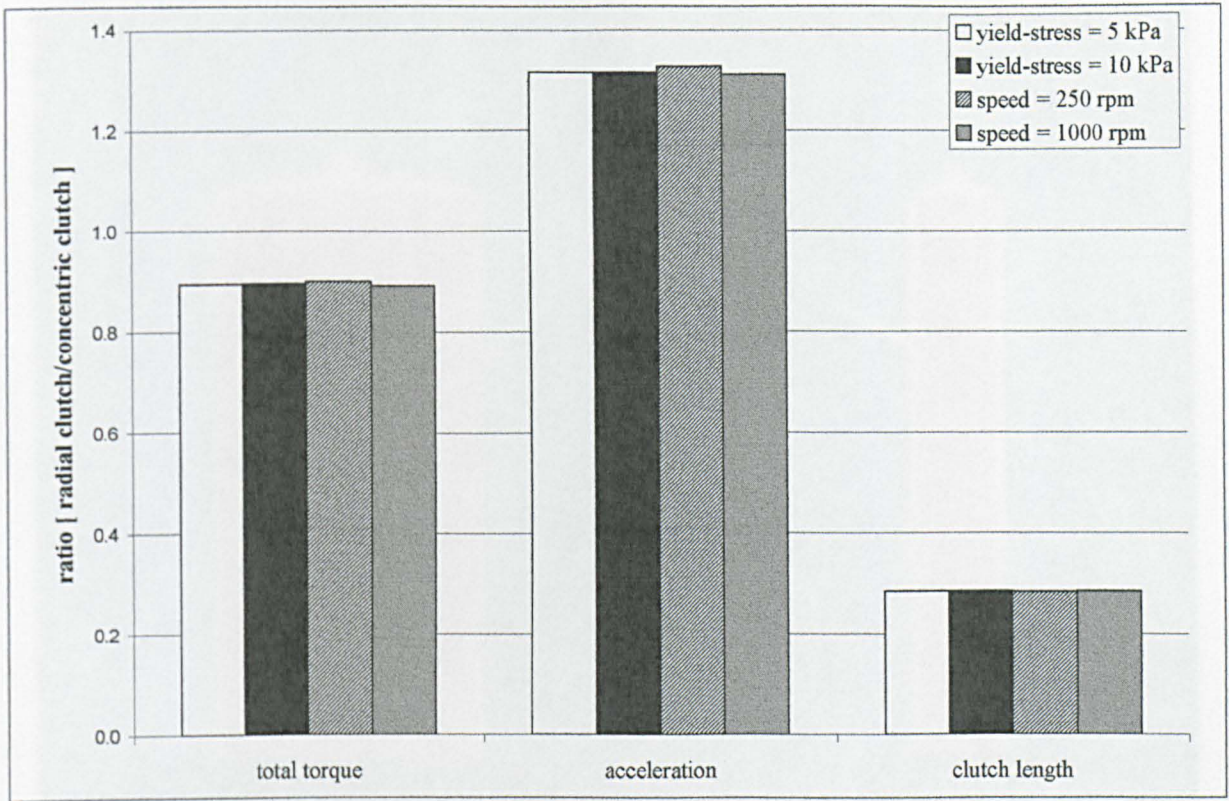


Fig. 6.17: Single rotor dual channel concentric and radial clutch design comparison. Ratio of torque, acceleration, and clutch length for the same clutch surface temperature.

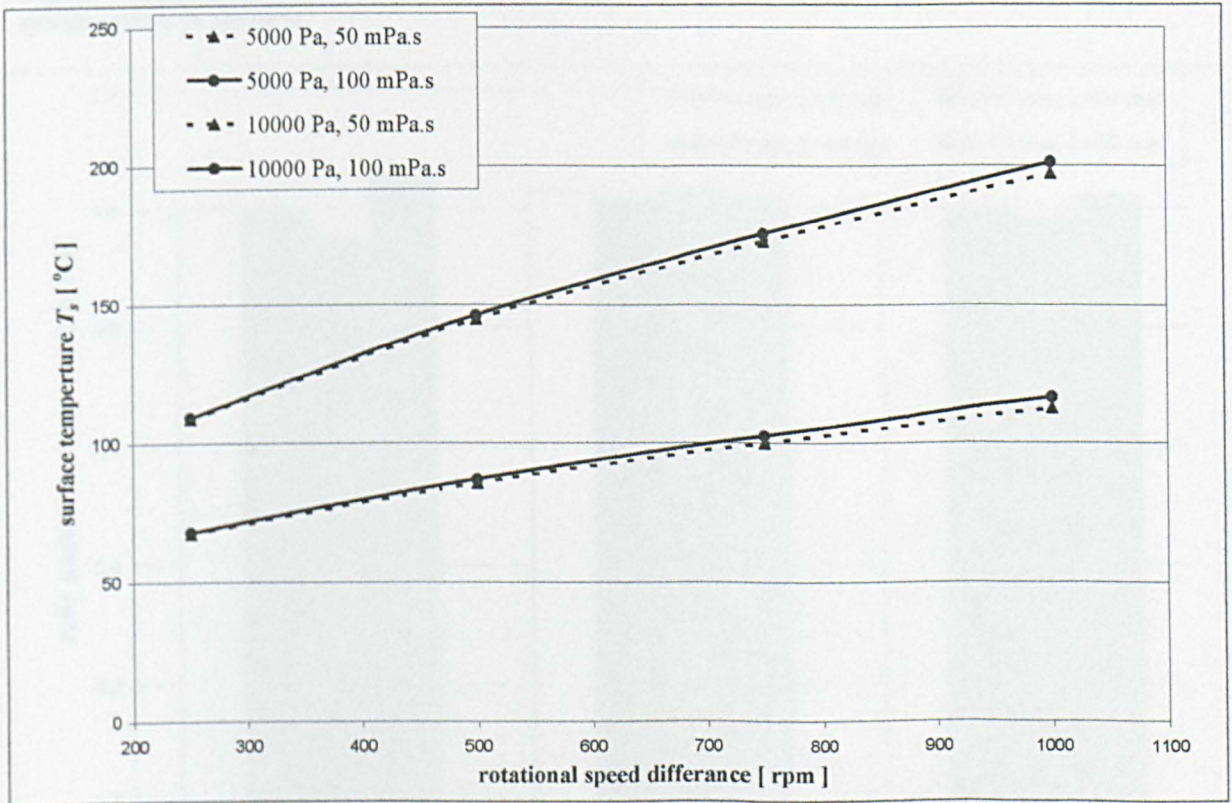


Fig. 6.18: Single dual channel concentric and radial clutch design comparison. Ratio of torque, acceleration, and clutch length for the same clutch outer surface temperature.

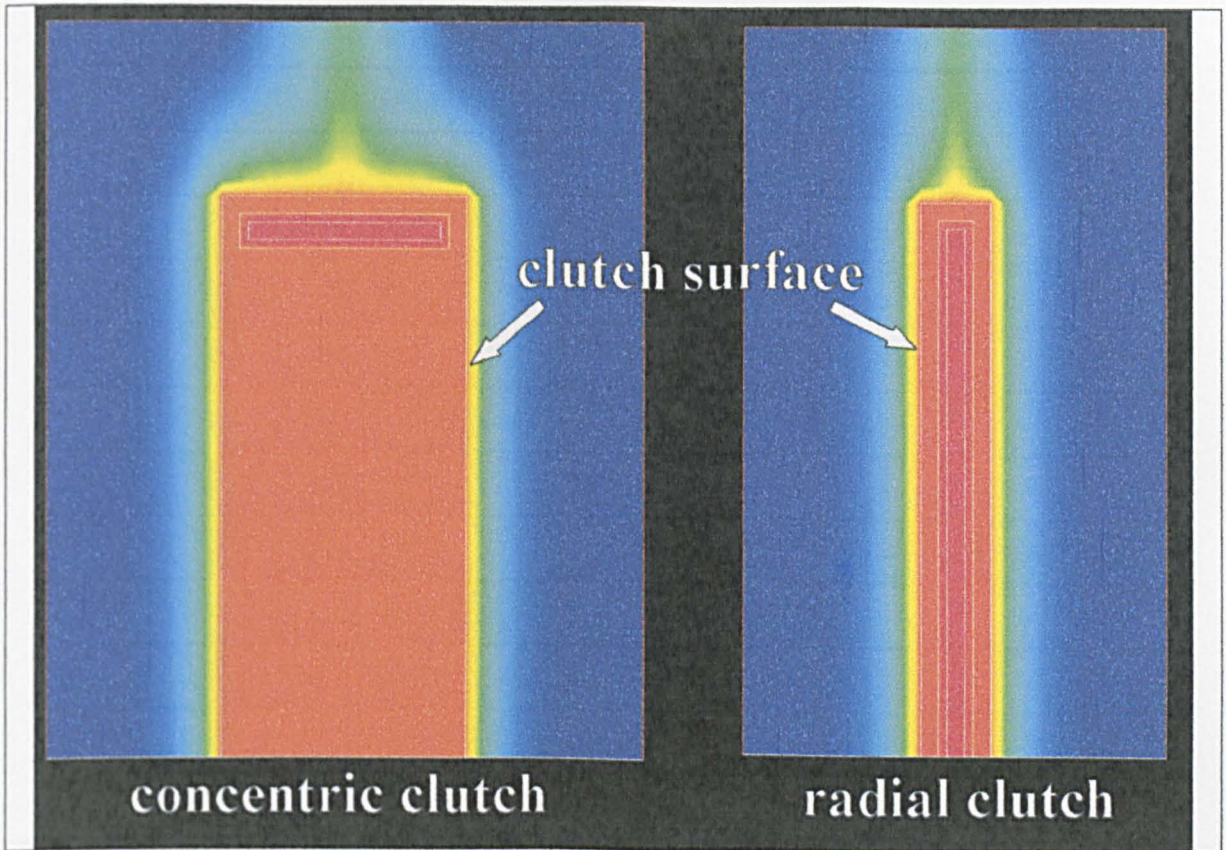


Fig. 6.19: Single dual channel concentric and radial clutch comparison. Temperature distribution on clutch surface is uniform.

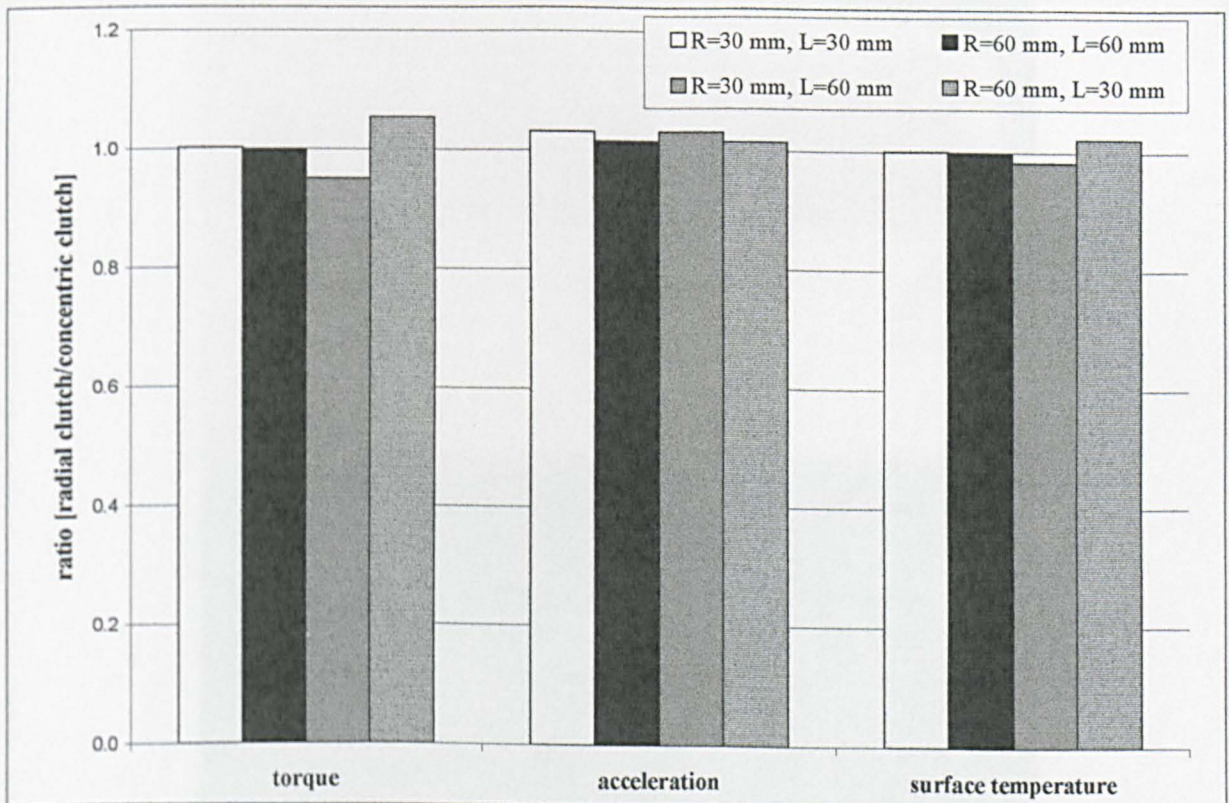


Fig. 6.20: Multi channel concentric and radial clutch design comparison. Ratio of torque, acceleration, and clutch length for the same clutch yield-stress value.

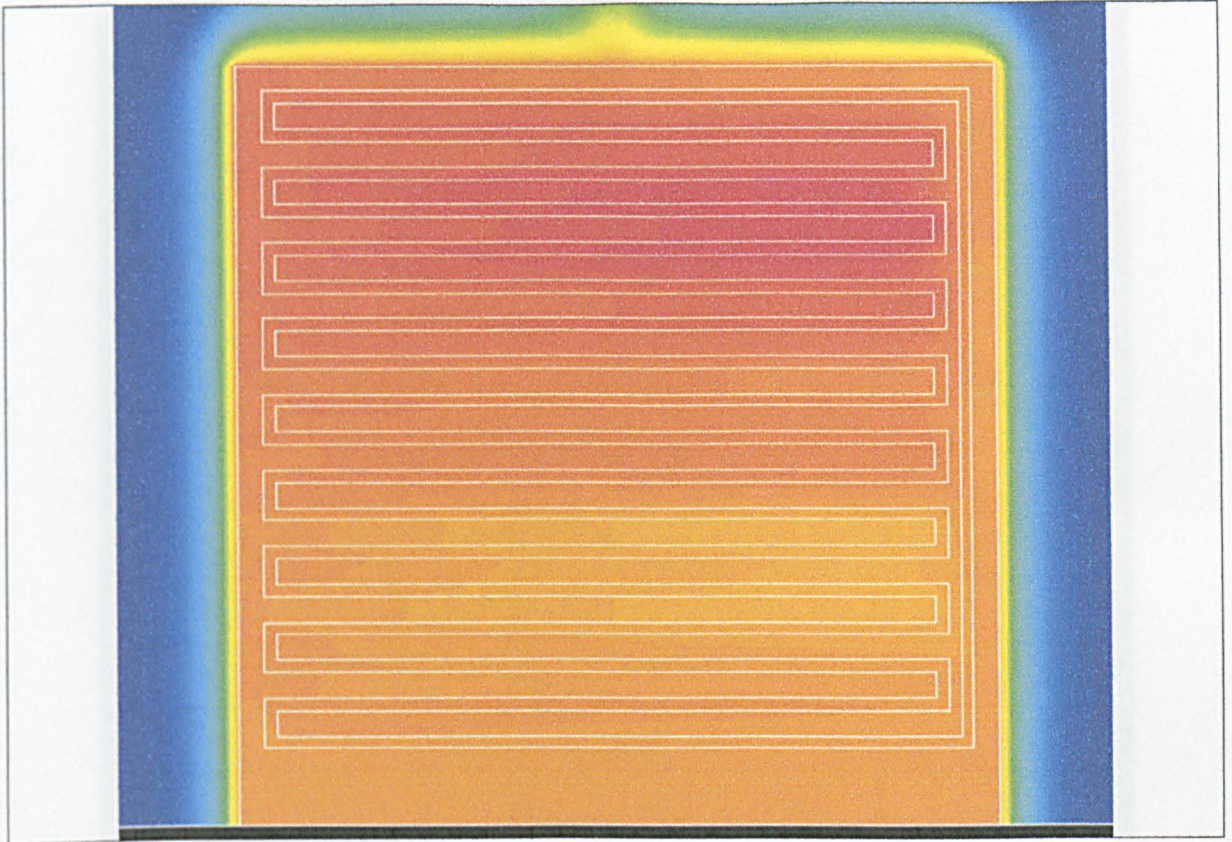


Fig. 6.21: CFD multi channel smart fluid concentric clutch. Distribution of temperature at 500 rpm. Range 300-311.298 °C. ($R = 60\text{mm}$, $L = 60\text{ mm}$)

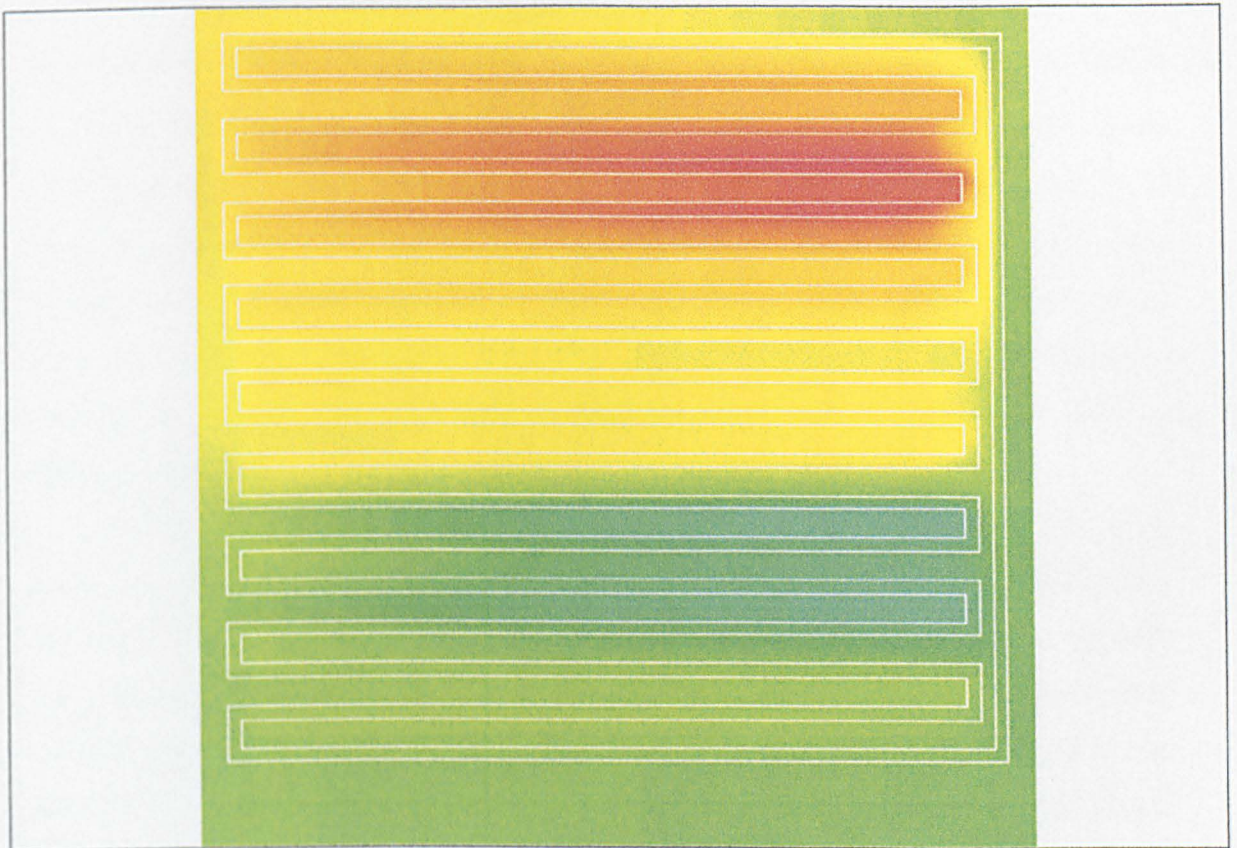


Fig. 6.22: CFD multi channel smart fluid concentric clutch. Distribution of temperature at 500 rpm. Range 309-311.298 °C ($\Delta T = 2.3^\circ\text{C}$). ($R = 60\text{mm}$, $L = 60\text{ mm}$)

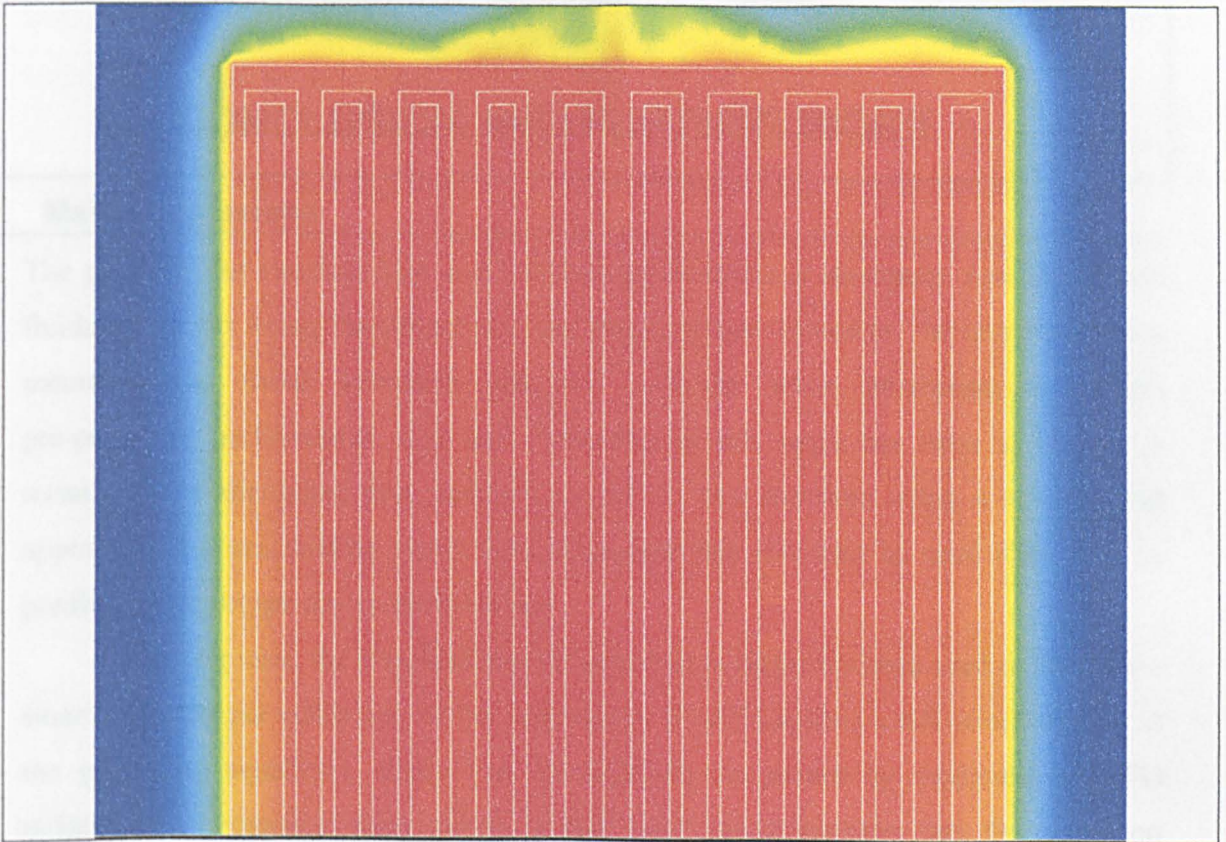


Fig. 6.23: CFD multi channel smart fluid concentric clutch. Distribution of temperature at 500 rpm. Range 300-311.491 °C. ($R = 60\text{mm}$, $L = 60\text{ mm}$)

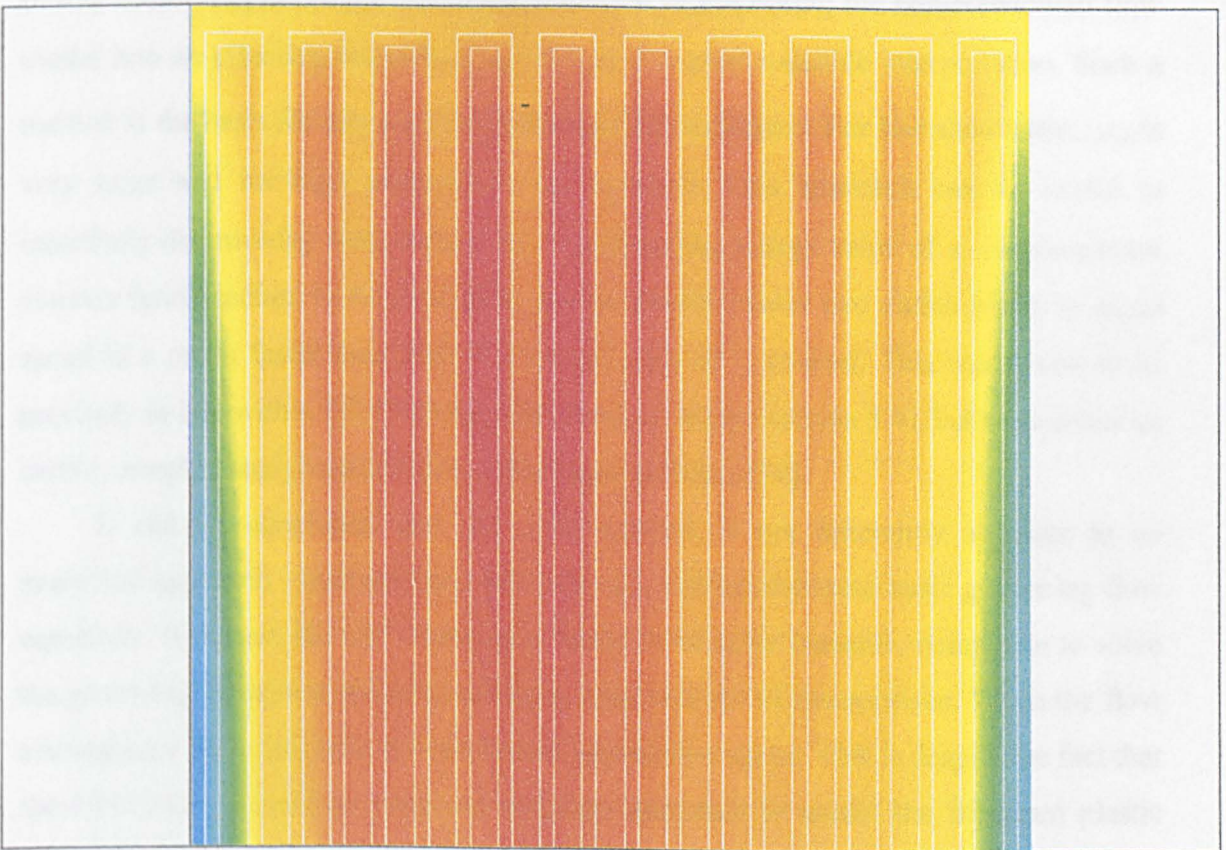


Fig. 6.24: CFD multi channel smart fluid concentric clutch. Distribution of temperature at 500 rpm. Range 310-311.491 °C ($\Delta T = 1.5^\circ\text{C}$). ($R = 60\text{mm}$, $L = 60\text{ mm}$)

CHAPTER 7 :

CONCLUSION AND FURTHER WORK

7.1 Main Conclusions

The potential for creating new and exciting applications is enormous now that smart fluids are finally being introduced into the market place. However, the non-Newtonian nature of the fluids introduces inherent difficulty when attempting to predict pre-prototype performance. The main objective of this work has been to identify a technique for alleviating this problem via CFD. This involves using a standardised approach for characterising smart fluid behaviour that can then be used with CFD to predict pre-prototype device performance.

For a long time, the Bingham plastic model has commonly been used to describe a smart fluid. Proper utilisation of the constitutive model requires a full consideration of the governing equations, which can subsequently be solved by analytical or CFD techniques. A common interpolation of this model is to consider that the excitation generates a yield-stress, above which the zero volts viscosity provides Newtonian flow. In this author's opinion, the rheologist's method of translating the non-Newtonian flow model into an effective viscosity $\{\mu_{nn} = f(\dot{\gamma})\}$ is a more valuable interpretation. Such a method is the basis for any continuum-based CFD technique. For low shear-rates, μ_{nn} is very large and for high shear-rates, μ_{nn} is small. This approach can be useful in intuitively determining basic behaviour. For example, a large value of τ_y causes a more viscous fluid medium to be produced, and so should reduce two clutch plates to equal speed in a much faster time than if a lower value of τ_y is used. This was found to be precisely in line with a full CFD and experimental study (section 5.4), but contradicts an earlier complex analytical solution of the same problem [38].

It can be concluded that the CFD method is not inherently superior to an analytical approach - both methods are, after all, solving the same basic governing flow equations. However, the CFD method is found to be more versatile, being able to solve the governing equations without making a large number of assumptions. When the flow assumptions are valid, both the continuum approaches agree. This is despite the fact that the CFD method used an effective viscosity approach to model the Bingham plastic equation, an approach which some people express reservations about.

One drawback of a direct analytical solution is the necessity of considering where the plug regions may occur and including them in the model. In CFD it is not necessary

to significantly consider plug formation; plug regions form and possess the appropriate values of momentum as determined by the fluid's density and velocity.

Exploitation of the continuum approach is very limited via direct analytical solutions. Even for the simplest flows, the formulations soon become too complex. The only sensible way forward is to use a CFD approach. However, both methods require the fluid to be a continuum, and furthermore to have been characterised.

A specific constant stress rheometer used in section 3.6 to characterise an ER fluid was found to indicate consistent continuum properties. However, it also suggested that the plastic-viscosity could be negative. This is believed to be impossible, but the truth remains to be established. These results were deemed not to be very accurate. This rheometer offers only simple steady state characterisation with no values of G' . Provided a smart fluid can be characterised in terms of continuum properties, a CFD approach promises to be a vitally important pre-prototyping tool and should improve the commercial utilisation of smart fluid technology.

7.1.1 Original Contributions and Significant Discoveries

Unsteady Flow

If the CFD method is to have significant practical purpose it must be able to model smart fluids in unsteady flow.

- A significant argument in support of the usefulness of smart fluids is their speed of response. The dynamic speed of response of a smart fluid annular valve and a Rayleigh step bearing was therefore investigated and found to be very fast.
- By assuming an instantaneous change in yield-stress some firm conclusions can be drawn, but problems associated with an unrealistic change in shear stress were encountered. This led to an investigation of a viscoelastic version of the Bingham plastic model that allows a much smoother change in shear stress. This model was found to give much more realistic results.
- The Rayleigh step bearing response was found to be fast and in range with experimental data obtained on new experimental rig. However, detailed fluid properties were not fully available for a more intricate analysis - the viscoelastic model requires a shear modulus parameter G' .
- It is not surprising that the CFD study showed that the density, and thus mass and inertia of unconstrained machine parts affected the fluid dynamic response. This is in disagreement with an analytical solution of the same problem. In the analytical solution it was difficult to properly account for the effect of the rotor. A smart fluid

typically operates as the medium between two machine parts, the dynamics of which affect the boundary conditions and vice versa.

- For a CFD clutch run-up problem to be useful, the model had to be aware of the mass of influencing parts (output rotor). Results are found to be clearly in line with experimental results for both Newtonian oil and ER fluid mediums.

Heat Transfer

To model viscous heating, heat flow and thus temperature distributions, it is almost as simple as introducing the energy equation.

- For a smart fluid device, comparisons of CFD data to results obtained by experimental and semi-empirical analysis analytical data show that CFD can correctly predict magnitudes of heat transfer.
- The only real difficulty encountered was in correctly modelling the convection from the device into the surrounding air. This has nothing to do with the smart fluid nature of the model.
- For a more complex set-up such as a multi-plated clutch, CFD promises to be a simple and important tool. Here CFD can handle the complex geometry, evaluate viscous heating, heat transfer across the plates and dissipation of heat from the clutch into the atmosphere.
- Heat transfer in non-Newtonian fluids is a complex subject. However, it is proposed that modelling heat transfer in a smart fluid using CFD need not be that complicated. In general, temperature distribution across a small gap-width is likely to be nominal as indicated in this study; the yield-stress is the most important variable contributing to heating and can be easily entered as a function of temperature; furthermore, non-Newtonian velocity profiles will give accurate rate of heat generation on cell-by-cell basis.

CFD Solution Technique in General

- With the use of user-defined sub-routines, the commercial CFD code (Fluent5 from Fluent.Inc) was found to be highly suitable for modelling a smart fluid.
- For a smart fluid the viscosity usually varies on a cell by cell basis, consequently computing is found to be significantly slower than that expected if the fluid is Newtonian. However, the continual increase in computational power will alleviate this problem.

- An adequately converged smart fluid solution always required the residual histories¹ to be reduced for more than usual. Convergence was best judged through monitoring overall variables.
- In general, the Fluent platform was quite stable. However, it often proved wise to compute a viscous Newtonian flow before the smart fluid model was activated.
- Minor problems encountered with the CFD package included, for example; incorrect calculation of the resultant shear rate when axisymmetric geometry was used. Once identified, such problems were relatively easy to fix. The Fluent CFD package is vastly powerful and versatile. The problems encountered will have been minuscule to those that would have been encountered if a new CFD code specific for modelling smart fluids had been built from scratch.

Other Advantages of the CFD Approach

It is sufficient to say that given enough computational power it should be straight forward to model a whole host of complex smart fluid machines and devices. This will allow promising designs and ideas to be rapidly identified, while those with less potential can be sidelined, thus allowing limited research resources to be directed more appropriately. The work in this thesis indicates that:

- Complex geometry by virtue of highly developed meshing software can be generated without difficulty.
- In using an already commercially available CFD code, the vast majority of the required programming has already been done. Adapting the CFD code specifically for the smart fluids is possible using suitable subroutines.
- Future rheometer studies may produce constitutive models that are more accurate. Within the CFD method, it will be relatively simple to utilise a more complex constitutive equation. Here μ_{mn} could be a function of time, temperature, excitation, yield-stress or elasticity constants and so forth.
- For an ER fluid, the field distribution can be readily determined by simply stating which boundaries are live, earthed and insulated. For a MR fluid, if the form of field distribution is known it will be a relatively simple matter to incorporate it in the overall model.
- Another potentially useful feature of later versions of commercial CFD packages includes the ability for the geometry to change. This would be a useful feature for

¹ the imbalance between a cell variable and its neighbouring values summed over the whole computational mesh

modelling, for example, a smart fluid damper.

7.2 Further Work

7.2.1 More Collaboration with Rheologists

For an experienced operator, the CFD method can readily be used to model a whole host of smart fluid devices. However, the significance of the results is limited by the adequacy and accuracy of the constitutive model and the data upon which it is based. The extent to which a continuum model is valid needs to be established. There is little point using a complex CFD model to account for minor field changes across a gap-width if the continuum assumption is not entirely satisfactory.

Building a specialised smart fluid rheometer can be very expensive (£100-500,000). A radial design of rheometer is likely to be more appropriate. During this study a detailed proposal to design and build an ER/MR rheometer in collaboration with Ravenfield Designs Limited (Makers of Viscometers and Scientific Instruments) was turned down by the EPSRC. However, re-written in light of the results of this thesis, the proposal would have much more potential.

In some respects, the necessity of attempting to achieve such accuracy still needs to be determined. For example, gap widths are generally very small, and so fluid temperature differences across them may be small and thus insignificant in the overall scheme of the engineering problem. In addition, one must remember that there is likely to be a limit as to how representative a homogenous continuum can ultimately be. Nevertheless, the CFD promises to be a formidable tool. Detailed rheological studies may highlight deviations from continuum behaviour in some areas, for example, at low shear rates or near wall regions. In the CFD method, it may be possible to introduce corrective functions to account for such behaviour. This would be similar to the way in which turbulence is modelled.

REFERENCES

1. Bullough, W.A., *The third wave of machines*. 1996: p. 50-55.
2. Khabibullaev, P.K., E.V. Gevorkian, and A.S. Lagunov, *Rheology of Liquid Crystals*. 1994: Allerton Pr. 0898640776
3. Winslow, W.M., *Method and means for translating electrical impulses into mechanical force*. 1947, 2 417 850: US Patent.
4. Jabinow, J., *The magnetic fluid clutch*. AIEE Trans., 1948. **67**: p. 1308-1315.
5. Rabinow, J., *Magnetic fluid torque and force transmitting device*. 1947, 2 575 360: US.
6. Kordonski, W.I. and S.D. Jacobs. *Magnetorheological finishing. Proc. 5th Int. Conf. on ER fluids MR suspensions and associated technology*. 1995. Sheffield, UK: World Scientific.
7. Kordonski, W.I. and S.D. Jacobs, *Magneto-rheological finishing*. International Journal of Modern Physics B, 1996. **10**: p. 2837-2848.
8. Rheonetic, *Lord Corporation company*, <http://www.rheonetic.com/>.
9. Stanway, R., *Cadillac Suspension Dampers*. 2002.
10. Block, H. and J.P. Kelly. *Materials and mechanisms in electro-rheology. First International Symposium on ER fluids*. 1989. Boston, Massachusetts: North Carolina State University Engineering Publications Raleigh, NC 27695.
11. Johnson, A.R., J. Makin, and W.A. Bullough. *Electro-Rheological catch/clutch : inertial simulations. 4th int. conf. : Electrorheological fluids mechanisms, properties, technology and applications*. 1993. Feldkirch, Austria: World Scientific.
12. Tan, K.P., *Application of an Electro-Rheological twin clutch mechanism to robot arm positioning*, Ph.D, Phd thesis Mechanical Engineering, University of Sheffield, 2001.
13. Wilkinson, W.L., *Non-Newtonian fluids*. 1960, Oxford: Pergamon Press
14. Peel, D.J. and W.A. Bullough. *Prediction of electro-rheological valve performance in steady flow. Proc. Instn. Mech. Engrs*. 1994.
15. Whittle, M., R. Firoozian, W.A. Bullough, and D.J. Peel, *Pressure coupling in the electrical response of ER valves*. Int. J. Mod. Phys. B, 1994. **8**: p. 2903-2919.
16. ERFD, *ER Fluid Developments Sheffield, now Smart Technologies*.
17. Sproston, J.L., S.G. Rigby, E.W. Williams, and R. Stanway, *A numerical simulation of ERFs in oscillatory compression squeeze-flow*. J. Appl. Phys. D, 1994. **27**: p. 338-343.
18. Bullough, W.A., D.J. Ellam, and R.J. Atkin, *Electro-structured fluid flow quantification*, in *Smart structures applications and related technologies*, A. Suleman, Editor. 2001, Springer-Verlag: Heidelberg. p. 145-166.
19. Bullough, W.A. and D.J. Peel, *Electro-rheological oil hydraulics. Proc. Japan Soc. Hydraulics and Pneumatics*, 1986. **17**: p. 30-36.
20. Bullough, W.A., *Electro-rheological fluid actuators*, in *Adaptronics and Smart Structures*, H. Janocha, Editor. 1999, Springer-Verlag Berlin Heidelberg New York. p. 161-179.
21. Bullough, W.A., A. Hossenini-Sianaki, J. Makin, R. Firoozian, and A.R. Johnson. *Power transmission via the ER catch: continuum basis, performance predictions and infrastructure requirements. Mech E*.
22. Bullough, W.A. and e. al., *The ER catch: design, performance, considerations and operation*, in *Proc. IMechE*. 1993. p. 253-266.
23. Atkin, R.J., X. Shi, and W.A. Bullough, *Solutions of the constitutive equations*

- for the flow of an electro-rheological fluid in radial configurations. *J. Rheol.*, 1991. 7: p. 1441-1491.
24. Bird, R.B., G.C. Dai, and B.J. Yarusso, *The rheology and flow of viscoplastic materials*. *Rev. Chem. Eng.*, 1983. 1: p. 1-70.
 25. Bullough, W.A., R.J. Atkin, S. Urang, T.G. Kum, C. Musch, and T. Rober, *Two dimensional flow of an ESF: experiment, CFD, Bingham plastic analysis*. *Int. Jnl. Mod. Phys. B*, 2001. 15: p. 745-757.
 26. Lipscomb, G.G. and M.M. Denn, *Flow of Bingham Fluids in Complex Geometries*. *J. of Non-Newtonian Fluid Mech.*, 1984. 14: p. 337-346.
 27. Atkin, R.J., X. Shi, and W.A. Bullough, *Effect of non-uniform field distribution on steady flow of an ERF*. *J. Non-Newtonian Fluid Mech.*, 1999. 86: p. 119-132.
 28. Leek, T.H., R.J. Atkin, S. Lingard, and W.A. Bullough, *Solutions for one dimensional combined Couette and Poiseuille flow of an ERF modelled as a Bingham plastic: to be published*.
 29. Atkin, R.J., D.J. Ellam, and W.A. Bullough, *Throughflow effect on slip torque in a ESF concentric clutch*, in *Proc. 13th Int. Congress on Rheology*. 2000, British Soc. of Rheology: Glasgow. p. 414-416.
 30. Cheng, D., P. Madhvi, and A.P. Kruszeski, *Course notes: Warren Spring laboratory foundation course in rheology*. 1994.
 31. Kecskes, L.J., *Assessment of two ER fluids for use in recoil abatement applications*. 2001, Army Research Laboratory.
 32. Peel, D.J., R. Stanway, and W.A. Bullough, *A generalised presentation of valve and clutch data for an ER fluid, and practical performance prediction methodology*. *International Journal of Modern Physics B*, 1996. 10: p. 3103-3114.
 33. Gorodkin, S., A. Lukianovich, and W. Kordonski. *MR Trrottle Valve in Passive Damping Systems*. 1998.
 34. Peel, D.J. and W.A. Bullough, *A technique for the normalisation of electro-rheological fluid performance data in cylindrical/shear and pressure/flow modes of steady operation*, in *Proc. of SPIE: Smart Materials, Structures and MEMS*. 1996: Bangalore, India, p. 511-523.
 35. Kinsella, J. *Computational Fluid Mechanics Modelling of ESFs*. 1996.
 36. Whittle, M., R. Firoozian, D.J. Peel, and W.A. Bullough, *Electrorheological relaxation times derived from pressure response experiments in the flow mode*. *J. Non-Newtonian Fluid Mech.*, 1995. 57: p. 1-25.
 37. Whittle, M., R.J. Atkin, and W.A. Bullough, *Dynamics of an ER valve*, in *Proc. 5th Int. Conf. ERFs MRSs and Associated Tech*. 1995: World Scientific. p. 100-117.
 38. Whittle, M., R.J. Atkin, and W.A. Bullough, *Fluid dynamic limitations on the performance of an electro-rheological clutch*, in *J. Non-Newtonian Fluid Mech.* 1995. p. 61-81.
 39. Whittle, M., R.J. Atkin, and W.A. Bullough. *Dynamics of a radial plate clutch*. *5th Int. conf. ER*. 1995. World Scientific.
 40. Carreau, P.J., *Rheological equations from molecular network theories*. *Trans. Soc. Rheol.*, 1972. 16: p. 99-127.
 41. Leek, T.H., S. Lingard, W.A. Bullough, and R.A. Atkin, *The time response of an Electro-Rheological Fluid in a hydrodynamic film*. *Int. J. Mod. Phys. B*, 1996. 10(23 & 24): p. 3343-3355.
 42. Simmonds, S., *CFD analysis of a Rayleigh step bearing using ER fluids*, MENG, BEng Thesis Mechanical Engineering, Sheffield, 1999.
 43. Atkin, R.J., *Personal Communication*. 2003: Department of Mathematics, University of Sheffield.
 44. Bullough, W.A., J. Kinsella, and D.J. Peel. *Particulate/liquid electrically*

- structured functional fluids - a computer fluid mechanic technique for engineering design. Smart Materials and Structures Proceedings of the 4th European and 2nd MIMR conference.* 1998. Harrogate, UK: Institute of Physics Publishing.
45. Ellam, D.J., R.J. Atkin, and W.A. Bullough, *Appraisal of an ESF radial plate clutch with cooling flow using a NNF CFD solver*, in *Proc. Rheology and Fluid Mechanics of Nonlinear Materials*. 2000, ASME: Florida. p. 117-125.
 46. Atkin, R.J., D.J. Ellam, and W.A. Bullough. *Electro-Structured Fluid Seals. Proc. 8th Int. Con. on ERFs, MRSs and Associated Technology*. 2001. Nice, France: World Scientific Publishing.
 47. Atkin, R.J., D.J. Ellam, and W.A. Bullough, *Electro-Structured Fluid Seals. J. Intelligent Material Systems and Structures*, 2002. **13**: p. 459-464.
 48. Atkin, R.J., *Personal Correspondence, University of Sheffield, Department of Mathematics*.
 49. Musch, C. and T.K. Rober, *Theoretical investigation of a concentric ER clutch*, Undergraduate, Mech. Eng., University of Sheffield, 1999.
 50. Urang, S., *Theoretical investigation of a concentric ER clutch*, Undergraduate, Mech. Eng., University of Sheffield, 1999.
 51. Atkin, R.J., T.J. Corden, T.G. Kum, and W.A. Bullough, *Two-dimensional Bingham plastic flow in a cylindrical pressurised clutch*. *Int. J. Mod. Phys. B*, 1994. **8**: p. 2955-2965.
 52. Kordonski, W.I. and S.R. Gorodkin, *Magnetorheological fluid seal*. *Proc. 6th int. con. on ERFs, MRSs and their applications*, 1997. **10**: p. 704-709.
 53. Li, W.H., X.J. Wang, X. Tang, and P.Q. Zhang.
 54. Bullough, W.A., *Electro-rheological fluids and Magneto-rheological suspensions and associated technology Proceedings of the 5th International Conference*. 1995: World Scientific. 981-02-2676-4
 55. Nakano, M. and K. Koyama, *Electro-rheological fluids and Magneto-rheological suspensions and their applications Proceedings of the 6th International Conference*. 1997: World Scientific. 908. 981-02-3750-2
 56. Tao, R., *Electro-rheological fluids and Magneto-rheological suspensions Proceedings of the 7th International Conference*. 1999: World Scientific. 864. 981-02-4258-1
 57. Bossis, G., *Electro-rheological fluids and Magneto-rheological suspensions Proceedings of the Eighth International Conference*. 2001: World Scientific. 904. 981-02-4937-3
 58. Weiss, K.D., J.D. Carlson, and D.A. Nixon, *Viscoelastic Properties of Magneto- and Electro-Rheological Fluids*. *J. Intelligent Material Systems and Structures*, 1994. **5**: p. 772-775.
 59. Roy, R.K., *Design of Experiments Using The Taguchi Approach*. 2001: Wiley. 560. 0-471-36101-1
 60. Kordonski, W. and D. Golini. *Progress update in magnetorheological finishing. Proceedings of the 6th international conference on ERFs, MRS and their applications*. 1997: World scientific Publishing.
 61. Tozer, R.C., *On-off excitation switch for ER devices*. 1994. **8**.
 62. Makin, J., *Electro-rheological fluid - fast response tolerance actuator application*, Ph.D thesis, Mechanical Engineering, The University of Sheffield, 2001.
 63. Oravsky, V. *Heat transfer from an ESF radial plate clutch surface - theory. Proc. 8th Int. Con. on ERFs, MRSs and Associated Technology*. 2001. Nice, France: World Scientific Publishing.
 64. Ellam, D.J., W.A. Bullough, and V. Oravsky. *Heat transfer from an ESF radial*

- plate clutch surface. Proc. 8th Int. Con. on ERFs, MRSs and associated technology.* 2002. Nice, France: World Scientific Publishing.
65. Ellam, D.J., W.A. Bullough, and V. Oravsky, *Heat transfer from an ESF radial plate clutch surface.* *J. Intelligent Material Systems and Structures*, 2003. **14**: p. 119-124.
66. Bullough, W.A., *Electro-structured fluids and smart machines.* 2000.
67. Wong, *Handbook of essential formulae and data on heat transfer for engineers.* 1977, New York: Longman Inc. 0-582-46050-6
68. Smyth, R., K.H. Tan, and W.A. Bullough, *Heat transfer modeling of a cylindrical ER catch.* *Int. Jnl. Mod. Phys.*, 1994. **8**: p. 3033-3050.
69. Fluent, *Fluent5 User's Guide.* 1998.

APPENDIX A : CFD SUB-ROUTINES

The following tables show examples of Fluent5 subroutines. These functions must be compiled into the main before they are available for selection. See Fluent5 manuals for details.

```

#include "udf.h"
#define MU 0.1
#define MUHI 1000
#define V 1000

#define DEDX (C_UDSI_G(c,t,0)[0])
#define DEDY (C_UDSI_G(c,t,0)[1])

#define DUDX C_DUDX(c,t)
#define DVDY C_DVDY(c,t)
#define DODY (C_OMEGA_G(c,t)[1])
#define DODX (C_OMEGA_G(c,t)[0])
#define DUDY C_DUDY(c,t)
#define DVDX C_DVDX(c,t)
#define W C_W(c,t)
#define V C_V(c,t)
#define R x[1]

DEFINE_PROPERTY(ne1000_100,c,t)
{
  real x[ND_ND];
  real Err;
  real Eoo;
  real Ezz;
  real Erz;
  real Ero;
  real Eoz;
  real strain_rate;

  real mu;
  real TAU;
  real EDOT;

  C_CENTROID(x,c,t);

  Err = 0.5*DVDY*DVDY;
  Eoo = 0.5*(V/R)*(V/R);
  Ezz = 0.5*DUDX*DUDX;
  Erz = (0.5*R*DODY)*(0.5*R*DODY);
  Ero = (0.5*(DUDY+DVDX))*(0.5*(DUDY+DVDX));
  Eoz = (0.5*R*DODX)*(0.5*R*DODX);

  strain_rate =2 * sqrt(Err+Eoo+Ezz+Erz+Ero+Eoz);

  EDOT = sqrt(DEDX*DEDX+DEDY*DEDY);

  if (EDOT < 100000)
    TAU = MU;
  else
    TAU = EDOT/1000;

  if (strain_rate < (TAU/(MUHI-MU)))
    mu = MUHI;

```

```

else
  mu = TAU/strain_rate + MU;

return mu;
}

```

Table A.1: Example of subroutine for calculating the resultant excitation and then viscosity.

```

#include "udf.h"
#define MU 0.1
#define MUHI 1000
#define TAU 5000
#define G 10000

DEFINE_PROPERTY(t2d_5000_100,c,t)
{
  real strain_rate;
  real mu, yield;
  real time = RP_Get_Real("flow-time");
  strain_rate = CELL_STRAIN_RATE_MAG(c,t);
  yield = TAU*(1 - exp(-G*strain_rate/TAU*time));
  mu = MU + (yield/strain_rate)*(1-MU/MUHI);

  if (mu > MUHI)
    mu = MUHI;

  return mu;
}

```

Table A.2: Example of a subroutine for calculating the non-Newtonian viscosity using a viscoelastic Bingham CFD model.

```

#include "udf.h"

DEFINE_PROFILE(shear_stress, thread, nv)
{
  face_t f;
  cell_t c;
  Thread *ct;
  real dt;
  real stress=0;
  real A=5.231;

  /* loop over each of the faces of this zone */
  begin_f_loop (f,thread)
  {
    if((rp_dual_time) && (n_time_levels >1))
    {
      c =F_C0(f,thread);
      ct =F_C0_THREAD(f,thread);

      if((rp_dual_time) && (n_time_levels >1))
      {
        dt = RP_Get_Real("physical-time-step");
        stress=(C_U(c,ct) - C_U_M1(c,ct))/dt
      }
    }
    F_PROFILE(f,thread,nv) = stress;
  }
  end_f_loop(f,thread)
}

```

```
}
```

Table A.3: Example of a subroutine for calculating the wall shear stress due the output rotors inertial value.

```
#include "udf.h"
#define J 16.0
#define E 2.0
DEFINE_SOURCE(qe, cell, thread, dS, eqn)
{
  real qe;
  real x[ND_ND];
  qe = -J*E;
  dS[eqn] = 0;
  return qe;
}
```

Table A.4: Example of a subroutine for calculating electrical heating in an ER fluid.

APPENDIX B : PUBLICATIONS

1. Bullough, W.A., D.J. Ellam, and R.J. Atkin, *Electro-structured fluid flow quantification, in Smart structures applications and related technologies*, A. Suleman, Editor. 2001, Springer-Verlag: Heidelberg. p. 145-166. (not in this appendix)
2. Ellam, D.J., R.J. Atkin, and W.A. Bullough, *Appraisal of an ESF radial plate clutch with cooling flow using a NNF CFD solver, in Proc. Rheology and Fluid Mechanics of Nonlinear Materials*. 2000, ASME: Florida. p. 117-125.
3. Atkin, R.J., D.J. Ellam, and W.A. Bullough, *Thoughflow effect on slip torque in a ESF concentric clutch, in Proc. 13th Int. Congress on Rheology*. 2000, British Soc. of Rheology: Glasgow. p. 414-416.
4. Atkin, R.J., D.J. Ellam, and W.A. Bullough. *Electro-Structured Fluid Seals*. Proc. 8th Int. Con. on ERFs, MRSs. July 2001. Nice, France: World Scientific Publishing. (not in this appendix)
5. Atkin, R.J., D.J. Ellam, and W.A. Bullough, *Electro-Structured Fluid Seals*. *J. Intelligent Material Systems and Structures*, 2002. 13: p. 459-464.
6. Ellam, D.J., W.A. Bullough, and V. Oravsky, *Heat transfer from an ESF radial plate clutch surface*. *J. Intelligent Material Systems and Structures*, 2003. 14: p. 119-124.
7. Ellam, D.J., W.A. Bullough, and V. Oravsky. *Heat transfer from an ESF radial plate clutch surface*. Proc. 8th Int. Con. on ERFs, MRSs. July 2001. Nice, France: World Scientific Publishing. (not in this appendix)

APPRAISAL OF AN ESF RADIAL PLATE CLUTCH WITH COOLING FLOW USING A NNF CFD SOLVER

Darren J. Ellam, Raymond J. Atkin and William A. Bullough
SMMART Engineering Network, University of Sheffield, Mappin Street, Sheffield, S1 3JD, UK

ABSTRACT

To aid the application of electro-structured fluid (ESF) devices, a virtual two plate radial clutch is examined in a pre-prototyping exercise to estimate the effect of a radial cooling flow on pre-set torque transmission. A throughflow of ESF will act to keep the fluid temperature under control making such devices more reliable over a wider operating range.

The ESF is treated as a Bingham viscoplastic material and clutch behaviour is investigated under steady state isothermal conditions. The resulting two-dimensional non-Newtonian fluid (NNF) model is solved using a computational fluid dynamics (CFD) package. The results are partially verified using analytical analysis and compared with sparse experimental data. This work is expected to lead to a more complex CFD model for which analytical methods will not be available.

Indications are that, for realistic rates of throughflow, torque transmission should not be overtly affected. Hence the cooling of slipping ESF clutches by throughflow can be contemplated.

NOMENCLATURE

C_v	J/kg ^o K	fluid specific heat capacity
$G(r)$	N/m ³	pressure gradient (function of radius)
T	Nm	applied torque
T_e	Nm	τ_e contribution to applied torque
T_o	Nm	Newtonian contribution to applied torque
dp	bar	pressure difference between inlet and outlet
h	m	gap width
\dot{m}	kg/s	mass flow rate
p	Pa	static pressure
\dot{q}_r	m ³ /s	flow rate through clutch
r	m	radial position
r_o	m	outer radius
r_i	m	inner radius

v_r	m/s	velocity in radial direction
v_θ	m/s	velocity in circumferential direction
z	m	axial position (from lower plate)
$\dot{\gamma}$	/s	magnitude of local deformation rate
μ	Pa.s	plastic viscosity
μ_{nn}	Pa.s	non-Newtonian (effective) viscosity
$\mu_{\dot{\gamma} \rightarrow 0}$	Pa.s	limiting viscosity (viscosity at low shear rates)
θ	radians	circumferential direction
ρ	kg/m ³	ESF density
τ	Pa	magnitude of local deformation stress
τ_e	Pa	electro-stress (yield stress)
τ_{rz}	Pa	radial shear stress
$\tau_{\theta z}$	Pa	circumferential shear stress
Ω	rad/s	relative angular speed

INTRODUCTION

An ESF provides a reliable means of coupling electronic and mechanical control. Unlike their mechanical counterparts ESF clutch controllers offer the ability to rapidly and smoothly actuate accelerating loads on a very regular basis without direct plate to plate contact.

In such ESF type devices fluid temperature is driven upwards by repeated switching of inertial loads at high accelerations and in high shear rate conditions. This is an unavoidable inefficiency in such transmission of power. In a closed system electro-rheological fluids (ERFs) experience avalanche current discharges in thermal runaway. In high yield stress magneto-rheological suspension (MRS) applications the heating effect can be intense. For both scenarios, the introduction of a cooling flow would seem to offer obvious benefits for clutch devices provided that the throughflow did not severely affect the torque transmission.

It should be noted that a valve controlled damper test rig has

worked trouble free for years (Peel et.al, 1994). It enjoys the control volume method of working where the fluid is continuously exhausted from the valve and cooled externally. Furthermore, analytical theory using the Bingham plastic equation is found to be very successful in predicting operation.

Electro-Structured Fluids

The aim is to appraise the clutch problem for ESFs that can be defined by the Bingham plastic type constitutive equation. This particularly includes MRSs, ERFs and ERF/MRS mixtures, which comprise of a suspension of particles in a fluid medium. The particles are $<10 \mu\text{m}$ in diameter, therefore on a macroscopic scale the fluid can be treated as a continuum. ESFs also include liquid-liquid non-miscible liquids and liquid crystals. Such fluid types can be potentially modelled using the NNF CFD technique presented in this paper.

In the unexcited state the Bingham type ESFs can be considered to behave as Newtonian fluids. On the application of a field the fluid can undergo a reversible microscopic interaction that generates a fluid yield stress capable of supporting a load. Altering the field strength simply generates a different electro-stress, τ_e , value. In this state the fluid behaviour can be described using non-Newtonian viscoplastic equations.

The Bingham plastic constitutive equation will closely represent the properties of most ESFs and is therefore used in this paper. On an individual fluid basis a more representative model may be used at a later time. Furthermore this work concentrates on the steady state case where the fluid is subject to a constant field strength, in which response time effects are not considered.

ESF Clutches

In the simplest case the ESF radial clutch comprises of two circular plates. The gap width, h , typically 0.5 mm, is filled with ESF and it is this fluid medium, rather than physical contact of the two plates, which transmits the torque. Varying the excitation and hence the ESF properties allows the transmitted torque to be controlled. A commercially viable clutch may be multi-plate in design and much more physically complex.

This paper follows a previous publication on the effect of an axial throughflow in a geometrically and therefore rheologically simpler concentric type clutch (Atkin et.al, 2000). In essence, the analysis shows that the axial and circumferential flows are coupled, but for practical parameters, the reduction in torque is negligible allowing such a device to be contemplated. In addition, the computed CFD flow field precisely complemented the analytical theory. Figure 1. shows a schematic of both types of clutch.

Approach Taken

In a real clutch situation, fluid properties will be temperature dependent, heat transfer will take place, difficult geometries will be encountered and the general mode of operation will be unsteady. In this respect only CFD holds out to the prospect of a meaningful pre-prototype procedure. Before moving directly to a complex CFD approach it is prudent to test whether the main proposition is valid:

will the torque be significantly affected by the rate of cooling flow? Also, can a current CFD package deal with a relatively complex two-dimensional situation.

Using the Bingham plastic constitutive theory, an approximate analytical theory is developed. This theory is then used to validate the results of a CFD model for exactly the same geometry and parameters. The results are also compared with some data from experiments carried out at low loading conditions, which correlates with the theoretical predictions.

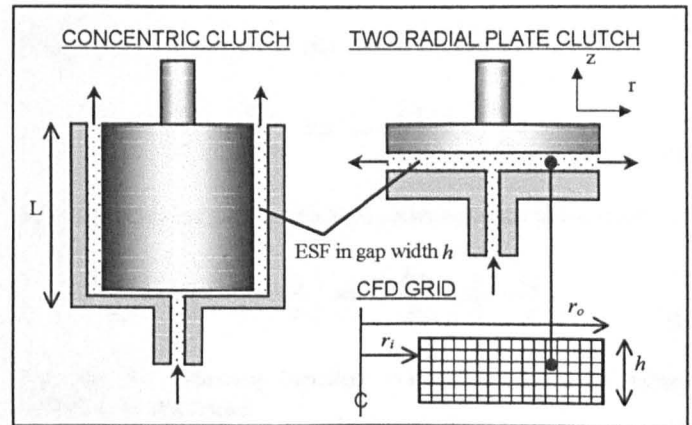


Figure 1. Schematic of radial and concentric type clutches and illustration of how the CFD model is set up.

ANALYTICAL THEORY

Modelling

The analysis of the two plate radial clutch arrangement (Fig. 1.) is simplified by assuming that the flow is steady, two-dimensional, laminar and isothermal. The ESF is considered to be a homogeneous, incompressible continuum with constant properties of electro-stress and plastic viscosity.

A distance of h in the z -direction separates the two clutch plates. Flow occurs in both circumferential and radial directions, the former caused by the relative angular speed, Ω , of the plates (Couette flow), the latter due to the difference in pressure between inlet and outlet radii (Poiseuille flow). For simplicity one plate is always considered to be stationary, the other rotates with a constant speed Ω . The velocity components are

$$v_r = v_r(r, z), \quad v_\theta = v_\theta(r, z), \quad v_z = 0. \quad (1)$$

In the absence of body forces the momentum equations are

$$\rho \left(\frac{\partial v_i}{\partial t} + v_j \frac{\partial v_i}{\partial x_j} \right) = - \frac{\partial p}{\partial x_i} + \frac{\partial \tau_{ij}}{\partial x_j}. \quad (2)$$

The 3-d Bingham plastic constitutive model (Bird et.al, 1983) is used to represent the stress tensor τ_{ij} in terms of the deformation rate

tensor d_{ij} , so that

$$\begin{aligned} \tau_{ij} &= \left(\frac{\tau_e}{\dot{\gamma}} + \mu \right) d_{ij}, & \tau > \tau_e \\ d_{ij} &= 0, & \tau < \tau_e \end{aligned} \quad (3)$$

where

$$d_{ij} = \frac{\partial v_i}{\partial x_j} + \frac{\partial v_j}{\partial x_i}, \quad (4)$$

$$\tau = \pm \sqrt{\frac{1}{2} \tau_{ij} \tau_{ij}}, \quad (5)$$

$$\dot{\gamma} = \pm \sqrt{\frac{1}{2} d_{ij} d_{ij}}. \quad (6)$$

An analysis of d_{ij} shows that provided $h \ll r$ the dominant terms are d_{rz} , d_{zr} , $d_{z\theta}$ and $d_{\theta z}$. This is equivalent to neglecting the normal stresses. As centrifugal acceleration terms are expected to be small, steady state acceleration terms are also neglected. Under the approximation $h \ll r$ the dominant terms in the momentum equations (Eq. (2.)) are then

$$-\frac{\partial p}{\partial r} + \frac{\partial \tau_{rz}}{\partial z} = 0, \quad \frac{\partial \tau_{\theta z}}{\partial z} = 0, \quad \frac{\partial p}{\partial z} = 0. \quad (7)$$

These partial differential equations can be integrated to give

$$\tau_{rz} = G(r)z + b(r), \quad \tau_{\theta z} = c(r), \quad p = p(r), \quad (8)$$

where

$$G(r) = \frac{dp}{dr}. \quad (9)$$

and G , b and c are functions of radius. Eq. (5). gives the magnitude of the resultant shear stress as

$$\tau = \sqrt{\tau_{rz}^2 + \tau_{\theta z}^2} = \sqrt{(G(r)z + b(r))^2 + c(r)^2}.$$

It can be deduced that flow will only occur if

$$\sqrt{b^2 + c^2} > \tau_e. \quad (10)$$

If $|c(r)| > \tau_e$ flow will occur across the whole gap. However if $|c(r)| < \tau_e$ flow can only occur if a central pseudo-plug region is present. A plug region is a section of solid material in which $\tau < \tau_e$. The term pseudo-plug is used because in this geometry it is impossible to have a solid central section moving at constant speed, but at given radius the velocity profiles have a central section in which the speed is constant.

The torque required to keep the upper plate moving with angular speed Ω is given by

$$T = \int_n^{r_0} dr \int_0^{2\pi} r^2 c(r) d\theta = 2\pi \int_n^{r_0} r^2 c(r) dr. \quad (11)$$

In the coupled flow case the total torque is calculated at discrete radii and summed over the range r_i and r_0 so that

$$T = 2\pi \sum_n^{r_0} r^2 c(r) \delta r. \quad (12)$$

Using the constitutive theory (Eq. (3.)) it follows that

$$\tau_{rz} = \left(\frac{\tau_e}{\dot{\gamma}} + \mu \right) \frac{\partial v_r}{\partial z} \quad \text{and} \quad \tau_{\theta z} = \left(\frac{\tau_e}{\dot{\gamma}} + \mu \right) \frac{\partial v_\theta}{\partial z}, \quad (13)$$

and, combining Eq. (8). and Eq. (13)., after suitable rearrangement

$$\mu \frac{\partial v_r}{\partial z} = (Gz + b) \left(1 - \frac{\tau_e}{\tau} \right) \quad \text{and} \quad \mu \frac{\partial v_\theta}{\partial z} = c \left(1 - \frac{\tau_e}{\tau} \right). \quad (14)$$

Applying the following boundary conditions allows the velocity profiles to be developed

$$\begin{aligned} z = 0, \quad v_r &= 0 \quad \& \quad v_\theta = 0 \\ z = h, \quad v_r &= 0 \quad \& \quad v_\theta = r\Omega \end{aligned} \quad (15)$$

In order to satisfy the boundary conditions on v_r ,

$$b = -\frac{G(r)h}{2}. \quad (16)$$

(i) Plug-less flow region $|c(r)| > \tau_e$

Here the velocity profiles are given as follows

$$v_r = V_r = \frac{1}{\mu} \left(\frac{Gz^2}{2} + bz - \frac{\tau_e}{G} \left[\sqrt{c^2 + (Gz + b)^2} - \sqrt{c^2 + b^2} \right] \right), \quad (17)$$

$$v_\theta = V_\theta = \frac{|c|}{\mu} \left(z - \frac{\tau_e}{G} \left[\sinh^{-1} \left(\frac{Gz + b}{|c|} \right) - \sinh^{-1} \left(\frac{b}{|c|} \right) \right] \right). \quad (18)$$

Both velocity components are therefore dependent on G and are so affected by a change in the pressure gradient. To satisfy the condition $v_\theta = r\Omega$ at $z = h$ the following expression determines $c(r)$ at position r

$$\mu r \Omega = |c| \left[h - \frac{2\tau_e}{G} \sinh^{-1} \left(\frac{Gh}{2|c|} \right) \right]. \quad (19)$$

An integration of the radial velocity profile (Eq. (17).) gives the radial flow rate

$$\dot{q}_r = -\frac{Gh^3\pi r}{6\mu} + \frac{2\pi r}{\mu} \left\{ \frac{\tau_e h}{4G} \sqrt{G^2 h^2 + 4c^2} - \frac{\tau_e c^2}{G^2} \sinh^{-1} \left(\frac{Gh}{2|c|} \right) \right\}. \quad (20)$$

Couette Flow Only. When $|Gh/2c| \ll 1$ Eq. (19). reduces to

$$c(r) = \frac{\mu r \Omega}{h} + \tau_e. \quad (21)$$

This is also the expression for $c(r)$ in the case when there is no axial flow (i.e $G = 0$). This expression can be integrated to give

$$T = T_o + T_e = \frac{\mu \pi \Omega}{2h} (r_o^4 - r_i^4) + \frac{2\pi \tau_e}{3} (r_o^3 - r_i^3). \quad (22)$$

It can be observed that when there is no throughflow the output torque consists of a Newtonian contribution (T_o) due to the shear rate, plus a fixed electro-stress contribution (T_e) due to the excitation of the ESF. The fixed value of T_e must be overcome before flow can occur.

(ii) Plug flow region $|c(r)| < \tau_e$

In this case τ_e alone is not large enough to cause flow and so a contribution from τ_z is required to satisfy the flow condition $\tau > \tau_e$. In this flow regime a central pseudo-plug is present. The plug boundaries can be determined by the condition that $\tau = \tau_e$ for which

$$G(r)^2 \left(z - \frac{h}{2} \right)^2 + c(r)^2 = \tau_e^2$$

hence

$$z_1 = \frac{h}{2} - \frac{\sqrt{\tau_e^2 - c^2}}{|G|}, \quad z_2 = \frac{h}{2} + \frac{\sqrt{\tau_e^2 - c^2}}{|G|}. \quad (23)$$

This gives a plug thickness of

$$z_2 - z_1 = \frac{2}{|G|} \sqrt{\tau_e^2 - c^2}, \quad (24)$$

which must be less than the gap size h . This inequality leads to a critical condition for flow to occur equivalent to Eq. (10). The velocity components are now

$$v_r = \begin{cases} V_r(r, z) & , & 0 \leq z \leq z_1, \\ V_r(r, z_1) & , & z_1 \leq z \leq z_2, \\ V_r(r, h-z) & , & z_2 \leq z \leq h, \end{cases} \quad v_\theta = \begin{cases} V_\theta(r, z) & , & 0 \leq z \leq z_1, \\ r\Omega/2 & , & z_1 \leq z \leq z_2, \\ r\Omega - V_\theta(r, h-z) & , & z_2 \leq z \leq h, \end{cases} \quad (25)$$

where V_r and V_θ are given by Eq. (17). and Eq. (18). The result for this solution which corresponds to Eq. (19) is

$$\mu r \Omega = |c| \left[h - \frac{2\sqrt{\tau_e^2 - c^2}}{|G|} \right] - \frac{2|c|\tau_e}{|G|} \times \left[\sinh^{-1} \left(\frac{Gh}{2|c|} \right) - \sinh^{-1} \left(\frac{\sqrt{\tau_e^2 - c^2}}{|c|} \right) \right]. \quad (26)$$

Again an integration of the velocity profile v_r gives the radial flow rate expression

$$\dot{q} = 2\pi r \left[2 \int_0^{z_1} v_r(r, z) dz + V_r(r, z_1)(z_2 - z_1) \right] = \dot{q}_1 + \dot{q}_2$$

$$\dot{q}_1 = \frac{2\pi r}{\mu_2} \left[-\frac{Gz^2}{12} (3h - 2z) + \frac{\tau_e z}{2G} \sqrt{G^2 h^2 + 4c^2} + \frac{\tau_e}{2G} (0.5h - z) \sqrt{c^2 + G^2 (0.5h - z)^2} + \frac{\tau_e c^2}{2G^2} \sinh^{-1} \left(\frac{G}{|c|} (0.5h - z) \right) \right]_0^{z_1}$$

$$\dot{q}_2 = 2\pi r (0.5h - z_1) V_r(r, z_1). \quad (27)$$

Poiseuille Flow only. If we consider radial flow only (i.e. $c(r) = 0$) then using Eq. (17). Eq. (27) reduces to

$$\dot{q}_r = \frac{\pi r h^3 G(r)}{6\mu} \left[-1 + 3 \left(\frac{\tau_e}{hG(r)} \right) - 4 \left(\frac{\tau_e}{hG(r)} \right)^3 \right]. \quad (28)$$

With appropriate change in notation this equation is the same as that presented by Bird et.al (1983).

COMPUTATIONAL FLUID DYNAMICS

The same problem as outlined above was solved using a commercial CFD package (Fluent IV). The same flow and fluid assumptions already outlined at the beginning of the analytical analysis section apply to the CFD solution. However the lubrication assumption, $h \ll r$, is not required and furthermore the steady state acceleration terms are not neglected.

The governing Navier-Stokes equations are discretised using a finite volume method that involves splitting the continuum into a finite number of cells allowing the partial differential equations to be integrated on a control volume basis. The Newtonian viscosity is replaced with a non-Newtonian viscosity, μ_{nm} which is solely dependent on the local deformation rate (Eq. (6.)) and fixed fluid properties; it is derived using the Bingham plastic equation:

$$\mu_{nm} = \frac{\tau_e}{\dot{\gamma}} + \mu \leq \mu_{\dot{\gamma} \rightarrow 0} \quad (29)$$

There is the potential for computational difficulties due to

unyielded sections of fluid having a zero deformation rate making μ_{nn} equal to infinity. Rather than computing the stresses and strains in unyielded regions here the entire material is treated as a fluid with an upper limit of μ_{nn} . This constitutive model is comparable to the bi-viscous model that utilises a Bingham plastic equation in yielded regions and treats unyielded regions as a highly viscous Newtonian fluid with viscosity $\mu_{i \rightarrow 0}$. The difference between the two is that CFD does not apply boundary conditions to determine plug regions; the plug boundaries occur when $\mu_{nn} \rightarrow \tau_e / \dot{\gamma}$; and then within this plug the viscosity increases to a possible maximum value of $\mu_{i \rightarrow 0}$. When this limiting viscosity is large enough there should be no noticeable difference between the bi-viscous, Bingham, or CFD method of representing the stress tensor. So long as $\mu_{i \rightarrow 0}$ is high enough to prevent μ_{nn} being cut off before any potential plug boundary occurs the particular value is quite insignificant. The viscosity $\mu_{i \rightarrow 0}$ was therefore set at 100 Pa, typically 1000 times the plastic viscosity.

Since the flow aligns with the grid a first order power law interpolation scheme was adequate to determine cell face values. Velocities are determined from the momentum equations, and pressure is determined using the SIMPLE pressure-velocity coupling algorithm. The viscosity, μ_{nn} , is calculated in a sub-routine linked to the main code. The fully discretised equations are then solved by a semi-iterative method using a Tri-diagonal Matrix Algorithm and treating off-line variables as known from the previous iteration. Convergence of a solution is usually interpreted by using the normalised residuals; these are a measure of the degree to which the equations are satisfied. The manual (Fluent, 1997) describes more fully the numerical and solution techniques.

The clutch was modelled as two radial plates; all derivatives are zero in the tangential direction allowing a 2-d axisymmetric grid to be used. A uniform inlet velocity boundary condition allowed the flow rate, \dot{q}_r , to be set, a relative static pressure condition of 0 Pa was used for the outlet. One plate wall is set as stationary the other is set to rotate at an angular speed Ω . Increasing grid resolution produces a model that more accurately simulates the continuum. However, this comes at the expense of computational speed therefore engineering judgment must be exercised.

EXPERIMENTAL INVESTIGATION

A small undergraduate investigation by Hon (1996) of this radial flow problem has been previously carried out on an ERF based apparatus. The two plate clutch arrangement had a 2 mm inner and 30 mm outer radii with a gap size h of 1 mm. Results were taken between 440-750 rpm steady state rotation at field strengths corresponding to electro-stress values of between 54-700 Pa.

The application of relatively small pressures at the inlet using the weight of the fluid in a vertical/axial supply line resulted in low flow rates (<0.1 lt/min). Small values of pressure result in $|Gh/2c| \ll 1$ being valid, making Eq. (21) and Eq. (22) relevant. Over the full range of experimental values the torque is within 30% of that predicted by Eq. (22). The accuracy in interpolating the manufacturers fluid data, in particular τ_e , plus the rudimentary nature of the apparatus and experimental technique is likely to be responsible for this discrepancy.

The important result to note is that at each particular field strength there was no measurable change in pre-set torque as increasing flow rates were imposed. This complements the analytical

theory in so much as it predicts this behaviour at low pressure gradients and hence low flow rates.

RESULTS

Poiseuille and Couette Flow

The computed CFD flow field for the case of radial flow only clearly shows the presence of pseudo-plug profiles (Fig. 2). The approximate analysis (Eq. (24) with $c(r) = 0$) suggests that the plug size should increase with radius due to $G(r)$ decreasing with radial position. To maintain mass continuity the velocity of the ESF reduces, this results in a more dominant plug at greater radii (Fig. 2.) due to a reduction in deformation rate, and a non-linear pressure profile (Fig. 3.).

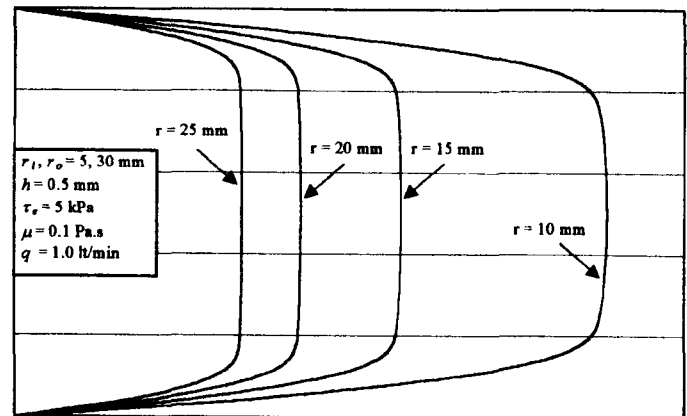


Figure 2. Radial velocity profiles for the case of Poiseuille flow only (i.e. no angular speed)

The pressure profile can be numerically differentiated to determine the gradient, $G(r)$, at discrete values of radius. If the CFD profile is correct then Eq. (28) must yield a constant value of \dot{q}_r at all radii if mass is to be conserved. Initial tests showed disagreement at small radii that could not be fully attributed to flow development. The discrepancy was found to be due to a lack of cell density in the radial direction. Unlike the concentric clutch case the pressure profile is non-linear particularly at and near the inlet radius. Increasing cell density resulted in good agreement over most of the radius range. The computed CFD flow field satisfies mass continuity over the whole radius. However, within the first 5 mm of the clutch the pressure profile is rather erratic due to the imposed uniform inlet velocity requiring some length to develop. As a consequence of using $G(r)$ calculated from the CFD pressure profile, the analytical equation that yields the flow rate (Eq. (28)) does not correspond to the CFD answer in this initial development length region.

When no throughflow is imposed the same grid was used to calculate the flow field for Couette flow only. Equation (22), which is relevant to this case, was found to be verified.

Coupled Flow

It is of interest to use theory and CFD to predict how T is affected

at higher values of flow rate when the approximation $|Gh/2c| \ll 1$ is no longer valid. As $|G(r)|$ increases $|c(r)|$ decreases and eventually there is a cross over from case (i) to (ii) (see Fig. (3)). For every computed flow field $G(r)$ was determined numerically allowing $c(r)$ to be calculated using the relevant equation (Eq. (19). or Eq. (26)). This allowed the total applied torque to be evaluated by summing the values at each discrete radii (Eq. (12)). This was achieved by importing CFD data into a spreadsheet allowing each CFD point to be checked.

A grid analysis showed that 80 cells in the axial direction gave grid independent answers. To achieve an accurate pressure field over the full radius requires about 400 cells. Eq. (22). shows that the majority of the torque is generated well away from the inlet, this meant that in practice only 100 cells in the radial direction were required for a grid independent answer. Considering the geometry $(r_o-r_i)/h$ the chosen grid of 80×100 gives a cell aspect ratio of 40. Such a cell ratio is acceptable for laminar flow problems in which derivatives are relatively linear. Engineering judgment was therefore used to set up a practical grid; the validity of which is demonstrated in the following results.

Figure (3). shows a non-linear pressure profile and how the shear stress, $c(r)$, varies with radius. The effect of the uniform inlet boundary condition can clearly be seen within the first 5 mm from the inlet radius, which is required for the parabolic type profiles to develop. This effect on the overall applied torque is not noticeable due to a large dependence on radius ($T = f(r^4)$). For this particular case both plug and plug-less regimes are present, the cross over point occurs at 5 kPa.

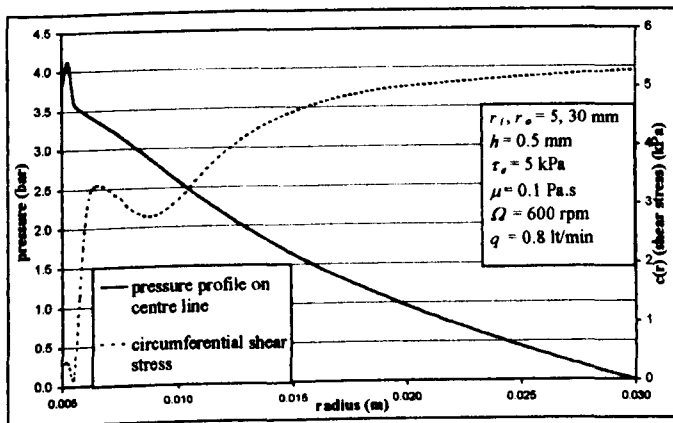


Figure 3. Static pressure and circumferential shear stress profiles within radial clutch.

Figure (4). & (5). show behaviour over a wide range of τ_s and flow rates at two typical speeds of operation. At 600 rpm there is a ~50 % reduction in T at 6 l/min at each value of τ_s , while at 1200 rpm the severity of the coupling loss is much less (~29 %). For a constant pressure difference reducing the speed also reduces the flow rate.

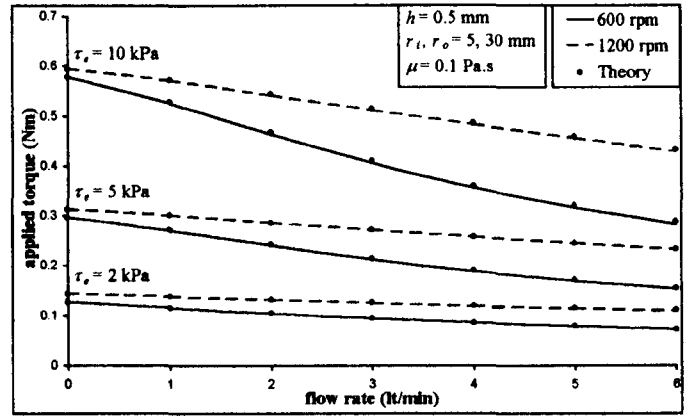


Figure 4. Torque coupling effect with flow rate.

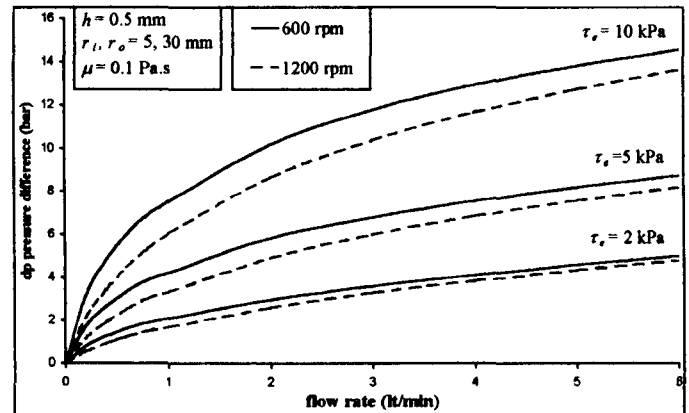


Figure 5. Effect of flow rate on dp corresponding to Fig. (4).

Next the effect of the geometry is considered. When there is no radial flow doubling the gap size halves the shearing rate and likewise the Newtonian contribution to torque (Eq. (22)). But for practical parameters the Newtonian shear stress is small in comparison to the electro-stress contribution, which means there is only a small reduction in T . In terms of coupling effect as shown in Fig. (6)., doubling the gap size results in a significantly better scenario. This is due to a doubling in the ratio between circumferential/radial velocity, resulting in a greater Couette flow domination and less coupling.

As shown in Fig. (6). a 17 % increase in radii from 30 to 35 mm gives a 91 % increase in applied torque. This is due to the large significance of radius ($T = f(r^4)$) and a resulting higher ratio of circumferential/radial velocity in this new section, radial velocity decreases with radius while circumferential velocity increases. At 6 l/min the loss in torque is now ~40% as opposed to ~50% previously.

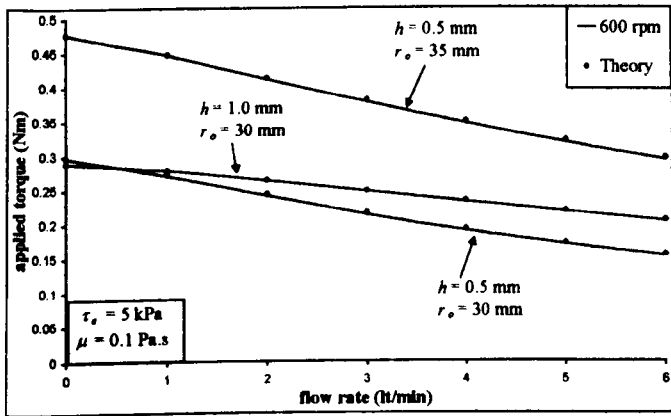


Figure 6. Torque coupling effect with flow rate for different geometry.

It is worth investigating the effect of the plastic viscosity. In the absence of radial flow, μ only contributes to the Newtonian term (T_o) that is typically much smaller than the electro-stress term (T_e) (Eq. (22)). Figure (7). shows that a high plastic viscosity could give a much greater Newtonian contribution but has little effect in terms of the coupling effect.

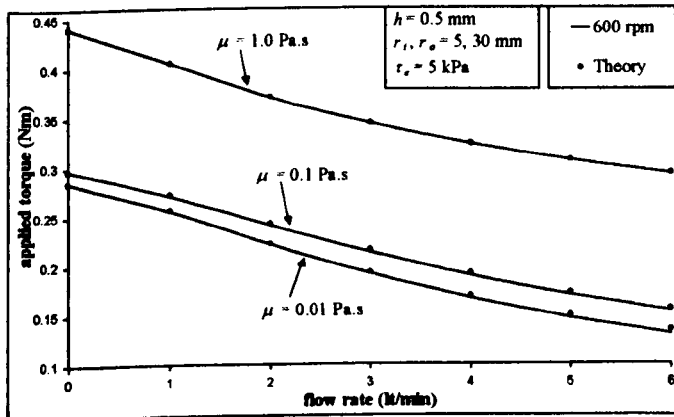


Figure 7. Torque coupling effect with flow rate for different values of plastic viscosity.

We now take a look at the velocity profiles. Figure (8). and Fig. (9). show the radial and circumferential velocity profiles for the case of 5 kPa at 0.8 lt/min corresponding to the data in Fig. (3).. In this case both plug and parabolic regions are present. The pseudo-plug regime is observed at small radii at and near the inlet where the Poiseuille flow is dominant. At larger radii, at and near the outlet, Couette flow dominates and the plug-less regime is present.

The pseudo-plug propagates from being present only at the inlet to the full radius at greater radial flow rates. When the Poiseuille flow is dominant at all radii the plug size is seen to increase with radius in a similar way to that observed for the Poiseuille flow only case (Fig. (2)). From Fig. (9). it can be seen that near the outlet where most of the torque is generated the circumferential velocity profiles are relatively linear.

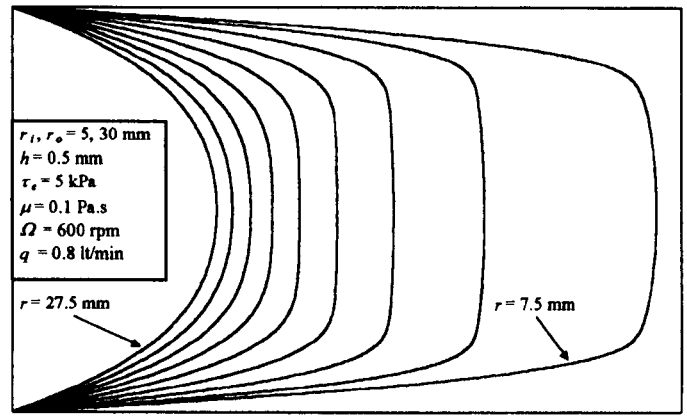


Figure 8. Radial velocity profiles for coupled flow at equally spaced radial positions corresponding to Fig. (3).

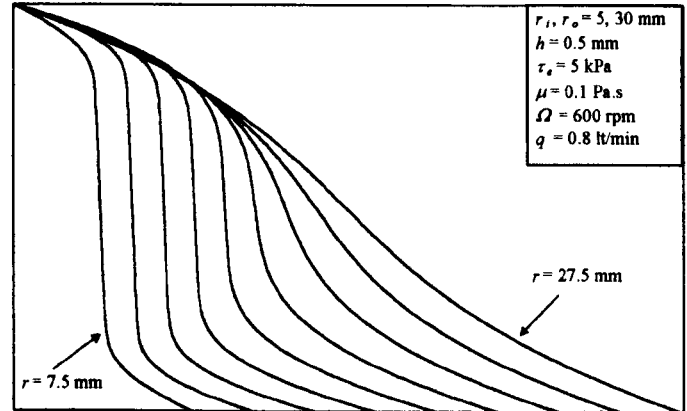


Figure 9. Circumferential velocity profiles for coupled flow at equally spaced radial positions corresponding to Fig. (3).

Required Range

To emphasise the effect of changing parameters and show good agreement between theory and CFD over a wide range, the results have so far been presented over the range [0 - 6 lt/min]. To determine the magnitude that is required in a practical situation, a basic heat balance calculation is carried out. Evaluating the power input and equating this to the amount of energy the fluid carries away gives the relation

$$\text{temperature change} = \frac{\Omega T}{\rho C_p q_r} \quad (30)$$

Even for low values of τ_e , the majority of the work done on the ESF is that needed to overcome the yield stress of the fluid. It is therefore the electro-stress as opposed to the Newtonian contribution that is responsible for heat generation. For the geometry used in this paper a electro-stress of 10 kPa generates a torque of 0.6 Nm; it follows from Eq. (30). that to stop the fluid rising by more than 2 °C a flow rate of 0.5 lt/min is required. In comparison an electro-stress of 20 kPa requires 1.0 lt/min.

A flow rate of 1.0 lt/min is therefore a substantial cooling flow for this situation and over the operational range 0 - 1.0 lt/min it can be seen that the drop in pre-set torque is less severe (Fig. (10).) - the loss in applied torque, for all values of τ_e , at 1.0 lt/min is $\sim 9\%$ @ 600 rpm and $\sim 4\%$ @ 1200 rpm. In this range we are mostly in the plug-less flow regime where the circumferential flow is dominant. But for low speeds the radial Poiseuille flow is seen to begin to become dominant - the loss in applied torque at 1.0 lt/min is $\sim 21\%$ @ 300 rpm.

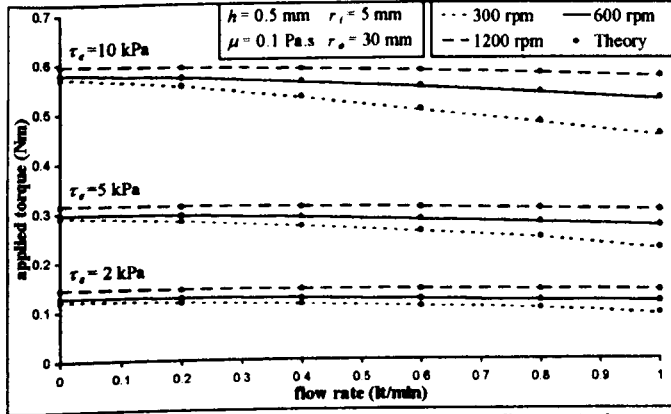


Figure 10. Torque coupling effect with flow rate in estimated required range of 0 - 1 lt/min.

DISCUSSION

Constitutive Theory

The 3-d Bingham plastic constitutive model (Eq. (3).) used for the analytical theory in this paper, states that regions in which $\tau < \tau_e$ have a zero deformation rate. On the boundary of a plug $\tau = \tau_e$, and the velocity is continuous. When the plug has a constant width, taking this region to be moving with a constant speed satisfies all conditions. But is this approach valid when the plug width varies? This problem forms the basis for why Lipscomb et al.(1984) state that in complex geometry solid plug regions cannot exist. They suggest the use of the bi-viscous model that, as already mentioned in the CFD section, regards unyielded fluid as almost solid in comparison to yielded sections of fluid. The model can be expressed as follows

$$\tau_{ij} = \begin{cases} \left(\frac{\tau_e}{\dot{\gamma}} + \mu \right) d_{ij} & \tau > \tau_e \\ \mu \dot{\gamma}_{\rightarrow 0} d_{ij} & \tau < \tau_e \end{cases} \quad (31)$$

We have analysed the radial and coupled flows when $h \ll r$ using the bi-viscous model. The theory presented here, using the Bingham plastic constitutive equation, are the results corresponding to high values of $\mu \dot{\gamma}_{\rightarrow 0}$. These expressions were used to derive all the data in this paper. The results clearly show that the CFD method, which uses a similar bi-viscous approach, is comparable to the Bingham plastic analytical theory. It can be concluded that for this particular case that the 3-d Bingham plastic model is a good

approximation. Allowing the pseudo-plug to be a fluid with a high viscosity results in insignificant extra terms - the modelling of unyielded regions is unimportant in comparison to the yielded regions.

ERFs and MRSs are expected to display very high values of $\mu \dot{\gamma}_{\rightarrow 0}$, the magnitude of which is therefore of little importance. It should however be noted, that some shear thinning NNFs are characterised by having a noticeable constant value of $\mu \dot{\gamma}_{\rightarrow 0}$ at low shear rates which then starts to decrease as particle interactions start to become significant. The CFD model used here could be a very useful tool for modelling such fluids. It can also be noted at high enough shear rates all materials and suspensions display Newtonian behaviour; for the Bingham plastic model μ_{nn} tends towards the plastic viscosity at high deformation rates.

Steady State Assumption

The main difference between the analytical and CFD model was that the former neglected steady state (centripetal) acceleration terms in the momentum equations. A simple conservation of angular momentum calculation, on a control volume placed around the boundaries of the clutch, shows that the magnitude of the output torque (that required to keep the lower plate stationary) will be less than the input torque (that required to rotate upper plate at speed Ω):

$$\dot{m} r_i v_{\theta i} \ll \dot{m} r_o v_{\theta o} \Rightarrow T_{output} = \dot{m} r_o v_{\theta o} - T_{input} \quad (32)$$

This first came to light from initial CFD results. The difference in torque is only noticeable at large flow rates when τ_e is low. The difference being up to 7% at 6 lt/min and 1200 rpm. In the estimated practical flow range of 0 - 1 lt/min the difference is less than 1%. The CFD torque values presented in this paper are those that correspond to the input plate - this is done to allow an accurate comparison between CFD and analytical theory.

Main Indications of Appraisal

The results basically show that provided the Couette flow is dominant the pre-set torque is relatively unaffected by the radial flow. The presence of pseudo-plugs is not desirable in as much as it means that the radial Poiseuille flow is dominates. On a more practical point, the presence of a plug means that the difference between plate speeds is distributed over smaller distances resulting in greater shear rates and hence more significant viscous heat generation. In this present application the presence of plugs is not desirable.

Fluid manufacturers have designed ESFs to have a low plastic viscosity, this gives a low Newtonian shear stress contribution and consequently a relatively constant shear stress for a given τ_e over a wide range of speeds. The plastic viscosity is found to have little effect in terms of the severity of the coupling effect. However, although the Newtonian contribution is small, for ERFs that display low τ_e , it can be a significant contribution to the overall applied torque. Since the rate of heat generation increases with speed it is advantageous that for the same pressure difference the flow rate increases with increased speed.

A larger gap size results in a lower radial velocity and therefore a smaller coupling effect for the same flow rate. Unfortunately a larger gap size requires a larger power supply to generate the same field strength. A compromise in this respect is therefore required.

Furthermore a small increase in outer radius results in a much greater applied torque and also a reduction in coupling effect. The outer radius is therefore a very significant consideration but, depending on the application, a compromise in terms of the device size may be required.

There are other consequences of having a throughflow. The condition (Eq. (10.)) that must be satisfied at the outer radius for flow to occur can be rewritten as:

$$\sqrt{\frac{G^2 h^2}{4} + c^2} > \tau_e. \quad (33)$$

This inequality suggests that, provided $|G(r)| > 2\tau_e/h$, even when both clutch plates are stationary the ESF will always be in a sheared flowing state. The requirement of a limiting torque (T_e , see Eq. (22.)) before any flow occurs is therefore eliminated. This suggests that the clutch cannot support any load, but as soon as there is any rotational flow the radial flow becomes less dominant allowing the clutch to support a torque (see Eq. (26)).

In practice for a clutch operating at the estimated low flow rates, $|G(r)| < 2\tau_e/h$, there will always be a considerable amount of load supporting ability at zero speed which is given by

$$G(r)^2 h^2 / 4 + c(r)^2 = \tau_e^2. \quad (34)$$

In the absence of a radial flow the $T - \Omega$ relationship is a linear one (Eq. (22.)). At relatively large radial flow rates, for high values of τ_e , non-linearity can be observed at low speeds - for the same flow rate the coupling effect becomes much more severe as the angular speed is reduced. This can be clearly seen in Fig. (10). at high τ_e . Here we are merely pointing out what the theory suggests, an experimental study is required to fully understand this scenario. It should however be noted when the clutch is operated at low speeds the work on the fluid is less severe, possibly allowing the radial flow rate to be reduced to a zero value at zero angular speed.

The severity of the coupling effect is similar for both concentric and radial types of clutch. It should however be noted that although significant the ability to maintain T while allowing the fluid to circulate is only one factor in deciding the best type of design and fluid specification. Response times and inertial effects, which are currently being studied, are expected to be important.

Complex Model

In essence it can be concluded that there is good agreement between the CFD and analytical theory. Any discrepancy appears to be due to a lack in the number of cells required to accurately represent the continuum model. The initial aims of this work have therefore been fulfilled. In the required flow range to keep the ESF thermally stable, at realistic angular speeds, the loading capabilities are little affected and the CFD analysis for this flow arrangement is proven to be correct.

The analytical theory in this paper is useful with regards to getting an overall view of the problem and in this case allowed the CFD results to be verified. However it is not readily adaptable for different flow conditions and geometry. In practice CFD will eventually be needed to predict prototype performance and even test concepts in the absence of analytical techniques.

This work has allowed confidence to be gained in the basic method allowing more complex CFD models to be contemplated involving difficult geometry, heat transfer and unsteady modes of operation. The Fluent CFD software already has a very sophisticated input and output interface and the internal code can be easily adapted using subroutines. This allows for the modelling of realistic fluids in which the main fluid property μ_{mn} can be dependent on field strength, temperature, local deformation rate and even the time domain. There is therefore no need to use idealistic viscoplastic models - for some ERFs the yield stress appears to reduce with increased shear rate (Peel et.al, 1994). In practice all that is required is the non-Newtonian viscosity function that can be derived from small fluid sample Couette type viscometer tests carried out over a temperature and field strength range (Bullough et.al, 2000).

ACKNOWLEDGMENTS

The authors wish to thank undergraduate students T.H.Hon and G.A. Karolemeas who played a part in the project foundation work and to D. Butcher and J. Hodgson who built and maintained the test equipment respectively.

REFERENCES

- Atkin, R. J., Bullough, W. A. and Ellam, D. J., 2000, "Throughflow effect on slip torque in an ESF concentric clutch," to appear in the Proceedings of the 13th International Congress on Rheology, Cambridge.
- Bird, R. B., Dai, G. C. and Yarusso, B. J., 1983, "The rheology and flow of viscoplastic materials," Rev. Chem. Eng. 1, pp. 1-70.
- Bullough, W. A., Ellam, D. J., and Atkin, R. J., 2000, "ESF fluid quantification," lecture given at Centre for International Sciences, Udine, Italy, June 2000, to be published by Springer Verlag Berlin 2001.
- Fluent Incorporated, Fluent 4.4 users guide, 1997, contact www.fluent.co.uk..
- Hon, T. H., 1996, "The effects of throughflow on the torque transmitting capabilities of an ER clutch device," BEng thesis, Department of Mechanical Engineering, University of Sheffield, UK.
- Lipscomb, G. G. and Denn, M. M., 1984, "Flow of Bingham fluids in complex geometries," Journal of Non-Newtonian Fluid Mechanics, Vol. 14, pp. 337-346.
- Peel, D. J. and Bullough W. A., 1994, "Prediction of electro-rheological valve performance in steady flow," Proc. Instn. Mech. Engrs., Vol. 208, pp. 253-266.

THROUGHFLOW EFFECT ON SLIP TORQUE IN AN ESF CONCENTRIC CLUTCH

R. J. ATKIN, W. A. BULLOUGH AND D. J. ELLAM

SMMART Engineering Network, University of Sheffield, Mappin Street, Sheffield, S1 3JD, UK

ABSTRACT

A problem of considerable interest in the development of ESF clutch devices operating at high shear rate is how to maintain a relatively constant fluid temperature whilst retaining the ability to control the transmitted torque by means of electrical excitation. In this paper the possibility of using an axial throughflow in a concentric cylinder Couette type device for typical operating conditions is investigated an ERF at different voltages and axial pressure gradients.

KEYWORDS: ELECTRO-STRUCTURED FLUIDS (ESF), ELECTRO-RHEOLOGICAL FLUIDS (ERF), COMPUTATIONAL FLUID DYNAMICS (CFD)

INTRODUCTION

Modelling the ESF at any given excitation as a homogeneous, incompressible continuum with fixed Bingham plastic properties [1], 2-d, analytical solutions for fully developed, isothermal flow between one stationary and one moving plate electrode are presented. Flows in both the circumferential and axial directions are coupled and, in general, these flow fields and the transmitted torque depend upon the relative rotational speed and axial pressure gradient. Results are compared with experimental data and corresponding results from a Bingham plastic CFD package. Test results at low, but realistic, loading conditions correlate with theoretical predictions at each field strength. Indications are that the rate of throughflow should not interfere overtly with set torque transmission. Hence the cooling of slipping ESF clutches by throughflow can be contemplated.

Verification of the CFD method constitutes a foundation for future work on ESFs. This is expected to include: the effect of temperature θ and shear rate on the electro-stress τ_e and plastic viscosity μ , heat transfer, non-linear field strengths, unsteady flows, and complex geometries. This degree of modelling will require the CFD approach.

THEORETICAL ANALYSIS

In the inter electrode space, where the field strength is assumed constant, flow occurs in both the circumferential (tangential) and axial directions, the former caused by rotation of the inner electrode and the latter due to the difference in pressure between inlet and outlet along the axis. Since the inter electrode gap width h is small compared to the mean radius r_m of the electrodes flow is considered to be between two flat plates, $x=0$ which moves with speed $V(=r_i\Omega)$ in the y -direction and a fixed plate $x=h$. The pressure gradient $G(=dp/dz=\Delta P/L)$ is in the z -direction. If $v(x)$ and $w(x)$ denote the velocity components in the y - and z - directions respectively the two rates of strain components $\frac{1}{2}(dv/dx)$ and $\frac{1}{2}(dw/dx)$ give an expression for the resultant 2-d shear rate

$$\dot{\gamma} = \frac{1}{2} \{ (dv/dx)^2 + (dw/dx)^2 \}^{1/2} \quad (1)$$

The non zero shear stresses τ_{xy} and τ_{xz} and the magnitude of the resultant shear stress, τ , are given by:

$$\tau_{xy} = a, \quad \tau_{xz} = Gx + b, \quad \tau = \sqrt{a^2 + (Gx + b)^2} \quad (2)$$

where a and b are constants.

Flow occurs when $\tau > \tau_e$. Here τ_e is a positive constant. Velocity components, which satisfy the no-slip condition on the boundaries $x=0$ and $x=h$, can be determined. To satisfy the boundary conditions on w it follows that $b = -Gh/2$. The main results are given below (see [1] & [2] section 2, for further details).

Case (i) $|a| > \tau_e$

Here flow occurs across the whole gap with no plugs present. Both v and w depend upon G and V and so are affected by varying either the axial pressure gradient or the speed of the plate. To satisfy the condition $v(h) = 0$

$$|a| \left[h - (2\tau_e/G) \sinh^{-1}(Gh/2|a|) \right] = \mu V \quad (3)$$

If the plate moves, for any finite pressure gradient flow occurs in the axial z -direction. The leakage flow rate \dot{q}_z is given by:

$$\dot{q}_z = -\frac{Gh^3\pi r_m}{6\mu} + \frac{2\pi r_m}{\mu} \left\{ \frac{\tau_e h}{4G} \sqrt{G^2 h^2 + 4a^2} - \frac{\tau_e a^2}{G^2} \sinh^{-1}(Gh/2|a|) \right\} \quad (4)$$

\dot{q}_z has Newtonian and Bingham contributions, the latter always trying to reduce the former. When $G=0$, $\dot{q}_z=0$ and at high values of G the Newtonian term dominates.

Case (ii) $|a| < \tau_e$

In this case there is a central plug symmetrically placed about $x=h/2$ of thickness $2(\tau_e^2 - a^2)^{1/2} / |G|$, which is less than h provided $|G| > 2(\tau_e^2 - a^2)^{1/2} / h$. Again both v and w depend upon G and V . The result for this case which corresponds to (3) is

$$|a| \left(h - 2\sqrt{\tau_e^2 - a^2} / G \right) - (2|a|\tau_e/G)x \left\{ \sinh^{-1}(Gh/2|a|) - \sinh^{-1} \left(\sqrt{\tau_e^2 - a^2} / |a| \right) \right\} = \mu V \quad (5)$$

The leakage flow rate is now given by:

$$\dot{q}_z = 2(\dot{q}_1 + \dot{q}_2) \quad (6)$$

where \dot{q}_1 is the flow rate between 0 and x_1 , the lower plug boundary, and \dot{q}_2 is the flow rate in the plug, (see [2], equations (14), (15)).

COMPUTATIONAL FLUID DYNAMICS PACKAGE

Without making the flat plate assumption, the same problem under identical flow assumptions as outlined above was solved using a commercial CFD package (FLUENT IV).

The governing Navier-Stokes equations are discretised using a finite volume method which involves splitting the continuum into a finite number of cells allowing the partial differential equations to be integrated on a control volume basis. The Newtonian viscosity is replaced with a non-Newtonian viscosity μ_m which is dependent only on the local deformation rate (Eq.1) and is derived from the Bingham plastic equation.

Since the flow aligns with the grid a first order power law interpolation scheme was adequate to determine cell face values. Velocities are determined from the momentum equations, and pressure is determined using the SIMPLE pressure-velocity coupling algorithm. The fully discretised equations are then solved by a semi-iterative method using a Tri-diagonal Matrix Algorithm and treating off-line variables as known from the previous iteration. Convergence of a solution is usually interpreted by using the normalised residuals; these are a measure of the degree to which the equations are satisfied. The FLUENT manual describes more fully the numerical and solution techniques.

The clutch was modelled using an inner and outer cylindrical wall; all derivatives are zero in the tangential direction allowing a 2-d axisymmetric grid to be used. A uniform inlet velocity boundary condition allowed the flow rate \dot{q}_z (based on the mean radius r_m) to be set, a fully developed flow condition was used for the outlet. The length of the clutch was increased by 20% to allow space for the parabolic velocity profile to develop. The inner cylinder wall was set to rotate at a tangential speed V .

RESULTS

The main objective was to investigate the dependence of the magnitude of the transmitted torque $T = 2\pi r_m^2 L |a|$ upon the axial flow rate \dot{q}_z . The clutch is considered to be operating in a 'slipping' state which means that a relative speed always exists between the two rotating members. When the clutch is in a locked state the torque on the device is not high enough to overcome the electro-stress; in this state there is no shear rate and therefore no cooling is required.

In general the shear stress $|a|$, given by either Eq. (3) or (5), depends upon the axial pressure gradient G , the speed V as well as the fluid parameters τ_e and μ and the gap width h .

Experiments have been carried out [3] at voltages corresponding to τ_e of 54-1460 Pa, and rotational speeds 300-1500 rpm. In all cases very low flow rates were involved and it was found theoretically that $|a| > \tau_e$ so that case (i) applies and that $|Gh/2a| \ll 1$ which allows the velocity profiles to be approximated as

$$v = V(1-x/h), \quad w = (G/2\mu)(1-\tau_e/|a|)x(x-h) \quad (6)$$

and Eqs. (3) and (4) reduce to

$$|a| = \mu(V/h) + \tau_e, \quad \dot{q}_z = -(Gh^3\pi r_m/6\mu)(1-\tau_e/|a|) \quad (7)$$

Here the velocity components are partially un-coupled. The transverse component being linear and independent of G whilst the axial component is parabolic, hence the term 'parabolic' theory. Also $|a|$ and hence T are independent of G (or \dot{q}_z). Typical results show good agreement between theory, experiment and CFD (see [2]).

Due to technical reasons experiments were only performed at low τ_e and \dot{q}_z . It is therefore of interest to use theory and CFD to predict how T is effected at higher values when the approximation $|Gh/2a| \ll 1$ is no longer valid. For higher pressure gradients $|a|$ decreases as $|G|$ increases and eventually there is a transition from case (i) $|a| > \tau_e$ to case (ii) $|a| < \tau_e$. The transition point is found to move to higher flow rates with decreasing τ_e and V . Behaviour for $\tau_e = 2$ and 10 kPa at 600 rpm is shown in Fig.1&2. The CFD results are found to be in very good agreement with the analytical predictions.

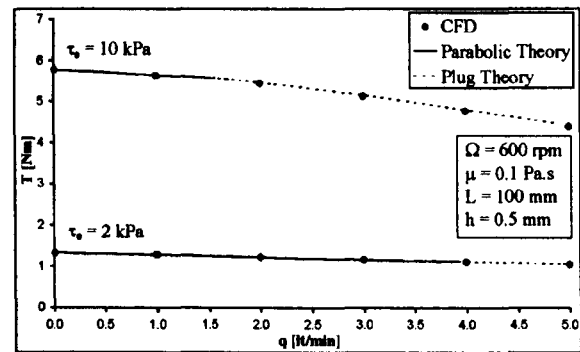


Figure 1: Torque vs. Flow rate: Theory and CFD

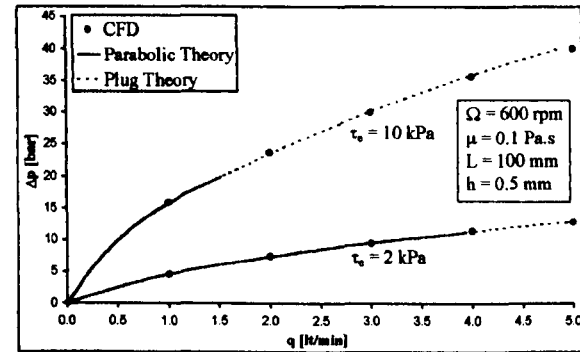


Figure 2: Pressure drop vs. Flow rate: Theory and CFD

Finally the velocity profiles are considered. In case(i) $v(h/2) = V/2$ (no plug), whereas in case (ii) the region $x_1 \leq x \leq x_2$ is occupied by a plug moving with this speed in the transverse direction. The axial component is symmetric about $x = h/2$ with maximum speed at $x = h/2$ in case (i) and in case (ii) the plug moves with speed $w(x_i)$ in this direction. These features agree with the profiles obtained from the CFD. Typical velocity profiles are shown in Fig.3&4. When the flow rate is less than the critical value as predicted by the analysis, no plug is present whereas above this value there is a central plug. Profiles given by CFD confirm that in the experimental range the tangential component is linear (Fig.3) and the axial component is

parabolic.

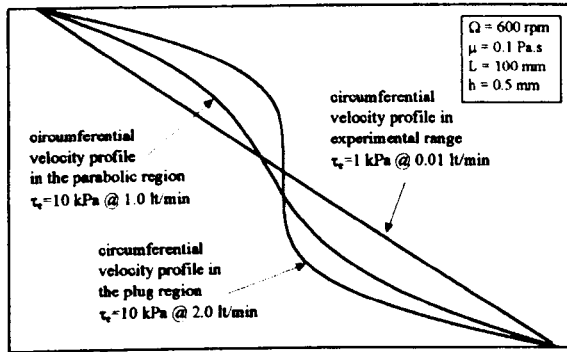


Figure 3: CFD circumferential velocity profiles

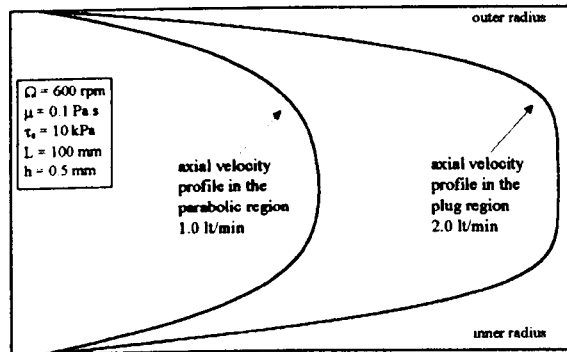


Figure 4: CFD axial velocity profiles

DISCUSSIONS

The present problem is will an induced axial throughflow affect the torque pre-set by the excitation voltage? A test rig built for a former sealing problem [4] was utilised for the present problem, thus, imposing limitations on the inlet pressure head of a few centimetres of ERF ($\dot{q}_z < 0.01 \text{ lt/min}$). Pressurisation of the inlet tank was not possible due to the small amount of fluid available.

The equations governing the 2-d flow/stress field give rise to two flows that are coupled. A spreadsheet was used to numerically solve the resulting equations for the torque and flow rate for set values of τ_s , μ , G and V and geometry. The number of cells in the gap width required to achieve a grid independent CFD solution was found to be much greater than that required for a similar Newtonian flow. Also the default convergence criteria (residual history of $1e-3$) was found to be insufficient; the residuals had to be taken down to $1e-7$ if convergence was to be guaranteed. These conditions were much more stringent than had been previously used [2]. The very high degree of correlation between the two methods complement each other showing that there little scope for error in the Bingham plastic analysis and for this realistic geometry the flat plate assumption appears valid.

In essence the results show that agreement between CFD 'parabolic' analysis and experiment is probable over the full range of experimentation [2]. Over a wider range of conditions it can be seen that the set torque is expected to be more and more influenced by the pressure difference G ,

which causes the throughflow. It is clear that for practical cases ($\dot{q}_z \approx 1.0 \text{ lt/min}$ based on rudimentary heat balance calculation) that the linearised approximation based on $|Gh/2a| \ll 1$ is not valid. The consequence of this is that there will be a drop in pre-set torque with increased throughflow (see Fig.1). However the results show that the severity of this loss in output is quite small allowing for an otherwise impractical (due to heating effects) device to be contemplated.

It will be noted that whilst the conditions for change over from 'parabolic' to 'plug' regions is reasonably well defined by $a = \tau_s$, no critical stability criteria are known (Reynolds or Taylor types). This is important since the analysis here assumes laminar flow of a continuum. It will be further noted that in the case of the higher flow rates, which are indicated to be linearly linked to the pressure drop required to induce them (see Fig.2), that $\dot{q}_z \times \Delta p$, the 'heating effect' provided by a circulation pump, will exceed $\omega \times T$, the shaft driving power heating component, that it is intended to carry away.

Perhaps the real importance of the present work is that it sets up a sound foundation for more accurate modelling of ESF devices. In a real engineering situation the ESF will not be an ideal Bingham plastic, geometry will be more complicated and heat transfer may well be a factor. This implies that the analysis given here will be insufficient to accurately predict operating conditions. This is why the opportunity was taken to test the CFD package for a two dimensional flow field encountered in experiments. Apart from the general advantages of CFD, on this occasion it also indicated that the original 'parabolic' axial flow theory may be insufficient: this led to the development of the plug flow analysis. More rigorous experimental tests that are extended into the 'plug' region are called for before the analysis can be proved to be useful for accurate analytical prediction.

REFERENCES

1. R. J. Atkin et al, "Solutions of the constitutive equations for the flow of an ERF in radial configurations", J. Rheol. **35** (1991), pp. 1441-1461.
2. W. A. Bullough et al, "Two dimensional flow of an ESF: experiment, CFD, Bingham plastic analysis", Int. Jnl. Mod. Phys. B. (2000 to appear)
3. T. G. Kum & T. H. Yap &, Exploratory investigations on ERF clutch devices, The University of Sheffield. B.Eng Thesis's (1996) & (1996).
4. R. J. Atkin et al, "Two dimensional Bingham plastic flow in a cylindrical pressurised clutch", Int. Jnl. Mod. Phys. B, **8** No. 20&21 (1994), pp. 2955-2965.

ELECTRO-STRUCTURED FLUID SEALS

R. J. ATKIN, D. J. ELLAM* & W. A. BULLOUGH

SMMART Engineering Network, University of Sheffield, Sheffield, S1 3JD, UK

**correspondence: mep99dje@shef.ac.uk, (44) 0114 2227794*

The aim of this paper is to bring together various works on concentrically located rotating shaft seals which utilize electro-structured fluid sealant, in order to produce a generalized approach to their design, thus resolving seemingly incompatible reports on the effects of rotational speed on sealing capabilities. In turn the results from these works are reviewed, a viscoplastic analysis of the two dimensional problem is presented and the effects on leakage rate of radius ratio, rotational speed and axial pressure gradient as they interact with fluid properties are illustrated.

KEYWORDS: ERF, MRF, SEAL, CFD

INTRODUCTION

Experiments, and analysis based on steady, two-dimensional flow induced by a pressure gradient in the axial (shaft) direction and rotary motion in the other (circumferential) direction carried out on an ERF by Atkin et. al. (1994), indicates that the motion in the circumferential direction of one surface with respect to the stationary surface always causes flow to take place in a direction appropriate to that of the pressure gradient inducing it. In a second work by Kordonski and Gorodkin (1995) no equivalent theory is supplied but experimentally a MRF seal is found to withstand a significant axial pressure gradient without leakage occurring. Since the constitutive equation for ERF and MRF is understood to be similar, both materials being modelled as a Bingham plastic, these conflicting results are in need of examination.

Recently the use of a Computational Fluid Dynamics package (CFD) has been used to solve viscoplastic flows by use of an algorithm attached to a fundamental Newtonian fluid solver that is inclusive of centrifugal effects. Given that the viscoplastic continuum analysis, albeit in some cases approximated by the absence of centrifugal terms and limited by use of the lubrication assumption, compares well with the CFD results in both radial plate and concentric cylindrical clutch cases (Ellam, Atkin and Bullough (2000), Atkin, Ellam and Bullough (2000)), it is now used to resolve the apparent paradox between the results reported by Atkin et. al. (1994) and Kordonski and Gorodkin, (1995).

From the outset due caution needs to be exercised at low shear rates when the exact properties of the various fluid types are not fully known. This can be due to the presence of surfactant and anti coagulant additives – see for example Tully, Binder and Carlson (1991). This position reinforces calls for a more comprehensive understanding and perhaps more accepted standard methods of fluid testing. CFD analysis is becoming very powerful yet the results of the analysis can vary significantly depending on the definition of yield stress and plastic viscosity. These difficulties may be overcome by the adaptation of the main basic effective viscosity vs. deformation rate vs. excitation test standard.

THEORETICAL ANALYSIS: BINGHAM PLASTIC FLAT PLATE THEORY

Since the publication by Atkin et. al. (1994) the theory has been developed to include the plug regime, which occurs when the effect of relative speed of the seal surfaces compared to the pressure gradient on the flow rate is relatively low. A review of this extended analysis is presented below.

Within the gap width, where the field strength is assumed constant, flow occurs in both the circumferential and axial directions, the former caused by rotation of the inner electrode and the latter due to the difference in pressure between inlet and outlet along the shaft. Since the inter electrode gap width h is small compared to the mean radius r_m of the electrodes the flow is considered to be between two flat plates, $x = 0$ which moves with speed $V (= r_m \Omega)$ in the y -direction and a fixed plate $x = h$ (See Figure 1 for a schematic). The pressure gradient $G (= dp/dz = \Delta P/L)$ is in the z -direction. If $v(x)$ and $w(x)$ denote the velocity components in the y - and z - directions respectively the two rates of strain components $\frac{1}{2}(dv/dx)$ and $\frac{1}{2}(dw/dx)$ give an expression for the resultant 2-d shear rate,

$$\dot{\gamma} = \sqrt{\left(\frac{dv}{dx}\right)^2 + \left(\frac{dw}{dx}\right)^2} \quad (1)$$

The non-zero shear stresses τ_{xy} and τ_{xz} and the magnitude of the resultant shear stress, τ , are given by:

$$\tau_{xy} = a, \quad \tau_{xz} = Gx + b, \quad \tau = \sqrt{a^2 + (Gx + b)^2}, \quad (2)$$

for which a and b are constants.

Flow occurs when $\tau > \tau_e$. Here the yield stress τ_e is a positive constant. Velocity components, which satisfy the no-slip condition on the boundaries $x = 0$ and $x = h$, can be determined. To satisfy the boundary conditions on w it follows that $b = -Gh/2$ and the resultant shear stress is symmetric about $x = h/2$. Using (2) (with $b = -Gh/2$) the condition $\tau > \tau_e$ can be recast in the form $a^2/\tau_e^2 + G^2/(2\tau_e/h)^2 > 1$. For a given material and known geometry this gives a criteria for the values of a and G for flow to occur. When the operating parameters are such that the values of a and G lie inside the ellipse $a^2/\tau_e^2 + G^2/(2\tau_e/h)^2 = 1$ no axial flow can occur and the shaft cannot rotate. The main results are given below (see Atkin et. al. (1994) & Bullough et. al. (2001) section 2, for further details).

Case (i) $|a| > \tau_e$

Here flow occurs across the whole gap with no plugs present. Both v and w depend upon G and V and so are affected by varying either the axial pressure gradient or the speed of the plate. To satisfy the condition $v(h) = 0$,

$$|a| \left[h - (2\tau_e/G) \sinh^{-1}(Gh/2|a|) \right] = \mu V. \quad (3)$$

The magnitude of the shear stress $|a|$ depends upon G and V as well as the fluid parameters τ_e and plastic viscosity μ and the gap width h . If the plate moves, for any finite pressure gradient flow occurs in the axial z -direction. The leakage flow rate is given by:

$$\dot{q}_z = -\frac{Gh^3 \pi r_m}{6\mu} + \frac{2\pi r_m}{\mu} \left\{ \frac{\tau_e h}{4G} \sqrt{G^2 h^2 + 4a^2} - \frac{\tau_e a^2}{G^2} \sinh^{-1}(Gh/2|a|) \right\}. \quad (4)$$

\dot{q}_z has Newtonian and Bingham contributions, the latter always trying to reduce the former. When $G = 0$, $\dot{q}_z = 0$ and at high values of G the Newtonian term dominates. For very low flow rates when $|Gh/2a| \ll 1$ (3) (4) reduce to

$$|a| = \mu(V/h) + \tau_e, \quad \dot{q}_z = -(Gh^3 \pi_e / 6\mu)(1 - \tau_e / |a|), \quad (5)$$

so that in this approximation $|a|$ is independent of G but \dot{q}_z depends upon G and V and is zero if either G or V vanish. Equation (5)₁ also arises from the analysis of shear flow when $w = 0$. For higher pressure gradients using (3) it is found that $|a|$ decreases as $|G|$ increases and eventually there is a transition from $|a| > \tau_e$ to $|a| < \tau_e$.

Case (ii) $|a| < \tau_e$

In this case there is a central plug symmetrically placed about $x = h/2$ of thickness $2(\tau_e^2 - a^2)^{1/2} / |G|$, which is less than h provided $|G| > 2(\tau_e^2 - a^2)^{1/2} / h$. Again both v and w depend upon G and V . Results corresponding to (3) and (4) are obtained. The transition point from case (i) to (ii) is found to move to higher flow rates with decreasing τ_e and V . Typical behaviour for $\tau_e = 2$ and 10 kPa at 600 rpm is shown in Figs. 1 & 2 of Atkin, Ellam and Bullough (2000). Flow profiles are shown in Figs. 3 & 4.

COMPUTATIONAL FLUID DYNAMICS PACKAGE

The same problem is solved under identical flow assumptions as those outlined above using a commercial CFD package (Fluent v4) for flow between two concentric cylinders but without making the flat plate approximation adopted in the theoretical analysis. The governing Navier-Stokes equations are discretised using a finite volume method which involves splitting the continuum into a finite number of cells, allowing the partial differential equations to be integrated on a control volume basis. Each cell volume has a viscosity that is dependent on the local deformation rate $\dot{\gamma}$. This non-Newtonian viscosity μ_{mn} is determined using the bi-viscous model where μ_{max} is set at 1000 Pa.

$$\mu_{mn} = \frac{\tau_e}{\dot{\gamma}} + \mu \leq \mu_{max} \quad (6)$$

Since the flow aligns with the grid a first order power law interpolation scheme is adequate to determine cell face values. Velocities are determined from the momentum equations, and the pressure is determined using the SIMPLE pressure-velocity coupling algorithm. The viscosity, μ_{mn} , is calculated in a sub-routine linked to the main code. The fully discretised equations are then solved by a semi-iterative method using a Tri-diagonal Matrix Algorithm and treating off-line variables as known from the previous iteration. Convergence of a solution is usually interpreted by using the normalised residuals; these are a measure of the degree to which the equations are satisfied. However for highly viscous flow it is found to be safer to monitor variable histories at various points in the flow to determine when the solution has converged. The FLUENT manual describes more fully the numerical and solution techniques (Fluent, 1995).

CFD Model

The seal is modelled using an axisymmetric grid. This is possible because, as stated in the earlier assumptions, all derivatives in the tangential direction are zero. The fluid is therefore confined by an inner and outer cylindrical wall boundary condition. The inner cylindrical wall is set to rotate at a tangential speed $V = r_1 \Omega$. Uniform pressure conditions are set at the inlet and outlet, allowing a pressure difference to be set over a certain seal length.

It is important to determine an adequate cell density for the CFD model to correctly represent a continuum. In the radial direction it is found that 20 cells are adequate. In theory fewer cells are needed in the axial direction because the flow is not changing with distance in that direction. However it is important not to skew the cells severely and so 100 cells are used in that direction.

REVIEW

The aim of this section is to consider why some experimental results in Atkin et. al. (1994) and the Bingham plastic flat plate theory suggest that it is impossible to have an effective ESF seal when the shaft is rotating whilst other experimental results reported by Kordonski and Gorodkin (1995) for their MRF indicate that the opposite is true. A list of the values of the relevant parameters used by these authors is given in Table 1; those indicated by a (*) are estimates.

	Atkin et. al. (1994)	Kordonski and Gorodkin (1995)
Yield stress	ERF: 256 – 1500 Pa	MRF: ~ 5 - 10 kPa *
Shaft diameter	60 mm	20 mm
Gap width	1 – 2 mm	0.075 - 0.15 mm
Shaft speed	500-2000 rpm (~50 - 200 rad/s)	< 250 rpm (~25 rad/s)
Pressure gradient	1000Pa/10mm = 0.1 GPa/m	10 min, 300 max GPa/m *

The experiments in Atkin et. al. (1994) were conducted in the range $|a| > \tau_e$ but, from the magnitudes of the yield stress and speed, it appears that the results reported in Kordonski and Gorodkin (1995) could be in the range $|a| < \tau_e$ when, in the parallel plate case, there is a central plug. It also seems pertinent at this point to consider any effects due to cylindrical geometry. For purely rotational flow ($w = 0$) between two concentric cylinders with radii r_1 and r_2 ($r_1 < r_2$), caused by either cylinder rotating with angular speed Ω with the other stationary, at small enough speeds it is possible to have flow in only part of the gap with a plug attached to outer cylinder. The angular speed at which the plug disappears for a Bingham plastic material is given by Wilkinson (1960)

$$\Omega_{limit} = \frac{\tau_e}{2\mu} \left(\frac{r_2^2}{r_1^2} - 1 - \ln \frac{r_2^2}{r_1^2} \right). \quad (7)$$

For $\Omega > \Omega_{limit}$ there is flow across the whole gap. Estimates of Ω_{limit} are given in Table 2.

Case	r_1	$r_2 - r_1$	τ_e	μ	Ω_{limit}
	mm	mm	Pa	Pa.s	rad/s
Kordonski and Gorodkin (1995)	10	0.15	10000	0.1	22
	10	0.15	10000	0.5	11
Atkin et. al. (1994)	30	2	1000	0.1	44
on smaller shaft	10	2	1000	0.1	4963

The value of Ω_{limit} is significantly affected by the fluid properties. It can be concluded from line 3 of the above table that experimental work in Atkin et. al. (1994) is likely to have been carried out at rotational speeds greater than Ω_{limit} , the limiting speed for plugs being present, when the theory predicts flow across the whole gap. This conclusion is further validated by the fact that the results (within experimental error) do match up to the theory. However with the same parameters and a smaller shaft radius very high speeds are needed. As illustrated in line 1 in the above table, for a smaller shaft (as used by Kordonski and Gorodkin (1995)) the limiting speed is much higher than many of the experimental speeds used. This consequently means that plugs are likely to be present which goes some way to explaining why it may be possible to have full sealing.

CFD ANALYSIS

Further insight into the effect of the relevant parameters when flow is present in both axial and circumferential directions is gained from the CFD analysis. Since shaft diameter is likely to be a significant factor, results are obtained for two sizes corresponding to the apparatus used in Atkin et. al. (1994) and Kordonski and Gorodkin (1995). To highlight the important parameters an orthogonal array, which limits the total number of simulations to 16, is used (Tagucci Analysis). The table below shows the flow rate results for all 16 simulations, also indicated is the theoretical transition speed Ω_{limit} .

Table 3: Chosen parameters and resulting flow rates

No	Ω rad/s	Gap Size mm	Yield Stress kPa	Vis. Pa.s	dP/dz GPa/m	Shaft radius 10 mm			Shaft radius 30 mm		
						Ω_{limit} eqn. (5)	Flow Rate [Lt/hr]		Ω_{limit} eqn. (5)	Flow Rate [Lt/hr]	
						rad/s	CFD	Diff [%]	rad/s	CFD	Diff [%]
1	10	0.5	10	0.05	10	492	0.20	84.8	55	4.03	60.7
2	30	0.5	10	0.10	20	246	4.71	40.3	28	39.85	30.8
3	10	0.2	10	0.10	10	40	0.05	47.1	4	0.64	12.4
4	10	0.5	5	0.05	20	246	7.47	38.8	28	60.71	26.5
5	30	0.2	10	0.05	20	79	0.41	46.7	9	4.21	14.5
6	30	0.5	5	0.10	10	123	4.51	36.4	14	35.56	23.0
7	10	0.2	5	0.10	20	20	0.44	37.5	2	3.52	20.8
8	30	0.2	5	0.05	10	40	0.43	28.6	4	4.06	6.7
Average						161	2.28	45.0	18	19.07	24.4

Here the values of Ω are close to the range used in Kordonski and Gorodkin (1995). For the chosen range of parameters the results from the CFD simulations differ from those of the flat plate theory between 7 - 85 %, the largest discrepancy occurring when $\Omega \ll \Omega_{limit}$ (simulation 1). The flow profiles corresponding to simulation 1 when $r_1 = 10$ mm are shown in Figure 2. The circumferential velocity is seen to exhibit plug-like behaviour, corresponding to high values of μ_{ms} , and the axial velocity is non-symmetric. The plug-like region is attached to the outer cylinder and extends over almost half the gap. The large discrepancy indicates that the flat plate approximation is inapplicable and that it is necessary to consider the cylindrical geometry. Other large discrepancies indicate that for this range of parameters care has to be taken when using the flat plate approximation. Care in interpreting the results of Figure 2 should be exercised on account of the concentric cylindrical arrangement and the selection of the value of μ_{max} . It will be noted that no constant velocity plug per se is evident.

The CFD results are used in Figure 3 to show the average effect of each parameter. A considerably lower flow rate on the smaller shaft can now be seen. At the relatively low speeds of 10 & 30 rad/s the shaft speed is found to be relatively unimportant. The yield stresses and pressure gradients are found to have an almost linear effect, i.e. double the yield stress halves the flow rate. As clearly represented in Figure 3 the significant parameter of most interest appears to be the gap size. It must be noted that the resulting flow rates are quite small (litres/hour).

It can also be shown that for smaller Ω_{limit}/Ω (less extensive plug behaviour) the results are generally closer. Also in all cases the larger r/h values (30 mm shaft) the results are considerably closer (Table 3). Over the range of parameters that were chosen the gap size is a more significant factor than yield stress and pressure gradient. Also it is found that the plastic viscosity and rotational speed are generally less important.

CONCLUSION

The present analyses indicate that, the results in Atkin et. al. (1994) and Kordonski and Gorodkin (1995) can both be reconciled. Although the analyses predict that there is leakage when rotation occurs, for some range of parameters this may be very small (see Figure 3). For all parameter values taken in Table 3 it is found that smaller flow rates are obtained with a smaller shaft radius. Since this model only approximates the real fluid, the flow rate could be zero as found experimentally in Kordonski and Gorodkin (1995) and Fujita et. al. (1999).

Whilst formula (6) for Ω_{limit} used to predict the occurrence of plugs in cylindrical geometry is restricted to purely rotational flow, the CFD results, which allow for flow in both the circumferential and axial directions, substantiate the occurrence of a plug-like region attached to the outer cylinder. The CFD analysis also allows for the effect of the relevant parameters on flow rate to be investigated and indicates that the gap width and the shaft radius are the most significant.

For some parameter values in Table 3 there are large discrepancies between the values for flow rates predicted by the CFD and those which follow from the theoretical analysis in which the flow is taken to be between two parallel flat plates. Here the speeds were chosen to be within the range used in Kordonski and Gorodkin (1995). However in earlier work (Atkin et. al. (1994), Ellam, Atkin and Bullough (2000), Atkin, Ellam and Bullough (2000) and Bullough et. al (2001)) where higher speeds are used very good agreement is found between this theory and the results from CFD. This indicates that care has to be taken when replacing the cylindrical geometry by two parallel flat plates.

Finally, in all the analysis presented the excitation field is assumed to be constant across the gap. The effect of a non-uniform field distribution can be included in both theoretical analysis and CFD and further work is in progress.

REFERENCES

- Atkin, R. J., Corden, T. J., Kum, T. G. and Bullough, W. A. 1994. "Two-dimensional Bingham plastic flow in a cylindrical pressurised clutch," *Int. J. Mod. Phys. B*, (8):2955-2965.
- Atkin, R. J., Ellam, D. J. and Bullough W. A. 2000. "Throughflow Effect on Slip Torque in an ESF Concentric Clutch," Proc. 13th Int. Congress on Rheology, Cambridge, (British Soc. Of Rheology) 414-416.
- Bullough, W. A., Atkin, R. J., Urang, S., Kum, T. G., Musch, C. and Rober, T. 2001. "Two-dimensional flow of an ESF: experiment, CFD, Bingham plastic analysis," *Int. J. Mod. Phys. B*, (15):745-757
- Ellam, D. J., Atkin, R. J. and Bullough, W. A. 2000. "Appraisal of an ESF radial plate clutch with cooling flow using a NNF CFD solver," 2000 ASME Int. Mech. Eng. Congress and Exposition, Orlando, Florida, (ASME) 117-125.
- Fluent. 1997. "Fluent 4.4 Users Guide," contact www.fluent.co.uk
- Fujita, T., Yoshimura, K., Seki, Y., Dodbiba, G. and Miyazaki, T. 1999. "Characteristics for characterisation of magnetorheological suspensions for seals," Proc. 7th Int. Con. on ERFs, MRSs and their applications, Honolulu, Hawaii, (World Scientific Publishing) 709-715.
- Kordonski, W. I. and Gorodkin, S. R. 1995. "Magnetorheological fluid seal," Proc. 5th Int. Con. on ERFs, MRSs and Associated Technology, Sheffield, UK, (World Scientific Publishing) 704-709.
- Tully, M. R., Binder, J. W. and Carlson, J. D. 1991. "Properties and applications of commercial magnetorheological fluids," 5th SPIE Symposium on Smart Structures and Materials, 202-214.
- Wilkinson, W. L. 1960. *Non-Newtonian fluids* (Pergamon Press, Oxford).

Figure 1: Schematic of seal

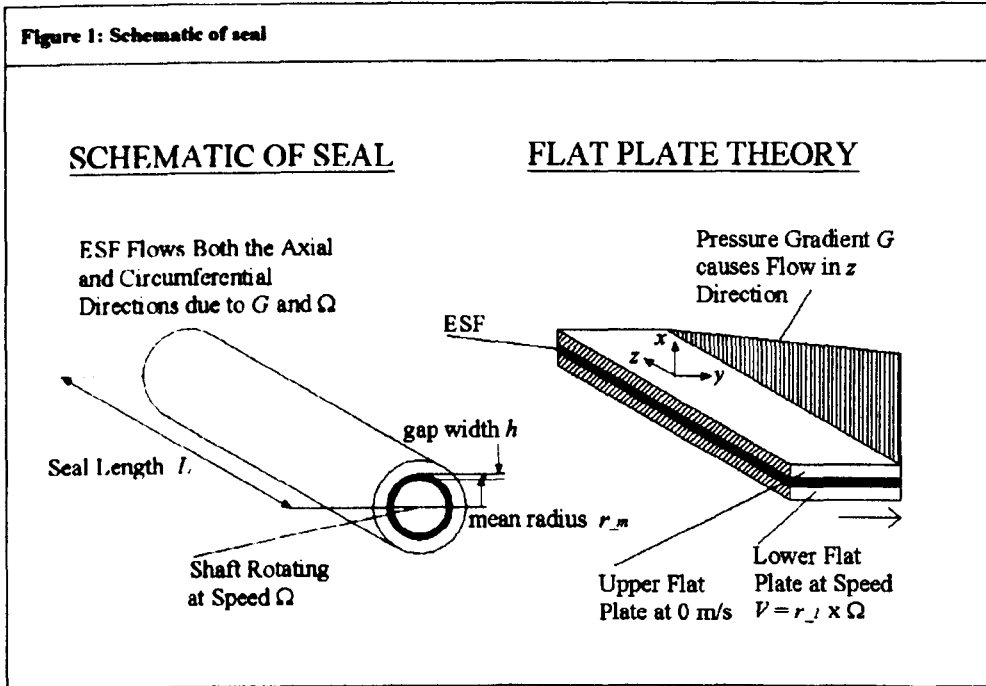
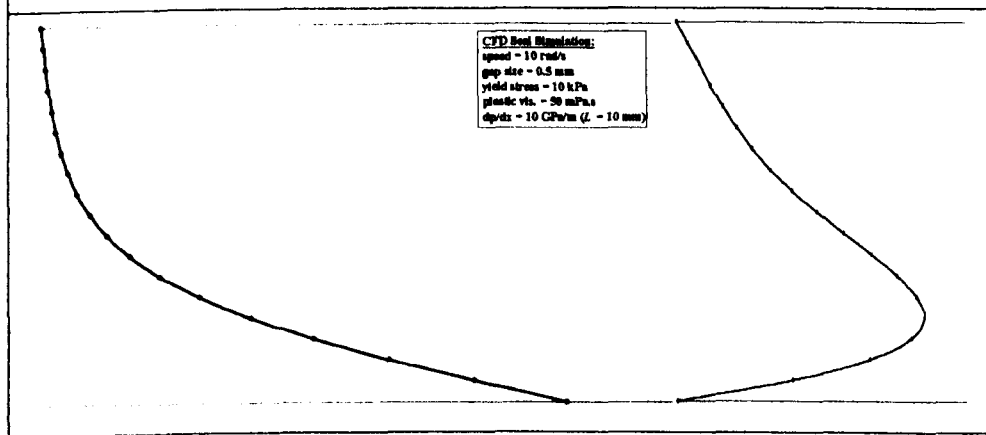
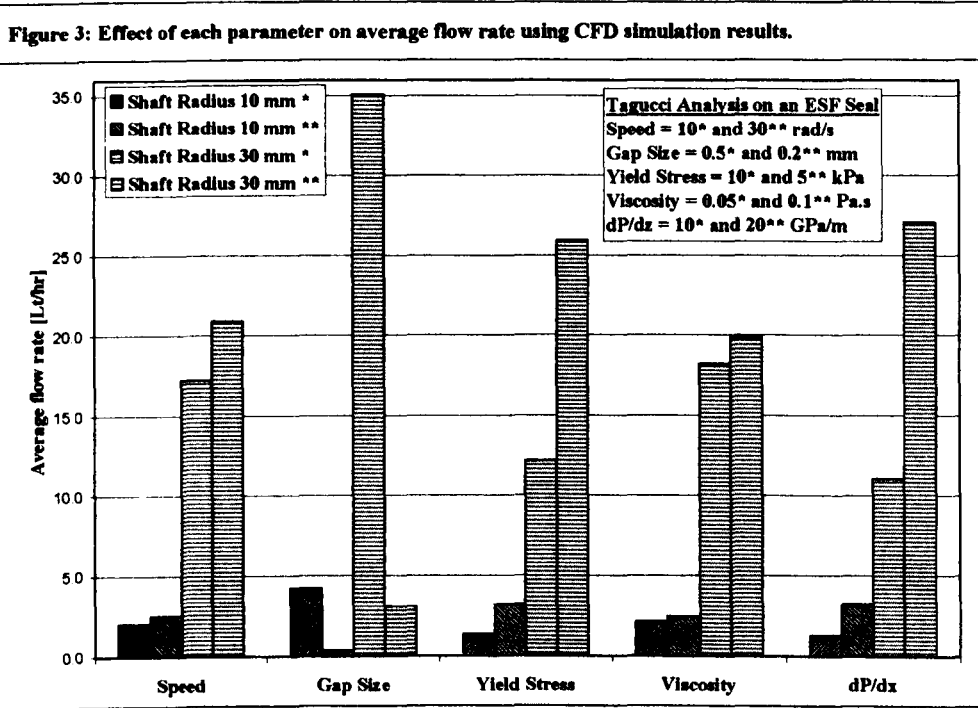


Figure 2: CFD results, velocity profiles for case no. 1 on 10 mm shaft. Circ. (left) and Axial (right).





HEAT TRANSFER FROM AN ESF RADIAL PLATE CLUTCH SURFACE

D. J. ELLAM*, W. A. BULLOUGH & V. ORAVSKY

*SMMART Engineering Network, University, Dpt. of Mechanical. Engng.
Mappin Street, Sheffield, S1 3JD, England*

**correspondence: mep99dje@shef.ac.uk, (44) 0114 2227794*

The aim of this work was to investigate the rate of heat transfer from a radial plate/clutch surface. The paper presents experimental results over a range of angular speeds (Ω) and fluid gap widths (h), which are then favourably compared to analytical and Computational Fluid Dynamics (CFD) solutions for the same geometry and operating conditions. Verifying the heat transfer capabilities of the latter goes some way towards validating the CFD package as a viable virtual prototyping method. The results allow a procedure to be established for the selection of a good Electro-Structured Fluid (ESF) clutch design.

Keywords: CFD, ERF, MRS, Heat Transfer

INTRODUCTION

An ESF clutch operates in the shear mode thereby requiring an adequate heat dissipation capability to keep the ESF at an acceptable operating temperature. This is particularly so when continually switching in order to achieve an electronically controlled variable configuration of output motion (Bullough, 2001a). In some instances multi-plate clutches will be required to provide a large output torque in a small, low inertia device. It follows that sooner or later a means of predicting the temperature within, and heat transfer through, a device of complex geometry will be required and that the non-linear properties of the ERF/MRS will give rise to a problem best handled by CFD in steady and unsteady non-isothermal situations.

For the same outer radius dimension both radial and concentric, dual channel, clutch type designs offer similar control ratio (T/T_c) and acceleration (T/I) capabilities. It may well be, therefore, that the capability for heat transfer dictates the best type of design.

In a previous work (Smyth, Tan and Bullough, 1994), the heat transfer from the surface of a concentric clutch was modelled and subsequent developments (Bullough, 2001b) have validated the technique. This model was latterly tested by running the outer rotor at speed whilst holding the inner stationary and measuring the temperature on the outer surface by a remote infra red thermometer. The use of a well known viscous fluid allowed the slipping torque and hence the work input ΩT to be calculated. A balance between the heat transfer from essentially the rotating outer case would equal the calculated work rate when the clutch reached equilibrium test conditions.

In the present work, much the same approach is followed but, this time on a radial plate clutch in which the upper plate is driven and the lower plate is held stationary and thermally insulated. Hence the heat transferred through the upper plate is equal to the power input ΩT . Unlike the predominately uniform shear field in the large diameter, small fluid gap concentric clutch the shear rate in the radial device varies with radius. This situation invites concern with respect to temperature gradients across and along the oil film and plates.

RADIAL CLUTCH DESCRIPTION

The clutch comprises two mild steel (EN3) radial discs (85 mm dia., \approx 10 mm thick). The upper disc is attached to a motor by a solid shaft of 20 mm dia. (shaft insulation 36 mm dia. x 60 mm) of the same material. Gauge blocks were used to set a gap between the discs, which contains hydraulic oil of known fluid properties (Shell Tellus 37).

The bottom plate was held stationary and was thermally insulated by the use of Tufnol and Kao Wool so that a zero heat flux boundary condition could be assumed. Five k-type thermocouples are implanted approximately 1.0 mm away from the wetted surface, located at radial positions of 0, 10, 20, 30 and 40 mm. To allow for a 1-d analysis the outer edges of the device and driving shaft are also insulated. Refer to Figure 1.

To determine the amount of heat that is conducted up through the shaft, in the CFD model, it is important to accurately know the temperature T_{sh} . The accuracy of an infrared camera which could remotely measure this temperature was deemed inadequate for this situation. The temperature T_{sh} was therefore inferred from the near air temperature. To calculate the amount of heat convected from the disc surface the bulk air temperature T_{∞} was also measured.

EXPERIMENTAL METHOD

All thermocouples were first checked to be working correctly and calibrated. The gap size was set at either 0.5, 0.75 or 1.0 mm. Temperature readings were taken and then the motor was set to rotate at 500, 750, or 1000 rpm. Temperature readings were then taken every twenty minutes or so until the temperatures had reached their steady state values. The readings consisted of the five lower plate temperatures T_i , two readings above the plate allowing an average T_{∞} to be determined and the near air temperature T_{sh} .

THEORETICAL MODEL AND SOLUTION OF HEAT TRANSFER IN THE EXPERIMENTAL DEVICE

Full details of the theoretical analysis can be found in the joint paper (Oravsky 2001). Only the rate of steady state heat transfer at constant rotational speed is considered. Insulation on circumferential surfaces allows 1-d heat transfer to be assumed. Furthermore, it is assumed that all mentioned temperatures are uniform in the radial direction. The fluid is taken to be Newtonian with viscosity dependent on the temperature ($T_i/2 + T_o/2$).

Frictional tangential forces in the fluid generate an amount of heat equal to $T\Omega$. As a result, heat is transferred through the oil, upper disc and shaft (via conduction). A proportion of the heat is transferred from the rotating disc into the surrounding air via convection, at a rate approximated by the Newton's law of cooling. The heat transfer coefficient for convection was given using a semi-empirical relation expressed through averaged Nusselt, $N\bar{u}$, Reynolds, Re , and Prandtl, Pr , numbers (Oravsky, 2001) & (Wong, 1997).

Two methods can be used to determine \dot{Q}_{shaft} . The first (*1st model* see joint paper (Oravsky, 2001), involves assuming that at a certain vertical position on the shaft the temperature reaches T_{∞} , the experimental data is then used to determine an empirical coefficient for the shaft ($W/m^2/C$) so that the theoretical temperatures match

experimental ones. This method also absorbs other uncertainties that may be present in the experimental set-up such as heat escaping through the insulated walls.

The second method (*2nd model*) assumes that the temperature of the air T_{sh} at a location very close to the shaft at known length above the disc surface L_{sh} is equal to the true temperature in the shaft at this location. This allows the conductivity equation to be applied for heat rate through the shaft. The geometry of the apparatus was such that very little heat could be convected from the shaft (small surface area) due to the attached motor and supporting metal structure providing a large heat sink and consequently a more favourable means for the heat to travel.

It was found that the *1st model* gives temperature results closer to experimental ones but the *2nd model* is very much less subjective and provides a fairer means for verification of the CFD method. In both cases mutual comparison of the heat flows provides a system of equations defining the three unknown temperatures T_s , T_i and T_o . The shaft T_{sh} and surrounding air T_∞ temperatures are known allowing the theoretical T_i to be determined using a simple iterative procedure.

CFD ANALYSIS (SOFTWARE PACKAGE FLUENT5)

The CFD model was set up in comparison to the *2nd theoretical model*. The exact geometry of the experimental device was used to produce an axis-symmetric grid required for the finite volume solution procedure. Table 1 outlines which relevant equations are applied and the boundary conditions that were used to close the system of equations. CFD applies the full set of Navier-Stokes and energy equations, thereby avoiding the requirement for the semi-empirical heat transfer coefficient for convection as used in theoretical analysis in the above two models.

Table 1: CFD parameters for analysis on Fluent5	
Flow	The flow of the oil and air is set to be laminar. Viscous heating terms are included. Furthermore, buoyancy terms in the air region are included.
Air(ρ, μ, k)	Ideal gas, properties as a function of cell temp..
Oil(μ, k)	Newtonian (Tellus 37), properties as a function of cell temp. (Oravsky, 2001)
Boundary Condition	Insulated walls are set to have zero heat flux. Rotating parts are set to the correct angular velocity. The shaft end is set to temp. T_{sh} . The boundary of the air region is placed at the vertical position equal to the T_∞ location. This boundary is then set to be equal to atmospheric pressure and temp. T_∞

Convergence was verified by making sure that the residual history of each equation was sufficiently low and that the net heat flux equated to $T\Omega$. Grid sufficiently was met using a built in grid adaptation facility, which increases the grid density in regions where the derivatives of variables are high. The temperature T_i and resulting heat fluxes though the various parts can then recorded.

RESULTS: EXPERIMENTAL VS. CFD VS. NUMERICAL

The experimental and CFD data verified that the assumption of uniform radial temperature distribution in all metal and fluid parts was correct. No variation on the lower plate was recorded in all experiments. The CFD analysis clearly showed that although there is a radial distribution in shear rate the high conductivity of the metal parts distributes the temperature out evenly. The essential results are shown in Table 2.

Table 2: Results: measured experimental temperatures and resulting theoretical predictions

Gap Width [mm]	Speed [rpm]	Experimental Temp.		Lower Plate Temp. (T_i)				Q_{sh}/Q_s	
		Shaft T_{sh} [°C]	Air T_∞ [°C]	Exp. [°C]	difference ($T - T_{exp.}$) theory model			Theory model two	CFD
					one	two	CFD		
0.5	500	24.9	25.4	28.1	0.3	2.1	1.8	3.9	3.1
		24.5	24.8	28.3	-0.5	1.5	1.2	3.7	2.9
	750	25.8	25.9	31.8	-0.2	3.1	2.4	2.9	2.2
		25.8	26.0	31.7	0.0	3.2	2.5	2.9	2.2
	1000	26.5	26.3	35.8	-0.7	3.5	2.5	2.4	1.9
		26.5	26.4	35.6	-0.4	3.7	2.7	2.4	1.9
0.75	500	26.6	27.0	29.1	0.1	1.3	0.8	3.9	3.1
		26.6	27.0	29.2	0.1	1.2	0.7	3.9	3.1
	750	26.6	26.5	31.6	-0.5	2.0	1.0	2.8	2.2
		26.4	26.4	31.4	-0.3	2.1	1.1	2.8	3.2
	1000	24.5	24.2	32.3	0.0	3.5	1.7	2.4	1.9
		24.5	24.5	31.7	0.8	4.1	2.3	2.4	1.9
1.00	500	27.4	27.6	29.0	0.5	1.5	0.9	3.7	3.0
		25.6	25.8	27.3	0.6	1.6	1.0	3.7	3.0
	750	25.4	25.4	30.1	-0.4	1.6	0.3	2.8	2.2
		27.1	27.2	31.0	0.2	2.1	0.8	2.9	2.3
	1000	25.4	25.3	32.0	0.3	3.0	1.0	2.4	1.9
		25.3	25.2	31.9	0.3	3.0	0.9	2.4	1.9

Theory *1st model* gives the closest predictions to the experiments. This is because it allows other uncertainties to be absorbed by virtue of the empirical coefficient for the shaft. Theory *2nd model* gives results that are rather high (4.1 °C in one case). The CFD results fare better, the reason for which is discussed below.

DISCUSSION

The semi-empirical expression used to calculate the heat transfer coefficient for the heat flow rate into the air from a complete circular rotating disc does not take into account shaft/wall constraints that are present in the experimental set up (see Figure 1). It was however hypothesized (Oravsky, 2001) that the expression would remain true if the area for convection were based on the disc area minus the shaft insulation area. In light of the results, it was thought prudent to check whether the expression was valid. In a CFD simulation, a hypothetical disc was set rotate in a large region of air (atmosphere), an

amount of heat flux was set to leave the disc and enter the atmosphere. Setting a far field temperature T_∞ closes the system of governing equations and allows T_s to be determined. Over a range of parameters, remarkably close coloration between theory and CFD was found. A shaft and wall constraint as seen in the experimental set-up was then introduced. It can be seen from Figure 2, which shows the results of this case, that the semi-empirical expression over predicts the surface temperature. This would explain why the CFD results are closer to the experimental data than the comparable *2nd theoretical model*, and why CFD gives lower values of $\dot{Q}_{shaft}/\dot{Q}_s$.

For theory *2nd model* and CFD all the temperatures predicted read high. This is due to the theoretical models being ideally insulated on the lower and outer parts whereas experimentally it was not. So that a 1-d assumption could be used in the theoretical analysis most of the apparatus was insulated. As a result the area assumed ideally insulated is relatively large in comparison to the non-ideally insulated surfaces. Although the conductivity of the insulating materials is low, the large surface could give rise to a significant heat loss through insulating parts. This fact along with the difficulty in accurately setting a uniform gap would explain the 0.3-2.7 °C error in the CFD results. In this case it is important to note the necessary inclusion of the driving shaft: it carries away a significant proportion of the generated heat.

It can be noted from Table 2 that for a gap width of 0.5 mm the shaft temperature increases with speed. The opposite effect is observed for 0.75 & 1.0 mm gap widths. The reason for this is likely to be related to the ratio of power being generated to that being able to leave through the disc. An increase in Ω which allows greater heat convection from the disc may not be sufficient to counter the increase in viscous heat generation. So for a small gap width in which the heat generation is larger the shaft may heat up as the speed is increased. Also the final shaft temperature is dependent on the outside air temperature T_∞ that can be different for each experiment.

COMPARISON OF CLUTCH DESIGNS

An attempt is now made to compare two different clutch designs. In order to produce a competitive commercial device it is important to consider acceleration (T_{total}/I) and control ration (T_{total}/T_s) as well as T_{total} . A variable speed driven rotor is therefore likely to be made of a lightweight material, whereas the outer casing that rotates at constant speed is likely to consist of a heavier highly conducting material to maximize heat dissipation from the device and help maintain run up speed on reduced regulation.

Dual channel, horizontal axis radial and concentric clutch designs are compared. The geometries are shown Figure 3. It is likely that the outer casing and consequent surface temperature T_s would be approximately uniform. Shafts will have similar effects in each design and are so therefore not included. Having chosen a mean radius, dimension z and gap size h , the overall geometry of the radial clutch outer casing (R_r and L_r) are known. For set speed differences Ω , fluid properties and air temperature T_∞ , a uniform surface temperature (T_s) can be calculated. It is assumed that,

$$T\Omega = (T_s - T_\infty)(A_r h_r + A_s h_s) \quad (1)$$

where h_r and h_s are the heat transfer coefficients for dissipation of heat by convection in the radial and axial directions. Such values are determined by the condition of the air at the outer clutch surface and are therefore independent of any yield stress values. These are calculated using the following semi-empirical formulas (Wong, 1977):

$$Nu = 0.4(Re^2 + Gr)^{0.25} \quad Gr = \rho^2 \beta g R^3 \pi^{1.5} \Delta\theta / \mu^2 \quad (2)$$

$$Nu = 0.18 \left[(0.5 Re^{0.5} + Gr) Pr \right]^{0.315} \quad Gr = \rho^2 \beta g D^3 \Delta\theta / \mu^2 \quad (3)$$

The Bingham plastic equation is used to determine the value of torque T_{total} . A further parameter, length of the electrode L_e , is required for the concentric clutch. This length was chosen to make T_e equal to that of the radial clutch. The amount of T_{total}/I for the same parameters giving the same T_e can now be compared as shown in Figure 4.

It is observed that the plastic viscosity plays a noticeable but relatively insignificant role when compared to the effects of fluid yield shear stress. It can be seen that the radial disc design gives the better results even though the concentric design was approximately twice as long in axial dimension. In all cases, T_{total}/T_e was approximately the same. Also coefficients h_r & h_a were similar.

It must be noted that L_e need not be constrained to being relatively small. Increasing this dimension has no direct effect on T_{total}/I but would give and improved T_{total} . However, the inner electrode being of a low conducting material will make it difficult to dissipate heat from the inner channel. To get good T_{total}/I a commercial device is likely to be of the form length > radius resulting in a large surface area for radial heat flow. A multi-plate radial clutch occupying similar dimensions would therefore be better since it would allow radial flow. Furthermore, a radial design does not exhibit plug behaviour over its full range of operation generally leading to lower viscous heating.

CONCLUSION

As is evident from comparisons of experimental and theoretical data, of a viscous clutch device set-up, the correct magnitudes of heat transfer can be predicted effectively. For more complex set-ups, such as multi plate clutches, in an unsteady operation, CFD promises to be a simple and important tool for heat transfer evaluation purposes.

In the experimental study, the viscous medium was Newtonian oil. Heat transfer in non-Newtonian fluids is a complex subject. However, it is proposed that modelling heat transfer in ESFs need not be that complicated due to the following three reasons:

- Most ESF devices operate with ESF in a very narrow channel for which the distribution of temperature across the gap width is likely to be nominal as indicated in our simulations.
- Using CFD the most important variable (yield stress) can be easily entered as a function of temperature, excitation and shear rate.
- Furthermore, correctly determined non-Newtonian velocity profiles will give the rate of heat generation on cell-by-cell basis.

Should the radial model prove effective then through flow could be used to cool the sheared fluid automatically, i.e. by a centrifugal pump type action. The range of cooling flow required without disrupting the electrically applied stress has already been established (Ellam, Atkin and Bullough, 2000).

REFERENCES

Bullough, W. A. 2001a. "Electrostructured fluids and smart machines," lecture given at Centre for Int. Sciences, Udine, Italy, June 2000 (in press, Springer-Verlag-Berlin).

Bullough, W. A. 2001b. "ESF clutch drive mechanisms and the ER linear reversing motion demonstrator," lecture given at Centre for Int. Sciences, Udine, Italy, June 2000, (in press, Springer-Verlag-Berlin).

Ellam, D. J., Atkin, R. J., and Bullough, W. A. 2000 "Appraisal of an ESF radial plate clutch with cooling flow using a NNF CFD solver," 2000 ASME Int. Mech. Eng. Congress and Exposition, Orlando, Florida, (ASME), 117-125.

Oravsky, V. 2001. "Heat transfer from an ESF radial plate clutch surface II - part 2 - theory," Proc. 8th Int. Con. on ERFs, MRSs and associated technology, Nice, France, (World Scientific Publishing).

Smyth, R., Tan, K. H. and Bullough, W. A. 1994. "Heat transfer modelling of a cylindrical ER catch," *Int. Jnl. Mod. Phys.*, 8:3033-3050.

Wong, H. Y. 1977. Handbook of essential formulae and data on heat transfer for engineers, (Logman, London & New York).

FIGURES

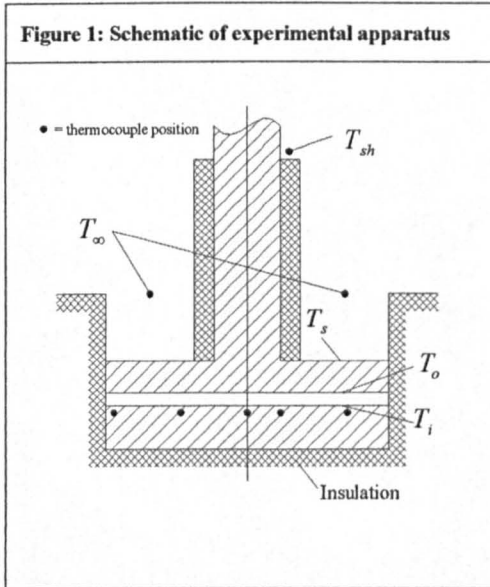


Figure 2: Rotating disc in air with shaft and wall constraint (as in Figure 1) Considering convection only (testing semi-empirical formulae).

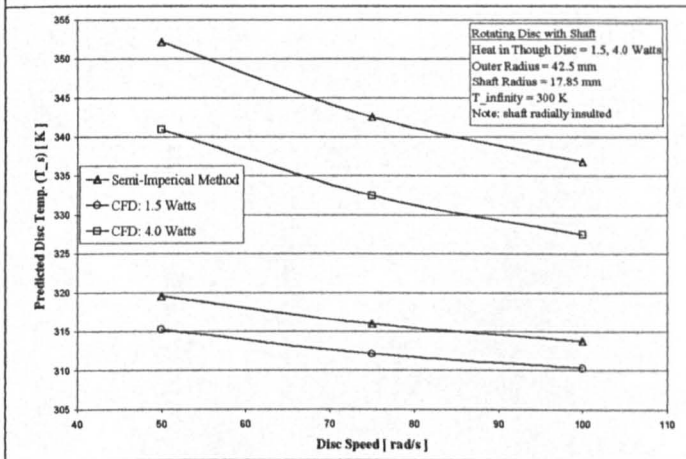


Figure 3: Clutch models

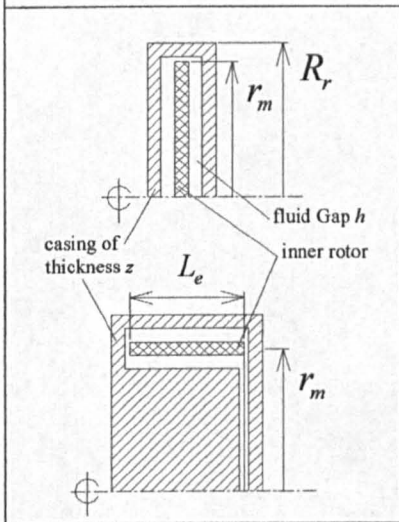


Figure 4: Comparison of radial and concentric dual channel designs. T/I for the same case surface temperature. Note: inertia's (I) are similar.

